2023

FUNDAMENTAL INVESTIGATION ON ANION BINDING EMPLOYING THE HYDROGEN BOND ENHANCED HALOGEN BOND

Jiyu Sun

FUNDAMENTAL INVESTIGATION ON ANION BINDING EMPLOYING THE HYDROGEN BOND ENHANCED HALOGEN BOND

By

JIYU SUN

Bachelor of Science, Nankai University, Tianjin, China, 2015

Dissertation/Thesis/Professional Paper (choose one)

presented in partial fulfillment of the requirements
for the degree of

Doctor of Philosophy
in Organic Chemistry

The University of Montana
Missoula, MT

December 2023

Approved by:

Ashby Kinch, Ph.D., Dean of The Graduate School
Graduate School

Orion B. Berryman, Ph.D., Advisor
Department of Chemistry and Biochemistry

Nigel D. Priestley, Ph.D.
Department of Chemistry and Biochemistry

Dong Wang, Ph.D.
Department of Chemistry and Biochemistry

Chris P. Palmer, Ph.D.
Department of Chemistry and Biochemistry

Andrea A. Stierle, Ph.D.
Department of Biomedical and Pharmaceutical Sciences

Sun, Jiyu, Ph.D., December 2023 Organic Chemistry

FUNDAMENTAL INVESTIGATION ON ANION BINDING EMPLOYING THE HYDROGEN BOND ENHANCED HALOGEN BOND

Advisor: Orion B. Berryman

Chairperson: Chris P. Palmer

Abstract

Noncovalent interactions play a critical role in chemistry and biochemistry. Understanding how to modulate closely situated noncovalent interactions is of utmost importance in the design of functional materials, supramolecular assemblies, pharmaceuticals, and catalysts. Over the past two decades, there has been a significant surge in research and applications on halogen bonds, driven by their exceptional properties such as high directionality and unique tunability when compared to hydrogen bonds. Taking inspiration from nature and other synthetic anion-binding receptors that effectively employ multiple noncovalent interactions in a concerted manner, we have developed an innovative preorganization strategy termed the "Hydrogen Bond Enhanced Halogen Bond." This unique combination of hydrogen and halogen bond interactions yields an anion-binding performance over an order of magnitude greater than that achieved with either hydrogen bonds or halogen bonds alone. In-depth investigations, including examinations of solvent effects and substituent impacts, have been undertaken to gain insights into this interaction. We have also pushed the boundaries of this interaction by incorporating non-traditional C-H hydrogen bond donors. This dissertation provides significant insights of this interaction fueling the development of new generations of halogen bond-based anion receptors with exciting applications in anion recognition, organocatalysis, anion transport, and anion sensing.

The ensuing chapters provide a comprehensive overview of this study. Chapter 1 introduces halogen bonding, tracing its evolution from hydrogen bonds, elucidating unique traits, and exploring preorganization strategies within the Hydrogen Bond Enhanced Halogen Bond (HBeXB). It also uncovers the captivating realm of anion binding through halogen bonds, highlighting their significance in applications. In Chapter 2, the investigation delves into intriguing solvatochromism and fluorescence responses to anions in halogen bonding anion receptors. Chapter 3 delves into the intricate interplay between hydrogen and halogen bonds, with a focus on quantification of the substituent effects in the hydrogen bond enhanced halogen bond. In Chapter 4, we delve into unconventional approaches to enhance halogen bonds using non-traditional hydrogen bonds, shedding light on anion binding in solution and offering innovative insights into this facet of XB···anion interaction. Finally, Chapter 5 summarizes our findings and offers a glimpse into the future.

ACKNOWLEDGEMENTS

I would like to express my deepest gratitude and appreciation to all those who has supported me throughout this academic adventure.

First and foremost, I am indebted to my advisor Orion Berryman, whose guidance, expertise, and unwavering support throughout this research journey have been invaluable. Your mentorship and encouragement have shaped my academic and research capabilities and have been crucial to the development of this thesis. Outside the lab, you have also been a role model for my continuous learning. Your ability to maintain a balance between your personal life and dedication to science has exemplified the essence of "work hard, play hard." I'm so greatful having you as my mentor. Thank you Orion!

I extend my sincere thanks to the members of my thesis committee, Dong Wang, Nigel Priestley, Chris Palmer and Andrea Stierle, for your insightful feedback, constructive criticism, and invaluable suggestions that greatly enriched the quality and depth of this work. I would like to also thank Earle Adams. He played a crucial role in the NMR and Mass Spec facilities, providing maintenance for the instruments and teaching me a lot useful techniqures during the first half of my PhD.

I am grateful to my dear lab mates of the Berryman lab group, who have been a constant source of inspiration, collaboration, and camaraderie. Our discussions and interactions have immensely contributed to the progression of my research. I would like to specifically thank Asia Riel, Dan Decato, Nick Wageling, Casey Massena, Eric John and Seth Helsley. It's you guys who have created such a relaxed vibe in the lab, allowing me to easily integrate when I first time left my hometown and came here on my own. Asia, you're my lab mentor and I have learnt so much from you and kept inspired by your positivity. Dan, your funny jokes and expertise in crystallography and computation help me so much during my lab life. Eric, it's truly wonderful to have you by my side all these years in this adventure!

To my family, my dad Weiping and my mom Jianxia, thank you for your uncondtional love, understanding, and encouragement throughout this academic journey. Your emotional support has been a pillar of strength and motivation. I cannot express enough how fortunate I am. It's your support empowers me to pursue my passion wholeheartedly.

I cannot fathom how I would have persevered on this journey without the love and support from my friends. Hongkai, Xiaoqi, and Mo, the moments we shared aided me in overcoming the toughest times throughout these years. To my sister Jiaping, I love you and miss you very much, don't leave me behind when I see you again.

Lastly, I want to express my heartfelt gratitude to all the participants and subjects involved in this research, without whom this work would not have been possible.

Thank you all for being an integral part of this incredible academic adventure.

The road ahead will be long, Our climb will be steep.
路漫漫其修远兮,吾将上下而求索。

TABLE OF CONTENTS

LIST OF TABLES

LIST OF FIGURES

Figure Page

LIST OF ABBREVIATIONS

$[BAr^F{}_4]^-$ – Tetrakis(3,5-bis(trifluoromethyl)phenyl)borate
C_6D_6 – deuterated benzene
^{13}C NMR – Carbon NMR
^{19}F NMR – Fluorine NMR
^1H NMR – Proton NMR
Br^- – Bromide
Br – Bromine
C – Carbon
CH_3CN – Acetonitrile (CD_3CN is the deuterated form)
$CHCl_3$ – Chloroform ($CDCl_3$ is the deuterated form)
CuI – Copper (I) iodide
DCM – Dichloromethane
DFT – Density functional theory
DIPEA – Diisopropylamine
DMF - Dimethylformamide
EDG – Electron donating group
e.g. – exempli gratia, “for example”
equiv. – Equivalent(s)
EMSL – DFT basis set exchange
ESI-HRMS – Electrospray ionization high-resolution mass spectrometry
ESI Q-TOF – electrospray ionization, quadrupole/time-of-flight
ESP – Electrostatic potential
Et_2O – Diethyl ether
EtOAc – Ethyl acetate
EWG – Electron withdrawing group
H – Host
HB – Hydrogen Bond
HBeXB – Hydrogen Bond Enhanced Halogen Bond
Hz – Hertz
G – Guest
G1XB – First Generation Halogen Bond
G1HB – First Generation Hydrogen Bond
G2XB – Second Generation Halogen Bond
G2HB – Second Generation Hydrogen Bond
G3XB – Third Generation Halogen Bond
G3HB – Third Generation Hydrogen Bond
I^- – Iodide
I – Iodine
I_2 – Molecular iodine
IUPAC – International Union of Pure and Applied Chemistry
J – Coupling constant

Ka – Association constant
kcal – kilocalorie
LA/LB – Lewis acid/base
MeCN – acetonitrile
MeOH – methanol
Mol – mole of substance
$MgSO_4$ – Magnesium sulfate
N – Nitrogen
N_2 – Nitrogen gas
$Na[BAr^F{}_4]$ – Sodium tetrakis(3,5-bis(trifluoromethyl)phenyl)borate
NaI – Sodium iodide
n-BuLi – *n*-Butyllithium
nHBeXB – G3XB without amine
NMR – Nuclear magnetic resonance
NOESY – Nuclear Overhauser effect spectroscopy
OTf^- – Triflate
pH – Logarithmic scale of acidity
Ph – phenyl
ppm – Parts per million
$ReO4^-$ – Perrhenate
RT or rt – Room temperature
TBA – Tetra-*n*-butylammonium
TBABr – Tetra-*n*-butylammonium bromide
TBACl – Tetra-*n*-butylammonium chloride
TBAI – Tetra-*n*-butylammonium iodide
TEA – Triethylamine
THA – Tetra-*n*-hexylammonium
THABr – Tetra-*n*-hexylammonium bromide
THACl – Tetra-*n*-hexylammonium chloride
THAI – Tetra-*n*-hexylammonium iodide
THF – Tetrahydrofuran
UV-Vis – Ultraviolet-visible
v/*v* – volume-volume ratio
vdW – van der Waals
XB – Halogen Bond
Δδ – Change in NMR chemical shift
∑vdW – Sum of the van der Waals
δ – Chemical shift
π – Pi electrons
σ – Hammett parameters

Chapter 1:
Halogen bond, the Hydrogen Bond Enhanced Halogen Bond and Halogen bond anion binding

1.1 Introduction to the Halogen Bond

1.1.1 From Hydrogen Bond to Halogen Bond

Noncovalent interactions encompass various attractive interactions between molecules or parts of molecules. Unlike covalent bonds, they do not rely on fully sharing or exchange of electrons. These weaker interactions arise from various physical and chemical properties, such as charge distribution, electron density, and molecular shape which play a crucial role in various biological and chemical processes. Among the myriad noncovalent interactions, hydrogen bonds (HBs) hold a privileged position due to their directional and tunable nature. HBs occur between a hydrogen atom which is covalently bound to an electronegative atom or group and an adjacent electron-rich acceptor (typically an oxygen, nitrogen, sulfur or halide), leading to a strong electrostatic attraction (Figure 1 left). These interactions are crucial in molecular recognition, solvation, and structural stability in biological systems.[1]

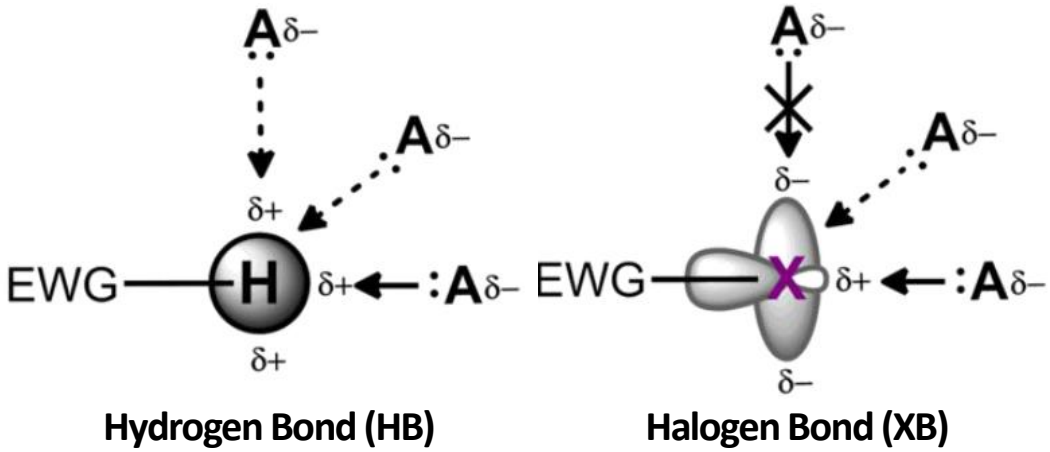

Figure 1. Schematic of HB interaction (left) and XB interaction (right).

In addition to the HB, another noteworthy noncovalent interaction is the halogen bond

(XB). The XB shares similarities with the HB but exhibits distinct characteristics. Unlike the HB where the hydrogen atom acts as the electron-deficient donor, the XB contains an electron-deficient halogen atom (such as chlorine, bromine, or iodine) that acts as an electron acceptor and forms a noncovalent interaction by accepting electron density from an electron-rich species (Figure 1, right). Higher directionality, tunability and enhanced binding with "soft" Lewis bases by polarized halogen atoms, makes the XB unique and complimentary to the HB. The XB was first noted in $I_2 \cdots NH_3$ complexes reported by J. J. Colin in 1814.[2] Much later, Mulliken introduced the concept of charge transfer complexes in the 1950s, where the $I_2 \cdots Et_2O$ complexes was stabilized by charge transfer forces.[3] With the development of X-ray crystallography, Hassel discovered that halogens can act as electron acceptors, and self-assemble into charge transfer complexes in the presence of electron donors and was awarded the 1969 Nobel prize in chemistry.[4] More recently, P. Politzer and J. S. Murray provided computational studies in the early 1990s on the distribution of the electron density in halogen atoms contributing to the understanding of the XB.[5,6] Many crucial concepts like the "σ-hole" (a region of depleted and often positive electrostatic potential on the surface of halogen atoms) have since been introduced.[7] With much debate, the XB was finally defined by IUPAC in 2013: "A halogen bond occurs when there is evidence of a net attractive interaction between an electrophilic region associated with a halogen atom in a molecular entity and a nucleophilic region in another, or the same, molecular entity."[8]

1.1.2 Nature of the Halogen Bond

A XB can be described as R-X···Y, where X is the donor which is a halogen atom that has an electrophilic region due to an attached electron withdrawing group (EWG) R. Y is the

acceptor which is electron-rich, usually a Lewis base, like an anion. The XB has several characteristic features: the interaction strength is in the range of 10 – 200 kJ mol^{-1}, the X···Y distance is shorter than the sum of van der Waals radii of the involved atoms, the R–X···Y angle is close to 180°, the strength of the interactions increase with decreasing electronegativity and increasing polarizability of the halogen atom X (I > Br > Cl >> F).[7]

The XB can be understood in term of electrostatics[7,9] and covalency[10,11]. An electrostatic description suggests that due to the polarizability of the halogen, its electron density can become anisotropic. Unshared electrons on the halogen atom X form a belt of negative electrostatic potential around its central region, generating a positive "σ-hole" along the extension of the R–X σ bond axis. The positive region termed the "σ-hole" can be quantified and compared by computing the maximum electrostatic potential ($V_{s,max}$) on the halogen. For instance, in the electrostatic potential (ESP) mapping of trifluoromethyl halides, it is observed that heavier halogen atoms have a larger "σ-hole" which act as a stronger XB donor (Figure 2).

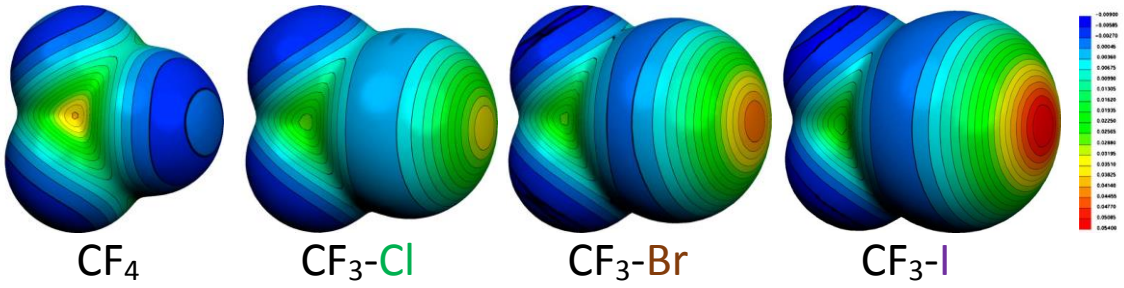

Figure 2. Electrostatic potential surfaces of molecules CF_3X (X = F, Cl, Br, I). Electron deficient regions are blue and electron rich regions are red (see scale). Copyright © 2006, Springer-Verlag.

The purely electrostatic σ-hole model is enriched by additional considerations. Analysis using density functional theory (DFT) has revealed that the halogen bond (XB) exhibits a significant covalent component, arising from interactions between the highest occupied molecular orbital (HOMO) and the lowest unoccupied molecular orbital (LUMO). Specifically, the p-orbital lone pair on the XB acceptor interacts with the antibonding σ* LUMO on the halogen of the XB donor (Figure 3).[10]

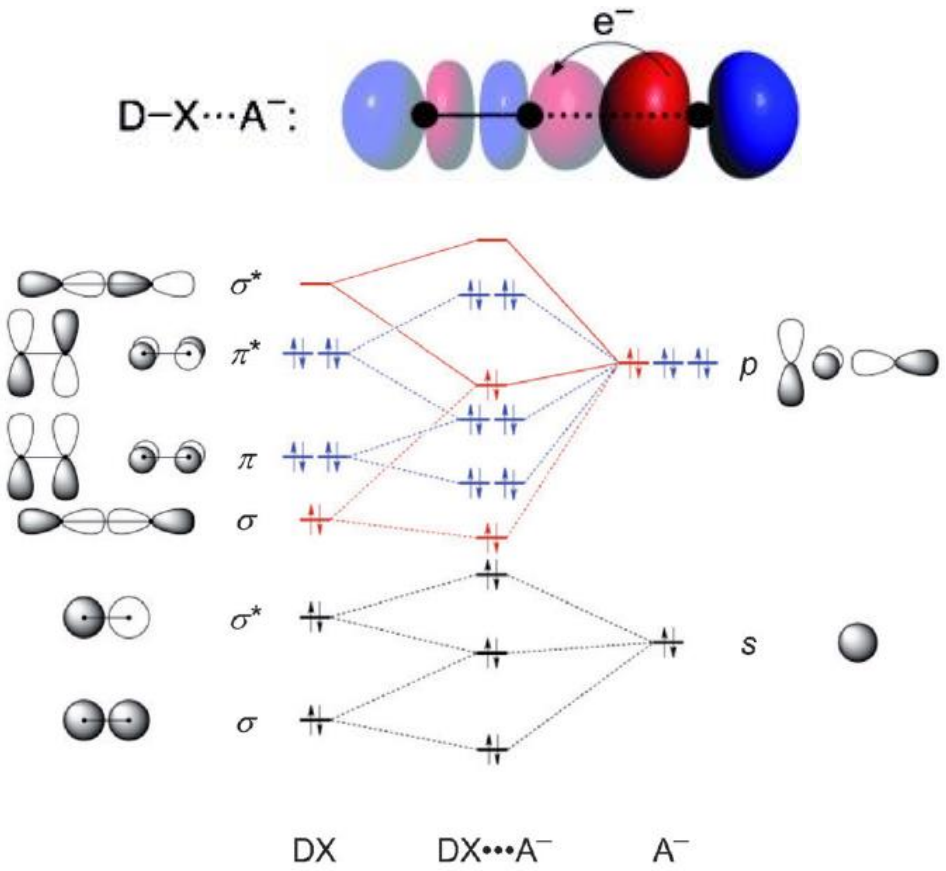

Figure 3. Kohn–Sham MO analysis of halogen-bonded complexes DX···A⁻. (a) HOMO–LUMO orbital interaction of XB. (b) Simplified orbital-interaction diagrams for DX···A⁻. Copyright © 2012 Wolters & Bickelhaupt.

As the comprehensive understanding of the XB incorporating principles of electrostatics, charge-transfer, and covalency has been improved, applications of this noncovalent

interaction are appearing at a rapid pace.[12] For example, strong XBing can assist the self-assembly of supramolecules.[13] Additionally, XB organocatalysts are being developed by researchers as an alternative to HB catalysts, and have successful examples been reported in recent years.[14] The charge transfer characteristics of the XB, along with its different solvent dependencies (more insensitive to water than HB)[101], make it highly advantageous and serves as a useful complement to other noncovalent interactions in the field of anion recognition and the design of anion sensors.[15]

1.2 The Hydrogen Bond Enhanced Halogen Bond (HBeXB) Preorganization

Understanding how to modulate both the strength of the XB and the structure of these molecules is of broad importance for the continued development of functional halogenated species. To this end, altering substituents proximal the XB donor and altering the halogen donor and remains the leading strategy. Understanding new ways to control preorganization and fine-tune XB strength will greatly aid in the development of functional XBing systems.

1.2.1 Preorganization strategy

Preorganization is an essential strategy of supramolecular chemistry which engenders natural and synthetic molecules with remarkable functions using noncovalent forces (e.g. HBing, steric effects, ion-pairing, and π-π stacking).[16-18] The principle of preorganization was stated by Cram as "the more highly hosts and guests are organized for binding and low solvation prior to their complexation, the more stable will be their complexes."[16] Intramolecular HBing has proven to be successful in preorganizing structure, such as helicies[19,20], cavitands[21-23] and ion transporters[24]. Two primary strategies employed for HB preorganization are internal[25] and external[26,27] intramolecular HBing. For example, as an

established method, “Polarization enhanced HBing”, was used to preorganize a HB receptor and result in a 8-fold increase for Cl^- binding by the through-bond polarization due to the external intramolecular amido NH···N^3 (triazole) HBings (Figure 4).[27]

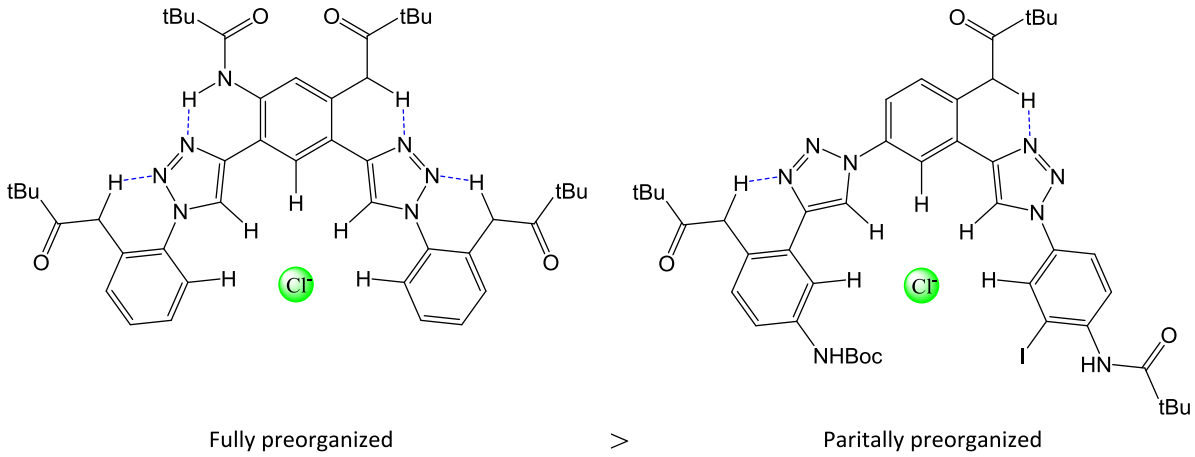

Figure 4. Example of stronger binding and more effective transport ability for fully preoganized HB receptor due to the intramolecular HBing preorgization.

1.2.2 The origin of the hydrogen bond enhanced halogen bond (HBeXB)

Recent studies have compared the XB and HB, but systematic studies to understand and quantify the effect of how they influence each other are critically lacking. Hence, our lab noticed the electronegative belt around the halogen atom due to the formation of the σ-hole. We came up with a new strategy which has an adjacent HB interact directly with the electron-rich belt of the halogen atom. In our published initial studies, intramolecular HBing from an amine polarizes the iodopyridinium XB donors of a bidentate anion receptor **G2XB** (Figure 5).[28] This interaction, which we coined “the hydrogen bond enhanced halogen bond” (HBeXB), can increase halide binding in solution by nearly 9-fold over **G1XB** which lacks intramolecular HBeXB. Additional crystal data shows a notable reduction in XB distance and better planarity of **G2XB**, confirming that HBeXB can preorganize the receptor while simultaneously strengthening the XB and keeping the receptors in more rigid, planar bidentate conformations

in the solid state. Furthermore, **G2XB** derivatives are fluorescent, solvatochromic and have photophysical response to anions (elaborated below in Chapter 2).[29] The HBeXB has also been used to improve the function of organocatalysts in a halide abstraction reaction.[30] In a parallel study, P. Shing Ho's lab showed that the HBeXB interaction can be used to increase enzyme stability and activity. Enhancing the relatively weak chlorine XB donor at just one amino acid residue of T4 lysozyme resulted in an increase of both thermal stability and enzymatic activity at elevated temperatures.[31-34]

Based on the aforementioned examples, the HBeXB has the potential to extend the utility of these interactions in chemistry and biochemistry, providing compelling alternative approaches to the classic HB and XB in the realm of molecular engineering. Ongoing research efforts are dedicated to gaining a more comprehensive understanding of the HBeXB, with the aim of devising a rational design methodology for its utilization in various applications, including self-assembly in synthetic anion channels, bolstering the binding strength in anion sensors, and enhancing the performance of organocatalysts.

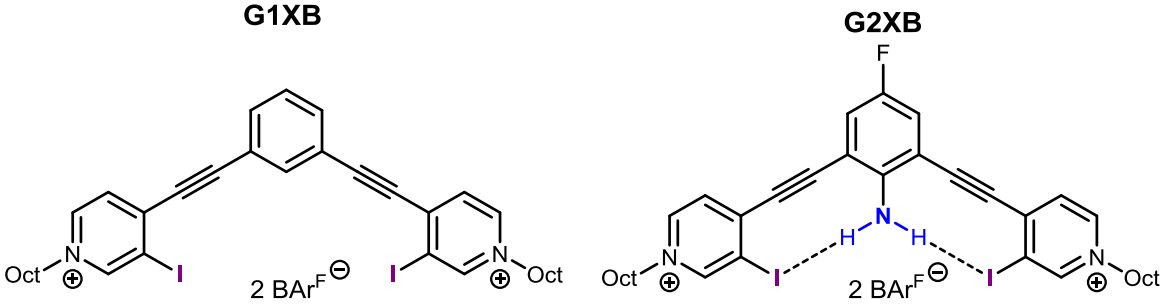

Figure 5. ChemDraw representations of first generation XB receptor **G1XB** (left) and second generation XB receptor that utilized the HBeXB strategy **G2XB** (right).

1.2.3 Computational insight of HBeXB interactions

The HBeXB interaction has garnered considerable attention from chemists ever since it was discovered. Over the past two years, several computational studies have been conducted

to gain a deeper understanding of these interactions. One noteworthy study was conducted by Dan Decato, who designed a series of trityl amide iodopyridinum XB donors featuring isolated HBeXBs.[35] Theoretical analysis revealed that the $V_{s,max}$ of the iodine XB donors for HBeXB derivatives (with an adjacent monodentate amide HB) are more positive by 3.58–3.89 kcal mol^{-1} compared to the isostructural non-HBing ester controls. Additionally, this HBeXB amplification tends to be more pronounced in electron-rich systems, where the iodine halogen is less polarized. Moreover, investigations into interaction energies with Cl^- showed that monodentate iodine XB donors can be strengthened by up to 3 kcal mol^{-1} when they simultaneously accept a single intramolecular amide HB. The study by Susana Portela[36] confirms this XB strength enhancement and provides evidence that this enhancement is attributable to intensified electrostatic and orbital attractions between the XB donor and the anion. These findings suggest a significant degree of covalency in these XBs. Quantum calculations by Steve Scheiner[37] indicate that the introduction of external molecules capable of forming a HB to the halogen atom of a molecule significantly augments its capacity to participate in a XB with a nucleophile. Each such HB raises the XB energy by an increment of more than a kcal mol^{-1}. These combined results lay the groundwork for future investigations concerning the interplay between HBs and XBs in close proximity. In the upcoming section, there will be an extended exploration of the practical uses and applications of the XB in anion binding.

1.3 Anion binding by Halogen Bonding

Anions hold significant importance in the modern world, as they play vital roles in chemistry, biology, medicine, and the environment.[38] With their electron-rich characteristics,

anions can be anticipated to form robust attractive interactions when serving as XB acceptors. The distinctive properties of the XB have led to a notable increase in research dedicated to exploring the fundamental and practical aspects of XB···anion interactions in the past two decades.[9] Various neutral or cationic XB donor motifs have been developed and incorporated into the design of synthetic anion receptors, such as neutral haloperfluoroarenes[39-44], halotriazoles[45-53], charged halotriazoliums[54-57], haloimidazoliums[58-63] and halopyridiniums[13,28,64-69]. The advantageous directionality of the XB···anion interactions make XB receptors often have superior binding affinities and provides them with the potential to selectively recognize and bind specific anions when compared to their analogous HB receptors.[70]

1.3.1 XB anion recognition

According to the Hard-Soft Acid-Base (HSAB) theory, the XB utilizes a soft Lewis acidic halogen as the electrophilic source. As a result, soft Lewis base acceptors are expected to have more favorable interactions with soft XB donors. Numerous experimental studies of XB receptors displayed a clear selectivity preference for halides (Cl^-, Br^-, I^-.) over oxoanions (NO_3^-, HSO_4^-, SO_4^{2-}, $H_2PO_4^-$, HPO_4^{2-}, AcO^-, ReO_4^-, etc.)[40,49,71,72]. The proposed reasons for this selectivity include potential charge transfer/dispersion contributions to the XB interactions, along with a significant electrostatic component, as well as the differences in receptor design. These findings provide insights into the design of selective receptors for “soft” anions. While the investigations into the factors influencing the binding trend of halides (Hofmeister bias[62,73-77]/anti-Hofmeister bias[78,79]) are still ongoing, there have been notable advancements in various areas. Examples include enantioselective anion recognition[80-82], the recognition of

biologically significant anions[83], and anion recognition in aqueous solvent media[84-86], which have emerged in recent years.

1.3.2 XB···anion interactions in organocatalysis

Inspired by the success of HBing in noncovalent organocatalysis[87], chemists have consistently become interested in exploring the use of XBing in organic synthesis and catalysis.[14,88-90] Building on the established halide recognition properties of haloimidazolium salts, the group of Huber has employed these compounds as halide-abstracting promoters of the Ritter reaction of benzhydryl bromide with acetonitrile in 2011.[91] Since then, several different types of XB donors were successfully used in halide abstraction reactions including the Ritter type reaction[92], the Koenigs-Knorr type glycosylation[93], the Friedel-Crafts alkylation reaction[94], the semipinacol rearrangement[95] and a controlled cationic living polymerization of isobutyl vinyl ether (IBVE)[96-98]. Meanwhile, the strong coordination of the XB donor to the anion also poses a potential risk of catalyst inhibition, which is an intrinsic challenge in halide abstraction reactions.[14] Hence, exploring novel approaches to modulate the XB and understand the interplay between binding affinity and catalysis efficiency becomes crucial.

1.3.3 XB···anion interactions in ion transport

XBing has shown potential for enhancing the mobility and selectivity of ions in various materials and systems. While the application of XBing in ion transport is a promising avenue, it is still a relatively new area of research, and further exploration is needed to fully understand and optimize its potential in practical use. As researchers delve deeper into this field, we can expect to see exciting advancements that may revolutionize ion transport-related technologies: (1) The exploration of XBing as a design strategy for ion-selective

membranes to amplify binding affinity for specific ions. This enhancement facilitates more efficient and selective ion transport across membranes.[99,100] (2) Incorporating XBing into ionic liquids and electrolytes can improve their ion mobility and conductivity, making them more effective for energy storage devices like batteries and supercapacitors.[101-103] (3) More efficient drug carriers that deliver therapeutic agents to targeted cells or tissues can be designed by exploiting XBing between drug molecules and cell receptors.[104,105] (4) The utilization of XBing in nanofluidic devices and nanotechnology allows for precise control and manipulation of ions at the nanoscale, leading to the development of advanced sensors, nanofluidic circuits, and nano-electromechanical systems (NEMS) with highly efficient ion transport and detection capabilities.[103,106]

1.3.4 XB anion sensing

The charge transfer nature of the XB allows the incorporation of XB interactions to provide an optical or electrochemical sensing response to anion guest binding. Due to its simplicity and ubiquity, the use of UV-Vis spectroscopy has received attention in the study of XB···anion interactions. Many examples of XB anion receptors have been shown to undergo changes in absorbance upon anion recognition but very few simple receptors undergo significant changes.[13,40,45,52,107] The Beer group introduced and employed a Mechanically Interlocked Molecules (MIMs) strategy in XB anion sensing, resulting in large scale, naked-eye colorimetric changes upon anion recognition.[108-110] In contrast to colorimetric sensors, the exploration of luminescent (particularly fluorescent) sensors utilizing XB interactions has been undertaken to enhance sensor readout sensitivity and utility.[15,52,84] The inherent traits of the XB, such as lower solvent dependency, higher hydrophobicity and stricter geometric binding

preferences make XB receptors potentially capable of anion sensing in increasingly competitive media and real-time sensing systems.

Bridge to Chapter 2:

The main approach to enhancing XBing is the utilization of substituent effects to modify the electronics of the halogen donors. Our lab has developed a novel design strategy called "Hydrogen bond enhanced Halogen bond", which was inspired by successful preorganization in supramolecular chemistry through the use of intramolecular HBs. This strategy takes advantage of the polarizbaility of halogen atoms and as a result, linear XB interactions benefit more from preorganization than other less directional interactions.

In our initial studies of HBeXB anion receptors, this interaction has been proved to significantly enhance the anion binding. Along with the charge transfer characteristics of the XB, this finding suggests that the HBeXB interaction could be utilized in the development of colorimetric and fluorescent anion sensors. However, there were still relatively few spectroscopic studies devoted to XBing anion receptors. Chapter 2 focuses on our exploration of the influence of XBing on the spectrophotometric properties of HBeXB anion receptors. This study expands our understanding of solvent dependency and anion induced fluorescence response for XB anion receptors and provides valuable insights for future design of anion sensors.

Chapter 2:

Solvatochromism and fluorescence response of a halogen bonding anion receptor

2.1 Preface

This chapter includes work that was published in *New Journal of Chemistry*, (2018, 42(13): 10489-10492.) which was co-authored by Asia Marie Riel and Prof. Orion B. Berryman. Asia Marie Riel aided in synthesis and assisted in computations. Prof. Orion B. Berryman assisted in data interpretation, provided editorial assistance and created the TOC and cover artwork. Jiyu Sun, first author, synthesized the molecules, conducted UV-Vis and fluorescence spectroscopic analysis, ran computations, performed data compilation and interpretation, wrote the manuscript and prepared the supporting information for the publication.

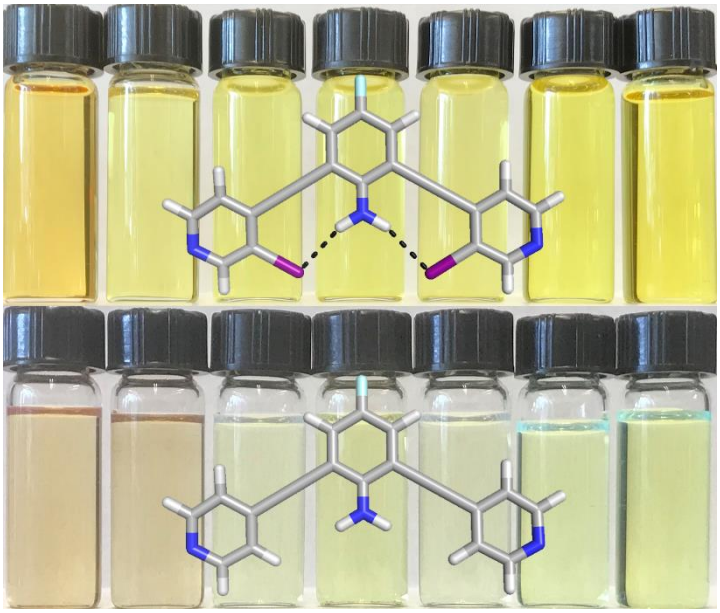

Figure 6. Table of contents photo from *New Journal of Chemistry*.

2.2 Introduction

A halogen bond (XB) is an attractive noncovalent interaction between an electron-deficient halogen atom and a Lewis base. XBs are more directional and display different solvent

dependencies[111,112] compared to hydrogen bonds (HB), and can be applied in anion recognition and sensing.[12,113,114] Recently, Beer's macrocycles[84], rotaxanes[115] and catenanes[15]; Molina and Alkorta's halotriazolium[55]; and Taylor's urea[40] were reported as leading examples of fluorescent and colorimetric anion sensors that employ XBs.[116] However, there are still relatively few spectroscopic studies devoted to XBing anion receptors. Herein we report a new UV-Vis/fluorescence responsive XB receptor that explores how XBing influences spectrophotometric properties in this system.

2.3 Results and Discussion

2.3.1 Design and Synthesis of XB Receptors

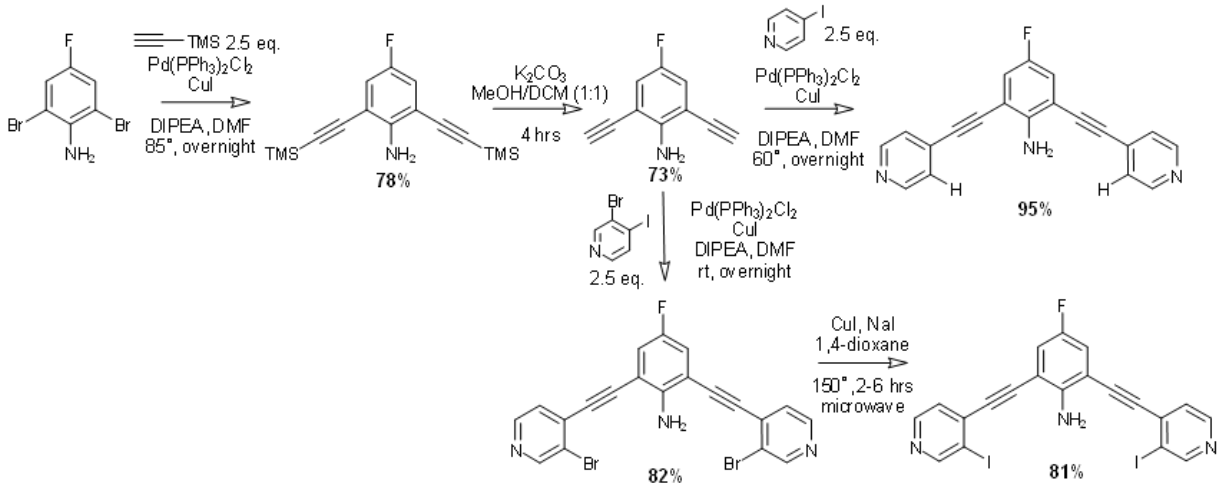

Scheme 1: Synthetic pathways of **G2XB** derivatives.

Building on previous studies conducted in our laboratory[65,66,117], we designed and synthesized a pair of 2,6-bis(4-ethynylpyridinyl)-4-fluoroaniline receptors (Scheme 1). Starting from 2,6-dibromo-4-fluoroaniline, a typical Sonogashira cross coupling reaction and following deprotection of trimethylsilyl groups were conducted to produce 2,6-bis(ethynyl)-4-fluoroaniline. By the second Sonogashira reaction with 3-bromo-4-

iodopyridine or 4-iodopyridine, respectively, neutral dibromo XB donor and HB donor (**1b**) were synthesized. To switch to better XB donor atoms, microwave halogen exchange reactions of the dibromo scaffold was performed producing the diiodo derivative (**1a**). Octlyating the pyridines of the neutral scaffolds activated the XB and HB donors. To increase solubility in organic solvent and minimize competitive intramolecular interactions, triflate counteranions were exchanged by metathesis for noncoordinating $[BAr^F{}_4]^-$ anions. Methyl derivatives were made in a similar way for X-ray diffraction studies.

Solution studies, crystal structures and computations supported our hypothesis that the intramolecular HB between the electron-deficient aniline and the two XB donor iodine atoms enhance the electrophilicity of the XB donors and preorganizes the bidentate XBing conformation.[28] We refer to this new preorganization strategy as intramolecular HBeXB. Receptor **2b**, lacks XB donors and was prepared to quantify C–H HBing and serve as a control. While synthesizing and characterizing the receptors, solvent dependent color changes were observed, especially under ultraviolet light. To better understand this solvatochromism, UV-Visible absorption and fluorescence emission studies were conducted for **1a**, **1b** and octyl derivatives **2a** and **2b** (Figure 7).

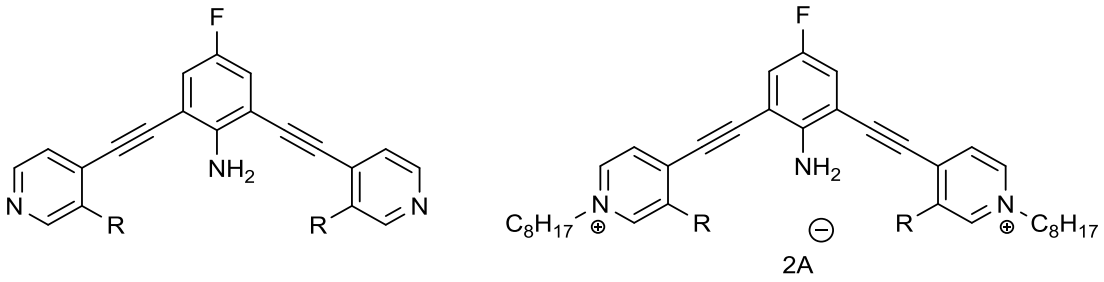

1a: R = I
1b: R = H

2a: R = I, A = BAr^F
2b: R = H, A = BAr^F

Figure 7. Structures of 2,6-bis(4-ethynylpyridinyl)-4-fluoroaniline XB donor **1a**, HB donor **1b** and octyl derivatives **2a**, **2b**.

2.3.2 Solvatochromism of neutral XB Receptors

Building on previous studies conduct Solvent dependence of both the absorption and emission spectra was observed for **1a** and **1b** (Figure 8). Receptors **1a** and **1b** exhibited a major absorbance band in the range of 300-600 nm (Figure S23 and S25). The absorption band of **1a** is red shifted from 405 nm to 416 nm as the dielectric constant of the solvent is increased with the exception of MeCN (Figure S31). A similar roughly linear correlation of bathochromic shift with increasing solvent dielectric constant was obtained for **1b** (Figure S25). Soret bands from π–π* transitions exhibit significant charge-transfer

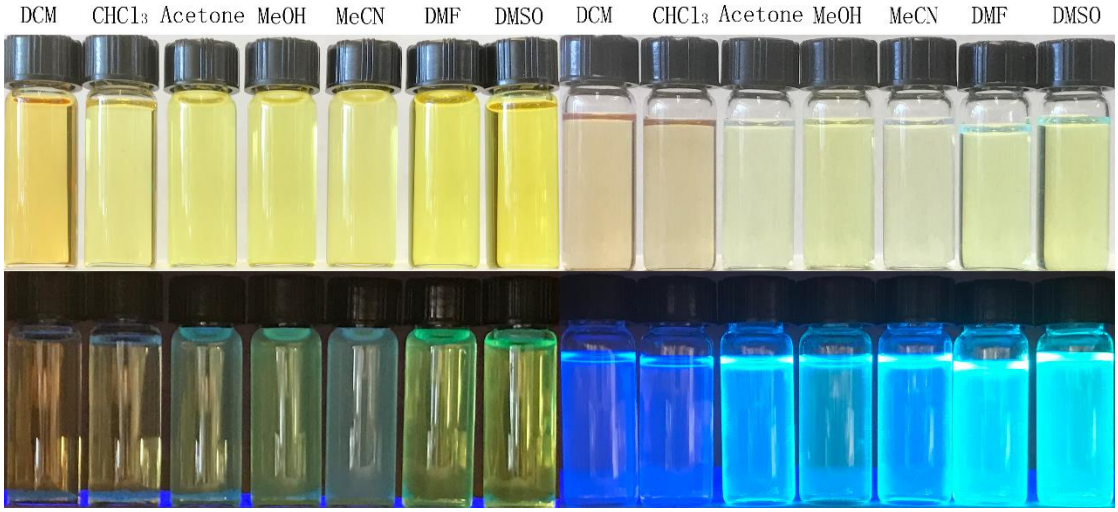

Figure 8. Solvatochromism of 1mM **1a** (top left: under sunlight; bottom left: under 365nm UV light) and **1b** (top right: under sunlight; bottom right: under 365nm UV light) in a set of solvents.

character resulting from the electron-deficient pyridine and electron donating aniline.[118,119] Other solvent parameters[120] (dipole moment, $E_T(30)$ and π* scale) were also analysed for both the neutral and charged receptors. However, no clear correlation between dipole moment, $E_T(30)$ or π*scale and absorbance ν_{max} (Figure S32-S34) was observed suggesting that nonspecific solvent polarity effects are not strong determinants of the HOMO and LUMO energy levels. This lack of correlation and solvents that deviate from the trend may be due to the Lewis acidic nature of the studied receptors. Taken together, these results suggest that the dielectric constant of the solvent most influences the HOMO and LUMO energy levels of the receptors. High dielectric solvents stabilize the excited state more than the ground state of the receptor. As a result, the energy for the HOMO to LUMO electron transition is lowered producing a bathochromic shift of the spectra with increasing solvent dielectric constant. The λ_{max} of **1a** is always red shifted when compared to **1b** in the same solvent, a result of the auxochrome iodine groups in **1a**.[121]

The solvatochromic effect on fluorescence was also investigated for **1a** and **1b**. The iodine atoms of **1a** produce a "heavy atom effect" that enhances the probability of intersystem crossing leading to reduced fluorescence of **1a** compared to **1b** (Figure 9).[122] The emission spectra of **1a** and **1b** obey the same direct correlation between solvent polarity and λ_{max} shift. However, methanol deviates from this trend for both **1a** and **1b** (Figure S24 and S26). For instance, the emission band of **1b** in methanol has a λ_{max} at 475 nm which is 15 nm and 14 nm longer than in acetone and acetonitrile, respectively, and is even close to dimethylformamide (DMF, λ_{max} = 476 nm) (Figure S26). This deviation could

result from the HB ability of the protic methanol. HBing to the amine of the fluoroaniline through an NH···O type HB or to a pyridine nitrogen through an OH···N HB could stabilize the excited state and shift the emission. Additionally, a drop in emission is observed for **1b**, perhaps due to HB enhanced internal conversion and intersystem crossing.[123]

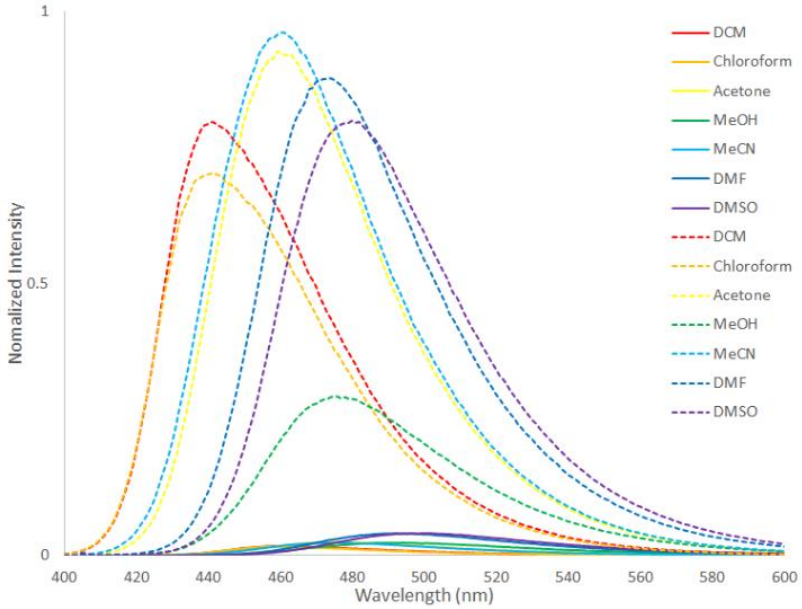

Figure 9. Normalized fluorescence emission spectra of **1a** (20 µM, solid line) and **1b** (20 µM, dashed line) in various solvents.

2.3.3 Solvatochromism of charged XB Receptors

To investigate the XB interaction and how it influences solvatochromism and fluorescence, the receptors were alkylated to increase their electron-deficiency and their binding affinity for anionic guests. Alkylation of the pyridines with octyl chains activated the XB and HB donors of **2a** and **2b**, respectively, while also enabling solubility in organic solvents.

The UV-Vis absorption and fluorescence emission spectra of **2a** and **2b** in various solvents are reported in Figure 10. A negative solvatochromism was observed in DCM, acetone, MeCN and DMF for the absorption of both **2a** and **2b** which has also been observed in other pyridinium systems.[124,125] This phenomenon has been explained by the ground state being more polar than

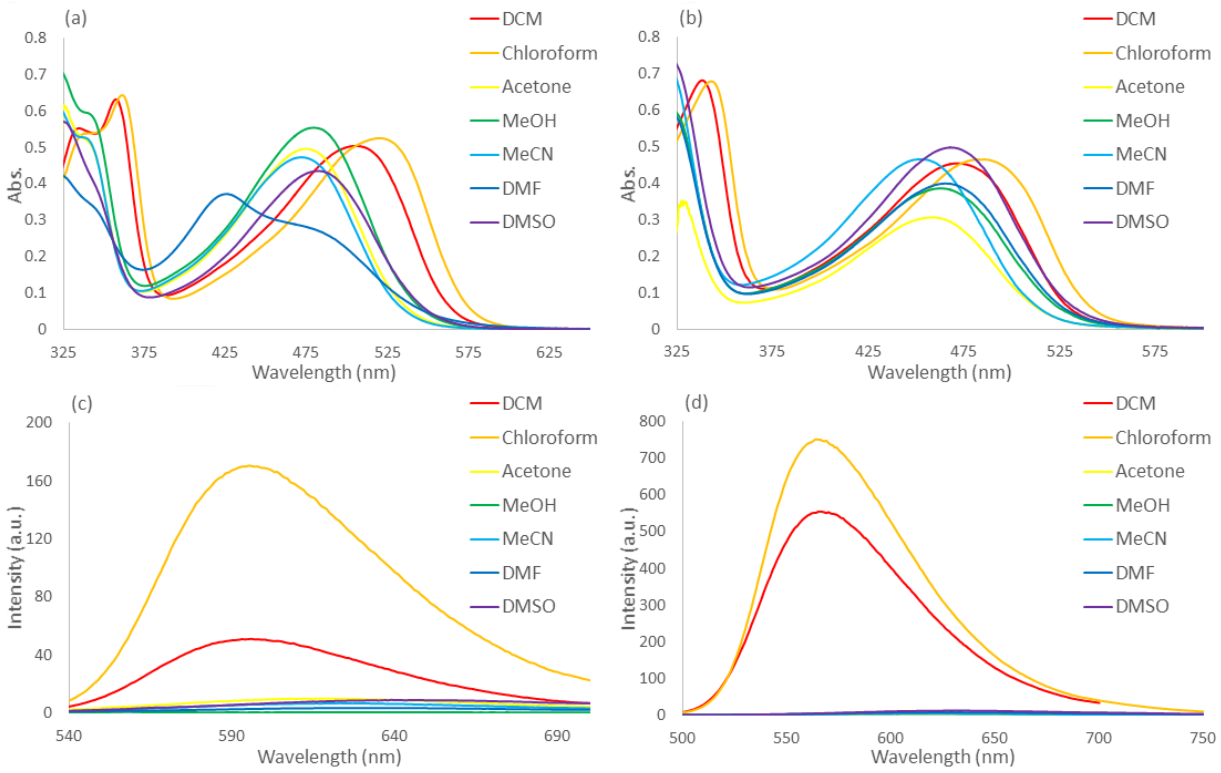

Figure 10. Absorption spectra of **2a** (a) and **2b** (b) in various solvents. Fluorescence emission spectra of **2a** (c) and **2b** (d) in various solvents (for excitation wavelengths and details see Experimental section). All spectra were recorded at 20 μM of receptor.

the excited state[126] and intramolecular charge transfer being favored by polar solvents.[124,125] This produces a larger energy difference between the ground and excited states as the polarity of the solvent increases. Chloroform, MeOH and DMSO deviate from this trend, perhaps, due to the binding between the receptors and solvents or environment effect which give rise to conformational changes in the receptor molecule.[13] Additionally, an obvious difference between **2a** and **2b** is the large blue shifting of **2a** in DMF. A linear free energy relationship between the absorbance (v_{max}) of **2a** and **2b** showed that the absorbance of **2a** is shifted more in DMF compared to **2b** (Figure S35b). We have solution and crystallographic evidence that derivatives of **2a** can XB to the DMF carbonyl oxygen.[66] This binding interaction may further stabilize the ground state. Ultimately, an 80 nm blue shift of absorbance in DMF is observed compared to DCM (Figure

10a). The HB in **2b** has a similar but weaker effect, shifting the absorption peak from 472 nm in DCM to 466 nm in DMF (Figure 10b).

2a was only fluorescent in nonpolar solvents (DCM and chloroform) and was nearly quenched in all other solvents (Figure 10c). In contrast, **2b** had stronger fluorescence than **2a** due to lack of the heavy atom effect, but was also quenched in polar solvents (Figure 10d). The fluorescence quenching is consistent with other probes that are weakly fluorescent in hydrophilic environments but strongly fluorescent in hydrophobic environments.[127]

2.3.4 Anion induced fluorescence response of charged XB Receptors

Qualitative evaluation of the anion sensing capability of **2a** and **2b** in DCM was performed with a series of anions as their tetrabutylammonium salts (Cl^-, Br^-, I^-, SCN^-, NO_3^-, HSO_4^-, $H_2PO_4^-$ and ReO_4^-). Considering both solubility and polarity which may affect the noncovalent interaction between receptor and anion, we chose DCM as the solvent for these studies. The results are illustrated in Figure 11 (see Experimental section for full details). In general, the absorption band of XB receptor **2a** at λ_{max} 507 nm is red shifted from 509 to 535 nm when one molar equivalent of anion is added, and hypochromically blue shifted after the addition of excess anion (50 molar equivalents). Additionally, the absorption band of HB receptor **2b** at 472 nm behaves similarly to **2a** which is red shifted from 479 to 513 nm in the presence of one equivalent of anion and hypochromically blue shifted upon addition of excess anion (50 molar equivalents).

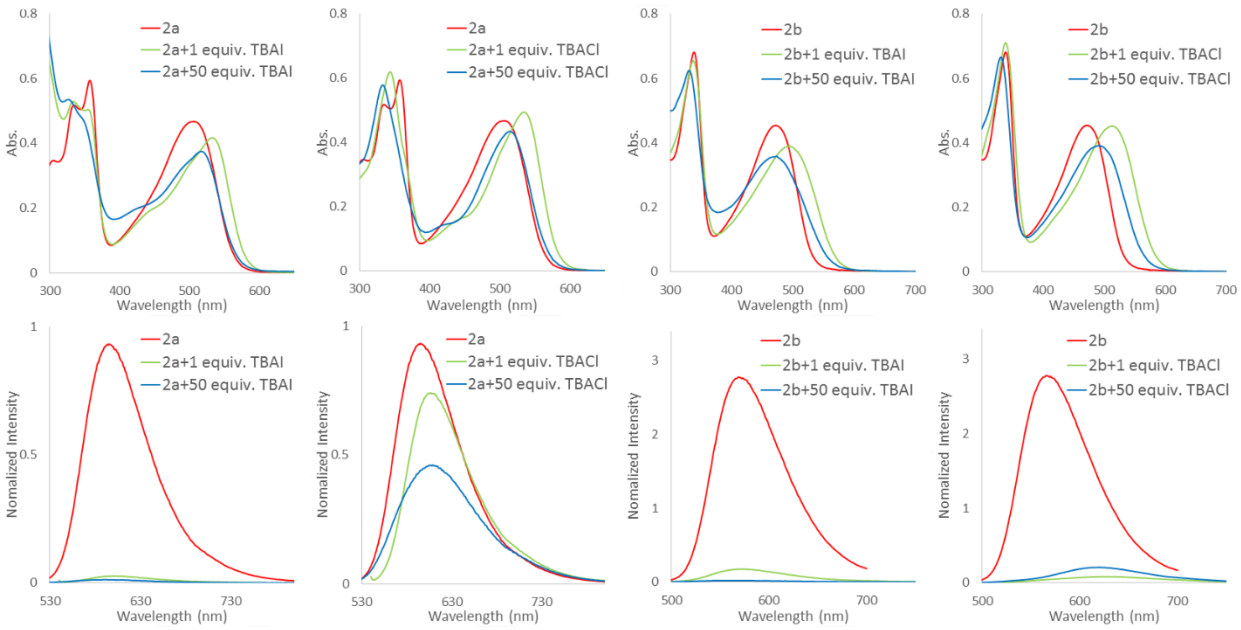

Figure 11. Absorption spectra of **2a** with TBA^+I^- (top left) and with TBA^+Cl^- (top middle-left), **2b** with TBA^+I^- (top middle-right) and with TBA^+Cl^- (top right); followed by fluorescence emission spectra of **2a** with TBA^+I^- (bottom left) and with TBA^+Cl^- (bottom middle-left), **2b** with TBA^+I^- (bottom middle-right) and with TBA^+Cl^- (bottom right). All spectra were recorded at 20 µM of receptor in DCM solution (for excitation wavelengths and details see Experimental section).

In the emission spectra, halides quenched the fluorescence of both **2a** and **2b** from 0 equivalent to 50 equivalents. For instance, fluorescence of **2a** decreased by 20% after adding one equivalent of TBA^+Cl^- and declined to 50% of the initial value after 50 equivalents (Figure 11, bottom middle-left). However, the receptor is more sensitive to iodide (Figure 11, bottom left). The intensity significantly dropped to 2% of the original level at just one equivalent of iodide. Inter and intramolecular HBing have been shown to facilitate fluorescence quenching.[128,129] The efficient fluorescence "turn-off" in **2a** correlates with previous NMR studies[28] that illustrate stronger binding between **2a** and I^- compared to other halide anions.[28] Specifically, the K_{11} values determined by titrations of **2a** with I^-, Br^- and Cl^- were 36,569 M^{-1}, 34,145 M^{-1} and 23,622 M^{-1} respectively in 40% $CDCl_3$/60% CD_3NO_2. In the current system, the formation of strong XBs (C-I···I^-) in the **2a**·I^- complex could allow the necessary spin-orbital coupling for fluorescence quenching

to occur.[130] Moreover, the iodine[131] and iodide[132] present can act as heavy-atom quenchers. Considering these effects, intersystem crossing could be favored which leads to fluorescence quenching. Compared to **2a**, fluorescence quenching of **2b** is more efficient with chloride and bromide, and similar with iodide. These results could partially be explained by the weaker binding ability of **2b** (K_{11} for I^-, Br^- and Cl^- are 1,820 M^{-1}, 2,122 M^{-1} and 2,326 M^{-1}, respectively in 40% $CDCl_3$/60% CD_3NO_2).[28] In addition, thiocyanate (SCN^-) quenched the fluorescence of both **2a** and **2b**. SCN^- decreased fluorescence intensity of **2a** to less than 35% of the original level at one equivalent but changed very little at 50 equivalents. However, the fluorescence of **2b** was almost totally quenched after 50 equivalents.

Some of the oxoanions studied elicited different fluorescence responses compared to halides and SCN^-. NO_3^- and ReO_4^- induced a similar fluorescence response in **2a** and **2b** as SCN^- did. However, $H_2PO_4^-$ produced a 51% and 60% decrease in **2a** and **2b**, respectively, at one equivalent and totally quenched fluorescence when in excess. HSO_4^- affected the fluorescence of **2b** in a similar way to SCN^-, NO_3^- and ReO_4^-. However, in **2a**, the solution turned cloudy and floccule formed, precipitating out the receptor in a couple minutes upon the addition of 50 equivalents of HSO_4^-. In general, **2b** is quenched more than **2a** with all anions, except for iodide. One hypothesis is that XB between **2a** and the anions rigidifies the structure of the **2a**·anion complex. The more planar/rigid structure which has less vibrational modes to absorb the excess energy leads to less efficient internal conversion. Thus, the more efficient internal conversion of **2b** causes the lower quantum yield, and correspondingly lower fluorescence intensity.[133]

2.3.5 Density Functional Theory (DFT) calculations

Table 1. Energy of HOMO, LUMO for receptors **1a**, **1b** and **2a**, **2b.**

	1a	**1b**	**2a**	**2b**
HOMO Energy (eV)	-2.672	-2.506	-8.268	-8.214
LUMO Energy (eV)	-6.011	-6.062	-10.833	-10.844
ΔE (eV)	3.339	3.556	2.565	2.630

Geometry optimizations and Frontier molecular orbital calculations were performed to further analyse the spectrophotometric properties of the receptors. Density Functional Theory (DFT) calculations were done using the B3LYP/6-31+G(d,p) functional. To simplify calculations, methyl derivatives of the charged receptors were evaluated. The electron density distributions of the HOMO and LUMO for all four receptors is depicted in Figure 12. The neutral receptors **1a** and **1b** have nearly equivalent HOMO and LUMO distributions. Additionally, **2a** and **2b** also have analogous HOMO and LUMO maps which is consistent with the similarly shaped absorption and emission spectra. The electron density in the HOMO is mainly populated on the central fluoroaniline ring. In the LUMO the electron density is increased on the two flanking pyridine rings. Such electronic configurations lead to the charge-transfer nature of the electronic

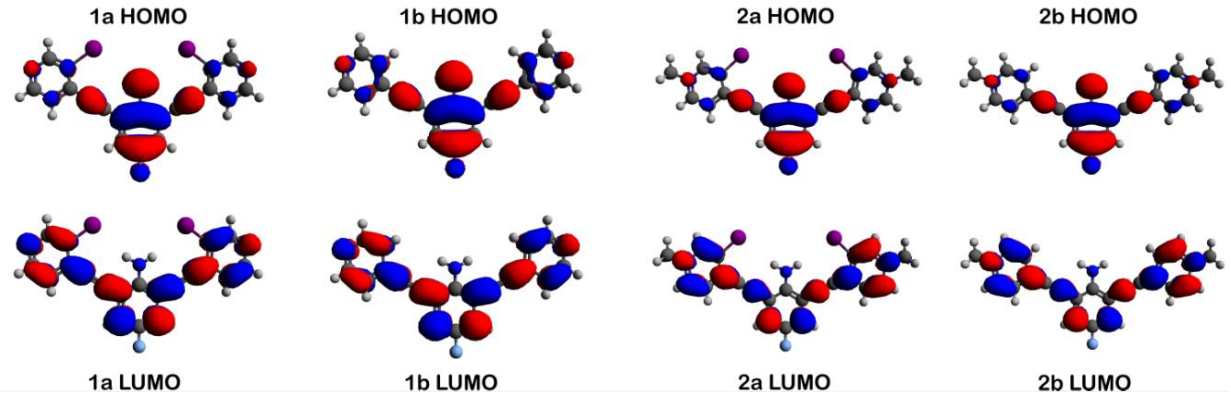

Figure 12. Calculated frontier molecular orbitals for neutral receptors **1a**, **1b** and charged receptors **2a**, **2b**.

transitions. The energy differences of the HOMO and LUMO are listed in Table 1. Narrower energy band gaps are predicted for the HOMO and LUMO for the halogen containing receptors (**1a** and **2a**) compared to the HB receptors (**1b** and **2b**) which correlate with the larger λ_{max} (for both the absorption and emission) observed for the halogen containing receptors **1a** and **2a**.

2.4 Conclusions

In summary, we have demonstrated that XB receptor **1a** and HB receptor **1b** exhibited similar solvatochromism in their UV-Vis and fluorescence spectra. As compared to **1a** and **1b**, octyl derivatives **2a** and **2b** exhibited opposite solvatochromism corresponding to their charged states and differences in binding ability. Theoretical estimations of the electron density distributions of the HOMOs and LUMOs highlighted the charge transfer nature of the receptors and supported the differences observed in the soret band λ_{max} in the UV-Vis spectra. The anion induced fluorescence quenching of XB derivative **2a** is less efficient than **2b** with most anions, possibly due to the loose bolt effect for the weaker binding **2b**. Additionally, **2a** can selectively sense I^- over other anions by a significant fluorescence quenching after the addition of one equivalent. Such effects have been explored to better understand the nature of XB and may provide the opportunity to exploit XB in fluorescent/colorimetric anion sensors.

Bridge to Chapter 3:

Chapter 2 demonstrated that XB receptors and HB receptors responded differently to the presence of anions. Specifically, selective sensing for iodide was established for the XB receptor. These results could be applied to the development of XBing colorimetric and fluorescent anion sensors. To further enhance the binding strength, modifying the electronics of the halogen donors through substituent effects is a promising approach. However, applying this approach to

modulate the HBeXB may not be straightforward, as there may be competing electronic effects. Therefore, in Chapter 3, we presented the first comprehensive investigation of substituent effects and Linear Free Energy Relationships (LFERs) studies on the HBeXB interaction, in the solution, gas, and solid phases.

Chapter 3:

The Interplay Between Hydrogen and Halogen Bonding: Substituent Effects and their role in the Hydrogen Bond Enhanced Halogen Bond

3.1 Preface

This chapter includes work that was published in *Chemical Science*, (2023) (Figure 13) which

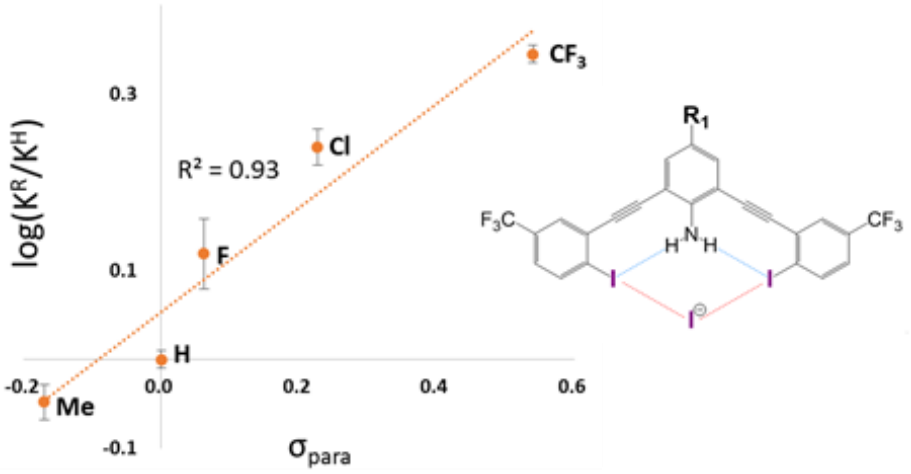

Figure 13. Table of contents photo from *Chemical Science*.

was co-authored by Daniel A. Decato, Vyacheslav S. Bryantsev, Eric A. John and Prof. Orion B. Berryman. Daniel A. Decato assisted in computations, collected diffraction data, solved single crystal X-ray structures, provided editorial assistance and wrote the crystal section of the manuscript. Vyacheslav S. Bryantsev conducted computations. Eric A. John assisted in synthesis. Orion B. Berryman assisted in conceiving this project and data interpretation and provided editorial assistance. Jiyu Sun, first author, synthesized all the molecules, conducted literature searches, grew diffraction quality crystals, performed data compilation and interpretation, wrote the manuscript, and prepared the supporting information for the publication.

3.2 Introduction

Understanding how to modulate noncovalent interactions that are in close proximity is paramount to engineering functional materials[134], supramolecular assemblies[135], drugs[136], and catalysts[137]. Foundational work has detailed the importance of substituent effects[138,139] to tune the electronics of noncovalent interactions.[140-143] Despite this pioneering work, few have looked at substituent effects involving multiple noncovalent interactions that are spatially close. Recently, Cockroft, and coworkers reported rare experimental data quantifying through-space substituent effects on noncovalent interactions and presented the inadequacy of describing substituent effects using classic Hammett parameters when through-space effects dominate.[144] Additionally, Zonta, and coworkers utilized similar methods to carry out an experimental survey of aromatic stacking interactions in solution.[145] Clearly, understanding how adjacent noncovalent interactions influence each other by substituent effects is critically lacking.

Among the myriad noncovalent interactions, HBs are privileged for their directionality and tunability. Halogen Bonds (XBs) share similarities with HBs, yet contain an electron deficient donor (halogen) that forms an attractive noncovalent interaction with an electron rich species. This interaction can be understood in term of electrostatics and covalency.[10,11,67,146-151] An electrostatic description suggests that due to the polarizability of the halogen, its electron density can become anisotropic. In this case, a partial positive potential develops on the halogen, opposite to the C-X σ bond which has been coined the *σ-hole*. Concurrently, an electron rich belt is generated on the XB donor which is orthogonal to the direction of the σ bond.[9,152,153] The high directionality, tunability and complementarity with "soft" Lewis bases [66,119,154], makes XBing accordant with HBing. Given these unique properties, exciting applications of XBing

supramolecule self-assembly[13], molecular recognition[59,155], anion binders[28,29,66], organocatalysts[14,88,30], and anion transporters[156] are appearing at a rapid pace. Understanding how to modulate both the strength of the XB and the structure of these molecules is of broad importance for the continued development of functional halogenated species. Using substituent effects to alter the electronics of the halogen donors remains a leading strategy. However, experimental substituent effects on XBing are limited (despite numerous computational studies[157-162]). Only Taylor[163], Diederich[164], Erdelyi[165], Stilinović[166] and Franz[167] have explicitly studied XBing substituent effects in solution—with different outcomes for each of their systems. Despite the critical importance of these substituent studies, the influence of a neighbouring noncovalent interaction has not been studied.

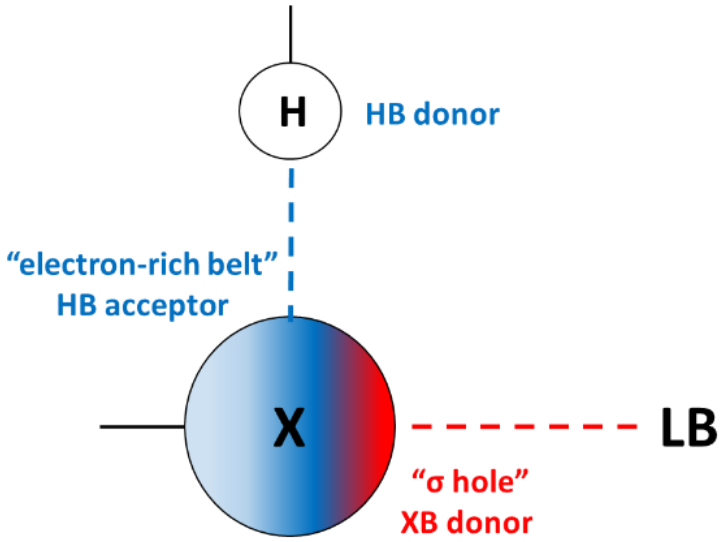

Figure 14. Cooperativity between HB and XB donors and acceptors in the HBeXB interaction. Blue dashed line: HB interaction, red dashed line: XB interaction, LB: Lewis base.

We recently introduced a new strategy—the Hydrogen Bond Enhanced Halogen Bond (HBeXB)—that directs intramolecular HBs to the electron rich belt of XB donors for preorganization and enhanced XB strength (Figure 14). Recently, the HBeXB interaction has been used to increase anion binding affinity by nearly an order of magnitude and to improve the

function of organocatalysts.[28,29] Similarly, Ho and his group have noted the HBeXB in biological settings and employed it to stabilize and improve a T4 lysozyme mutant.[31-34] These studies have been complemented by fundamental studies as well.[28,35-37,168] Over the course of these seminal works there are implications of reciprocity between the HB and XB, especially when considering circumstances where augmentation and preorganization are simultaneously operating. In fact, using substituent effects to modulate the HBeXB may not be straightforward as there are potentially competing electronic effects. Making the halogen atom more electron rich may decrease the XB donor ability but will increase the strength of the adjacent HB. The subtle interplay between these two interactions naturally leads one to ask important questions. For example, when optimizing binding, is it more efficient to tune the XB strength or the HB strength with electronic effects? Additionally, how does this influence molecular conformations? To address these questions and more, we present the first HBeXB substituent and LFER studies in solution, gas, and solid phases.

3.3 Results and Discussion

3.3.1 Design and Synthesis of XB Receptors

3.3.1.1 Receptor Design

We previously developed two generations of bis-ethynyl XB receptors that presented two charged pyridinium XB donors in a convergent manner (Figure 15 top). In the 2nd-generation receptor we introduced an amine substituent to the core that provided intramolecular N-H···I HBs to the XB donors. This innovation improved binding by nearly an order of magnitude over a control lacking the amine.[28] We coined this effect the *HBeXB* and showed that the enhancement was due to both preorganization of the receptor into a bidentate binding conformation and

strengthening of the XB. The success of the HBeXB and our experience with this scaffold prompted us to evaluate HBeXB substituent effects using a 3rd-generation anion receptor presented here (**G3XB**, Figure 15 bottom). This latest iteration replaces the flanking iodopyridinium rings with neutral aromatic rings to improve solubility in organic solvents. The redesign also reduced the number of synthetic steps to produce the diverse range of receptors needed to examine substituent effects. Specifically, we prepared a series of compounds that contained substituents of varying electronic properties that were *para* to both the amine (**R_1-G3XB**) and the iodine donors (**$2R_2$-G3XB**). This design permitted systematic modulation of the electron density on both the HB and XB donor rings to test substituent effects. Controls with trifluoromethyl substituents (the strongest electron withdrawing groups in this study) were also prepared without the amine (**nHBeXB**) and without the iodine XB donors (**G3HB**).

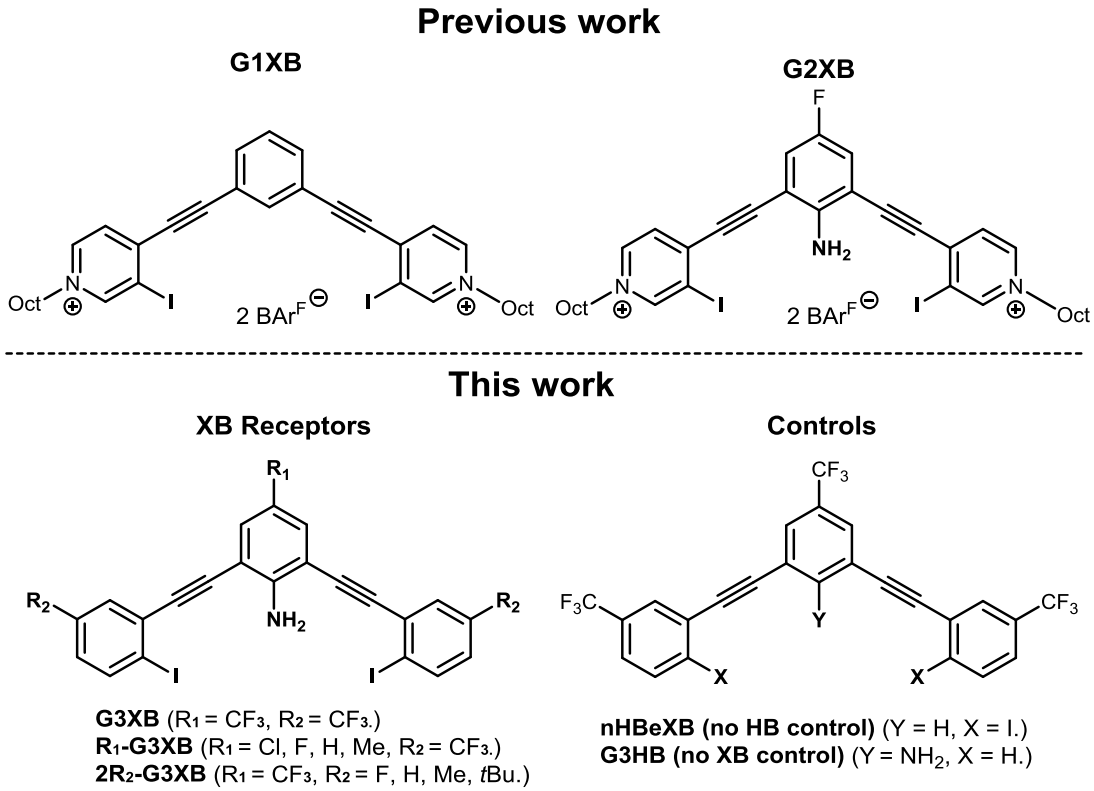

Figure 15. ChemDraw representation of previous XB receptors and **G3XB** derivatives in this work.

3.3.1.2 Synthesis and Characterization

The synthesis of **G3XB** derivatives is outlined in Scheme 2. 2,6-bis(ethynyl)-4-R_1-aniline (**2**) was synthesized by Sonogashira cross-coupling 2,6-dibromo-4-R_1-aniline (**1**) with

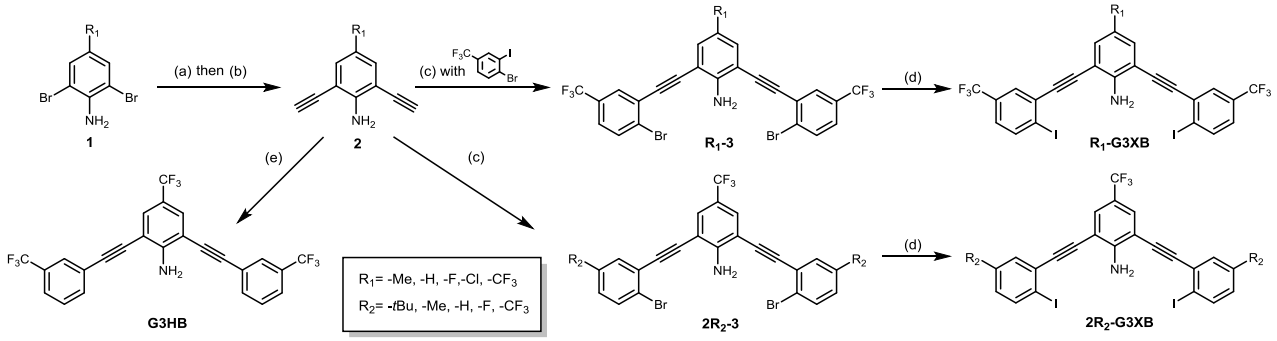

Scheme 2. Synthesis of **G3XB** derivatives and controls used to study HBeXB substituent effects. Reagents and conditions: (a) TMS-acetylene, $Pd(PPh_3)_2Cl_2$, Cu(I)I, DIPEA, DMF, overnight, N_2, 80˚C, ; (b) K_2CO_3, MeOH/DCM(1:1 v/v), 4 hours, rt, 45-96%. (c) 4-bromo-3-iodo-R_2-benzene, $Pd(PPh_3)_2Cl_2$, Cu(I)I, DIPEA, DMF, overnight, N_2, rt, 53-87%; (d) NaI, Cu(I)I, *trans-N,N*-dimethylcyclohexane-1,2-diamine, 1,4-dioxane, microwave reactor, 12-24 hours, 150˚C, 33-84%; (e) 3-bromotrifluoromethylbenzene, $Pd(PPh_3)_2Cl_2$, Cu(I)I, DIPEA, DMF, overnight, N_2, 80˚C, 60%.

trimethylsilylacetylene followed by removal of the trimethylsilyl protecting groups with potassium carbonate. Precursor scaffolds containing bromine (**R_1-3**, **$2R_2$-3**, and HB receptor **G3HB**) were synthesized by Sonogashira cross coupling **2** at the iodo-functionality of 4-bromo-3-iodo-R_2-benzene or 3-bromotrifluoromethylbenzene, respectively. The iodine containing **R_1-G3XB** and **$2R_2$-G3XB** were obtained by microwave assisted halogen exchange of **R_1-3** or **$2R_2$-3**. The complete experimental procedures can be found in the Experimental section.

3.3.1.3 Experimental Evidence of Intramolecular Hydrogen Bonding

Analysis of the amine ^{1}H NMR resonances provided initial indication of intramolecular HBing between the amine and the electron rich belt of the XB donor (N–H···I). The analysis provided a preliminary evaluation of substituent effects and provided rare experimental evidence of HBing to larger halogens.[98,169-172] Control receptor **G3HB**, lacking XB donors to accept HBs, had an amine ^{1}H chemical shift of 4.64 ppm in C_6D_6, whereas the chemical shift for **G3XB**, with iodine acceptors,

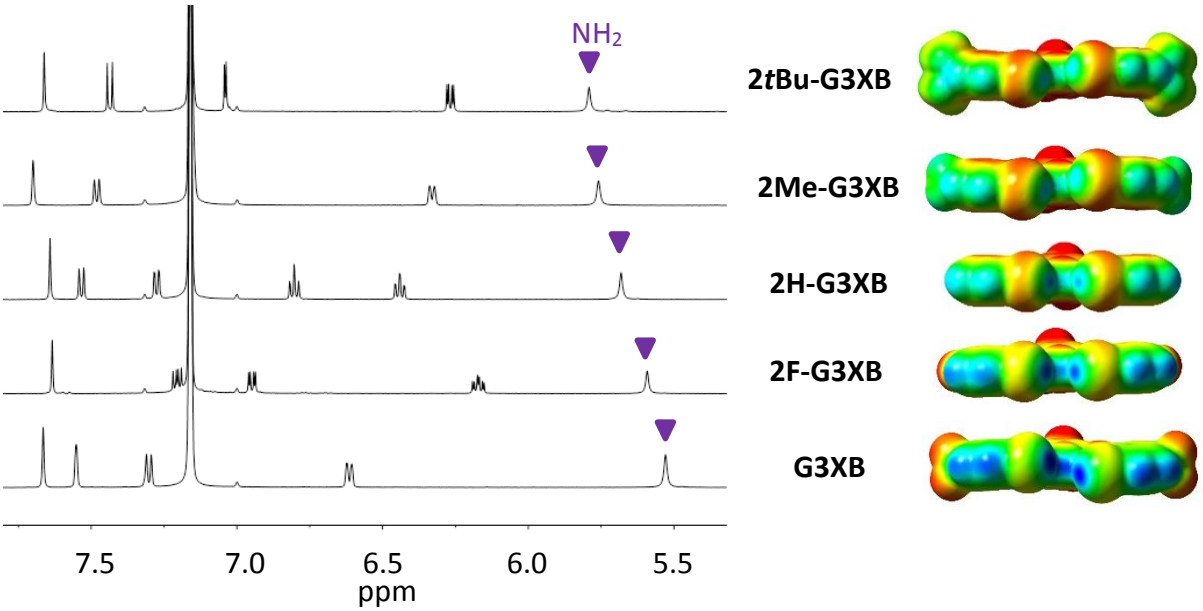

Figure 16. ^{1}H NMR spectra (C_6D_6, 500 MHz, 5mM) of **$2R_2$-G3XB** derivatives (left) highlighting the HBing downfield shift of the amine as the halogen becomes more electron rich; ESP maps (isovalue= 0.001 a.u.) for **$2R_2$-G3XB** derivatives (right) are displayed on the same scale. Electron deficient regions are blue and electron rich regions are red.

was 5.53 ppm. This 0.89 ppm *downfield* shift is indicative of intramolecular HBing. The series of **2R$_2$-G3XB** derivatives (Figure 15, left) showed that as the *para* substituent on the XB donor ring became more electron donating, the HBing amine proton shifted *downfield* from 5.53 ppm to 5.80 ppm. This *downfield* shift occurs despite the expectation that adding electron donating substituents should shield the nuclei and would produce an *upfield* shift for the proton. However, the electron donating groups in the **2R$_2$-G3XB** compounds transfer additional electron density onto the iodine atoms (*vide infra*) making the iodine a better HB acceptor, resulting in the *downfield shift*.§ Overall this NMR analysis suggests that the intramolecular HBing is formed and the strength of this HBing correlates with the electron density of the halogens.

3.3.2 Computational Evaluations

To garner preliminary insight into substituent effects of HBeXBs, *in silico* studies were performed. All the receptors were evaluated using Gaussian 16 at the M06-2X/def2TZVPP level of theory (see Experimental section for further details). A systematic use of conformational analysis and electrostatic potential (ESP) mapping provided early insight into the synergy between the HB and XB and helped to stimulate deeper LFER analysis.

3.3.2.1 σ-hole Calculations

σ-hole analysis (maximum/minimum electrostatic potentials, denoted by $V_{S,max}$/$V_{S,min}$) showed several trends regarding the influence of the intramolecular HB on XB donor strength. Consistent with our previous studies, the HB from the amine to the iodine augments the σ-hole

§No clear trend was observed among **R$_1$-G3XB** derivatives. The amine proton peak is 5.53 ppm for R_1=CF_3, 5.25 ppm R_1=Cl, 5.17 ppm R_1=F, 5.40 ppm R_1=H and 5.31 ppm R_1=Me. The deviation for the fluorine and chlorine substituents might be a result of their π electron donating property affecting the amine. We rationalize the trend observed of **2R$_2$-G3XB** derivatives based on how the substituents influence the electronics on the HB acceptor (in this case the XB donor) rather than the HB donor.

(greater $V_{s,max}$). For example, **G3XB** in the bidentate conformation has a $V_{s,max}$ that is 4.02 kcal mol^{-1} greater than **nHBeXB**—a consequence of the HBeXB (Table 2).

Table 2. Halogen $V_{s,max}$ of **G3XB** derivatives [a]

	Bidentate	S conformation (HBed iodine/ non-HBed iodine)	$\Delta V_{s,max}$ [b]
G3XB	32.05	31.45/24.46	6.99
nHBeXB	28.03	26.64/25.39	1.25
2F-G3XB	28.40	28.52/20.94	7.58
2H-G3XB	24.98	26.05/17.95	8.10
2Me-G3XB	23.03	24.69/16.94	7.75
2*t*Bu-G3XB	22.41	24.37/16.15	8.22
Cl-G3XB	30.84	29.85/24.16	5.69
F-G3XB	30.12	29.33/24.61	4.72
H-G3XB	28.72	28.08/24.07	4.01
Me-G3XB	28.11	27.36/24.04	3.31

[a] $V_{s,max}$ (kcal mol^{-1}) were calculated at 0.001 Å isoelectric surface.
[b] $\Delta V_{s,max} = V_{s,max\ HBed\ iodine} - V_{s,max,\ non\text{-}HBed\ iodine}$

3.3.2.1.1 Substitution on the HB Donor Ring

Modulation of the $\mathbf{R_1}$ group helped determine if stronger HBs would correlate to greater XB enhancement. Within the $\mathbf{R_1}$ series, the $V_{s,max}$ values on the XB donors ranged from 32.05 kcal mol^{-1} for the most electron withdrawing **G3XB** in the bidentate conformation to 28.11 kcal mol^{-1} for **Me-G3XB** (Table 1). The data verify that stronger HB donors correlate with a more positive $V_{s,max}$—confirming a notion alluded to in our previous HBeXB systems.[28,35] Our results here highlight that tuning the HB donor with a single remote substituent can influence the XB donor $V_{s,max}$ by 3.94 kcal mol^{-1}.

3.3.2.1.2 Substitution on the XB Donor Ring

Next, the $V_{s,max}$ of the **2$\mathbf{R_2}$-G3XB** derivatives in the bidentate conformation was probed to determine how substituent electronics on the XBing ring influence XB donor strength. As

expected, the $V_{s,max}$ becomes larger as the substituent *para* to the XB donor increases in electron withdrawing capacity. The **G3XB** derivative with CF_3 substituents represents the upper end in this series with a $V_{s,max}$ of 32.05 kcal mol^{-1} whereas, **2*t*Bu-G3XB** represents the lower end at 22.41 kcal mol^{-1}. These studies align with previous reports[163,164,167] showing that XB donors can be directly influenced by electronic substituent effects. For instance, the $V_{s,max}$ of the XB donors in Talyor's 4-R-C_6F_4I studies differ by 6.9 kcal mol^{-1} when a *para* fluoro substituent is changed to a piperidyl group.[163] However, it is notable that in this bisethynyl system the $V_{s,max}$ varies by 9.64 kcal mol^{-1} by direct substitution on the XB ring.

In contrast to the above discussion on XB donor strength (i.e. $V_{s,max}$), we also considered the $V_{s,min}$ of the iodine atoms as a measure of HB acceptor capacity. As the substituent *para* to the XB donor becomes more electron donating, the iodine species becomes more electron-rich (Figure 16, right). The $V_{s,min}$ of the **2R_2-G3XB** compounds (-1.11 to -11.14 kcal mol^{-1}, for details see Experimental section) trend with the downfield NMR shifting—suggesting that **R_2** electron donating groups strengthen the intramolecular HBing between the amine and the XB donor.

3.3.2.2 Conformational Effects on the XB donor

3.3.2.2.1 R_1 - Minimal through Bond Effects on the XB donor

ESP maps were calculated for the **R_1-G3XB** derivatives in the S conformation (Figure 17). The S conformation contains one XB donor that accepts a HB and one that does not. This S arrangement was used to determine whether substitution on the HB donor ring has a through bond electronic effect on the XB donor. The S conformation of **R_1-G3XB** derivatives all exhibit similar $V_{s,max}$ values (≈ 24 kcal mol^{-1}) for the iodine not accepting a HB. *This demonstrates that substituents on the central HB donor ring do not directly inductively alter the electronics of the XB*

donor.§§

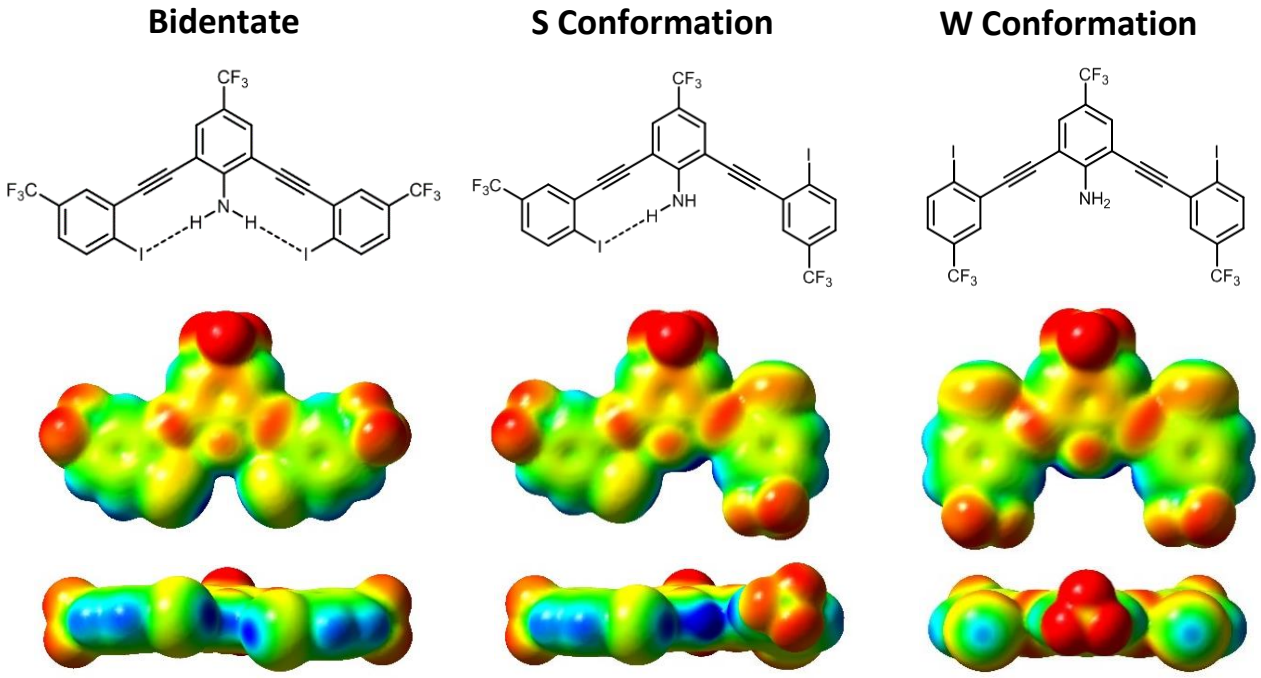

Figure 17. ChemDraws and ESP maps for **G3XB** in all three planar conformations. The bidentate conformation (left), where both XB donors are convergent; the S conformation (middle), where the XB donors are on opposite sides of the molecule; and the W conformation (right), where both XBs are directed away from the amine. All ESP maps are displayed on the same scale. Electron deficient regions are blue and electron rich regions are red.

3.3.2.2.2 R_1 - Through Space Effects on the XB Donor

In contrast, the potency of the HB donor does have an influence on the XB donor strength. The $V_{s,max}$ of the halogen accepting a HB has a greater ESP than the non-HB accepting iodine. The $V_{s,max}$ values for the iodine in **G3XB** that accepts a HB was 31.45 kcal mol^{-1} and 27.36 kcal mol^{-1} for **Me-G3XB** which has the most electron donating substituent $\mathbf{R_1}$. Thus, strengthening the intramolecular HB donor can modulate the $V_{s,max}$ of a single XB donor by 4.09 kcal mol^{-1}, a value similar to the bidentate assessment described above.

§§This finding also correlates with computational data from Scheiner[173] illustrating that the through bond influence of the electron withdrawing group on the XB properties diminishes with its distance from the halogen atom.

The through space influence of a HB on the XB donor was analyzed by computing the difference ($\Delta V_{s,max}$) between the two iodine donors in the S conformation ($\Delta V_{s,max}$ = $V_{s,max}$ HBed iodine - $V_{s,max}$ non-HBed iodine). Here the weakest HB donor **Me-G3XB** derivative had a $\Delta V_{s,max}$ of 3.31 kcal mol^{-1} while the strongest HB donor **G3XB** had the largest $\Delta V_{s,max}$ of 6.99 kcal mol^{-1}. Collectively the $\Delta V_{s,max}$ values of the **R_1-G3XB** derivatives adhere to the trend that increasing the electron withdrawing ability of **R_1**, strengthens the HB which in turn has a larger influence on the XB donor.

3.3.2.2.3 R_2 - Through Bond Effects on the XB Donor Ring

$V_{s,max}$ values for **2R_2-G3XB** derivatives in the S conformation were used to quantify how changing the electronics of the XB donor ring influences the iodine σ-hole. For example, the $V_{s,max}$ of the externally directed iodine (non-HBed iodine) generally followed the trends expected from the electronic contributions of the **R_2** group (i.e. $V_{s,max}$ values for **2R_2-G3XB** trended in the order CF_3 > F > H > Me > *t*Bu) ranging from 24.46 to 16.15 kcal mol^{-1}. The internally directed iodine atoms (accepting a HB) all had larger $V_{s,max}$ values ranging from 31.45 to 24.37 kcal mol^{-1} and generally followed the same trend.

3.3.2.2.4 R_2 - Through Space Effects on the XB Donor†

The strength of the HB donor in the **2R_2-G3XB** derivatives is constant (i.e. a CF_3 group *para*

† Comparing the entire **2R_2-G3XB** series, we noted that the $V_{s,max}$ of **2Me-G3XB** is smaller than **2H-G3XB** which deviates from the expected electronic trend. This is likely due to small differences in the planarity of the structures during the calculations that affect the electronic environment of the halogens (see Experimental section). For **2R_2-G3XB** derivatives which have more electron donating substituents (**R_2** = F, H, Me, *t*Bu), it was observed that the iodine in the S conformation which accepts a HB has a 0.1 to 2.0 kcal mol^{-1} higher $V_{s,max}$ than the iodines in the bidentate conformation (which also accept HBs). We hypothesized that the S conformation provides more flexibility for the only N–H···I HB thus producing a stronger HB. However, when considering receptor design, this small difference would likely be compensated by allowing two convergent XBs to be available in the bidentate conformation.

to the central amine). Thus, the $\Delta V_{s,max}$ values here are a measure of how the **R_2** electronics impact the halogen as both a XB donor and a HB acceptor. The $\Delta V_{s,max}$ values of 6.99, 7.58, 8.10, 7.75 and 8.22 kcal mol^{-1} were obtained for **G3XB**, **2F-G3XB**, **2H-G3XB**, **2Me-G3XB** and **2*t*Bu-G3XB**, respectively. The trend parallels previous evaluations and shows that generally, more electron rich iodines experience a greater augmentation.

Comparing **2R_2-G3XB** and **R_1-G3XB** $\Delta V_{s,max}$ values provides a measure of which substituent position impacts XBing the most by a through space effect. The smaller range of values for the **2R_2-G3XB** series (1.23 kcal mol^{-1}), as compared to the **R_1-G3XB** derivatives (3.68 kcal mol^{-1}), suggests that the influence of HBing on the halogen atom is more sensitive to substitution on the HB donor ring. For example, altering one **R_1** substituent from CF_3 to Me results in a 3.68 kcal mol^{-1} $\Delta V_{s,max}$ difference. However, altering two **R_2** substituents from CF_3 to Me results in a 0.76 kcal mol^{-1} $\Delta V_{s,max}$ difference.

3.3.2.3 Influence of R_1 and R_2 on Conformation

To assess the role of preorganization in **G3XB** derivatives, their relative stabilities were assessed based on electronic energies from DFT. The difference between the S and bidentate conformation energy illustrates that intramolecular HBeXBs stabilize the bidentate conformation of the receptors (Table 3). The bidentate conformation of **G3XB** contains two intramolecular HBs (N–H···I) and is more stable than the S conformation by 1.53 kcal mol^{-1}. The W form, lacking intramolecular HBs is 3.11 kcal mol^{-1} higher in energy than the bidentate conformation. For the **2R_2-G3XB** series, as **R_2** becomes more electron donating, the energy differences between the bidentate and S conformation increases from 1.76 kcal mol^{-1} for **2F-G3XB** to 2.15 kcal mol^{-1} for **2*t*Bu-G3XB**. This suggests a greater stabilization when the iodine HB acceptor is more electron

rich. These results track with the amine ^{1}H NMR chemical shift analysis for **2R$_2$-G3XB.** In contrast, the difference between the bidentate and S conformation for the **R$_1$-G3XB** series is comparatively attenuated; however, only a single substituent group is modified. The ΔE is 1.42 kcal mol^{-1}, 1.33 kcal mol^{-1}, 1.43 kcal mol^{-1}, and 1.36 kcal mol^{-1} for **Cl-G3XB**, **F-G3XB**, **H-G3XB** and **Me-G3XB**, respectively. These data indicate that conformational preference is sensitive to the electronics of both the XB and HB donor.

Table 3. Electronic energy difference (ΔE) between S and bidentate conformations of **G3XB** derivatives

	ΔE (kcal mol^{-1})
G3XB	1.53
nHBeXB	-0.01
2F-G3XB	1.76
2H-G3XB	1.83
2Me-G3XB	1.90
2*t*Bu-G3XB	2.15
Cl-G3XB	1.42
F-G3XB	1.33
H-G3XB	1.43
Me-G3XB	1.36

3.3.3 Solution Studies

3.3.3.1 NMR Titrations and Association Constants

^{1}H NMR anion binding titrations were performed to quantify HBeXB substituent effects in solution. Titrations were conducted in C_6D_6 with tetra-*n*-hexylammonium Iodide (THAI) as the guest to ensure all complexes remained in solution. The addition of THAI resulted in downfield shifts for nearly all of the ^{1}H NMR signals on the receptors, (except for a center core singlet of

nHBeXB). Bindfit[174] was used to fit the changes in the ^{1}H NMR signals to a 1:1 binding model. Iterative and simultaneous refinement of multiple isotherms provided association constants (K_a) for all scaffolds (Table 4).

Table 4. Measured association constants and binding energies for **G3XB** derivatives with THA iodide.

Host	K_a (M^{-1})	$\Delta G_{binding}$ (kcal mol^{-1})
G3XB	420	-3.6
G3HB	30	-2.1
nHBeXB	10	-1.5
2F-G3XB	170	-3.0
2H-G3XB	70	-2.5
2Me-G3XB	50	-2.3
2*t*Bu-G3XB	50	-2.3
Cl-G3XB	330	-3.4
F-G3XB	250	-3.3
H-G3XB	190	-3.1
Me-G3XB	170	-3.0

The K_a values are reported as the average of three titration experiments. All titrations were performed in C_6D_6; Two significant figures are reported and errors are estimated at 10%. Tetra-*n*-hexylammonium iodide was used and titrations were performed at 25 ˚C. Bindfit was used to fit changes in chemical shift to a stepwise 1:1 host-guest binding model. The free energy of binding ($\Delta G_{binding}$) was calculated from the association constant.

3.3.3.2 Role of intramolecular HBing on anion binding

G3XB (all R groups -CF_3) had the strongest binding (420 M^{-1}) which was nearly 14 times greater than the isostructural no XB control (**G3HB**) (30 M^{-1}). The substantially lower binding affinity of **G3HB** suggests that the amine doesn't significantly HB to the iodide guest; the amine of the **G3XB** derivatives largely forms intramolecular HBs with the iodine XB donors. The considerable influence of the intramolecular N–H···I HBs is evident when comparing **G3XB** to the control lacking an amine (**nHBeXB**). **nHBeXB** exhibited very weak binding in solution with a K_a = 10 M^{-1}. The nearly 50-fold difference in K_a between **G3XB** and **nHBeXB** demonstrates the striking

impact that a weak intramolecular N–H···I HB can have on receptor performance. The HBeXB enhancement is far greater than our original HBeXB study using a dicationic receptor where only a 9-fold increase was observed.[28] The greater HBeXB influence in this study could be due to the iodine XB donors of **G3XB** being more electron rich (i.e. neutral receptor) than the iodopyridinium donors previously evaluated—allowing for stronger HBeXB and greater preorganization. It could also be attributed to solvent effects as the two studies were conducted in significantly different media (C_6D_6 vs. 60% CD_3NO_2/40% $CDCl_3$). These binding studies highlight that the central amine interacts minimally with the iodide and largely operates as an intramolecular HB donor to the iodine XB donor atoms.

3.3.3.3 2R_2-G3XB substituent effects on anion binding

The **2R_2-G3XB** (R_2 = CF_3, F, H, Me, *t*Bu) series of molecules were used to quantify how substituents *para* to the XB donor influence the HBeXB. Varying these substituents resulted in association constants for THAI ranging from 50 M^{-1} to 420 M^{-1} (Table 4). Having a stronger electron withdrawing group *para* to the XB donor increases the XB strength and for this series of compounds this generally holds true. **G3XB** (**R_2** = CF_3) maintained the greatest affinity followed by **2F-G3XB** with a K_a = 170 M^{-1}, which is 60% less than **G3XB**. **2H-G3XB** binding was further diminished to a K_a of 70 M^{-1}. The most electron rich **2*t*Bu-G3XB** exhibited similar iodide binding with the **2Me-G3XB** derivative (50 vs 50 M^{-1}, respectively). Nevertheless, the general trend in substituent effects matches previous studies for XB derivatives.[163-167]

3.3.3.4 R_1-G3XB substituent effects on anion binding

While studies have evaluated the influence of functional groups on the XB and HB independently none have considered their interplay. Here binding studies of **R_1-G3XB** derivatives

represent the first experimental consideration of this. The binding data for **R_1-G3XB** derivatives (**R_1** = CF_3, Cl, F, H, Me) highlights that stronger intramolecular HBing enhances the XB receptor binding affinity. By increasing the electron withdrawing capacity of the substituent *para* to the amine (strengthening the HB donor) from a Me group to a CF_3 group the binding increased 2.5-fold. **Me-G3XB**, the most electron rich of the **R_1-G3XB** series, had the lowest association constant (170 M^{-1}), while the most electron deficient **G3XB** had the highest (420 M^{-1}). This result reveals an effective way to increase the overall XB binding ability in a system which includes an intramolecular HB to XB donor—electronically tuning the HB with substituents rather than the XB.

3.3.3.5 R_1 and R_2 Interplay: Receptor performance

As noted above, the receptor performance can be modulated by either changing the substituents *para* to the XB donor or *para* to the HB donor. To further quantify the substituent effects on binding $\Delta G_{binding}$ was calculated for each receptor. The binding energy for **$2R_2$-G3XB** derivatives can be tuned by 1.3 kcal mol^{-1} simply by changing out the two CF_3 groups to Me groups on the XBing rings. Intriguingly, altering only one substituent (from CF_3 to Me) on the center ring can elicit a 0.6 kcal mol^{-1} change. This suggests that binding can be modified by a comparable amount with a smaller structural change to the receptor. These small energetic changes can have large implications, as previously demonstrated in a study of XB catalyst transition state binding.[90]

3.3.3.6 R_1 and R_2 Interplay: Linear Free Energy Relationships

Linear free energy relationships (LFERs) are gaining importance in understanding substituent effects on noncovalent interactions like HBing, XBing, chalcogen bonding, cation-π and π-π.[157-162,175-180] There are surprisingly few studies that have experimentally examined substituent effects by evaluating LFERs on the XB.[163-167] Taylor and coworkers adeptly used this approach to evaluate the XB between *para*-substituted tetrafluoro-iodobenzene and tributylphosphine oxide (Figure 18a). These studies showed the best correlation of association constants with the σ_{meta} parameter ($R^2(\sigma_m)$ = 0.94 vs σ_{para} $R^2(\sigma_p)$ = 0.82) which they attributed to inductive/field effects being more dominant.[163] In contrast, Diederich[164] and Franz[167] interestingly reported strong correlation for the σ_{para} parameters. Diederich evaluated XBing between 4-R-iodoethynylbenzene and quinuclidine ($R^2(\sigma_p)$ = 0.97 vs $R^2(\sigma_m)$ = 0.82, Figure 18b). The strong correlation with the σ_{para} parameter in this case indicated that substituents largely influence the halogen donor through resonance in this conjugated system. Finally, Erdélyi[165] and Stilinović[166] investigated substituent effects on XB acceptors. In Erdélyi's case, the three-center $[N{-}I{-}N]^+$ XB (Figure 18c) exhibited linear correlation (R^2 = 0.97) between the calculated natural atomic populations with σ_{para} parameters. In all cases, substituent effects were shown to have a significant influence on XBing.

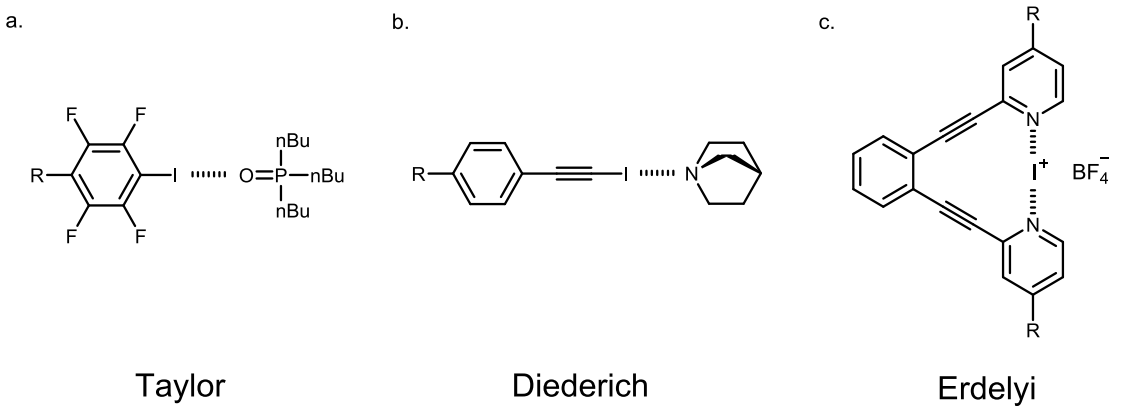

Figure 18. Select previous LFER studies on halogen bonding.

Nevertheless, each of these examples showed great correlation with different parameters for their LFERs. Despite these important studies, there are no experimental examples analyzing substituent effects on adjacent noncovalent interactions. Supramolecular contacts don't occur in an isolated environment and as such, it is essential to understand whether traditional substituent effects hold true in these situations. Herein, we evaluated substituent effects on the HBeXB and used LFERs to establish whether changing the electronics of the HB donor has the same influence on the overall binding as changing the electronics of the XB donor.

Our initial evaluation of LFERs compared the bidentate ESP values ($V_{s,max}$) of receptors with experimental ΔG values from titration studies. While XBing is known to encompass both covalent and electrostatic components, plots of ESP vs ΔG can establish the degree of electrostatic contribution in these particular HBeXB complexes. The following results demonstrate that in this system, the substituent influence is largely electrostatic in nature.

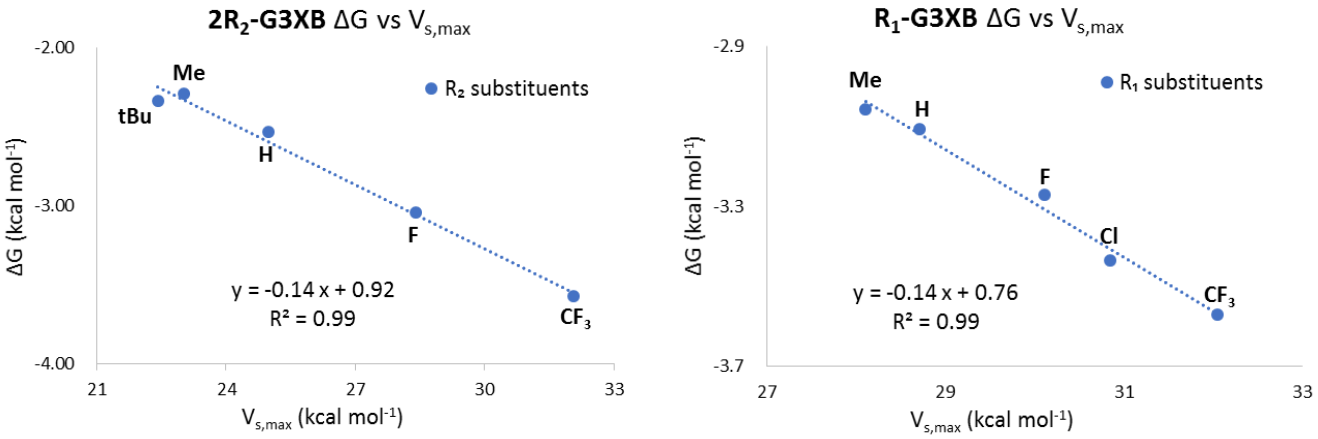

Figure 19. Non-normalized plots of the ESPs and binding energies for **$2R_2$-G3XB** (left) and **R_1-G3XB** (right)

The **$2R_2$-G3XB** derivatives show strong correlation between the electrostatics ($V_{s,max}$) of the XB donor and the iodide binding in solution. The non-normalized plots (Figure 19, left) are linear for the **$2R_2$-G3XB** derivatives (R^2 = 0.99). Since the modification was directly on the XBing ring,

this finding was expected given previous LFER studies on the XB.[163]

In contrast, the **R_1-G3XB** derivatives provided original insight into how the amine HB donor augments the XB donor strength. The LFER analysis for the **R_1-G3XB** series certainly suggests an electrostatic origin (Figure 19, right) as the plots are again linear (R^2 = 0.99). Collectively the ESP vs ΔG plots indicates that the HBeXB iodide binding of the **G3XB** derivatives is largely governed by electrostatics and that ESP maps accurately model the influence of intramolecular HBs on the XBs in this system.

We extended our LFER analysis by evaluating the correlation between our experimental association constants and Hammett parameters (σ_{meta} and σ_{para}). While Hammett parameters were originally used to model the ionization reaction of benzoic acid, they have been increasingly used to study noncovalent interactions.[140-145] We used Hammett parameters to analyze possible inductive (or field effects as proposed by Wheeler and Houk[181,182]) and resonance effects on the HBeXB receptor binding—an approach recently used by Hunter to effectively assess HB cooperativity.[183]

Normalized association constants ($\log(K_R/K_H)$) and the corresponding substituent parameters (**σ**) were fit using the Hammett equation shown below. **ρ** represents the slope.

$$\log(K_R/K_H) = \rho\sigma$$

The **R_1-G3XB** derivatives show a more linear correlation with the σ_{para} parameter (R^2 (σ_p) = 0.93) than with the σ_{meta} ($R^2(\sigma_m)$ = 0.87), indicating resonance effects are more important than inductive effects on the HB donor of the HBeXB (Figure 20, left). Electron withdrawing **R_1**

substituents enhance the amine donor strength, thus leading to stronger intramolecular N–H···I HBing. A stronger HB in turn makes the XB donor more electron deficient. Thus, the resonance of the **R_1** substituent work in concert with both the HB and XB donors, resulting in a linear correlation with the σ_{para} parameters.

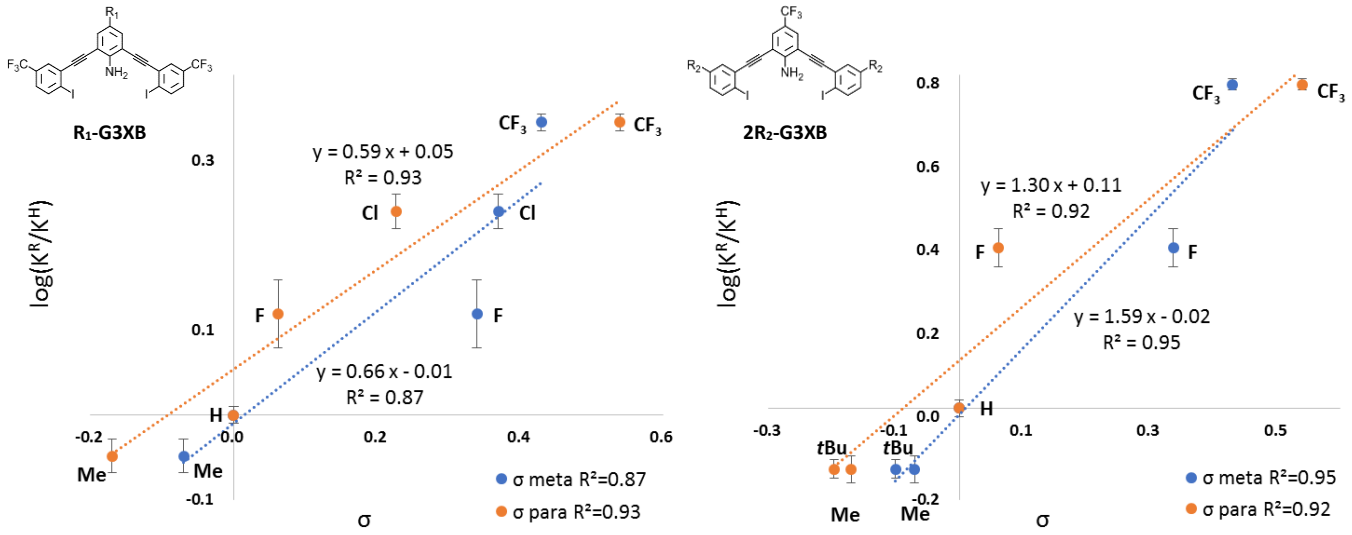

Figure 20. Normalized Hammett plots of K values of **R_1-G3XB** (left) and **$2R_2$-G3XB** (right) with σ_{meta} (blue) and σ_{para} (orange).

Curiously, normalized Hammett plots of K_a values for **$2R_2$-G3XB** resulted in *similar* linear fits with both the σ_{meta} and σ_{para} parameters (Figure 20, right). The fit with the σ_{meta} parameters is R^2 (σ_{meta}) = 0.95 while the fit with the σ_{para} parameters is R^2 (σ_{para}) = 0.92, implying that inductive effects may play a modestly more important role on substituent effects. As noted above, substituent effects on the XB have been found to be attributed to either inductive[163] or π-resonance effects[164,165]. It is atypical in LFER studies to obtain linear fits for both the σ_{para} and the σ_{meta} parameters simultaneously.[184] Unlike previous LFER studies, in this case there are two noncovalent interactions involved (N–H···I HBing and C–I···I^- XBing). The halogen here functions as both a XB donor and a HB acceptor. The electronics of the **R_2** substituents can have competing

influences on the noncovalent interactions. Thus, increasing the electron density on the halogen should weaken the XB donor but strengthen the intramolecular HBs with the amine. This competing effect produces good correlation with both the σ_{para} and the σ_{meta} parameters. Thus, when competing electronic influences are present, selecting an appropriate *para* substituent for a XB donor could be tricky if relying on Hammett parameters. We also looked for linear correlations between the association constants and other parameters including Taft's σ_I, σ_R[143], sEDA and pEDA.[185] However, no linear correlations were obtained (see Experimental section). The combined LFERs herein, suggest that choosing an appropriate substituent (**R_1**) to tune *adjacent* noncovalent interactions could complement the common strategy of directly altering the electronics of the XB donor (**R_2**) to modulate binding.

Classically, the slope ρ in the Hammett equation describes the susceptibility of the reaction to substituents. While studying noncovalent interactions, ρ provides a measure of how sensitive the interaction is to substituent effects as compared to the ionization of benzoic acid. The ρ value of the **R_1-G3XB** Hammett plot (ρR_1 = 0.59) is between 0 and 1 indicating that the binding is sensitive to electronics (although not as much as the ionization of benzoic acid). More importantly, the ρ value for **R_1-G3XB** can be compared to **2R_2-G3XB** (statistically taking into consideration the number of substituents); thereby, determining quantitatively which substituent position has a greater influence on receptor performance. There are two **R_2** groups affecting the anion binding per receptor, so half the ρ value was used for comparison. The 1/2ρ value for **R_2-G3XB** ($1/2\rho R_2$ = 0.79) is only modestly higher than the one obtained for the **R_1-G3XB** series (ρR_1 = 0.59). This is notable as the **R_1** substituents are much further from the binding site and maintain minimal through bond electronic influence on the XB. The data here indicate that altering the electronics

of an HB donor within the context of the HBeXB can have a similar effect on XB strength as traditional substituent effects.

For a more thorough picture of how resonance contributes to the interaction, multivariable linear regression of the normalized association constants ($\log(K_r/K_H)$) with the field (F) and resonance (R) parameters in the Swain–Lupton equation[139] were conducted in Matlab. The percent resonance contribution (%R) in this equation affords a simple and meaningful way to assess the relative importance of field (F) and resonance (R) effects.

$$\log(K_X/K_H) = \rho_f F + \rho_r R + i$$

$$\%R = \rho_r/(\rho_f + \rho_r) \times 100$$

Table 5. Field and Resonance Fitting

	ρ_f	ρ_r	R^2	%R
$2R_2$-G3XB	0.95	0.90	0.99	49%
R_1-G3XB	0.37	0.44	0.99	54%

As shown in Table 5, %R = 49 % for **$2R_2$-G3XB** which suggests that the binding is slightly more governed by inductive/field effects from the substituents. In contrast, the substituent effects in **R_1-G3XB** are more dependent on resonance where %R = 54 %. However, it should be noted that the Hammett studies employed used relatively few parameters which limits the statistical strength of this Swain Lupton analysis. The %R for **$2R_2$-G3XB** reveals the similarity in the impacts of resonance and inductive/field effects on the XB donor ring's **R_2** substituents. This similarity aligns with the **$2R_2$-G3XB** Hammett plots, which exhibit linear relationships with both the σ_{para} and σ_{meta} parameters due to the competing influences from the electronics of the **R_2**.

3.3.4 Crystal Structures

3.3.4.1 HBeXB Impact on Solid-State Features

Crystal structures of several receptors were obtained to further evaluate substituent effects. While previous studies have evaluated the HBeXB in the solid-state,[28,66,31,35] the HBeXB bidentate receptors reported here are the first structures considered the structures within the context of substituent effects.

The initial solid-state assessment of the neutral receptors focused on three species (**G3XB**, **G3HB**, **nHBeXB**) to identify the influence of the HBeXB. Previous generations were charged and thus in the solid state could be more influenced by induced fit binding. This series further confirms that the amine HBs promote a bidentate conformation.

As shown in Figure 21 (left), the **G3XB** structure displays convergent bidentate XBing conformations promoted by the intramolecular HBing with N-H···I distances and angles of 3.12(4) Å, 163(3)° and 3.20(3) Å, 165(4)°. **G3XB** crystalized in the monoclinic space group *P*21/*c* with a single molecule in the asymmetric unit. The XB donors are directed towards an iodine atom of an adjacent molecule. One of the iodine atoms forms a XB with C-I···I distances and angles of 3.9379(6) and 167.38(11)° (R_{II}=0.97).[186] The other halogen while directed at an iodine, is too far to XB with a C-I···I distance of 4.2007(11) and 173.56(9)°.

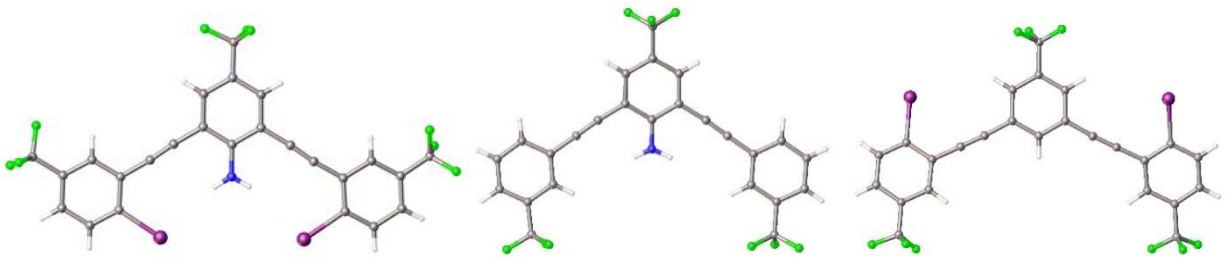

Figure 21. Crystal structures of **G3XB** molecule (left), **G3HB** (middle)*, and **nHBeXB** (right) highlighting the importance of the intramolecular HB to produce the bidentate conformation. *Representative example from the orthorhombic polymorph.

Notably, the exchange of the central amine group for a CH proton results in a molecule that adopts the W conformation (Figure 21 right), the form energetically favoured in the computational analysis. **nHBeXB** crystalizes in *P*21/*c* with a single molecule in the asymmetric unit. One of the iodine atoms forms a XB with a symmetrically equivalent species on an adjacent molecule (C-I···I of 160.91(16)° and 3.8065(6) Å (R_{II}=0.93)). The other iodine has Type II halogen contacts[187] with disordered fluorine atoms of an adjacent molecule, with contacts that are less than the sum of the Van der Waals radii.

Two crystal structures were obtained of **G3HB**, a triclinic and orthorhombic polymorph. Neither structure adopted a bidentate conformation. The triclinic (*P*-1) form has a single molecule in the asymmetric unit, and does not adopt one of the planar forms (i.e. bidentate, S, or W). The central amine does not play a significant role in the packing. The orthorhombic (*Fdd*2) structure of **G3HB** has two molecules in the asymmetric unit. While each molecule adopts a W conformation, one molecule is much less planar than the other. The distortion of one species in the asymmetric unit may come from the arms having to deflect to maintain a head-to-tail HBing chain.

The systematic changes of XB donors and HB donors in the **G3XB**, **G3HB**, **nHBeXB** series highlights that the N–H···I intramolecular HBing plays a key role in the receptor adopting the bidentate conformation. This is further demonstrated in the structures of derivatives containing different substituents on the flanking iodine containing arms.

3.3.4.2 2R_2-G3XB in the Solid State

To further consider the interplay between the XB and HB we obtained crystal structures of species that modulate the electron density on the XB donating arms. Altering the functional group

para to the iodine donor permitted us to evaluate two different features related to HBeXB within this system. First, the ability of the N–H···I HBing to bias the bidentate conformation was evaluated. Second, the first solid state evaluation of substituent effects with relation to the HB acceptor capacity of iodine donors was investigated.

Despite great efforts, only **G3XB** and **2H-G3XB** were crystallized from the **2R$_2$-G3XB** series. As expected, each of the molecules in this series maintains intramolecular N–H···I HBs and adopt bidentate conformations. **2H-G3XB** crystalizes in the monoclinic *P*21 space group with two molecules in the unit cell. The **2H-G3XB** molecules have HB parameters of 3.16(4)Å 164(4)°, 3.00(7)Å, 170(7)°, 3.16(7)Å 165(5)°, and 2.99(6)Å 169(6)°, that are shorter than **G3XB.**

The planarity of the molecules did not follow the expected trend. For example, despite having shorter HB contacts **2H-G3XB** was more distorted than **G3XB**. Angles between flanking rings and central rings of the two unique **2H-G3XB** species were 1.68° and 15.54° for one receptor and for the other was 4.66° and 17.53°. A partial explanation for this is that the two structures have different long range packing features (see Experimental section Fig. S158).

The angle formed by the centroids of the three rings (i.e. flanking-core-flanking angle) provides another structural measurement that indicates HBing strength between the amine hydrogen and more electron rich iodine atoms. For example, a smaller angle would suggest a stronger attraction distorting the alkyne bonds linking the core to the arms. Comparing **G3XB**, and **2H-G3XB**, the increasing electron density on the iodine led to greater distortion with angles of 118.94° for **G3XB** vs 117.18° for **2H-G3XB**.

3.3.4.3 R$_1$-G3XB in the Solid State

Several **R$_1$-G3XB** derivatives (**Me-G3XB**, **F-G3XB**, and **G3XB**) that modulate the electron

density of the central amine were also crystalized to evaluate the effects that these substituents have on the solid-state structures.

Similar to the **2R$_2$-G3XB** series, initial analysis compared the HB distances. **G3XB** maintained the shortest N–H···I HB contacts (see above for distances and angles) as suggested from the electron withdrawing nature of the CF_3 group. In contrast, the longest N–H···I HB contacts came from the **Me-G3XB** derivative. This methyl species crystalized in the monoclinic space group $P2_1/c$ with a single receptor in the asymmetric unit that adopts the bidentate conformation. The N–H···I HB contacts were 3.16(6)Å, 154(7)°, and 3.48(5)Å, 148(5)°. The longer HB contacts are attributed to the electron donating nature of the methyl group.

Unfortunately, **F-G3XB** adopted the S conformation making comparisons across the series irrelevant. However, comparison of the bidendate **G3XB** and **Me-G3XB** suggests that the electronics of the aniline core may have some structural impact on the receptor. For example, the weaker HBs of **Me-G3XB** resulted in a less planar receptor. For **Me-G3XB** the angles between the planes of the core and flanking arms were 5.29° and 8.75° as compared to **G3XB** which was 1.06° and 8.59°. Another parameter evaluated was the angle formed by the centroids of the three rings. For the electron rich **Me-G3XB** this angle is 123.16° whereas for **G3XB** the angle is 118.94°. This suggests that the amine donors are stronger in **G3XB** causing a slight distortion due to the stronger HBs between the amine hydrogen atoms and the iodine atoms.

3.3.4.4 G3XB and Derivatives as Cocrystal-Salts

To probe receptor binding in the solid-state the various derivatives were crystalized with tetraalkylammonium chloride salts. Despite our efforts only four successful cocrystal-salts were obtained (**G3XB·Cl^{-1}**, **2H-G3XB·Cl^{-1}**, **2Me-G3XB·Cl^{-1}**, and **H-G3XB·Cl^{-1}**). Unfortunately, the different

tetraalkylammonium salts present and the crystal packing differences, made comparisons difficult (see Experimental section). Despite this, all the structures maintain a bidentate conformation. Additionally, the XB contacts are quite strong with reduction ratios ≤0.85.

3.4 Conclusions

In this work, we reported the first LFER studies for substituent effects on the HBeXB interaction. Electrostatic Surface Potentials (ESP) were used to assess the electrostatic contribution to the interaction. A strong correlation between computational ESP values and solution binding data illustrated the electrostatic nature of this cooperative interaction. Hammett plots constructed with iodide association constants for **R_1-G3XB** and **$2R_2$-G3XB** showed that the electronics of both the HB and XB are critically important to the binding. Resonance effects of electron withdrawing **R_1** substituents strengthened both the HB and XB and enhanced the overall HBeXB binding. Electron withdrawing groups of **R_1** substituents generated a more potent HB donor which better polarized the XB and further promoted the bidentate conformation. In contrast, the electronics of the **R_2** substituents had competing effects on the HB and XB. Specifically, electron donating groups *para* to the iodine atoms (**R_2**) decreased the XB donor ability but made the halogen a better HB acceptor. From a design standpoint, this implies that when modulating electron density on the halogen one can enhance the preorganization of a receptor by increasing electron density on the halogen (improved HB acceptor capacity) at the expense of a slightly weakened XB. Our X-ray crystallography studies further demonstrated the role of the HBeXB on preorganizing molecular structure. Combined, the solution experiments, computations and crystallography provided a rare example of how substituents affect proximal noncovalent interactions. The results from this study also provides important insights for the design of

receptors or catalysts—altering remote substituents which electronically influence adjacent noncovalent interactions (instead of direct *para* substitution) can have similar impact to traditional substituent effects and should be considered for molecular design.

Bridge to Chapter 4:

Chapter 3 described the important role of the intramolecular HBing between amine and iodine XB donor on the anion binding. However, as -OH or -NH HB donors have certain limitations in biochemical contexts, like their pH sensitivity and chemical reactivity (e.g. oxidation and glycosylation). It led us to consider pushing the boundaries of the HBeXB designs. In Chapter 4, we investigate the effects of C–H HBs to iodine atoms and their impact on receptor performance in anion binding.

Chapter 4:

Anion binding using non-traditional Hydrogen Bond enhanced Halogen Bonds

4.1 Preface

This chapter includes parts of published work in Chemical Science (2022, 13(37): 11156-11162.) which was co-authored by Daniel A. Decato, Madeleine R. Boller and Prof. Orion B. Berryman. Daniel Decato, first author, conceptualized the project, conducted synthesis and characterization, computational and solid-state studies, and wrote the paper. Madeleine R. Boller aided in synthesis. Prof. Orion B. Berryman conceptualized the project, supervised the investigation and provided editorial assistance during manuscript preparation. Jiyu Sun, synthesized the molecules and conducted the solution studies.

4.2 Non-traditional C–H Hydrogen Bonds enhanced Halogen Bonds (HBeXBs)

4.2.1 Design Considerations

Halogen Bonds enhanced by Hydrogen Bonds (HBeXBs) have been demonstrated to significantly increase anion binding by an order of magnitude. The influence of substituents effect on this interaction has also been quantified in a fundamental solution study, as detailed in Chapter 3. However, current studies have primarily focused on using "traditional" -OH or -NH HB donors which may exhibit pH sensitivity, thereby restricting their applicability in certain situations.

While HBs involving C-H donors are generally weaker than those involving O-H and N-H donors, they exhibit remarkable effects in various chemical systems. Notably, C-H HBs play a crucial role in stabilizing hydrophobic interactions, leading to the formation of hydrophobic pockets in proteins that are essential for ligand binding and enzymatic activity. Moreover, C-H HBs are more stable and preferred over polar interactions (HBs involving O-H and N-H donors) in lipid bilayers and hydrophobic regions of biomolecules. Given these unique properties and the lack of comprehensive studies, there is a compelling need to explore whether they can function similarly to the previously studied N-H donors in preorganizing the receptor and enhancing anion binding.

To test this, a set of four bidentate halogen bond receptors was designed, all featuring a

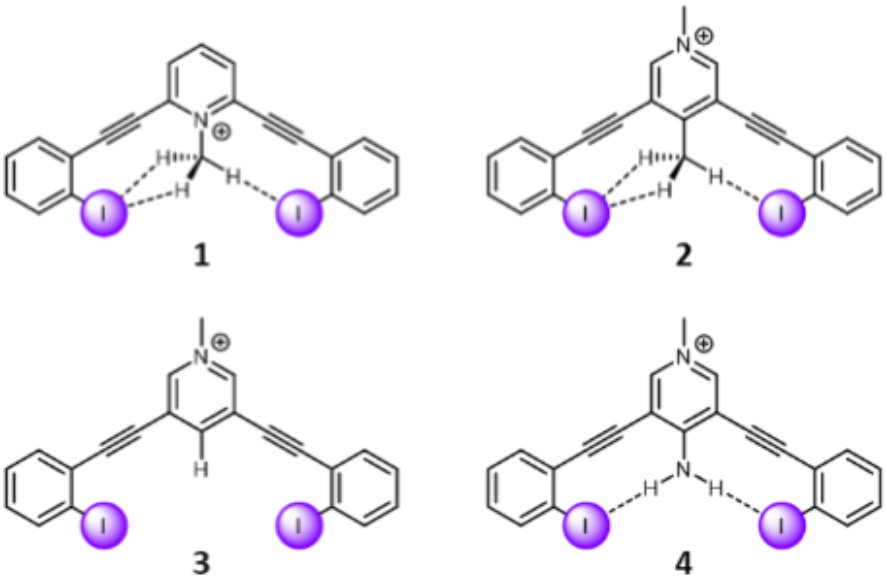

Figure 22.The receptors designed to evaluate C–H “non-traditional” HBeXB.

bisethynyl pyridinium core and flanking benzene arms (Figure 22). Each receptor's core was subjected to different substitutions, resulting in two receptors capable of forming C-H hydrogen bond enhanced halogen bonds (HBeXBs) denoted as **1** and **2**, a proto-control receptor denoted as **3**, and an amine control receptor forming NH_2 HBeXB denoted as **4**. The pyridinium core of these receptors served multiple purposes: it acted as an electron-withdrawing group to enhance

the strength of the XB donor, it generated potent C-H HB donors in **1** and **2**, and it ensured the solid-state evaluations.

In receptor **1**, the N-methylpyridinium group was positioned toward the receptor binding pocket, enabling C-H HBing to the XB donors in the bidentate conformation. It was hypothesized that receptor **1** would exhibit stronger XBing than **2** or **3** due to the location of the pyridinium group, which would have a greater through-bond and through-space effect on the XB.

In receptors **2** and **3**, the pyridinium methyl functionality was placed on the backside of the receptor, away from the binding pocket. Receptor **2** had a methyl group positioned para to the pyridinium nitrogen, directed into the binding pocket to assess C-H HBing to the XB donors. Scaffold **3** served as a control molecule for **2**, where the methyl group was replaced with a hydrogen atom.

Receptor **4** shared structural similarities with receptors **2** and **3**, with the pyridinium methyl group directed away from the pocket. However, it included an internally directed -NH_2 group, serving as a benchmark for C-H HBeXB interactions.

4.2.2 Synthesis of HBeXB receptors

The synthesis of C-H HBeXB receptors is outlined in Scheme 3. Bis-ethynyl pyridinium core was synthesized by Sonogashira cross-coupling dibromo pyridinium core with trimethylsilylacetylene followed by removal of the trimethylsilyl protecting groups with

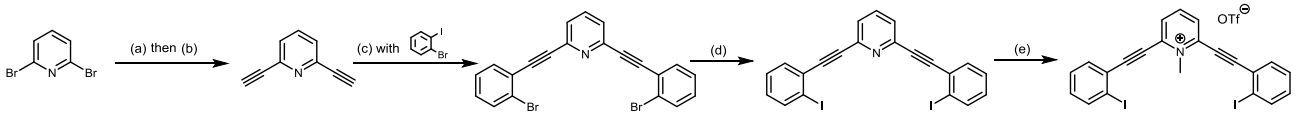

Scheme 3. Synthesis pathways of C-H HBeXB receptor **1** (top) and controls **2**, **3** and **4** (bottom). Reagents and conditions: (a) TMS-acetylene, $Pd(PPh_3)_2Cl_2$, Cu(I)I, DIPEA, DMF, overnight, N_2, 80˚C, ; (b) K_2CO_3, MeOH/DCM(1:1 v/v), 4 hours, rt. (c) 4-bromo-3-iodo-R_2-benzene, $Pd(PPh_3)_2Cl_2$, Cu(I)I, DIPEA, DMF, overnight, N_2, rt. (d) NaI, Cu(I)I, *trans-N,N*-dimethylcyclohexane-1,2-diamine, 1,4-dioxane, microwave reactor, 12 hours, 150˚C; (e) Methyl trifluoromethanesulfonate, DCM, overnight, rt.

potassium carbonate. Precursor scaffolds containing bromine were synthesized by Sonogashira cross coupling bis-ethynyl pyridinium core at the iodo-functionality of 1-bromo-2-iodobenzene. The iodine containing scaffolds were obtained by microwave assisted halogen exchange. Methylation of the iodine containing scaffolds with methyl trifluoromethanesulfonate produced the final charge-assisted HBeXB receptors. The complete experimental procedures can be found in the Experimental section.

4.3 Solution Binding Studies

To quantify the effectiveness of C-H HBeXBs, ^{1}H NMR titrations was initially carried out by Daniel A. Decato. However, minimal shifting of ^{1}H resonances were observed upon introduction of anions in various solvent systems (DMSO-d_6, Acetonitrile-d_3, etc.) Hence, we employed UV-Vis spectroscopic titrations of HBeXB receptors **1**–**4**. Considering both the solubilities and changes of absorbance, the solvent mixture used in all titrations is made by 90% spectra grade Tetrahydrofuran, 9.9% spectra grade Dimethyl sulfoxide, and 0.1% deionized water.†† Tetra-n-butylammonium bromide (TBABr) salt was chosen as anion guest due to the measureable

†† 0.1% deionized water is used to ensure a constant amount of water is present in all titration experiments.

changes of absorbance in THF/DMSO/H_2O (90/9.9/0.1) solvent mixture at 20°C.

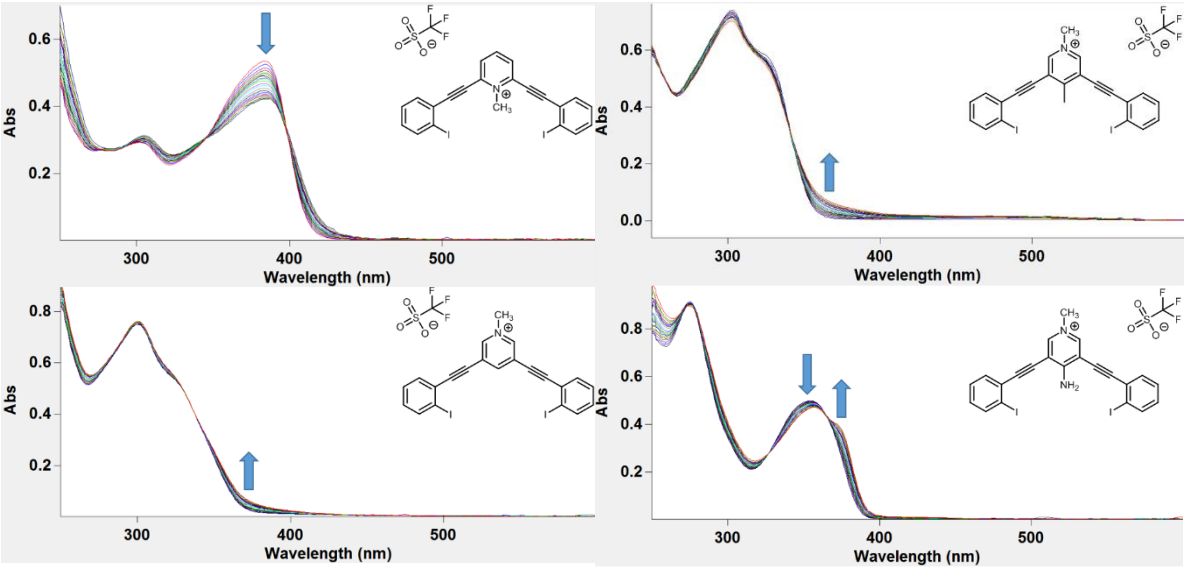

Figure 23. Uv-Vis Absorption titration spectra of **1-4** with TBABr in THF-DMSO-H_2O solvent mixture at 20 °C. Top left: **1** with TBABr; top right: **2** with TBABr; bottom left: **3** with TBABr; bottom right: **4** with TBABr.

Upon adding TBABr to the free host solution of **1**, the absorbance band around 385 nm exhibited a hypochromic shift (Figure 23 top left). In contrast, the addition of TBABr to receptor **2** (Figure 23 top right) and **3** (Figure 23 bottom left) resulted in hyperchromic shifts of absorbance around 365 nm and 375 nm, respectively. For NH_2 HBeXB control **4**, absorption bands around 375 nm and 350 nm grew and decreased, respectively, upon the addition of TBABr, leading to an isosbestic point around 363 nm (Figure 23 bottom right top left). These spectroscopic changes were analyzed to determine the association constants (K_a) by fitting the absorbance changes to a 1:1 binding model using Bindfit. The measured K_a values were listed in Table 6.

Table 6. Measured association constants for HBeXB receptors with TBA bromide.[a]

Receptor	**1**	**2**	**3**	**4**
K_a (M^{-1})	26000	15000	12000	18000

[a] The K_a values are reported as the average of three titration experiments. Two significant figures are reported and errors are estimated at 10%. Tetra-n-hexylammonium bromide was used and titrations were performed in 90% THF/9.9% DMSO/0.1% deionized H_2O at 20 ˚C. Bindfit was used

to fit changes in chemical shift to a stepwise 1:1 host-guest binding model.

Specifically, receptor **1** exhibited the strongest binding (26,000 M^{-1}). When comparing the K_a values for **2** and **3**, there was a slight difference in receptor performance, with **2** having a slightly higher association constant than **3** (15,000 M^{-1} vs. 12,000 M^{-1}), indicating that C-H HBeXB improved binding. This observation aligns with the theoretical evaluations and previous HBeXB papers, suggesting a combination of preorganization and XB enhancement. In addition, receptor **4**, with the amine HB donor, exhibited stronger binding (18,000 M^{-1}) than **2** and **3**.

4.4 Conclusions

A series of XB anion receptors was synthesized to conduct a systematic assessment of C-H HBeXB. Consistent with the computational and solid-state analysis, the anion binding studies in the solution phase indicate that C-H HBing to iodine atoms can enhance the performance of XB receptors. The positioning of the charge is a crucial factor—placing the charge close to the binding pocket can yield C-H HBeXB receptors that surpass traditional amine HB donors, where the charge is more distant. On the other hand, weaker C-H donors might represent the limit to this polarization-enhanced noncovalent interaction.

Chapter 5:

Concluding marks and Future work

5.1 Conclusion

We have presented three generations of bis(ethynylpyridinium)-fluoroaniline (**G2XB**), and bis(arylethynyl)-trifluoromethylaniline (**G3XB**) receptors and non-traditional C-H HBeXB receptors designed for anion binding studies. Solvatochromism investigations with the **G2XB** molecules revealed the charge transfer nature of these receptors. Additionally, the charged **G2XB** demonstrated selective sensing for iodide, making them potential candidates for developing colorimetric and fluorescent anion sensors (Chapter 2). To gain a deeper understanding of HBeXB interaction, we further developed third-generation arylethynyl scaffolds (**G3XB** derivatives) using a modular synthetic pathway which allowed systematic evaluation of substituent effects on both the HB and XB donors. Our *in silico*, solution and solid state analysis indicated that modifying distant substituents, which impact nearby noncovalent interactions, should be taken into account as a viable alternative to conventional *para* substitution substituent effects for molecular design (Chapter 3). To further explore the limits of the HBeXB interaction, we designed and evaluated a series of HBeXB receptors. The anion binding studies in solution confirmed the ability of C–H HBs to iodine atoms, which facilitated preorganization of the molecular structure and enhancement of XBs (Chapter 4).

I take great pride in stating that the research presented in this dissertation has yielded significant fundamental discoveries with far-reaching implications. These findings will potentially inspire the development of new generations of XB based anion receptors, offering robust

alternatives to the traditional XB or HB approaches in the field of supramolecular chemistry. At the same time, I also believe fundamental studies should lead to applications. In our lab, we have successfully showcased the first application of HBeXB in organocatalysis. Currently, we are also conducting studies on HBeXB anion-induced high-order helicates. However, there is still a significant dearth of research on the application of HBeXB in anion sensing, self-assembly, catalysis, and ion transport, which represents critical areas requiring further exploration.

To achieve this objective, there are still unresolved issues to be taken into consideration. For example, the applications of the XB have predominantly been restricted to reactions in organic solvents, with only very few reports present in the literature that show XB interactions in water or in aqueous media.[21,68,72,84-86,115,188] Nonetheless, XBs have shown great potential for use in aqueous environments. Unlike HBs, which are very sensitive to solvent polarity, XBs are not as disrupted even by polar alcohol solvents.[111] Furthermore, the pH-independence of XBs provides significant benefits for the binding of anions in aqueous media.[67,72] Hence, the incorporation of HBeXB interactions into competitive aqueous media could be an important step towards the design of functional anion receptor molecules with real world applications. The limitation nowdays likely stems from the scarce aqueous solubility of common XB donor frameworks, such as the XB receptors designed by Taylor, which contains polyfluoroaromatic moieties.[71] While some limited examples have demonstrated promising abilities of XB-based host systems to function effectively for anion recognition[21,68,72] and anion sensing[84-86] in aqueous solvents, the performance of HBeXB interaction in aqueous environments remains largely unknown.

A pivotal challenge lies in devising strategies to enhance the water solubility of HBeXB receptors through thoughtful and tailored design approaches. Overcoming this challenge is

crucial for unlocking the full potential of XB interactions in aqueous media, paving the way for their broader application in the realm of anion recognition and sensing. Commonly utilized approaches to enhance the water solubility of organic compounds encompass incorporating hydrophilic functional groups, adjusting pH, forming inclusion complexes, and incorporating water-soluble tags (e.g., PEGylation). Ongoing investigations aim to ascertain the effectiveness of augmenting the water solubility of HBeXB receptors, as well as to evaluate how the design impacts intramolecular HBing and the broader spectrum of HBeXB interactions.

5.2 Future work

5.2.1 Multi-charged assisted HBeXB receptors

Based on our investigations of **G2XB** in previous studies, we discovered that introducing a positive charge to these molecules significantly enhances their affinity for anion binding. This improvement is a result of the combined effects of charge assistance and stronger polarization of the C-X halogen bond. Furthermore, higher positive charges also lead to increased solubility of the molecules in polar solvents.

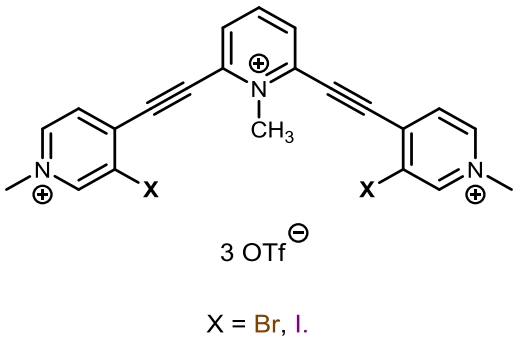

X = Br, I.

Figure 24. ChemDraw representation of triple-charged HBeXB receptor.

By making slight adjustments to the previous design, we can utilize a charged-assisted methyl pyridinium as the C-H HB donor and a flanking iodopyridinium arm as the XB donor. This modification allows us to create a triple-charged HBeXB receptor (Figure 24). Preliminary results

of crude reaction material have shown that this receptor (X = Br) can achieve solubility in 100% D_2O at NMR concentrations at room temperature. Quantification of the strength of XB interactions between the developed triple-charged HBeXB receptors and both anionic and neutral guests will be conducted in aqueous solution via NMR or UV-Vis titration methods. The binding investigations with different halides (Cl^-, Br^-, I^-.) and oxoanions (NO_3^-, HSO_4^-, $H_2PO_4^-$ and ReO_4^-) guests will be conducted to test the size selectivity of the triple-charged HBeXB receptors. Once reasonable binding affinity was observed, catalytic screenings are planned to delve into the prospective application of this HBeXB receptor as a catalyst for halide abstraction type reactions. As an illustration, we will initiate the Ritter-type solvolysis of benzhydryl bromide to serve as the benchmark reaction.[91] The degree of conversion to *N*-benzhydryl acetamide will be assessed using ^1H NMR spectroscopy, and achieving a high yield (>90%) will be considered a successful outcome. Additionally, efforts will be made to reduce reaction time and decrease catalyst loading in order to evaluate the reactivity of the catalysts in comparison to existing HB and XB catalysts. Consequently, the advancement of HBeXB catalysts with enhanced water solubility could unveil novel outlooks within the realm of XB-driven organocatalysis.

5.2.2 Halonium HBeXB receptors

Most of the XB receptors discussed above utilize a C-X bond. However, due to the greater polarity of the N-I bond compared to the common C-I bond, and the increased electron deficiency resulting from nitrogen's higher electronegativity during the elongation of the N-I bond, along with the formal positive charge that is generated, a more potent XB can be formed.[189] The study of halonium XB donors were mostly focused on the three-center, four-electron $[N\cdots X\cdots N]^+$ systems.[165,189] For example, [Bis(pyridine)iodine(I)]+ tetrafluoroborate, also known as Barluenga's

reagent, has been widely applied as a catalyst for alkene related reactions such as 1,2-iodofunctionalization[190], iodocyclizations[191] and alcohol oxidations[192], etc.

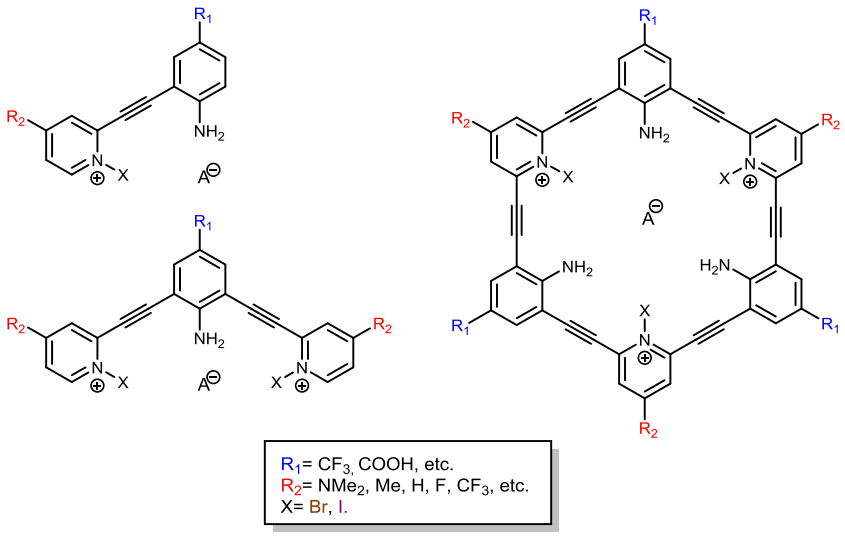

Figure 25. ChemDraw representations of halonium HBeXB receptors.

To the best of our knowledge, few have developed multidentate halonium XB receptors.[193] Along with our prior experience with HBeXB preorganization, we aim to create halonium scaffolds that incorporate HBeXB interactions. This approach will not only enhance the strength of the XBs but also maintain the multidentate scaffolds in rigid, planar conformations. By doing so, we can reduce the entropic cost and improve interactions with the substrate. Additionally, we will explore macrocyclization strategy to further minimize the entropic penalty of binding, ultimately enhancing the affinity of the receptor for the substrate. Comparing to impressive examples of primarily HB macrocycles[194,195], there are only a few reported XB macrocycles[84,86,196]. The unique properties (triple charged, multidentate XB donors) of the proposed HBeXB macrocycles will make them highly impactful and would enrich the exploitation of the XB in various practical applications like catalysis, anion sensing, ion transport, etc.

5.3 Final thoughts

It's worth noting that, it has been only 10 years since the official IUPAC definition was given to the halogen bond. This timeframe is relatively short in the context of scientific progress for the emergence of noteworthy applications. As we continue to deepen our understanding of HBeXB, we will gain valuable insights into the specific requirements of this interaction, making it a novel and potentially powerful variant of XBing in the fields of chemistry and biochemistry.

During the fundemental studies of the HBeXB receptors, more inquiries emerged regarding the factors influencing intramolecular HBeXB strength. What are the most effective geometric arrangements and configurations for achieving strong and selective HBeXB interactions? How do different solvents and environmental conditions (e.g., polarity, temperature) influence the strength and dynamics of HBeXB interactions? Can HBeXB interactions be effectively utilized in aqueous or biological environments, considering the potential challenges related to solvent effects and water interactions? By addressing these inquiries, we stand to gain comprehensive insights that could propel advancements in applications. For instance, unraveling the function of HBeXB interactions in biological systems, including biomolecular recognition or drug-receptor interactions, could guide their targeted utilization. Additionally, understanding how to tailor and apply HBeXB interactions in crafting functional materials like catalysts, sensors, or drug delivery systems is crucial. Moreover, exploring the potential of HBeXB interactions for the innovation of novel therapeutic agents or drug delivery systems holds significant promise.

REFERENCES

1. Smith, D. A. (Ed.). (1994). Modeling the hydrogen bond. *American chemical society: Washington DC*, 1994 ; pp 1–4..
2. Colin, J.-J., Ann. *Chem*. 1814, 91, 251-272.
3. Mulliken, R. S. (1952). Molecular compounds and their spectra. III. The interaction of electron donors and acceptors. *The Journal of Physical Chemistry*, 56(7), 801-822.
4. Hassel, O. (1970). Structural aspects of interatomic charge-transfer bonding. *Science*, 170(3957), 497-502.
5. Brinck, T., Murray, J. S., & Politzer, P. (1992). Surface electrostatic potentials of halogenated methanes as indicators of directional intermolecular interactions. *International Journal of Quantum Chemistry*, 44(S19), 57-64.
6. Murray, J. S., Paulsen, K., & Politzer, P. (1994, April). Molecular surface electrostatic potentials in the analysis of non-hydrogen-bonding noncovalent interactions. *In Proceedings of the Indian Academy of Sciences-Chemical Sciences* (Vol. 106, pp. 267-275). Springer India.
7. Clark, T., Hennemann, M., Murray, J. S., & Politzer, P. (2007). Halogen bonding: The σ-hole: Proceedings of "Modeling interactions in biomolecules II", Prague, September 5th–9th, 2005. *Journal of molecular modeling*, 13, 291-296.
8. Desiraju, G. R., Ho, P. S., Kloo, L., Legon, A. C., Marquardt, R., Metrangolo, P., ... & Rissanen, K. (2013). Definition of the halogen bond (IUPAC Recommendations 2013). *Pure and applied chemistry*, 85(8), 1711-1713.
9. Cavallo, G., Metrangolo, P., Milani, R., Pilati, T., Priimagi, A., Resnati, G., & Terraneo, G. (2016). The halogen bond. *Chemical reviews*, *116*(4), 2478-2601.
10. L. P. Wolters and F. M. Bickelhaupt, ChemistryOpen, 2012, 1, 96-105.
11. Wolters, L. P., & Bickelhaupt, F. M. (2012). Halogen bonding versus hydrogen bonding: a molecular orbital perspective. *ChemistryOpen*, *1*(2), 96-105.
12. Beale, T. M., Chudzinski, M. G., Sarwar, M. G., & Taylor, M. S. (2013). Halogen bonding in solution: thermodynamics and applications. *Chemical Society Reviews*, *42*(4), 1667-1680.
13. Massena, C. J., Wageling, N. B., Decato, D. A., Martin Rodriguez, E., Rose, A. M., & Berryman, O. B. (2016). A Halogen-Bond-Induced Triple Helicate Encapsulates Iodide. *Angewandte Chemie*, *128*(40), 12586-12590.
14. Bulfield, D., & Huber, S. M. (2016). Halogen bonding in organic synthesis and organocatalysis. *Chemistry–A European Journal*, *22*(41), 14434-14450.
15. Caballero, A., Zapata, F., White, N. G., Costa, P. J., Félix, V., & Beer, P. D. (2012). A halogen-bonding catenane for anion recognition and sensing. *Angewandte Chemie*, *124*(8), 1912-1916.
16. Cram, D. J. (1986). Preorganization—from solvents to spherands. *Angewandte Chemie International Edition in English*, *25*(12), 1039-1057.
17. Lehn, J. M. (2009). Towards complex matter: supramolecular chemistry and self-organization. *European Review*, *17*(2), 263-280.
18. J. B. Wittenberg and L. Isaacs, *Supramolecular Chemistry: From Molecules to Nanomaterials*, ed. P. A. Gale and J. W. Steed, John Wiley & Sons Ltd, Chichester, UK, 2012, vol. 1, ch. 3, pp. 25–44.

19. Gong, B., Yan, Y., Zeng, H., Skrzypczak-Jankunn, E., Kim, Y. W., Zhu, J., & Ickes, H. (1999). A new approach for the design of supramolecular recognition units: hydrogen-bonded molecular duplexes. *Journal of the American Chemical Society*, *121*(23), 5607-5608.
20. Yang, X., Brown, A. L., Furukawa, M., Li, S., Gardinier, W. E., Bukowski, E. J., ... & Gong, B. (2003). A new strategy for folding oligo (m-phenylene ethynylenes). *Chemical Communications*, (1), 56-57.
21. Biros, S. M., & Rebek Jr, J. (2007). Structure and binding properties of water-soluble cavitands and capsules. *Chemical Society Reviews*, *36*(1), 93-104.
22. Purse, B. W., & Rebek Jr, J. (2005). Functional cavitands: chemical reactivity in structured environments. *Proceedings of the National Academy of Sciences*, *102*(31), 10777-10782.
23. Rudkevich, D. M., Hilmersson, G., & Rebek, J. (1997). Intramolecular hydrogen bonding controls the exchange rates of guests in a cavitand. *Journal of the American Chemical Society*, *119*(41), 9911-9912.
24. Vargas Jentzsch, A., Hennig, A., Mareda, J., & Matile, S. (2013). Synthetic ion transporters that work with anion− π interactions, halogen bonds, and anion–macrodipole interactions. *Accounts of Chemical Research*, *46*(12), 2791-2800.
25. Hamuro, Y., Geib, S. J., & Hamilton, A. D. (1994). Novel molecular scaffolds: formation of helical secondary structure in a family of oligoanthranilamides. *Angewandte Chemie International Edition in English*, *33*(4), 446-448.
26. Kline, M. A., Wei, X., Horner, I. J., Liu, R., Chen, S., Chen, S., ... & Gong, B. (2015). Extremely strong tubular stacking of aromatic oligoamide macrocycles. *Chemical Science*, *6*(1), 152-157.
27. Shang, J., Si, W., Zhao, W., Che, Y., Hou, J. L., & Jiang, H. (2014). Preorganized aryltriazole foldamers as effective transmembrane transporters for chloride anion. *Organic letters*, 16(15), 4008-4011.
28. Riel, A. M. S., Decato, D. A., Sun, J., Massena, C. J., Jessop, M. J., & Berryman, O. B. (2018). The intramolecular hydrogen bonded–halogen bond: a new strategy for preorganization and enhanced binding. *Chemical science*, *9*(26), 5828-5836.
29. Sun, J., Riel, A. M. S., & Berryman, O. B. (2018). Solvatochromism and fluorescence response of a halogen bonding anion receptor. *New Journal of Chemistry*, *42*(13), 10489-10492.
30. Riel, A. M. S., Decato, D. A., Sun, J., & Berryman, O. B. (2022). Halogen bonding organocatalysis enhanced through intramolecular hydrogen bonds. *Chemical Communications*, *58*(9), 1378-1381.
31. Riel, A. M. S., Rowe, R. K., Ho, E. N., Carlsson, A. C. C., Rappé, A. K., Berryman, O. B., & Ho, P. S. (2019). Hydrogen bond enhanced halogen bonds: a synergistic interaction in chemistry and biochemistry. *Accounts of chemical research*, *52*(10), 2870-2880.
32. Scholfield, M. R., Ford, M. C., Carlsson, A. C. C., Butta, H., Mehl, R. A., & Ho, P. S. (2017). Structure–energy relationships of halogen bonds in proteins. *Biochemistry*, *56*(22), 2794-2802.
33. Carlsson, A. C. C., Scholfield, M. R., Rowe, R. K., Ford, M. C., Alexander, A. T., Mehl, R. A., & Ho, P. S. (2018). Increasing enzyme stability and activity through hydrogen bond-enhanced halogen bonds. *Biochemistry*, *57*(28), 4135-4147.

34. Rowe, R. K., & Ho, P. S. (2017). Relationships between hydrogen bonds and halogen bonds in biological systems. *Acta Crystallographica Section B: Structural Science, Crystal Engineering and Materials*, *73*(2), 255-264.
35. Decato, D. A., Riel, A. M. S., May, J. H., Bryantsev, V. S., & Berryman, O. B. (2021). Theoretical, Solid-State, and Solution Quantification of the Hydrogen Bond-Enhanced Halogen Bond. *Angewandte Chemie International Edition*, *60*(7), 3685-3692.
36. Portela, S., & Fernández, I. (2021). Nature of the hydrogen bond enhanced halogen bond. *Molecules*, *26*(7), 1885.
37. Scheiner, S. (2022). Ability of Peripheral H Bonds to Strengthen a Halogen Bond. *The Journal of Physical Chemistry A*, *126*(51), 9691-9698.
38. Schmidtchen, F. P., & Berger, M. (1997). Artificial organic host molecules for anions. *Chemical reviews*, *97*(5), 1609-1646.
39. Mele, A., Metrangolo, P., Neukirch, H., Pilati, T., & Resnati, G. (2005). A halogen-bonding-based heteroditopic receptor for alkali metal halides. *Journal of the American Chemical Society*, *127*(43), 14972-14973.
40. Chudzinski, M. G., McClary, C. A., & Taylor, M. S. (2011). Anion receptors composed of hydrogen-and halogen-bond donor groups: modulating selectivity with combinations of distinct noncovalent interactions. *Journal of the American Chemical Society*, *133*(27), 10559-10567.
41. Jungbauer, S. H., Schindler, S., Herdtweck, E., Keller, S., & Huber, S. M. (2015). Multiple multidentate halogen bonding in solution, in the solid state, and in the (calculated) gas phase. *Chemistry–A European Journal*, *21*(39), 13625-13636.
42. Vargas Jentzsch, Andreas, et al. "Ditopic ion transport systems: anion–π interactions and halogen bonds at work." Angewandte Chemie 123.49 (2011): 11879-11882.
43. Vargas Jentzsch, A., & Matile, S. (2013). Transmembrane halogen-bonding cascades. *Journal of the American Chemical Society*, *135*(14), 5302-5303.
44. Liu, Z. X., Sun, Y., Feng, Y., Chen, H., He, Y. M., & Fan, Q. H. (2016). Halogen-bonding for visual chloride ion sensing: a case study using supramolecular poly (aryl ether) dendritic organogel systems. *Chemical Communications*, *52*(11), 2269-2272.
45. Gilday, L. C., White, N. G., & Beer, P. D. (2013). Halogen-and hydrogen-bonding triazole-functionalised porphyrin-based receptors for anion recognition. *Dalton Transactions*, *42*(44), 15766-15773.
46. Tepper, R., Schulze, B., Görls, H., Bellstedt, P., Jäger, M., & Schubert, U. S. (2015). Preorganization in a cleft-type anion receptor featuring iodo-1, 2, 3-triazoles as halogen bond donors. *Organic letters*, *17*(23), 5740-5743.
47. Tepper, R., Schulze, B., Bellstedt, P., Heidler, J., Görls, H., Jäger, M., & Schubert, U. S. (2017). Halogen-bond-based cooperative ion-pair recognition by a crown-ether-embedded 5-iodo-1, 2, 3-triazole. *Chemical Communications*, *53*(14), 2260-2263.
48. Maugeri, L., Asencio-Hernández, J., Lébl, T., Cordes, D. B., Slawin, A. M., Delsuc, M. A., & Philp, D. (2016). Neutral iodotriazoles as scaffolds for stable halogen-bonded assemblies in solution. *Chemical science*, *7*(10), 6422-6428.
49. Borissov, A., Lim, J. Y., Brown, A., Christensen, K. E., Thompson, A. L., Smith, M. D., & Beer, P. D. (2017). Neutral iodotriazole foldamers as tetradentate halogen bonding anion receptors. *Chemical Communications*, *53*(16), 2483-2486.

50. Lim, J. Y., & Beer, P. D. (2017). A halogen bonding 1, 3-disubstituted ferrocene receptor for recognition and redox sensing of azide. *European Journal of Inorganic Chemistry*, *2017*(2), 220-224.
51. Zapata, F., Caballero, A., & Molina, P. (2017). Ferrocene–Triazole Combination as a Benchmark for the Electrochemical Detection of Noncovalent Halogen-Bonding Interactions. *European Journal of Inorganic Chemistry*, *2017*(2), 237-241.
52. Mole, T. K., Arter, W. E., Marques, I., Félix, V., & Beer, P. D. (2015). Neutral bimetallic rhenium (I)-containing halogen and hydrogen bonding acyclic receptors for anion recognition. *Journal of Organometallic Chemistry*, *792*, 206-210.
53. Chowdhury, B., Sinha, S., & Ghosh, P. (2016). Selective Sensing of Phosphates by a New Bis-heteroleptic RuII Complex through Halogen Bonding: A Superior Sensor over Its Hydrogen-Bonding Analogue. *Chemistry–A European Journal*, *22*(50), 18051-18059.
54. Tepper, R., Schulze, B., Jäger, M., Friebe, C., Scharf, D. H., Görls, H., & Schubert, U. S. (2015). Anion receptors based on halogen bonding with halo-1, 2, 3-triazoliums. *The Journal of organic chemistry*, *80*(6), 3139-3150.
55. Zapata, F., Caballero, A., Molina, P., Alkorta, I., & Elguero, J. (2014). Open bis (triazolium) structural motifs as a benchmark to study combined hydrogen-and halogen-bonding interactions in oxoanion recognition processes. *The Journal of Organic Chemistry*, *79*(15), 6959-6969.
56. Gonzalez, L., Zapata, F., Caballero, A., Molina, P., Ramirez de Arellano, C., Alkorta, I., & Elguero, J. (2016). Host–Guest Chemistry: Oxoanion Recognition Based on Combined Charge-Assisted C− H or Halogen-Bonding Interactions and Anion⋯ Anion Interactions Mediated by Hydrogen Bonds. *Chemistry–A European Journal*, *22*(22), 7533-7544.
57. Tepper, R., Bode, S., Geitner, R., Jäger, M., Görls, H., Vitz, J., ... & Schubert, U. S. (2017). Polymeric Halogen-Bond-Based Donor Systems Showing Self-Healing Behavior in Thin Films. *Angewandte Chemie International Edition*, *56*(14), 4047-4051.
58. Serpell, C. J., Kilah, N. L., Costa, P. J., Félix, V., & Beer, P. D. (2010). Halogen bond anion templated assembly of an imidazolium pseudorotaxane. *Angewandte Chemie*, *122*(31), 5450-5454.
59. Caballero, A., Bennett, S., Serpell, C. J., & Beer, P. D. (2013). Iodo-imidazolium salts: halogen bonding in crystals and anion-templated pseudorotaxanes. *CrystEngComm*, *15*(16), 3076-3081.
60. Cametti, M., Raatikainen, K., Metrangolo, P., Pilati, T., Terraneo, G., & Resnati, G. (2012). 2-Iodo-imidazolium receptor binds oxoanions via charge-assisted halogen bonding. *Organic & Biomolecular Chemistry*, *10*(7), 1329-1333.
61. Jungbauer, S. H., & Huber, S. M. (2015). Cationic multidentate halogen-bond donors in halide abstraction organocatalysis: Catalyst optimization by preorganization. *Journal of the American Chemical Society*, *137*(37), 12110-12120.
62. Wageling, N. B., Neuhaus, G. F., Rose, A. M., Decato, D. A., & Berryman, O. B. (2016). Advantages of organic halogen bonding for halide recognition. *Supramolecular chemistry*, *28*(7-8), 665-672.
63. Chakraborty, S., Dutta, R., & Ghosh, P. (2015). Halogen bonding assisted selective removal of bromide. *Chemical Communications*, *51*(79), 14793-14796.

64. Nepal, B., & Scheiner, S. (2015). Competitive Halide Binding by Halogen Versus Hydrogen Bonding: Bis-triazole Pyridinium. *Chemistry–A European Journal*, *21*(38), 13330-13335.
65. Massena, C. J., Riel, A. M. S., Neuhaus, G. F., Decato, D. A., & Berryman, O. B. (2015). Solution and solid-phase halogen and C–H hydrogen bonding to perrhenate. *Chemical Communications*, *51*(8), 1417-1420.
66. Riel, A. M. S., Jessop, M. J., Decato, D. A., Massena, C. J., Nascimento, V. R., & Berryman, O. B. (2017). Experimental investigation of halogen-bond hard–soft acid–base complementarity. *Acta Crystallographica Section B: Structural Science, Crystal Engineering and Materials*, *73*(2), 203-209.
67. Robinson, S. W., Mustoe, C. L., White, N. G., Brown, A., Thompson, A. L., Kennepohl, P., & Beer, P. D. (2015). Evidence for halogen bond covalency in acyclic and interlocked halogen-bonding receptor anion recognition. *Journal of the American Chemical Society*, *137*(1), 499-507.
68. Cornes, S. P., Sambrook, M. R., & Beer, P. D. (2017). Selective perrhenate recognition in pure water by halogen bonding and hydrogen bonding alpha-cyclodextrin based receptors. *Chemical Communications*, *53*(27), 3866-3869.
69. Amendola, V., Bergamaschi, G., Boiocchi, M., Fusco, N., La Rocca, M. V., Linati, L., ... & Miljkovic, A. (2016). Novel hydrogen-and halogen-bonding anion receptors based on 3-iodopyridinium units. *RSC advances*, *6*(72), 67540-67549.
70. Pancholi, J., & Beer, P. D. (2020). Halogen bonding motifs for anion recognition. *Coordination Chemistry Reviews*, *416*, 213281.
71. Sarwar, M. G., Dragisic, B., Sagoo, S., & Taylor, M. S. (2010). A tridentate halogen-bonding receptor for tight binding of halide anions. *Angewandte Chemie*, *122*(9), 1718-1721.
72. Robinson, S. W., & Beer, P. D. (2017). Halogen bonding rotaxanes for nitrate recognition in aqueous media. *Organic & Biomolecular Chemistry*, *15*(1), 153-159.
73. Lim, J. Y., & Beer, P. D. (2015). Superior perrhenate anion recognition in water by a halogen bonding acyclic receptor. *Chemical Communications*, *51*(17), 3686-3688.
74. Klein, H. A., & Beer, P. D. (2019). Iodide Discrimination by Tetra-Iodotriazole Halogen Bonding Interlocked Hosts. *Chemistry–A European Journal*, *25*(12), 3125-3130.
75. Li, X., Lim, J. Y., & Beer, P. D. (2017). Cationic all-halogen bonding rotaxanes for halide anion recognition. *Faraday Discussions*, *203*, 245-255.
76. Lim, J. Y., & Beer, P. D. (2019). Electrochemical bromide sensing with a halogen bonding [2] rotaxane. *European Journal of Organic Chemistry*, *2019*(21), 3433-3441.
77. Lim, J. Y., Bunchuay, T., & Beer, P. D. (2017). Strong and Selective Halide Anion Binding by Neutral Halogen-Bonding [2] Rotaxanes in Wet Organic Solvents. *Chemistry–A European Journal*, *23*(19), 4700-4707.
78. Mungalpara, D., Stegmüller, S., & Kubik, S. (2017). A neutral halogen bonding macrocyclic anion receptor based on a pseudocyclopeptide with three 5-iodo-1, 2, 3-triazole subunits. *Chemical Communications*, *53*(37), 5095-5098.
79. Li, X., Lim, J. Y., & Beer, P. D. (2018). Acid-Regulated Switching of Metal Cation and Anion Guest Binding in Halogen-Bonding Rotaxanes. *Chemistry–A European Journal*, *24*(67), 17788-17795.

80. Lim, J. Y., Marques, I., Felix, V., & Beer, P. D. (2017). Enantioselective anion recognition by chiral halogen-bonding [2] rotaxanes. *Journal of the American Chemical Society*, *139*(35), 12228-12239.
81. Lim, J. Y., Marques, I., Ferreira, L., Félix, V., & Beer, P. D. (2016). Enhancing the enantioselective recognition and sensing of chiral anions by halogen bonding. *Chemical Communications*, *52*(32), 5527-5530.
82. Pancholi, J., & Beer, P. D. (2020). Halogen bonding motifs for anion recognition. *Coordination Chemistry Reviews*, *416*, 213281.
83. Lim, J. Y., Marques, I., Félix, V., & Beer, P. D. (2018). A Chiral Halogen-Bonding [3] Rotaxane for the Recognition and Sensing of Biologically Relevant Dicarboxylate Anions. *Angewandte Chemie International Edition*, *57*(2), 584-588.
84. Zapata, F., Caballero, A., White, N. G., Claridge, T. D., Costa, P. J., Félix, V., & Beer, P. D. (2012). Fluorescent charge-assisted halogen-bonding macrocyclic halo-imidazolium receptors for anion recognition and sensing in aqueous media. *Journal of the American Chemical Society*, *134*(28), 11533-11541.
85. Caballero, A., White, N. G., & Beer, P. D. (2011). A bidentate halogen-bonding bromoimidazoliophane receptor for bromide ion recognition in aqueous media. *Angewandte Chemie*, *123*(8), 1885-1888.
86. Bunchuay, T., Boonpalit, K., Docker, A., Ruengsuk, A., Tantirungrotechai, J., Sukwattanasinitt, M., ... & Beer, P. D. (2021). Charge neutral halogen bonding tetradentate-iodotriazole macrocycles capable of anion recognition and sensing in highly competitive aqueous media. *Chemical Communications*, *57*(90), 11976-11979.
87. Pihko, P. M. (Ed.). (2009). *Hydrogen bonding in organic synthesis*. John Wiley & Sons.
88. Sutar, R. L., & Huber, S. M. (2019). Catalysis of organic reactions through halogen bonding. *ACS Catalysis*, *9*(10), 9622-9639.
89. Yang, H., & Wong, M. W. (2020). Application of halogen bonding to organocatalysis: A theoretical perspective. *Molecules*, *25*(5), 1045.
90. Gliese, J. P., Jungbauer, S. H., & Huber, S. M. (2017). A halogen-bonding-catalyzed Michael addition reaction. *Chemical Communications*, *53*(88), 12052-12055.
91. Walter, S. M., Kniep, F., Herdtweck, E., & Huber, S. M. (2011). Halogen-bond-induced activation of a carbon–heteroatom bond. *Angewandte Chemie International Edition*, *50*(31), 7187-7191.
92. Perera, M. D., & Aakeröy, C. B. (2019). Organocatalysis by a multidentate halogen-bond donor: An alternative to hydrogen-bond based catalysis. *New Journal of Chemistry*, *43*(21), 8311-8314.
93. Castelli, R., Schindler, S., Walter, S. M., Kniep, F., Overkleeft, H. S., Van der Marel, G. A., ... & Codée, J. D. (2014). Activation of glycosyl halides by halogen bonding. *Chemistry–An Asian Journal*, *9*(8), 2095-2098.
94. Dreger, A., Engelage, E., Mallick, B., Beer, P. D., & Huber, S. M. (2018). The role of charge in 1, 2, 3-triazol (ium)-based halogen bonding activators. *Chemical Communications*, *54*(32), 4013-4016.
95. Tsuji, N., Kobayashi, Y., & Takemoto, Y. (2014). Electrophilic iodine (i) compounds induced semipinacol rearrangement via C–X bond cleavage. *Chemical communications*, *50*(89), 13691-13694.

96. Takagi, K., Yamauchi, K., & Murakata, H. (2017). Halogen-bonding-mediated and controlled cationic polymerization of isobutyl vinyl ether: expanding the catalytic scope of 2-iodoimidazolium salts. *Chemistry–A European Journal*, *23*(40), 9495-9500.
97. Takagi, K., & Okamura, K. (2019). Cationic polymerization of n-hexyloxyallene by using halogen-bonding organocatalysts. *Journal of Polymer Science Part A: Polymer Chemistry*, *57*(24), 2436-2441.
98. Takagi, K., Murakata, H., Yamauchi, K., & Hashimoto, K. (2020). Cationic polymerization of vinyl monomers using halogen bonding organocatalysts with varied activity. *Polymer Chemistry*, *11*(42), 6739-6744.
99. Govindaraj, V., Ungati, H., Jakka, S. R., Bose, S., & Mugesh, G. (2019). Directing Traffic: Halogen-Bond-Mediated Membrane Transport. *Chemistry–A European Journal*, *25*(48), 11180-11192.
100. Jentzsch, A. V., Emery, D., Mareda, J., Nayak, S. K., Metrangolo, P., Resnati, G., ... & Matile, S. (2012). Transmembrane anion transport mediated by halogen-bond donors. *Nature communications*, *3*(1), 905.
101. Saccone, M., Palacio, F. F., Cavallo, G., Dichiarante, V., Virkki, M., Terraneo, G., ... & Metrangolo, P. (2017). Photoresponsive ionic liquid crystals assembled via halogen bond: en route towards light-controllable ion transporters. *Faraday Discussions*, *203*, 407-422.
102. Yan, C., & Mu, T. (2014). Investigation of ionic liquids for efficient removal and reliable storage of radioactive iodine: a halogen-bonding case. *Physical Chemistry Chemical Physics*, *16*(11), 5071-5075.
103. Fave, C., & Schöllhorn, B. (2019). Electrochemical activation of halogen bonding. *Current Opinion in Electrochemistry*, *15*, 89-96.
104. Que, C., Qi, Q., Zemlyanov, D. Y., Mo, H., Deac, A., Zeller, M., ... & Taylor, L. S. (2020). Evidence for halogen bonding in amorphous solid dispersions. *Crystal Growth & Design*, *20*(5), 3224-3235.
105. Nunes, R. S., Vila-Viçosa, D., & Costa, P. J. (2021). Halogen bonding: an underestimated player in membrane–ligand interactions. *Journal of the American Chemical Society*, *143*(11), 4253-4267.
106. Turunen, L., Warzok, U., Schalley, C. A., & Rissanen, K. (2017). Nano-sized I12L6 molecular capsules based on the [N⋯ I+⋯ N] halogen bond. *Chem*, *3*(5), 861-869.
107. Cheong Tse, Y., Hein, R., Mitchell, E. J., Zhang, Z., & Beer, P. D. (2021). Halogen-Bonding Strapped Porphyrin BODIPY Rotaxanes for Dual Optical and Electrochemical Anion Sensing. *Chemistry–A European Journal*, *27*(58), 14550-14559.
108. Barendt, T. A., Docker, A., Marques, I., Félix, V., & Beer, P. D. (2016). Selective Nitrate Recognition by a Halogen-Bonding Four-Station [3] Rotaxane Molecular Shuttle. *Angewandte Chemie International Edition*, *55*(37), 11069-11076.
109. Barendt, T. A., Robinson, S. W., & Beer, P. D. (2016). Superior anion induced shuttling behaviour exhibited by a halogen bonding two station rotaxane. *Chemical Science*, *7*(8), 5171-5180.
110. Klein, H. A., Kuhn, H., & Beer, P. D. (2019). Anion and pH dependent molecular motion by a halogen bonding [2] rotaxane. *Chemical Communications*, *55*(67), 9975-9978.
111. Robertson, C. C., Perutz, R. N., Brammer, L., & Hunter, C. A. (2014). A solvent-resistant halogen bond. *Chemical Science*, *5*(11), 4179-4183.

112. Laurence, C., Graton, J., Berthelot, M., & El Ghomari, M. J. (2011). The diiodine basicity scale: toward a general halogen-bond basicity scale. *Chemistry–A European Journal*, *17*(37), 10431-10444.
113. Erdelyi, M. (2012). Halogen bonding in solution. *Chemical Society Reviews*, *41*(9), 3547-3557.
114. Metrangolo, P., Meyer, F., Pilati, T., Resnati, G., & Terraneo, G. (2008). Halogen bonding in supramolecular chemistry. *Angewandte Chemie International Edition*, *47*(33), 6114-6127.
115. Mullaney, B. R., Thompson, A. L., & Beer, P. D. (2014). An all-halogen bonding rotaxane for selective sensing of halides in aqueous media. *Angewandte Chemie International Edition*, *53*(43), 11458-11462.
116. Saccone, M., Palacio, F. F., Cavallo, G., Dichiarante, V., Virkki, M., Terraneo, G., ... & Metrangolo, P. (2017). Photoresponsive ionic liquid crystals assembled via halogen bond: en route towards light-controllable ion transporters. *Faraday Discussions*, *203*, 407-422.
117. Riel, A. M. S., Decato, D. A., & Berryman, O. B. (2016). Protonation and Alkylation Induced Multidentate C–H··· Anion Binding to Perrhenate. *Crystal growth & design*, *16*(2), 974-980.
118. Kaletaş, B. K., Mandl, C., van der Zwan, G., Fanti, M., Zerbetto, F., De Cola, L., ... & Williams, R. M. (2005). Unexpected photophysical properties of symmetric indolylmaleimide derivatives. *The Journal of Physical Chemistry A*, *109*(29), 6440-6449.
119. Kaletaş, B. K., Joshi, H. C., van der Zwan, G., Fanti, M., Zerbetto, F., Goubitz, K., ... & Williams, R. M. (2005). Asymmetric Indolylmaleimide Derivatives and Their Complexation with Zinc (II)− Cyclen. *The Journal of Physical Chemistry A*, *109*(42), 9443-9455.
120. Webb, J. A., Klijn, J. E., Hill, P. A., Bennett, J. L., & Goroff, N. S. (2004). Experimental studies of the 13C NMR of iodoalkynes in Lewis-basic solvents. *The Journal of Organic Chemistry*, *69*(3), 660-664.
121. Dash, D. C. (2017). *Analytical Chemistry*, Second Edition, 384-385. PHI Learning Pvt. Ltd.
122. Xiang, Y., Zhao, Y., Xu, N., Gong, S., Ni, F., Wu, K., ... & Yang, C. (2017). Halogen-induced internal heavy-atom effect shortening the emissive lifetime and improving the fluorescence efficiency of thermally activated delayed fluorescence emitters. *Journal of Materials Chemistry C*, *5*(46), 12204-12210.
123. Lin, T., Liu, X., Lou, Z., Hou, Y., & Teng, F. (2016). Intermolecular-charge-transfer-induced fluorescence quenching in protic solvent. *Journal of Molecular Structure*, *1123*, 49-54.
124. Mazzoli, A., Carlotti, B., Bonaccorso, C., Fortuna, C. G., Mazzucato, U., Miolo, G., & Spalletti, A. (2011). Photochemistry and DNA-affinity of some pyrimidine-substituted styryl-azinium iodides. *Photochemical & Photobiological Sciences*, *10*, 1830-1836.
125. Carlotti, B., Cesaretti, A., Fortuna, C. G., Spalletti, A., & Elisei, F. (2015). Experimental evidence of dual emission in a negatively solvatochromic push–pull pyridinium derivative. *Physical Chemistry Chemical Physics*, *17*(3), 1877-1882.
126. Carlotti, B., Consiglio, G., Elisei, F., Fortuna, C. G., Mazzucato, U., & Spalletti, A. (2014). Intramolecular charge transfer of push–pull pyridinium salts in the singlet manifold. *The Journal of Physical Chemistry A*, *118*(20), 3580-3592.
127. Homocianu, M., Airinei, A., & Dorohoi, D.O. (2011). *Journal of Advanced Research in Physics*, 2(1), 1-9.

128. Zhao, G. J., & Han, K. L. (2009). Role of intramolecular and intermolecular hydrogen bonding in both singlet and triplet excited states of aminofluorenones on internal conversion, intersystem crossing, and twisted intramolecular charge transfer. *The Journal of Physical Chemistry A*, *113*(52), 14329-14335.
129. Shimada, H., Nakamura, A., Yoshihara, T., & Tobita, S. (2005). Intramolecular and intermolecular hydrogen-bonding effects on photophysical properties of 2'-aminoacetophenone and its derivatives in solution. *Photochemical & Photobiological Sciences*, *4*(4), 367-375.
130. Ottolenghi, M., Goldschmidt, C. R., & Potashnik, R. (1971). Intersystem crossing in the charge-transfer quenching of molecular fluorescence. *The Journal of Physical Chemistry*, *75*(8), 1025-1031.
131. Davidson, R. S., Bonneau, R., Joussot-Dubien, J., & Trethewey, K. R. (1980). Intramolecular quenching of the excited singlet state of a naphthyl group by halogeno substituents. *Chemical Physics Letters*, *74*(2), 318-320.
132. Chmyrov, A., Sandén, T., & Widengren, J. (2010). Iodide as a Fluorescence Quencher and Promoter-Mechanisms and Possible Implications. *The Journal of Physical Chemistry B*, *114*(34), 11282-11291.
133. Abdel-Mottaleb, M. S. A. (1984). *Laser Chemistry*, 4(1-6), 305-310.
134. Liu, K., Kang, Y., Wang, Z., & Zhang, X. (2013). 25th anniversary article: Reversible and adaptive functional supramolecular materials:"Noncovalent interaction" matters. *Advanced Materials*, *25*(39), 5530-5548.
135. Rest, C., Kandanelli, R., & Fernández, G. (2015). Strategies to create hierarchical self-assembled structures via cooperative non-covalent interactions. *Chemical Society Reviews*, *44*(8), 2543-2572.
136. Rehman, S. U., Sarwar, T., Husain, M. A., Ishqi, H. M., & Tabish, M. (2015). Studying non-covalent drug–DNA interactions. *Archives of biochemistry and biophysics*, *576*, 49-60.
137. Raynal, M., Ballester, P., Vidal-Ferran, A., & van Leeuwen, P. W. (2014). Supramolecular catalysis. Part 1: non-covalent interactions as a tool for building and modifying homogeneous catalysts. *Chemical Society Reviews*, *43*(5), 1660-1733.
138. Hansch, C., Leo, A., & Taft, R. W. (1991). A survey of Hammett substituent constants and resonance and field parameters. *Chemical reviews*, *91*(2), 165-195.
139. Swain, C. G., & Lupton, E. C. (1968). Field and resonance components of substituent effects. *Journal of the American Chemical Society*, *90*(16), 4328-4337.
140. Wheeler, S. E. (2013). Understanding substituent effects in noncovalent interactions involving aromatic rings. *Accounts of chemical research*, *46*(4), 1029-1038.
141. Wilcox, C. S., Kim, E. I., Romano, D., Kuo, L. H., Burt, A. L., & Curran, D. P. (1995). Experimental and theoretical studies of substituent effects in hydrogen bond based molecular recognition of a zwitterion by substituted arylureas. *Tetrahedron*, *51*(2), 621-634.
142. Tresca, B. W., Hansen, R. J., Chau, C. V., Hay, B. P., Zakharov, L. N., Haley, M. M., & Johnson, D. W. (2015). Substituent effects in CH hydrogen bond interactions: linear free energy relationships and influence of anions. *Journal of the American Chemical Society*, *137*(47), 14959-14967.
143. Charton, M. (1981). Electrical effect substituent constants for correlation analysis. *Progress in physical organic chemistry*, 119-251.

144. Burns, R. J., Mati, I. K., Muchowska, K. B., Adam, C., & Cockroft, S. L. (2020). Quantifying Through-Space Substituent Effects. *Angewandte Chemie*, *132*(38), 16860-16867.
145. Bravin, C., Piękoś, J. A., Licini, G., Hunter, C. A., & Zonta, C. (2021). Dissection of the Polar and Non-Polar Contributions to Aromatic Stacking Interactions in Solution. *Angewandte Chemie International Edition*, *60*(44), 23871-23877.
146. Pinter, B., Nagels, N., Herrebout, W. A., & De Proft, F. (2013). Halogen bonding from a hard and soft acids and bases perspective: investigation by using density functional theory reactivity indices. *Chemistry–A European Journal*, *19*(2), 519-530.
147. Pendás, A. M., Casals-Sainz, J. L., & Francisco, E. (2019). On electrostatics, covalency, and chemical dashes: Physical interactions versus chemical bonds. *Chemistry–A European Journal*, *25*(1), 309-314.
148. Wang, H., Wang, W., & Jin, W. J. (2016). σ-Hole bond vs π-hole bond: a comparison based on halogen bond. *Chemical reviews*, *116*(9), 5072-5104.
149. Oliveira, V., Kraka, E., & Cremer, D. (2016). The intrinsic strength of the halogen bond: Electrostatic and covalent contributions described by coupled cluster theory. *Physical Chemistry Chemical Physics*, *18*(48), 33031-33046.
150. Thirman, J., Engelage, E., Huber, S. M., & Head-Gordon, M. (2018). Characterizing the interplay of Pauli repulsion, electrostatics, dispersion and charge transfer in halogen bonding with energy decomposition analysis. *Physical Chemistry Chemical Physics*, *20*(2), 905-915.
151. Loy, C., Holthoff, J. M., Weiss, R., Huber, S. M., & Rosokha, S. V. (2021). "Anti-electrostatic" halogen bonding in solution. *Chemical Science*, *12*(23), 8246-8251.
152. Murray, J. S., Lane, P., & Politzer, P. (2009). Expansion of the σ-hole concept. *Journal of molecular modeling*, *15*, 723-729.
153. Politzer, P., Murray, J. S., & Clark, T. (2013). Halogen bonding and other σ-hole interactions: A perspective. *Physical Chemistry Chemical Physics*, *15*(27), 11178-11189.
154. Chudzinski, M. G., & Taylor, M. S. (2012). Correlations between computation and experimental thermodynamics of halogen bonding. *The Journal of Organic Chemistry*, *77*(7), 3483-3491.
155. Berger, G., Frangville, P., & Meyer, F. (2020). Halogen bonding for molecular recognition: New developments in materials and biological sciences. *Chemical communications*, *56*(37), 4970-4981.
156. Jentzsch, A. V. (2014). S. Matile in Topics in Current Chemistry, Vol. 358: *Halogen Bonding I: Impact on Materials Chemistry and Life Sciences*, 205-239.
157. Alkorta, I., Sánchez-Sanz, G., & Elguero, J. (2013). Linear free energy relationships in halogen bonds. *CrystEngComm*, *15*(16), 3178-3186.
158. Solimannejad, M., Malekani, M., & Alkorta, I. (2013). Substituent effects on the cooperativity of halogen bonding. *The Journal of Physical Chemistry A*, *117*(26), 5551-5557.
159. Nepal, B., & Scheiner, S. (2015). Substituent effects on the binding of halides by neutral and dicationic bis (triazolium) receptors. *The Journal of Physical Chemistry A*, *119*(52), 13064-13073.
160. Domagała, M., & Palusiak, M. (2014). The influence of substituent effect on noncovalent interactions in ternary complexes stabilized by hydrogen-bonding and halogen-bonding. *Computational and Theoretical Chemistry*, *1027*, 173-178.

161. Nguyen, S. T., Ellington, T. L., Allen, K. E., Gorden, J. D., Rheingold, A. L., Tschumper, G. S., ... & Watkins, D. L. (2018). Systematic experimental and computational studies of substitution and hybridization effects in solid-state halogen bonded assemblies. *Crystal Growth & Design*, *18*(5), 3244-3254.
162. Adasme-Carreño, F., Munoz-Gutierrez, C., & Alzate-Morales, J. H. (2016). Halogen bonding in drug-like molecules: A computational and systematic study of the substituent effect. *RSC advances*, *6*(66), 61837-61847.
163. Sarwar, M. G., Dragisic, B., Salsberg, L. J., Gouliaras, C., & Taylor, M. S. (2010). Thermodynamics of halogen bonding in solution: substituent, structural, and solvent effects. *Journal of the American Chemical Society*, *132*(5), 1646-1653.
164. Dumele, O., Wu, D., Trapp, N., Goroff, N., & Diederich, F. (2014). Halogen bonding of (iodoethynyl) benzene derivatives in solution. *Organic letters*, *16*(18), 4722-4725.
165. Carlsson, A. C. C., Mehmeti, K., Uhrbom, M., Karim, A., Bedin, M., Puttreddy, R., ... & Erdelyi, M. (2016). Substituent effects on the $[N–I–N]^+$ halogen bond. *Journal of the American Chemical Society*, *138*(31), 9853-9863.
166. Stilinović, V., Horvat, G., Hrenar, T., Nemec, V., & Cinčić, D. (2017). Halogen and hydrogen bonding between (N-halogeno)-succinimides and pyridine derivatives in solution, the solid state and in silico. *Chemistry–A European Journal*, *23*(22), 5244-5257.
167. Chang, Y. P., Tang, T., Jagannathan, J. R., Hirbawi, N., Sun, S., Brown, J., & Franz, A. K. (2020). NMR quantification of halogen-bonding ability to evaluate catalyst activity. *Organic Letters*, *22*(16), 6647-6652.
168. Orenha, R. P., Furtado, S. S. P., Caramori, G. F., Piotrowski, M. J., Muñoz–Castro, A., & Parreira, R. L. T. (2023). Anion recognition using enhanced halogen bonding through intramolecular hydrogen bonds–a computational insight. *New Journal of Chemistry*, *47*(9), 4439-4447.
169. Brammer, L., Bruton, E. A., & Sherwood, P. (2001). Understanding the behavior of halogens as hydrogen bond acceptors. *Crystal Growth & Design*, *1*(4), 277-290.
170. Zhu, Y. Y., Yi, H. P., Li, C., Jiang, X. K., & Li, Z. T. (2008). The N H··· X (X= Cl, Br, and I) Hydrogen-Bonding Pattern in Aromatic Amides: A Crystallographic and 1H NMR Study. *Crystal Growth and Design*, *8*(4), 1294-1300.
171. Shang, J., Gallagher, N. M., Bie, F., Li, Q., Che, Y., Wang, Y., & Jiang, H. (2014). aromatic triazole foldamers induced by C–H··· X (X= F, Cl) intramolecular hydrogen bonding. *The Journal of Organic Chemistry*, *79*(11), 5134-5144.
172. Liu, Y. H., Xu, X. N., Zhao, X., & Li, Z. T. (2015). Assessment of intermolecular N–H… F and N–H… Cl hydrogen bonding in stabilising hetero-and homodimers in solution. *Supramolecular Chemistry*, *27*(5-6), 310-320.
173. Lapp, J., & Scheiner, S. (2021). Proximity effects of substituents on halogen bond strength. *The Journal of Physical Chemistry A*, *125*(23), 5069-5077.
174. http://supramolecular.org
175. McGrath, J. M., & Pluth, M. D. (2014). Linear Free Energy Relationships Reveal Structural Changes in Hydrogen-Bonded Host–Guest Interactions. *The Journal of Organic Chemistry*, *79*(23), 11797-11801.

176. Docker, A., Guthrie, C. H., Kuhn, H., & Beer, P. D. (2021). Modulating Chalcogen Bonding and Halogen Bonding Sigma-Hole Donor Atom Potency and Selectivity for Halide Anion Recognition. *Angewandte Chemie International Edition*, *60*(40), 21973-21978.
177. Hunter, C. A., Low, C. M., Rotger, C., Vinter, J. G., & Zonta, C. (2002). Substituent effects on cation–π interactions: a quantitative study. *Proceedings of the National Academy of Sciences*, *99*(8), 4873-4876.
178. Chen, Z., Fimmel, B., & Würthner, F. (2012). Solvent and substituent effects on aggregation constants of perylene bisimide π-stacks–a linear free energy relationship analysis. *Organic & biomolecular chemistry*, *10*(30), 5845-5855.
179. Wheeler, S. E., McNeil, A. J., Müller, P., Swager, T. M., & Houk, K. N. (2010). Probing substituent effects in aryl− aryl interactions using stereoselective Diels− Alder cycloadditions. *Journal of the American Chemical Society*, *132*(10), 3304-3311.
180. Hwang, J., Li, P., Carroll, W. R., Smith, M. D., Pellechia, P. J., & Shimizu, K. D. (2014). Additivity of substituent effects in aromatic stacking interactions. *Journal of the American Chemical Society*, *136*(40), 14060-14067.
181. Wheeler, S. E., & Houk, K. N. (2009). Through-space effects of substituents dominate molecular electrostatic potentials of substituted arenes. *Journal of chemical theory and computation*, *5*(9), 2301-2312.
182. Wheeler, S. E., & Houk, K. N. (2008). Substituent effects in the benzene dimer are due to direct interactions of the substituents with the unsubstituted benzene. *Journal of the American Chemical Society*, *130*(33), 10854-10855.
183. Soloviev, D. O., Hanna, F. E., Misuraca, M. C., & Hunter, C. A. (2022). H-bond cooperativity: polarisation effects on secondary amides. *Chemical Science*, *13*(40), 11863-11868.
184. Teng, Q., Ng, P. S., Leung, J. N., & Huynh, H. V. (2019). Donor strengths determination of pnictogen and chalcogen ligands by the Huynh electronic parameter and its correlation to sigma Hammett constants. *Chemistry–A European Journal*, *25*(61), 13956-13963.
185. Ozimiński, W. P., & Dobrowolski, J. C. (2009). σ-and π-electron contributions to the substituent effect: natural population analysis. *Journal of Physical Organic Chemistry*, *22*(8), 769-778.
186. Alvarez, S. (2013). A cartography of the van der Waals territories. *Dalton Transactions*, *42*(24), 8617-8636.
187. Desiraju, G. R., & Parthasarathy, R. (1989). The nature of halogen…halogen interactions: are short halogen contacts due to specific attractive forces or due to close packing of nonspherical atoms?. *Journal of the American Chemical Society*, *111*(23), 8725-8726.
188. Bergamaschi, G., Lascialfari, L., Pizzi, A., Espinoza, M. I. M., Demitri, N., Milani, A., ... & Metrangolo, P. (2018). A halogen bond-donor amino acid for organocatalysis in water. *Chemical Communications*, *54*(76), 10718-10721.
189. Turunen, L., & Erdélyi, M. (2020). Halogen bonds of halonium ions. *Chemical Society Reviews*, *49*(9), 2688-2700.
190. Barluenga, J. (1999). Transferring iodine: more than a simple functional group exchange in organic synthesis. *Pure and applied chemistry*, *71*(3), 431-436.

191. Okitsu, T., Yumitate, S., Sato, K., In, Y., & Wada, A. (2013). Substituent effect of bis (pyridines) iodonium complexes as iodinating reagents: control of the iodocyclization/oxidation process. *Chemistry–A European Journal*, *16*(19), 4992-4996.
192. Barluenga, J., González-Bobes, F., Murguía, M. C., Ananthoju, S. R., & González, J. M. (2004). Bis (pyridine) iodonium tetrafluoroborate (IPy2BF4): A versatile oxidizing reagent. *Chemistry–A European Journal*, *10*(17), 4206-4213.
193. Yan, R., Chen, K., Li, Z., Qu, Y., Gao, L., Tong, H., ... & Guo, K. (2021). Fixation of CO2 into Cyclic Carbonates by Halogen-Bonding Catalysis. *ChemSusChem*, *14*(2), 738-744.
194. Choi, K., & Hamilton, A. D. (2003). Macrocyclic anion receptors based on directed hydrogen bonding interactions. *Coordination chemistry reviews*, *240*(1-2), 101-110.
195. Mayoral, M. J., Bilbao, N., & González-Rodríguez, D. (2016). Hydrogen-Bonded Macrocyclic Supramolecular Systems in Solution and on Surfaces. *ChemistryOpen*, *5*(1), 10-32.
196. Yu, S., Kalenius, E., Frontera, A., & Rissanen, K. (2021). Macrocyclic complexes based on $[N\cdots I\cdots N]^+$ halogen bonds. *Chemical Communications*, *57*(93), 12464-12467.

Experimental Section

General:

All reagents were obtained from commercial sources and were used without further purification unless otherwise noted. Thin layer chromatography (TLC) was performed using normal-phase silica gel glass-backed plates (0.25 mm, F-254, SiliCycle) and observed under UV light. Flash column chromatography was performed using normal-phase silica gel (230–400 mesh, SiliaFlash®P60, SiliCycle). Activated molecular sieves were used when anhydrous solvents were required. All compounds were dried in vacuo at room temperature as needed. High-resolution mass spectrometry was carried out using an Agilent 6520 Accurate-Mass Q-TOF LC/MS. Elemental analysis results were obtained from Micro Analysis, Inc. Nuclear magnetic resonance (NMR) spectra were obtained with a VNMRS Varian 500 MHz or a Bruker Avance 400 MHz or an Agilent 400 MHz spectrometer. Chemical shifts are reported in parts per million (ppm) from high to low frequency using the residual solvent peak as the internal reference ($CHCl_3$= 7.26 ppm or C_6H_6= 7.16 ppm). For the ^{19}F NMR spectra hexafluorobenzene C_6F_6 (δ – 164.9 ppm) was used as an internal standard. Signal splitting patterns are indicated as s, singlet; d, doublet; t, triplet; m, multiplet, b, broad. Coupling constants (J) are given in Hz.

Chapter 2

Synthesis of Second Generation Molecules (G2XB, G2HB)

General Procedure for Octylation. In an oven dried round bottom, **4** or **5** (1 equiv.) was dissolved in dry DCM. Octyl triflate (4.5 equiv., prepared according to literature procedure1) was dissolved in dry DCM. Both round bottoms were sparged with dry N2 gas for 15 min. The octyl triflate solution was then added dropwise to the solution of **4** or **5**. The solution was stirred for 16 h under inert atmosphere. Removal of the DCM by rotoevaporation left a solid/oil that was triturated with hexanes followed by filtration.

General Procedure for Anion Metathesis. Octylated triflate salt of **4** or **5** was dissolved in the smallest amount of acetonitrile (enough to solubilize the receptor salt but not dilute it). 2.2 equivalents of tetra-*n*-butylammonium chloride were added to the acetonitrile mixture. Red precipitate formed upon addition of TBACl, reaction was stirred overnight at room temperature. Vapor diffusion of Et2O afforded a precipitate that was isolated by filtration. To remove excess tetra-*n*6 butylammonium chloride, the precipitate was washed with acetone which left a powder/oil. ^1H and ^{19}F NMR showed precipitate was clean product and no further purification was needed.

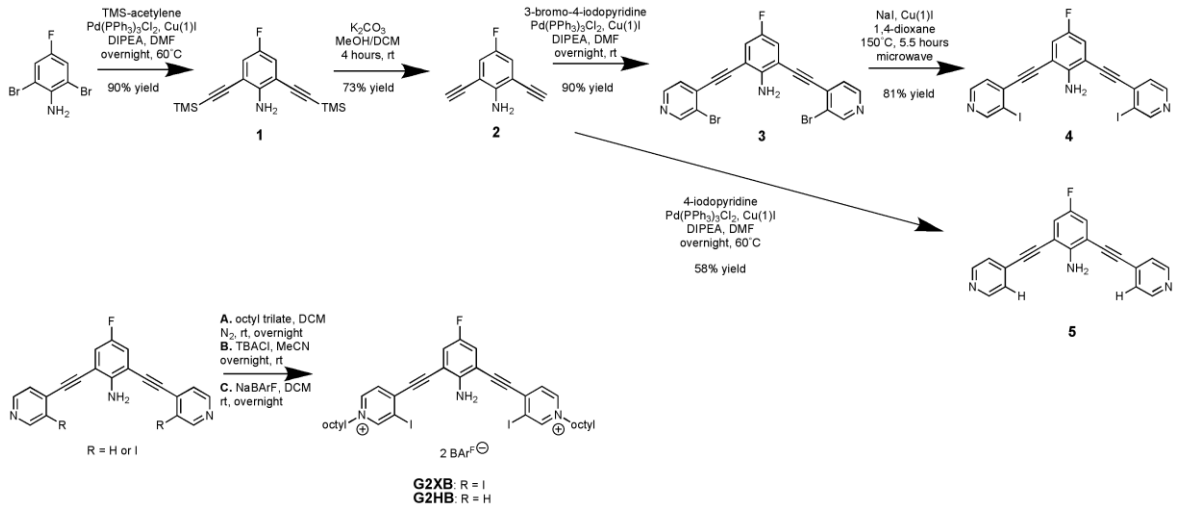

Figure S1. Synthetic Pathway of **G2XB** derivatives molecules.

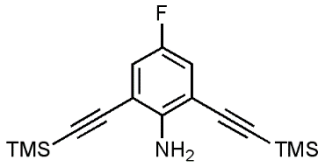

4-fluoro-2,6-bis((trimethylsilyl)ethynyl)aniline (1). To an oven dried Schlenk flask was charged with 2,6-dibromo-4-fluoroaniline (4.9787 g, 18.51 mmol), then vacuumed and backfilled with dry N_2 gas (3x). Bis(triphenylphosphine)palladium(II) dichloride (0.778 g, 1.10 mmol) was added, vacuumed and backfilled with dry N_2 (3x). Copper (I) iodide (0.354 g, 1.86 mmol) was added, vacuumed and backfilled with dry N_2 (3x). The dry reagents were dissolved in 150 mL dry dimethylformamide (DMF). N,N-diisopropylamine (16 mL, 91.85 mmol) and TMS-acetylene (6.65 mL, 46.56 mmol) were added to the DMF solution. The flask was carefully vacuumed and backfilled with dry N_2 (3x). The dark brown solution stirred overnight at 60˚C. The reaction mixture was first run through a silica plug with a hexane/ethyl acetate solvent mixture (50:50) to remove any excess salts and catalysts. Subsequent removal of DMF, hexanes and ethyl acetate by roto-evaporation left a brown solid that was purified by column chromatography (gradient column of pure hexanes to 5% EtOAc/95% Hexanes) to afford **1** (5.04 g, 16.6 mmol, 90%) as a golden yellow colored oil. ^{1}H (400 MHz, $CDCl_3$, 25˚C): 6.9916-6.9697 (2H, d, *J* = 8.76 Hz), 4.6717 (2H, s), 0.2598 (18H, s). ^{13}C (125.7 MHz, $CDCl_3$, 25˚C): 154.7221-152.8471 (d, *J* = 235.7 Hz), 146.8236, 119.3367 (d, *J* = 23.9 Hz), 108.0455 (d, *J* = 9.7 Hz), 101.5135, 100.2913, 0.1138. ^{19}F (470.6 MHz, $CDCl_3$, 25˚C): -130.7549 (1F, t, *J* = 8.73 Hz). HRMS (ESI pos) *m/z*: 304.1353 (M^++1, 100%); $C_{16}H_{23}FNSi_2^+$+1 (304.1377).

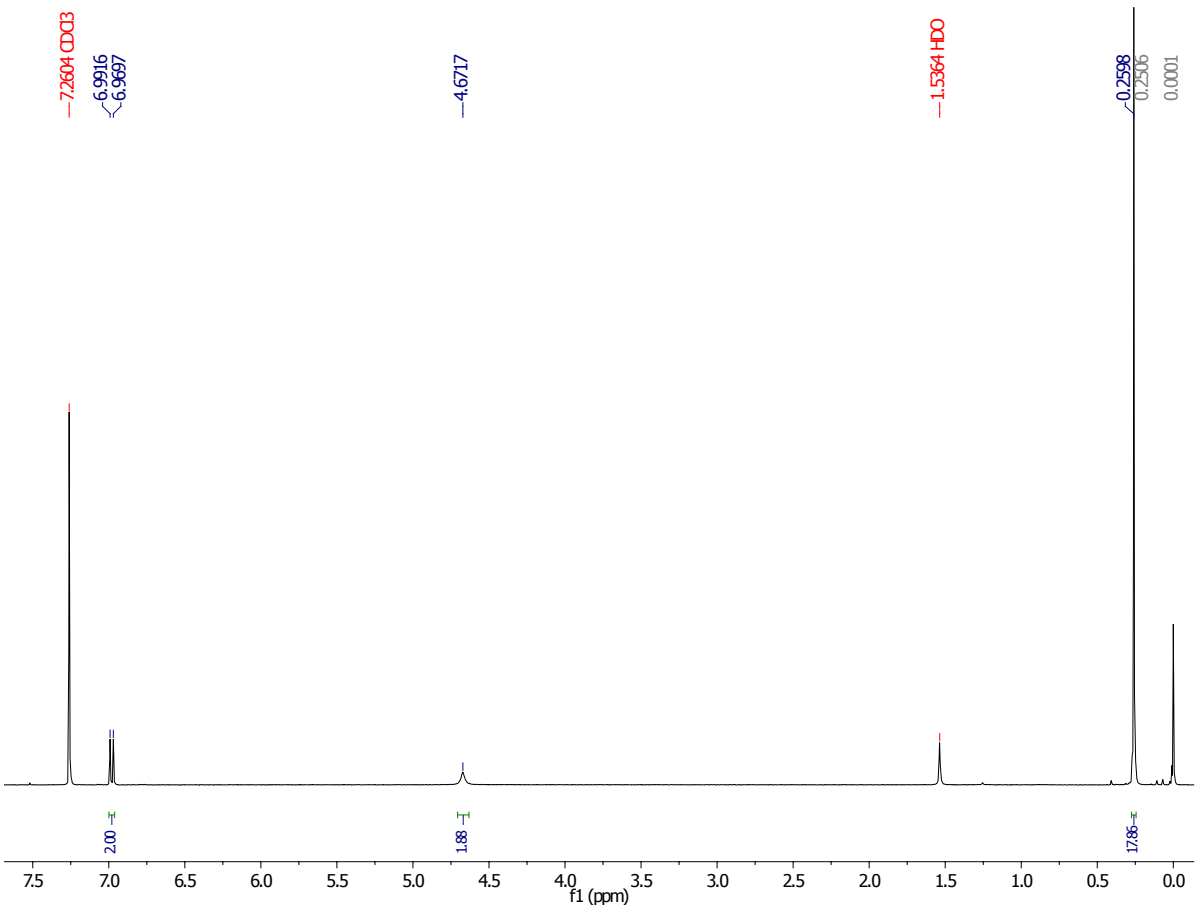

Figure S2. ^{1}H NMR of spectrum of **1** ($CDCl_3$, 25˚C, 400 MHz).

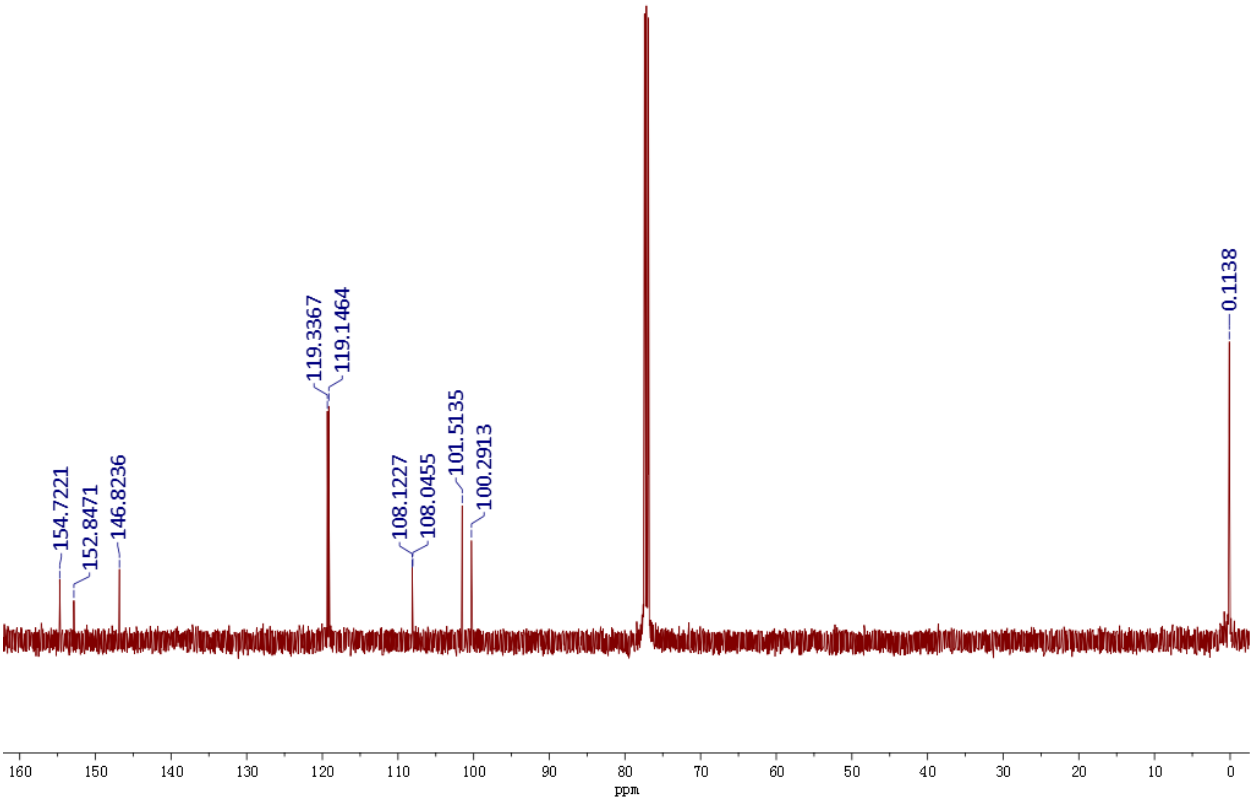

Figure S3. ^{13}C NMR of spectrum of **1** ($CDCl_3$, 25˚C, 125.7 MHz).

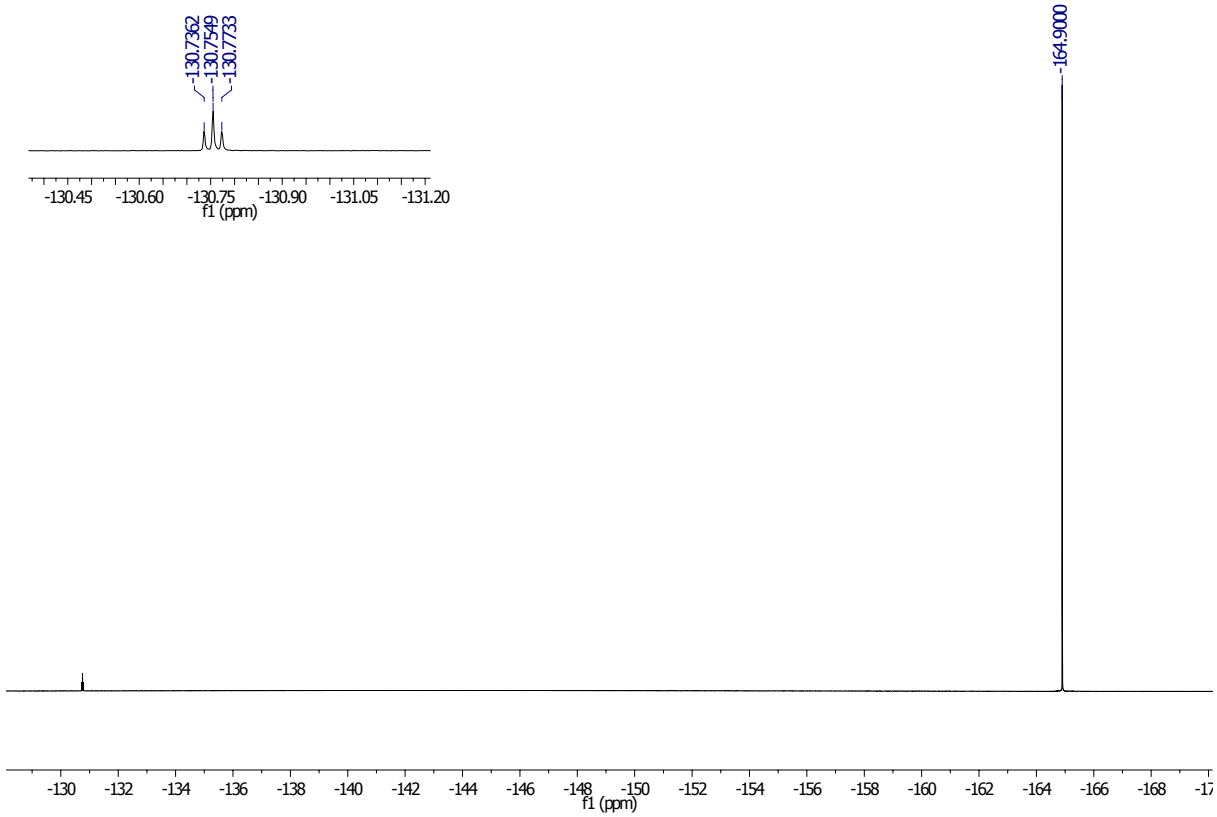

Figure S4. ^{19}F NMR of spectrum of **1** ($CDCl_3$, 25˚C, 470.6 MHz).

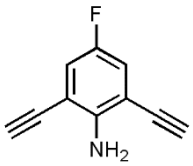

2,6-bisethynyl-4-fluoroaniline (2). 1 (1.59 g, 5.24 mmol) was dissolved in 15 mL methanol and 15 mL DCM in a 250 mL round bottom flask. Potassium carbonate (1.85 g, 13.11 mmol) was added to the organic mixture. The reaction stirred vigorously for 4 hours at room temperature and reaction progress was checked via TLC. If the reaction was not finished, it was stirred overnight. When the reaction came to completion, water was added to quench the reaction. The crude product was extracted with ethyl acetate, dried over magnesium sulfate and vacuum filtered. The organic mixture was reduced under vacuum and crude product remained a brown solid. The clean yellow solid **2** (0.610 g, 73 % yield) was obtained by column chromatography (10% DCM/90 % Hexanes). ^1H (400 MHz, $CDCl_3$, 25˚C): 7.0602-7.0387 (2H, d, *J* = 8.6 Hz), 4.7013 (2H, s), 3.4343 (2H, s). ^{13}C (125.7 Hz, $CDCl_3$, 25˚C): 154.6664-152.7916 (d, *J* = 235.7 Hz), 147.2792, 120.1869 (d, *J* = 24.1 Hz), 107.0369 (d, *J* = 9.8 Hz), 83.8922, 79.2389. ^{19}F (470.6 MHz, $CDCl_3$, 25˚C): -130.5275 (1F, t, *J* = 8.66 Hz). HRMS (ESI pos) *m/z*: 160.0563 (M^++1, 100%); $C_{10}H_7FN^+$+1 (160.0563).

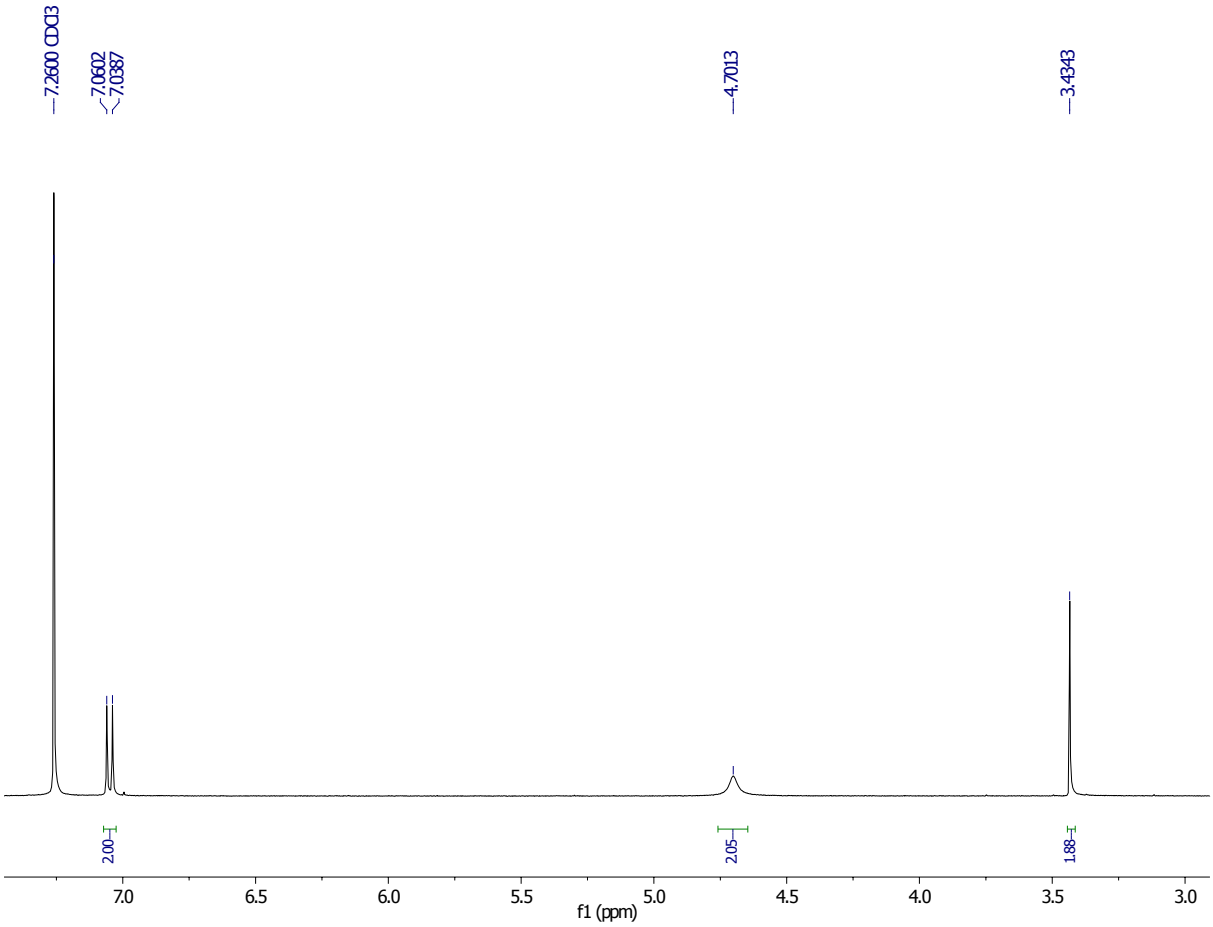

Figure S5. ^{1}H NMR of spectrum of **2** ($CDCl_3$, 25˚C, 400 MHz).

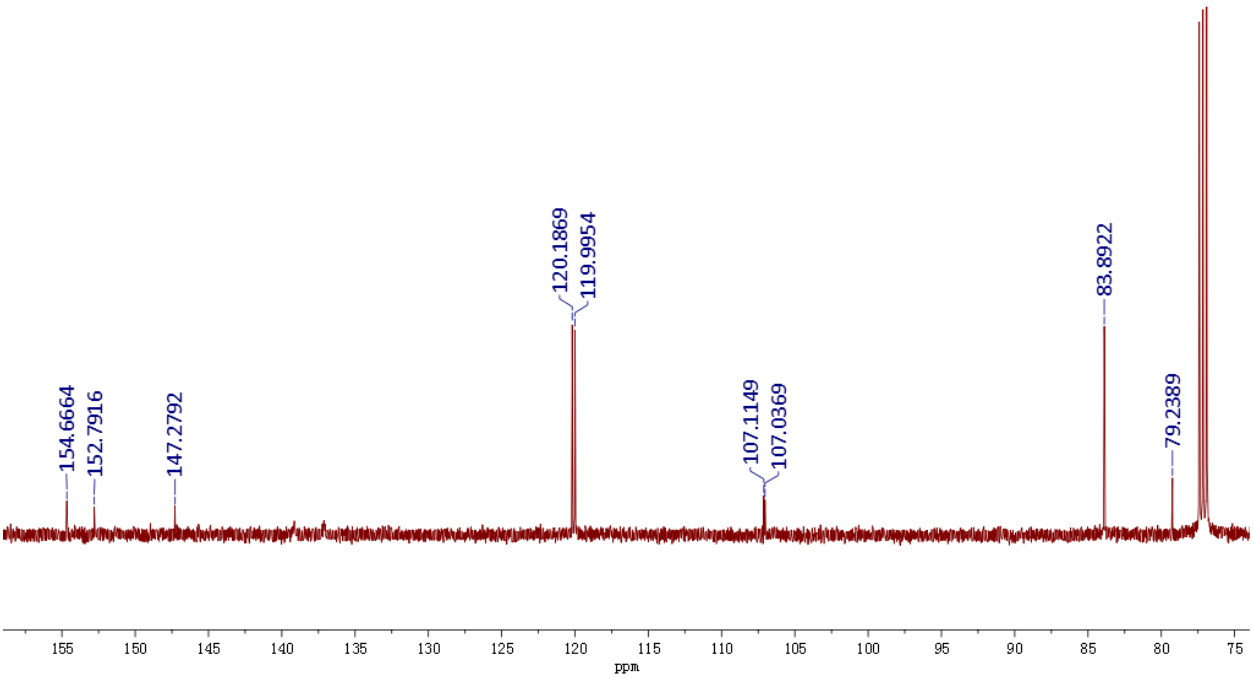

Figure S6. ^{13}C NMR of spectrum of **2** ($CDCl_3$, 25˚C, 125.7 MHz).

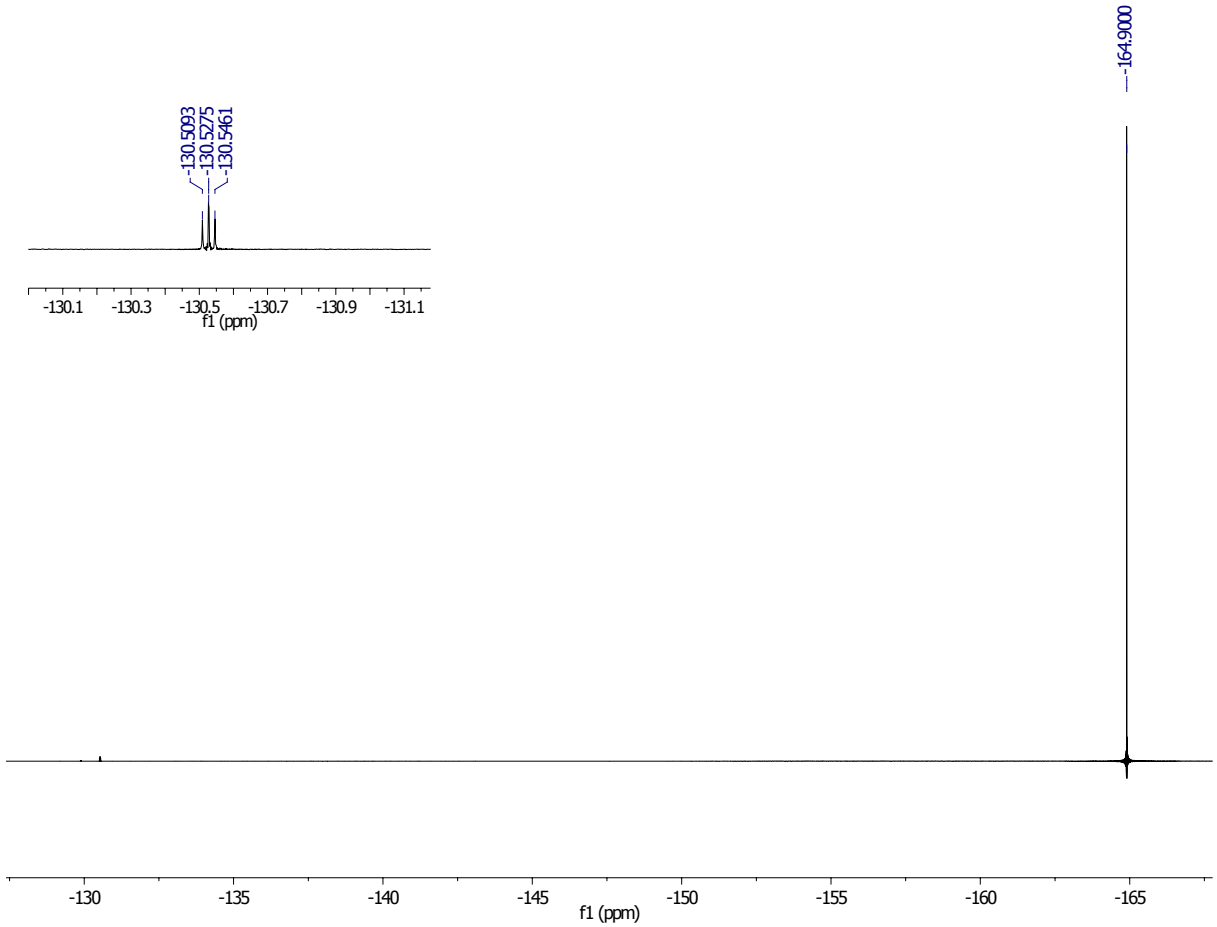

Figure S7. ^{19}F NMR of spectrum of **2** ($CDCl_3$, 25˚C, 470.6 MHz).

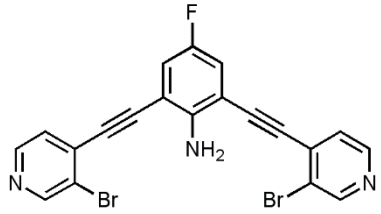

2,6-bis(4-ethynyl-3-bromopyridinyl)-4-fluoroaniline (3). To an oven dried Schlenk flask was charged with **2** (0.300 g, 1.88 mmol) and 4-bromo-3-iodopyridine (1.125 g, 4.71 mmol) then vacuumed and backfilled with dry N_2 gas (3x). Bis(triphenylphosphine)palladium (II) dichloride (0.0793 g, 0.113 mmol) was added, vacuumed and backfilled with dry N_2 (3x). Copper (I) iodide (0.035 g, 0.188 mmol) was added, vacuumed and backfilled with dry N_2 (3x). The dry reagents were dissolved in 60 mL dry DMF. N,N-diisopropylamine (1.6 mL, 9.4 mmol) was added to the DMF solution. The flask was carefully vacuumed and backfilled with dry N_2 (3x). The dark brown solution stirred overnight at room temperature. The reaction mixture was first run through a silica plug with a hexane/ethyl acetate solvent mixture (50:50) to remove any excess salts and catalysts. Subsequent removal of DMF, hexanes and ethyl acetate by roto-evaporation left and brown solid that was purified by column chromatography (gradient from 30% EtOAc/70% Hexanes to 75% EtOAc/25% Hexanes) to afford **3** (5.04 g, 16.6 mmol, 90%) as a bright yellow

solid. ^{1}H (400 MHz, $CDCl_3$, 25˚C): 8.8199 (2H, s), 8.5531-8.5406 (2H, d, *J* = 5 Hz), 7.4405-7.4280 (2H, d, *J* = 5 Hz), 7.2255-7.2045 (2H, d, *J* = 8.4 Hz), 5.2456 (2H, s). ^{13}C (125.7 MHz, CDCl3, 25˚C): 155.42, 153.07-152.16 (d, *J* = 114.4 Hz), 148.43, 133.02, 132.69, 126.81, 123.06, 121.46 (d, *J* = 30.2 Hz), 107.77 (d, *J* = 43.0 Hz), 94.45, 92.76. ^{19}F (470.6 MHz, $CDCl_3$, 25˚C): -129.9064 (1F, t, *J* = 8.35 Hz). HRMS (ESI pos) *m/z*: 471.9283 (M^++1, 100%); $C_{20}H_{11}Br_2FN_3^+$+1 (471.9350).

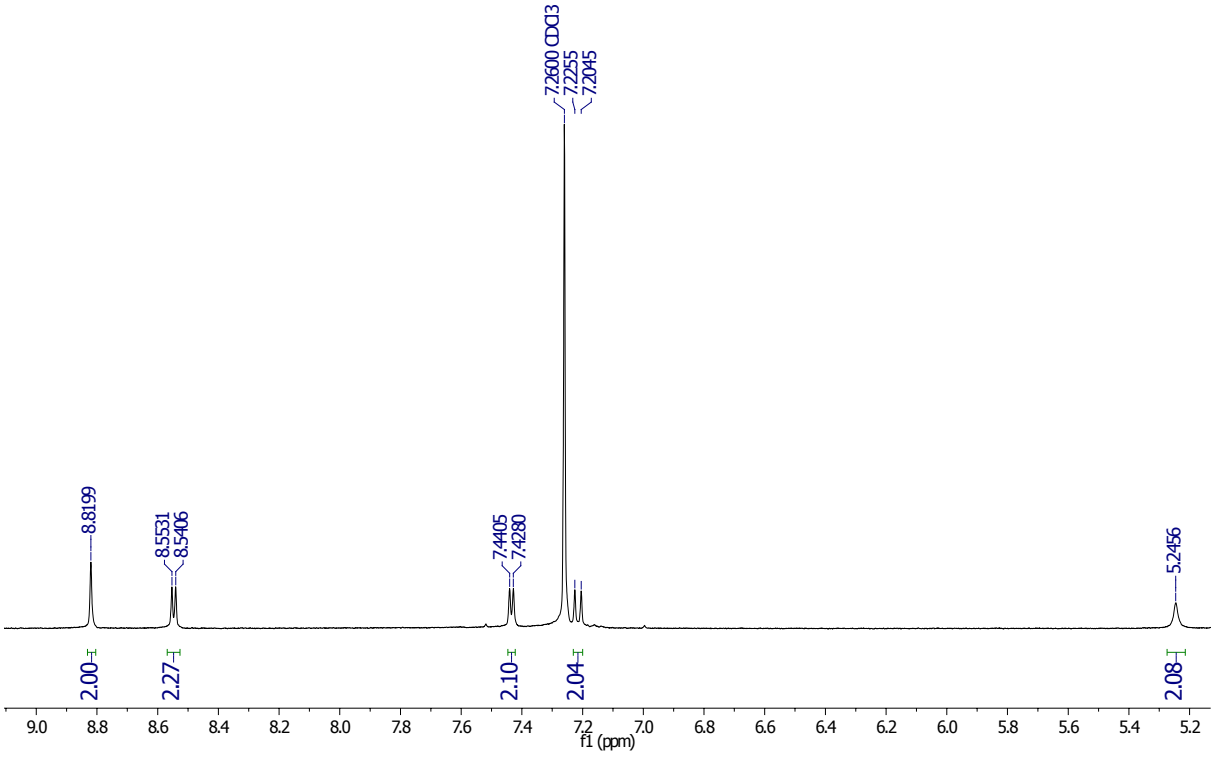

Figure S8. ^{1}H NMR of spectrum of **3** ($CDCl_3$, 25˚C, 400 MHz).

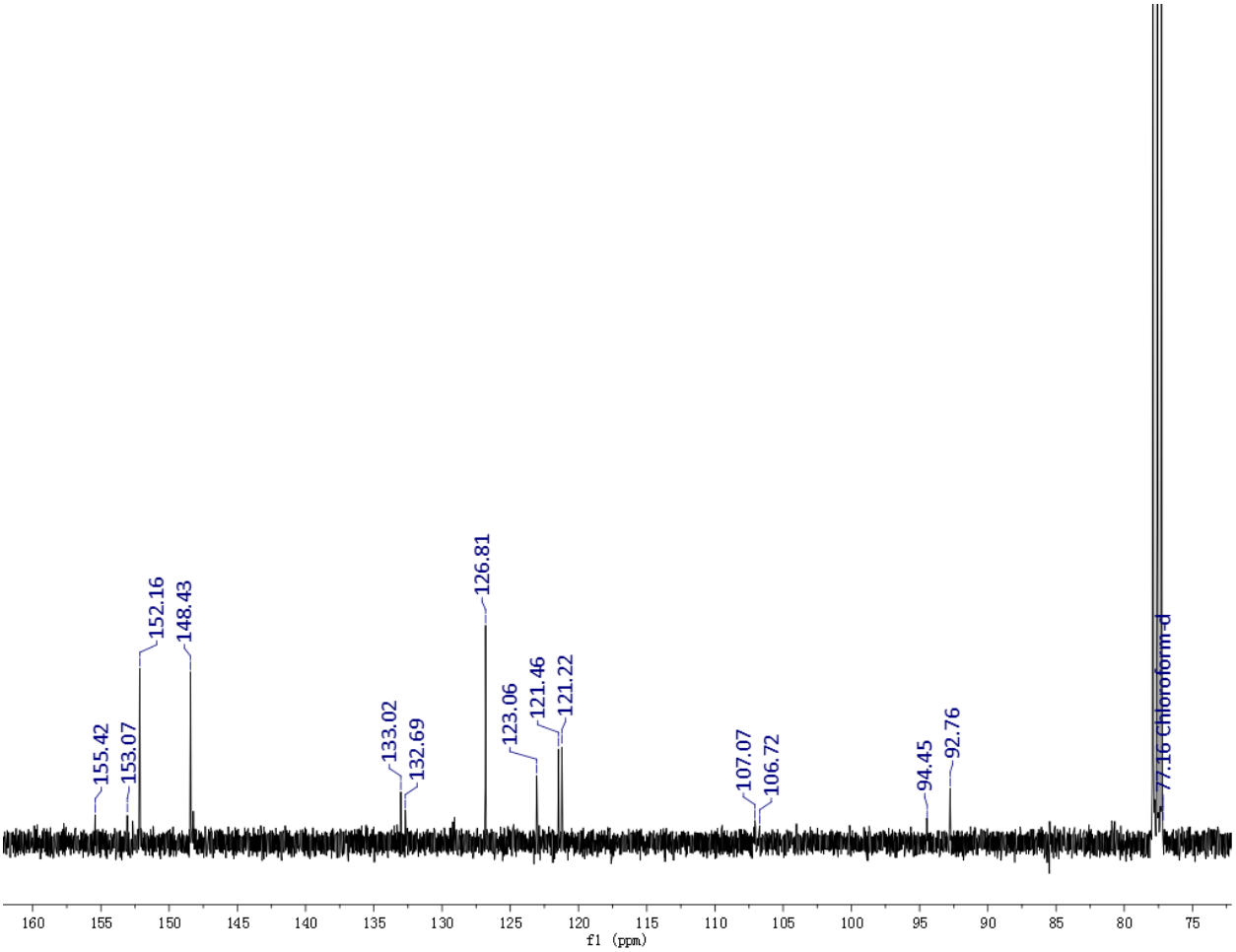

Figure S9. ^{13}C NMR of spectrum of **3** ($CDCl_3$, 25˚C, 125.7 MHz).

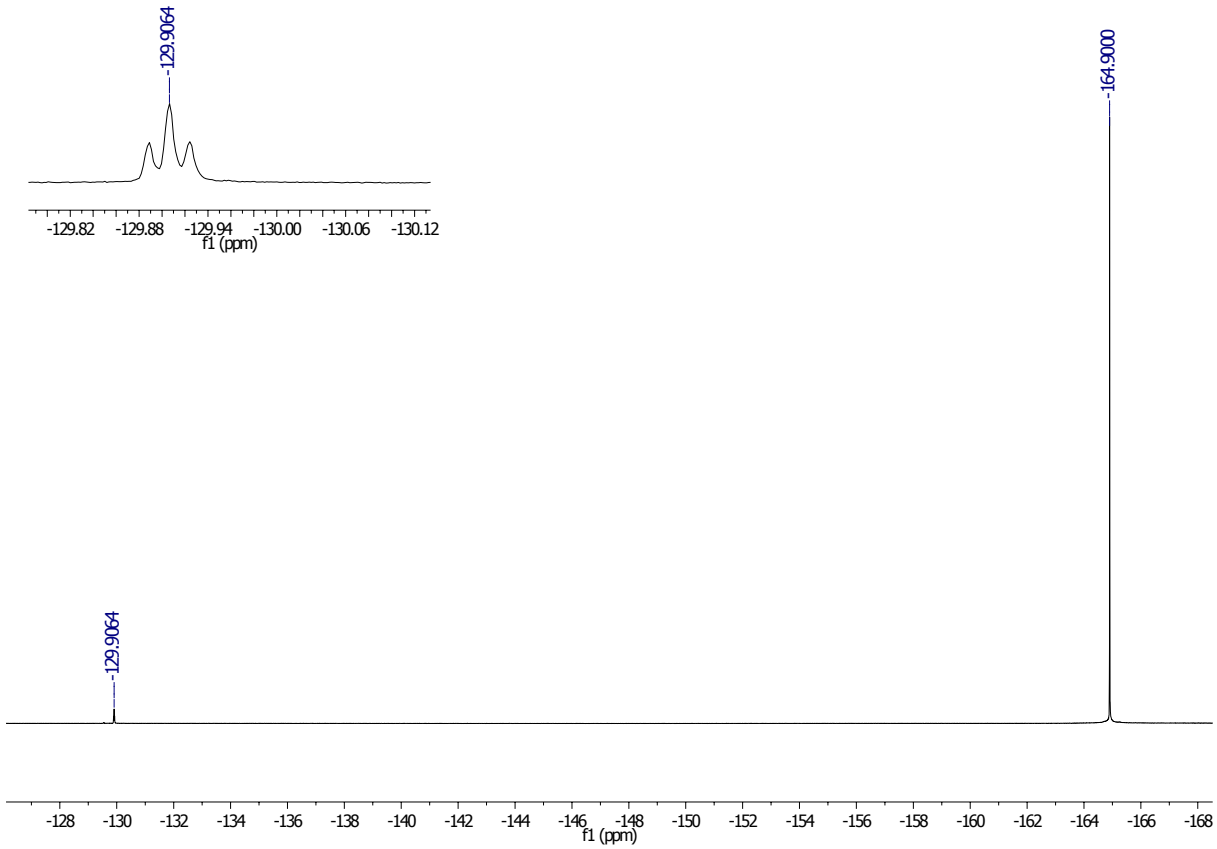

Figure S10. ^{19}F NMR of spectrum of **3** ($CDCl_3$, 25˚C, 470.6 MHz).

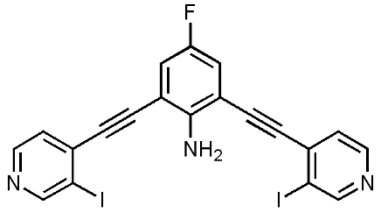

2,6-bis(4-ethynyl-3-iodopyridinyl)-4-fluoroaniline (4). 3 (0.225 g, 0.47 mmol), copper iodide (0.009 g, 0.047 mmol), sodium iodide (0.286 g, 1.91 mmol) were added to a 10-20 mL microwave reaction vial containing a stir bar and dissolved in 13 mL 1,4-dioxane. To the vibrant yellow reaction mixture, trans-N,N'-dimethylcyclohexane-1,2-diamine (0.23 mL, 1.45 mmol) was added which turned the solution color green-brown. The microwave vial was sealed and placed in a microwave. The reaction was performed in a Biotage Initiator+ microwave reactor for 5.5 hours at 150 ˚C. After cooling, an aliquot was ran through pipet silica plug with EtOAc to remove catalysts and salts. The EtOAc crude was then ran through GCMS in order to obtain % conversion of bromines to iodines. If the reaction was unfinished, it would be submitted again at 30 min incriments. When the reaction ran to completion, the crude reaction was run through a silica plug with EtOAc. The bright yellow product (0.219 g, 0.39 mmol, 81%) was purified via column chromatography (gradient column 30% EtOAc/70% Hexanes to 70% EtOAc/30%

Hexanes). ^{1}H (400 MHz, $CDCl_3$, 25˚C): 9.0073 (2H, s), 8.5603-8.5478 (2H, d, *J* = 5 Hz), 7.4334-7.4209 (2H, d, *J* = 5 Hz), 7.2380-7.21770 (2H, d, *J* = 8.4 Hz), 5.3240 (2H, s). ^{13}C (125.7 MHz, CDCl3, 25˚C): 157.1417, 154.7946-152.9078 (d, *J* = 237.2 Hz), 148.6974, 147.7629, 136.7807, 126.3512, 120.8622 (d, *J* = 24.0 Hz), 106.7141 (d, *J* = 9.7 Hz), 98.9006, 95.5187, 92.9690. ^{19}F (470.6 MHz, $CDCl_3$, 25˚C): -129.8910 (1F, t, *J* = 8.3 Hz). HRMS (ESI pos) *m/z*: 565.9026 (M^++1, 100%); $C_{20}H_{11}FI_2N_3^+$+1 (565.9040).

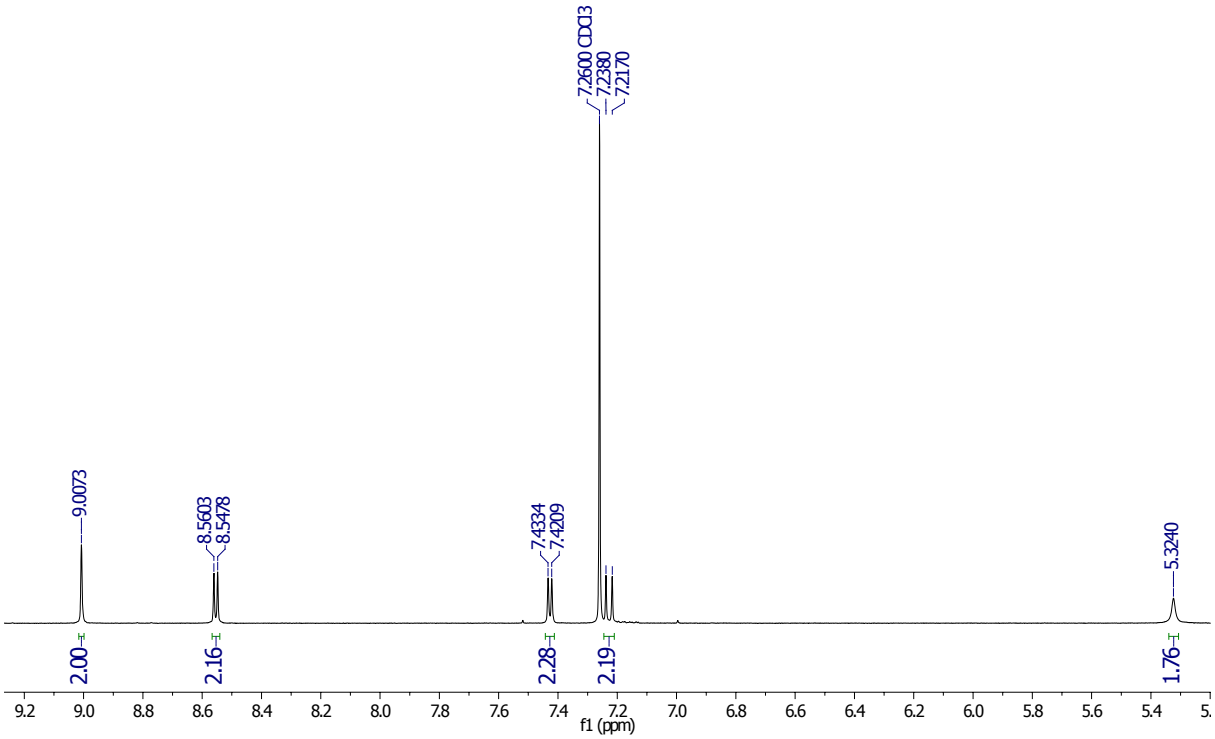

Figure S11. ^{1}H NMR of spectrum of **4** ($CDCl_3$, 25˚C, 400 MHz).

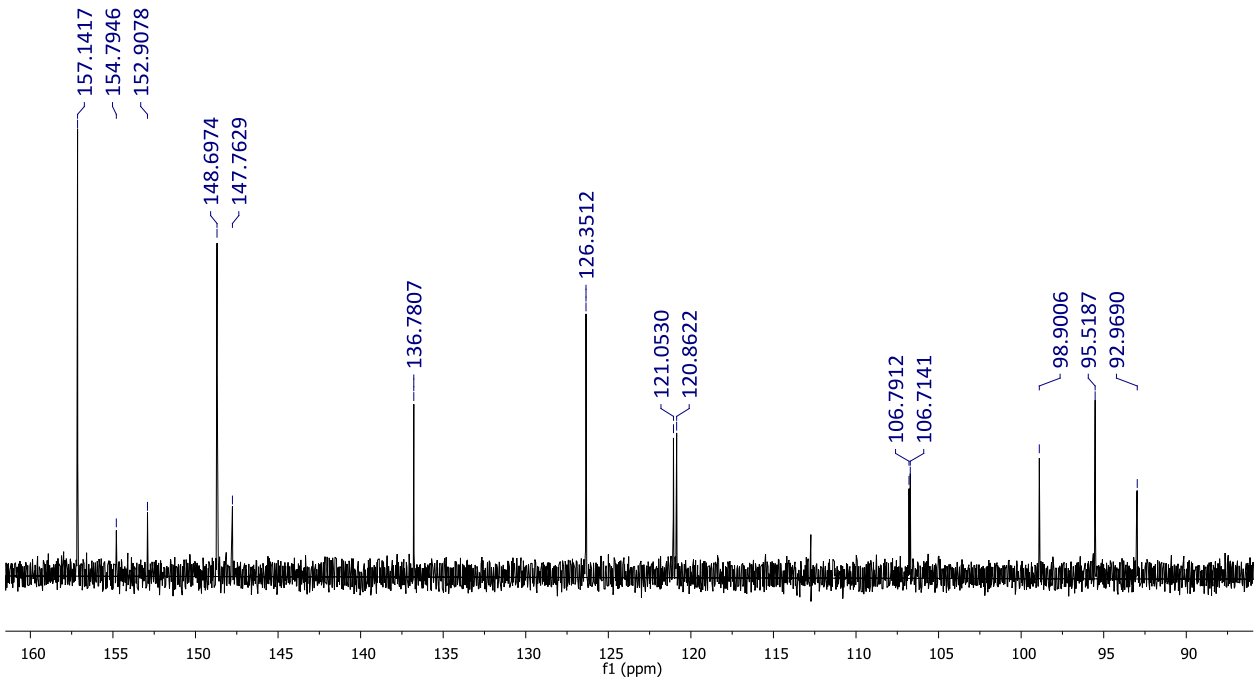

Figure S12. ^{13}C NMR of spectrum of **4** ($CDCl_3$, 25˚C, 125.7 MHz).

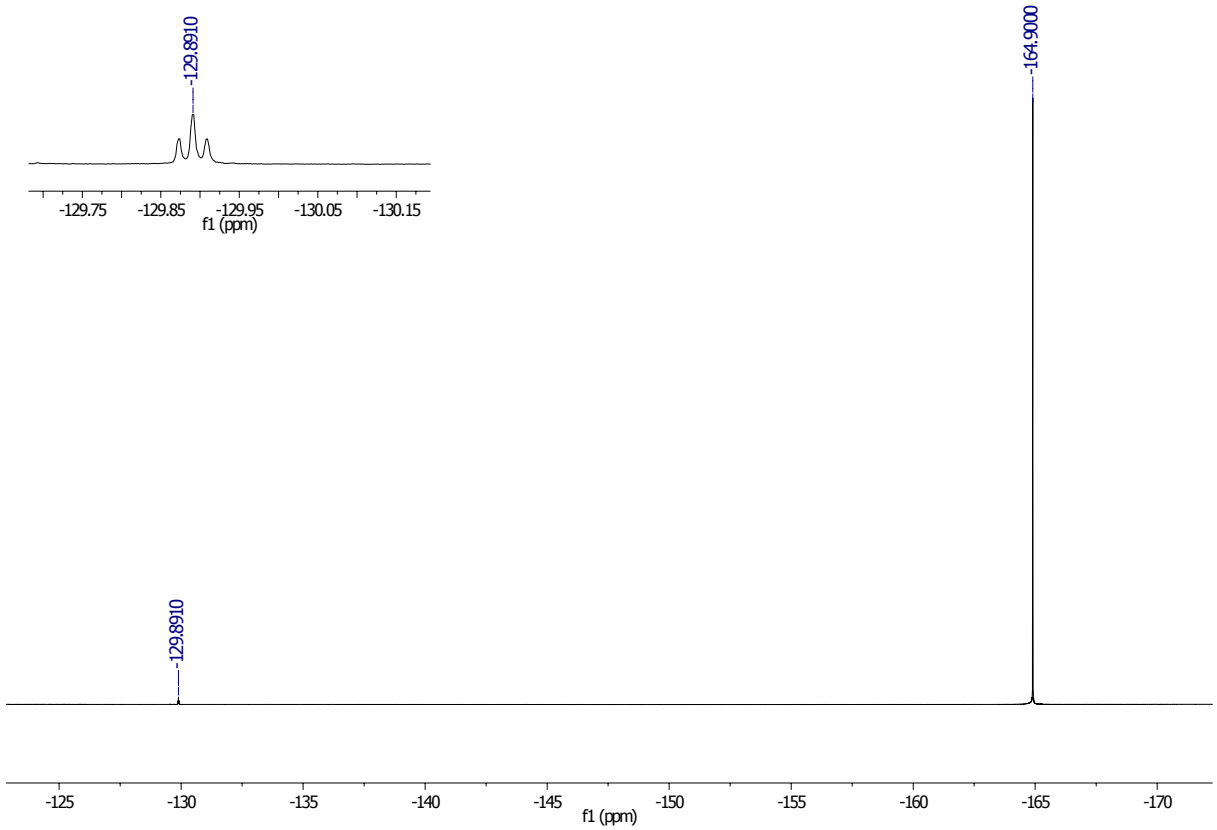

Figure S13. ^{19}F NMR of spectrum of **4** ($CDCl_3$, 25˚C, 470.6 MHz).

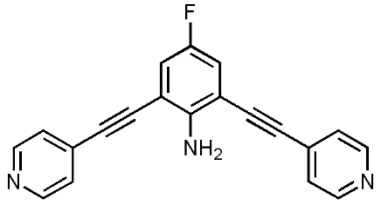

2,6-bis(4-ethynylpyridinyl)-4-fluoroaniline (5). To an oven dried Schlenk flask was charged with **2** (0.85 g, 5.34 mmol) and 4-iodopyridine (2.5 g, 12.2 mmol) then vacuumed and backfilled with dry N_2 gas (3x). Bis(triphenylphosphine)palladium (II) dichloride (0.226 g, 0.342 mmol) was added, vacuumed and backfilled with dry N_2 (3x). Copper (I) iodide (0.101 g, 0.53 mmol) was added, vacuumed and backfilled with dry N_2 (3x). The dry reagents were dissolved in 40 mL dry DMF. N,N-diisopropylamine (4.6 mL, 26.4 mmol) was added to the DMF solution. The flask was carefully vacuumed and backfilled with dry N_2 (3x). The dark brown solution stirred overnight at 150 ˚C. The reaction mixture was first run through a silica plug with an ethyl acetate/methanol solvent mixture (90:10) to remove any excess salts and catalysts. Subsequent removal of DMF, hexanes and ethyl acetate by roto-evaporation left and brown solid that was purified by column chromatography (gradient from 30% EtOAc/70% Hexanes to 75% EtOAc/25% Hexanes) to afford **5** (0.96 g, 3.1 mmol, 58%) as a bright yellow solid. ^1H (500 MHz, CD_3CN, 25˚C): 8.6234-

8.6114 (2H, d, *J* = 6 Hz), 7.5059-74938 (4H, d, *J* = 6.05 Hz), 7.2422-7.2245 (2H, d, *J* = 8.85 Hz), 5.2600 (2H, s). ^{13}C (125.7 MHz, CD_3CN, 25˚C): 155.3862, 150.9501 (d, *J* = 6.9 Hz), 148.4883, 131.3914, 126.2978, 121.2470 (d, *J* = 24.2 Hz), 107.7302 (d, *J* = 10.13 Hz), 93.8579, 89.3999. ^{19}F (470.6 MHz, CD_3CN, 25˚C): -129.6846 (1F, t, *J* = 8.82 Hz). HRMS (ESI pos) *m/z*: 314.1094 (M^++1, 100%); $C_{20}H_{13}FN_3^+$+1 (314.1107).

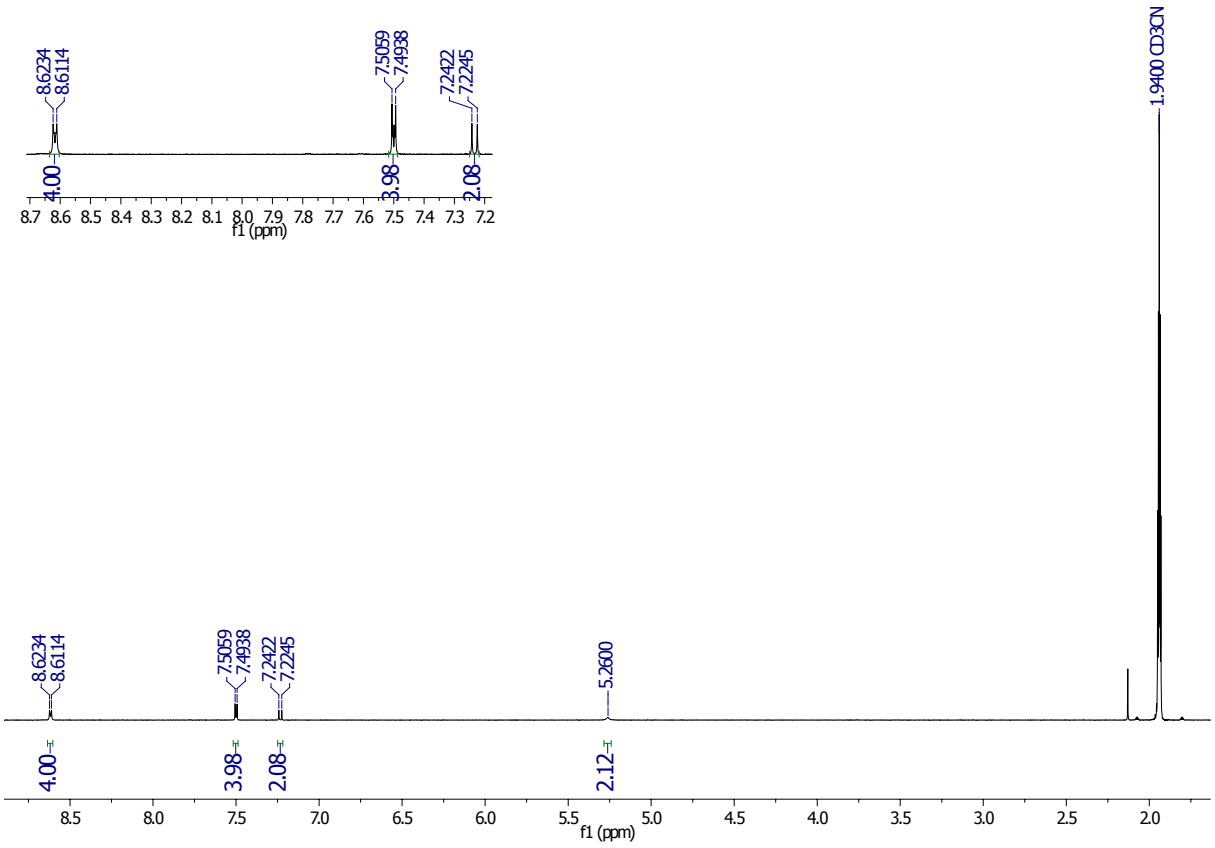

Figure S14. ^1H NMR of spectrum of **5** (CD_3CN, 25˚C, 500 MHz).

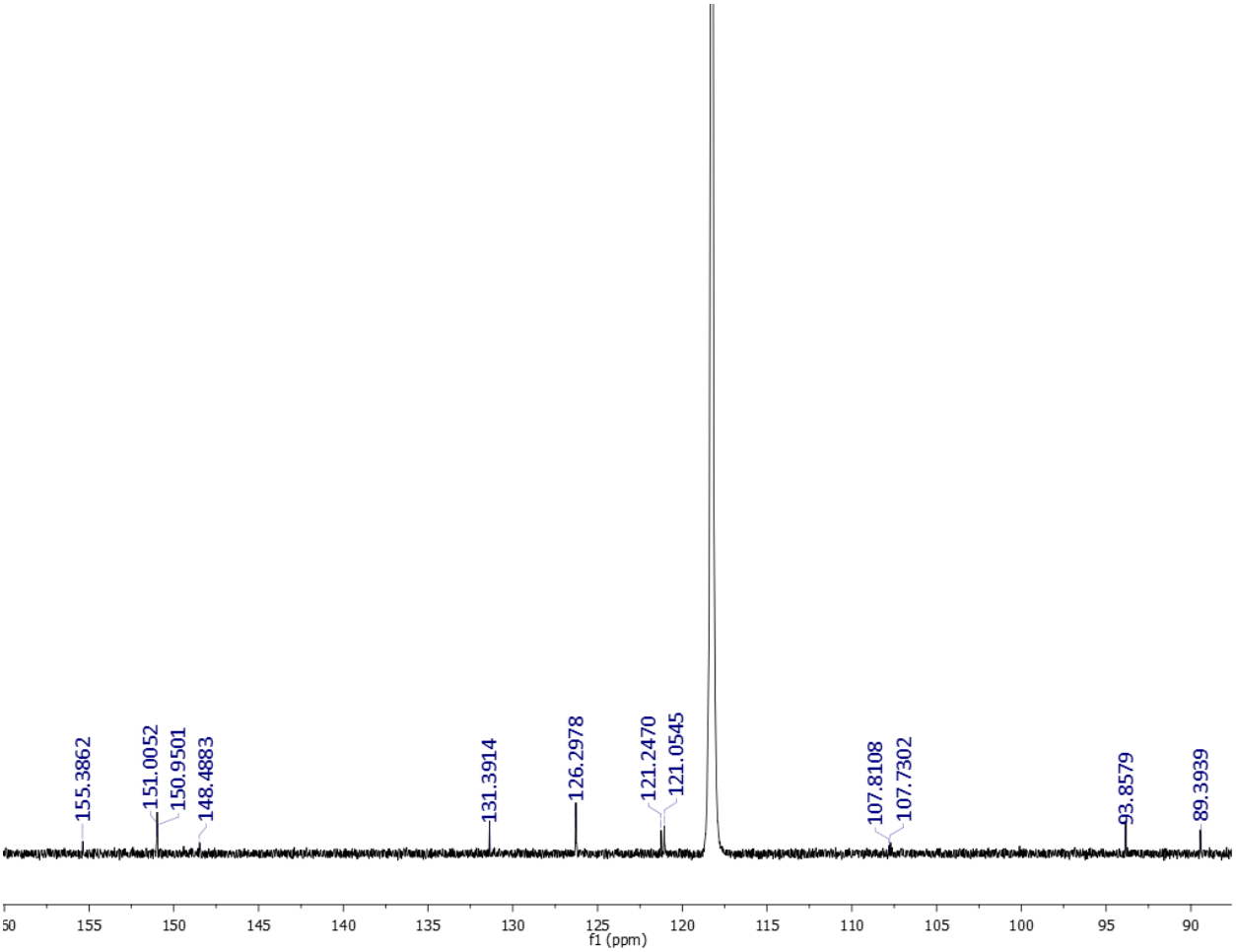

Figure S15. ^{13}C NMR of spectrum of **5** (CD_3CN, 25˚C, 125.7 MHz).

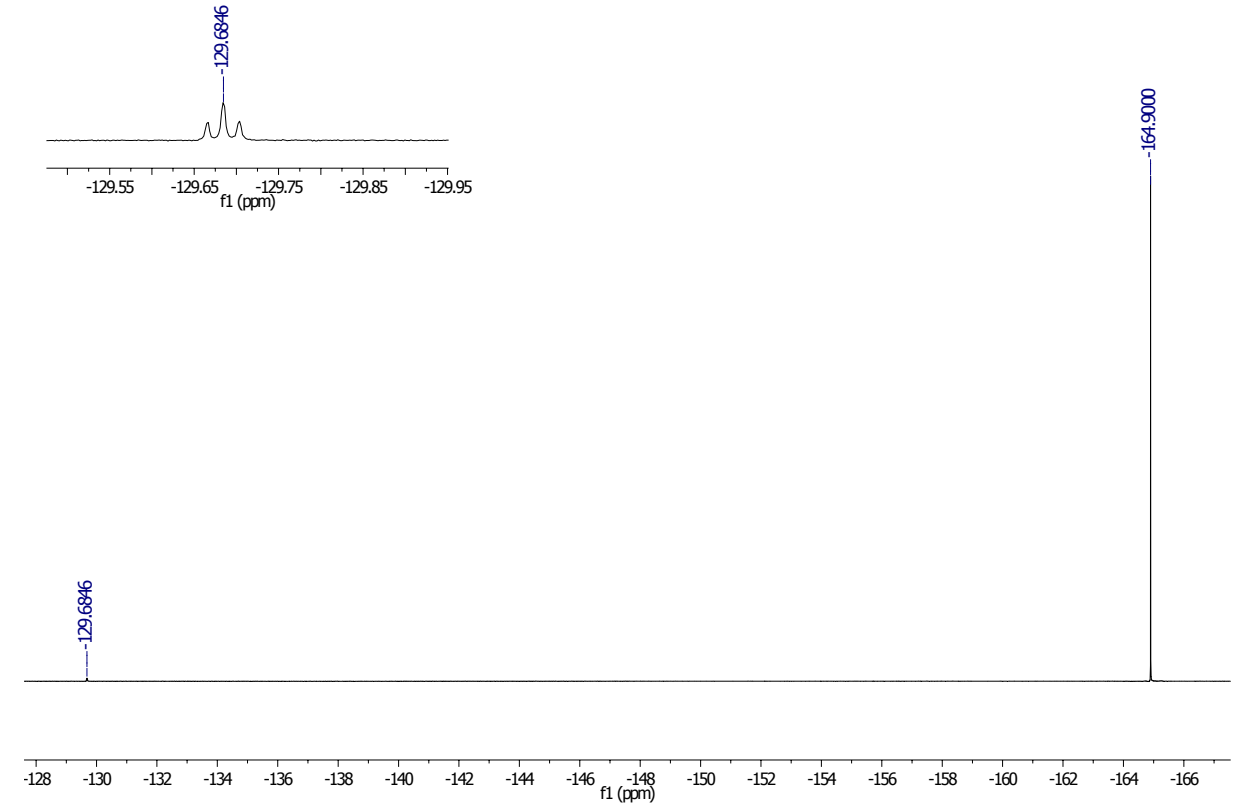

Figure S16. ^{19}F NMR of spectrum of **5** (CD_3CN, 25˚C, 470.6 MHz).

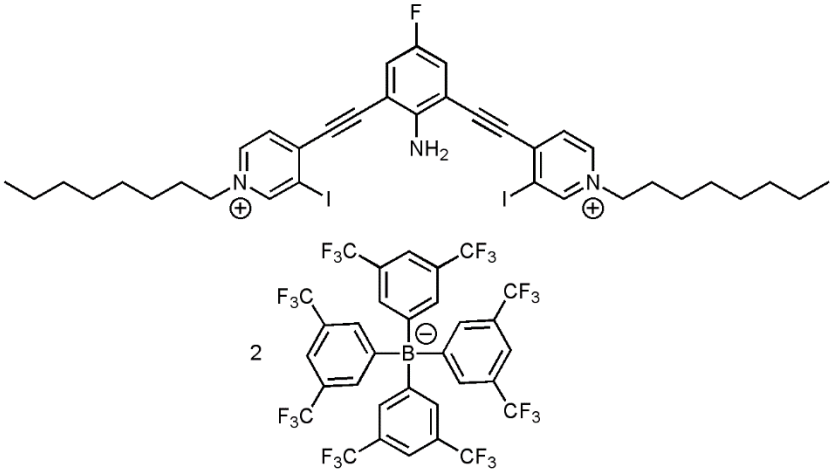

G2XB (6). ^1H (500 MHz, $CDCl_3$, 25˚C): 8.6111 (2H, s), 8.0362-8.0211 (2H, d, *J* = 7.55 Hz), 7.6914 (16H, b), 7.6045-7.5917 (2H, d, *J* = 6.54 Hz), 7.4989 (8H, b), 7.3652-7.3500 (2H, d, *J* = 7.65 Hz), 5.2924 (2H, s), 4.2338 (4H, t, *J* = 7.05 Hz), 1.9174 (4H, b), 1.3144-1.2317 (20H, b), 0.8460 (6H, t). ^{13}C (125.7MHz, $CDCl_3$, 25˚C): 162.2529 (dd, *J* = 99.95 Hz, *J* = 45.55 Hz), 149.3866, 147.4292, 141.0047, 135.1731, 129.4505 (qq, *J* = 34.07 Hz), 125.9575 (q, *J* = 272.61 Hz), 125.5778,

125.3818, 117.9445, 106.9363, 105.1553 (d, *J* = 7.41 Hz), 99.6546, 95.5300, 63.1093, 31.7955, 31.7420, 29.0824, 28.9629, 26.3058, 22.8052, 14.2414. ^{19}F (470.6 MHz, $CDCl_3$, 25˚C): -126.7810 (1F, t, *J* = 7.65 Hz), -65.3734 (48F, s). HRMS (ESI pos) *m/z*: 395.5805 (M^{+2}, 100%), 1654.2257 (M^{+}-1BAr^{F}); $C_{36}H_{44}FI_2N_3^{+2}$ (395.5814), $C_{68}H_{56}BF_{25}I_2N_3^{+}$ (1654.2241).

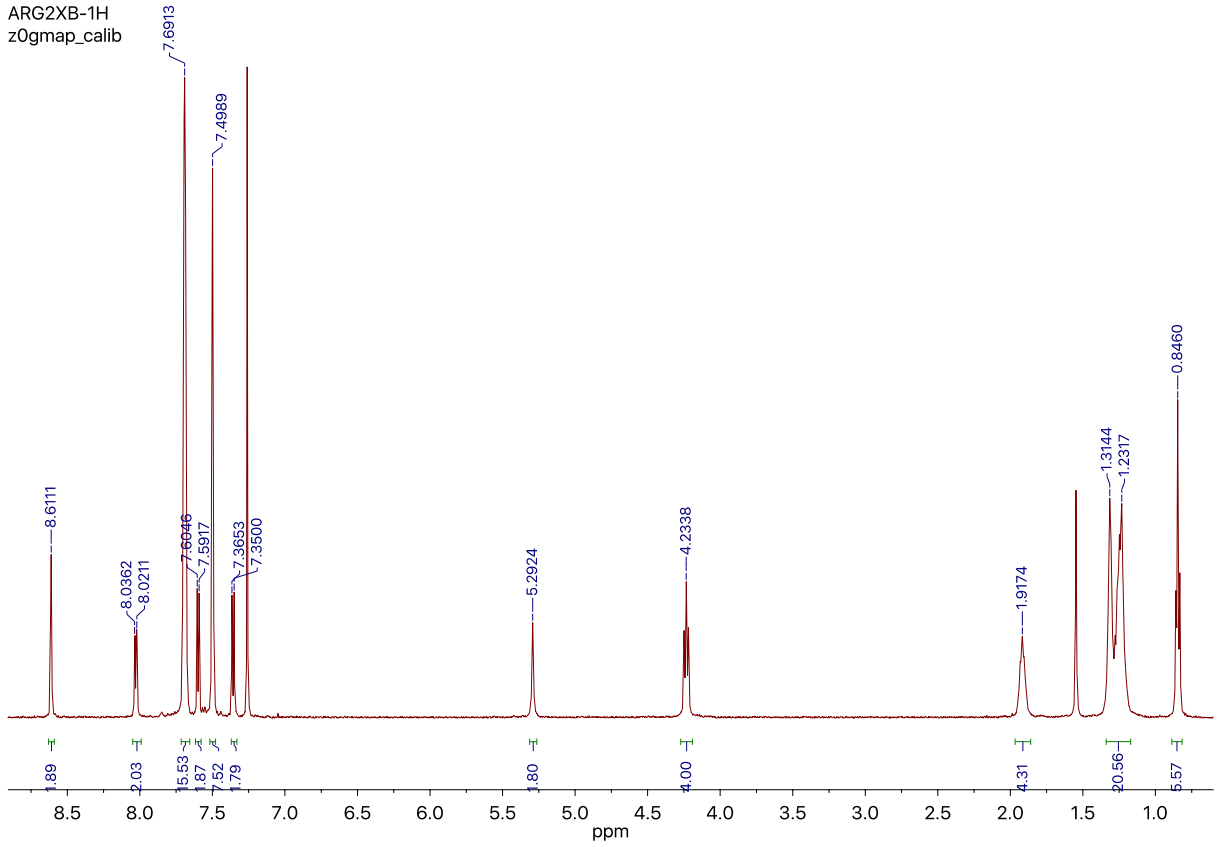

Figure S17. ^{1}H NMR of spectrum of **6** ($CDCl_3$, 25˚C, 500 MHz).

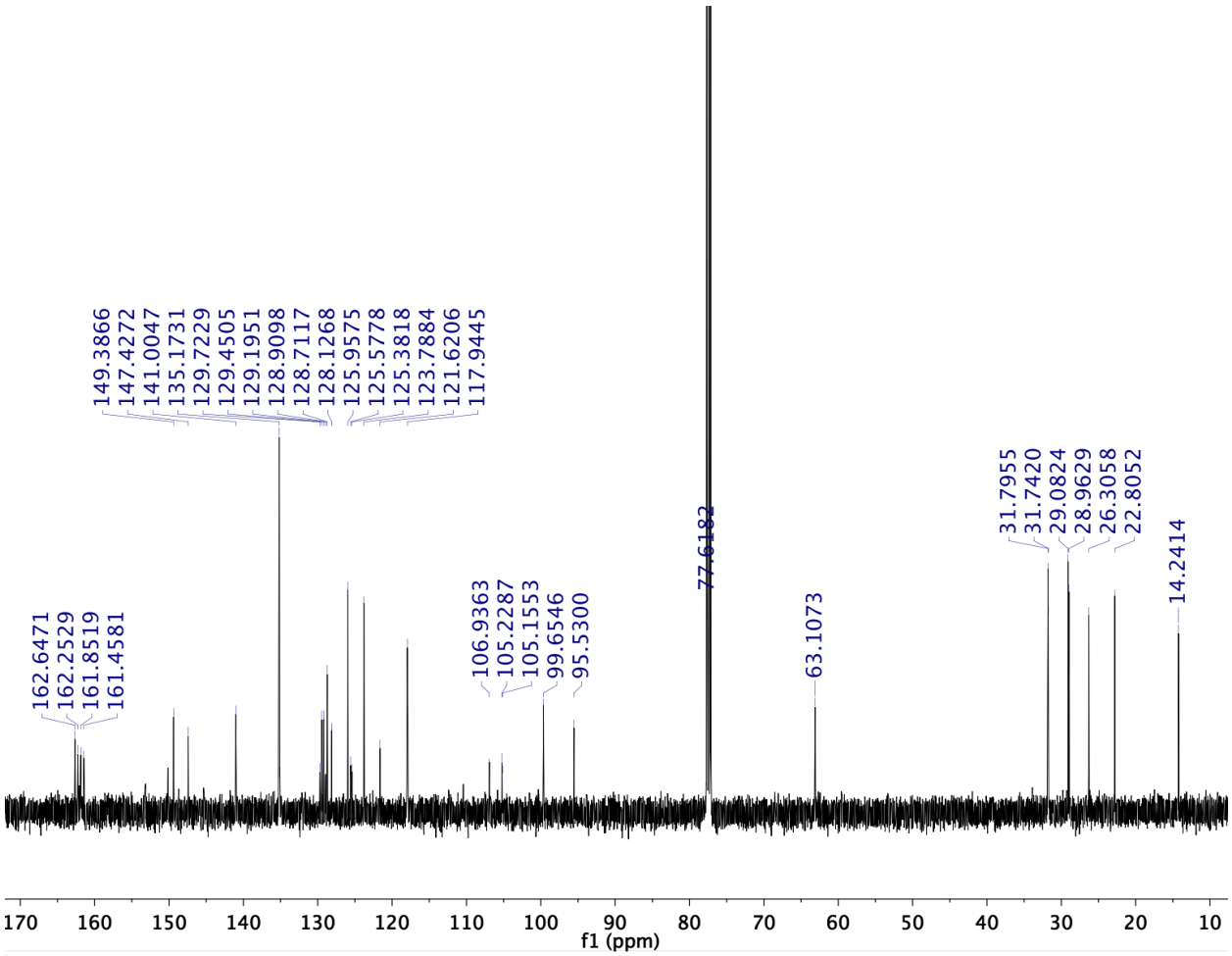

Figure S18. ^{13}C NMR of spectrum of **6** ($CDCl_3$, 25˚C, 125.7 MHz).

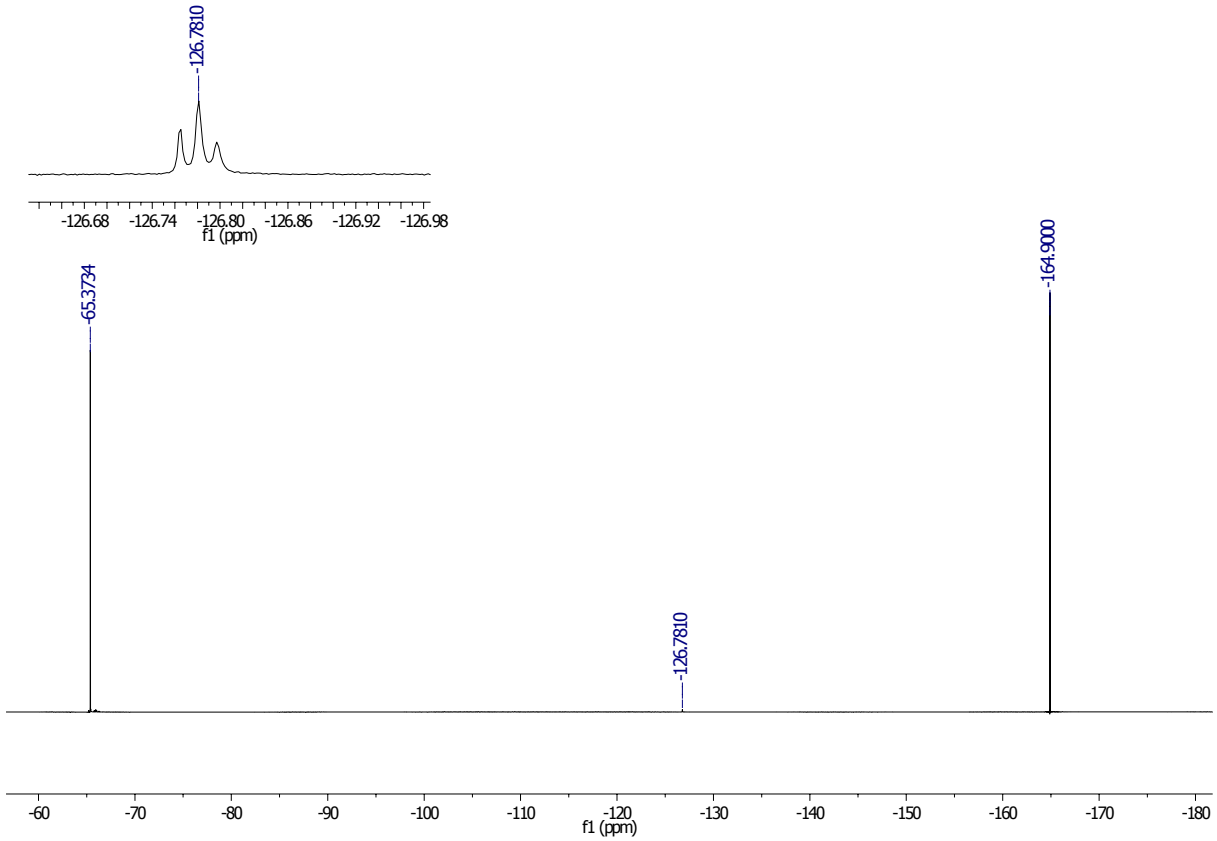

Figure S19. ^{19}F NMR of spectrum of **6** ($CDCl_3$, 25˚C, 470.6 MHz).

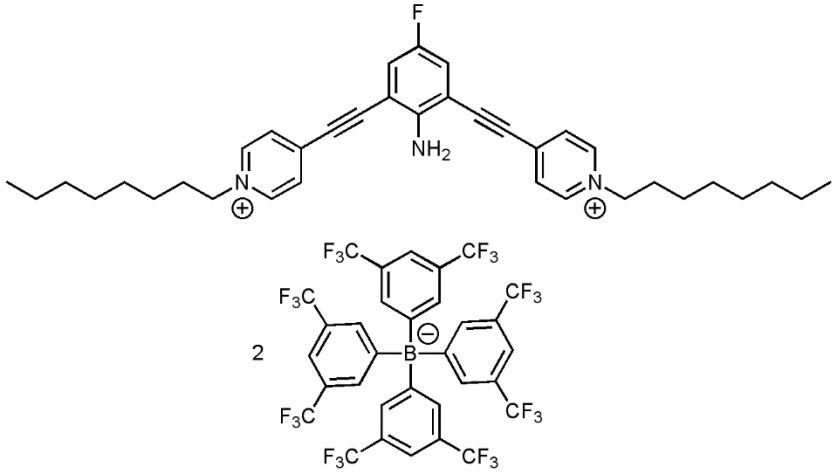

G2HB (7). ^1H (500 MHz, $CDCl_3$, 25˚C): 8.0731-8.0598 (4H, d, *J* = 6.65 Hz), 7.6842 (16H, b), 7.6559-7.6427 (4H, d, *J* = 6.6 Hz), 7.4937 (8H, b), 7.2376 (2H, d), 4.7532 (2H, s), 4.2531 (4H, t, *J* = 7.53 Hz), 1.9058 (4H, b), 1.3076 (20H, b), 0.8548 (6H, t). ^{13}C (125.7 MHz, $CDCl_3$, 25˚C): 161.9838 (dd, *J* = 99.24 Hz, *J* = 49.59 Hz), 148.6799, 142.4386, 141.5833, 134.8523, 129.6429, 129.2233 (qq, *J* = 29.85 Hz), 125.6782 (q, *J* = 272.61 Hz), 124.5287, 124.3342, 117.6843, 117.6541,

105.0244 (d, *J* = 7.55 Hz), 102.6996, 91.0861, 62.9674, 31.5562, 31.4401, 28.8630, 26.0454, 22.5690. ^{19}F (470.6 MHz, $CDCl_3$, 25˚C): -126.9895 (t, *J* = 7.81 Hz, 1F), -65.4280 (48F, s). HRMS (ESI pos) *m/z*: 269.6838 (M^{+2}, 100%), 1402.4325 (M^{+}-1BAr^{F}); $C_{36}H_{44}FI_2N_3^{+2}$ (269.6840), $C_{68}H_{56}BF_{25}I_2N_3^{+}$ (1402.4325).

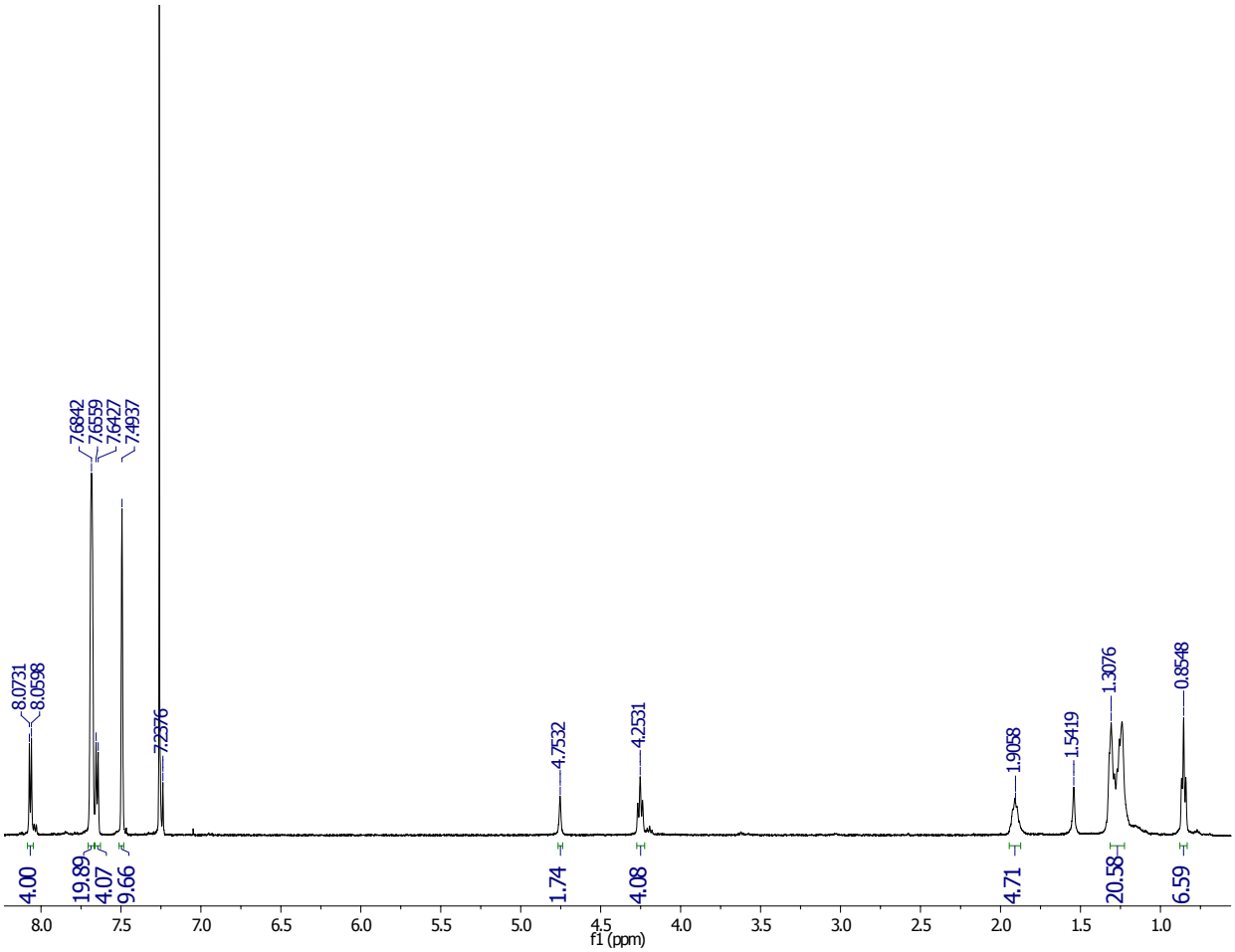

Figure S20. ^{1}H NMR of spectrum of **7** ($CDCl_3$, 25˚C, 500 MHz).

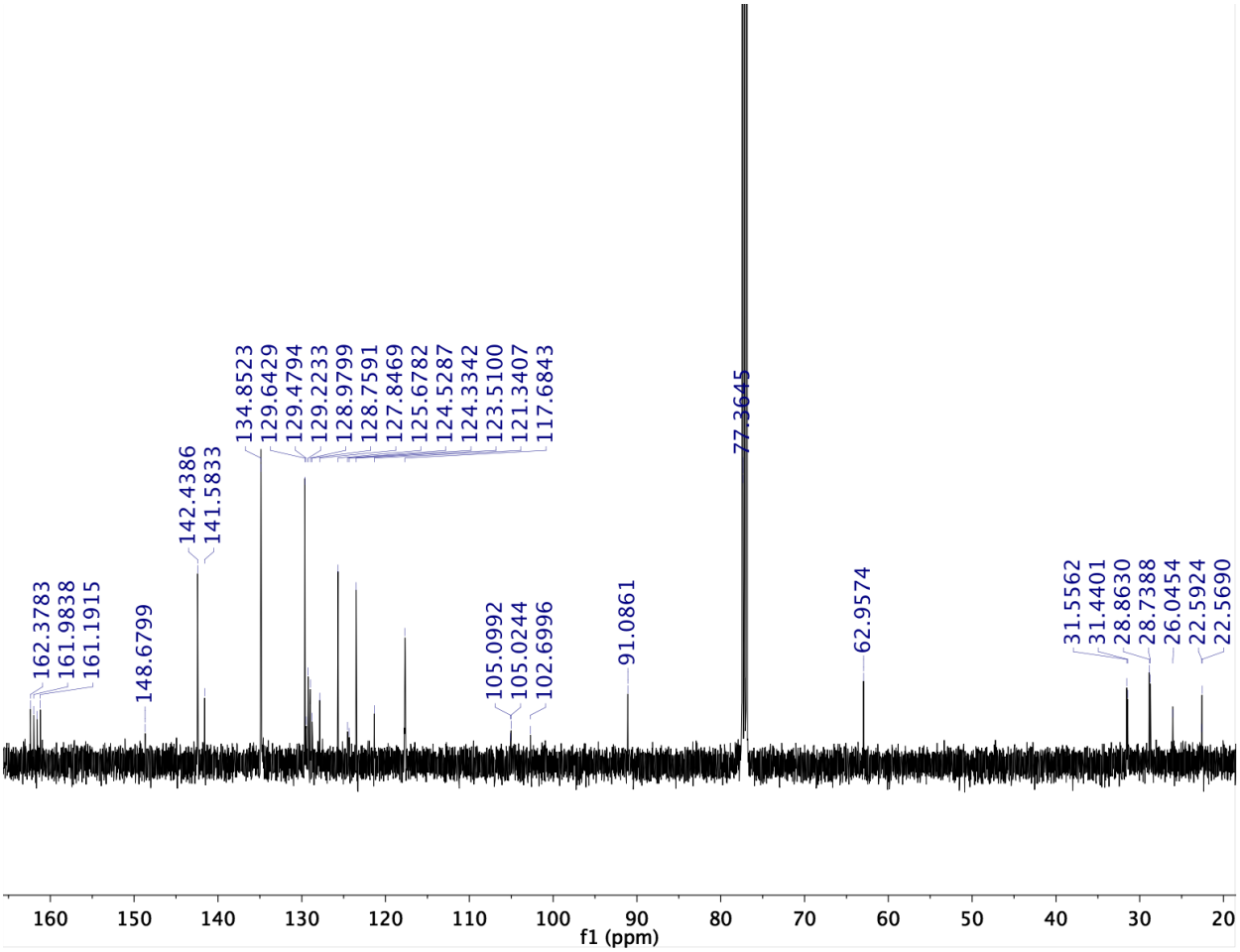

Figure S21. ^{13}C NMR of spectrum of **7** ($CDCl_3$, 25˚C, 125.7 MHz).

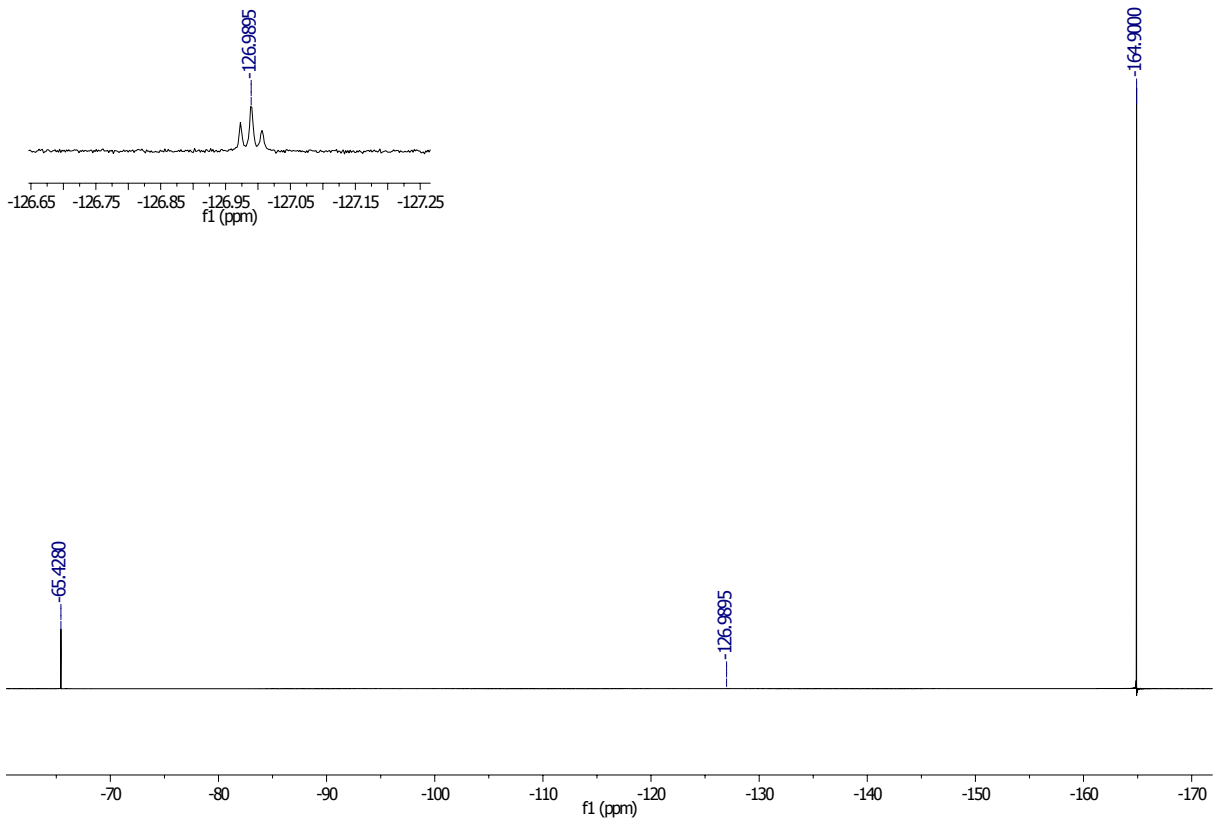

Figure S22. ^{1}H NMR of spectrum of **7** ($CDCl_3$, 25˚C, 470.6 MHz).

UV-Vis and fluorescence studies

General methods of UV-Vis and fluorescence experiments

All the solvents used for UV-Vis and fluorescence studies were spectrophotometric grade (99.7+%). All UV-Vis spectra were collected on a Cary 60 spectrometer at 298 K. All fluorescence spectra were collected on a Cary Eclipse spectrometer at 298 K. All spectra were collected using a quartz cell fitted with a Teflon stopper, with a path length of 10.0 mm. In all cases, 0.02mM was chosen as the working concentration for each receptor such that the peak absorbance value was approximately 0.2 to 0.5. Measurements were carried out using Hamilton gastight syringes and titrations were carried out using Hamilton microliter syringes. After each addition, the cell was stoppered and shook for two minutes to ensure complete mixing. In order to keep the concentration of the receptor (host) constant throughout the titration, the receptor solution was used to prepare the anion (guest) solution. UV-Vis titrations were carried out by adding aliquots of the anion (guest) solution to a known volume of receptor (host) solution.

Solvatochromism of neutral receptors 1a and 1b

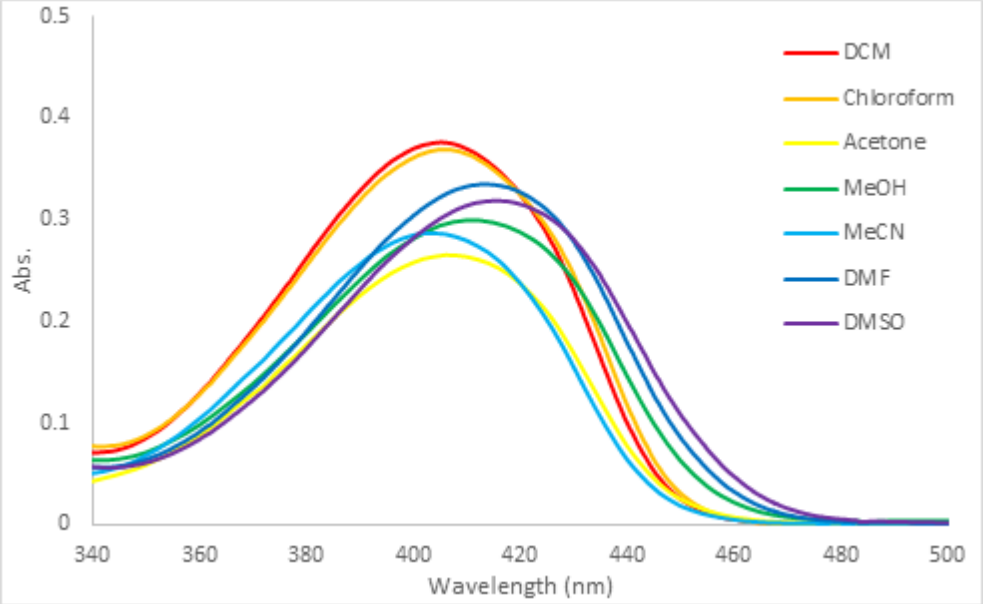

Figure S23. UV-Vis absorption spectrum of **1a** in various solvents.

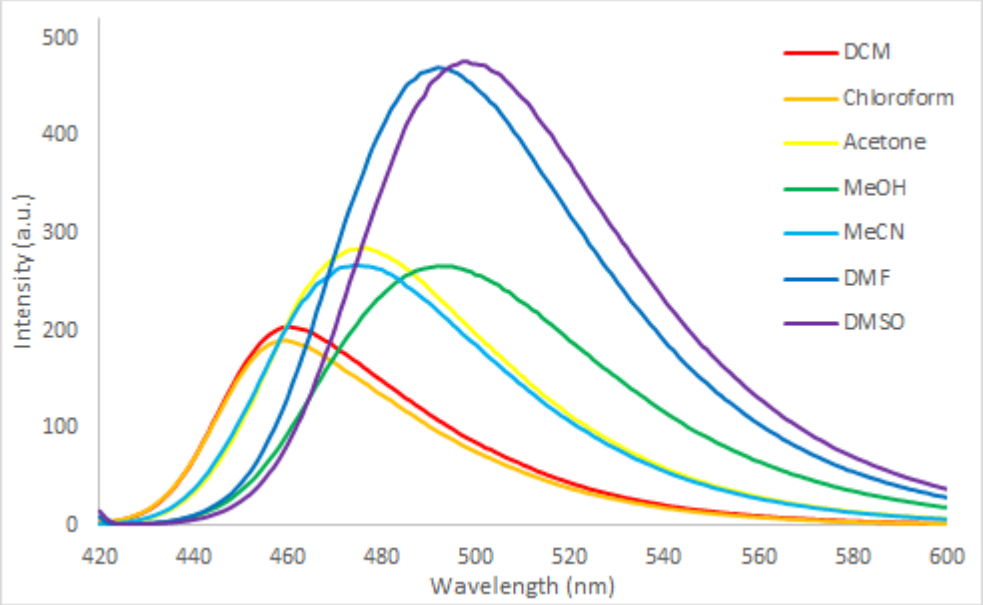

Figure S24. Fluorescence emission spectrum of **1a** in various solvents. Slit (excitation/emission) = 5 nm.

$\lambda_{ex\ DCM}$= 405 nm, $\lambda_{ex\ Chloroform}$= 406 nm, $\lambda_{ex\ Acetone}$= 406 nm, $\lambda_{ex\ methanol}$= 411 nm, $\lambda_{ex\ MeCN}$= 405 nm, $\lambda_{ex\ DMF}$= 413.5 nm, $\lambda_{ex\ DMSO}$= 415.5 nm.

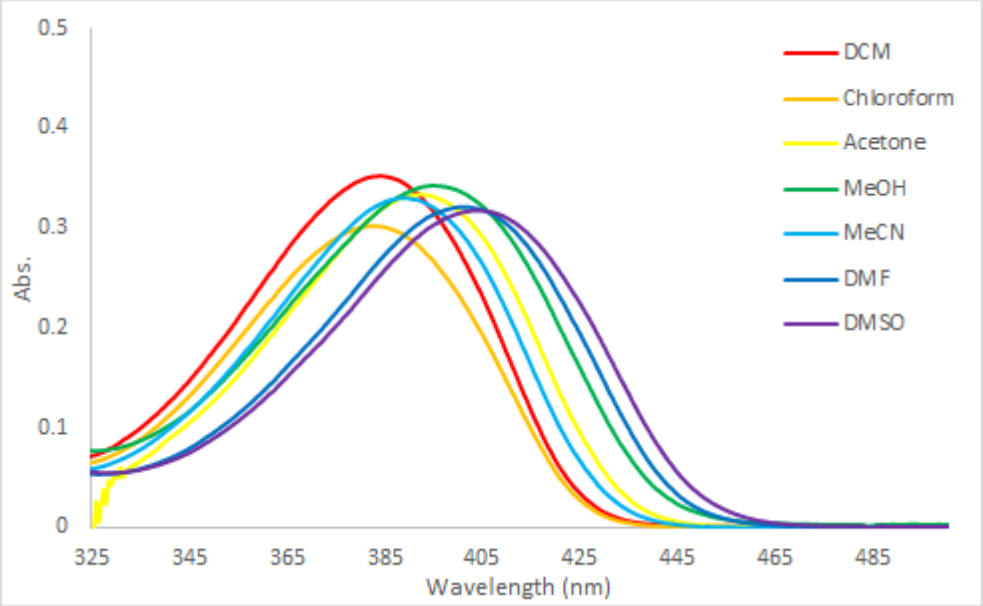

Figure S25. UV-Vis absorption spectrum of **1b** in various solvents.

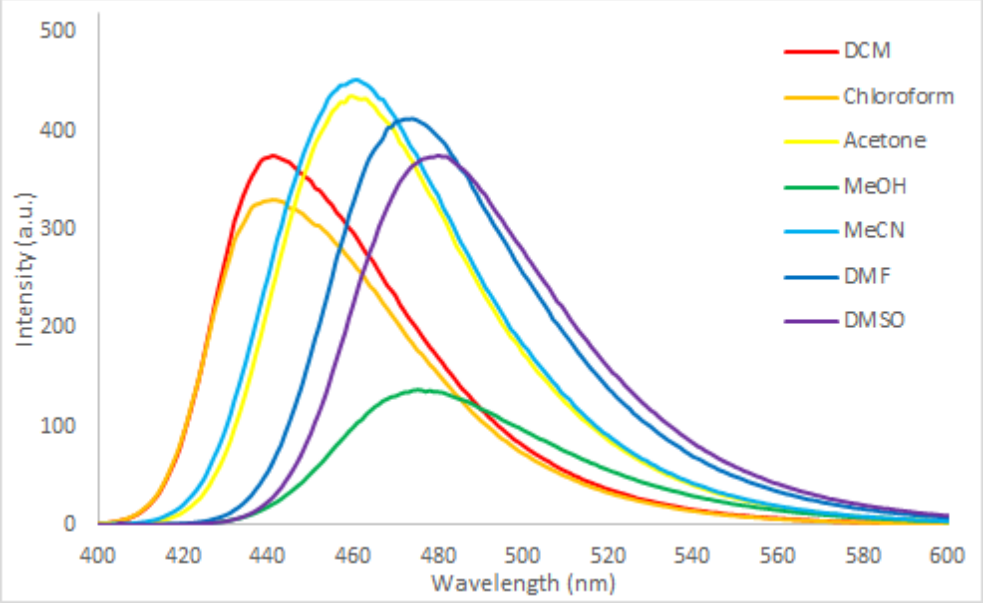

Figure S26. Fluorescence emission spectrum of **1b** in various solvents. Slit (excitation/emission) = 2.5 nm.

$\lambda_{ex\ DCM}$= 384.5 nm, $\lambda_{ex\ Chloroform}$= 382 nm, $\lambda_{ex\ Acetone}$= 392.5 nm, $\lambda_{ex\ methanol}$= 395 nm, $\lambda_{ex\ MeCN}$ = 388 nm, $\lambda_{ex\ DMF}$= 401.5 nm, $\lambda_{ex\ DMSO}$= 404 nm.

Solvatochromism of charged receptors 2a and 2b

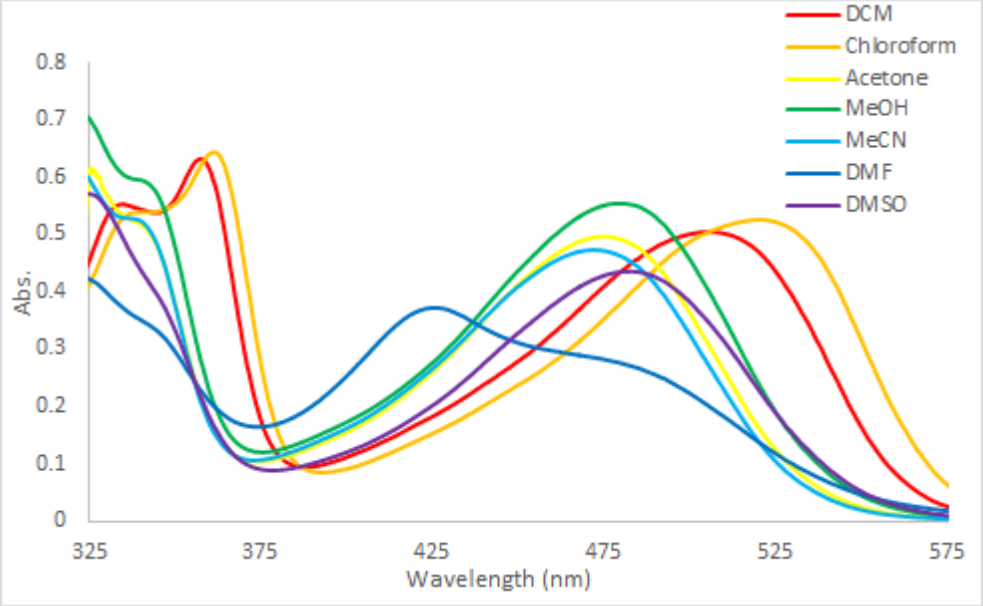

Figure S27. UV-Vis absorption spectrum of **2a** in various solvents.

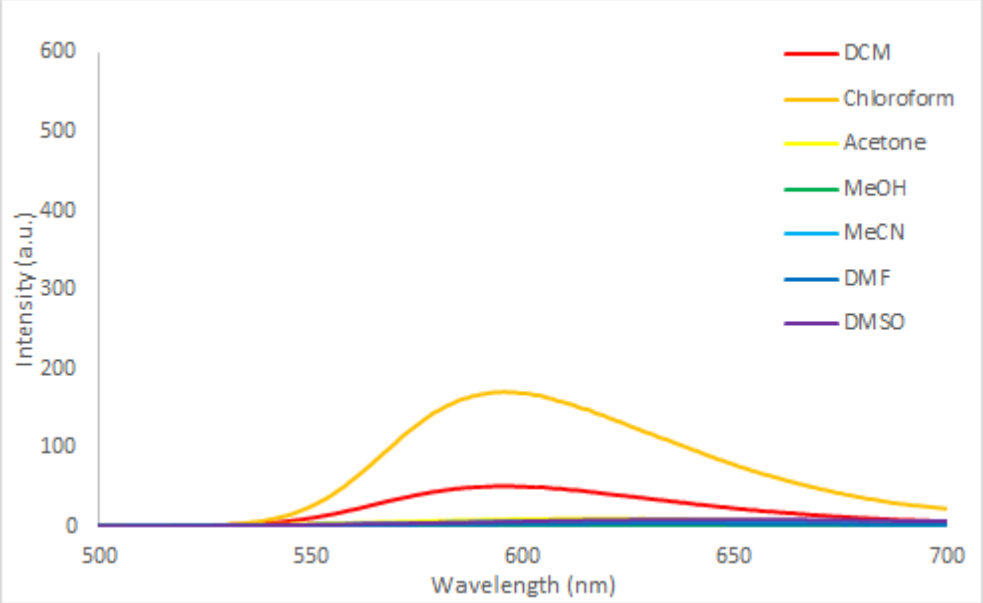

Figure S28. Fluorescence emission spectrum of **2a** in various solvents. Slit (excitation/emission) = 5 nm.

$\lambda_{ex\ DCM}$= 505.5 nm, $\lambda_{ex\ Chloroform}$= 521 nm, $\lambda_{ex\ Acetone}$= 475 nm, $\lambda_{ex\ methanol}$= 479 nm, $\lambda_{ex\ MeCN}$ = 472 nm, $\lambda_{ex\ DMF}$= 425.5 nm, $\lambda_{ex\ DMSO}$= 482.5 nm.

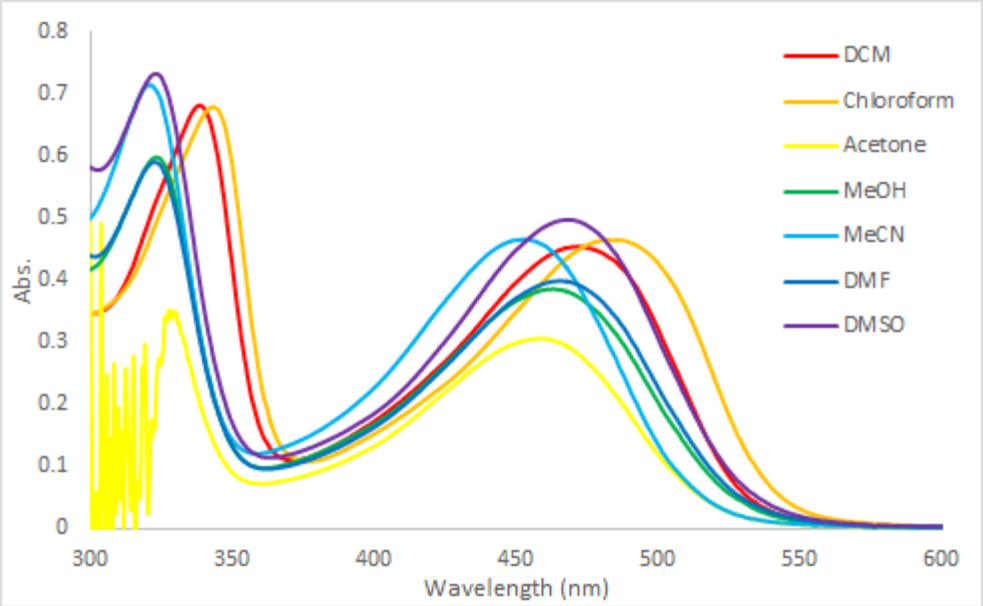

Figure S29. UV-Vis absorption spectrum of **2b** in various solvents.

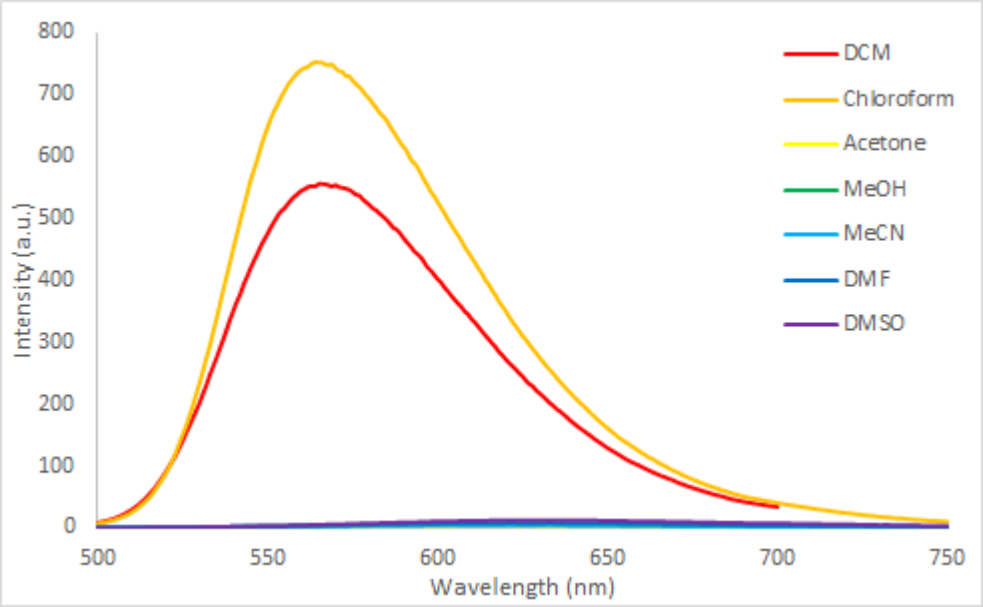

Figure S30. Fluorescence emission spectrum of **2b** in various solvents. Slit (excitation/emission) = 5 nm.

$\lambda_{ex\ DCM}$= 472 nm, $\lambda_{ex\ Chloroform}$= 482.5 nm, $\lambda_{ex\ Acetone}$= 458.5 nm, $\lambda_{ex\ methanol}$= 463.5 nm, $\lambda_{ex\ MeCN}$ = 453.5 nm, $\lambda_{ex\ DMF}$= 465.5 nm, $\lambda_{ex\ DMSO}$= 468 nm.

Linear free energy relationships

Linear correlations between $1/\lambda_{max}$ of UV-Vis spectra and solvent polarity were conducted for neutral receptors **1a**,**b** and charged receptors **2a**,**b** using four solvent polarity parameters (dielectric constant, dipole moment, $E_T(30)$[1] and π*scale[2]), respectively.

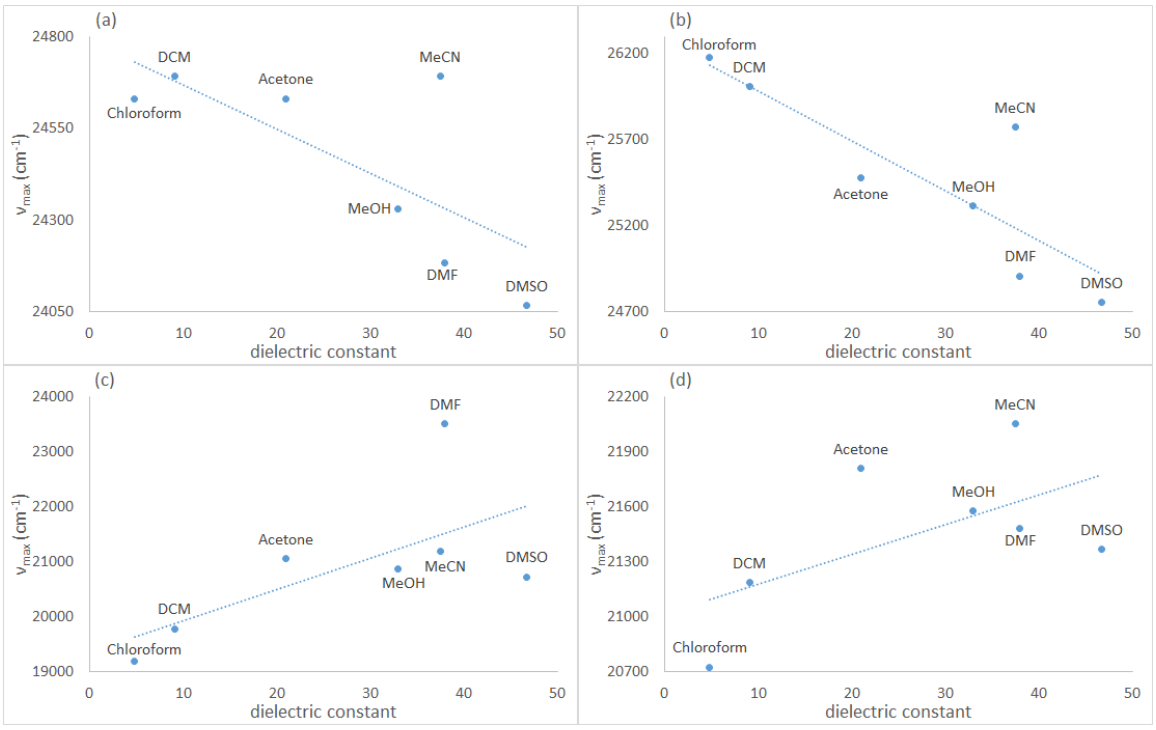

Figure S31. Linear correlation between v_{max} and dielectric constant for neutral receptors **1a** (a), **1b** (b) and charged receptors **2a** (c), **2b** (d).

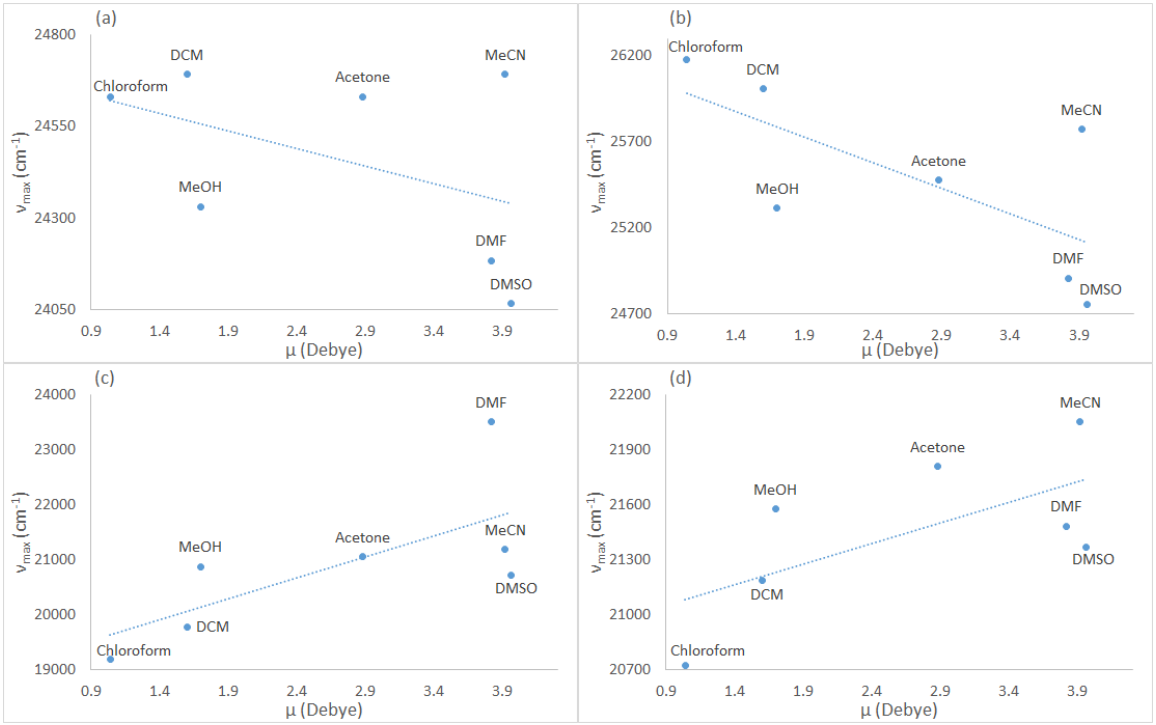

Figure S32. Linear correlation between v_{max} and dipole moment for neutral receptors **1a** (a), **1b** (b) and charged receptors **2a** (c), **2b** (d).

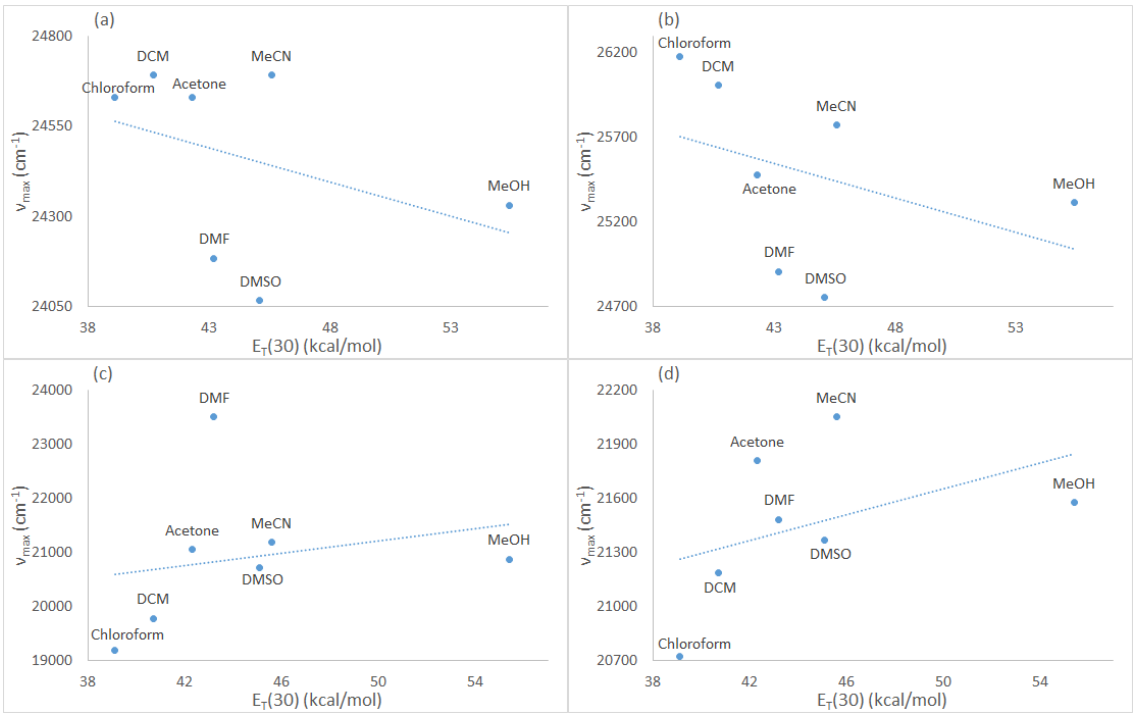

Figure S33. Linear correlation between ν_{max} and $E_T(30)$ for neutral receptors **1a** (a), **1b** (b) and charged receptors **2a** (c), **2b** (d).

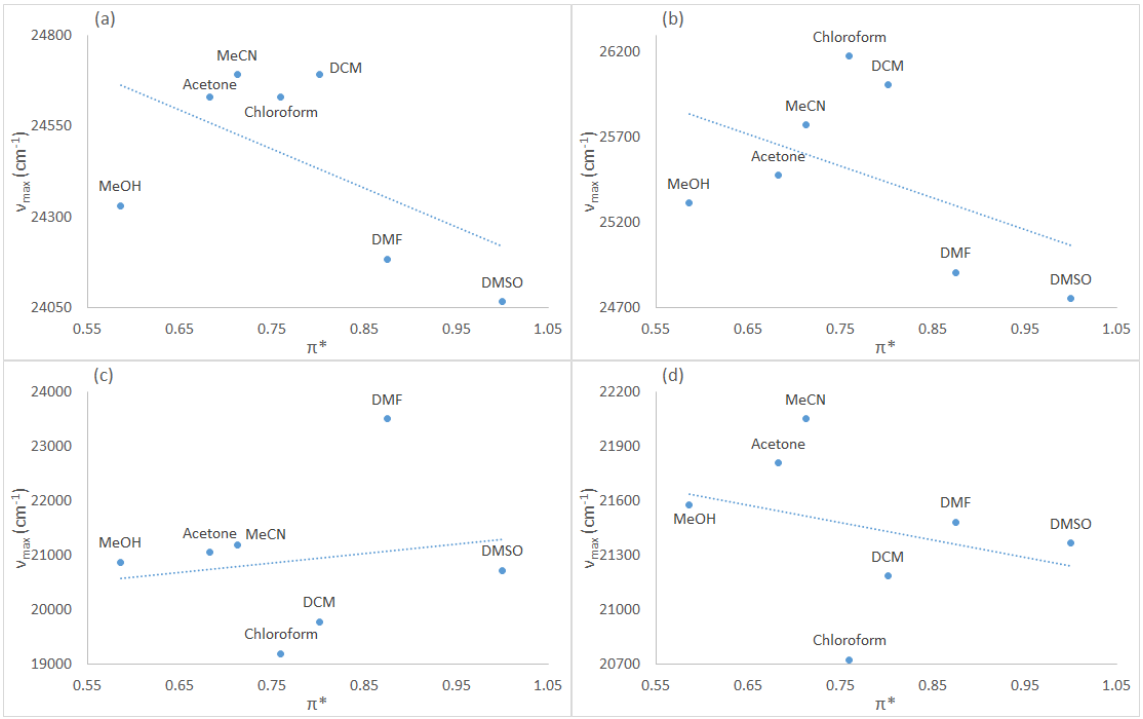

Figure S34. Linear correlation between ν_{max} and π* for neutral receptors **1a** (a), **1b** (b) and charged receptors **2a** (c), **2b** (d).

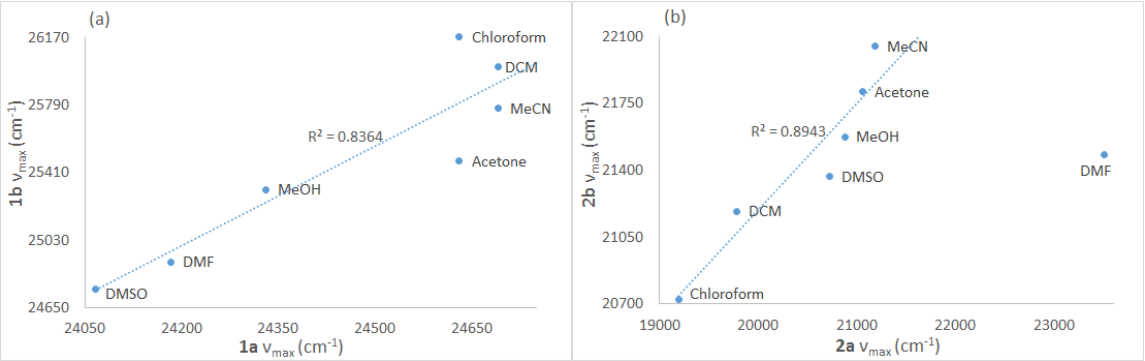

Figure S35. Linear correlation between (a) absorbance ν_{max} of neutral iodinated receptor **1a** and non-iodinated receptor **1b**, (b) absorbance ν_{max} of charged iodinated receptor **2a** and non-iodinated receptor **2b**.

Anion binding studies

All spectra were recorded at 20 μM of receptor in dichloromethane solution. Slit of excitation and emission for fluorescence experiment in this section is set up to 5 nm unless otherwise noted.

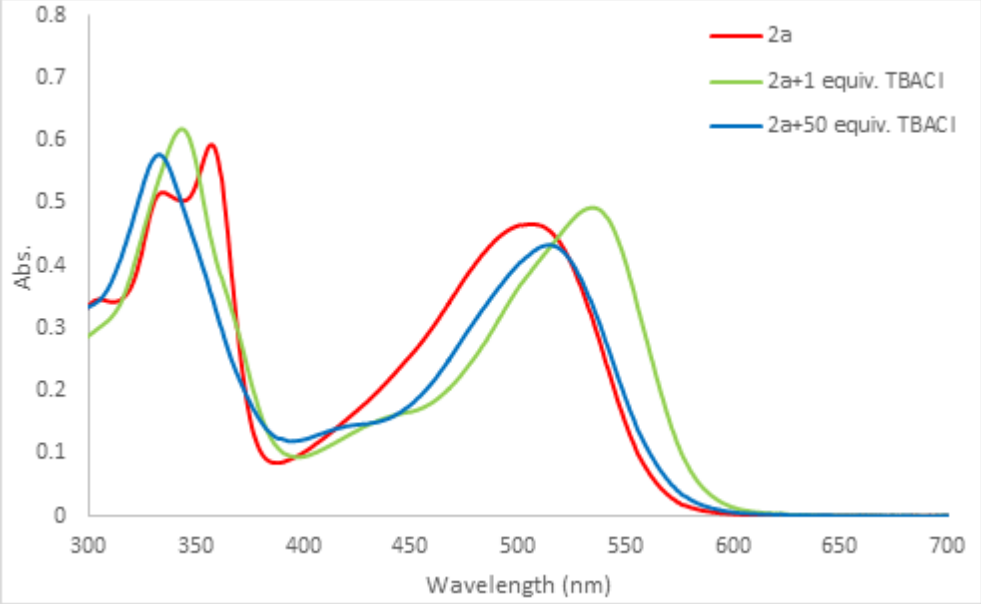

Figure S36. UV-Vis absorption spectrum of **2a** upon addition of $TBA^{+}Cl^{-}$.

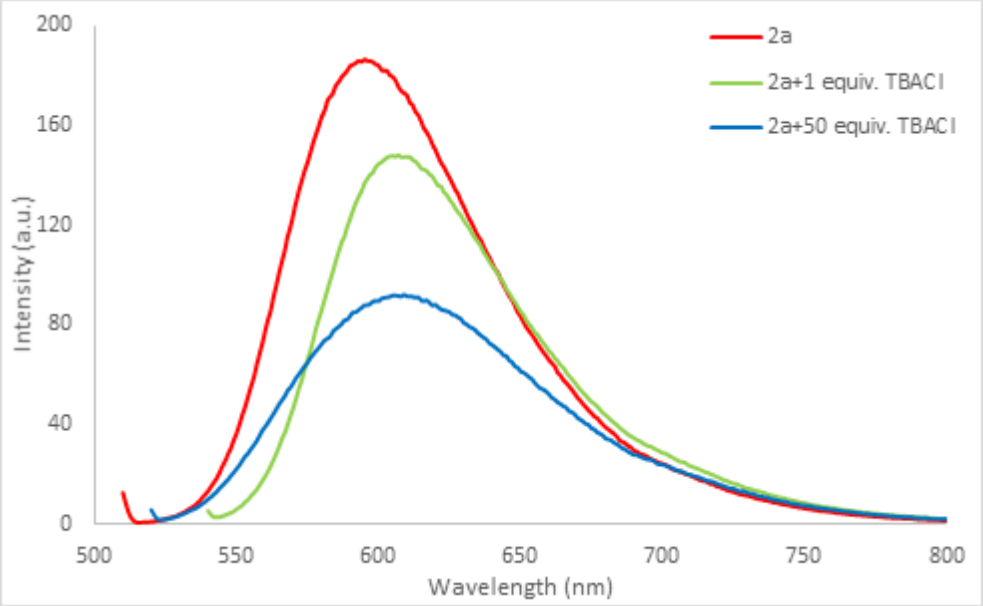

Figure S37. Fluorescence emission spectrum of **2a** upon addition of $TBA^{+}Cl^{-}$. λ_{ex} red= 506.5 nm, λ_{ex} green= 534.5 nm, λ_{ex} blue= 514.5 nm.

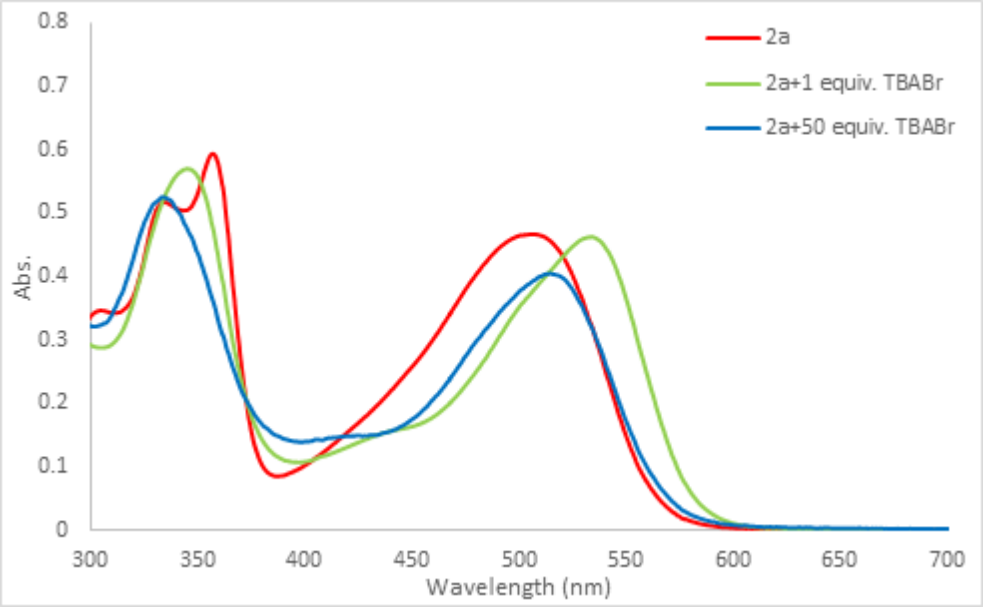

Figure S38. UV-Vis absorption spectrum of **2a** upon addition of $TBA^{+}Br^{-}$.

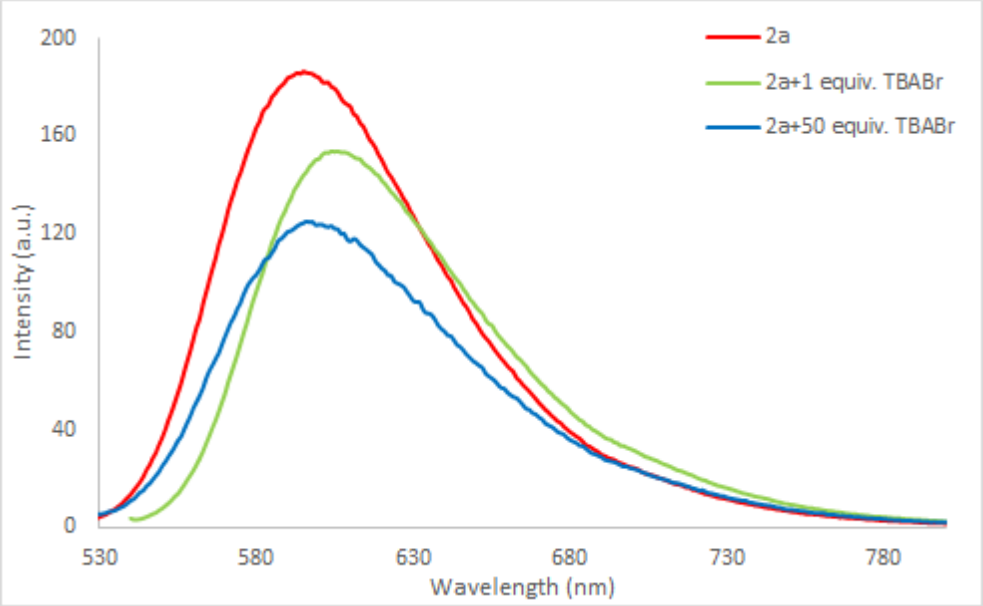

Figure S39. Fluorescence emission spectrum of **2a** upon addition of $TBA^{+}Br^{-}$. λ_{ex} red= 506.5 nm, λ_{ex} green= 534 nm, λ_{ex} blue= 514.5 nm.

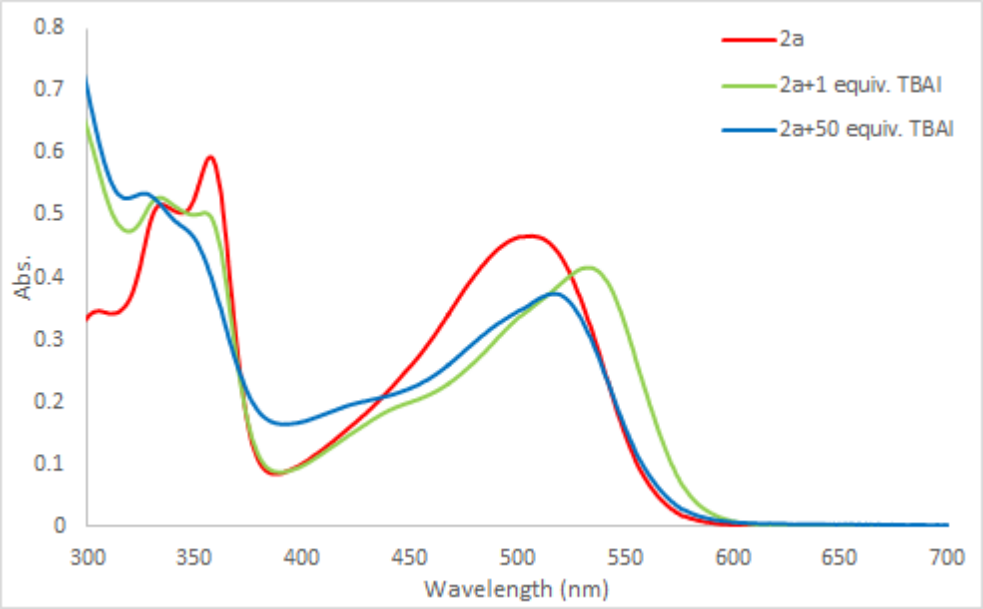

Figure S40. UV-Vis absorption spectrum of **2a** upon addition of $TBA^{+}I^{-}$.

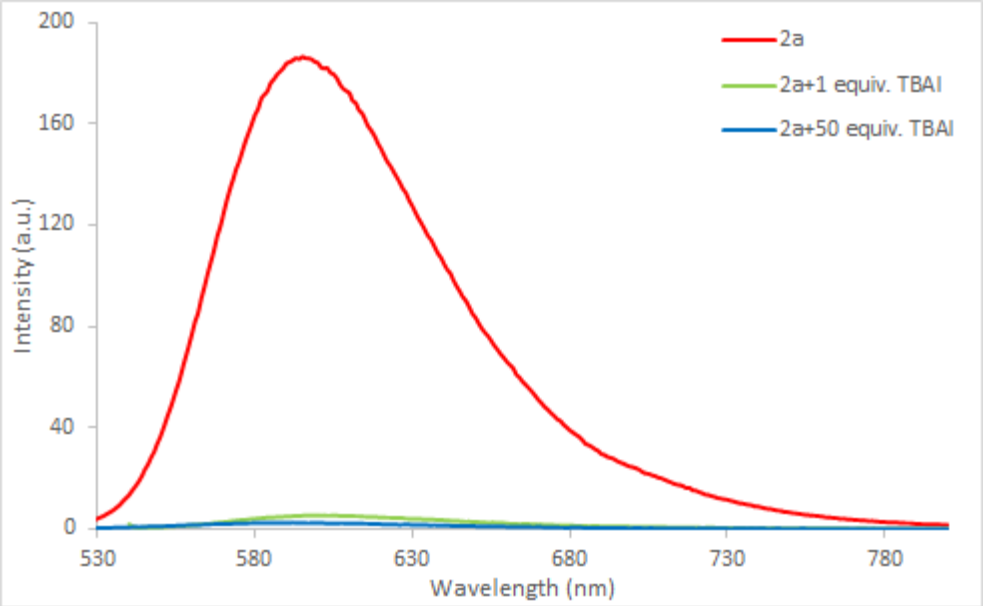

Figure S41. Fluorescence emission spectrum of **2a** upon addition of $TBA^{+}I^{-}$. λ_{ex} red= 506.5 nm, λ_{ex} green= 534 nm, λ_{ex} blue= 517.5 nm.

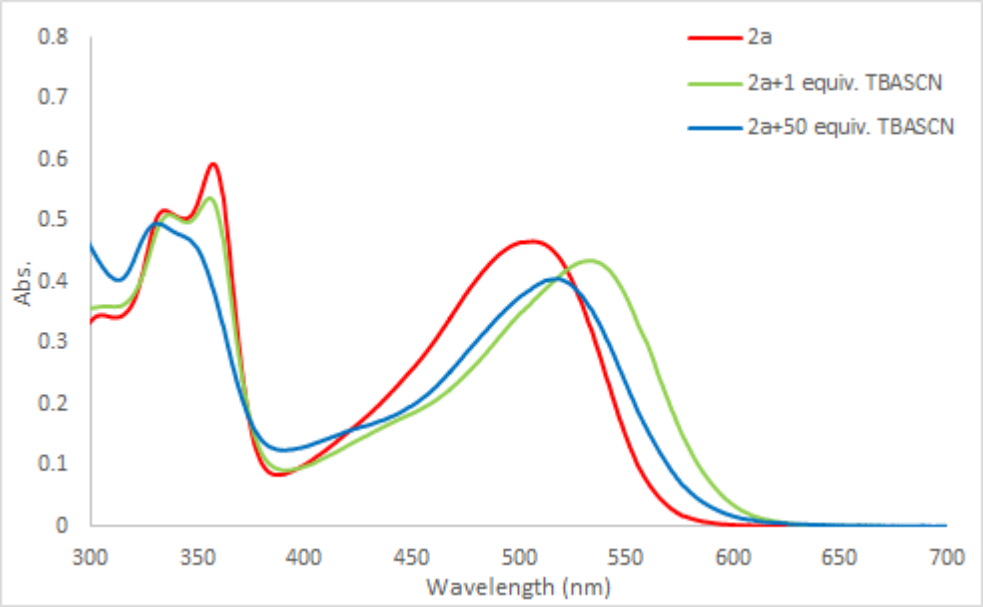

Figure S42. UV-Vis absorption spectrum of **2a** upon addition of $TBA^{+}SCN^{-}$.

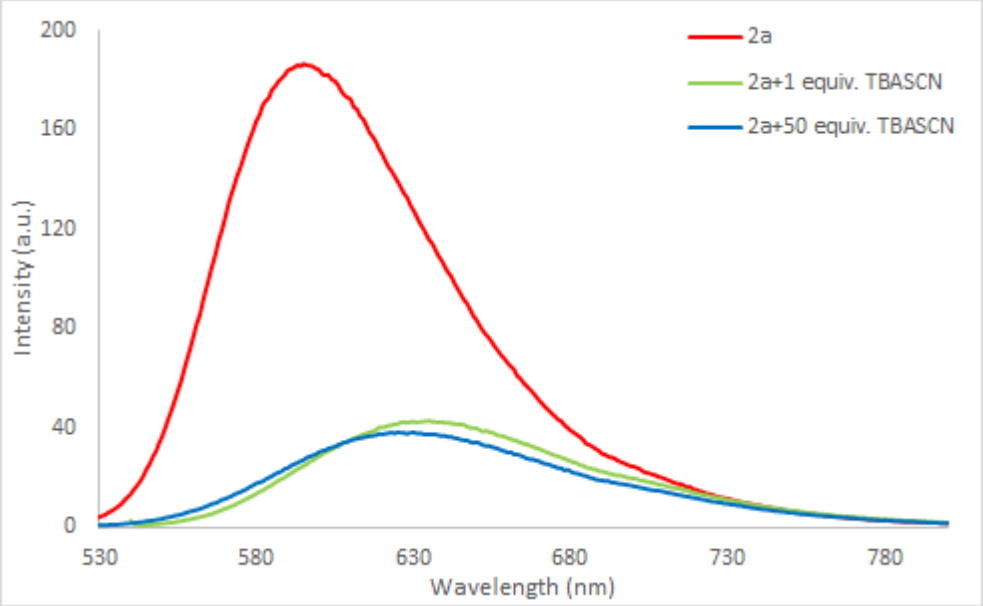

Figure S43. Fluorescence emission spectrum of **2a** upon addition of $TBA^{+}SCN^{-}$. λ_{ex} red= 506.5 nm, λ_{ex} green= 534 nm, λ_{ex} blue= 518.5 nm.

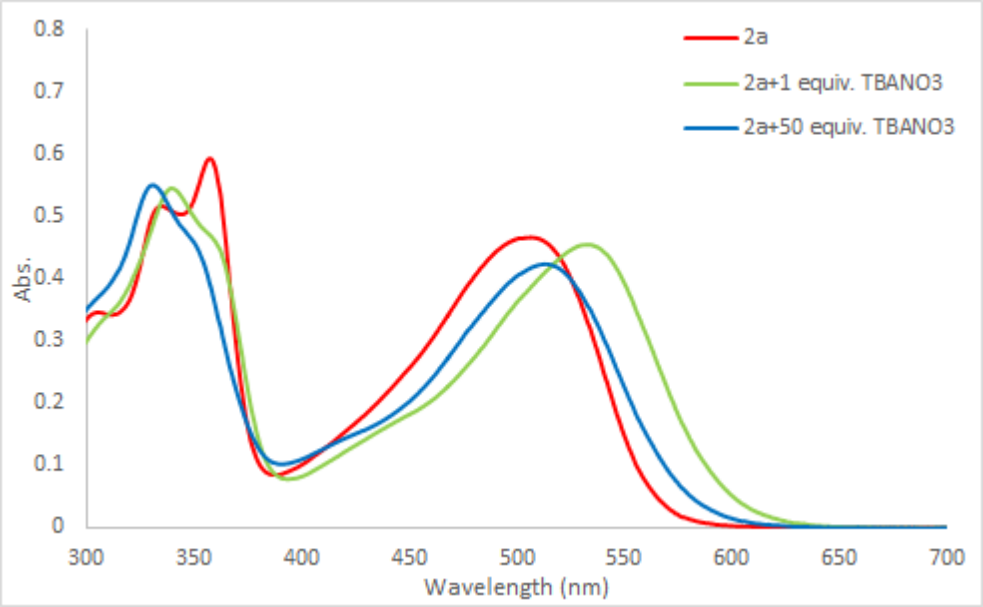

Figure S44. UV-Vis absorption spectrum of **2a** upon addition of $TBA^{+}NO_3^{-}$.

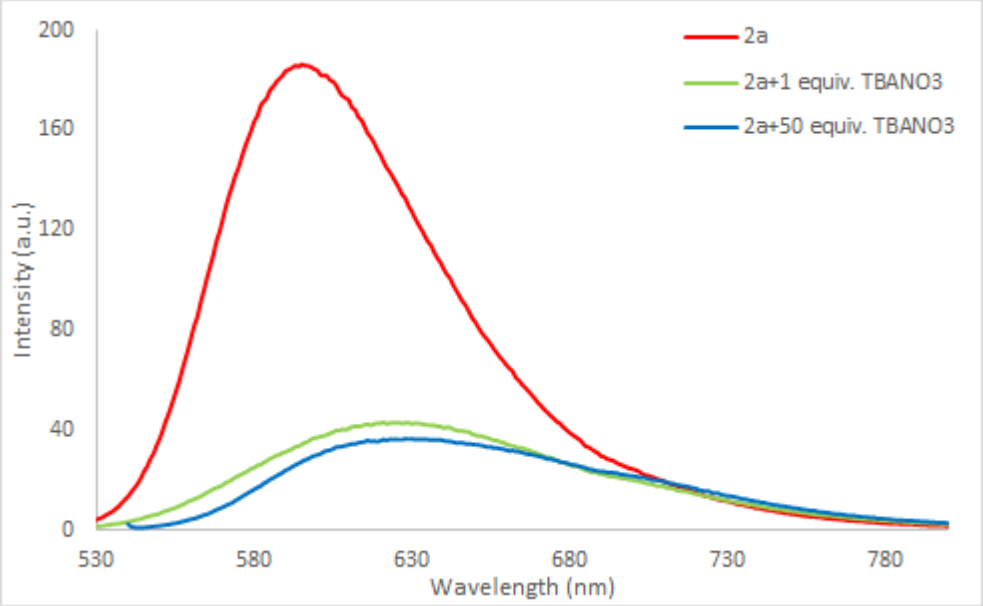

Figure S45. Fluorescence emission spectrum of **2a** upon addition of $TBA^{+}NO_3^{-}$. λ_{ex} red= 506.5 nm, λ_{ex} green= 534 nm, λ_{ex} blue= 513 nm.

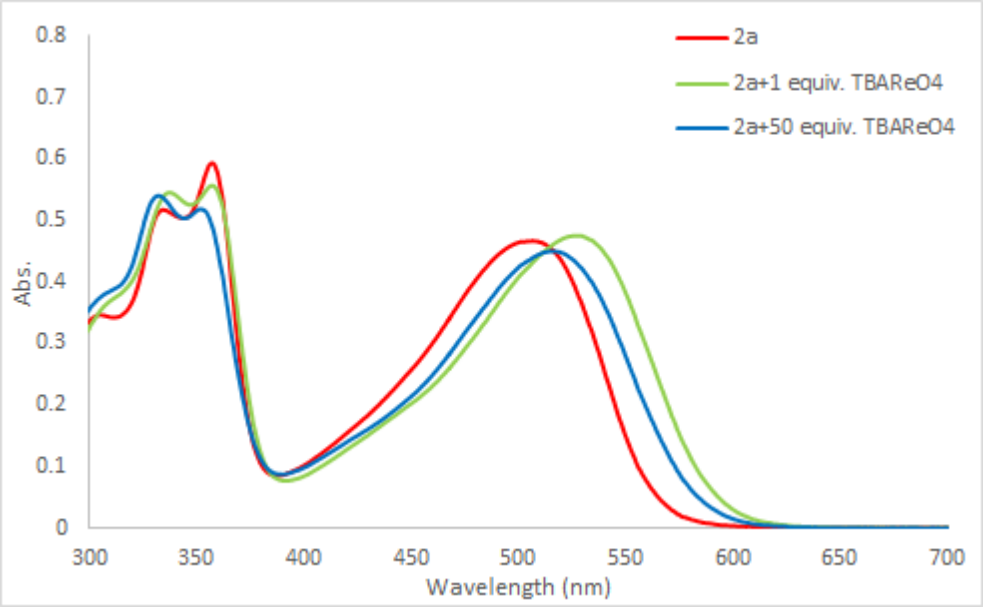

Figure S46. UV-Vis absorption spectrum of **2a** upon addition of $TBA^{+}ReO_4^{-}$.

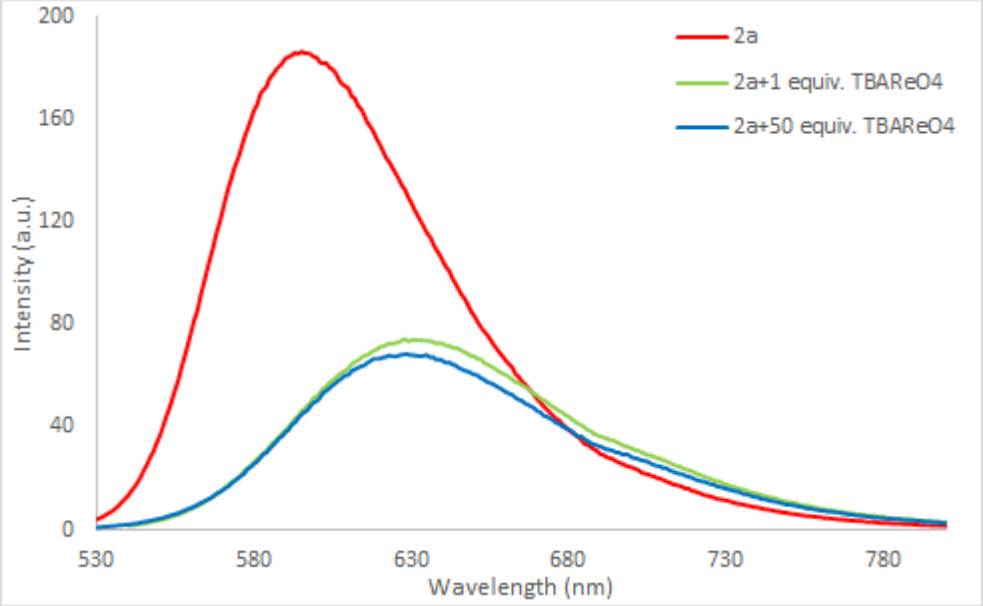

Figure S47. Fluorescence emission spectrum of **2a** upon addition of $TBA^{+}ReO_4^{-}$. λ_{ex} red= 506.5 nm, λ_{ex} green= 526.5 nm, λ_{ex} blue= 514.5 nm.

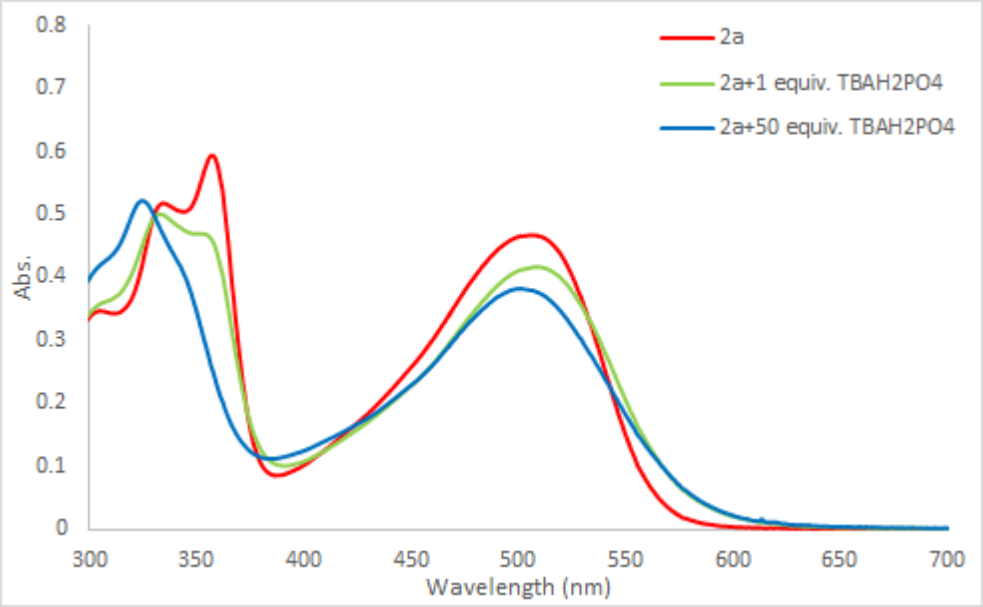

Figure S48. UV-Vis absorption spectrum of **2a** upon addition of $TBA^{+}H_2PO_4^{-}$.

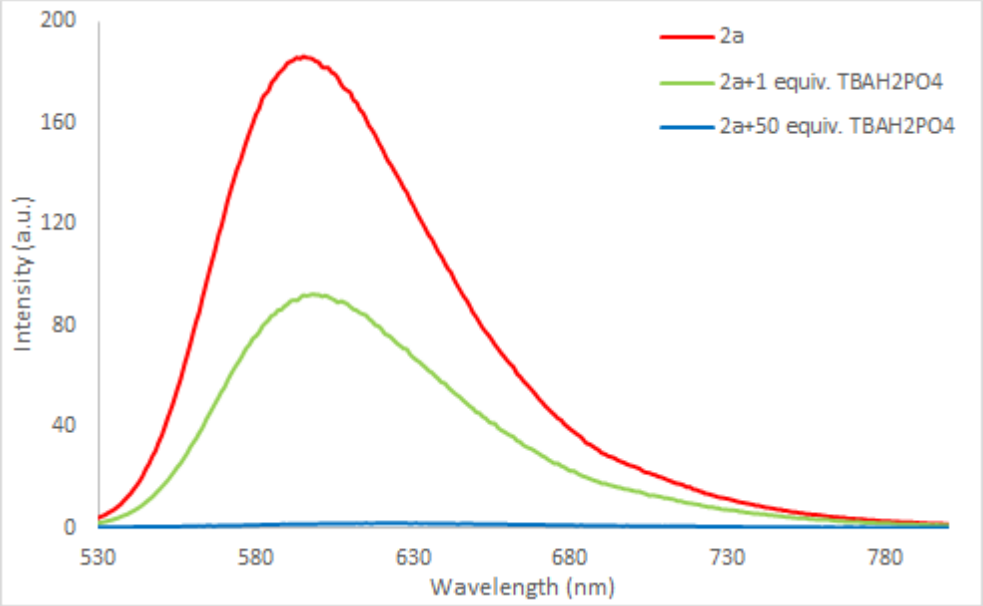

Figure S49. Fluorescence emission spectrum of **2a** upon addition of $TBA^{+}H_2PO_4^{-}$. λ_{ex} red= 506.5 nm, λ_{ex} green= 509 nm, λ_{ex} blue= 501 nm.

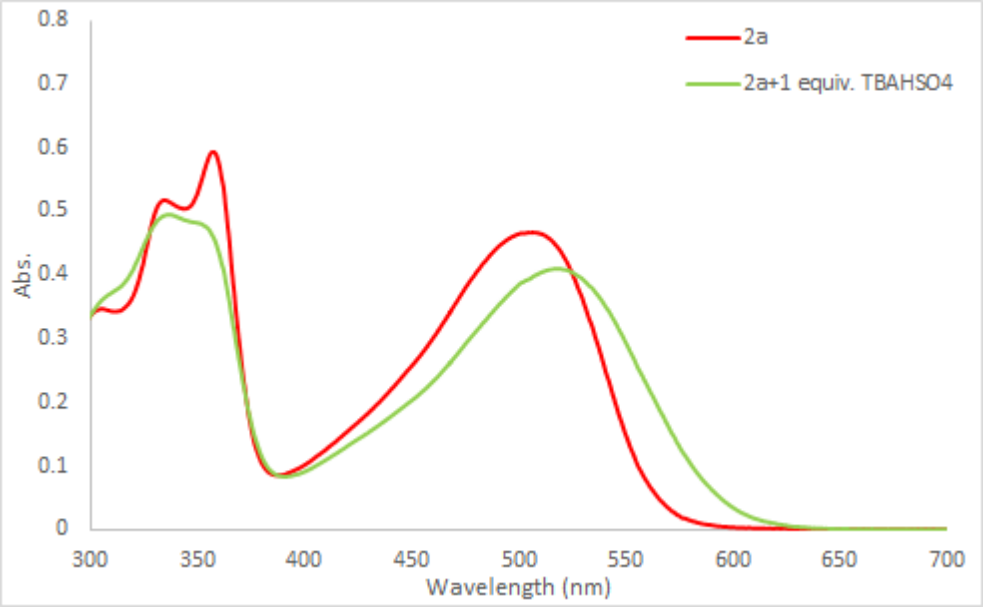

Figure S50. UV-Vis absorption spectrum of **2a** upon addition of $TBA^{+}HSO_4^{-}$.

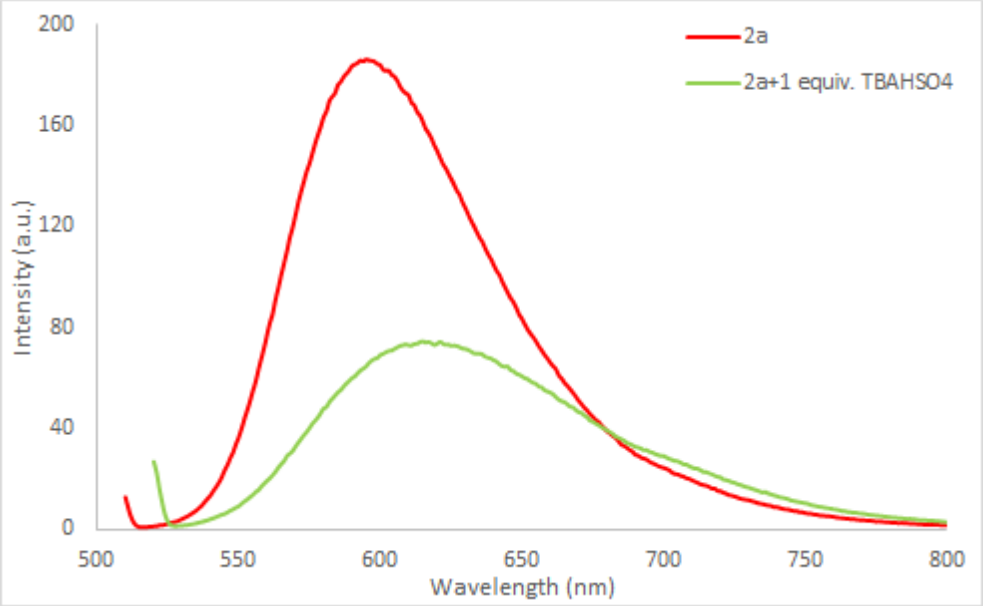

Figure S51. Fluorescence emission spectrum of **2a** upon addition of $TBA^{+}HSO_4^{-}$. λ_{ex} red= 506.5 nm, λ_{ex} green= 518.5 nm.

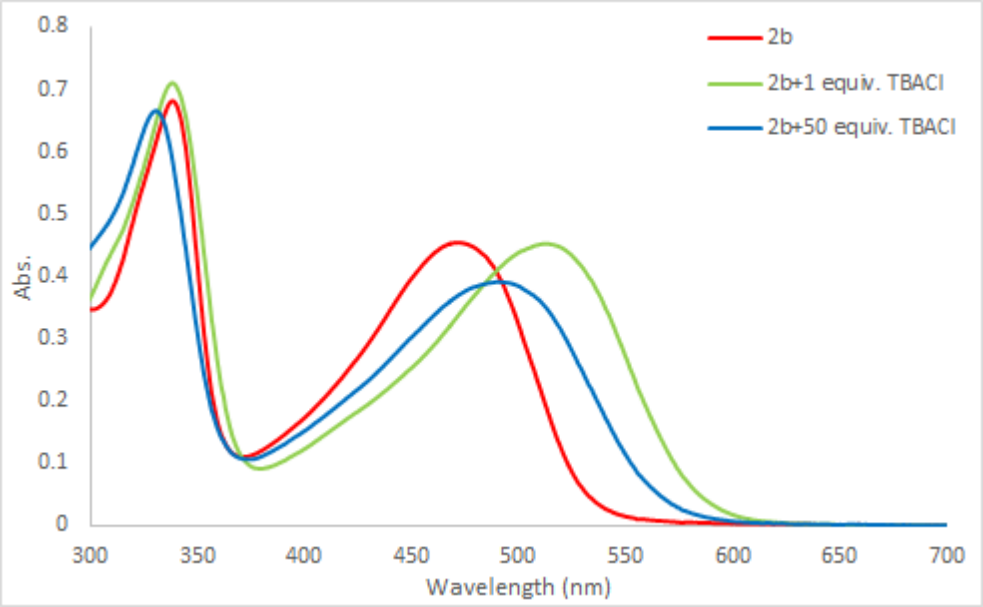

Figure S52. UV-Vis absorption spectrum of **2b** upon addition of $TBA^{+}Cl^{-}$.

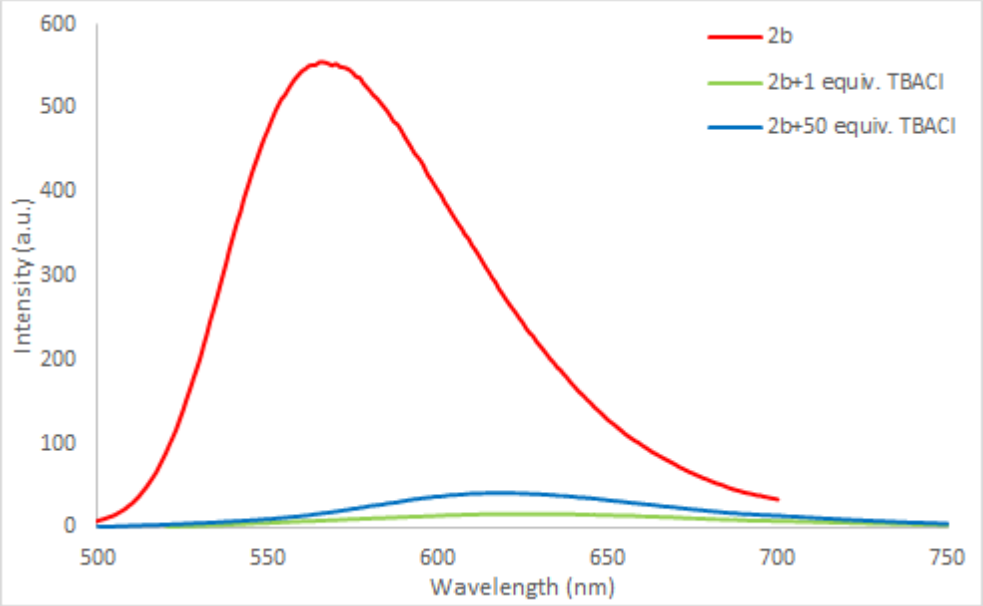

Figure S53. Fluorescence emission spectrum of **2b** upon addition of $TBA^{+}Cl^{-}$. λ_{ex} red= 472 nm, λ_{ex} green= 513 nm, λ_{ex} blue= 492.5 nm.

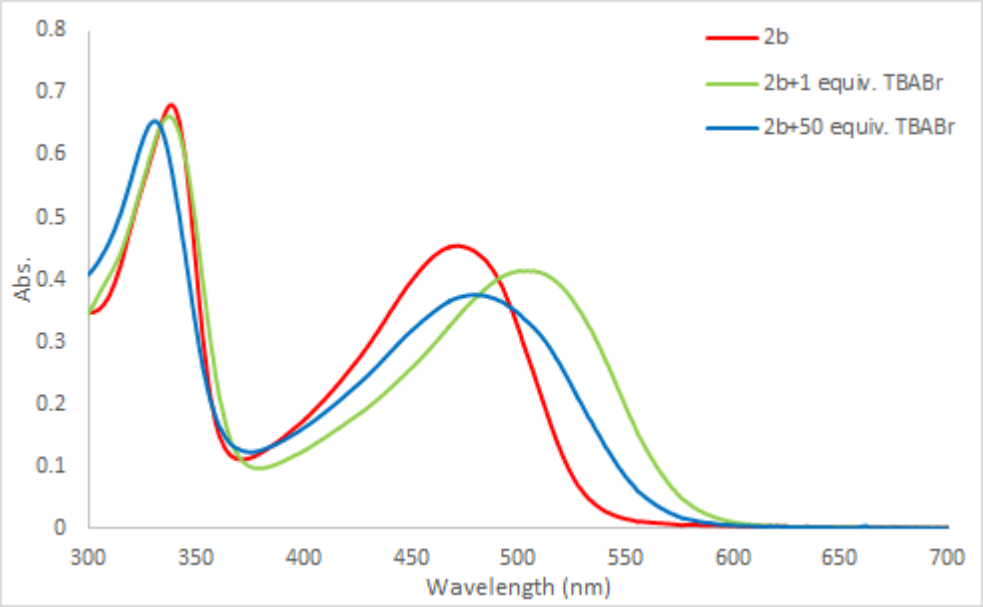

Figure S54. UV-Vis absorption spectrum of **2b** upon addition of $TBA^{+}Br^{-}$.

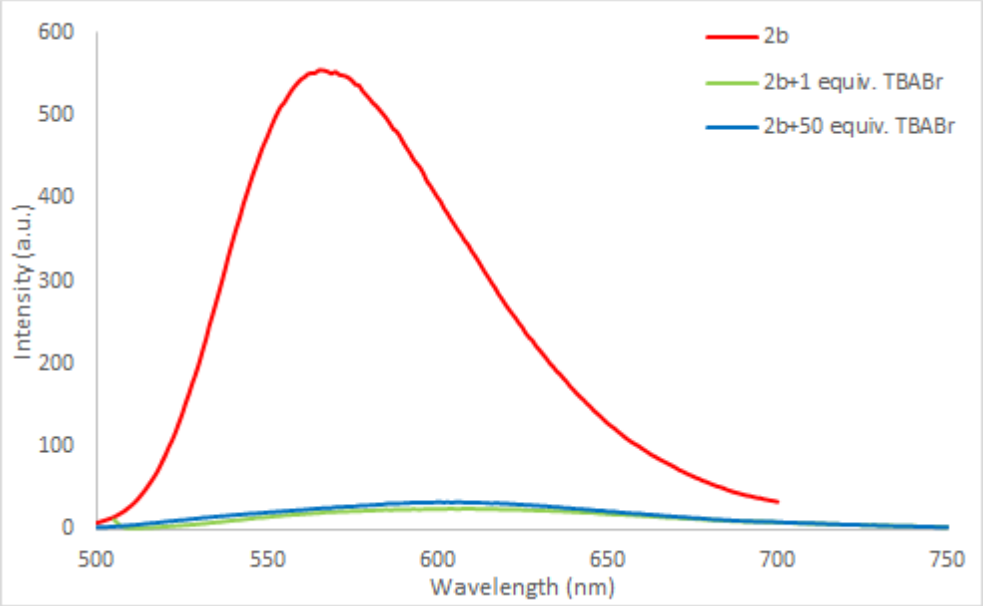

Figure S55. Fluorescence emission spectrum of **2b** upon addition of $TBA^{+}Br^{-}$. λ_{ex} red= 472 nm, λ_{ex} green= 501 nm, λ_{ex} blue= 480 nm.

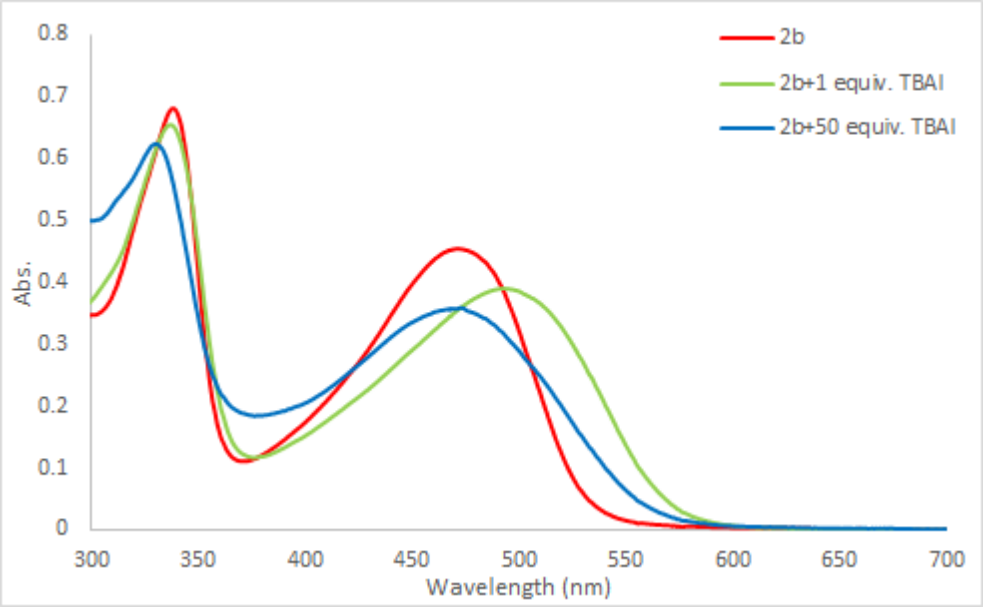

Figure S56. UV-Vis absorption spectrum of **2b** upon addition of $TBA^{+}I^{-}$.

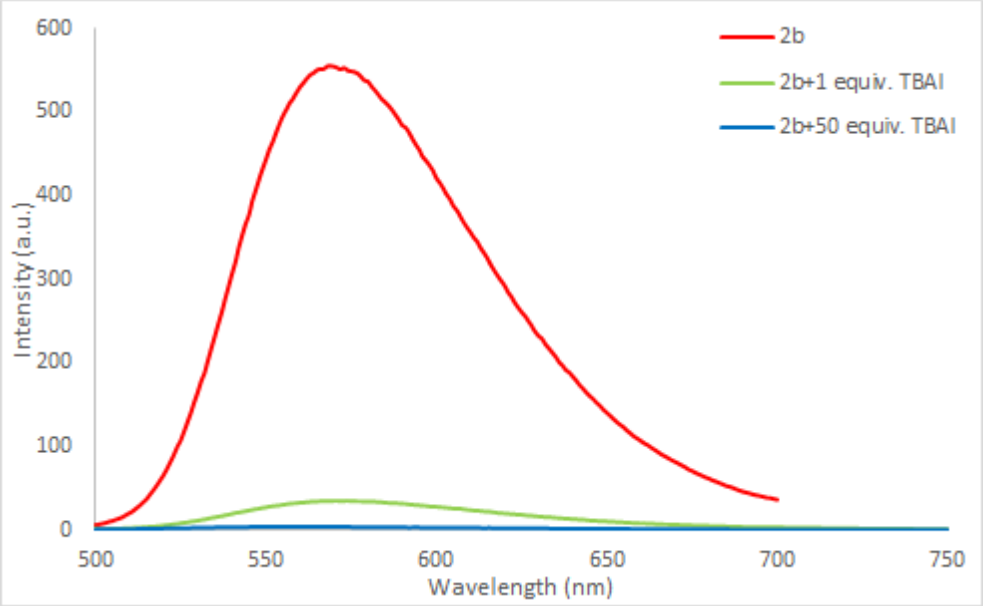

Figure S57. Fluorescence emission spectrum of **2b** upon addition of $TBA^{+}I^{-}$. λ_{ex} red= 472 nm, λ_{ex} green= 493.5 nm, λ_{ex} blue= 472.5 nm.

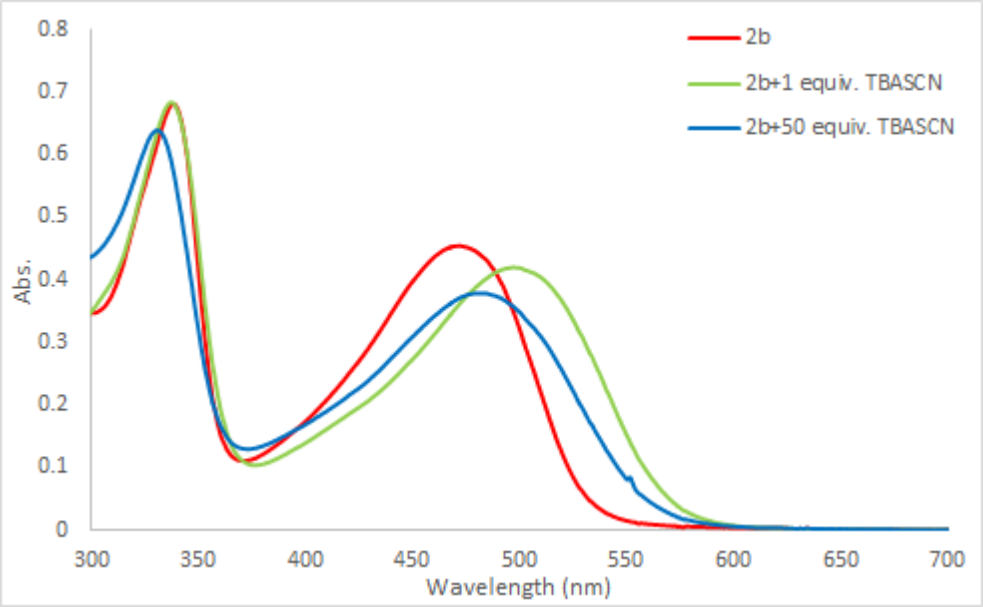

Figure S58. UV-Vis absorption spectrum of **2b** upon addition of $TBA^{+}SCN^{-}$.

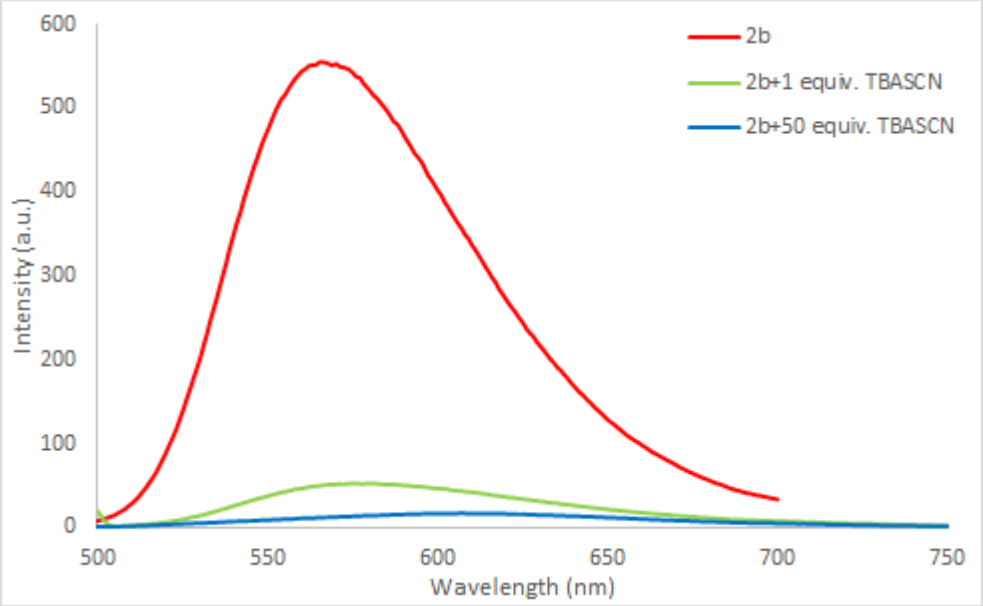

Figure S59. Fluorescence emission spectrum of **2b** upon addition of $TBA^{+}SCN^{-}$. λ_{ex} red= 472 nm, λ_{ex} green= 497 nm, λ_{ex} blue= 481 nm.

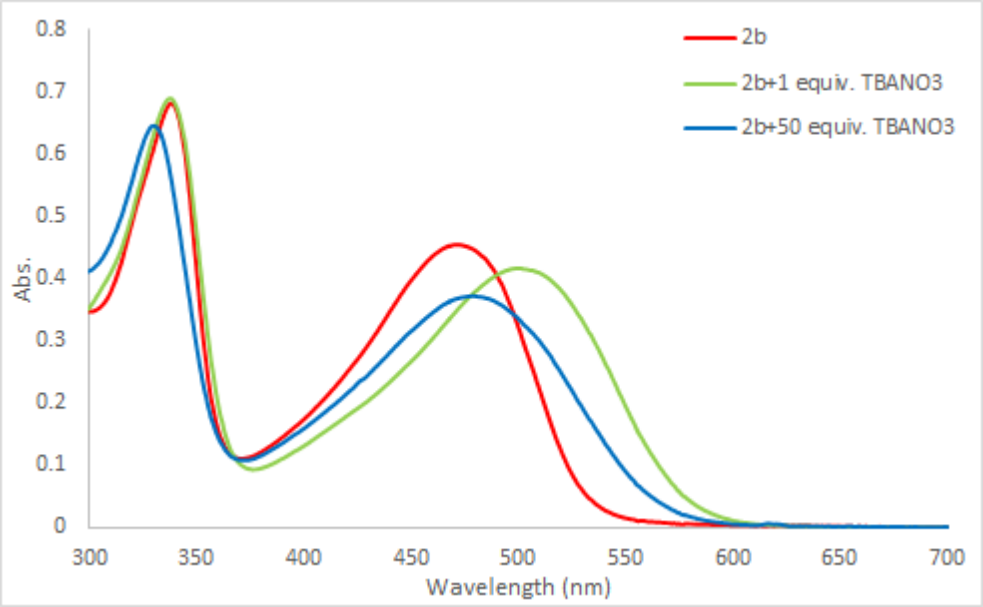

Figure S60. UV-Vis absorption spectrum of **2b** upon addition of $TBA^{+}NO_3^{-}$.

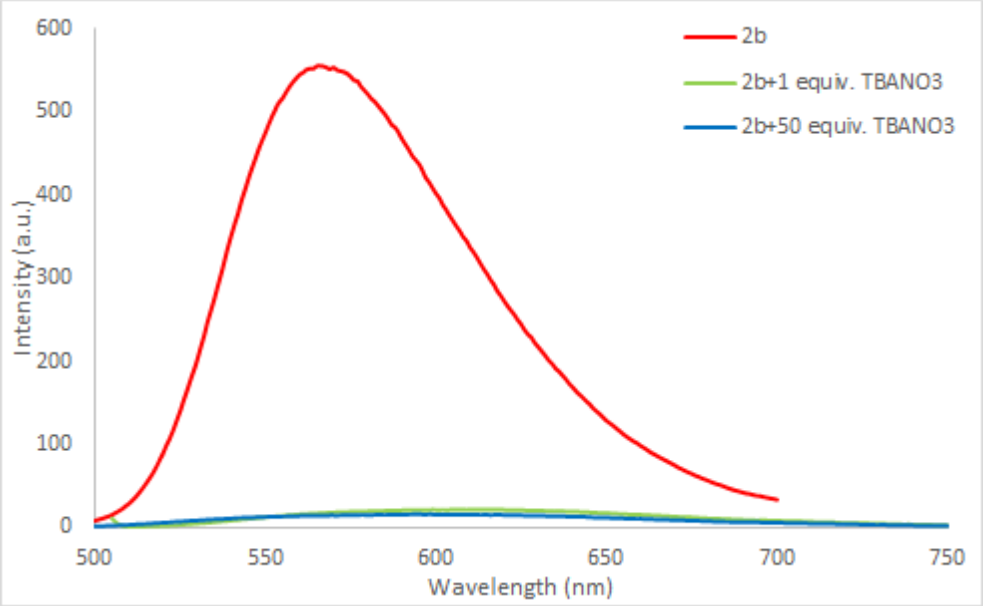

Figure S61. Fluorescence emission spectrum of **2b** upon addition of $TBA^{+}NO_3^{-}$. λ_{ex} red= 472 nm, λ_{ex} green= 501 nm, λ_{ex} blue= 478.5 nm.

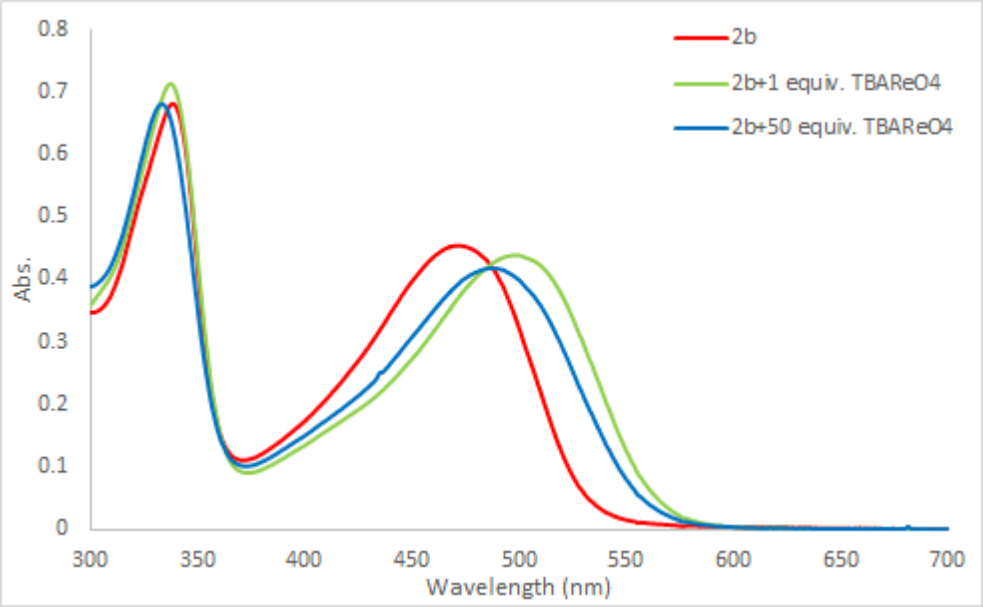

Figure S62. UV-Vis absorption spectrum of **2b** upon addition of $TBA^{+}ReO_4^{-}$.

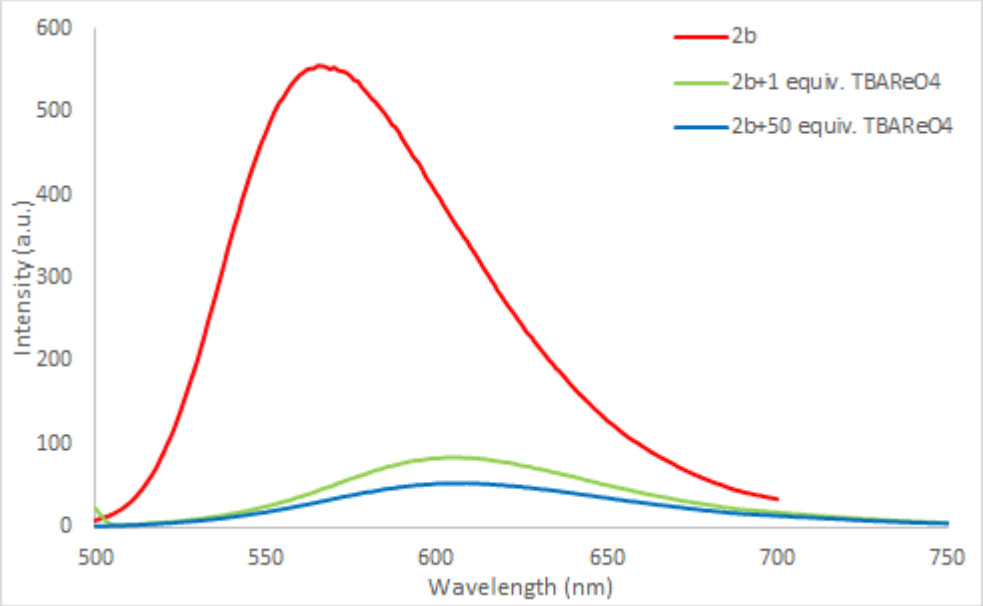

Figure S63. Fluorescence emission spectrum of **2b** upon addition of $TBA^{+}ReO_4^{-}$. λ_{ex} red= 472 nm, λ_{ex} green= 499 nm, λ_{ex} blue= 488 nm.

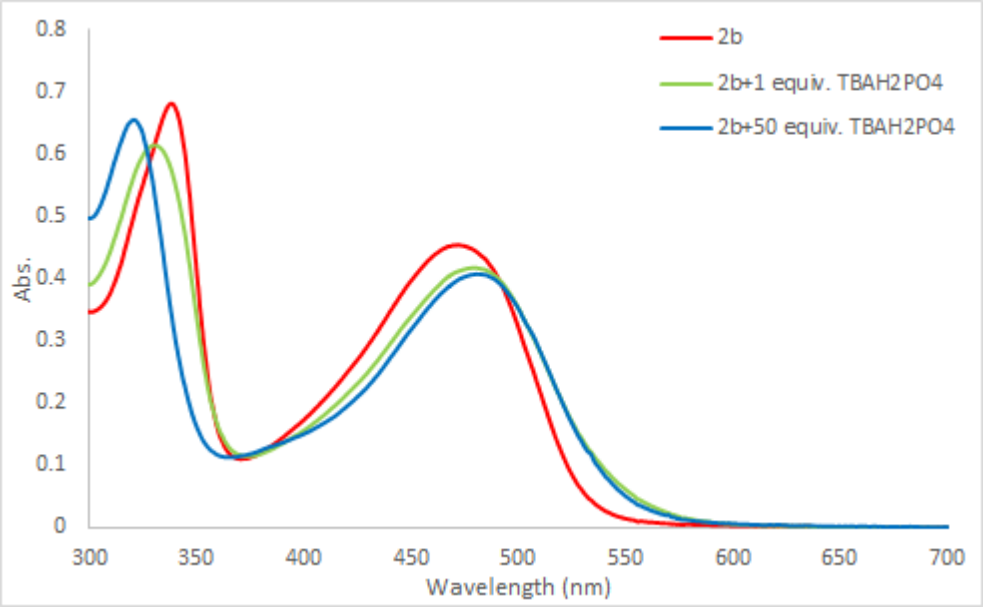

Figure S64. UV-Vis absorption spectrum of **2b** upon addition of $TBA^{+}H_2PO_4^{-}$.

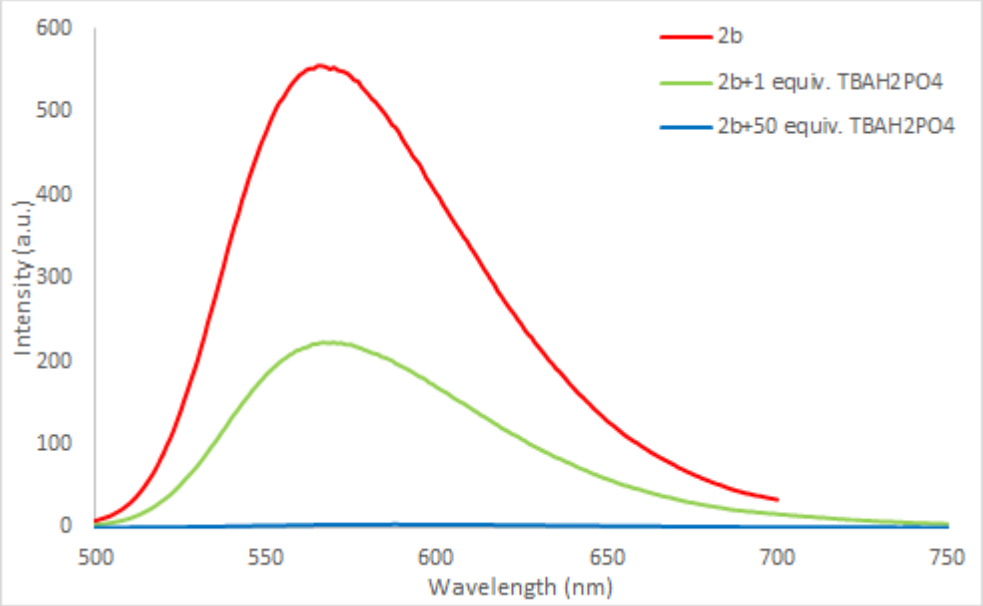

Figure S65. Fluorescence emission spectrum of **2b** upon addition of $TBA^{+}H_2PO_4^{-}$. λ_{ex} red= 472 nm, λ_{ex} green= 479 nm, λ_{ex} blue= 481 nm.

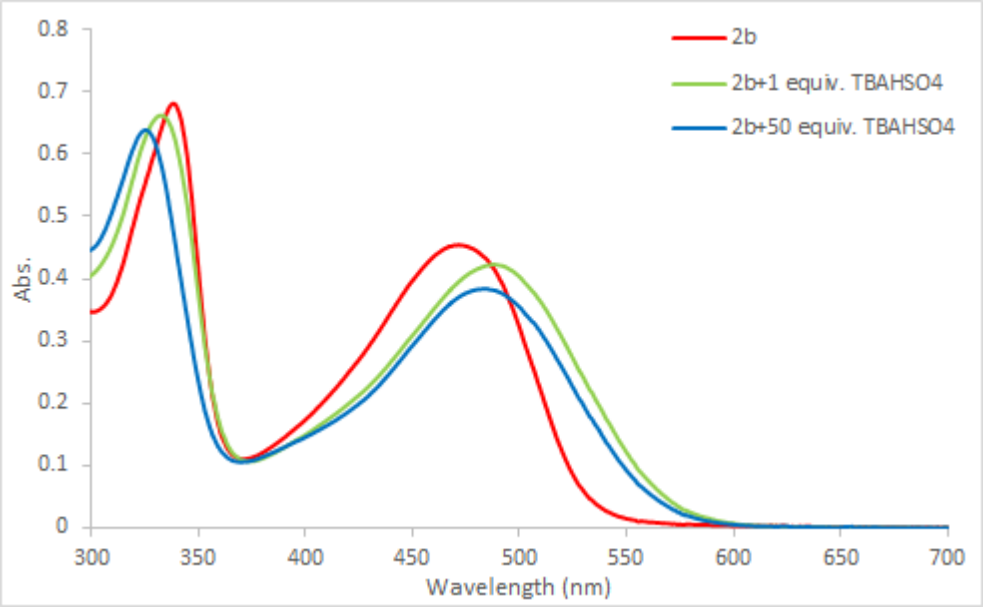

Figure S66. UV-Vis absorption spectrum of **2b** upon addition of $TBA^{+}HSO_4^{-}$.

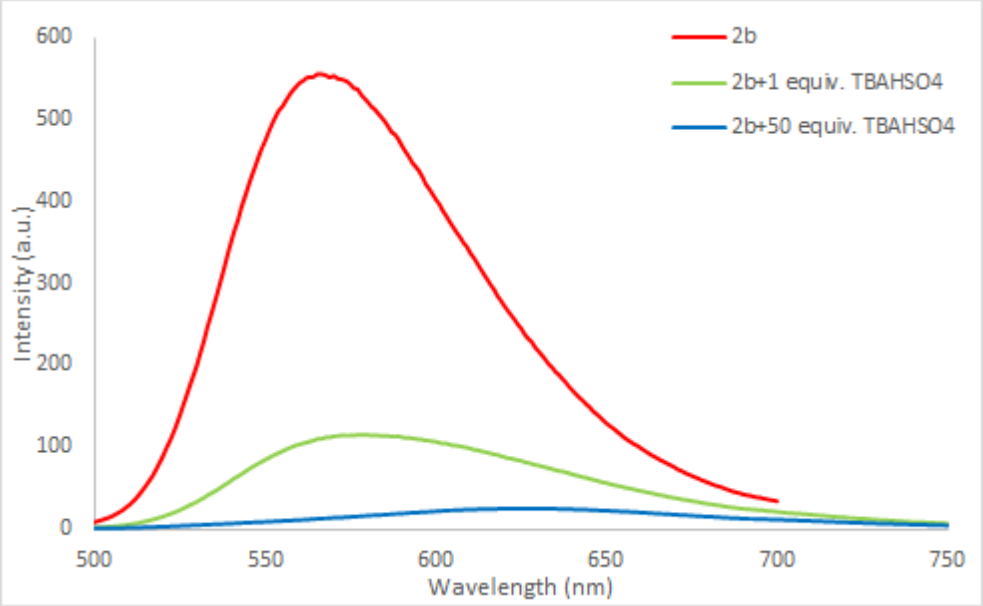

Figure S67. Fluorescence emission spectrum of **2b** upon addition of $TBA^{+}HSO_4^{-}$.
λ_{ex} red= 472 nm, λ_{ex} green= 488 nm, λ_{ex} blue= 484 nm.

Computational methods

Computations for **1a**,**b** and **2a**,**b** calculations were carried out with the Gaussian '09 suite of programs using B3LYP functional employing the 6-31+G(d,p) basis set for all atoms except nitrogen and iodine. For which nitrogen—aug-cc-pVTZ basis set and iodide— LANL2DZdp and effective core potential (ECP) were used. The LANL2DZdp ECP basis set was downloaded from the EMSL Basis Set Exchange[3]. To simplify calculations, methyl derivative of charged receptors were evaluated. Crystal structures of methyl derivative of charged XB receptor were employed as a starting point for optimization.

Neutral XB receptor **1a**
B3LYP/GEN = -1055.00099255 au

I	3.14731	-2.09014	-0.00006
F	0.	6.0774	0.00037
N	0.	0.55182	0.00003
H	0.86617	0.03944	0.00002
H	-0.86617	0.03944	-0.00002
N	7.23619	-0.71105	0.00009
C	4.72274	0.58018	0.00012
C	4.83728	-0.82734	0.00004
C	3.48258	1.27079	0.00014
C	1.22751	2.63753	0.00018
C	2.45708	1.93045	0.00016
C	6.106	-1.41582	0.00003
H	6.20673	-2.49817	-0.00004
C	0.	1.90735	0.00012

C	-2.45708	1.93045	0.00007
C	1.21173	4.04473	0.00027
H	2.14215	4.60098	0.00032
C	-1.22751	2.63753	0.00014
C	-3.48258	1.27079	0.00001
C	0.	4.71583	0.00029
C	5.93451	1.30647	0.00018
H	5.90825	2.39103	0.00025
C	7.14417	0.62322	0.00016
H	8.08391	1.17093	0.00021
C	-1.21173	4.04473	0.00022
H	-2.14215	4.60098	0.00024
N	-7.23619	-0.71105	-0.00019
C	-4.72274	0.58018	-0.00006
C	-7.14417	0.62322	-0.00011
H	-8.08391	1.17093	-0.0001
C	-5.93451	1.30647	-0.00004
C	-4.83728	-0.82734	-0.00015
C	-6.106	-1.41582	-0.00021
H	-6.20673	-2.49817	-0.00027
I	-3.14731	-2.09014	-0.00018
H	-5.90825	2.39103	0.00002

Neutral HB receptor **1b**

B3LYP/GEN = -1033.43979671 au

F	0.	4.72839	0.0515
N	0.	-0.80336	0.04693
H	-0.85694	-1.279	-0.18102
H	0.85694	-1.279	-0.18102
N	-7.21555	-2.10564	-0.02912
C	-4.74721	-0.7419	-0.0094
C	-4.81019	-2.14535	0.08701
C	-3.50336	-0.04691	-0.00012
C	-1.22643	1.2898	0.02044
C	-2.45977	0.58317	0.00842
C	-6.05776	-2.76591	0.07187
H	-6.12789	-3.84949	0.14559
C	0.	0.56622	0.01783
C	2.45977	0.58317	0.00842
C	-1.21243	2.69739	0.03204
H	-2.14288	3.25337	0.03433
C	1.22643	1.2898	0.02044
C	3.50336	-0.04691	-0.00012
C	0.	3.36725	0.03947

C	-5.96769	-0.04677	-0.11509
H	-5.97981	1.03531	-0.19204
C	-7.15688	-0.77303	-0.11947
H	-8.11059	-0.25507	-0.20026
C	1.21243	2.69739	0.03204
H	2.14289	3.25337	0.03433
N	7.21555	-2.10564	-0.02912
C	4.74721	-0.7419	-0.0094
C	7.15688	-0.77303	-0.11947
H	8.11059	-0.25507	-0.20025
C	5.96769	-0.04677	-0.11509
C	4.81019	-2.14535	0.087
C	6.05776	-2.76591	0.07186
H	6.12789	-3.84949	0.14558
H	5.97981	1.03531	-0.19204
H	3.90357	-2.73497	0.17513
H	-3.90357	-2.73497	0.17514

Charged XB receptor **2a**

B3LYP/GEN = -1134.32828236 au

I	3.5839	-2.10992	-0.00315
F	0.00003	5.95285	-0.00265
N	0.	0.4334	0.00022
H	0.8642	-0.08224	-0.00004
H	-0.86421	-0.08223	-0.00005
N	7.46036	-0.26288	-0.00263
C	4.84095	0.72302	0.00066
C	5.10564	-0.67599	-0.00027
C	3.54736	1.27087	0.00002
C	1.2288	2.52038	-0.00093
C	2.46828	1.84753	-0.00047
C	6.41736	-1.12233	-0.00105
H	6.66683	-2.17589	-0.00153
C	0.00001	1.78238	-0.00059
C	-2.46827	1.84756	-0.0005
C	1.20939	3.93058	-0.0016
H	2.13813	4.48998	-0.00185
C	-1.22879	2.5204	-0.00094
C	-3.54736	1.27093	-0.00006
C	0.00002	4.60678	-0.00197
C	5.96936	1.58514	-0.00005
H	5.82786	2.65927	-0.00135
C	7.24596	1.07644	-0.00118
H	8.12686	1.70708	-0.00217

C	-1.20935	3.93059	-0.00162
H	-2.13808	4.49001	-0.00189
N	-7.46039	-0.26278	-0.00294
C	-4.84096	0.7231	0.00055
C	-7.24598	1.07652	-0.00145
H	-8.12684	1.70721	-0.00252
C	-5.96935	1.58521	-0.00024
C	8.85204	-0.77428	0.02542
H	9.27652	-0.61192	1.01894
H	9.44102	-0.24414	-0.72438
H	8.84678	-1.83882	-0.20391
C	-5.10567	-0.67593	-0.00038
C	-6.41737	-1.12224	-0.00123
H	-6.66688	-2.1758	-0.00171
C	-8.85188	-0.77463	0.0263
H	-9.27169	-0.62311	1.02355
H	-8.84765	-1.83659	-0.21479
H	-9.44443	-0.23644	-0.71483
I	-3.58393	-2.10985	-0.00325
H	-5.82786	2.65934	-0.00162

Charged HB receptor **2b**

B3LYP/GEN = -1112.77851060 au

H	4.31962	-1.41665	-0.00176
F	0.00003	5.95285	-0.00265
N	0.	0.4334	0.00022
H	0.8642	-0.08224	-0.00004
H	-0.86421	-0.08223	-0.00005
N	7.46036	-0.26288	-0.00263
C	4.84095	0.72302	0.00066
C	5.10564	-0.67599	-0.00027
C	3.54736	1.27087	0.00002
C	1.2288	2.52038	-0.00093
C	2.46828	1.84753	-0.00047
C	6.41736	-1.12233	-0.00105
H	6.66683	-2.17589	-0.00153
C	0.00001	1.78238	-0.00059
C	-2.46827	1.84756	-0.0005
C	1.20939	3.93058	-0.0016
H	2.13813	4.48998	-0.00185
C	-1.22879	2.5204	-0.00094
C	-3.54736	1.27093	-0.00006
C	0.00002	4.60678	-0.00197
C	5.96936	1.58514	-0.00005

H	5.82786	2.65927	-0.00135
C	7.24596	1.07644	-0.00118
H	8.12686	1.70708	-0.00217
C	-1.20935	3.93059	-0.00162
H	-2.13808	4.49001	-0.00189
N	-7.46039	-0.26278	-0.00294
C	-4.84096	0.7231	0.00055
C	-7.24598	1.07652	-0.00145
H	-8.12684	1.70721	-0.00252
C	-5.96935	1.58521	-0.00024
C	8.85204	-0.77428	0.02542
H	9.27652	-0.61192	1.01894
H	9.44102	-0.24414	-0.72438
H	8.84678	-1.83882	-0.20391
C	-5.10567	-0.67593	-0.00038
C	-6.41737	-1.12224	-0.00123
H	-6.66688	-2.1758	-0.00171
C	-8.85188	-0.77463	0.0263
H	-9.27169	-0.62311	1.02355
H	-8.84765	-1.83659	-0.21479
H	-9.44443	-0.23644	-0.71483
H	-4.31965	-1.41659	-0.00186
H	-5.82786	2.65934	-0.00162

References

1. Kamlet, M. J., Abboud, J. L., & Taft, R. W. (1977). *Journal of the American Chemical Society*, 99(18), 6027-6038.
2. Reichardt, C. (1994). *Chemical Reviews*, *94*(8), 2319-2358.
3. https://bse.pnl.gov/bse/portal

Chapter 3

Synthesis of Third Generation Molecules (G3XB derivatives)

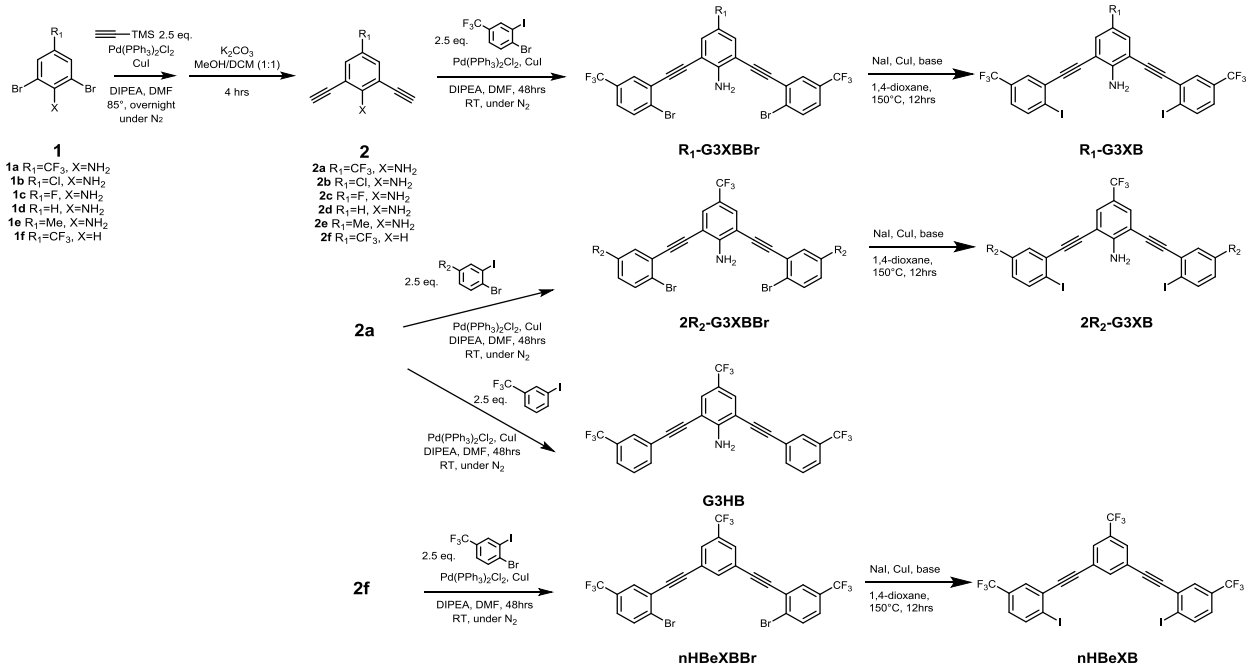

Figure S68. ChemDraw schematic of all **G3XB** derivatives molecules.

2,6-bisethynyl-4-(trifluoromethyl)aniline (2a). To an oven dried Schlenk flask was charged with 2,6-dibromo-4-(trifluoromethyl)aniline (**1a**)(0.638 g, 2 mmol), then vacuumed and backfilled with dry N2 gas (3x). Bis(triphenylphosphine)palladium(II) dichloride (0.07 g, 0.1 mmol) was added, vacuumed and backfilled with dry N2 (3x). Copper (I) iodide (0.038 g, 0.2 mmol) was added, vacuumed, and backfilled with dry N2 (3x). The dry reagents were dissolved in 60 mL dry dimethylformamide (DMF). N,N-diisopropylethylamine (1.74 mL, 10 mmol) and TMS-acetylene (0.692 mL, 5 mmol) were added to the DMF solution. The flask was carefully vacuumed and backfilled with dry N2 (3x). The dark brown solution stirred overnight at 85˚C. The reaction mixture was run through a silica plug with a hexane/ethyl acetate solvent mixture (50:50) to remove any excess salts and catalysts. Subsequent removal of DMF, hexanes and ethyl acetate by rotary evaporation left a brown liquid that was used directly in the next step with no purification. The brown liquid was dissolved in 50 mL methanol and 50 mL DCM in a 250 mL round bottom flask. Potassium carbonate (0.69 g, 0.5 mmol) was added to the organic mixture. The reaction stirred vigorously for 4 hours at room temperature and reaction progress was monitored via TLC. Upon completion, water was added to quench the reaction. The crude product was extracted with ethyl acetate, dried over magnesium sulfate and gravity filtered. The organic mixture was reduced under vacuum and crude product was purified by column chromatography (gradient from 5% EtOAc/95% Hexanes to 30% EtOAc/70% Hexanes) to afford a dark yellow solid (0.343 g, 85 % yield).

^{1}H NMR (400 MHz, $CDCl_3$): δ (ppm) = 7.55 (s, 2H), 5.17 (s, 2H), 3.46 (s, 2H).

^{13}C NMR (125 MHz, $CDCl_3$): δ (ppm) = 152.38, 130.42 (q, J = 3.8 Hz), 123.88 (q, J = 269.3 Hz), 119.28 (q, J = 33.5 Hz), 106.19, 84.23, 78.78.

^{19}F NMR (470 MHz, $CDCl_3$): δ (ppm) = –59.86.

Elemental analysis, Found: C, 60.7; H, 2.66; N, 6.70%. Calc. for $C_{11}H_6F_3N$: C, 63.1; H, 2.89; N, 6.55%.

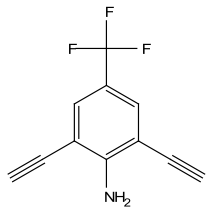

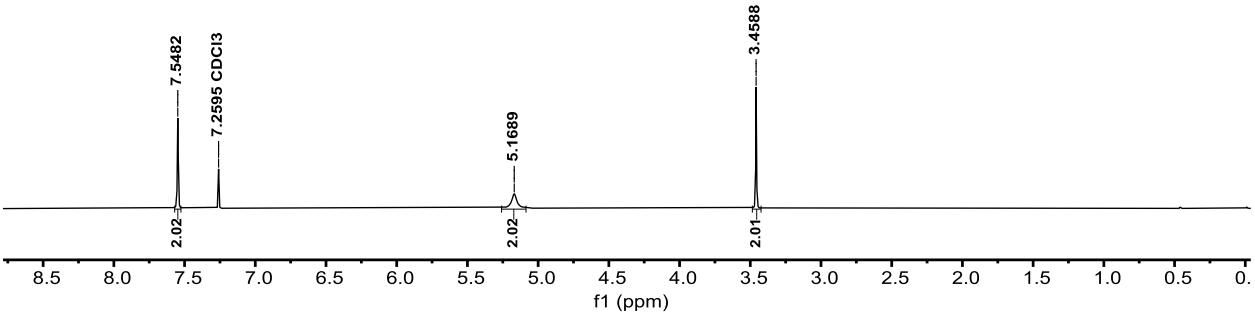

Figure S69. ^{1}H NMR of **2a** (400 MHz, $CDCl_3$).

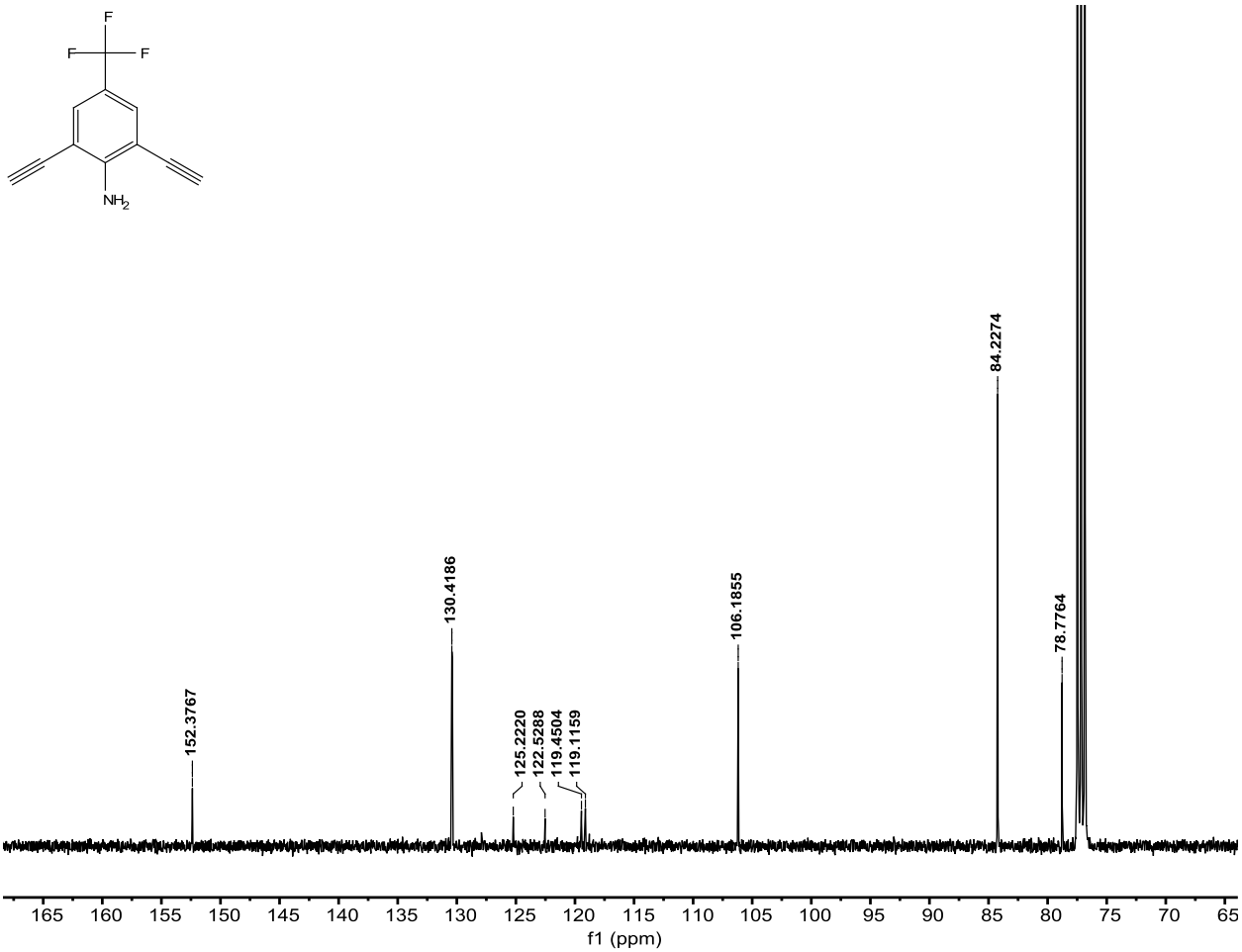

Figure S70. ^{13}C NMR of **2a** (100 MHz, $CDCl_3$).

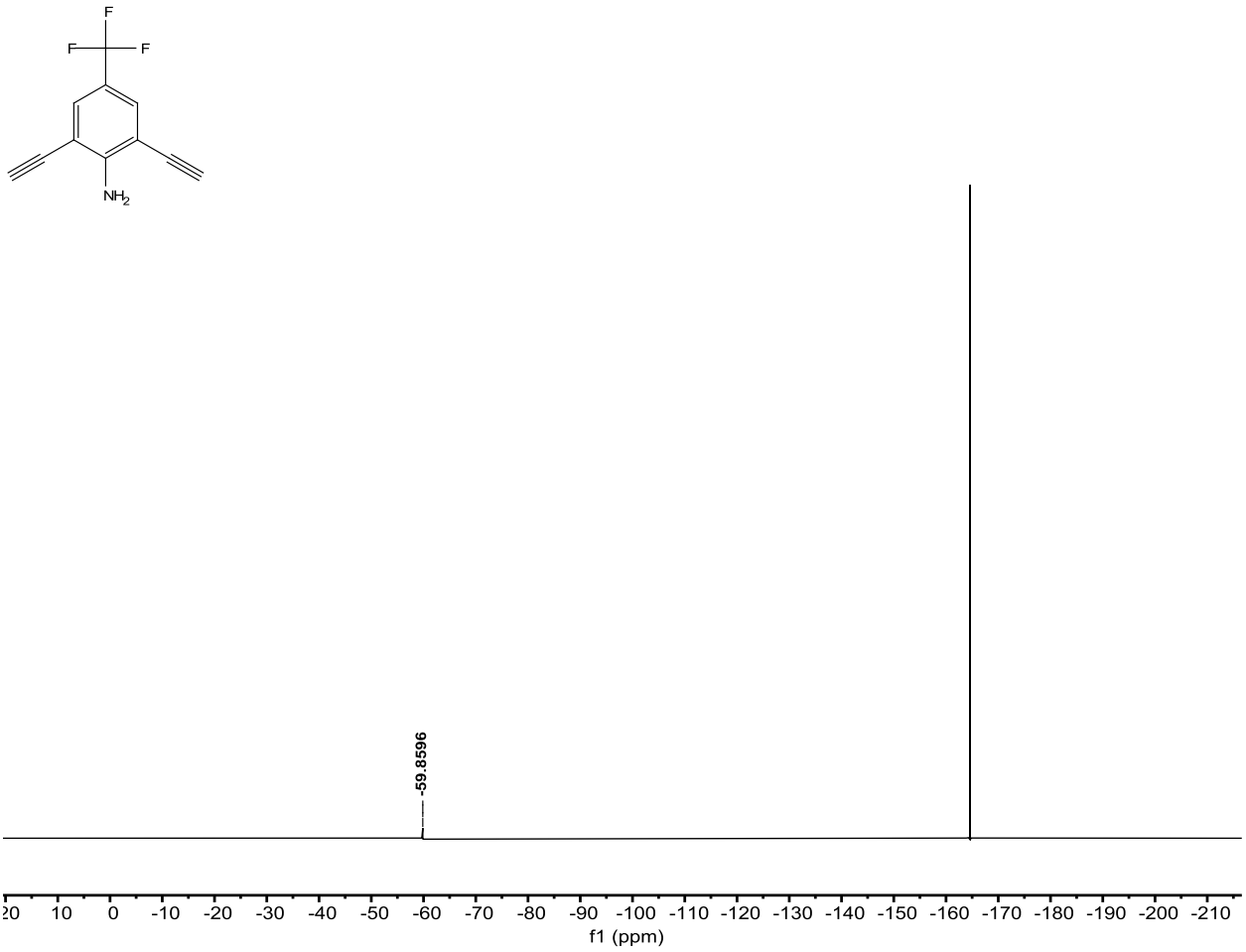

Figure S71. ^{19}F NMR of **2a** (376 MHz, $CDCl_3$). Hexafluorobenzene (C_6F_6) internal reference.

2,6-bisethynyl-4-chloroaniline (2b). To an oven dried Schlenk flask was charged with 2,6-dibromo-4-chloroaniline (**1b**)(0.571 g, 2 mmol), then vacuumed and backfilled with dry N2 gas (3x). Bis(triphenylphosphine)palladium(II) dichloride (0.07 g, 0.1 mmol) was added, vacuumed and backfilled with dry N2 (3x). Copper (I) iodide (0.038 g, 0.2 mmol) was added, vacuumed, and backfilled with dry N2 (3x). The dry reagents were dissolved in 60 mL dry dimethylformamide (DMF). N,N-diisopropylethylamine (1.74 mL, 10 mmol) and TMS-acetylene (0.692 mL, 5 mmol) were added to the DMF solution. The flask was carefully vacuumed and backfilled with dry N2 (3x). The dark brown solution stirred overnight at 75°C. The reaction mixture was run through a silica plug with a hexane/ethyl acetate solvent mixture (50:50) to remove any excess salts and catalysts. Subsequent removal of DMF, hexanes and ethyl acetate by rotary evaporation left a brown liquid that was used directly in the next step with no purification. The brown liquid was dissolved in 50 mL methanol and 50 mL DCM in a 250 mL round bottom flask. Potassium carbonate (0.69 g, 0.5 mmol) was added to the organic mixture. The reaction stirred vigorously for 2 hours at room temperature and reaction progress was monitored via TLC. Upon completion, water was added to quench the reaction. The crude product was extracted with ethyl acetate, dried over magnesium sulfate and gravity filtered. The organic mixture was reduced under vacuum and crude product was purified by column

chromatography (gradient from 5% EtOAc/95% Hexanes to 30% EtOAc/70% Hexanes) to afford a brown solid (0.295 g, 84 % yield).

^{1}H NMR (400 MHz, $CDCl_3$): δ (ppm) = 7.28 (s, 2H), 4.84 (s, 2H), 3.44 (s, 2H).

^{13}C NMR (125 MHz, $CDCl_3$): δ (ppm) = 149.08, 139.92, 121.06, 107.63, 84.11, 78.95.

Elemental analysis, Found: C, 67.85; H, 2.93; N, 8.55%. Calc. for $C_{10}H_6ClN$: C, 68.39; H, 3.44; N, 7.98%.

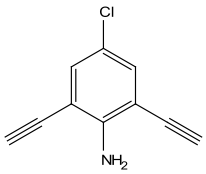

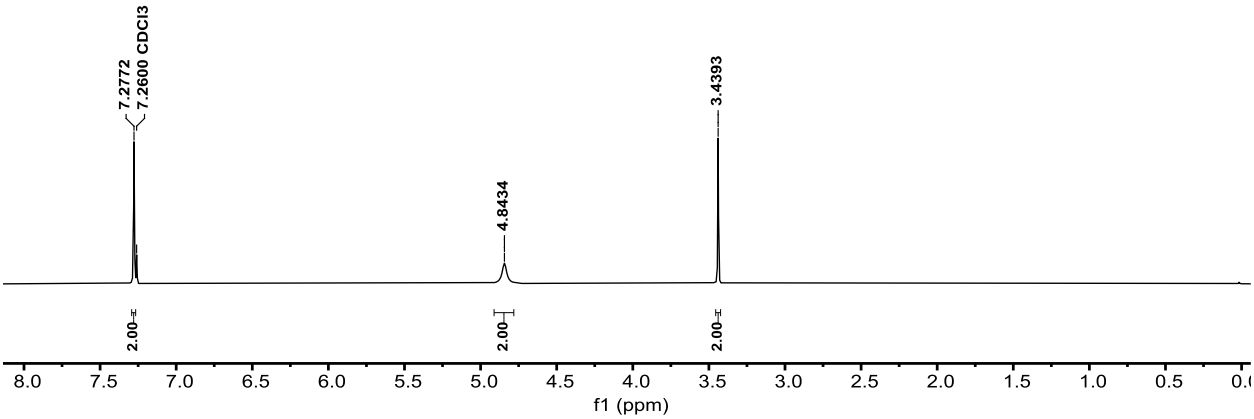

Figure S72. ^{1}H NMR of **2b** (400 MHz, $CDCl_3$).

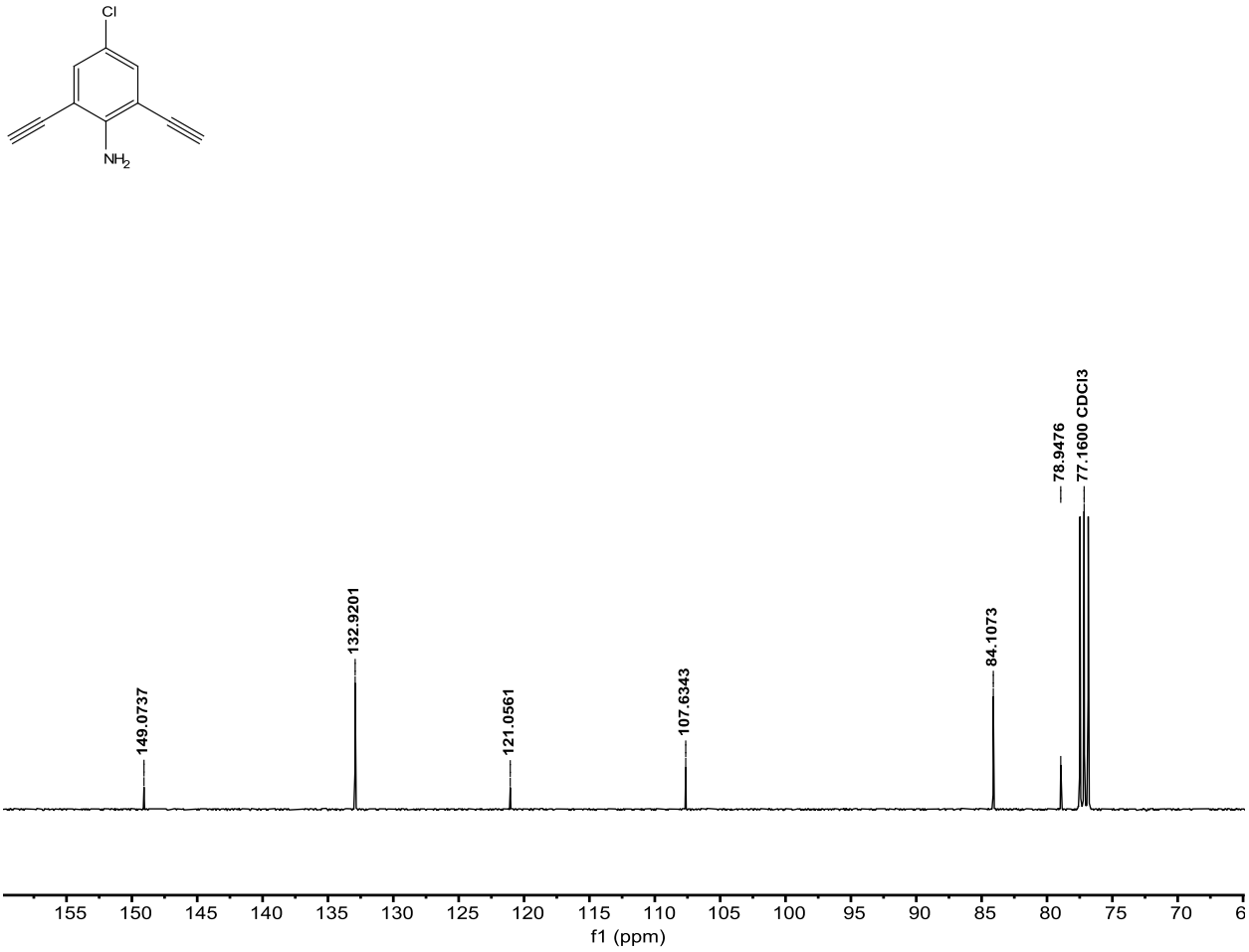

Figure S73. ^{13}C NMR of **2b** (100 MHz, $CDCl_3$).

2,6-bisethynyl-4-fluoroaniline (2c). To an oven dried Schlenk flask was charged with 2,6-dibromo-4-fluoroaniline (**1c**)(0.534 g, 2 mmol), then vacuumed and backfilled with dry N2 gas (3x). Bis(triphenylphosphine)palladium(II) dichloride (0.07 g, 0.1 mmol) was added, vacuumed and backfilled with dry N2 (3x). Copper (I) iodide (0.038 g, 0.2 mmol) was added, vacuumed, and backfilled with dry N2 (3x). The dry reagents were dissolved in 60 mL dry dimethylformamide (DMF). N,N-diisopropylethylamine (1.74 mL, 10 mmol) and TMS-acetylene (0.692 mL, 5 mmol) were added to the DMF solution. The flask was carefully vacuumed and backfilled with dry N2 (3x). The dark brown solution stirred overnight at 75°C. The reaction mixture was run through a silica plug with a hexane/ethyl acetate solvent mixture (50:50) to remove any excess salts and catalysts. Subsequent removal of DMF, hexanes and ethyl acetate by rotary evaporation left a brown liquid that was used directly in the next step with no purification. The brown liquid was dissolved in 50 mL methanol and 50 mL DCM in a 250 mL round bottom flask. Potassium carbonate (0.69 g, 0.5 mmol) was added to the organic mixture. The reaction stirred vigorously for 4 hours at room temperature and reaction progress was monitored via TLC. Upon completion, water was added to quench the reaction. The crude product was extracted with ethyl acetate, dried over magnesium sulfate and gravity filtered. The organic mixture was reduced under vacuum and crude product was purified by column

chromatography (gradient from 5% EtOAc/95% Hexanes to 30% EtOAc/70% Hexanes) to afford a yellow solid (0.251 g, 79 % yield). Molecule **2c** spectra in accordance with previously reported.[1]

2,6-bisethynylaniline (2d). To an oven dried Schlenk flask was charged with 2,6-dibromoaniline (**1d**) (0.502 g, 2 mmol), then vacuumed and backfilled with dry N2 gas (3x). Bis(triphenylphosphine)palladium(II) dichloride (0.07 g, 0.1 mmol) was added, vacuumed and backfilled with dry N2 (3x). Copper (I) iodide (0.038 g, 0.2 mmol) was added, vacuumed, and backfilled with dry N2 (3x). The dry reagents were dissolved in 60 mL dry dimethylformamide (DMF) at 0°C and stirred for 1 hour. Tetraethylamine (50 mL, excess) and TMS-acetylene (0.692 mL, 5 mmol) were added to the DMF solution. The flask was carefully vacuumed and backfilled with dry N2 (3x). The dark brown solution stirred overnight at 60°C. The reaction mixture was run through a silica plug with a hexane/ethyl acetate solvent mixture (50:50) to remove any excess salts and catalysts. Subsequent removal of DMF, hexanes and ethyl acetate by rotary evaporation left a brown liquid that was used directly in the next step with no purification. The brown liquid was dissolved in 50 mL methanol and 50 mL DCM in a 250 mL round bottom flask. Potassium carbonate (0.69 g, 0.5 mmol) was added to the organic mixture. The reaction stirred vigorously for 4 hours at room temperature and reaction progress was monitored via TLC. Upon completion, water was added to quench the reaction. The crude product was extracted with ethyl acetate, dried over magnesium sulfate and gravity filtered. The organic mixture was reduced under vacuum and crude product was purified by column chromatography (gradient from 100% Hexanes to 5% EtOAc/95% Hexanes) to afford a yellow solid (0.152 g, 54 % yield). Molecule **2d** spectra in accordance with previously reported.[2]

2,6-bisethynyl-4-methylaniline (2e). To an oven dried Schlenk flask was charged with 2,6-dibromo-4-methylaniline (**1e**) (0.530 g, 2 mmol), then vacuumed and backfilled with dry N2 gas (3x). Bis(triphenylphosphine)palladium(II) dichloride (0.07 g, 0.1 mmol) was added, vacuumed and backfilled with dry N2 (3x). Copper (I) iodide (0.038 g, 0.2 mmol) was added, vacuumed, and backfilled with dry N2 (3x). The dry reagents were dissolved in 60 mL dry dimethylformamide (DMF) at 0°C and stirred for 1 hour. Tetraethylamine (50 mL, excess) and TMS-acetylene (0.692 mL, 5 mmol) were added to the DMF solution. The flask was carefully vacuumed and backfilled with dry N2 (3x). The dark brown solution stirred overnight at 60°C. The reaction mixture was run through a silica plug with a hexane/ethyl acetate solvent mixture (50:50) to remove any excess salts and catalysts. Subsequent removal of DMF, hexanes and ethyl acetate by rotary evaporation left a brown liquid that was used directly in the next step with no purification. The brown liquid was dissolved in 50 mL methanol and 50 mL DCM in a 250 mL round bottom flask. Potassium carbonate (0.69 g, 0.5 mmol) was added to the organic mixture. The reaction stirred vigorously for 4 hours at room temperature and reaction progress was monitored via TLC. Upon completion, water was added to quench the reaction. The crude product was extracted with ethyl acetate, dried over magnesium sulfate and gravity filtered. The organic mixture was reduced under vacuum and crude product was purified by column chromatography (gradient from 100% Hexanes to 3% EtOAc/97% Hexanes) to afford a brown solid (0.139 g, 45 % yield). Molecule **2e** spectra in accordance with previously reported.[3]

3,5-bisethynyl-trifluoromethylbenzene (2f). To an oven dried Schlenk flask was charged with Bis(triphenylphosphine)palladium(II) dichloride (0.231 g, 0.33 mmol) and then vacuumed and backfilled with dry N2 (3x). Copper (I) iodide (0.125 g, 0.66 mmol) was added, vacuumed, and backfilled with dry N2 (3x). The dry reagents were dissolved in 150 mL dry dimethylformamide (DMF). 3,5-dibromo-trifluoromethylbenzne (**1f**) (1.0 mL, 6.6 mmol), N,N-diisopropylethylamine (5.66 mL, 33 mmol) and TMS-acetylene (2.28 mL, 16.5 mmol) were added to the DMF solution. The flask was carefully vacuumed and backfilled with dry N2 (3x). The dark brown solution stirred overnight at 85°C. The reaction mixture was run through a silica plug with hexane to remove any excess salts and catalysts. Subsequent removal of DMF and hexane by rotary evaporation left a brown liquid that was used directly in the next step with no purification. The brown liquid was dissolved in 50 mL methanol and 50 mL DCM in a 250 mL round bottom flask. Potassium carbonate (2.28 g, 16.5 mmol) was added to the organic mixture. The reaction stirred vigorously for one hour at room temperature and reaction progress was monitored via TLC. Upon completion, water was added to quench the reaction. The crude product was extracted with ethyl acetate, dried over magnesium sulfate and gravity filtered. The organic mixture was reduced under vacuum and crude product was purified by column chromatography (gradient from 5% EtOAc/95% Hexanes to 30% EtOAc/70% Hexanes) to afford a light orange oil (1.232 g, 96 % yield). Molecule 4 spectra in accordance with previously reported.[4]

2,6-bis(2-ethynyl-4-(trifluoromethyl)bromophenyl)-4-(trifluoromethyl)aniline (G3HB). To an oven dried Schlenk flask was charged with 2,6-bisethynyl-4-(trifluoromethyl)aniline **(2a)** (0.211g 1mmol), then vacuumed and backfilled with dry N2 gas (3x). Bis(triphenylphosphine)palladium (II) dichloride (0.035 g, 0. 05 mmol) was added, vacuumed and backfilled with dry N2 gas (3x). Copper (I) iodide (0.019 g, 0.1 mmol) was added, vacuumed and backfilled with dry N2 (3x). The dry reagents were dissolved in 60 mL dry DMF. 3-iodo-trifluoromethylbenzene (0.36 mL, 2.5 mmol) and N,N-diisopropylethylamine (0.86 mL, 5 mmol) were added to the DMF solution. The flask was carefully vacuumed and backfilled with dry N2 (3x). The dark brown solution stirred overnight at room temperature. The reaction mixture was extracted with ethyl acetate then washed with water to remove any excess salts and catalysts, then was dried over magnesium sulfate and gravity filtered. Subsequent removal of DMF, hexanes and ethyl acetate by rotary evaporation left and brown solid that was purified by column chromatography (gradient from 5% DCM/95% Hexanes to 10% DCM/95% Hexanes) to afford **G3HB** (0.395 g, 60%) as a dull yellow solid.

^{1}H NMR (400 MHz, $CDCl_3$): δ (ppm) = 7.81 (s, 2H), 7.72 (d, J = 7.8 Hz, 2H), 7.64 (d, J = 6.1 Hz, 2H), 7.63 (s, 1H), 7.52 (t, J = 7.7 Hz, 2H), 5.22 (s, 2H).

^{13}C NMR (100 MHz, $CDCl_3$): δ (ppm) = 151.13, 134.78, 131.40 (q, J = 35.8 Hz), 130.03 (q, J = 4.6 Hz), 129.29, 128.51 (q, J = 3.6 Hz), 125.58 (q, J = 4.0 Hz), 123.96 (q, J = 268.9 Hz), 123.76 (q, J = 271.1 Hz), 123.50, 120.10 (q, J = 33.2 Hz), 107.01, 95.65, 85.53.

^{19}F NMR (376 MHz, $CDCl_3$): δ (ppm) = –60.19, -61.37.

HRMS (ESI neg) m/z for $C_{25}H_{11}F_9N^-$ $[M\text{-}H^+]^-$: calculated: 496.0753; found: 496.0758.

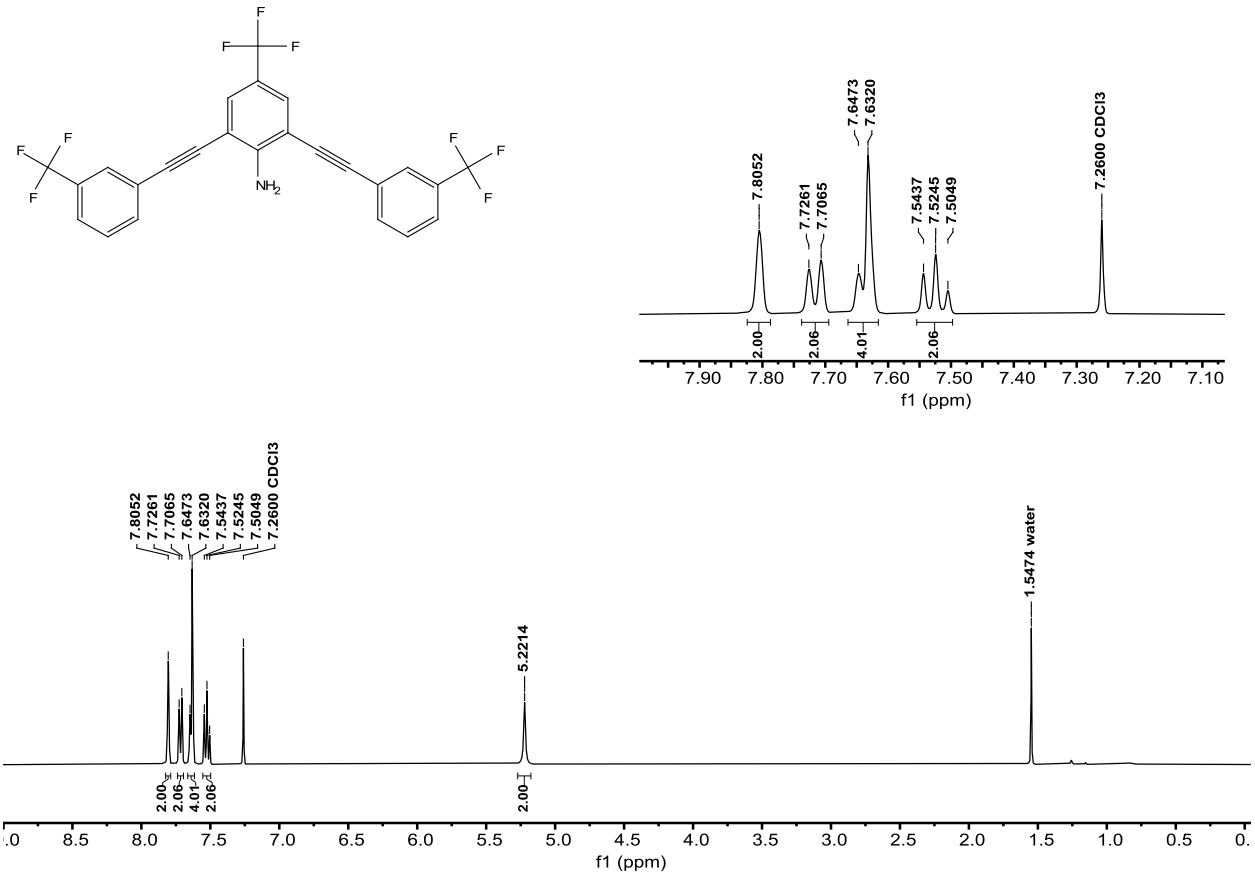

Figure S74. ^{1}H NMR of **G3HB** (400 MHz, $CDCl_3$).

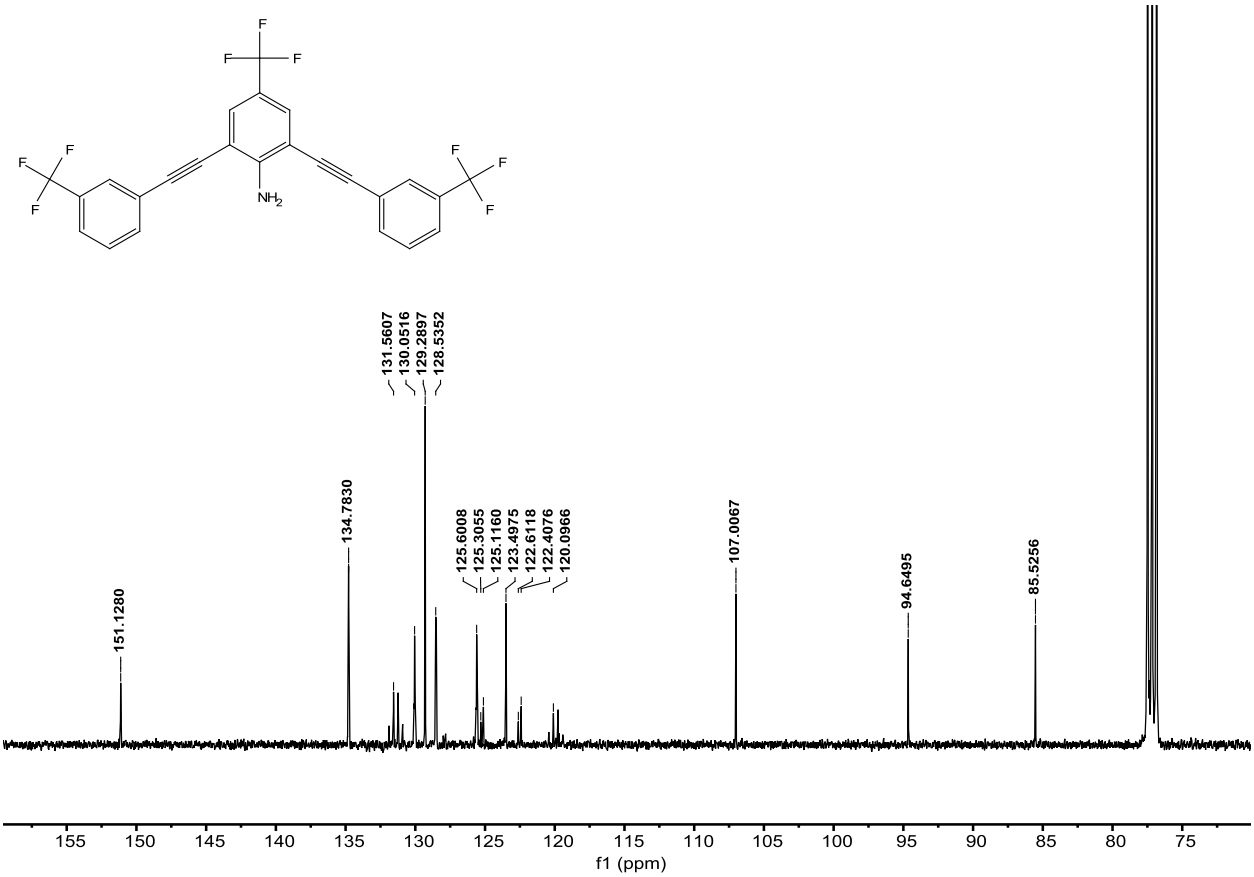

Figure S75. ^{13}C NMR of **G3HB** (100 MHz, $CDCl_3$).

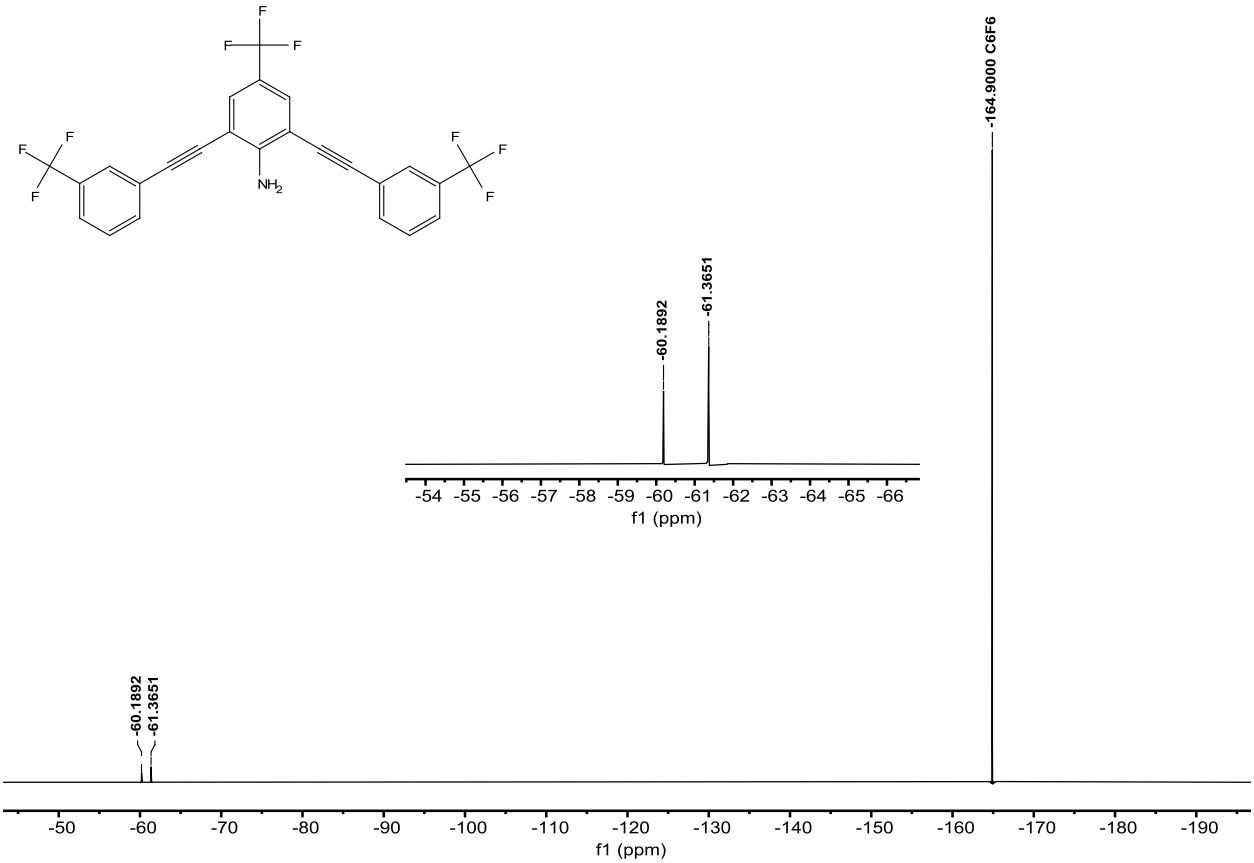

Figure S76. ^{19}F NMR of **G3HB** (376 MHz, $CDCl_3$). Hexafluorobenzene (C_6F_6) internal reference.

2,6-bis(2-ethynyl-4-(trifluoromethyl)bromophenyl)-4-(trifluoromethyl)aniline (G3XBBr). To an oven dried Schlenk flask was charged with 2,6-bisethynyl-4-(trifluoromethyl)aniline **(2a)** (0.211g 1mmol), then vacuumed and backfilled with dry N2 gas (3x). Bis(triphenylphosphine)palladium (II) dichloride (0.034 g, 0. 05 mmol) was added, vacuumed and backfilled with dry N2 gas (3x). Copper (I) iodide (0.019 g, 0.1 mmol) was added, vacuumed and backfilled with dry N2 (3x). The dry reagents were dissolved in 60 mL dry DMF. 1-Bromo-2-iodo-4-(trifluoromethyl)benzene (0.4 mL, 2.5 mmol) and N,N-diisopropylethylamine (0.86 mL, 5 mmol) were added to the DMF solution. The flask was carefully vacuumed and backfilled with dry N2 (3x). The dark brown solution stirred overnight at room temperature. The reaction mixture was extracted with ethyl acetate then washed with water to remove any excess salts and catalysts, then was dried over magnesium sulfate and gravity filtered. Subsequent removal of DMF, hexanes and ethyl acetate by rotary evaporation left and brown solid that was purified by column chromatography (gradient from 100% Hexanes to 5% EtOAc/95% Hexanes) to afford **G3XBBr** (0.492 g, 75%) as a dull yellow solid.

^{1}H NMR (400 MHz, $CDCl_3$): δ (ppm) = 7.84 (s, 2H), 7.79 (d, J = 7.8 Hz, 2H), 7.67 (s, 2H), 7.47 (d, J = 6.1 Hz, 2H), 5.65 (s, 2H).

^{13}C NMR (100 MHz, $CDCl_3$): δ (ppm) = 152.09, 133.24, 130.57 (q, J = 33.5 Hz), 130.36 (q, J = 3.7 Hz), 129.99 (q, J = 3.7 Hz), 128.98, 126.36 (q, J = 3.7 Hz), 125.82, 123.89 (q, J = 265.4 Hz), 123.47 (q, J = 269.7 Hz), 119.89 (q, J = 34.1 Hz), 106.46, 93.57, 90.49.

^{19}F NMR (376 MHz, $CDCl_3$): δ (ppm) = –60.14, -61.33.

HRMS (ESI neg) m/z for $C_{25}H_9F_9Br_2N^-$ [M-H^+]$^-$: calculated: 653.8943; found: 653.8943.

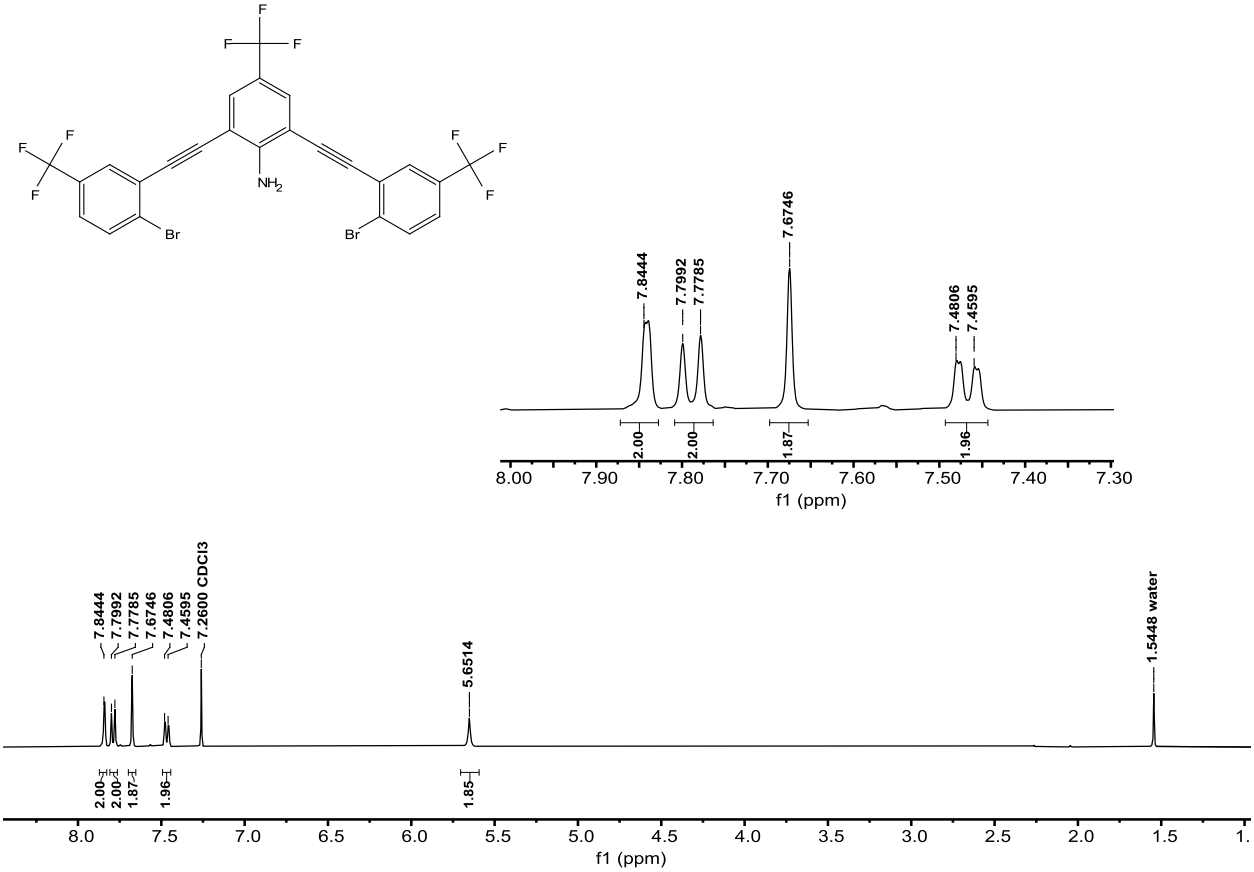

Figure S77. ^{1}H NMR of **G3XBBr** (400 MHz, $CDCl_3$).

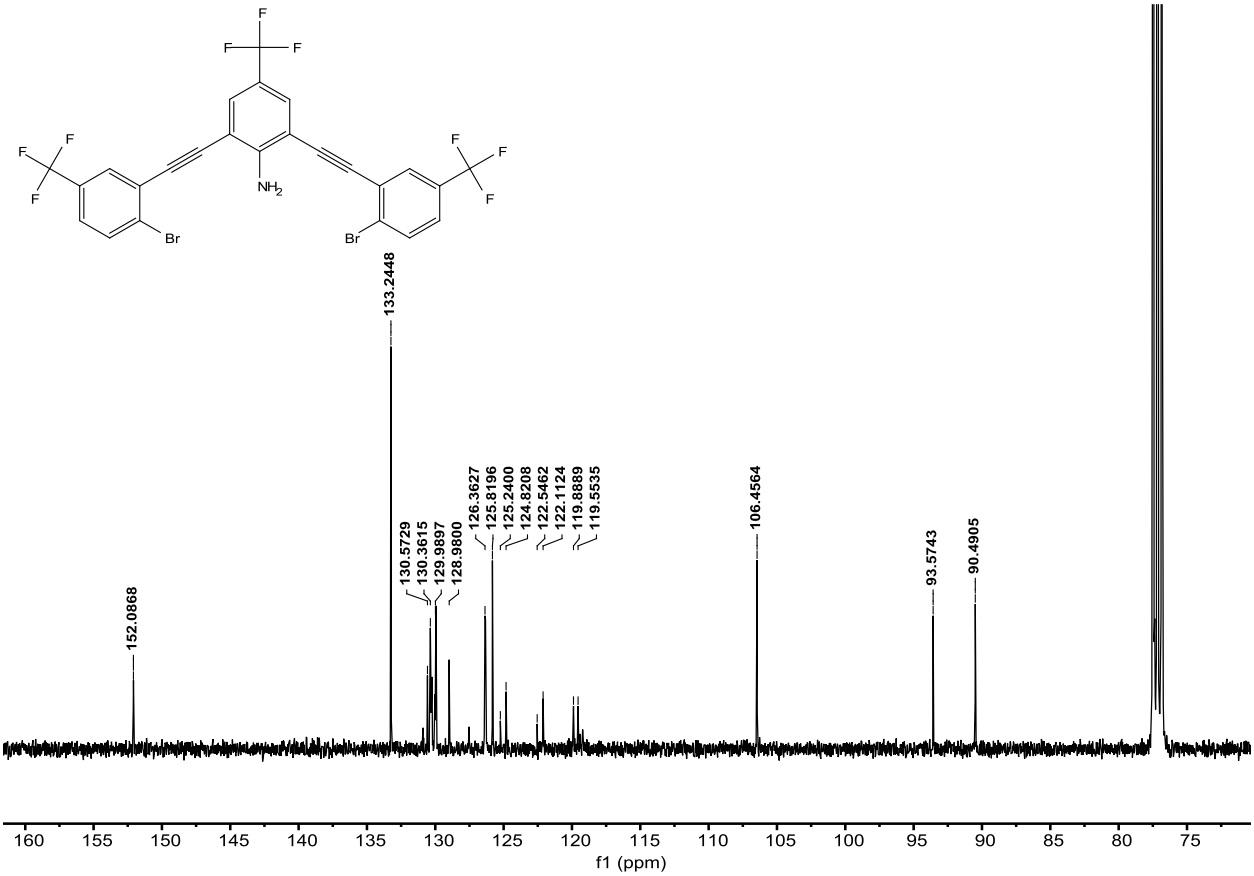

Figure S78. ^{13}C NMR of **G3XBBr** (100 MHz, $CDCl_3$).

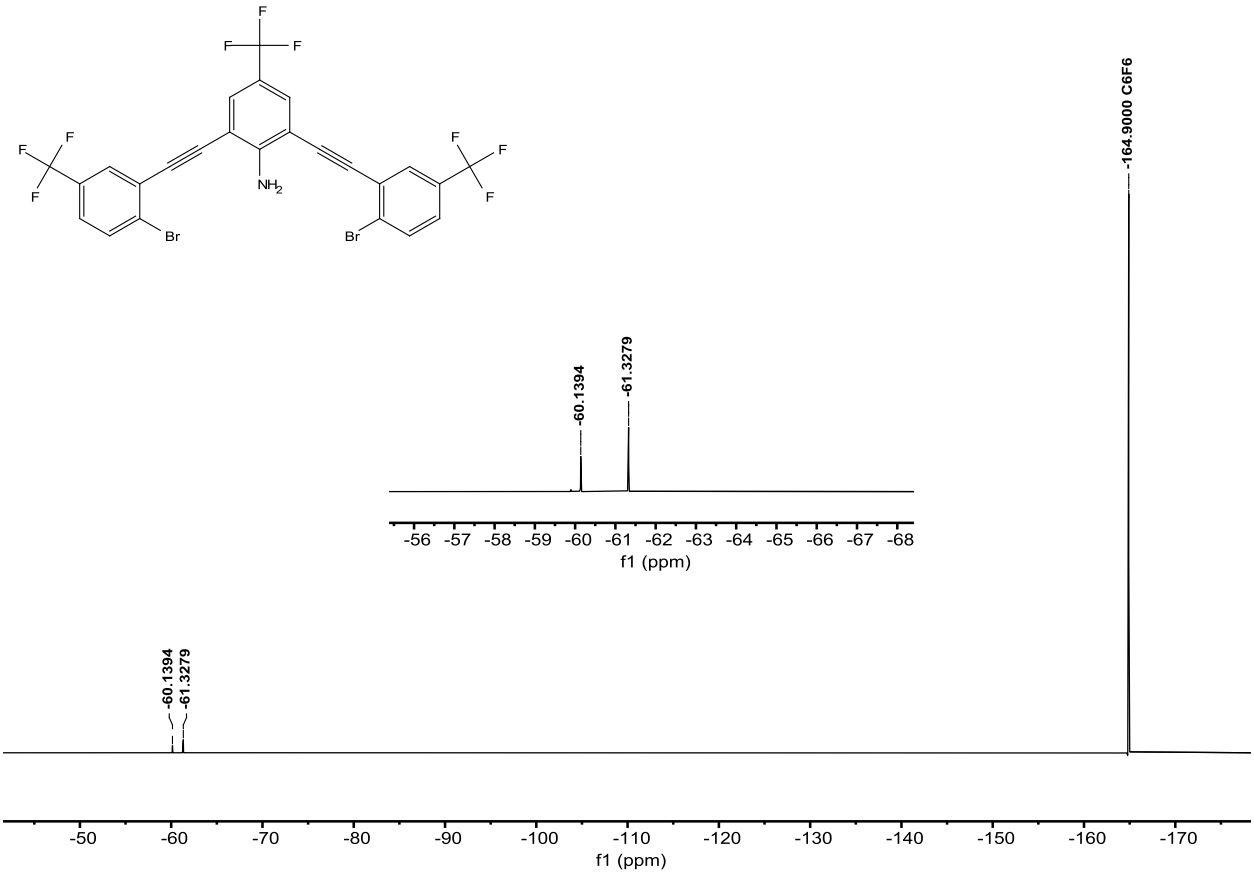

Figure S79. ^{19}F NMR of **G3XBBr** (376 MHz, $CDCl_3$). Hexafluorobenzene (C_6F_6) internal reference.

2,6-bis(2-ethynyl-4-(trifluoromethyl)iodophenyl)-4-(trifluoromethyl)aniline (G3XB). G3XBBr (0.200 g, 0.305 mmol), copper iodide (0.006 g, 0.030 mmol), sodium iodide (0.183 g, 1.22 mmol) were added to a 10-20 mL microwave reaction vial containing a stir bar and dissolved in 13 mL 1,4-dioxane. To the vibrant yellow reaction mixture, trans-N,N'-dimethylcyclohexane-1,2-diamine (0.1 mL) was added. The microwave vial was sealed and placed in a Biotage Initiator+ microwave reactor for 12.5 hours at 150 ˚C. After cooling, the reaction was run through pipet silica plug with EtOAc to remove catalysts and salts. The EtOAc crude was then ran through GCMS in order to obtain % conversion of bromines to iodines. If the conversion from bromine to iodine was 99% or greater, then the reaction was concentrated. The beige/yellow product (0.13 g, 58%) was obtained after purified via high performance liquid chromatography (reverse phase column gradient from 80% water/20% acetonitrile to 100% acetonitrile).

^{1}H NMR (400 MHz, $CDCl_3$): δ (ppm) = 8.04 (d, J = 8.2 Hz, 2H), 7.81 (s, 2H), 7.69 (s, 2H), 7.29 (d, J = 8.4 Hz, 2H), 5.73 (s, 2H).

^{13}C NMR (100 MHz, $CDCl_3$): δ (ppm) = 152.16, 145.84, 139.54, 131.05 (q, J = 33.5 Hz), 130.36 (q, J = 3.6 Hz), 129.23 (q, J = 4.0 Hz), 126.15 (q, J = 4.0 Hz), 123.91 (q, J = 269.4 Hz), 123.60 (q, J = 270.5 Hz), 119.63 (q, J = 33.2 Hz), 106.50, 104.78, 96.85, 89.67.

^{19}F NMR (376 MHz, $CDCl_3$): δ (ppm) = –60.15, -61.56.

HRMS (ESI neg) m/z for $C_{25}H_9F_9I_2N^-$ [M-H^+]$^-$: calculated: 747.8686; found: 747.8689.

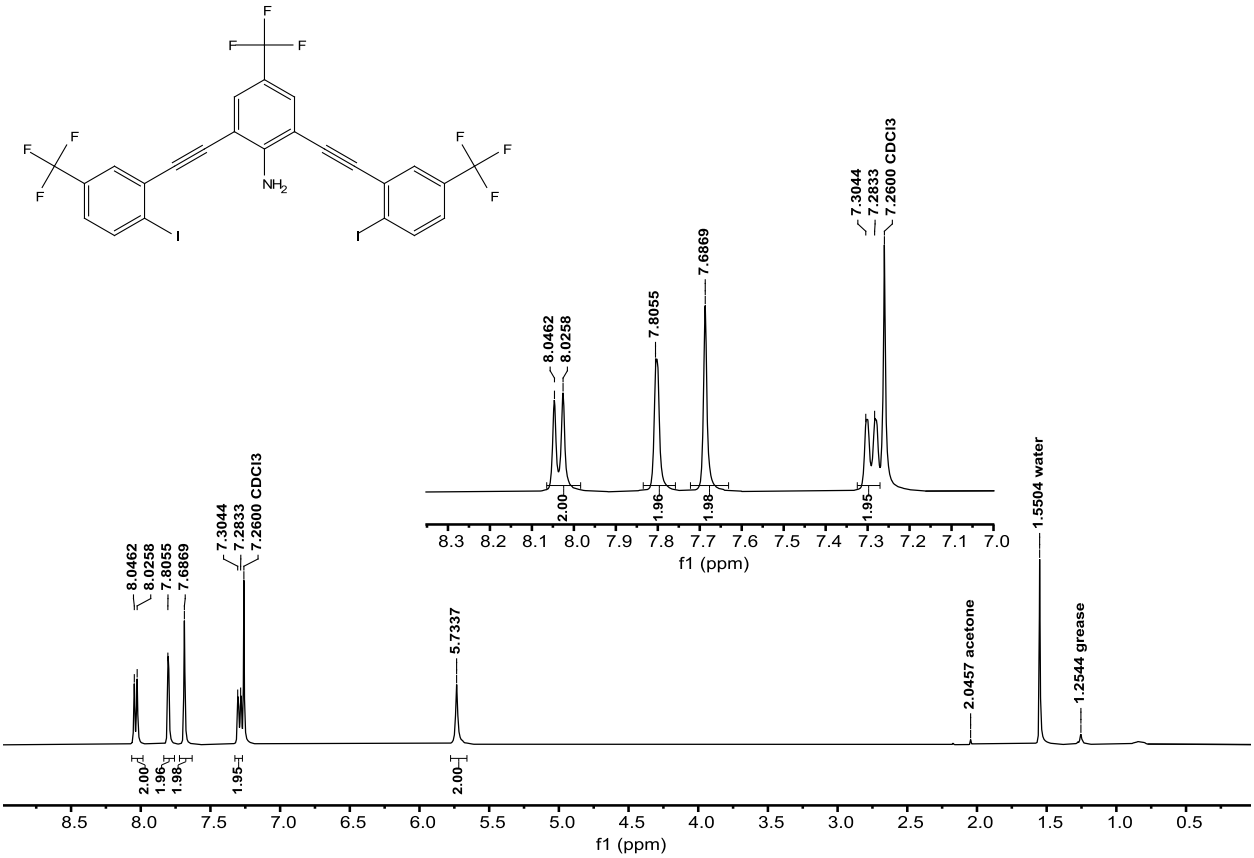

Figure S80. ^{1}H NMR of **G3XB** (400 MHz, $CDCl_3$).

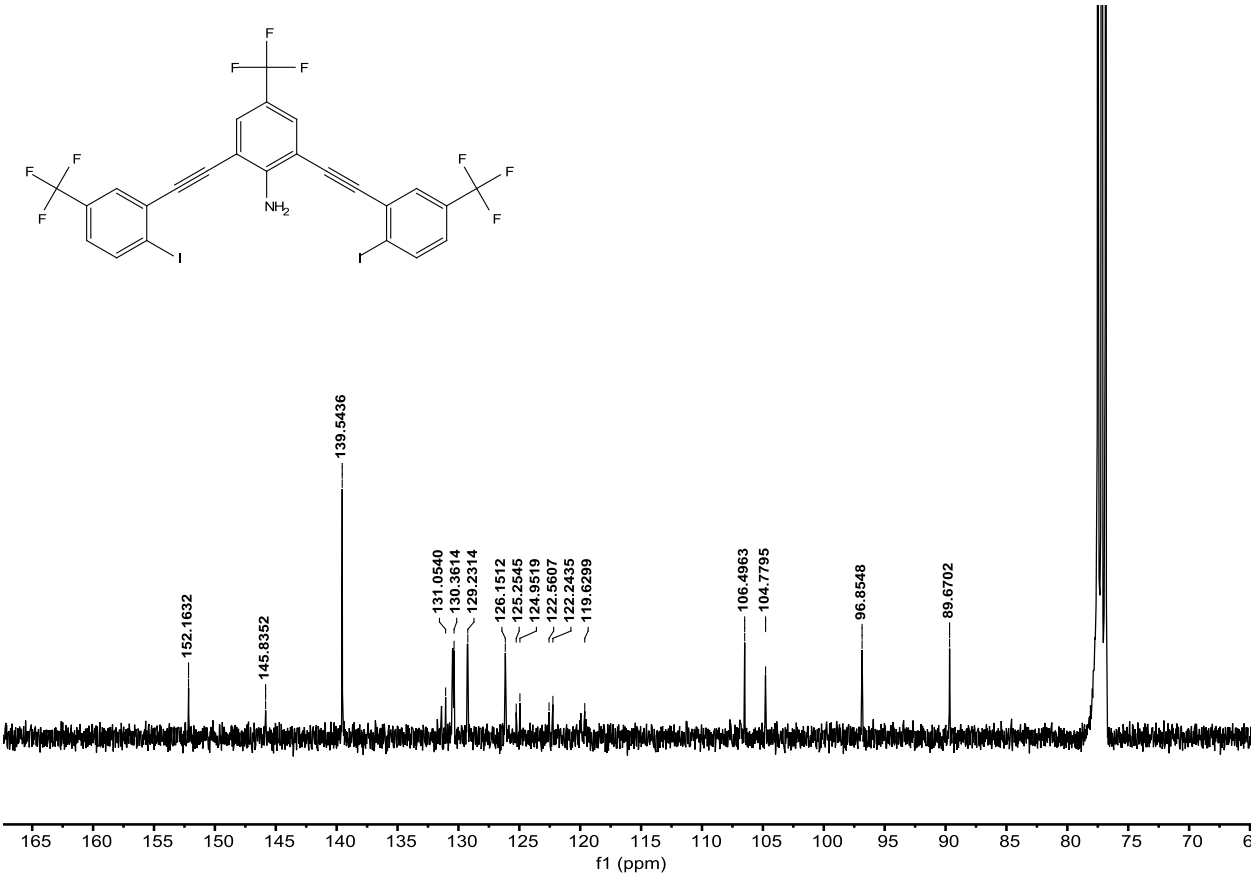

Figure S81. ^{13}C NMR of **G3XB** (100 MHz, $CDCl_3$).

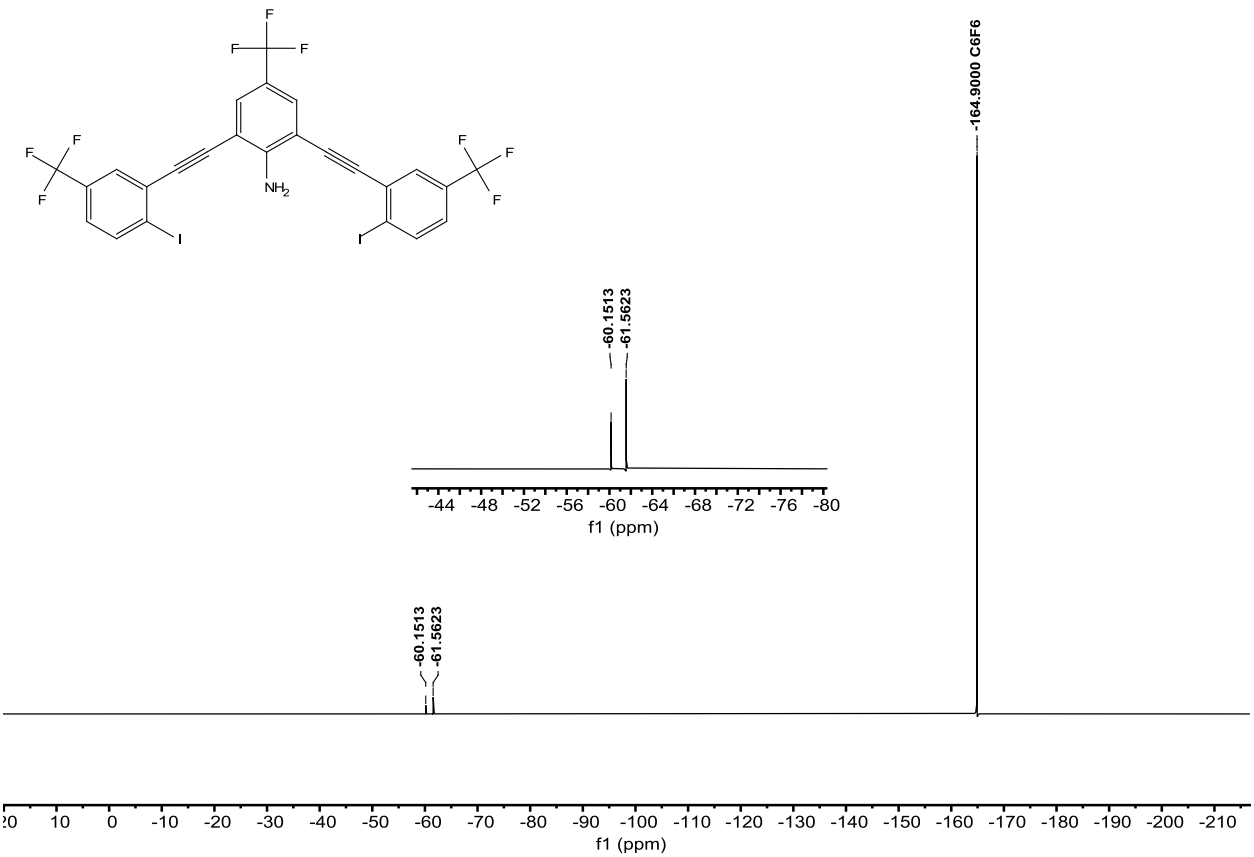

Figure S82. ^{19}F NMR of **G3XB** (376 MHz, $CDCl_3$). Hexafluorobenzene (C_6F_6) internal reference.

2,6-bis(2-ethynyl-4-(trifluoromethyl)bromophenyl)-4-(trifluoromethyl)aniline (2F-G3XBBr). To an oven dried Schlenk flask was charged with 2,6-bisethynyl-4-(trifluoromethyl)aniline **(2a)** (0.211g 1mmol), then vacuumed and backfilled with dry N2 gas (3x). Bis(triphenylphosphine)palladium (II) dichloride (0.035 g, 0. 05 mmol) was added, vacuumed and backfilled with dry N2 gas (3x). Copper (I) iodide (0.019 g, 0.1 mmol) was added, vacuumed and backfilled with dry N2 (3x). The dry reagents were dissolved in 60 mL dry DMF. 1-Bromo-2-iodo-4-fluorobenzene (0.33 mL, 2.5 mmol) and N,N-diisopropylethylamine (0.86 mL, 5 mmol) were added to the DMF solution. The flask was carefully vacuumed and backfilled with dry N2 (3x). The dark brown solution stirred overnight at room temperature. The reaction mixture was extracted with ethyl acetate then washed with water to remove any excess salts and catalysts, then was dried over magnesium sulfate and gravity filtered. Subsequent removal of DMF, hexanes and ethyl acetate by rotary evaporation left and brown solid that was purified by column chromatography (gradient from 100% Hexanes to 3% EtOAc/97% Hexanes) to afford **2F-G3XBBr** (0.480 g, 87%) as a dull yellow solid.

^{1}H NMR (400 MHz, $CDCl_3$): δ (ppm) = 7.82 (dd, J = 8.8 Hz, 2H), 7.65 (s, 2H), 7.30 (dd, J = 8.9 Hz, 2H), 6.87-7.82 (dt, J = 8.1 Hz, 2H), 5.76 (s, 2H).

^{13}C NMR (100 MHz, $CDCl_3$): δ (ppm) = 162.64 (d, J = 247.5 Hz), 152.19, 140.18 (d, J = 8.4 Hz), 130.96 (d, J = 9.5 Hz), 130.26 (q, J = 3.6 Hz), 123.96 (q, J = 269.4 Hz), 119.80 (d, J = 23.7 Hz), 119.73 (q, J = 33.5 Hz), 117.99 (d, J = 21.9 Hz), 106.53, 96.99, 98.93, 89.15.

^{19}F NMR (376 MHz, $CDCl_3$): δ (ppm) = –60.08, -111.79.

HRMS (ESI neg) m/z for $C_{23}H_9F_5Br_2N^-$ $[M-H^+]^-$: calculated: 553.9007; found: 553.9007.

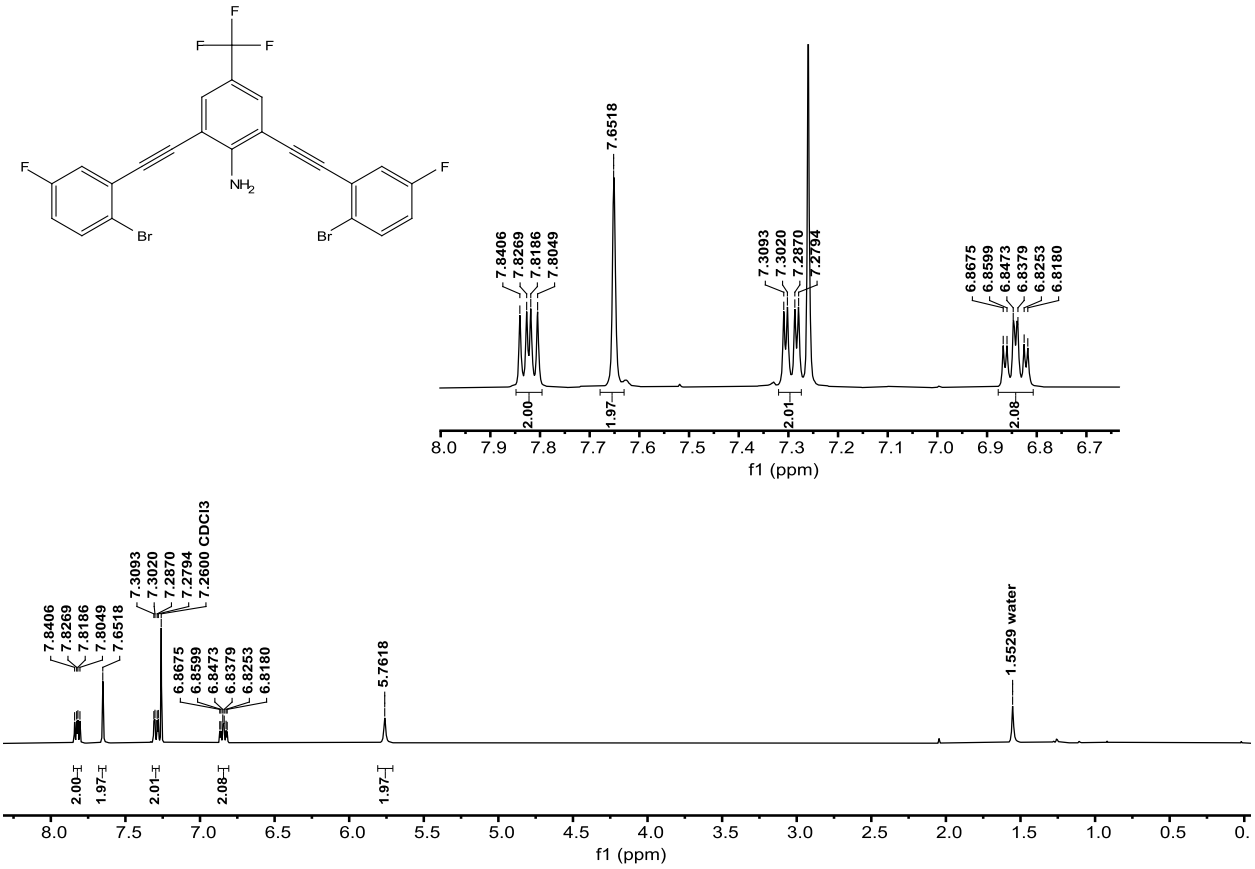

Figure S83. ^{1}H NMR of **2F-G3XBBr** (400 MHz, $CDCl_3$).

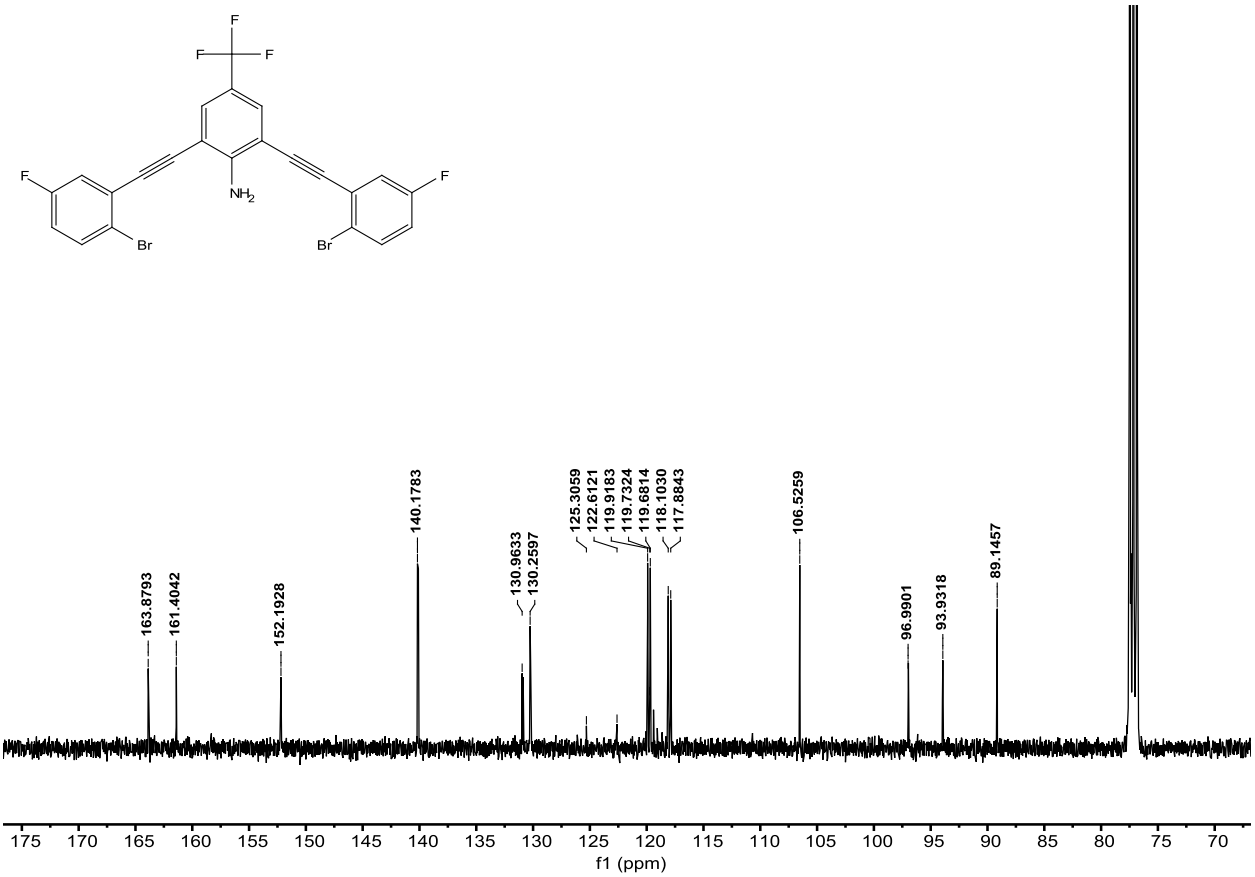

Figure S84. ^{13}C NMR of **2F-G3XBBr** (100 MHz, $CDCl_3$).

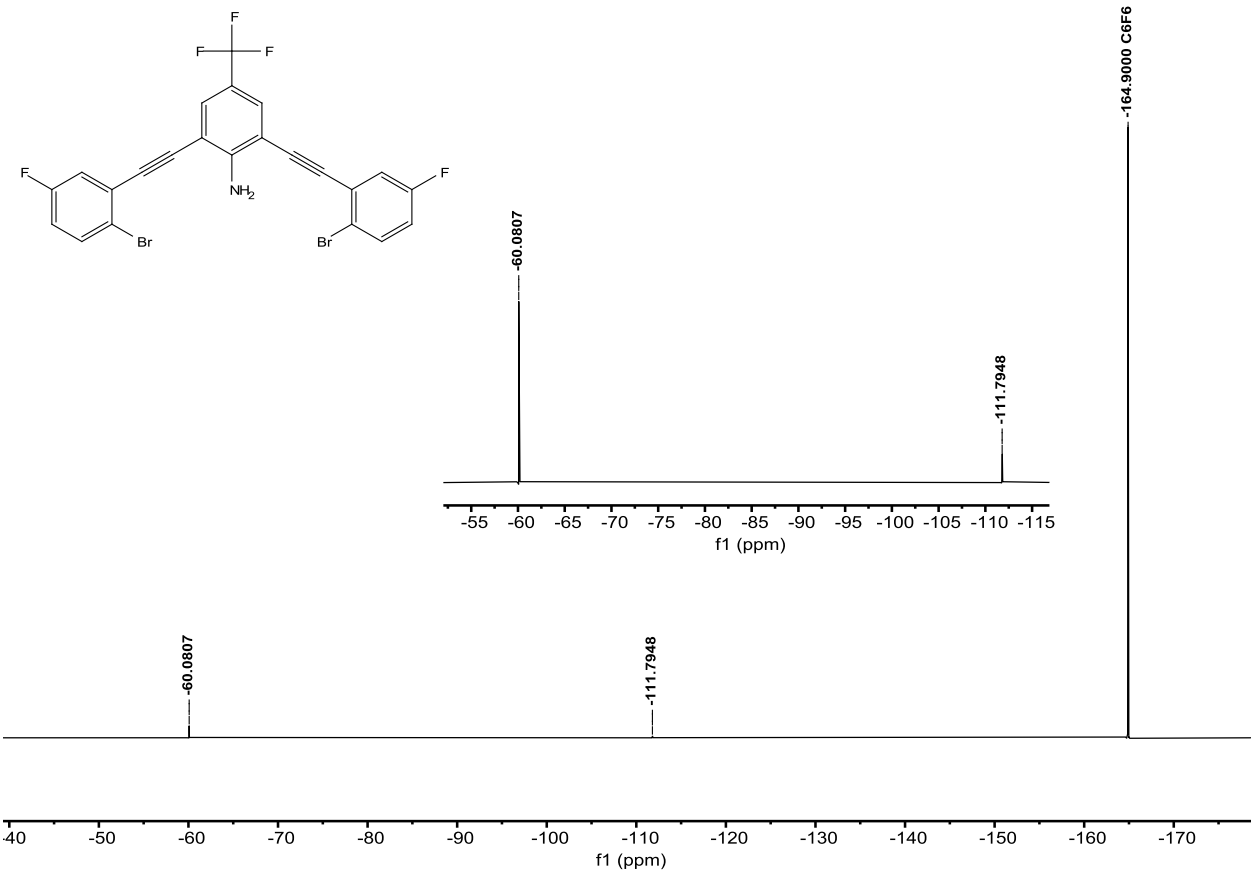

Figure S85. ^{19}F NMR of **2F-G3XBBr** (376 MHz, $CDCl_3$). Hexafluorobenzene (C_6F_6) internal reference.

2,6-bis(2-ethynyl-4-fluoro-iodophenyl)-4-(trifluoromethyl)aniline (2F-G3XB). 2F-G3XBBr (0.200 g, 0.360 mmol), copper iodide (0.006 g, 0.036 mmol), sodium iodide (0.216 g, 1.44 mmol) were added to a 10-20 mL microwave reaction vial containing a stir bar and dissolved in 13 mL 1,4-dioxane. To the vibrant yellow reaction mixture, trans-N,N'-dimethylcyclohexane-1,2-diamine (0.1 mL) was added. The microwave vial was sealed and placed in a Biotage Initiator+ microwave reactor for 16 hours at 150 ˚C. After cooling, the reaction was run through pipet silica plug with EtOAc to remove catalysts and salts. The EtOAc crude was then ran through GCMS in order to obtain % conversion of bromines to iodines. If the conversion from bromine to iodine was 99% or greater, then the reaction was concentrated. The beige/yellow product (0.187 g, 80%) was obtained after purified via high performance liquid chromatography (reverse phase column gradient from 80% water/20% acetonitrile to 100% acetonitrile).

^{1}H NMR (400 MHz, $CDCl_3$): δ (ppm) = 7.82 (dd, J = 5.5 Hz, 2H), 7.65 (s, 2H), 7.30 (dd, J = 6.0 Hz, 2H), 6.87-6.82 (dt, J = 8.0 Hz, 2H), 5.76 (s, 2H).

^{13}C NMR (100 MHz, $CDCl_3$): δ (ppm) = 162.63 (d, J = 247.5 Hz), 152.18, 140.17 (d, J = 8.4 Hz), 130.95 (d, J = 9.1 Hz), 130.21 (q, J = 3.6 Hz), 123.95 (q, J = 269.4 Hz), 119.80 (d, J = 23.7 Hz) 119.72 (q, J = 33.5 Hz), 117.98 (d, J = 21.9 Hz), 106.52, 96.95, 93.92, 89.14.

^{19}F NMR (376 MHz, $CDCl_3$): δ (ppm) = –60.08, -111.80.

HRMS (ESI neg) m/z for $C_{23}H_9F_5I_2N^-$ [M-H$^+$]$^-$: calculated: 647.8750; found: 647.8750.

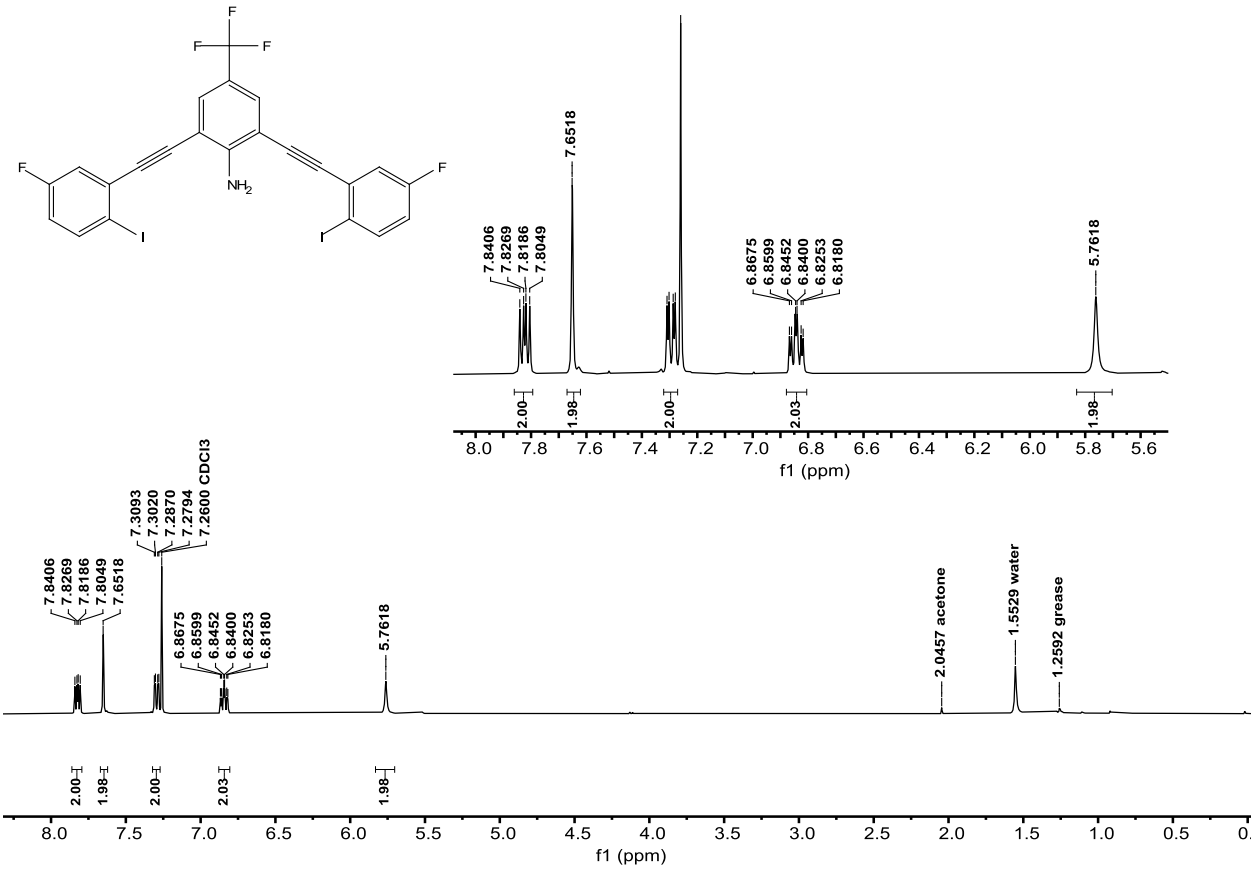

Figure S86. ^{1}H NMR of **2F-G3XB** (400 MHz, $CDCl_3$).

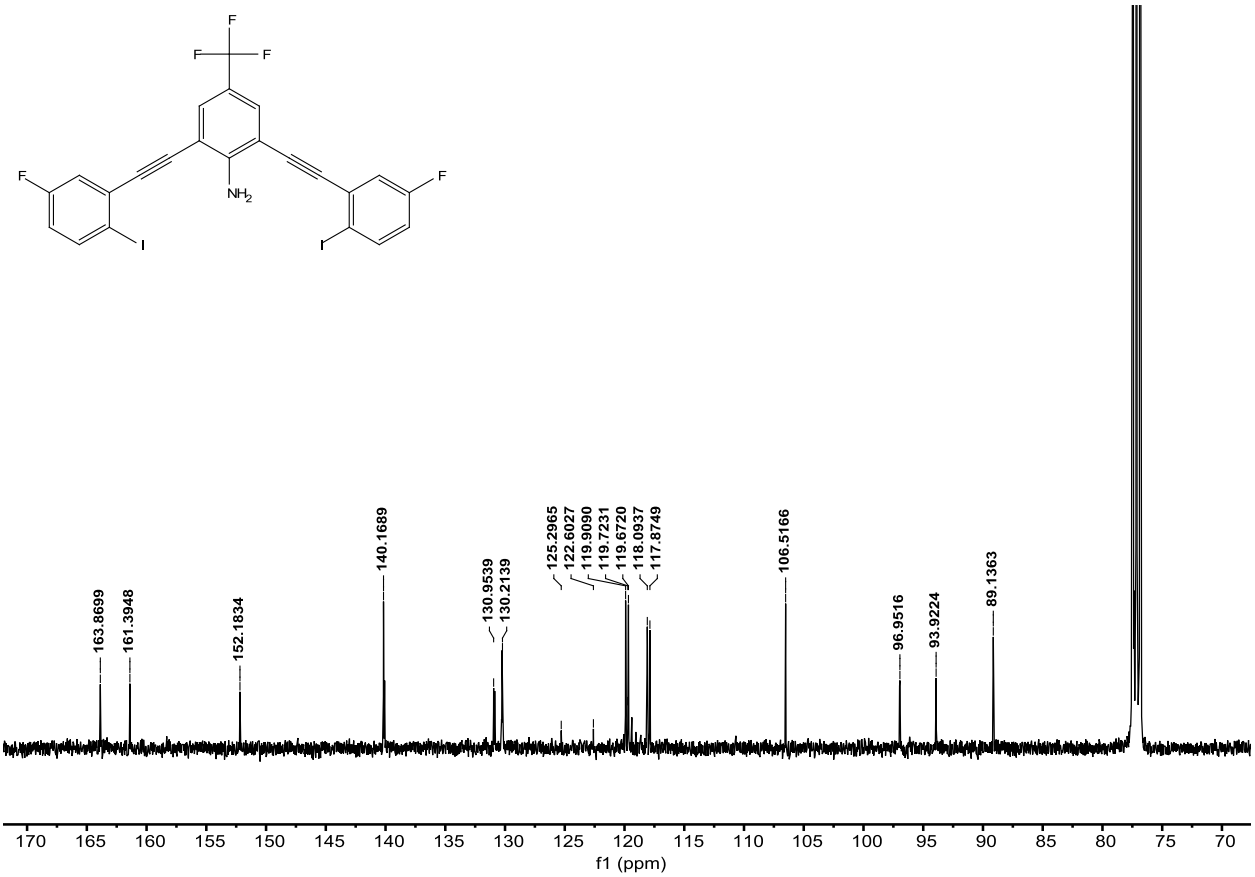

Figure S87. ^{13}C NMR of **2F-G3XB** (100 MHz, $CDCl_3$).

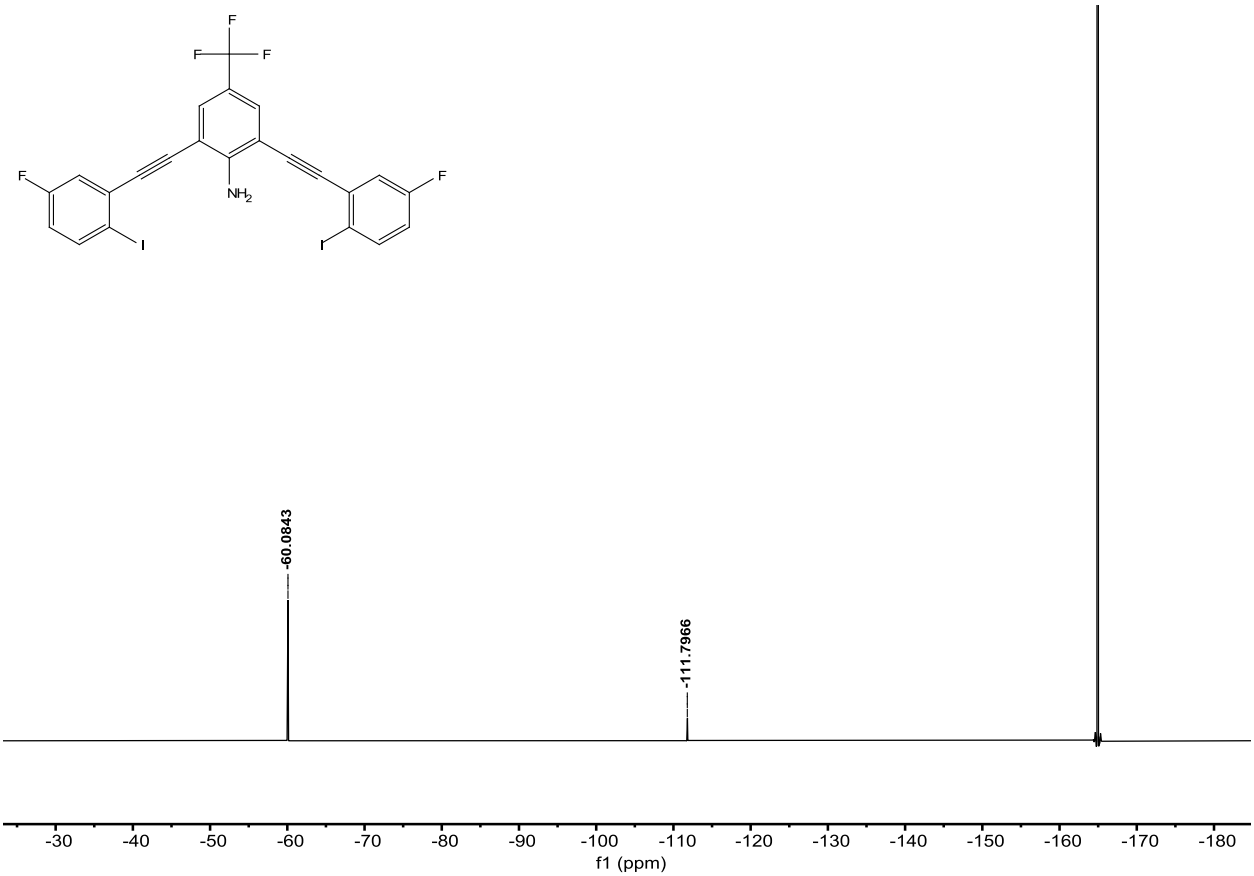

Figure S88. ^{19}F NMR of **2F-G3XB** (376 MHz, $CDCl_3$). Hexafluorobenzene (C_6F_6) internal reference.

2,6-bis(2-ethynyl-bromophenyl)-4-(trifluoromethyl)aniline (2H-G3XBBr). To an oven dried Schlenk flask was charged with 2,6-bisethynyl-4-(trifluoromethyl)aniline **(2a)** (0.375g 1.78mmol), then vacuumed and backfilled with dry N2 gas (3x). Bis(triphenylphosphine)palladium (II) dichloride (0.063 g, 0. 089 mmol) was added, vacuumed and backfilled with dry N2 gas (3x). Copper (I) iodide (0.034 g, 0.178 mmol) was added, vacuumed and backfilled with dry N2 (3x). The dry reagents were dissolved in 100 mL dry DMF. 1-Bromo-2-iodo-benzene (0.57 mL, 4.45 mmol) and N,N-diisopropylethylamine (1.53 mL, 8.9 mmol) were added to the DMF solution. The flask was carefully vacuumed and backfilled with dry N2 (3x). The dark brown solution stirred overnight at room temperature. The reaction mixture was extracted with ethyl acetate then washed with water to remove any excess salts and catalysts, then was dried over magnesium sulfate and gravity filtered. Subsequent removal of DMF, hexanes and ethyl acetate by rotary evaporation left and brown solid that was purified by column chromatography (gradient from 100% Hexanes to 5% EtOAc/95% Hexanes) to afford **2H-G3XBBr** (0.647 g, 70%) as a yellow solid.

^{1}H NMR (400 MHz, $CDCl_3$): δ (ppm) = 7.65 (d, J = 8.0 Hz, 2H), 7.63 (s, 2H), 7.59 (d, J = 7.7 Hz, 2H), 7.35 (t, J = 7.6 Hz, 2H), 7.23 (t, J = 7.6 Hz, 2H), 5.70 (s, 2H).

^{13}C NMR (100 MHz, $CDCl_3$): δ (ppm) = 152.02, 133.29, 132.57, 129.99, 129.61 (q, J = 3.7 Hz), 127.49, 125.33, 124.91, 124.11 (q, J = 269.4 Hz), 119.47 (q, J = 33.4 Hz), 106.91, 94.74, 89.09.

^{19}F NMR (376 MHz, $CDCl_3$): δ (ppm) = –59.99.

HRMS (ESI neg) m/z for $C_{23}H_{11}F_3Br_2N^-$ $[M-H^+]^-$: calculated: 517.9195; found: 517.9196.

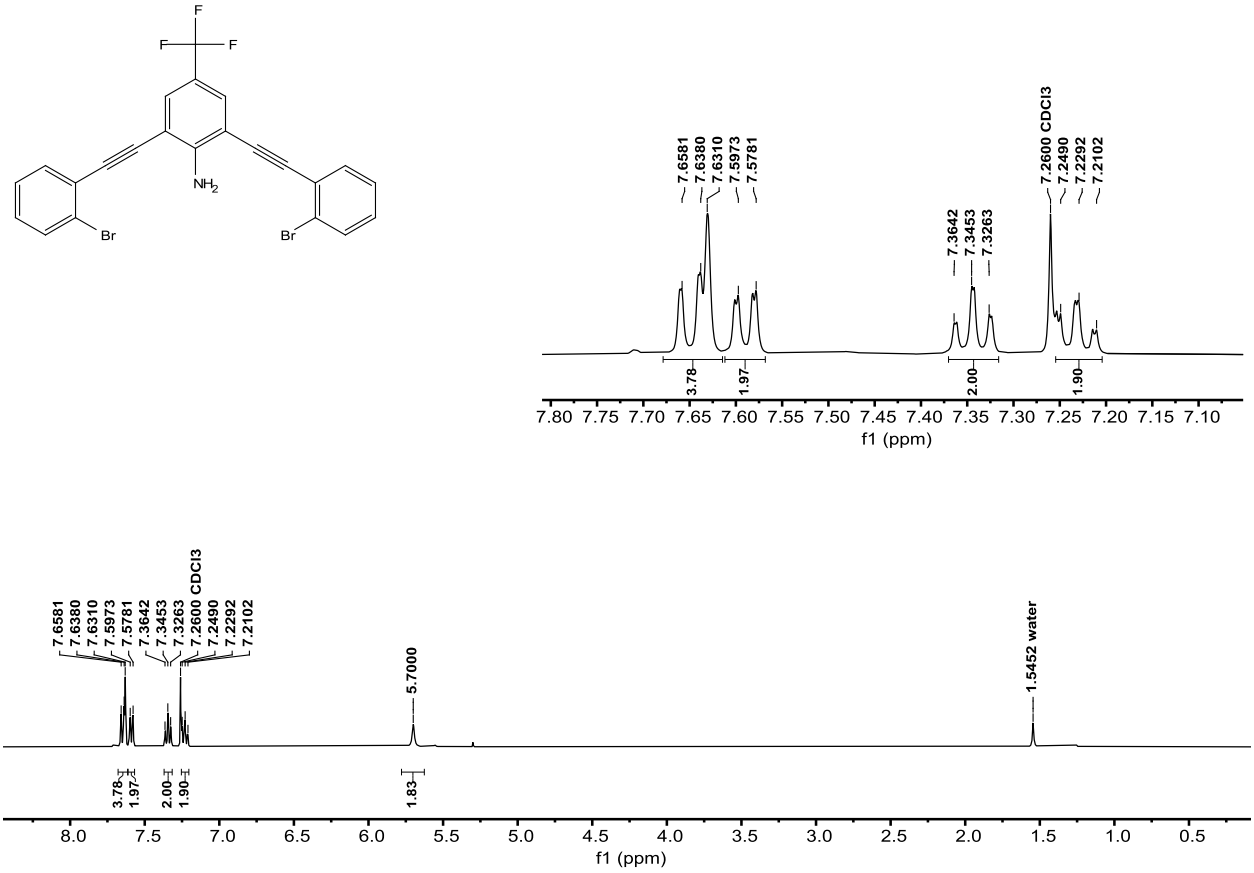

Figure S89. ^{1}H NMR of **2H-G3XBBr** (400 MHz, $CDCl_3$).

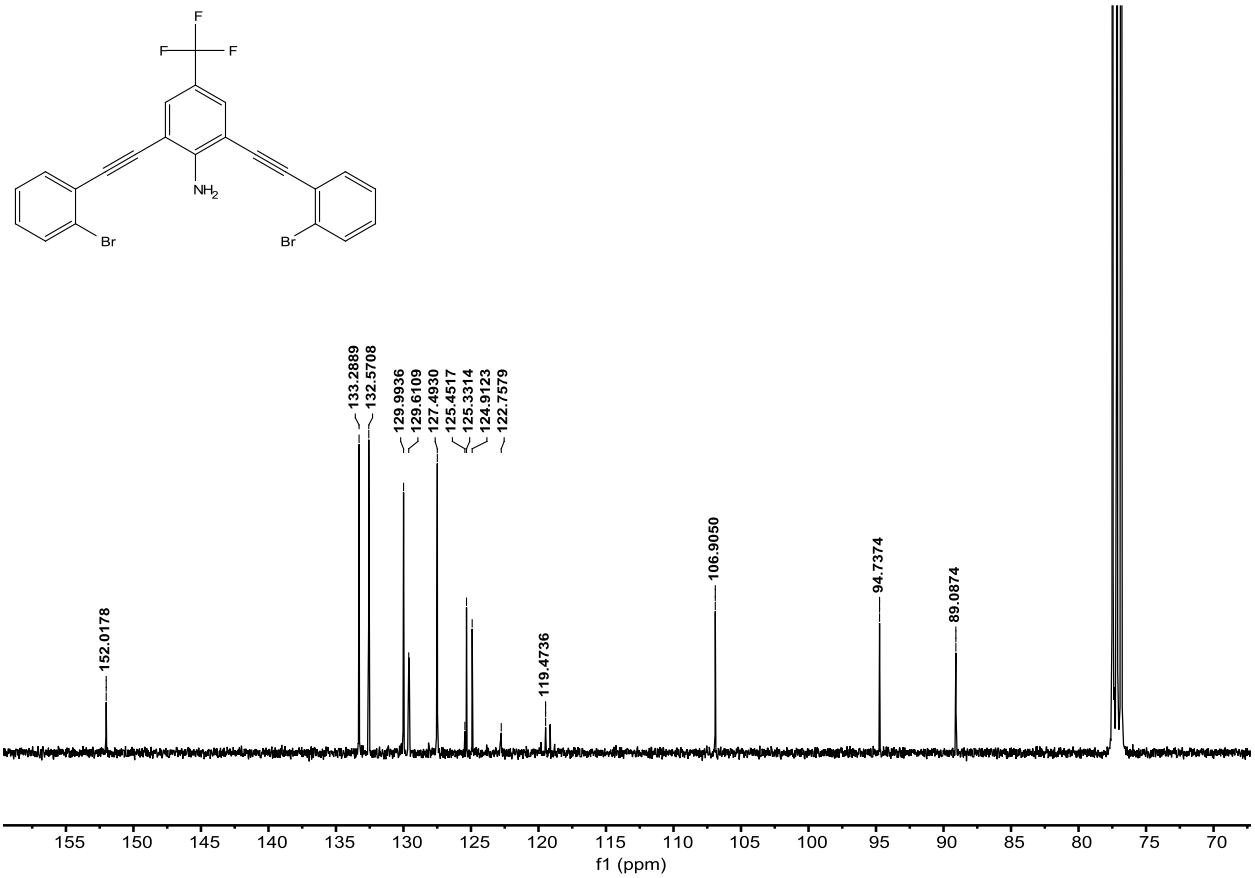

Figure S90. ^{13}C NMR of **2H-G3XBBr** (100 MHz, $CDCl_3$).

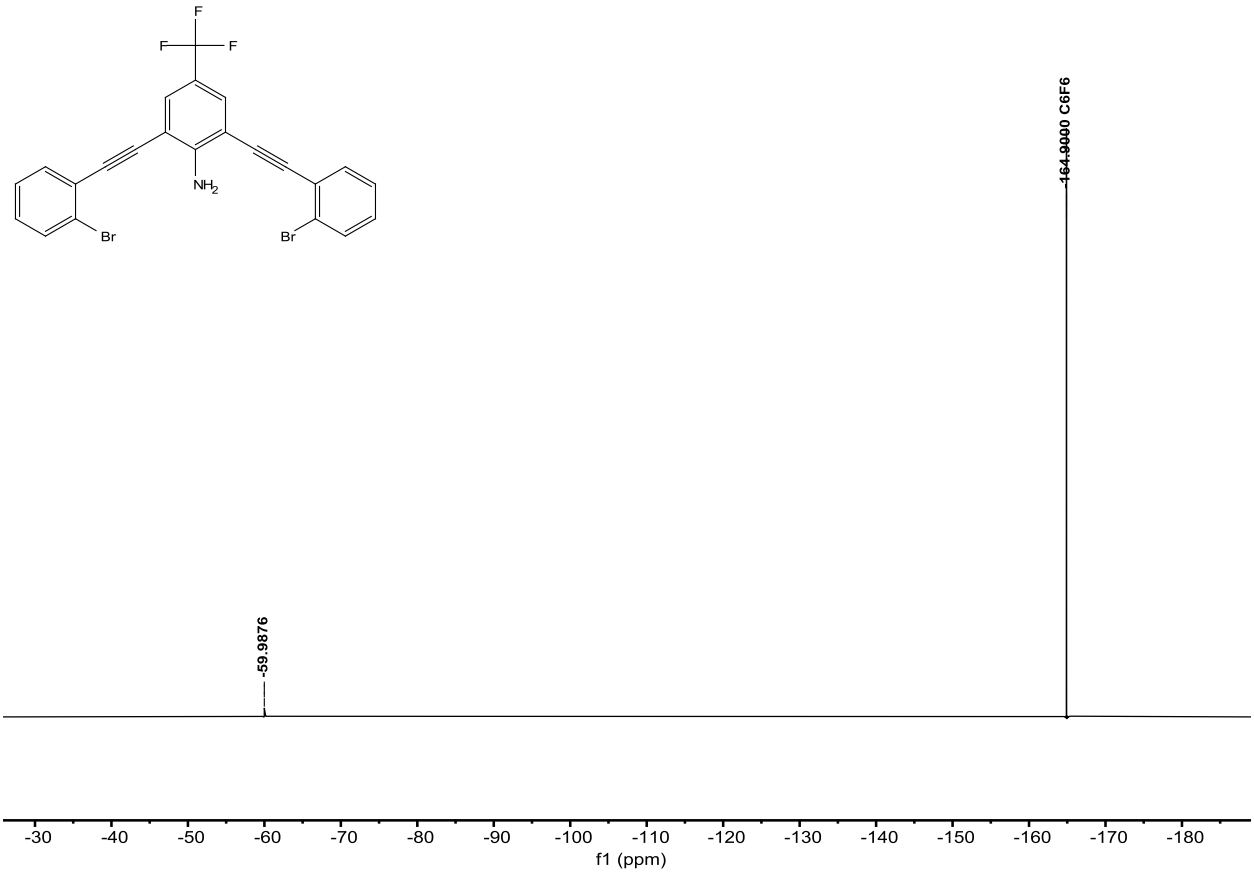

Figure S91. ^{19}F NMR of **2H-G3XBBr** (376 MHz, $CDCl_3$). Hexafluorobenzene (C_6F_6) internal reference.

2,6-bis(2-ethynyl-iodophenyl)-4-(trifluoromethyl)aniline (2H-G3XB). 2H-G3XBBr (0.121 g, 0.233 mmol), copper iodide (0.005 g, 0.026 mmol), sodium iodide (0.140 g, 0.93 mmol) were added to a 10-20 mL microwave reaction vial containing a stir bar and dissolved in 13 mL 1,4-dioxane. To the vibrant yellow reaction mixture, trans-N,N'-dimethylcyclohexane-1,2-diamine (0.1 mL) was added. The microwave vial was sealed and placed in a Biotage Initiator+ microwave reactor for 12 hours at 150 ˚C. After cooling, the reaction was run through pipet silica plug with EtOAc to remove catalysts and salts. The EtOAc crude was then ran through GCMS in order to obtain % conversion of bromines to iodines. If the conversion from bromine to iodine was 99% or greater, then the reaction was concentrated. The beige/yellow product (0.100 g, 70%) was obtained after purified via high performance liquid chromatography (reverse phase column gradient from 80% water/20% acetonitrile to 100% acetonitrile).
^{1}H NMR (400 MHz, $CDCl_3$): δ (ppm) = 7.90 (d, J = 8.0 Hz, 2H), 7.64 (s, 2H), 7.57 (d, J = 7.7 Hz, 2H), 7.38 (t, J = 8.8 Hz, 2H), 7.06 (t, J = 5.8 Hz, 2H), 5.78 (s, 2H).
^{13}C NMR (100 MHz, $CDCl_3$): δ (ppm) = 152.08, 138.83, 132.85, 129.97, 129.72 (q, J = 3.9 Hz), 129.38, 128.25, 124.10 (q, J = 269.4 Hz), 119.35 (q, J = 33.5 Hz), 106.91, 100.71, 97.93, 88.27.
^{19}F NMR (376 MHz, $CDCl_3$): δ (ppm) = –60.00.
HRMS (ESI neg) m/z for $C_{23}H_{11}F_3I_2N^-$ [M-H$^+$]$^-$: calculated: 611.8938; found: 611.8938.

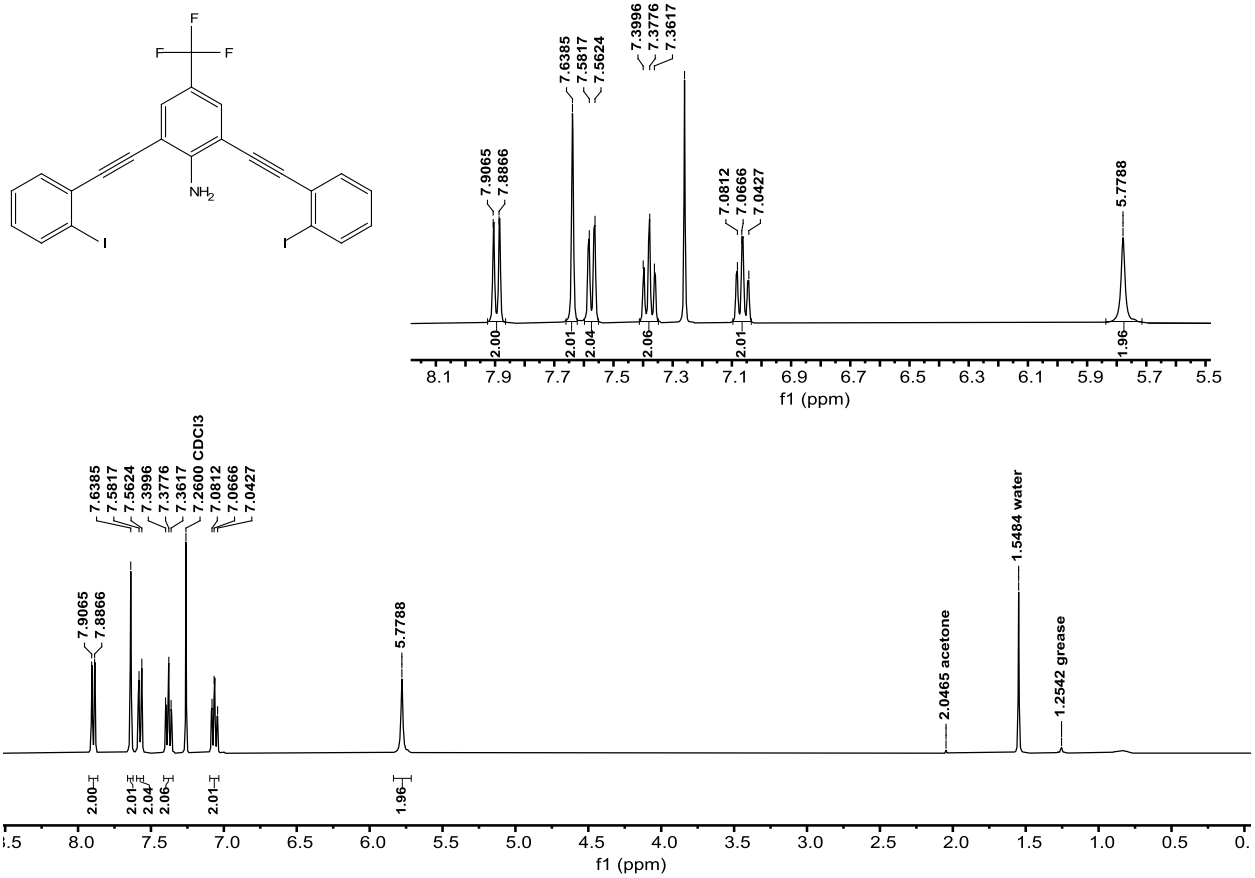

Figure S92. ^{1}H NMR of **2H-G3XB** (400 MHz, $CDCl_3$).

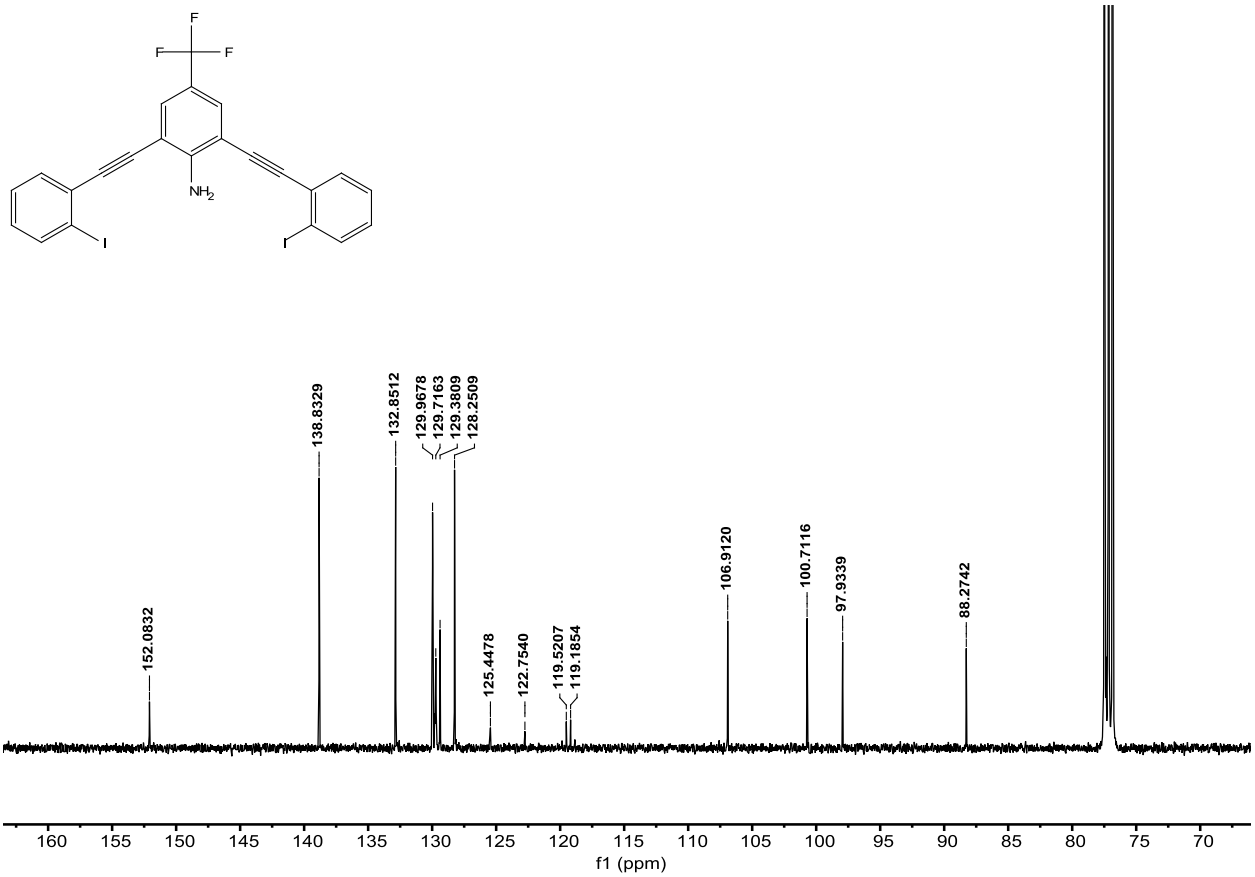

Figure S93. ^{13}C NMR of **2H-G3XB** (100 MHz, $CDCl_3$).

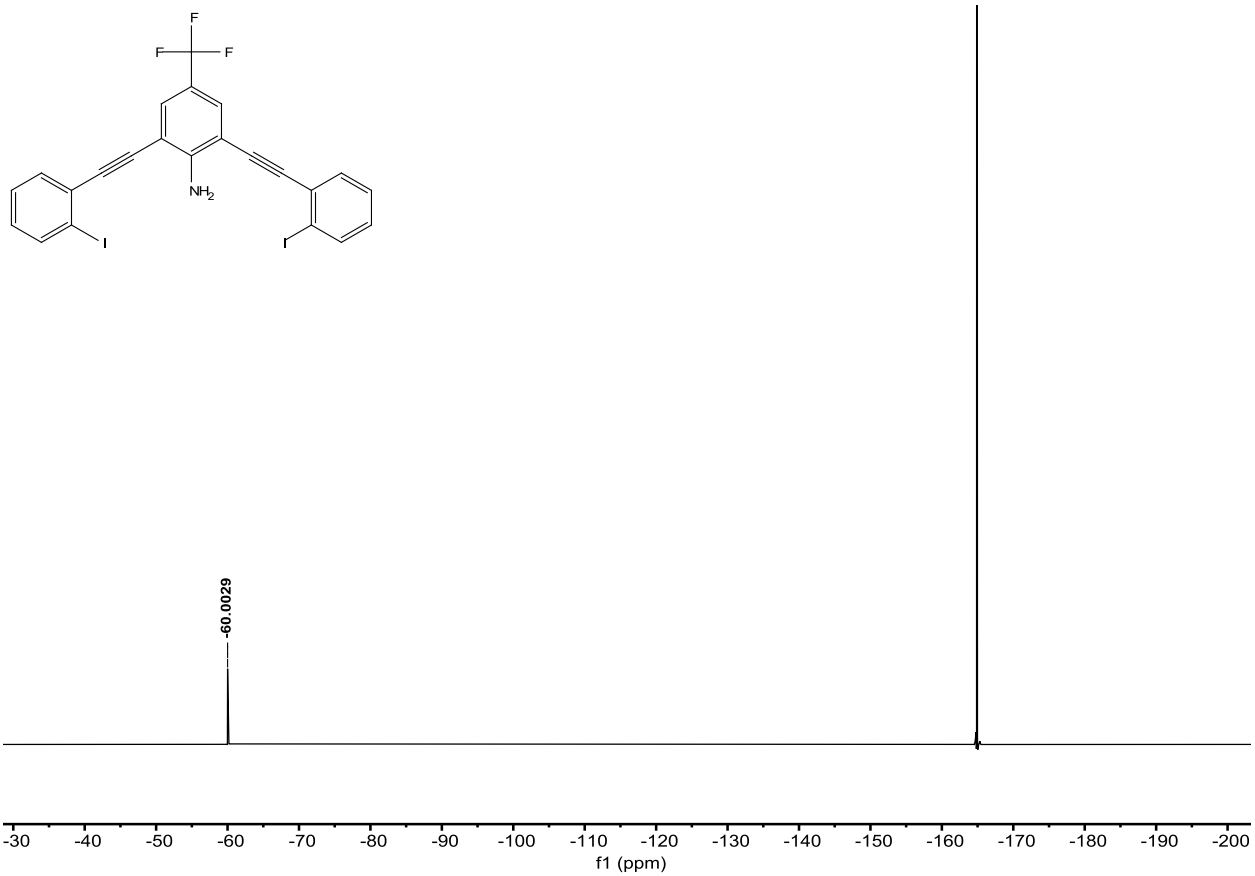

Figure S94. ^{19}F NMR of **2H-G3XB** (376 MHz, $CDCl_3$). Hexafluorobenzene (C_6F_6) internal reference.

2,6-bis(2-ethynyl-4-methyl-bromophenyl)-4-(trifluoromethyl)aniline (2Me-G3XBBr). To an oven dried Schlenk flask was charged with 2,6-bisethynyl-4-(trifluoromethyl)aniline **(2a)** (0.211g 1mmol), then vacuumed and backfilled with dry N2 gas (3x). Bis(triphenylphosphine)palladium (II) dichloride (0.035 g, 0. 05 mmol) was added, vacuumed and backfilled with dry N2 gas (3x). Copper (I) iodide (0.019 g, 0.1 mmol) was added, vacuumed and backfilled with dry N2 (3x). 1-Bromo-2-iodo-4-methylbenzene (0.742 g, 2.5 mmol) was added, vacuumed and backfilled with dry N2 gas (3x). The dry reagents were dissolved in 60 mL dry DMF. N,N-diisopropylethylamine (0.86 mL, 5 mmol) were added to the DMF solution. The flask was carefully vacuumed and backfilled with dry N2 (3x). The dark brown solution stirred for 20 hours at room temperature. The reaction mixture was extracted with ethyl acetate then washed with water to remove any excess salts and catalysts, then was dried over magnesium sulfate and gravity filtered. Subsequent removal of DMF, hexanes and ethyl acetate by rotary evaporation left and brown solid that was purified by column chromatography (gradient from 100% Hexanes to 3% EtOAc/97% Hexanes) to afford **2Me-G3XBBr** (0.375 g, 69%) as a dull yellow solid.
^{1}H NMR (400 MHz, $CDCl_3$): δ (ppm) = 7.61 (s, 2H), 7.52-7.50 (d, J = 8.3 Hz, 2H), 7.41 (s, 2H), 7.04-7.02 (d, J = 8.2 Hz, 2H), 5.69 (s, 2H), 2.33 (s, 6H).
^{13}C NMR (100 MHz, $CDCl_3$): δ (ppm) = 152.00, 137.53, 133.80, 132.24, 131.04, 129.47 (q, J = 3.7 Hz), 124.53, 124.13 (q, J = 269.4 Hz), 121.96, 119.40 (q, J = 34.0 Hz), 106.96, 94.90, 88.67, 20.92.

^{19}F NMR (376 MHz, $CDCl_3$): δ (ppm) = –59.99.

HRMS (ESI neg) m/z for $C_{25}H_{15}F_3Br_2N^-$ $[M\text{-}H^+]^-$: calculated: 545.9508; found: 545.9508.

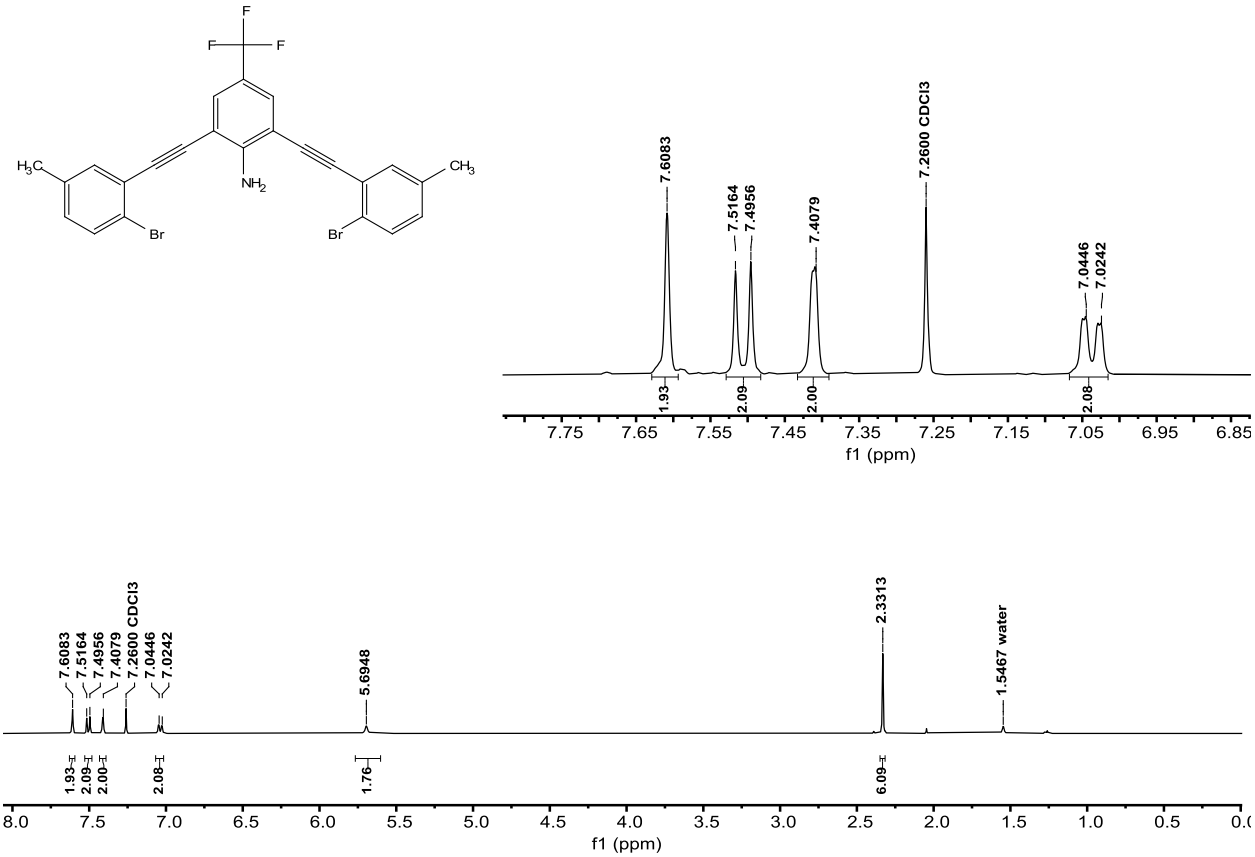

Figure S15. ^{1}H NMR of **2Me-G3XBBr** (400 MHz, $CDCl_3$).

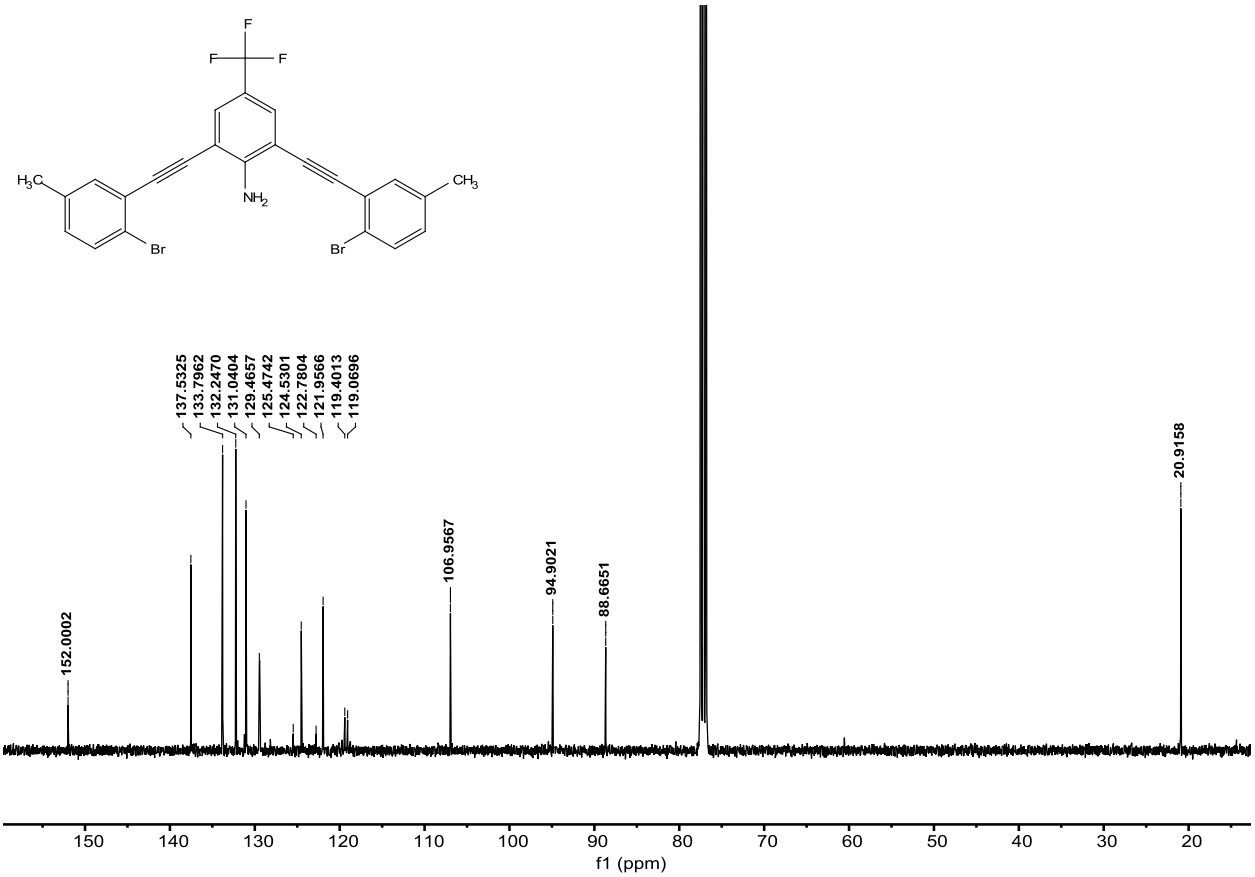

Figure S96. ^{13}C NMR of **2Me-G3XBBr** (100 MHz, $CDCl_3$).

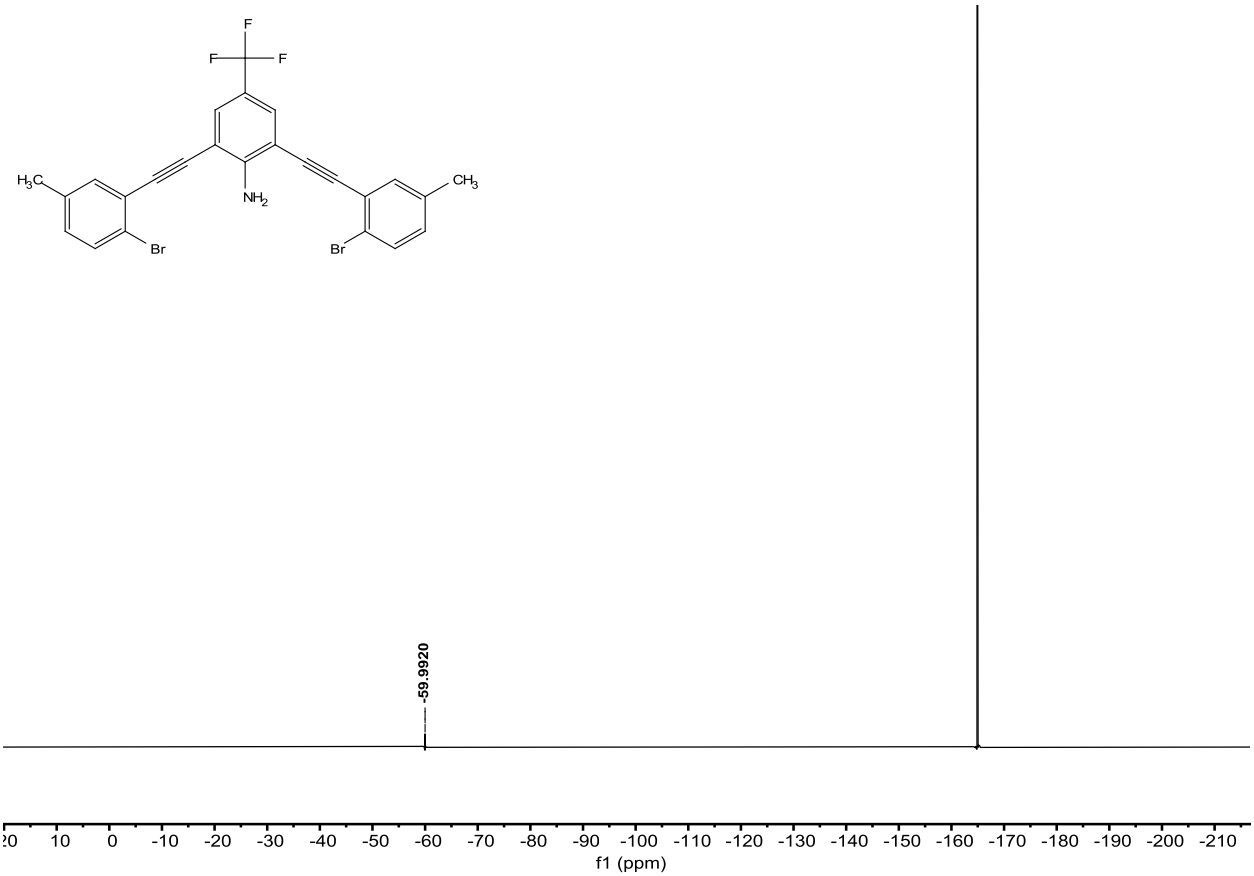

Figure S97. ^{19}F NMR of **2Me-G3XBBr** (376 MHz, $CDCl_3$). Hexafluorobenzene (C_6F_6) internal reference.

2,6-bis(2-ethynyl-4-methyl-iodophenyl)-4-(trifluoromethyl)aniline (2Me-G3XB). 2Me-G3XBBr (0.100 g, 0.183 mmol), copper iodide (0.0035 g, 0.018 mmol), sodium iodide (0.110 g, 0.732 mmol) were added to a 10-20 mL microwave reaction vial containing a stir bar and dissolved in 13 mL 1,4-dioxane. To the vibrant yellow reaction mixture, trans-N,N'-dimethylcyclohexane-1,2-diamine (0.1 mL) was added. The microwave vial was sealed and placed in a Biotage Initiator+ microwave reactor for 24 hours at 150 ˚C. After cooling, the reaction was run through pipet silica plug with EtOAc to remove catalysts and salts. The EtOAc crude was then ran through GCMS in order to obtain % conversion of bromines to iodines. If the conversion from bromine to iodine was 99% or greater, then the reaction was concentrated. The beige/yellow product (0.081 g, 69%) was obtained after purified via high performance liquid chromatography (reverse phase column gradient from 80% water/20% acetonitrile to 100% acetonitrile).
^{1}H NMR (400 MHz, $CDCl_3$): δ (ppm) = 7.74 (d, J = 8.2 Hz, 2H), 7.62 (s, 2H), 7.41 (s, 2H), 6.88 (d, J = 10.7 Hz, 2H), 5.78 (s, 2H), 2.32 (s, 6H).
^{13}C NMR (100 MHz, $CDCl_3$): δ (ppm) = 152.08, 138.54, 138.38, 133.55, 131.20, 129.62 (q, J = 3.9 Hz), 129.09, 124.13 (q, J = 269.4 Hz), 119.46 (q, J = 33.9 Hz), 106.97, 98.03, 96.60, 87.88, 20.98.
^{19}F NMR (376 MHz, $CDCl_3$): δ (ppm) = –59.99.
HRMS (ESI neg) m/z for $C_{25}H_{15}F_3I_2N^-$ [M-H$^+$]$^-$: calculated: 639.9251; found: 639.9252.

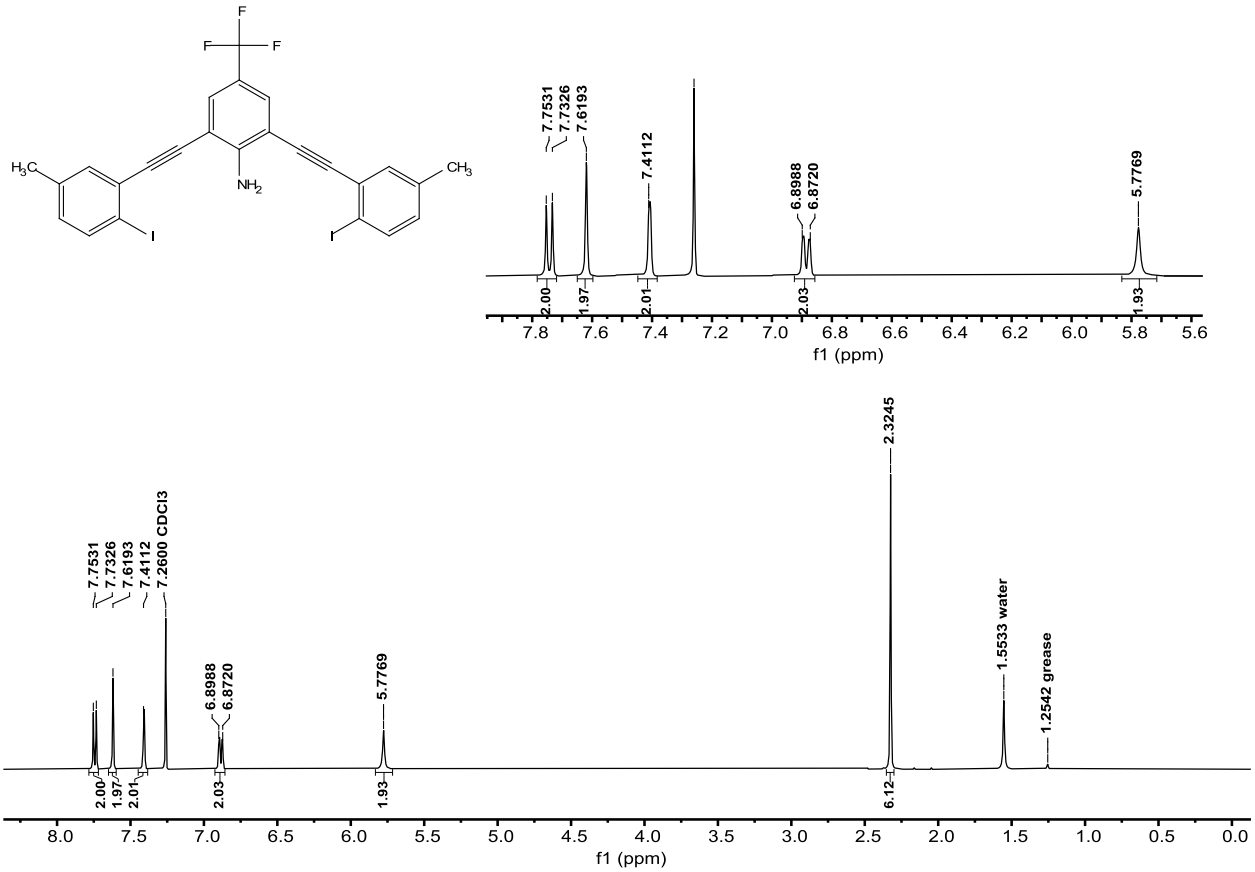

Figure S98. ^{1}H NMR of **2Me-G3XB** (400 MHz, $CDCl_3$).

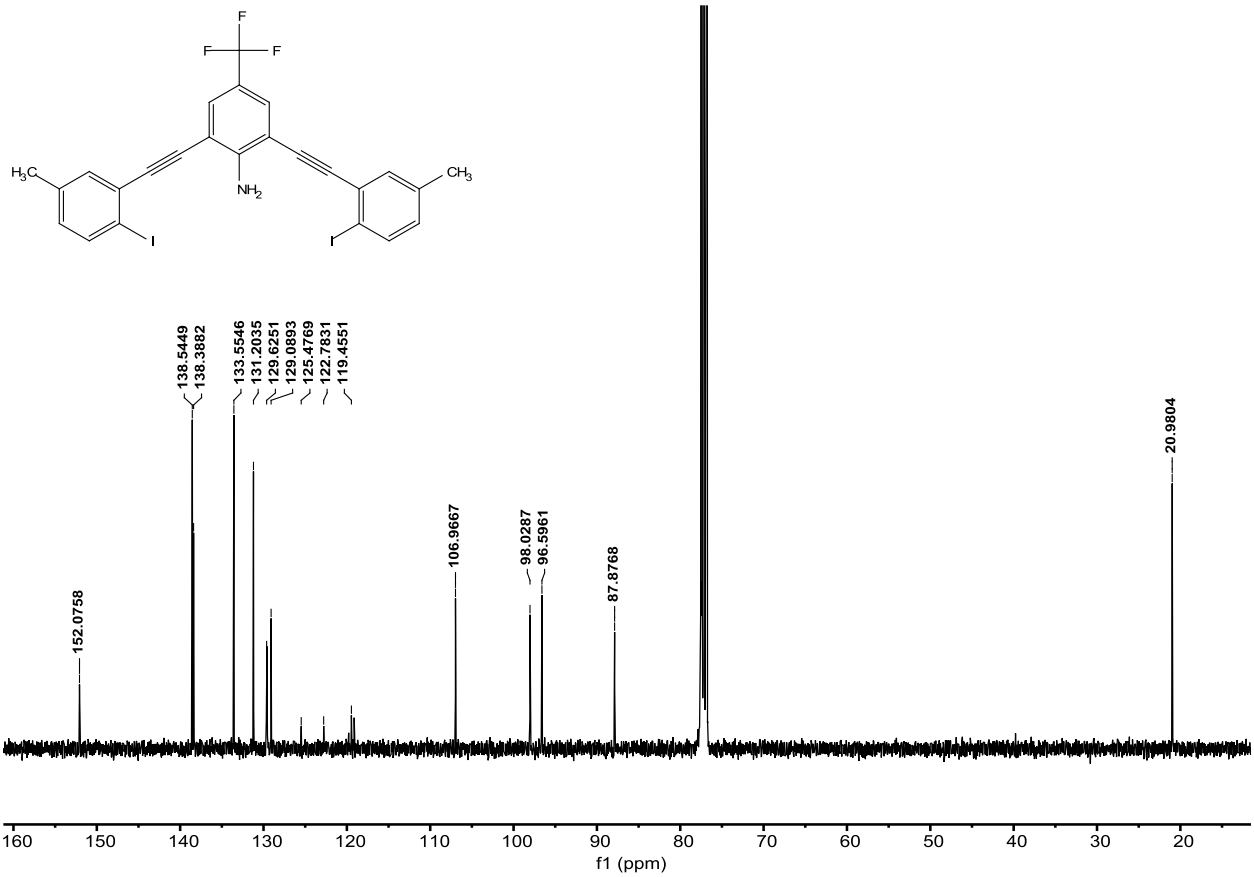

Figure S99. ^{13}C NMR of **2Me-G3XB** (100 MHz, $CDCl_3$).

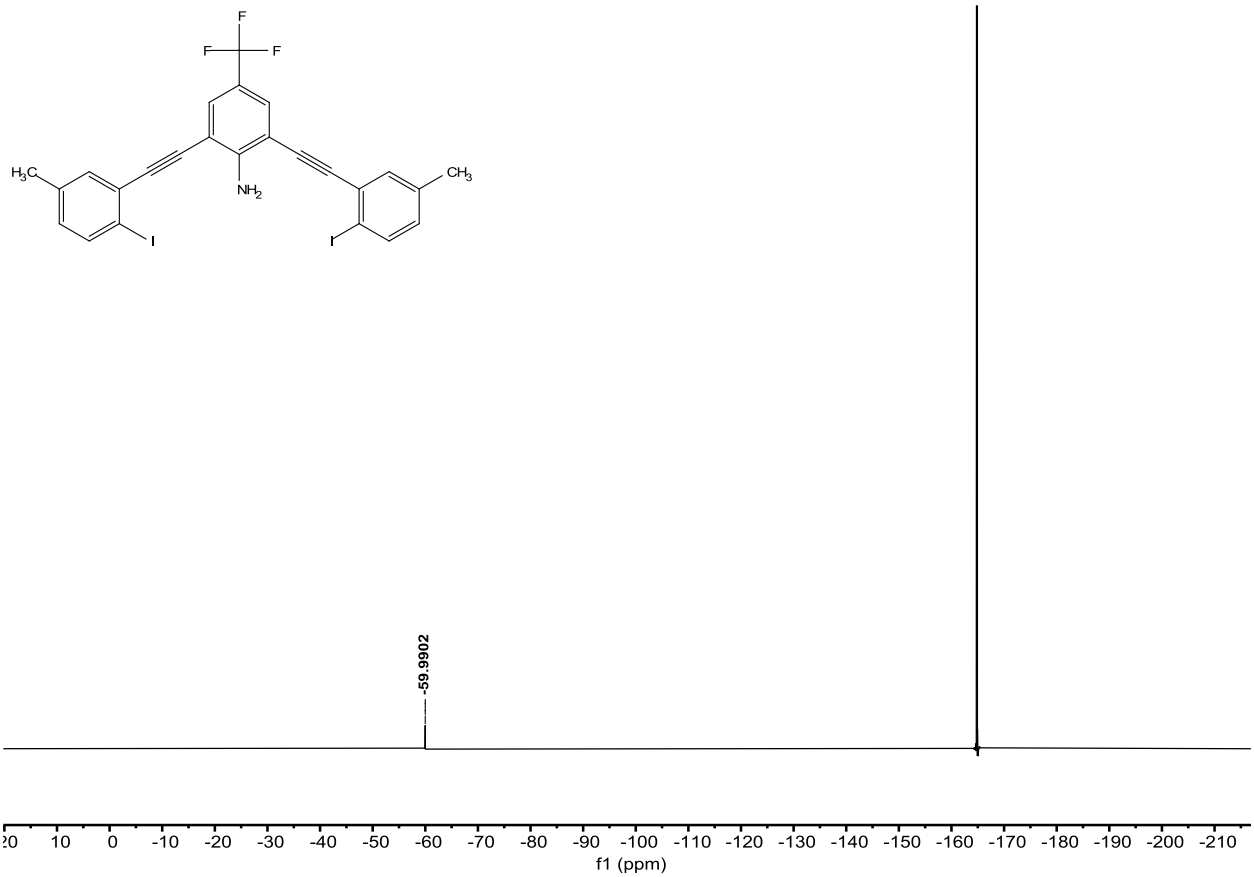

Figure S100. ^{19}F NMR of **2Me-G3XB** (376 MHz, $CDCl_3$). Hexafluorobenzene (C_6F_6) internal reference.

2,6-bis(2-ethynyl-4-*tert*-butyl-bromophenyl)-4-(trifluoromethyl)aniline (2*t*Bu-G3XBBr). To an oven dried Schlenk flask was charged with 2,6-bisethynyl-4-(trifluoromethyl)aniline **(2a)** (0.633g 3mmol), then vacuumed and backfilled with dry N2 gas (3x). Bis(triphenylphosphine)palladium (II) dichloride (0.105 g, 0. 15 mmol) was added, vacuumed and backfilled with dry N2 gas (3x). Copper (I) iodide (0.057 g, 0.3 mmol) was added, vacuumed and backfilled with dry N2 (3x). 1-Bromo-2-iodo-4-*tert*-butylbenzene (1.015 g, 7.5 mmol) was added, vacuumed and backfilled with dry N2 gas (3x). The dry reagents were dissolved in 60 mL dry DMF. N,N-diisopropylethylamine (2.58 mL, 15 mmol) were added to the DMF solution. The flask was carefully vacuumed and backfilled with dry N2 (3x). The dark brown solution stirred for 24 hours at room temperature. The reaction mixture was extracted with ethyl acetate then washed with water to remove any excess salts and catalysts, then was dried over magnesium sulfate and gravity filtered. Subsequent removal of DMF, hexanes and ethyl acetate by rotary evaporation left and brown solid that was purified by column chromatography (gradient from 100% Hexanes to 3% EtOAc/97% Hexanes) to afford **2*t*Bu-G3XBBr** (0.9 g, 50%) as a white solid. **^{1}H NMR (400 MHz, $CDCl_3$):** δ (ppm) = 7.65 (s, 2H), 7.59 (d, J = 2.3 Hz, 2H), 7. 55 (d, J = 8.5 Hz, 2H), 7. 26 (dd, J = 8.5 Hz, 2H), 5.72 (s, 2H), 1.34 (s, 18H).

^{13}C NMR (100 MHz, $CDCl_3$): δ (ppm) = 152.01, 150.89, 132.08, 130.42, 129.47 (q, J = 3.7 Hz), 127.60, 124.28, 124.15 (q, J = 269.3 Hz), 122.07, 119.38 (q, J = 33.2 Hz), 106.97, 95.25, 88.41, 34.80, 31.25.

^{19}F NMR (376 MHz, $CDCl_3$): δ (ppm) = –59.95.

HRMS (ESI neg) m/z for $C_{31}H_{27}F_3Br_2N^-$ [M-H^+]$^-$: calculated: 545.9508; found: 545.9508.

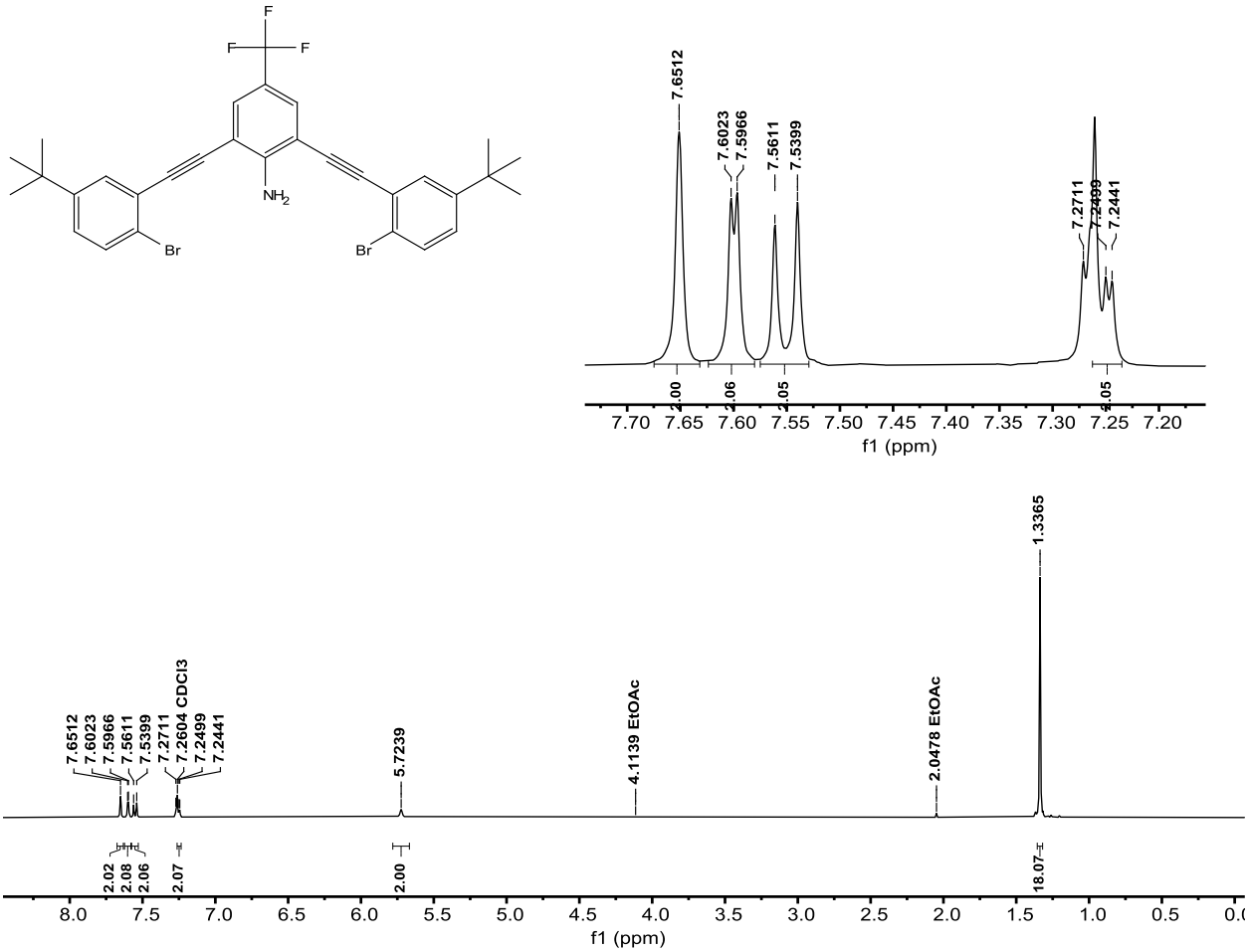

Figure S101. ^{1}H NMR of **2*t*Bu-G3XBBr** (400 MHz, $CDCl_3$).

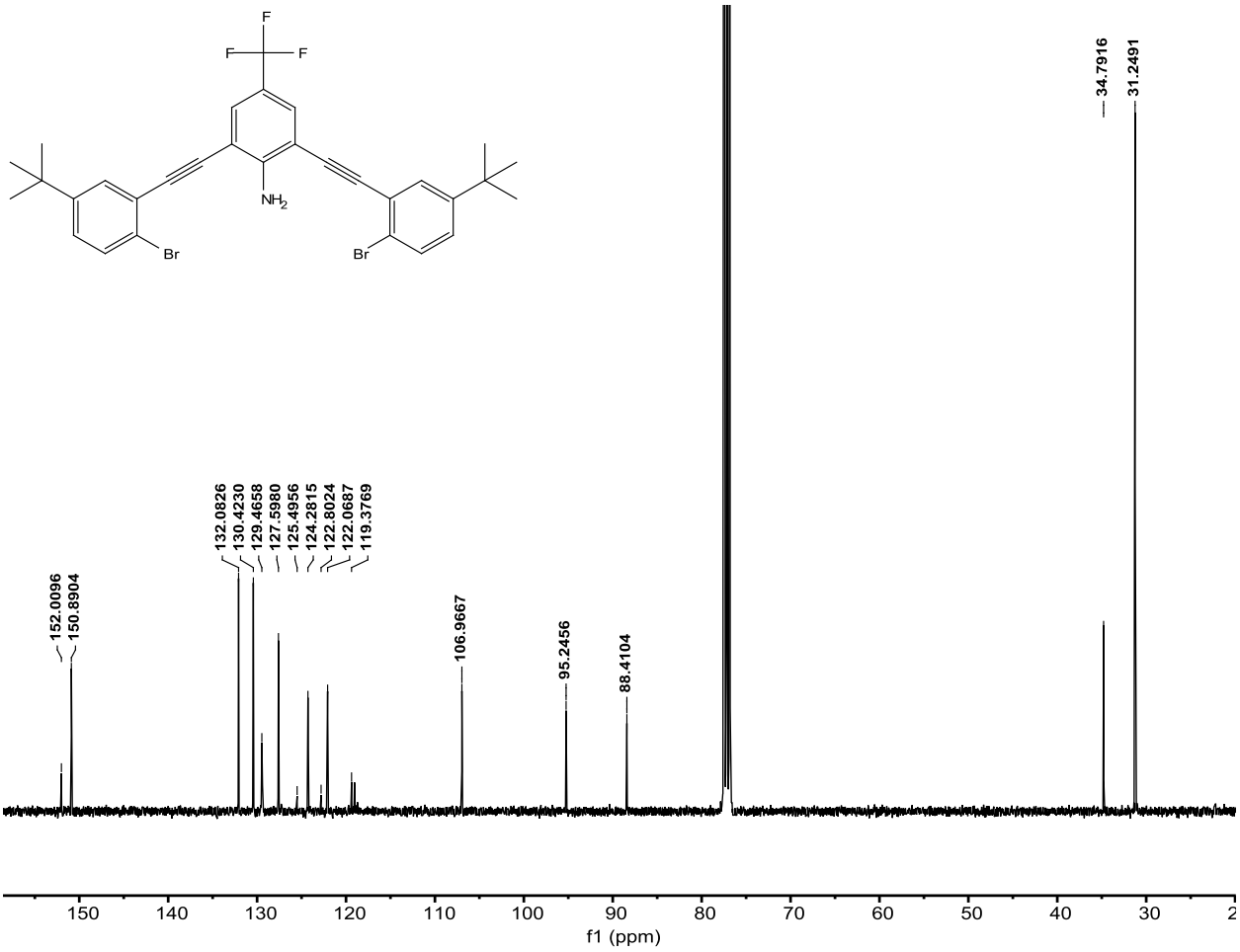

Figure S102. ^{13}C NMR of **2*t*Bu-G3XBBr** (100 MHz, $CDCl_3$).

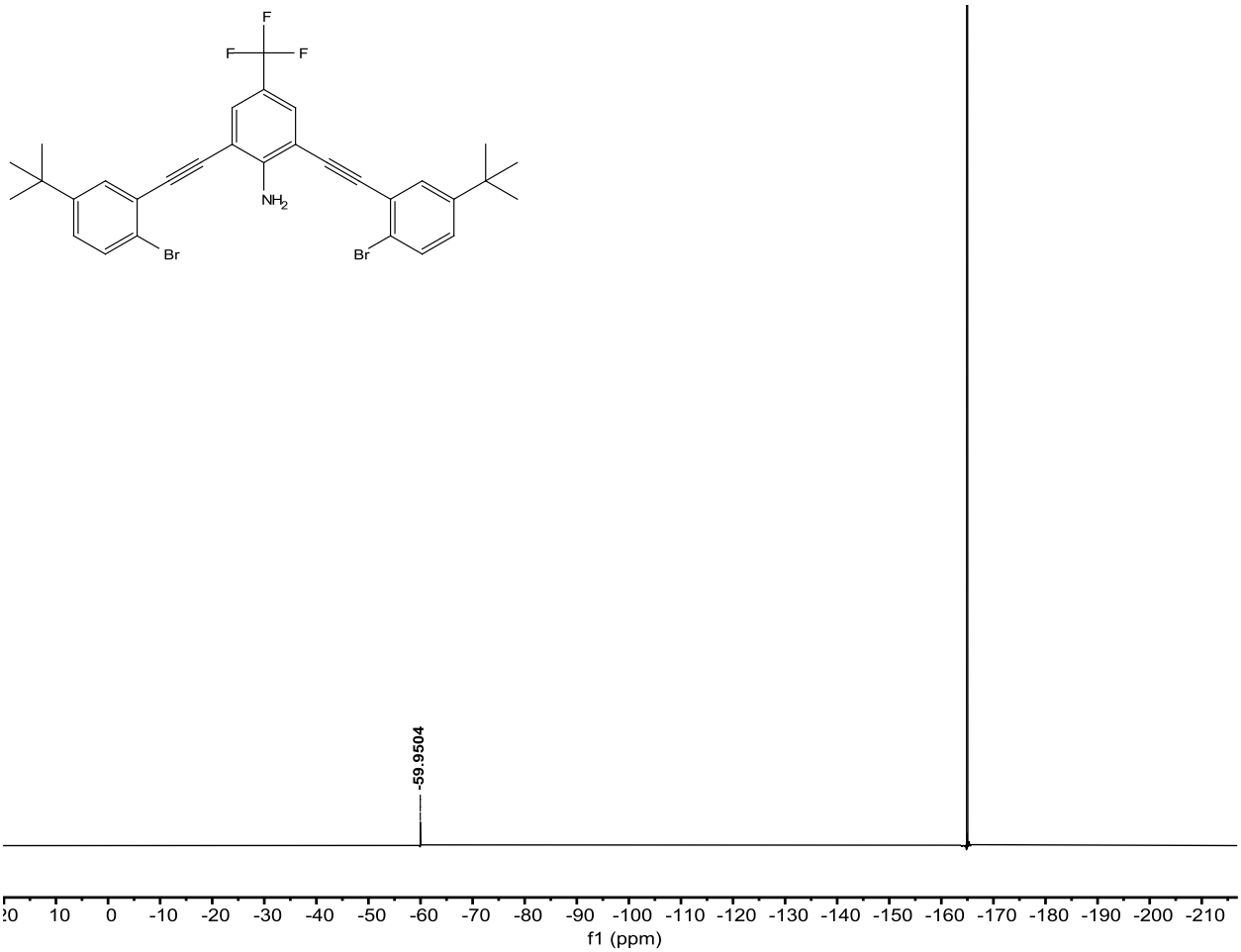

Figure S103. ^{19}F NMR of **2*t*Bu-G3XBBr** (376 MHz, $CDCl_3$). Hexafluorobenzene (C_6F_6) internal reference.

2,6-bis(2-ethynyl-4-*tert*-butyl-iodophenyl)-4-(trifluoromethyl)aniline (2*t*Bu-G3XB). 2*t*Bu-G3XBBr (0.200 g, 0.317 mmol), copper iodide (0.0060 g, 0.032 mmol), sodium iodide (0.190 g, 1.267 mmol) were added to a 10-20 mL microwave reaction vial containing a stir bar and dissolved in 13 mL 1,4-dioxane. To the vibrant yellow reaction mixture, trans-N,N'-dimethylcyclohexane-1,2-diamine (0.1 mL) was added. The microwave vial was sealed and placed in a Biotage Initiator+ microwave reactor for 64 hours at 160˚C. After cooling, the reaction was run through pipet silica plug with EtOAc to remove catalysts and salts. The EtOAc crude was then ran through GCMS in order to obtain % conversion of bromines to iodines. If the conversion from bromine to iodine was 99% or greater, then the reaction was concentrated. The white product (0.154 g, 67%) was obtained after purified via high performance liquid chromatography (reverse phase column gradient from 80% water/20% acetonitrile to 100% acetonitrile).

^{1}H NMR (400 MHz, $CDCl_3$): δ (ppm) = 7.79 (d, J = 8.4 Hz, 2H), 7.66 (s, 2H), 7.59 (d, J = 2.2 Hz, 2H), 7.10 (dd, J = 8.4 Hz, 2H), 5.81 (s, 2H), 1.33 (s, 18H).

^{13}C NMR (100 MHz, $CDCl_3$): δ (ppm) = 152.10, 151.77, 138.39, 130.15, 129.63 (q, J = 3.7 Hz), 128.86, 127.73, 124.15 (q, J = 269.3 Hz), 119.42 (q, J = 33.2 Hz), 106.97, 98.35, 96.93, 87.61, 34.83, 31.20.

^{19}F NMR (376 MHz, $CDCl_3$): δ (ppm) = –59.92.

HRMS (ESI neg) m/z for $C_{31}H_{27}F_3I_2N^-$ [M-H^+]$^-$: calculated: 724.0190; found: 724.0194.

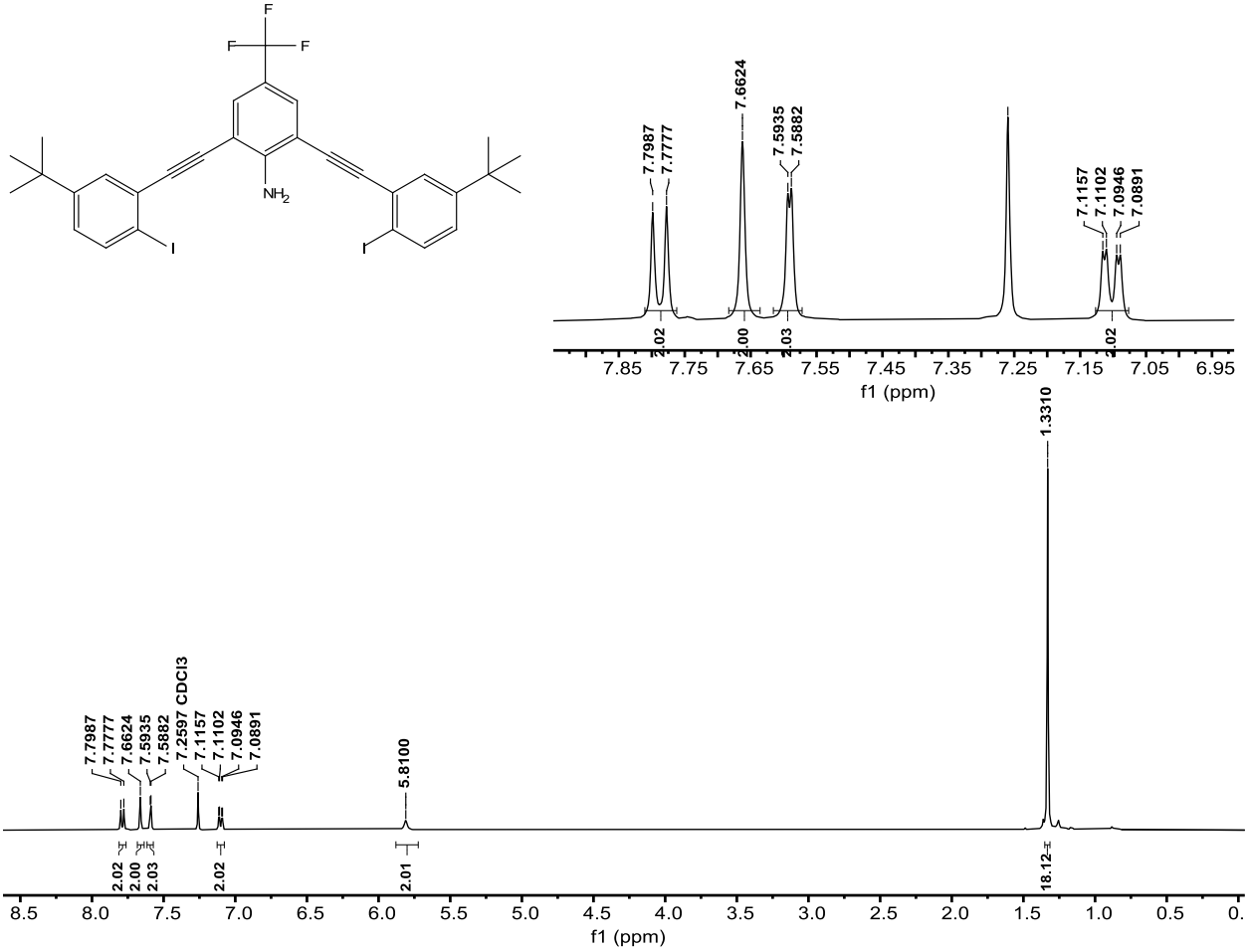

Figure S104. ^{1}H NMR of **2*t*Bu-G3XB** (400 MHz, $CDCl_3$).

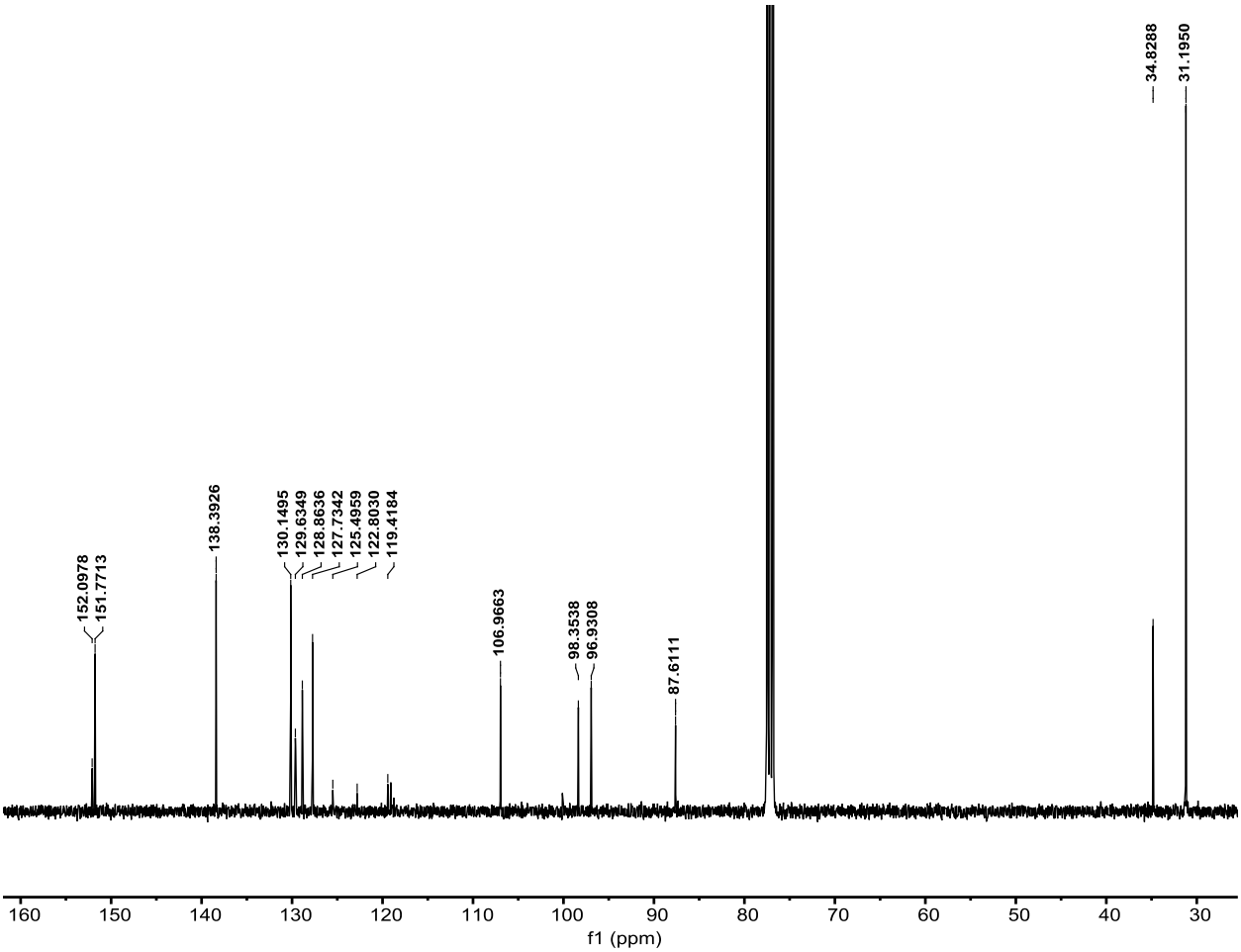

Figure S105. ^{13}C NMR of **2*t*Bu-G3XB** (100 MHz, $CDCl_3$).

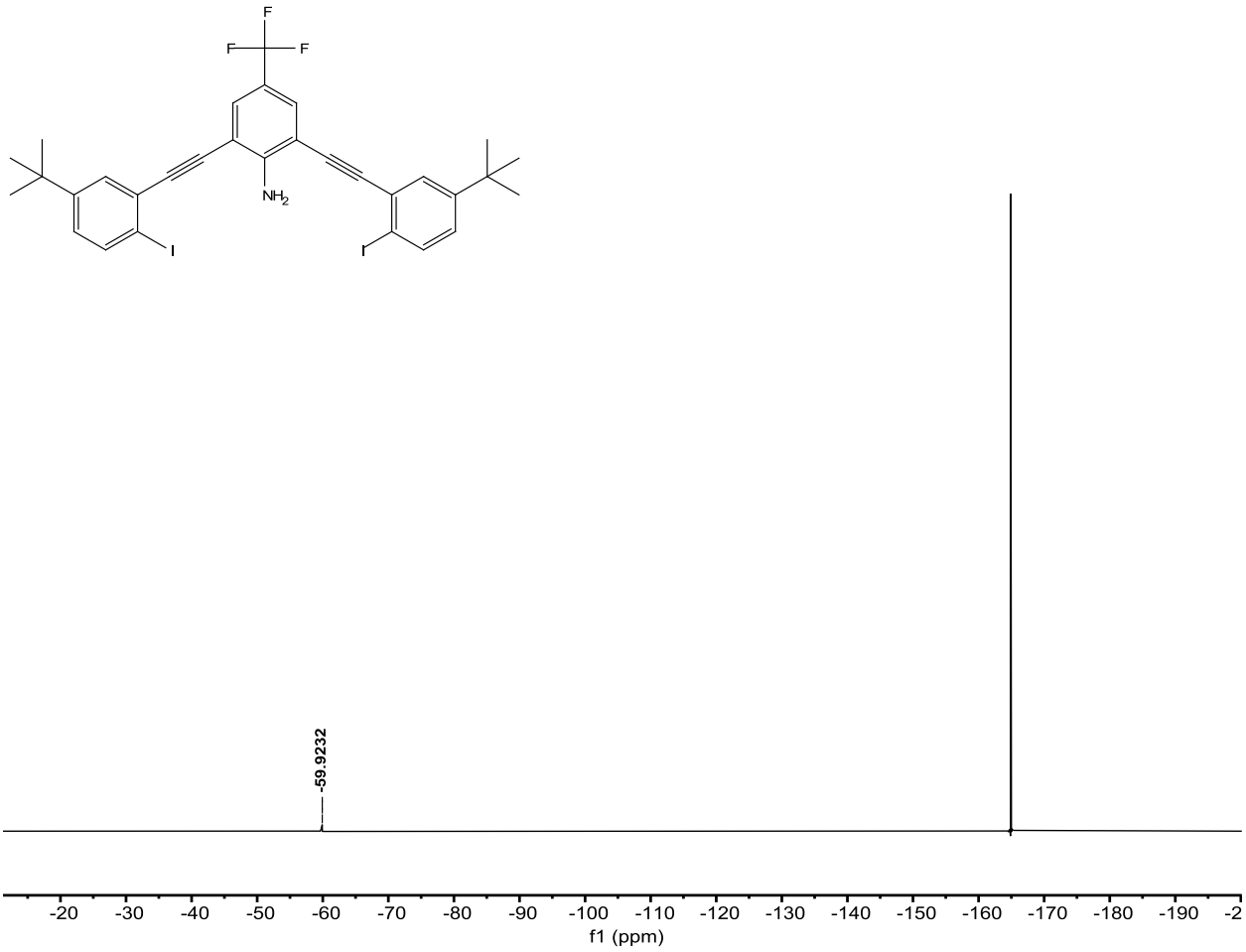

Figure S106. ^{19}F NMR of **2*t*Bu-G3XB** (376 MHz, $CDCl_3$). Hexafluorobenzene (C_6F_6) internal reference.

2,6-bis(2-ethynyl-4-methoxy-bromophenyl)-4-(trifluoromethyl)aniline (2MeO-G3XBBr). To an oven dried Schlenk flask was charged with 2,6-bisethynyl-4-(trifluoromethyl)aniline **(2a)** (0.211g 1mmol), then vacuumed and backfilled with dry N2 gas (3x). Bis(triphenylphosphine)palladium (II) dichloride (0.035 g, 0. 05 mmol) was added, vacuumed and backfilled with dry N2 gas (3x). Copper (I) iodide (0.019 g, 0.1 mmol) was added, vacuumed and backfilled with dry N2 (3x). The dry reagents were dissolved in 60 mL dry DMF. 1-Bromo-2-iodo-4-methoxybenzene (0.38 mL, 2.5 mmol) and N,N-diisopropylethylamine (0.86 mL, 5 mmol) were added to the DMF solution. The flask was carefully vacuumed and backfilled with dry N2 (3x). The dark brown solution stirred for 20 hours at room temperature. The reaction mixture was extracted with ethyl acetate then washed with water to remove any excess salts and catalysts, then was dried over magnesium sulfate and gravity filtered. Subsequent removal of DMF, hexanes and ethyl acetate by rotary evaporation left and brown solid that was purified by column chromatography (gradient from 100% Hexanes to 3% EtOAc/97% Hexanes) to afford **2MeO-G3XBBr** (0.357 g, 62%) as a dull yellow solid.

^{1}H NMR (400 MHz, $CDCl_3$): δ (ppm) = 7.63 (s, 2H), 7.50 (d, J = 8.9 Hz, 2H), 7.110 (d, J = 3.0 Hz, 2H), 6.81 (dd, J = 8.9 Hz, 2H), 5.72 (s, 2H), 3.83 (s, 6H).

^{13}C NMR (100 MHz, $CDCl_3$): δ (ppm) = 158.82, 152.11, 133.20, 129.62 (q, J = 3.6 Hz), 125.39, 124.09 (q, J = 269.3 Hz), 119.26 (q, J = 33.0 Hz), 117.68, 117.18, 115.97, 106.80, 94.80, 88.83, 55.80.

^{19}F NMR (376 MHz, $CDCl_3$): δ (ppm) = –59.99.

HRMS (ESI neg) m/z for $C_{25}H_{15}F_3Br_2NO_2^-$ $[M\text{-}H^+]^-$: calculated: 577.9407; found: 577.9406.

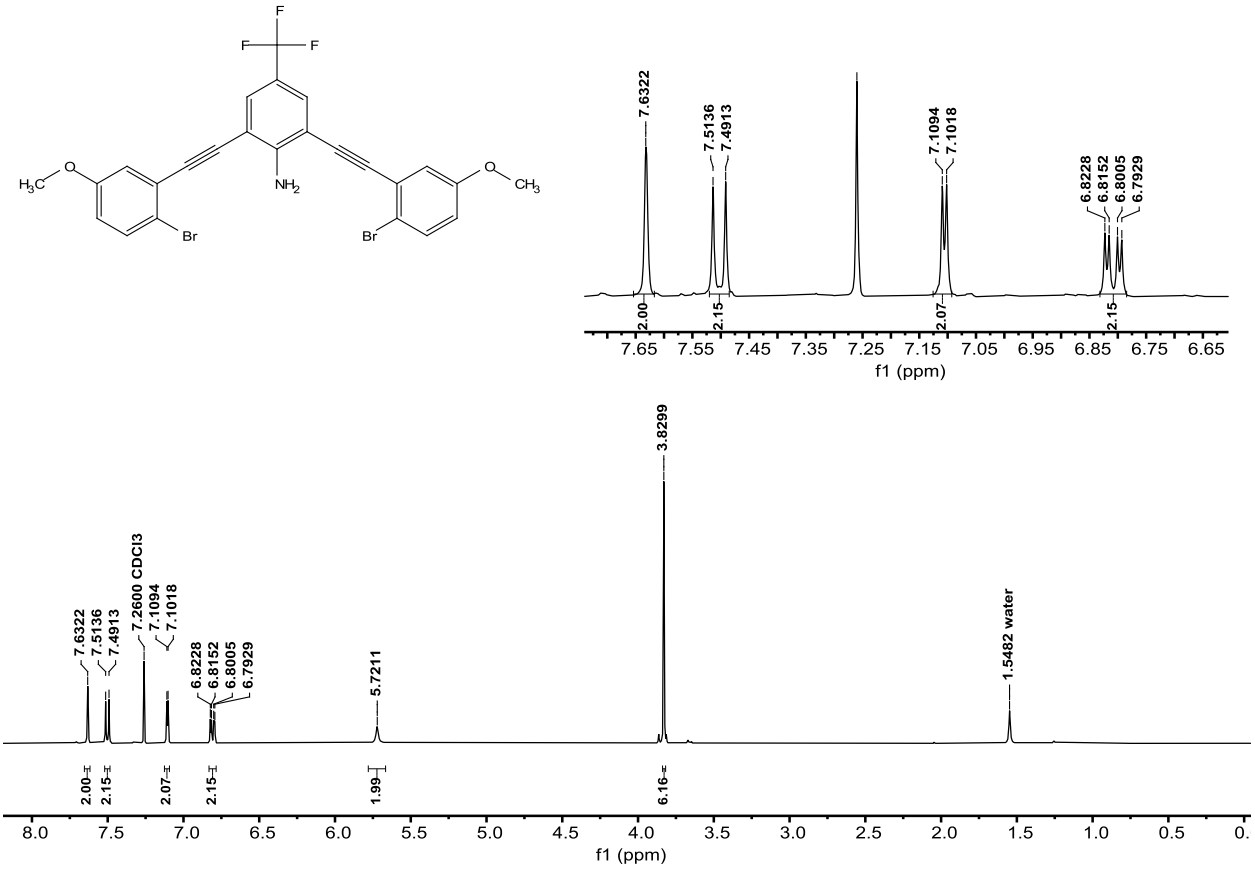

Figure S107. ^{1}H NMR of **2MeO-G3XBBr** (400 MHz, $CDCl_3$).

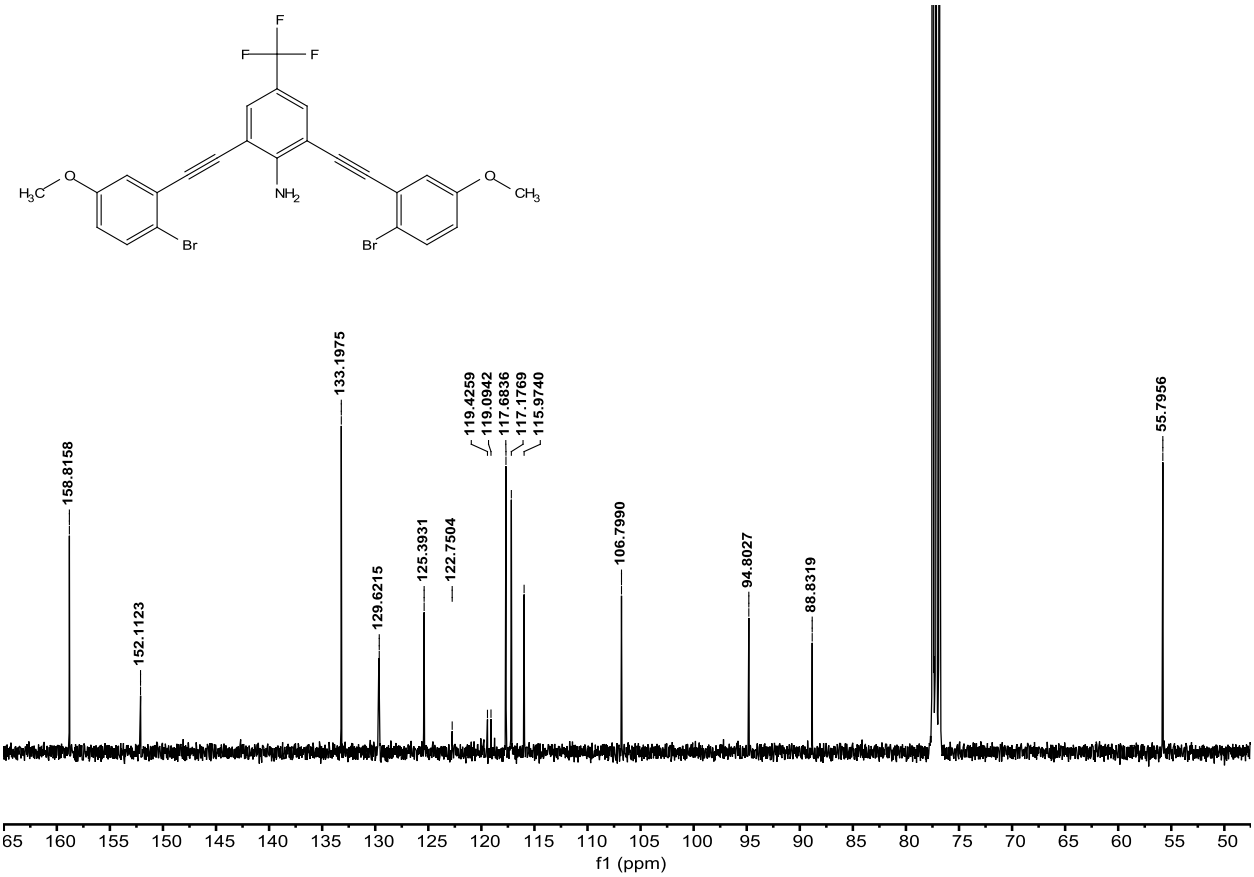

Figure S108. ^{13}C NMR of **2MeO-G3XBBr** (100 MHz, $CDCl_3$).

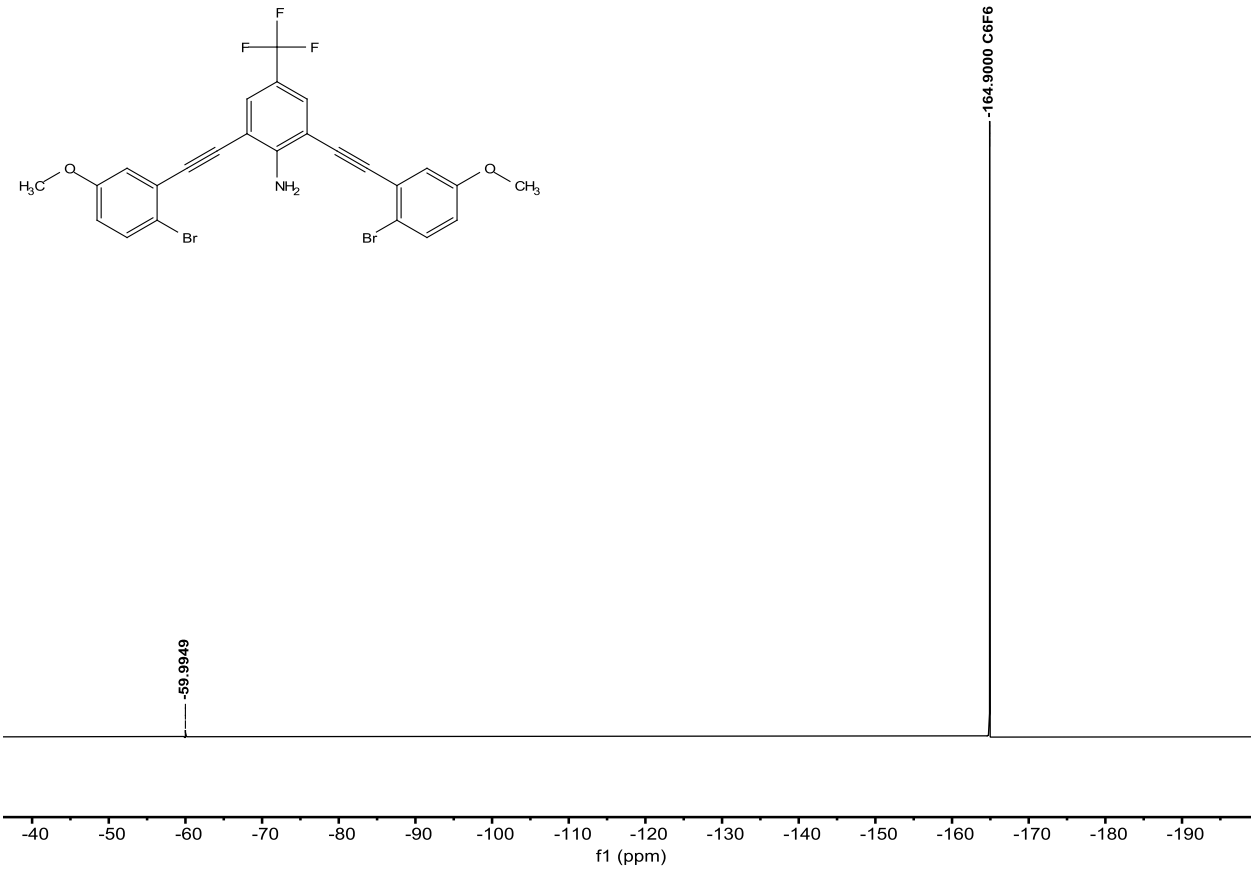

Figure S109. ^{19}F NMR of **2MeO-G3XBBr** (376 MHz, $CDCl_3$). Hexafluorobenzene (C_6F_6) internal reference.

2,6-bis(2-ethynyl-4-methoxy-iodophenyl)-4-(trifluoromethyl)aniline (2MeO-G3XB). 2MeO-G3XBBr (0.100 g, 0.173 mmol), copper iodide (0.0033 g, 0.017 mmol), sodium iodide (0.104 g, 0.692 mmol) were added to a 10-20 mL microwave reaction vial containing a stir bar and dissolved in 13 mL 1,4-dioxane. To the vibrant yellow reaction mixture, trans-N,N'-dimethylcyclohexane-1,2-diamine (0.1 mL) was added. The microwave vial was sealed and placed in a Biotage Initiator+ microwave reactor for 12 hours at 150 ˚C. After cooling, the reaction was run through pipet silica plug with EtOAc to remove catalysts and salts. The EtOAc crude was then ran through GCMS in order to obtain % conversion of bromines to iodines. If the conversion from bromine to iodine was 99% or greater, then the reaction was concentrated. The beige/yellow product (0.98 g, 84.4%) was obtained after purified via high performance liquid chromatography (reverse phase column gradient from 80% water/20% acetonitrile to 100% acetonitrile).

^{1}H NMR (400 MHz, $CDCl_3$): δ (ppm) = 7.72 (d, J = 8.9 Hz, 2H), 7.64 (s, 2H), 7.12 (d, J = 3.0 Hz, 2H), 6.68 (dd, J = 8.8 Hz, 2H), 5.81 (s, 2H), 3.83 (s, 6H).

^{13}C NMR (100 MHz, $CDCl_3$): δ (ppm) = 159.76, 152.19, 139.38, 129.96, 129.78 (q, J = 3.6 Hz), 124.10 (q, J = 269.4 Hz), 119.46 (q, J = 33.4 Hz), 117.71, 117.54, 106.80, 97.86, 89.40, 88.03, 55.69.

^{19}F NMR (376 MHz, $CDCl_3$): δ (ppm) = –59.98.

HRMS (ESI neg) m/z for $C_{25}H_{15}F_3I_2NO_2^-$ $[M-H^+]^-$: calculated: 671.9150; found: 671.9150.

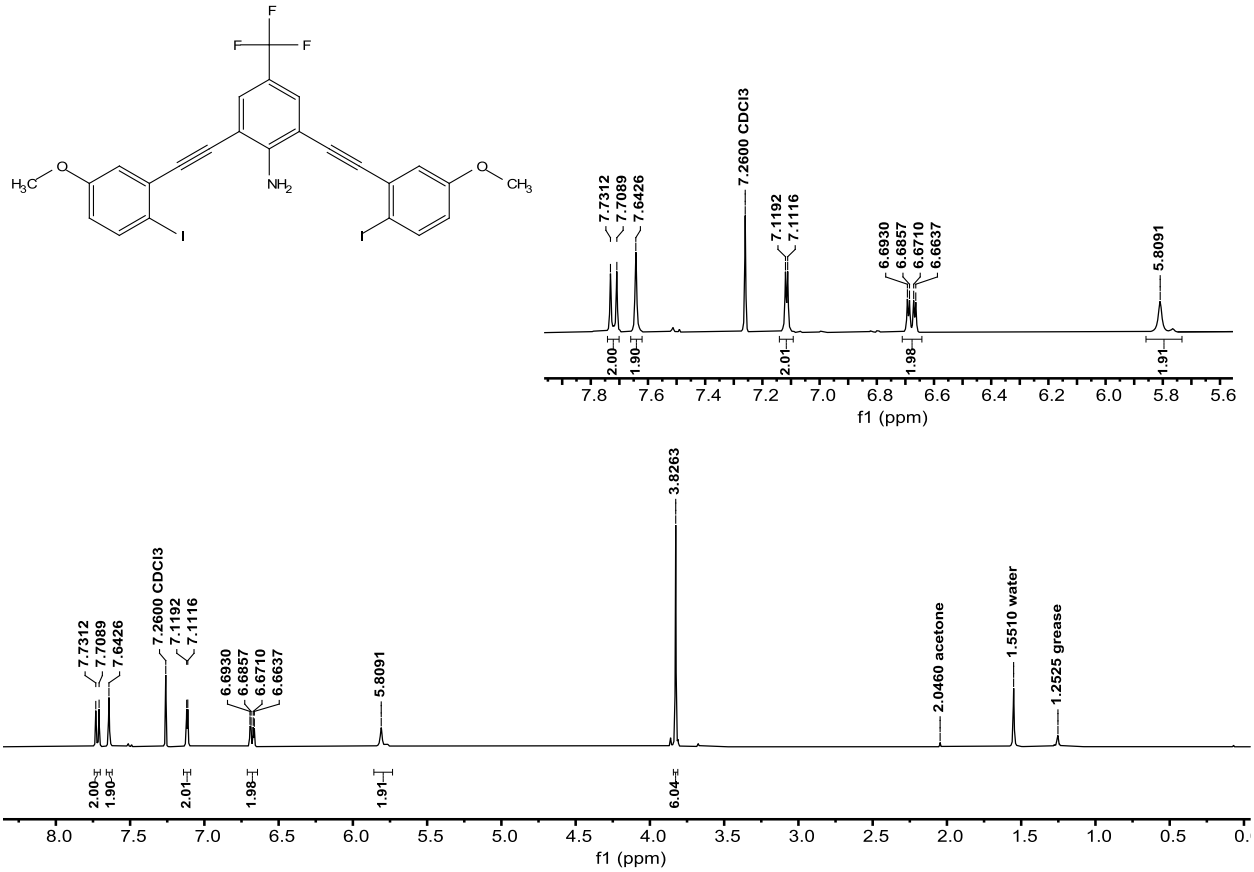

Figure S110. ^{1}H NMR of **2MeO-G3XB** (400 MHz, $CDCl_3$).

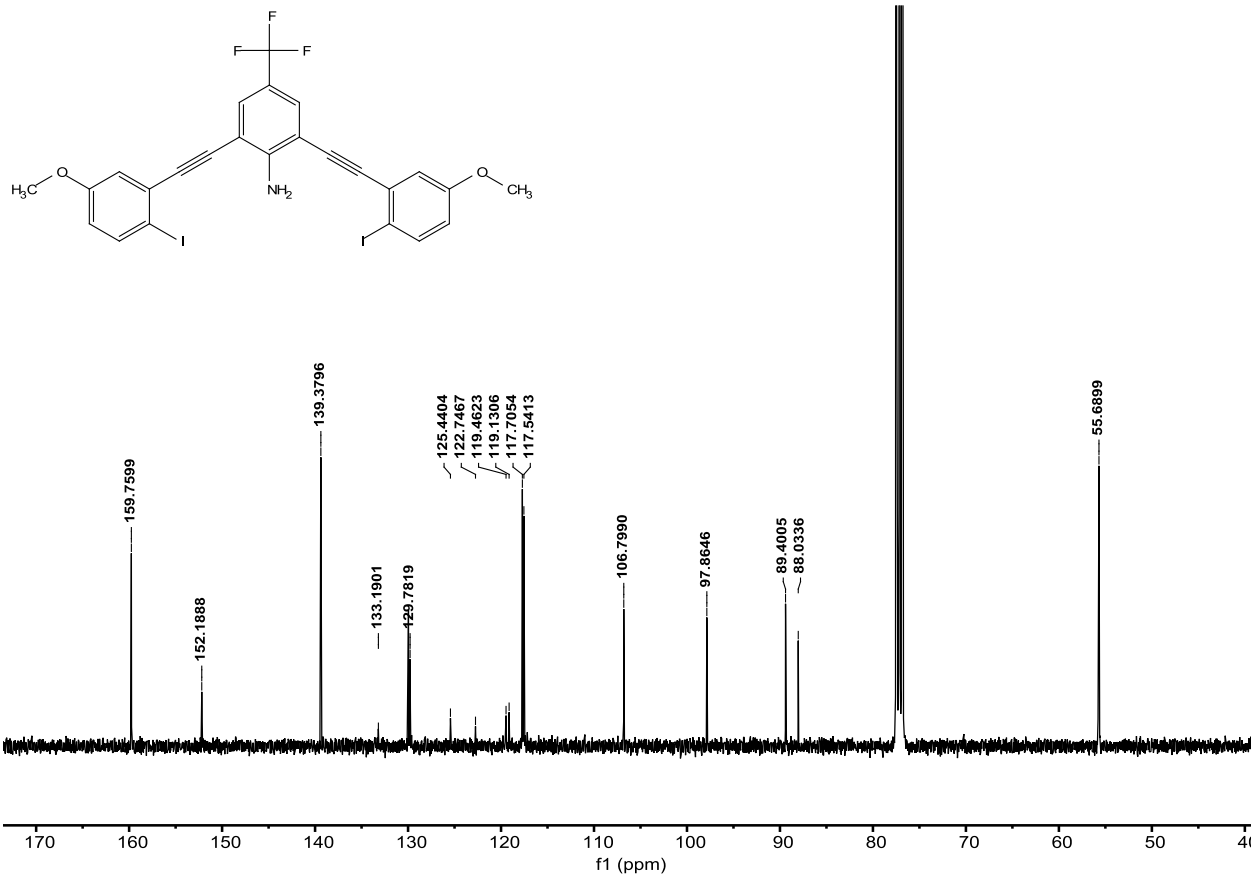

Figure S111. ^{13}C NMR of **2MeO-G3XB** (100 MHz, $CDCl_3$).

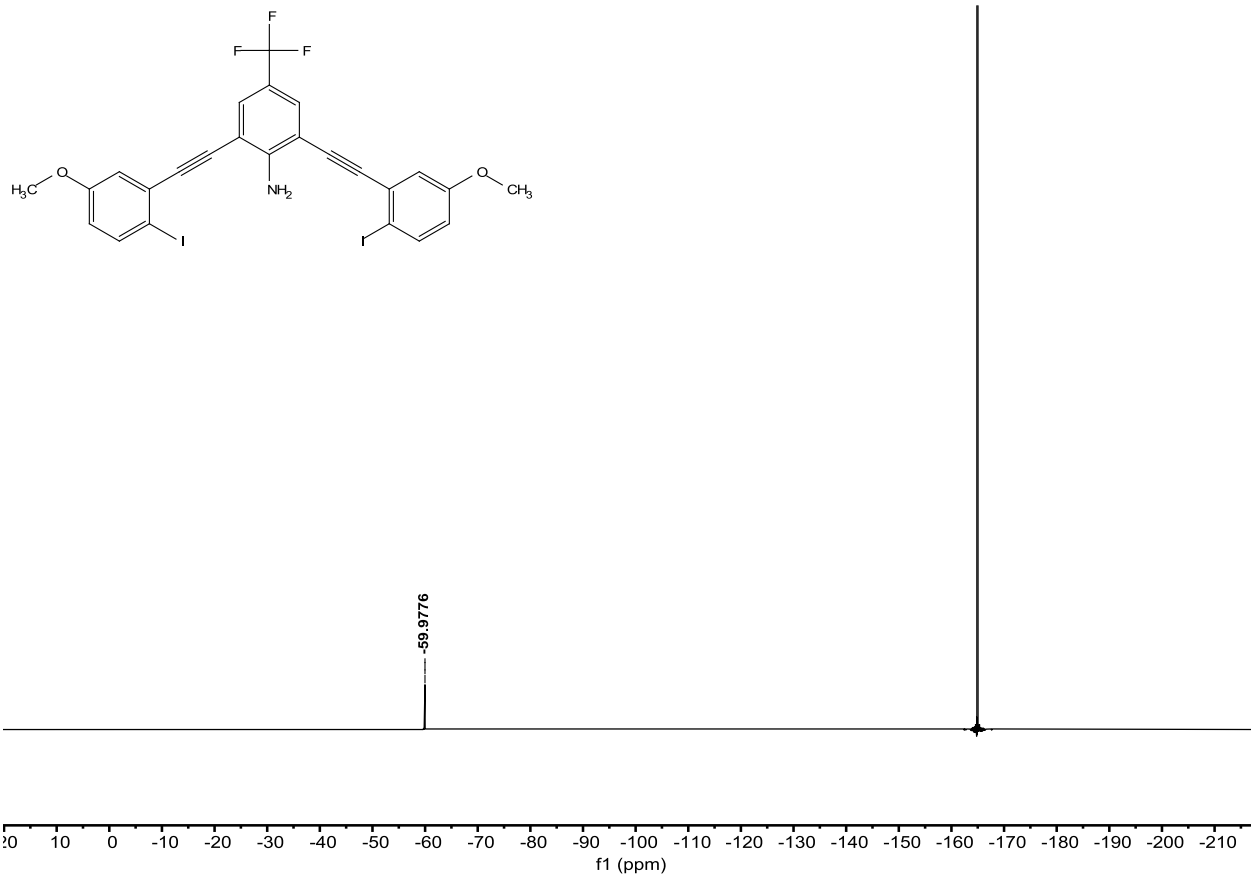

Figure S112. ^{19}F NMR of **2MeO-G3XB** (376 MHz, $CDCl_3$). Hexafluorobenzene (C_6F_6) internal reference.

2,6-bis(2-ethynyl-4-(trifluoromethyl)bromophenyl)-4-chloroaniline (Cl-G3XBBr). To an oven dried Schlenk flask was charged with 2,6-bisethynyl-4-chloroaniline **(2b)** (0.43g 2.45mmol), then vacuumed and backfilled with dry N2 gas (3x). Bis(triphenylphosphine)palladium (II) dichloride (0.086 g, 0. 125 mmol) was added, vacuumed and backfilled with dry N2 gas (3x). Copper (I) iodide (0.047 g, 0.245 mmol) was added, vacuumed and backfilled with dry N2 (3x). The dry reagents were dissolved in 100 mL dry DMF. 1-Bromo-2-iodo-4-(trifluoromethyl)benzene (0.98 mL, 6.1 mmol) and N,N-diisopropylethylamine (2.11 mL, 12.25 mmol) were added to the DMF solution. The flask was carefully vacuumed and backfilled with dry N2 (3x). The dark brown solution stirred overnight at room temperature. The reaction mixture was extracted with ethyl acetate then washed with water to remove any excess salts and catalysts, then was dried over magnesium sulfate and gravity filtered. Subsequent removal of DMF, hexanes and ethyl acetate by rotary evaporation left and brown solid that was purified by column chromatography (gradient from 100% Hexanes to 10% EtOAc/90% Hexanes) to afford **Cl-G3XBBr** (1.18 g, 78%) as a dull yellow solid.

^{1}H NMR (400 MHz, $CDCl_3$): δ (ppm) = 7.82 (s, 2H), 7.78 (d, J = 8.2 Hz, 2H), 7.46 (d, J = 8.5 Hz, 2H), 7.41 (s, 2H), 5.32 (s, 2H).

^{13}C NMR (100 MHz, $CDCl_3$): δ (ppm) = 148.91, 133.24, 132.87, 130.50 (q, J = 33.2 Hz), 129.93 (q, J = 3.7 Hz), 129.00, 126.22 (q, J = 3.7 Hz), 125.95, 123.95 (q, J = 270.0 Hz), 121.50, 107.82, 93.55, 90.75.

^{19}F NMR (376 MHz, $CDCl_3$): δ (ppm) = –61.31.

HRMS (ESI neg) m/z for $C_{24}H_9F_6Br_2ClN^-$ $[M-H^+]^-$: calculated: 619.8680; found: 619.8680.

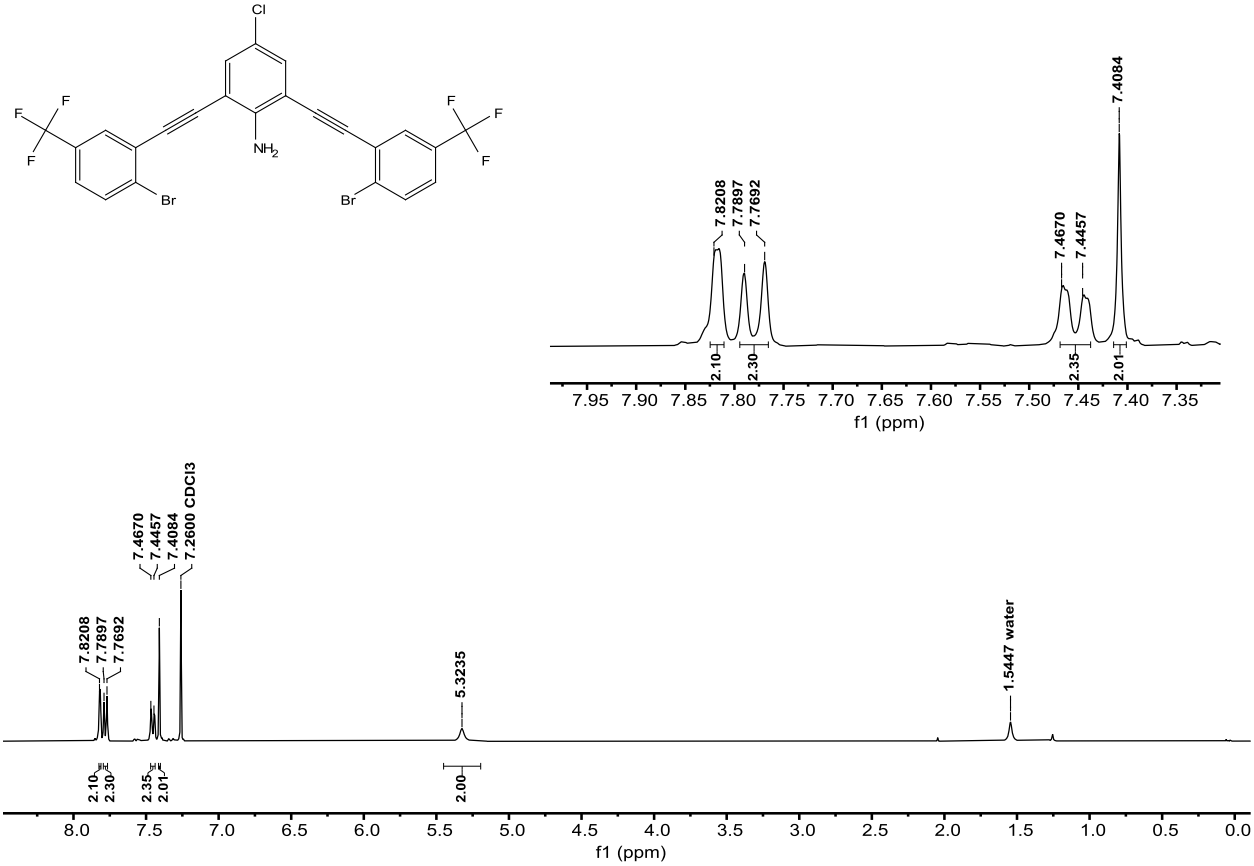

Figure S113. ^{1}H NMR of **Cl-G3XBBr** (400 MHz, $CDCl_3$).

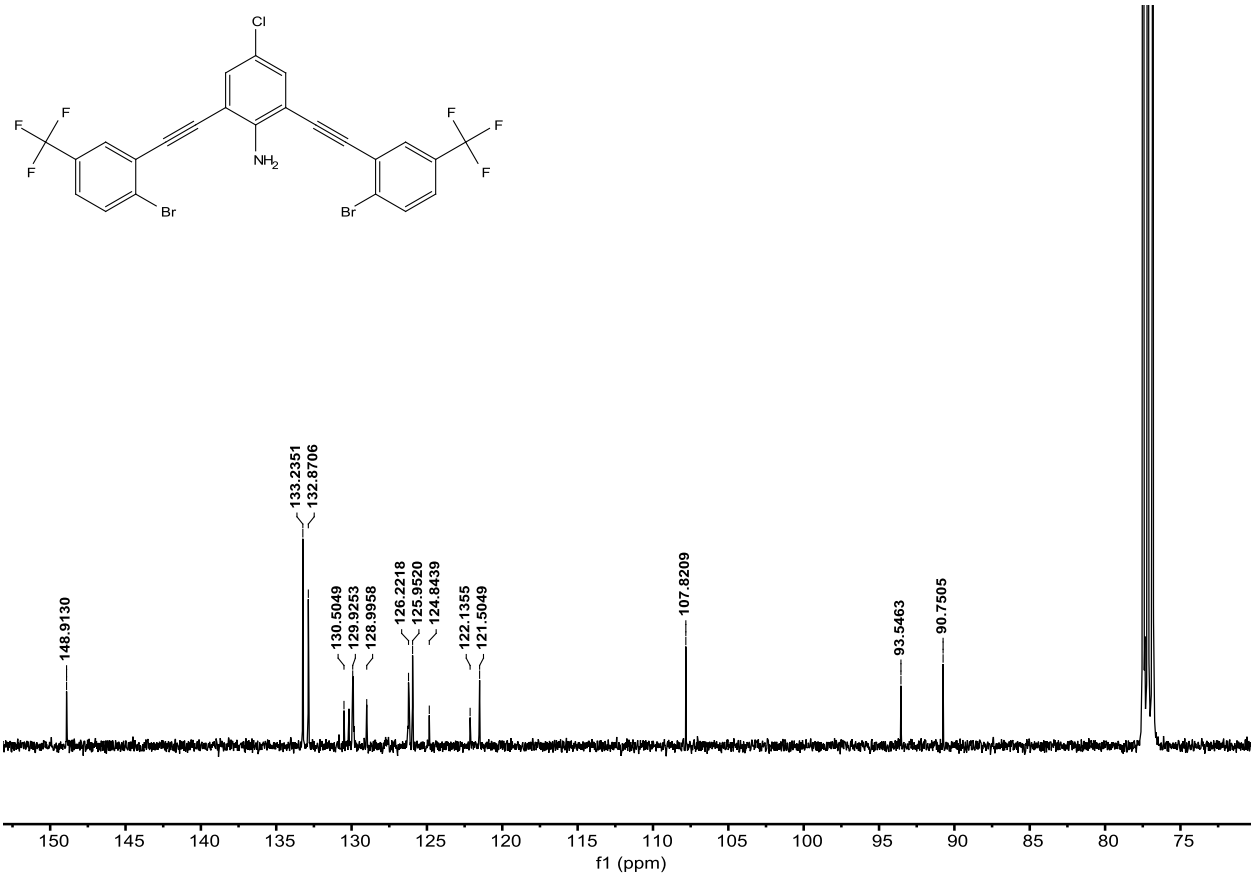

Figure S114. ^{13}C NMR of **Cl-G3XBBr** (100 MHz, $CDCl_3$).

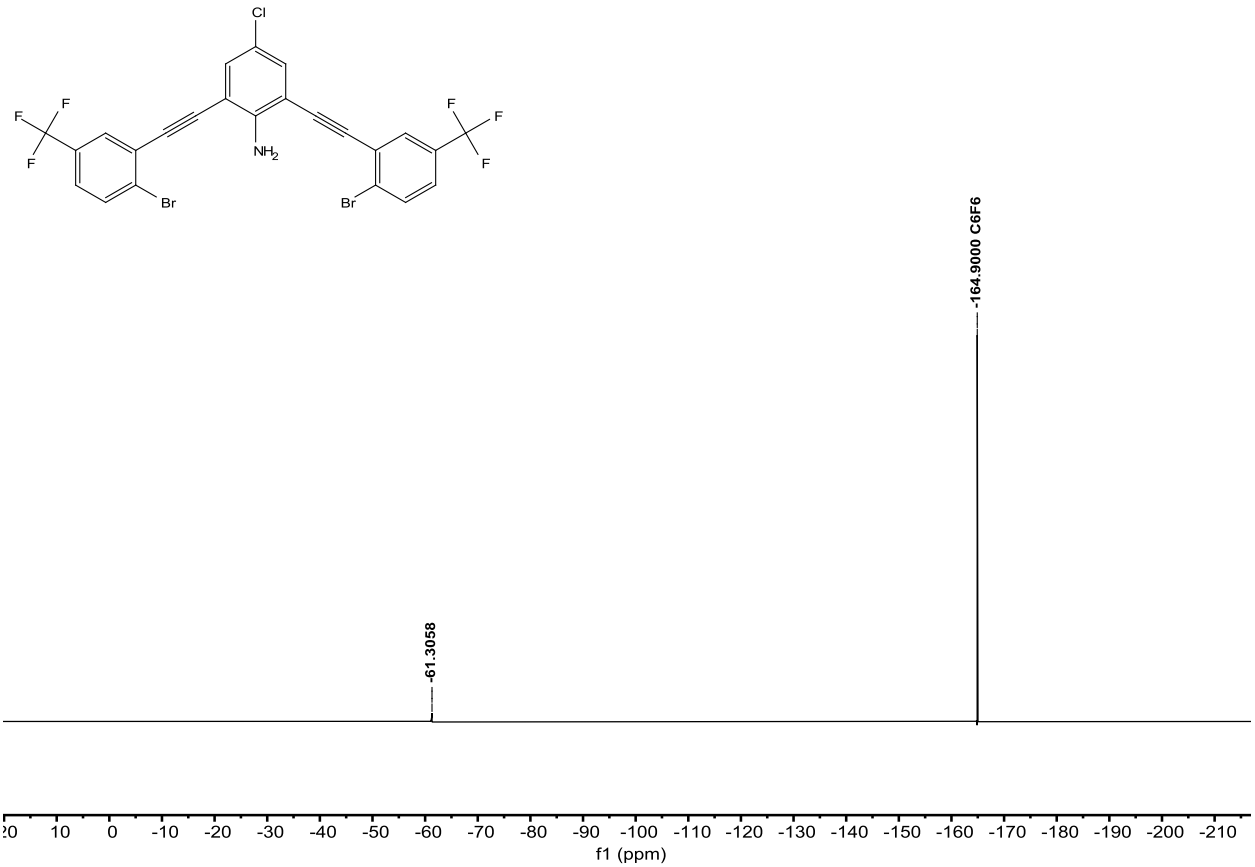

Figure S115. ^{19}F NMR of **Cl-G3XBBr** (376 MHz, $CDCl_3$). Hexafluorobenzene (C_6F_6) internal reference.

2,6-bis(2-ethynyl-4-(trifluoromethyl)iodophenyl)-4-chloroaniline (Cl-G3XB). Cl-G3XBBr (0.200 g, 0.323 mmol), copper iodide (0.006 g, 0.030 mmol), sodium iodide (0.193 g, 1.29 mmol) were added to a 10-20 mL microwave reaction vial containing a stir bar and dissolved in 13 mL 1,4-dioxane. To the vibrant yellow reaction mixture, trans-N,N'-dimethylcyclohexane-1,2-diamine (0.15 mL) was added. The microwave vial was sealed and placed in a Biotage Initiator+ microwave reactor for 12.5 hours at 150 ˚C. After cooling, the reaction was run through pipet silica plug with EtOAc to remove catalysts and salts. The EtOAc crude was then ran through GCMS in order to obtain % conversion of bromines to iodines. If the conversion from bromine to iodine was 99% or greater, then the reaction was concentrated. The beige/yellow product (0.076 g, 33%) was obtained after purified via high performance liquid chromatography (reverse phase column gradient from 80% water/20% acetonitrile to 100% acetonitrile).

^{1}H NMR (400 MHz, $CDCl_3$): δ (ppm) = 8.03 (d, J = 8.2 Hz, 2H), 7.77 (s, 2H), 7.42 (s, 2H), 7.28 (d, J = 9.2 Hz, 2H), 5.39 (s, 2H).

^{13}C NMR (100 MHz, $CDCl_3$): δ (ppm) = 148.96, 139.53, 132.97, 131.29 (q, J = 42.7 Hz), 130.46, 129.17 (q, J = 5.9 Hz), 126.01 (q, J = 3.5 Hz), 123.62 (q, J = 270.8 Hz), 121.53, 107.84, 104.83, 96.84, 89.91.

^{19}F NMR (376 MHz, $CDCl_3$): δ (ppm) = –61.52.

HRMS (ESI neg) m/z for $C_{24}H_9F_6I_2ClN^-$ [M-H$^+$]$^-$: calculated: 713.8423; found: 713.8422.

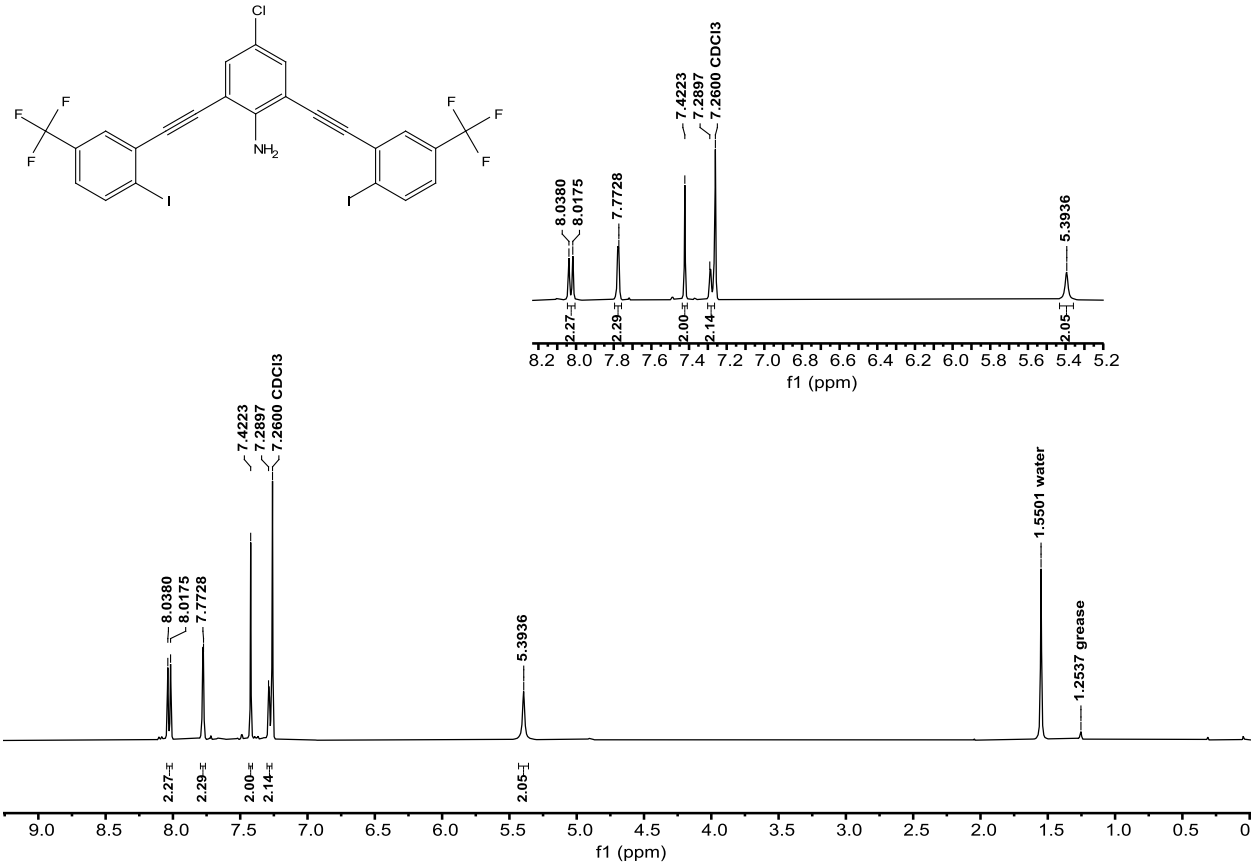

Figure S116. ^{1}H NMR of **Cl-G3XB** (400 MHz, $CDCl_3$).

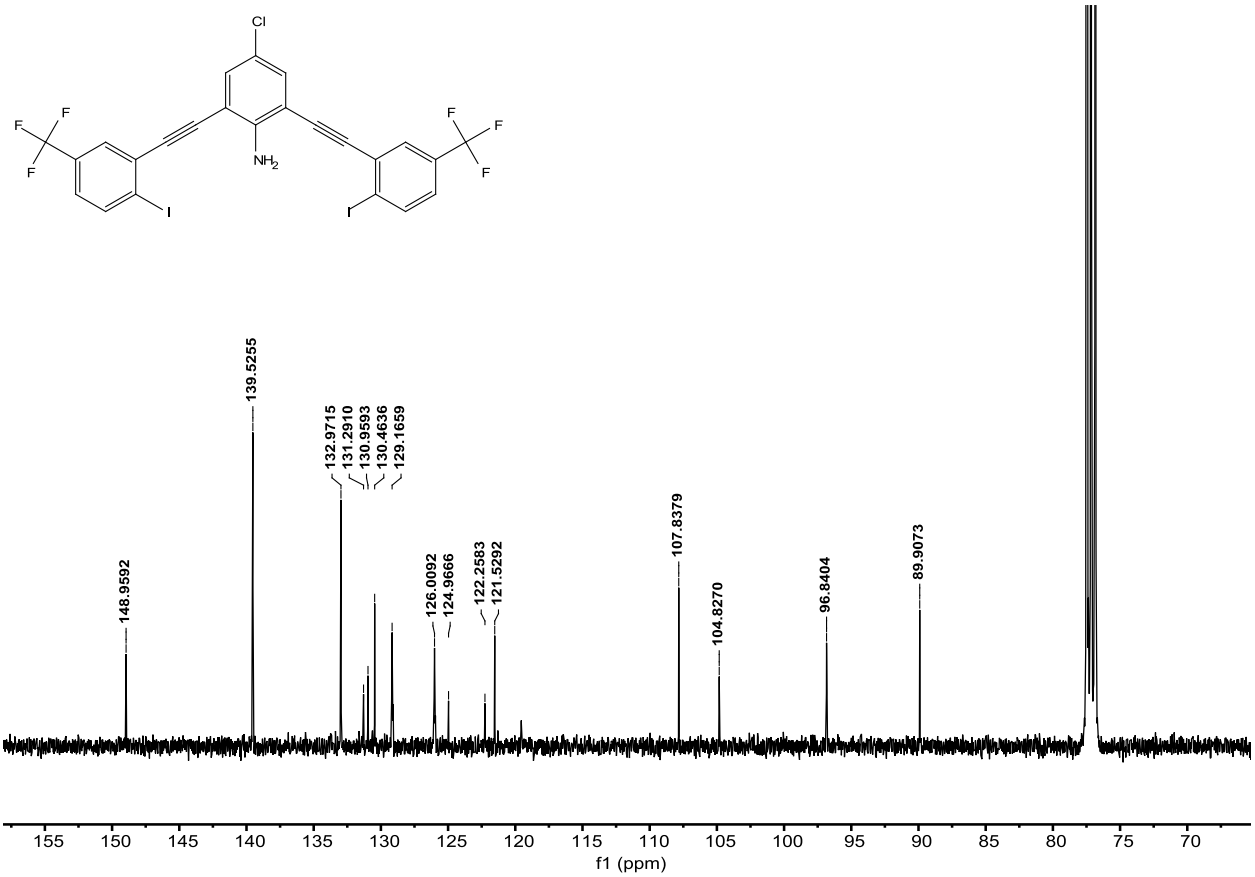

Figure S117. ^{13}C NMR of **Cl-G3XB** (100 MHz, $CDCl_3$).

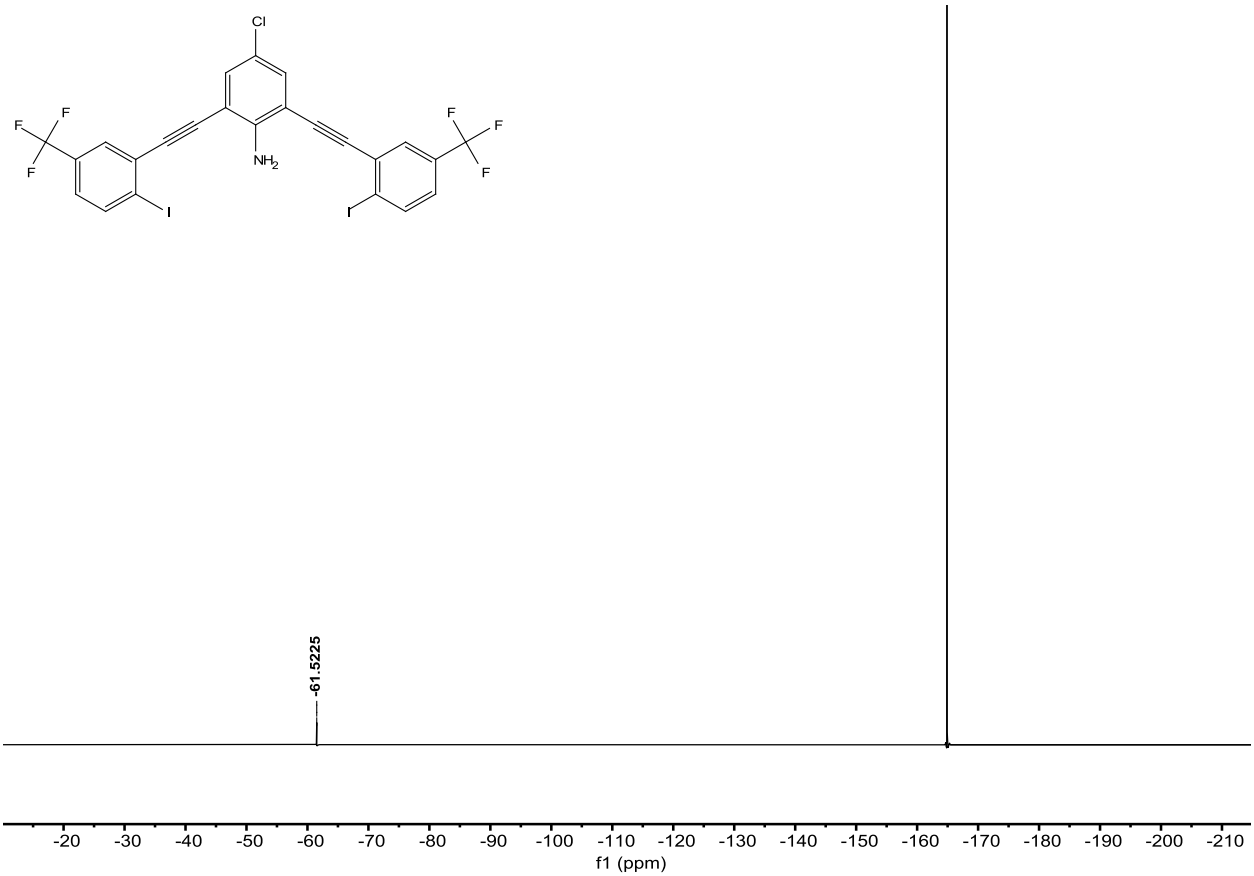

Figure S118. ^{19}F NMR of **Cl-G3XB** (376 MHz, $CDCl_3$). Hexafluorobenzene (C_6F_6) internal reference.

2,6-bis(2-ethynyl-4-(trifluoromethyl)bromophenyl)-4-fluoroaniline (F-G3XBBr). To an oven dried Schlenk flask was charged with 2,6-bisethynyl-4-fluoroaniline **(2c)** (0.159g 1mmol), then vacuumed and backfilled with dry N2 gas (3x). Bis(triphenylphosphine)palladium (II) dichloride (0.035 g, 0. 05 mmol) was added, vacuumed and backfilled with dry N2 gas (3x). Copper (I) iodide (0.019 g, 0.1 mmol) was added, vacuumed and backfilled with dry N2 (3x). The dry reagents were dissolved in 60 mL dry DMF. 1-Bromo-2-iodo-4-(trifluoromethyl)benzene (0.4 mL, 2.5 mmol) and N,N-diisopropylethylamine (0.86 mL, 5 mmol) were added to the DMF solution. The flask was carefully vacuumed and backfilled with dry N2 (3x). The dark brown solution stirred overnight at room temperature. The reaction mixture was extracted with ethyl acetate then washed with water to remove any excess salts and catalysts, then was dried over magnesium sulfate and gravity filtered. Subsequent removal of DMF, hexanes and ethyl acetate by rotary evaporation left and brown solid that was purified by column chromatography (gradient from 100% Hexanes to 3% EtOAc/97% Hexanes) to afford **F-G3XBBr** (0.28 g, 53%) as a dull yellow solid.

^{1}H NMR (400 MHz, $CDCl_3$): δ (ppm) = 7.82 (s, 2H), 7.78 (d, J = 8.4 Hz, 2H), 7.45 (d, J = 8.4 Hz, 2H), 7.18 (d, J = 8.4 Hz, 2H), 5.16 (s, 2H).

^{13}C NMR (100 MHz, $CDCl_3$): δ (ppm) = 153.95 (d, J = 235.2 Hz), 147.23, 133.23, 130.48 (q, J = 33.2 Hz), 129.95 (q, J = 4.0 Hz), 129.00, 126.21 (q, J = 3.6 Hz), 125.96, 123.50 (q, J = 272.1 Hz), 120.18 (d, J = 24.0 Hz), 107.23 (d, J = 9.8 Hz), 93.33, 91.08 (d, J = 3.4 Hz).
^{19}F NMR (376 MHz, $CDCl_3$): δ (ppm) = –61.31, -125.31.
HRMS (ESI neg) m/z for $C_{24}H_9F_7Br_2N^-$ [M-H$^+$]$^-$: calculated: 603.8975; found: 603.8976.

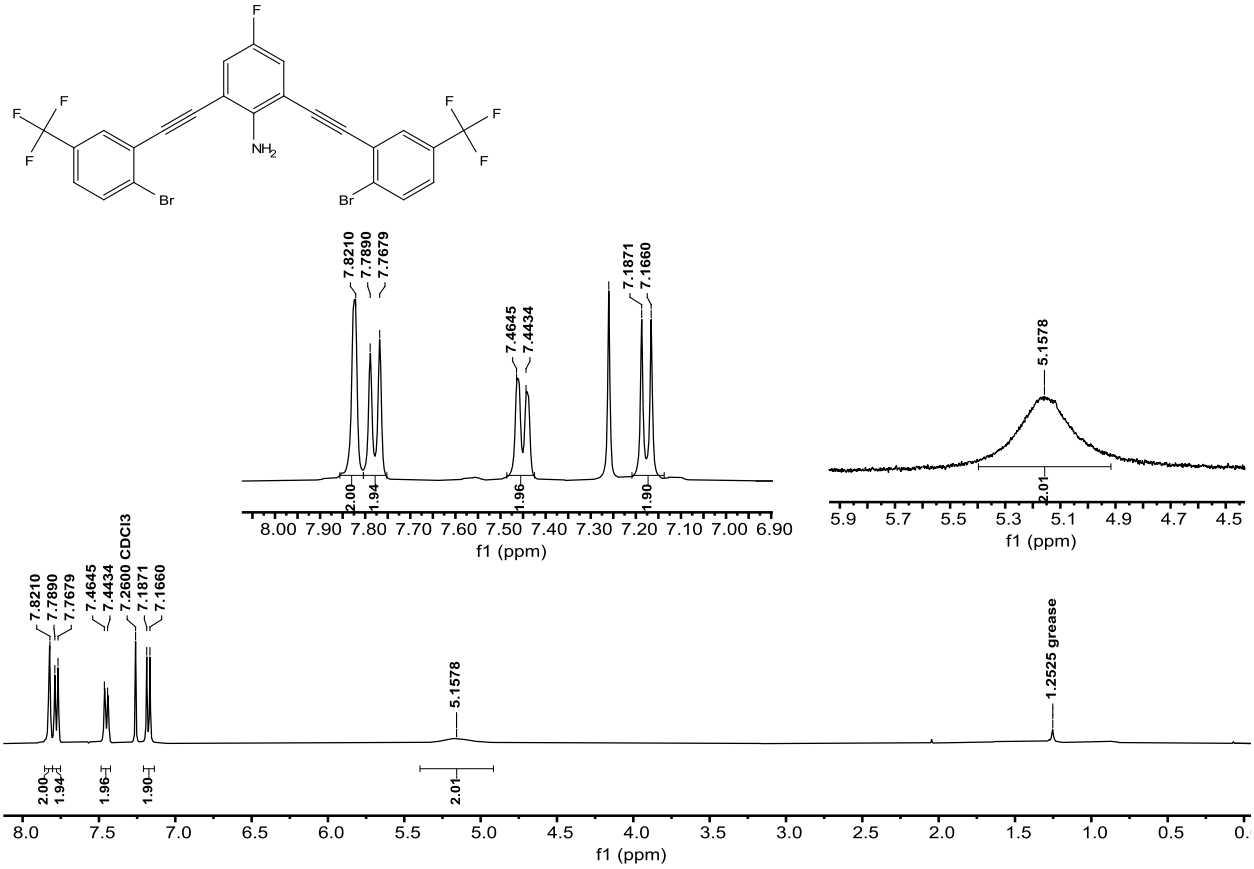

Figure S119. ^{1}H NMR of **F-G3XBBr** (400 MHz, $CDCl_3$).

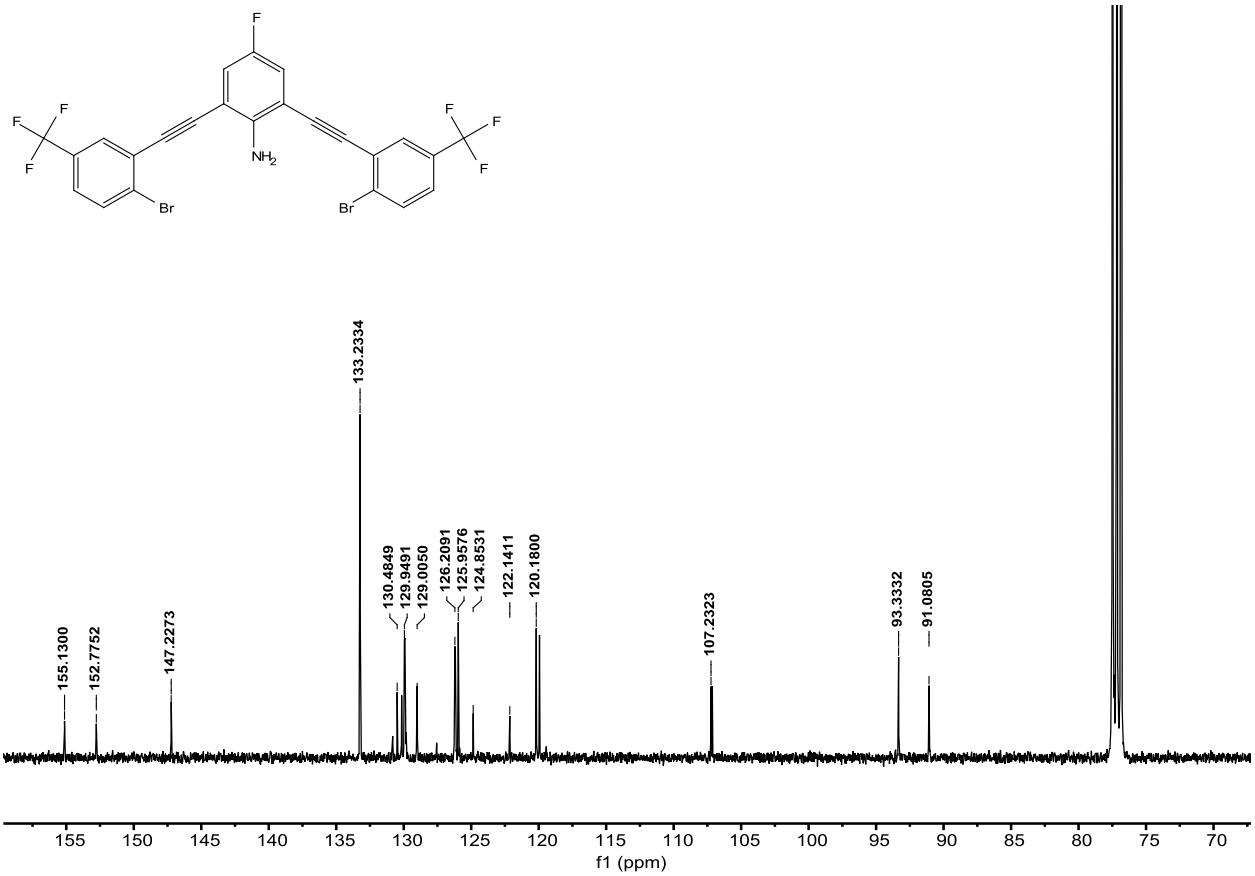

Figure S120. ^{13}C NMR of **F-G3XBBr** (100 MHz, $CDCl_3$).

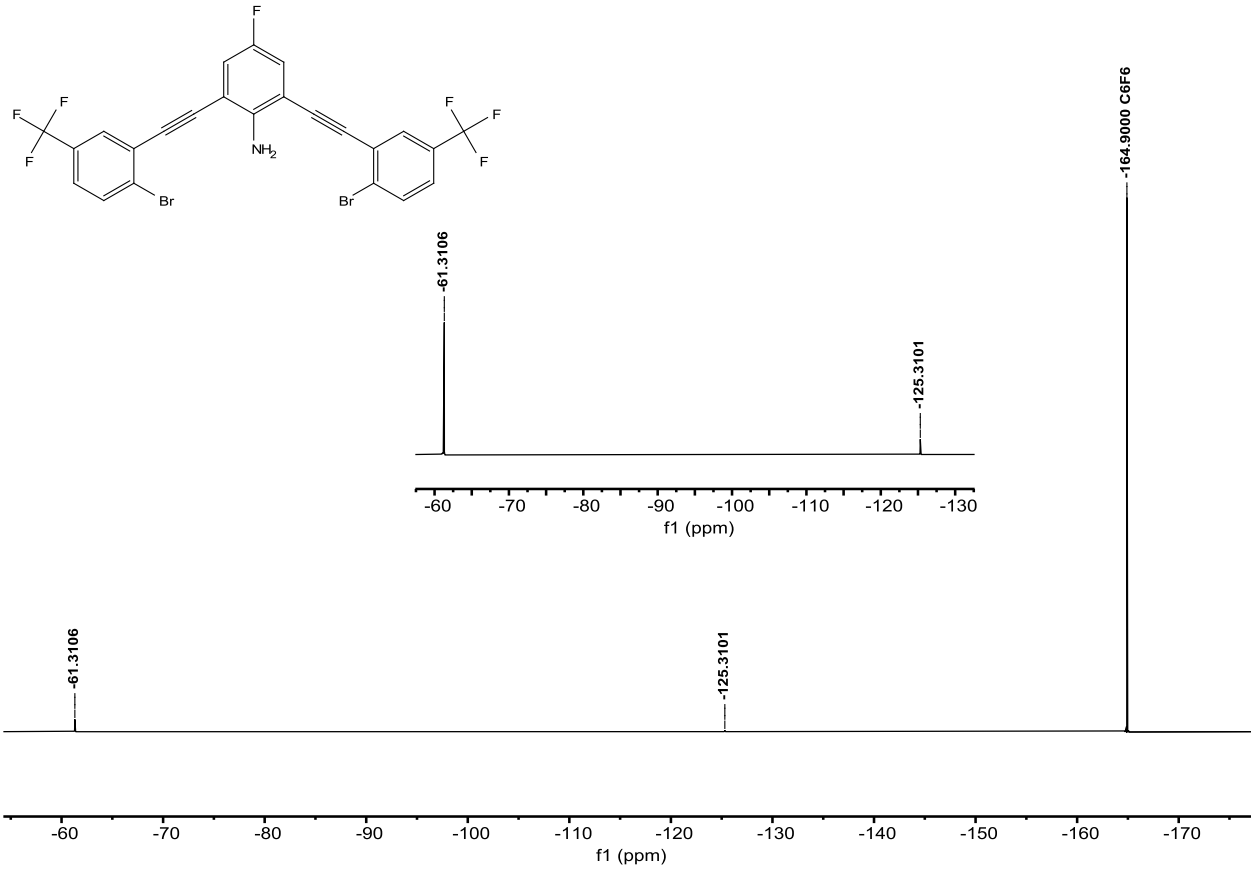

Figure S121. ^{19}F NMR of **F-G3XBBr** (376 MHz, $CDCl_3$). Hexafluorobenzene (C_6F_6) internal reference.

2,6-bis(2-ethynyl-4-(trifluoromethyl)iodophenyl)-4-fluoroaniline (F-G3XB). F-G3XBBr (0.100 g, 0.165 mmol), copper iodide (0.003 g, 0.016 mmol), sodium iodide (0.102 g, 0.68 mmol) were added to a 10-20 mL microwave reaction vial containing a stir bar and dissolved in 13 mL 1,4-dioxane. To the vibrant yellow reaction mixture, trans-N,N'-dimethylcyclohexane-1,2-diamine (0.1 mL) was added. The microwave vial was sealed and placed in a Biotage Initiator+ microwave reactor for 13 hours at 150 ˚C. After cooling, the reaction was run through pipet silica plug with EtOAc to remove catalysts and salts. The EtOAc crude was then ran through GCMS in order to obtain % conversion of bromines to iodines. If the conversion from bromine to iodine was 99% or greater, then the reaction was concentrated. The beige/yellow product (0.099 g, 86%) was obtained after purified via high performance liquid chromatography (reverse phase column gradient from 80% water/20% acetonitrile to 100% acetonitrile).

^{1}H NMR (400 MHz, $CDCl_3$): δ (ppm) = 8.03 (d, J = 8.2 Hz, 2H), 7.79 (s, 2H), 7.28 (d, J = 8.0 Hz, 2H), 7.20 (d, J = 6.4 Hz, 2H), 5.25 (s, 2H).

^{13}C NMR (100 MHz, $CDCl_3$): δ (ppm) = 153.99 (d, J = 235.1 Hz), 147.26, 139.54, 131.28 (q, J = 33.3 Hz), 130.47, 129.20 (q, J = 3.8 Hz), 126.01 (q, J = 3.7 Hz), 123.62 (q, J = 270.0 Hz), 120.29 (d, J = 23.3 Hz), 107.27 (d, J = 11.9 Hz), 104.83, 96.62, 90.23 (d, J = 3.3 Hz).

^{19}F NMR (376 MHz, $CDCl_3$): δ (ppm) = –61.51, -125.30.

HRMS (ESI neg) m/z for $C_{24}H_9F_7I_2N^-$ [M-H$^+$]$^-$: calculated: 697.8718; found: 697.8718.

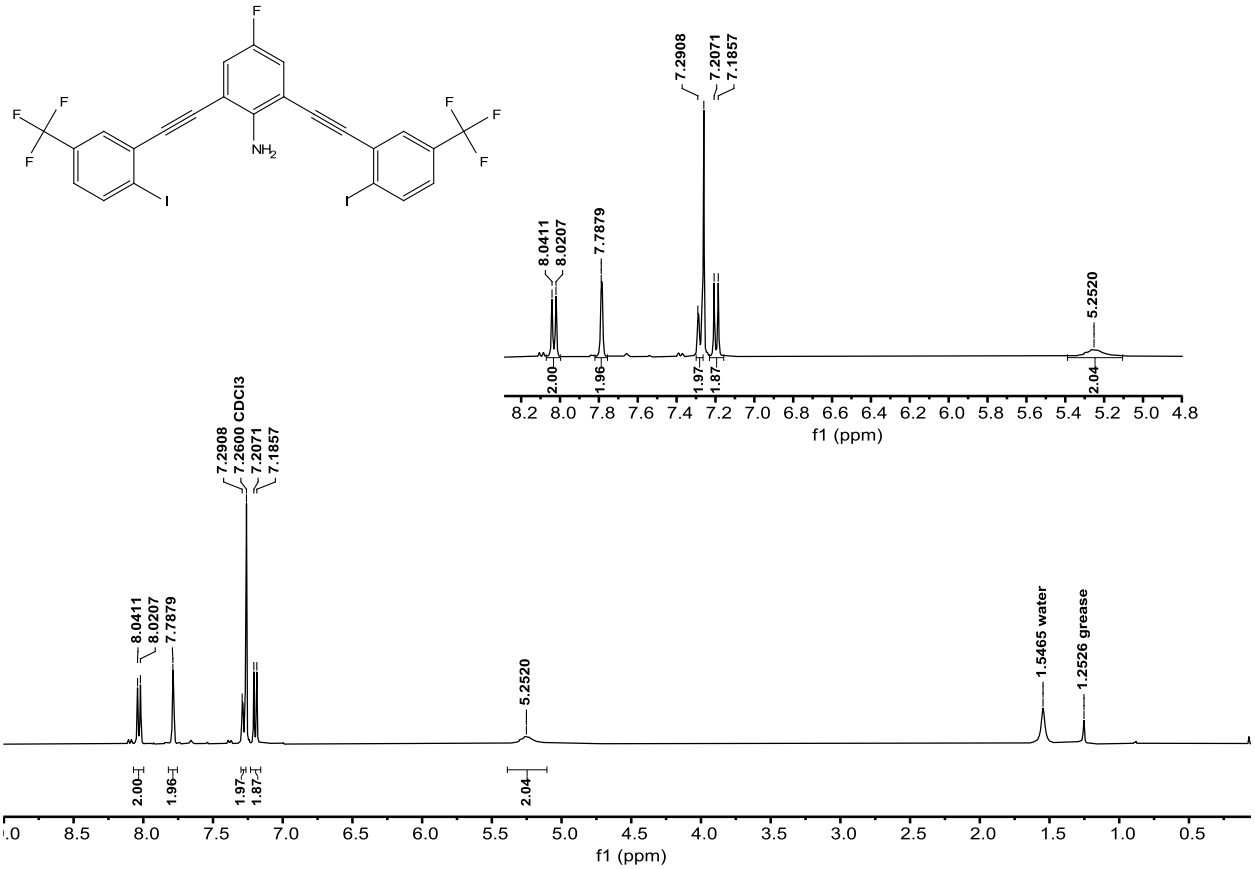

Figure S122. ^{1}H NMR of **F-G3XB** (400 MHz, $CDCl_3$).

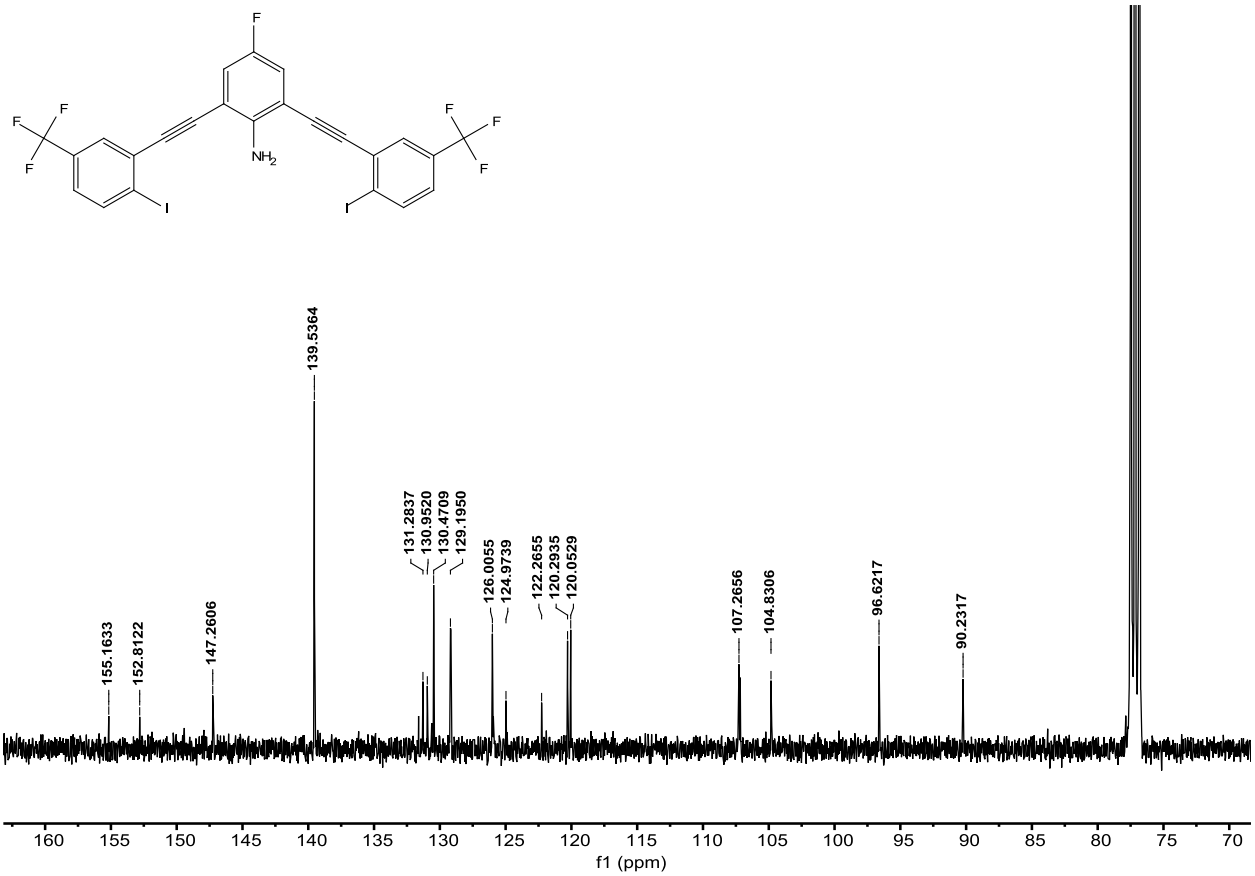

Figure S123. ^{13}C NMR of **F-G3XB** (100 MHz, $CDCl_3$).

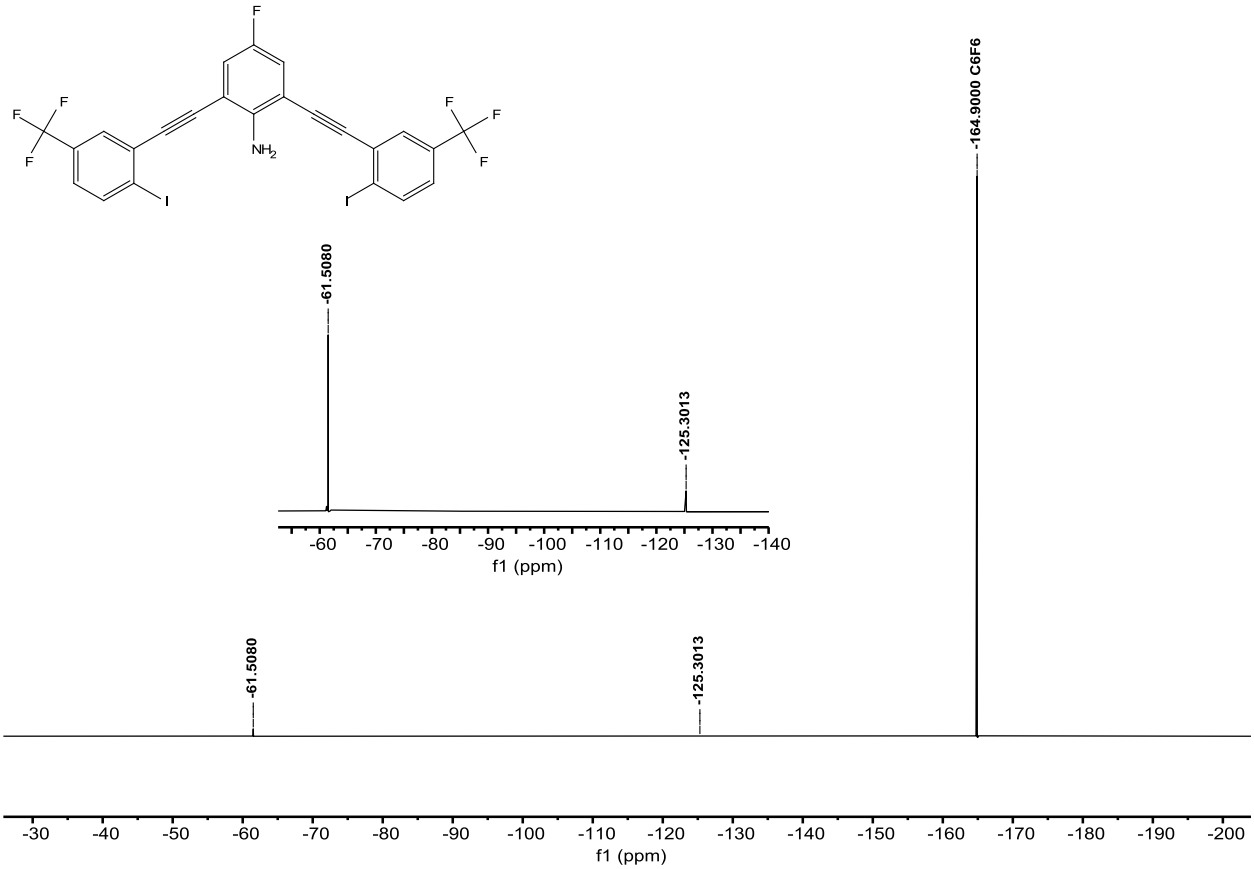

Figure S124. ^{19}F NMR of **F-G3XB** (376 MHz, $CDCl_3$). Hexafluorobenzene (C_6F_6) internal reference.

2,6-bis(2-ethynyl-4-(trifluoromethyl)bromophenyl)-aniline (H-G3XBBr). To an oven dried Schlenk flask was charged with 2,6-bisethynyl-aniline **(2d)** (0.305g 2.16 mmol), then vacuumed and backfilled with dry N2 gas (3x). Bis(triphenylphosphine)palladium (II) dichloride (0.077 g, 0. 11 mmol) was added, vacuumed and backfilled with dry N2 gas (3x). Copper (I) iodide (0.042 g, 0.22 mmol) was added, vacuumed and backfilled with dry N2 (3x). The dry reagents were dissolved in 60 mL dry DMF. 1-Bromo-2-iodo-4-(trifluoromethyl)benzene (0.86 mL, 5.4 mmol) and N,N-diisopropylethylamine (1.86 mL, 10.8 mmol) were added to the DMF solution. The flask was carefully vacuumed and backfilled with dry N2 (3x). The dark brown solution stirred for 48 hours at room temperature. The reaction mixture was extracted with ethyl acetate then washed with water to remove any excess salts and catalysts, then was dried over magnesium sulfate and gravity filtered. Subsequent removal of DMF, hexanes and ethyl acetate by rotary evaporation left and brown solid that was purified by column chromatography (gradient from 100% Hexanes to 3% EtOAc/97% Hexanes) to afford **H-G3XBBr** (0.773 g, 61%) as a dull yellow solid.

^{1}H NMR (400 MHz, $CDCl_3$): δ (ppm) = 7.83 (s, 2H), 7.78 (d, J = 8.3 Hz, 2H), 7.44 (d, J = 7.6 Hz, 2H), 7.44 (d, J = 7.2 Hz, 2H), 7.73 (t, J = 7.7 Hz, 1H), 5.30 (s, 2H).

^{13}C NMR (100 MHz, $CDCl_3$): δ (ppm) = 150.34, 134.68, 133.17, 130.43 (q, J = 33.2 Hz), 129.82 (q, J = 4.0 Hz), 128.91, 126.42, 125.84 (q, J = 3.6 Hz), 123.57 (q, J = 270.8 Hz), 117.41, 106.54, 92.78, 92.14.

^{19}F NMR (376 MHz, $CDCl_3$): δ (ppm) = –61.29.

HRMS (ESI neg) m/z for $C_{24}H_{10}F_6Br_2N^-$ [M-H^+]$^-$: calculated: 585.9069; found: 585.9069.

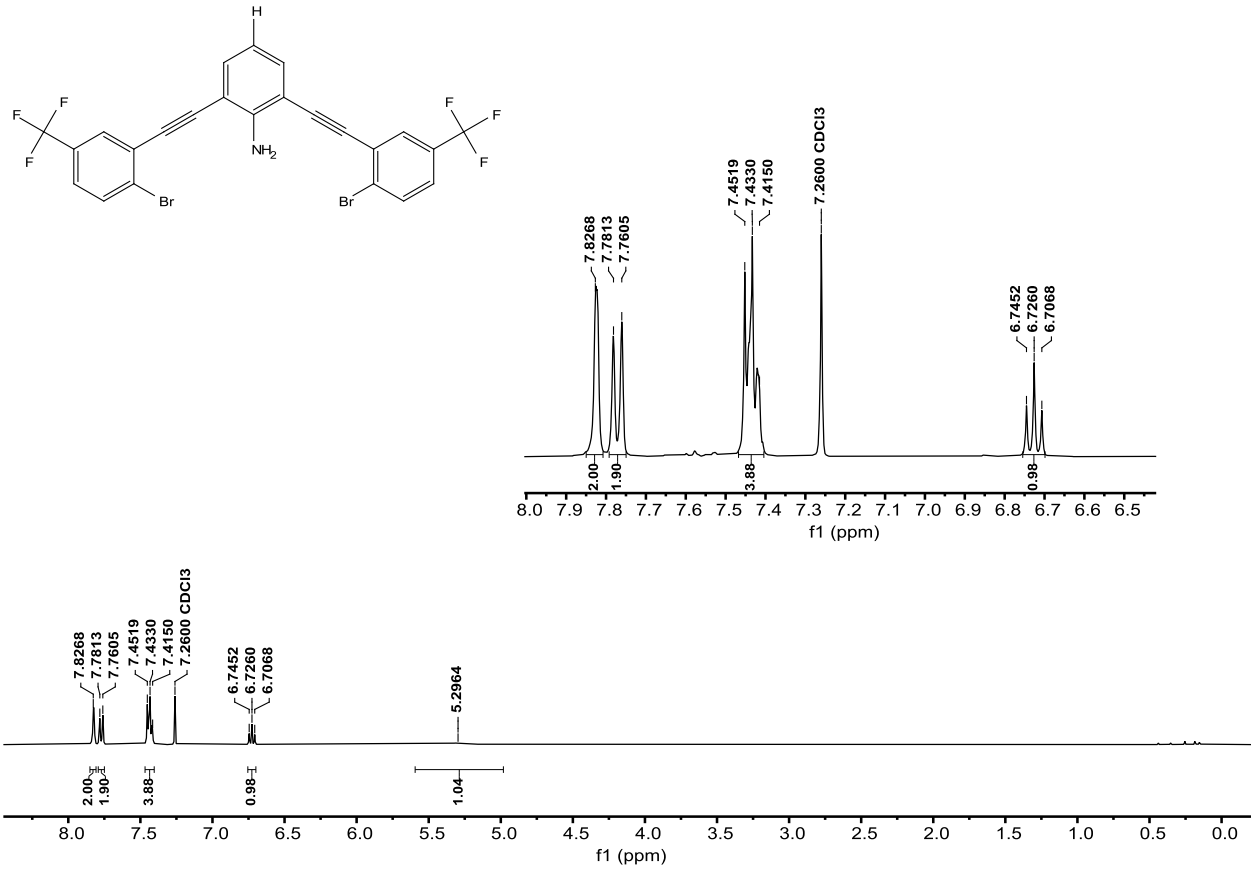

Figure S125. ^{1}H NMR of **H-G3XBBr** (400 MHz, $CDCl_3$).

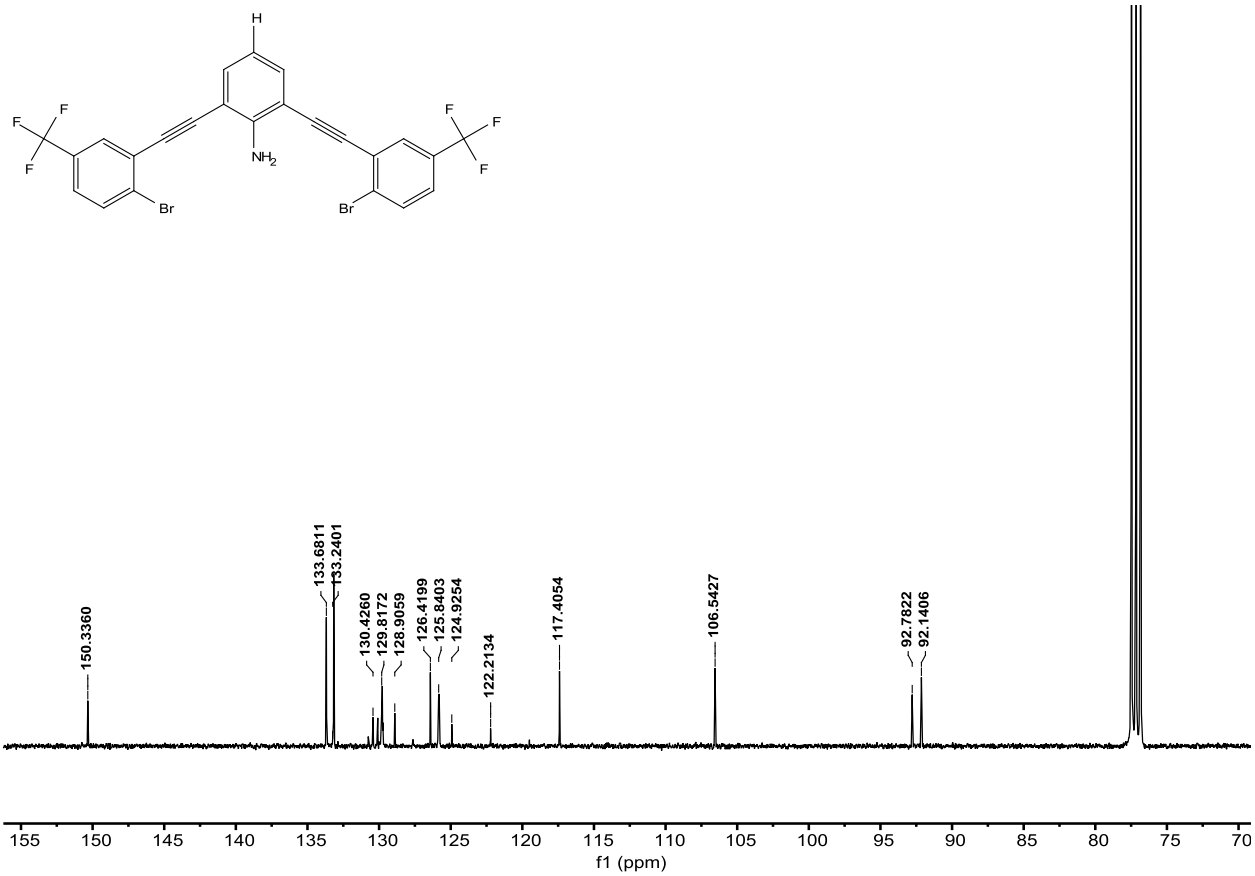

Figure S126. ^{13}C NMR of **H-G3XBBr** (100 MHz, $CDCl_3$).

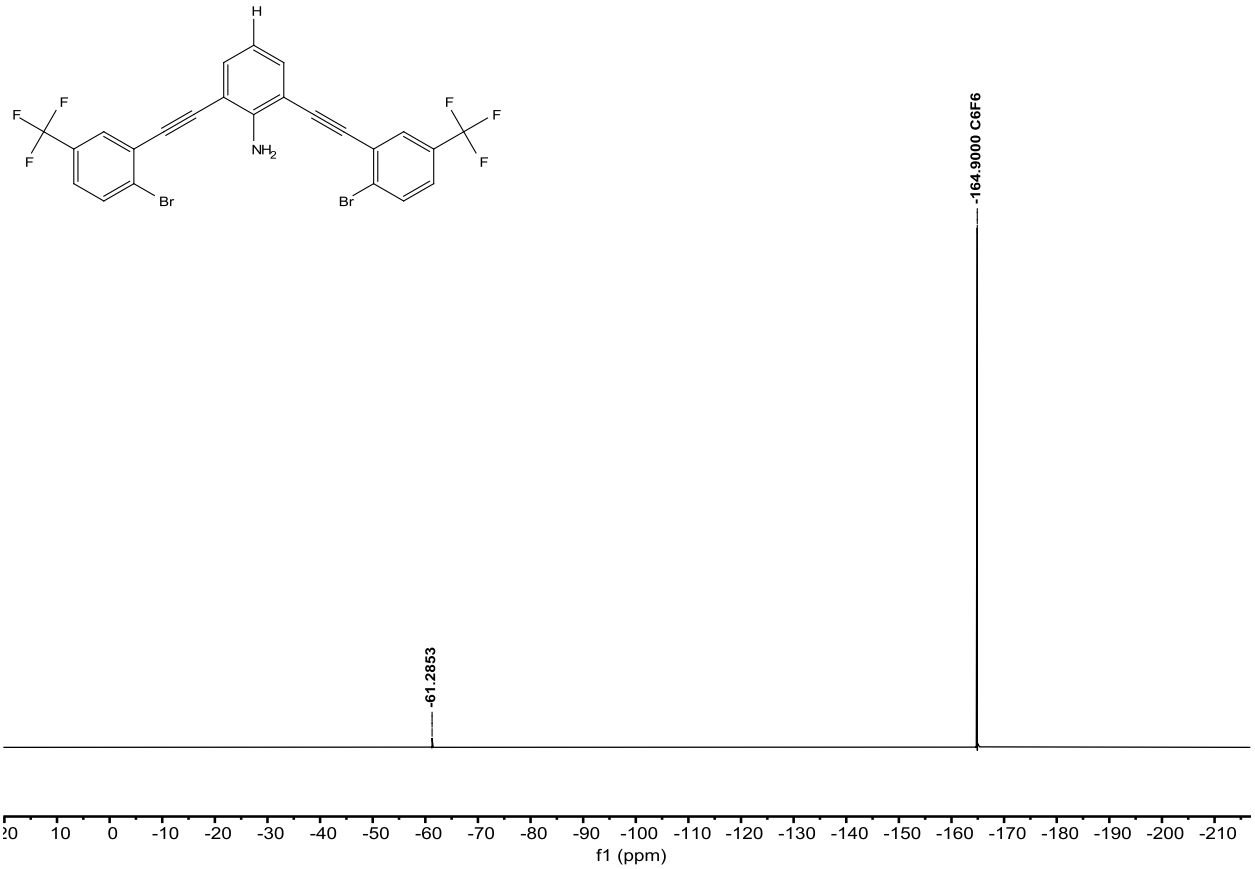

Figure S127. ^{19}F NMR of **H-G3XBBr** (376 MHz, $CDCl_3$). Hexafluorobenzene (C_6F_6) internal reference.

2,6-bis(2-ethynyl-4-(trifluoromethyl)iodophenyl)-aniline (H-G3XB). H-G3XBBr (0.200 g, 0.341 mmol), copper iodide (0.006 g, 0.030 mmol), sodium iodide (0.183 g, 1.22 mmol) were added to a 10-20 mL microwave reaction vial containing a stir bar and dissolved in 13 mL 1,4-dioxane. To the vibrant yellow reaction mixture, trans-N,N'-dimethylcyclohexane-1,2-diamine (0.15 mL) was added. The microwave vial was sealed and placed in a Biotage Initiator+ microwave reactor for 16 hours at 150 ˚C. After cooling, the reaction was run through pipet silica plug with EtOAc to remove catalysts and salts. The EtOAc crude was then ran through GCMS in order to obtain % conversion of bromines to iodines. If the conversion from bromine to iodine was 99% or greater, then the reaction was concentrated. The beige/yellow product (0.103 g, 44%) was obtained after purified via high performance liquid chromatography (reverse phase column gradient from 80% water/20% acetonitrile to 100% acetonitrile).

^{1}H NMR (400 MHz, $CDCl_3$): δ (ppm) = 8.02 (d, J = 8.3 Hz, 2H), 7.78 (s, 2H), 7.46 (d, J = 7.7 Hz, 2H), 7.25 (d, J = 7.4 Hz, 2H), 6.73 (t, J = 7.7 Hz, 1H), 5.35 (s, 2H).

^{13}C NMR (100 MHz, $CDCl_3$): δ (ppm) = 150.37, 139.46, 133.80, 131.04 (q, J = 33.0 Hz), 130.02, 128.99 (q, J = 3.7 Hz), 125.65 (q, J = 3.7 Hz), 123.69 (q, J = 270.8 Hz), 117.44, 106.53, 104.79, 96.09, 91.30.

^{19}F NMR (376 MHz, $CDCl_3$): δ (ppm) = –61.50.

HRMS (ESI neg) m/z for $C_{24}H_{10}F_6I_2N^-$ [M-H$^+$]$^-$: calculated: 679.8812; found: 679.8812.

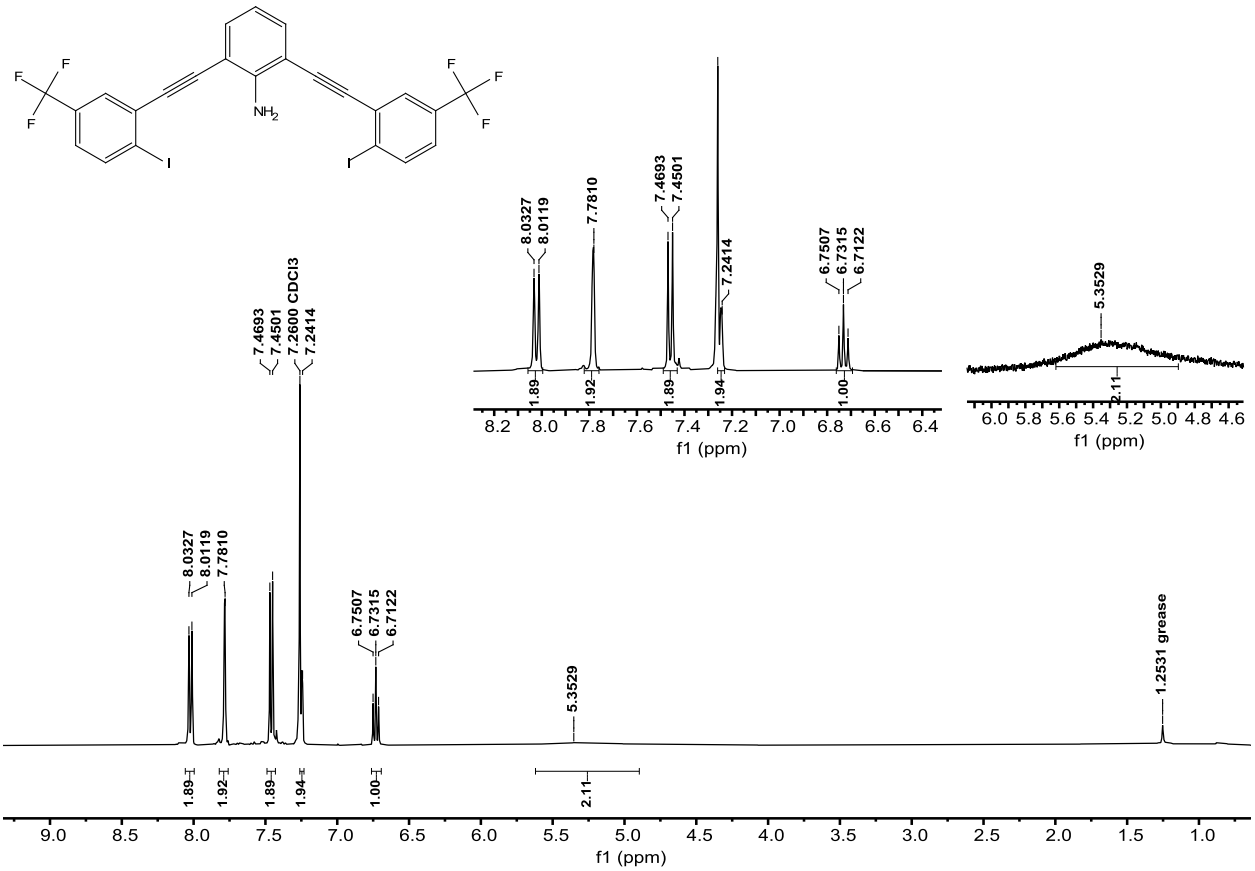

Figure S128. ^{1}H NMR of **H-G3XB** (400 MHz, $CDCl_3$).

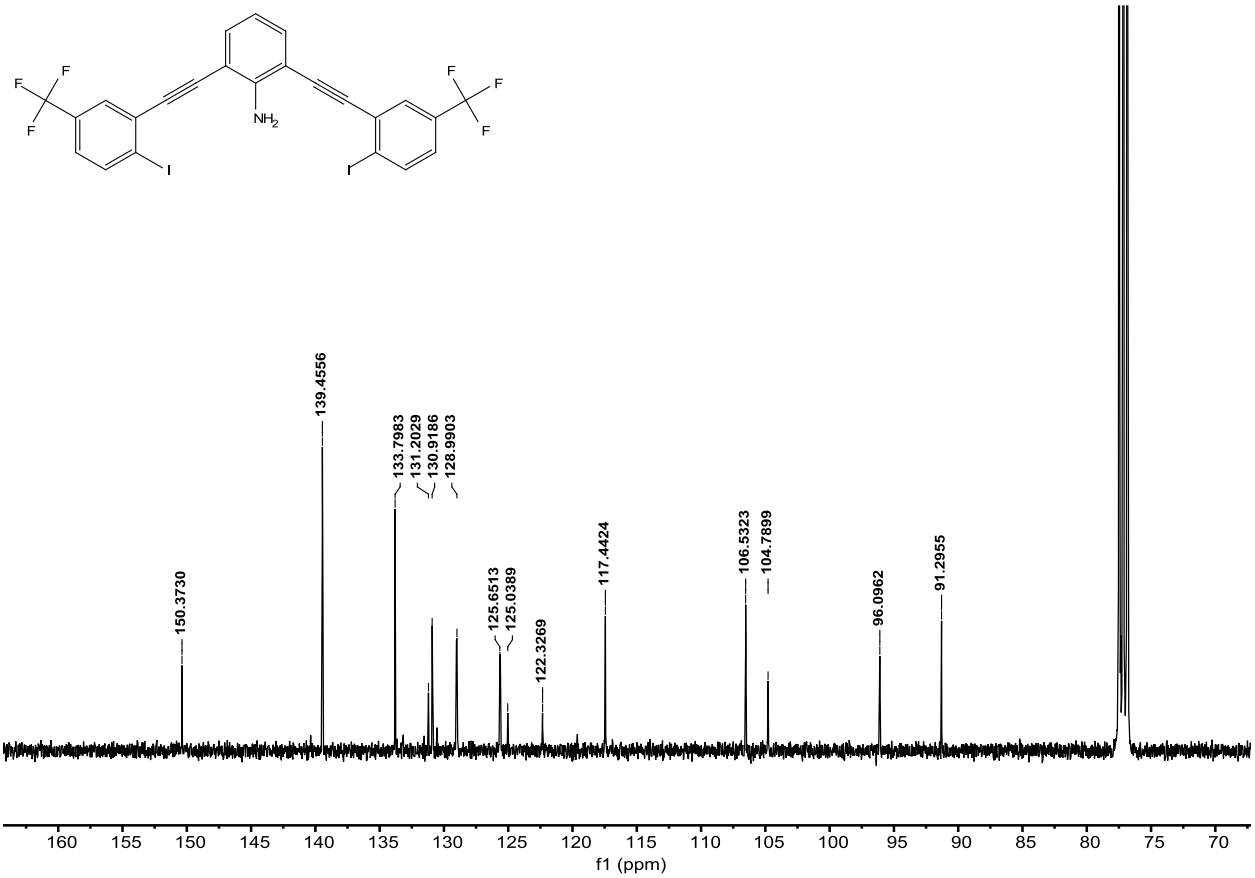

Figure S129. ^{13}C NMR of **H-G3XB** (100 MHz, $CDCl_3$).

Figure S130. ^{19}F NMR of **H-G3XB** (376 MHz, $CDCl_3$). Hexafluorobenzene (C_6F_6) internal reference.

2,6-bis(2-ethynyl-4-(trifluoromethyl)bromophenyl)-4-methylaniline (Me-G3XBBr). To an oven dried Schlenk flask was charged with 2,6-bisethynyl-4-methylaniline **(2e)** (0.133 g 0.86 mmol), then vacuumed and backfilled with dry N2 gas (3x). Bis(triphenylphosphine)palladium (II) dichloride (0.035 g, 0. 05 mmol) was added, vacuumed and backfilled with dry N2 gas (3x). Copper (I) iodide (0.019 g, 0.1 mmol) was added, vacuumed and backfilled with dry N2 (3x). The dry reagents were dissolved in 60 mL dry DMF. 1-Bromo-2-iodo-4-(trifluoromethyl)benzene (0.4 mL, 2.5 mmol) and N,N-diisopropylethylamine (0.86 mL, 5 mmol) were added to the DMF solution. The flask was carefully vacuumed and backfilled with dry N2 (3x). The dark brown solution stirred overnight at room temperature. The reaction mixture was extracted with ethyl acetate then washed with water to remove any excess salts and catalysts, then was dried over magnesium sulfate and gravity filtered. Subsequent removal of DMF, hexanes and ethyl acetate by rotary evaporation left and brown solid that was purified by column chromatography (gradient from 100% Hexanes to 3% EtOAc/97% Hexanes) to afford **Me-G3XBBr** (0.344 g, 67%) as a dull yellow solid.

^{1}H NMR (400 MHz, $CDCl_3$): δ (ppm) = 7.80 (s, 2H), 7.75 (d, J = 8.4 Hz, 2H), 7.41 (d, J = 8.4 Hz, 2H), 7.25 (s, 2H), 5.13 (s, 2H), 2.25 (s, 3H).

^{13}C NMR (100 MHz, $CDCl_3$): δ (ppm) = 148.35, 139.45, 134.27, 131.01 (q, J = 32.8 Hz), 131.00, 128.98 (q, J = 4.0 Hz), 126.72, 125.57 (q, J = 3.7 Hz), 123.70 (q, J = 270.8 Hz), 106.57, 104.79, 95.85, 91.54, 20.24.

^{19}F NMR (376 MHz, $CDCl_3$): δ (ppm) = -61.29.

HRMS (ESI neg) m/z for $C_{25}H_{12}F_6Br_2N^-$ $[M\text{-}H^+]^-$: calculated: 599.9226; found: 599.9224.

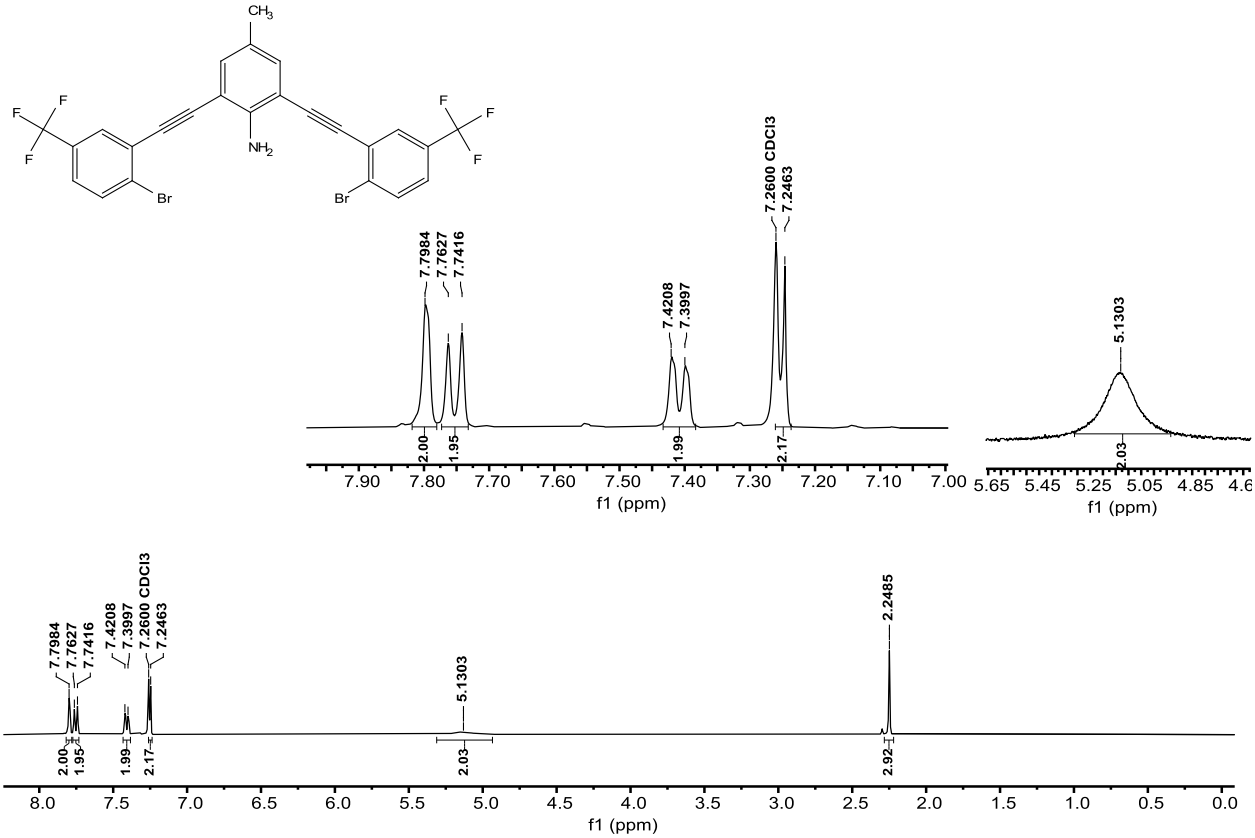

Figure S131. ^{1}H NMR of **Me-G3XBBr** (400 MHz, $CDCl_3$).

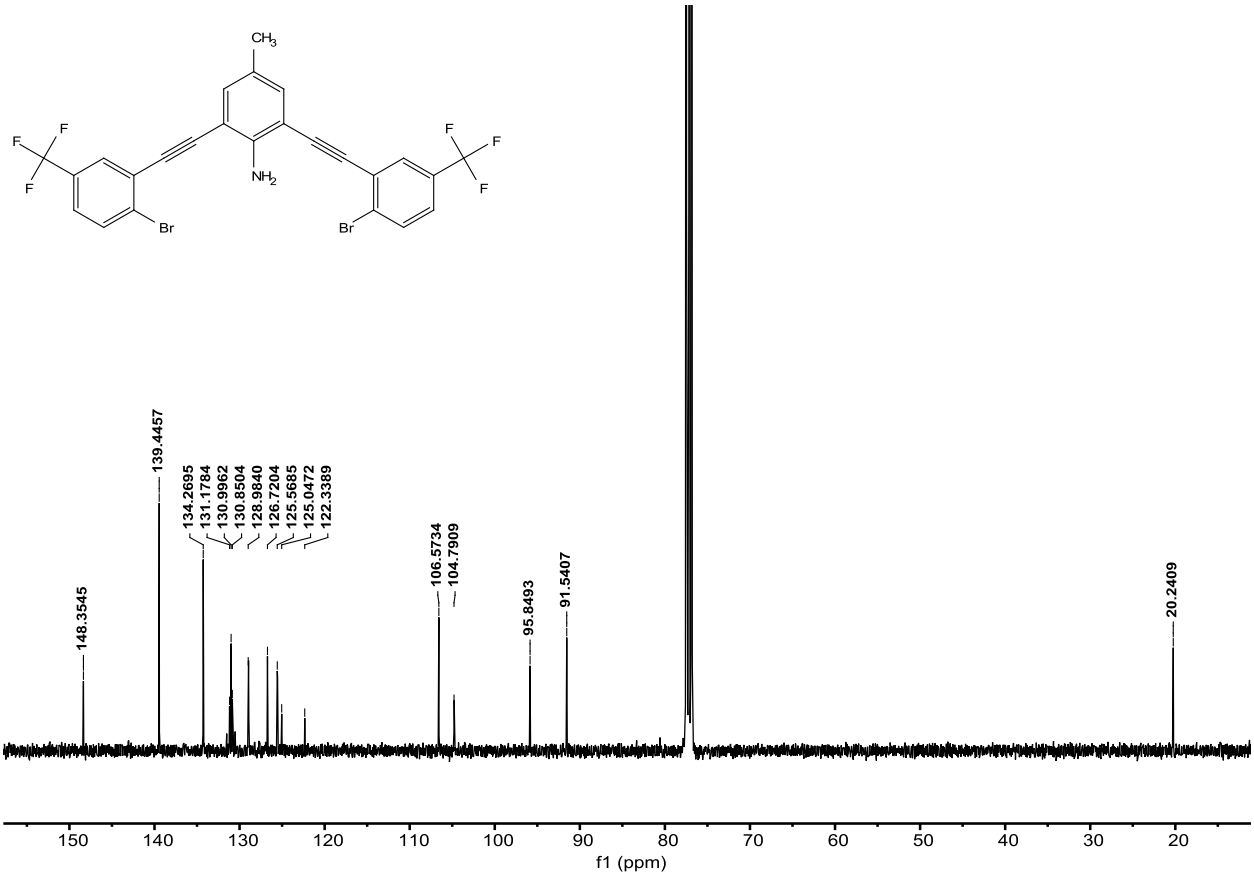

Figure S132. ^{13}C NMR of **Me-G3XBBr** (100 MHz, $CDCl_3$).

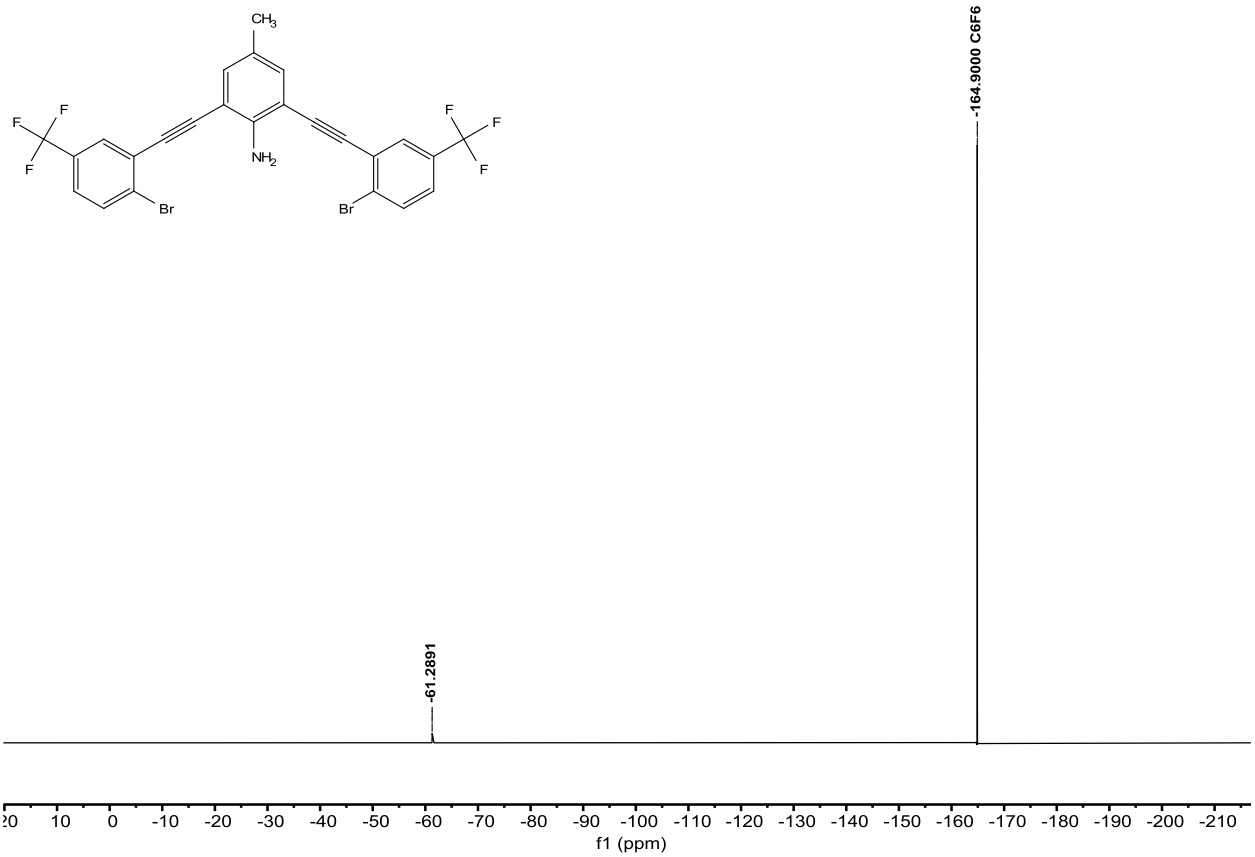

Figure S133. ^{19}F NMR of **Me-G3XBBr** (376 MHz, $CDCl_3$). Hexafluorobenzene (C_6F_6) internal reference.

2,6-bis(2-ethynyl-4-(trifluoromethyl)iodophenyl)-4-methylaniline (Me-G3XB). Me-G3XBBr (0.200 g, 0.332 mmol), copper iodide (0.006 g, 0.033 mmol), sodium iodide (0.200 g, 1.33 mmol) were added to a 10-20 mL microwave reaction vial containing a stir bar and dissolved in 13 mL 1,4-dioxane. To the vibrant yellow reaction mixture, trans-N,N'-dimethylcyclohexane-1,2-diamine (0.15 mL) was added. The microwave vial was sealed and placed in a Biotage Initiator+ microwave reactor for 17 hours at 150 ˚C. After cooling, the reaction was run through pipet silica plug with EtOAc to remove catalysts and salts. The EtOAc crude was then ran through GCMS in order to obtain % conversion of bromines to iodines. If the conversion from bromine to iodine was 99% or greater, then the reaction was concentrated. The beige/yellow product (0.100 g, 43%) was obtained after purified via high performance liquid chromatography (reverse phase column gradient from 80% water/20% acetonitrile to 100% acetonitrile).

^{1}H NMR (400 MHz, $CDCl_3$): δ (ppm) = 8.02 (d, J = 8.2 Hz, 2H), 7.77 (s, 2H), 7.29 (s, 2H), 7.64 (d, J = 6.1 Hz, 2H), 7.25 (d, J = 5.8 Hz, 2H), 5.20 (s, 2H), 2.27 (s, 3H).

^{13}C NMR (100 MHz, $CDCl_3$): δ (ppm) = 148.35, 139.45, 134.27, 131.01 (q, J = 32.8 Hz), 131.00, 128.98 (q, J = 4.0 Hz), 126.72, 125.57 (q, J = 3.7 Hz), 123.70 (q, J = 270.8 Hz), 106.57, 104.79, 95.85, 91.54, 20.24.

^{19}F NMR (376 MHz, $CDCl_3$): δ (ppm) = –61.50.

HRMS (ESI neg) m/z for $C_{25}H_{12}F_6Br_2N^-$ $[M-H^+]^-$: calculated: 693.8969; found: 693.8968.

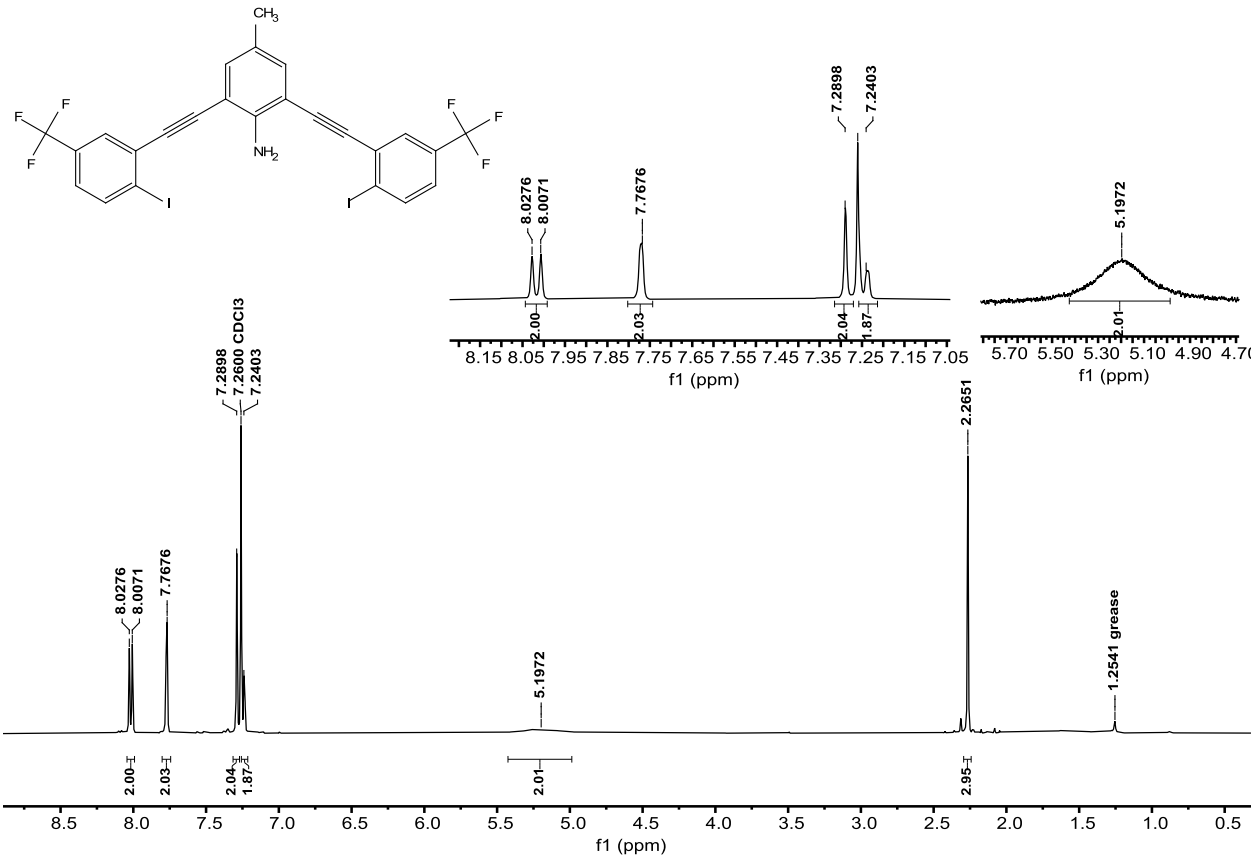

Figure S134. ^{1}H NMR of **Me-G3XB** (400 MHz, $CDCl_3$).

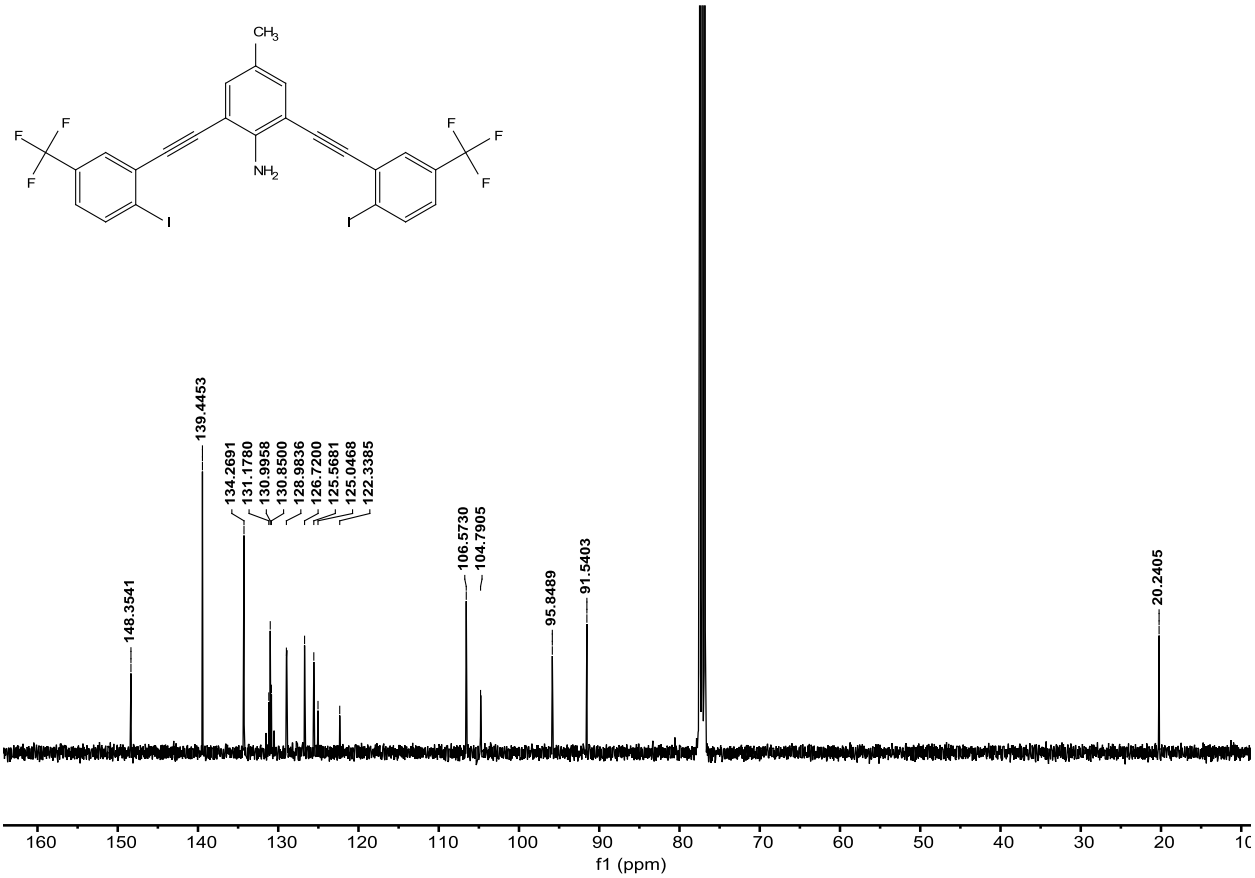

Figure S135. ^{13}C NMR of **Me-G3XB** (100 MHz, $CDCl_3$).

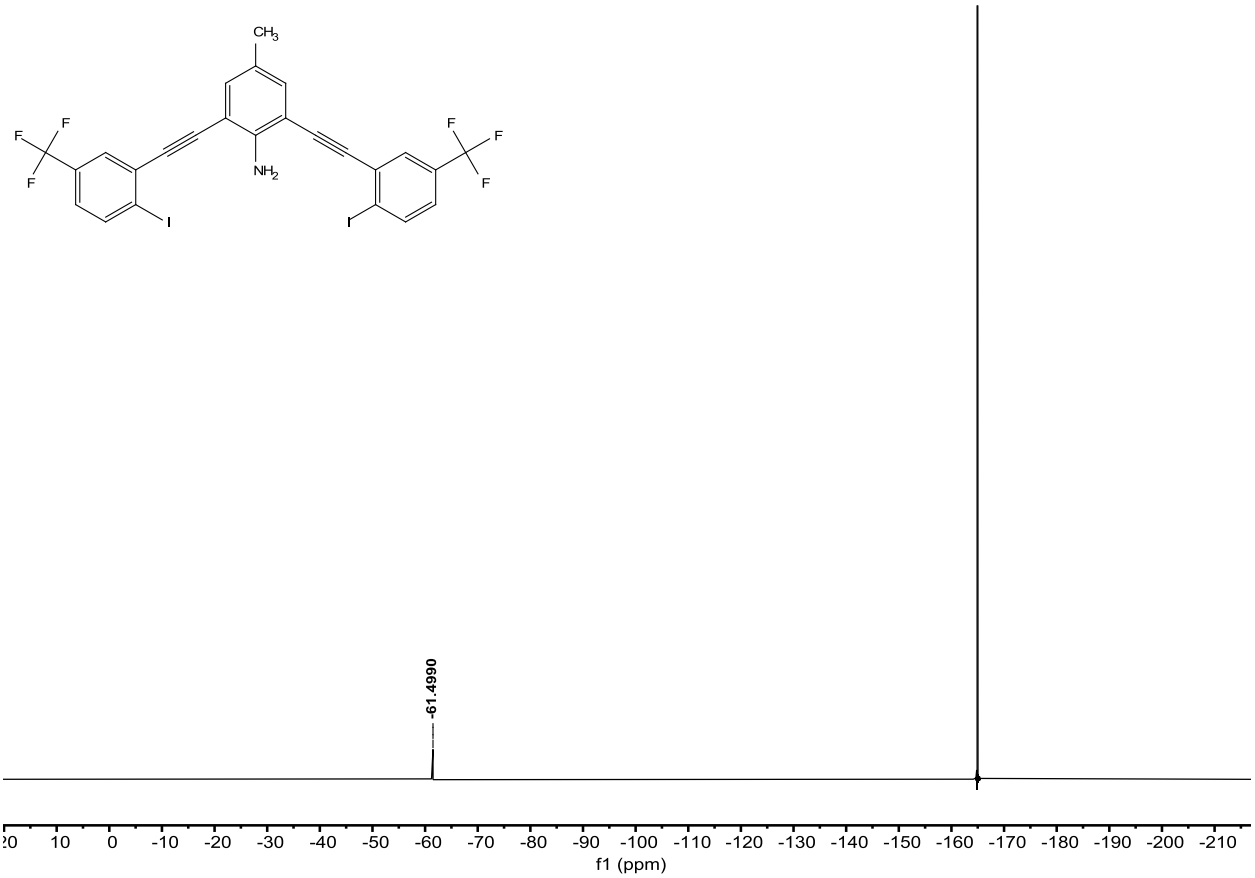

Figure S136. ^{19}F NMR of **Me-G3XB** (376 MHz, $CDCl_3$). Hexafluorobenzene (C_6F_6) internal reference.

3,5-bis(2-ethynyl-4-(trifluoromethyl)bromophenyl)-(trifluoromethyl)benzene (nHBeXBBr). To an oven dried Schlenk flask was charged with 3,5-bisethynyl-trifluoromethylbenzene **(2f)** (0.234g 1.2 mmol), then vacuumed and backfilled with dry N2 gas (3x). Bis(triphenylphosphine)palladium (II) dichloride (0.042 g, 0. 06 mmol) was added, vacuumed and backfilled with dry N2 gas (3x). Copper (I) iodide (0.023 g, 0.12 mmol) was added, vacuumed and backfilled with dry N2 (3x). The dry reagents were dissolved in 60 mL dry DMF. 1-Bromo-2-iodo-4-(trifluoromethyl)benzene (0.48 mL, 3 mmol) and N,N-diisopropylethylamine (1.03 mL, 6 mmol) were added to the DMF solution. The flask was carefully vacuumed and backfilled with dry N2 (3x). The dark brown solution stirred overnight at room temperature. The reaction mixture was extracted with ethyl acetate then washed with water to remove any excess salts and catalysts, then was dried over magnesium sulfate and gravity filtered. Subsequent removal of DMF, hexanes and ethyl acetate by rotary evaporation left and brown solid that was purified by column chromatography (gradient from 100% Hexanes to 5% EtOAc/95% Hexanes) to afford **nHBeXBBr** (0.466 g, 60%) as a dull yellow solid.
^{1}H NMR (400 MHz, $CDCl_3$): δ (ppm) = 7.94 (s, 1H), 7.83 (s, 4H), 7.78 (d, J = 8.3 Hz, 2H), 7.48 (d, J = 8.4 Hz, 2H).

^{13}C NMR (100 MHz, $CDCl_3$): δ (ppm) = 137.73, 133.42, 132.12 (q, J = 33.2 Hz), 130.221 (q, J = 33.2 Hz), 130.37 (q, J = 4.0 Hz), 129.72, 128.82 (q, J = 3.7 Hz), 126.64 (q, J = 3.6 Hz), 125.62, 123.49 (q, J = 270.8 Hz), 124.07, 123.25 (q, J = 271.2 Hz), 92.71, 89.03.
^{19}F NMR (376 MHz, $CDCl_3$): δ (ppm) = –61.32, -61.48.
Elemental analysis, Found: C, 47.02; H, 1.39%. Calc. for $C_{25}H_9Br_2F_9$: C, 46.91; H, 1.42%.

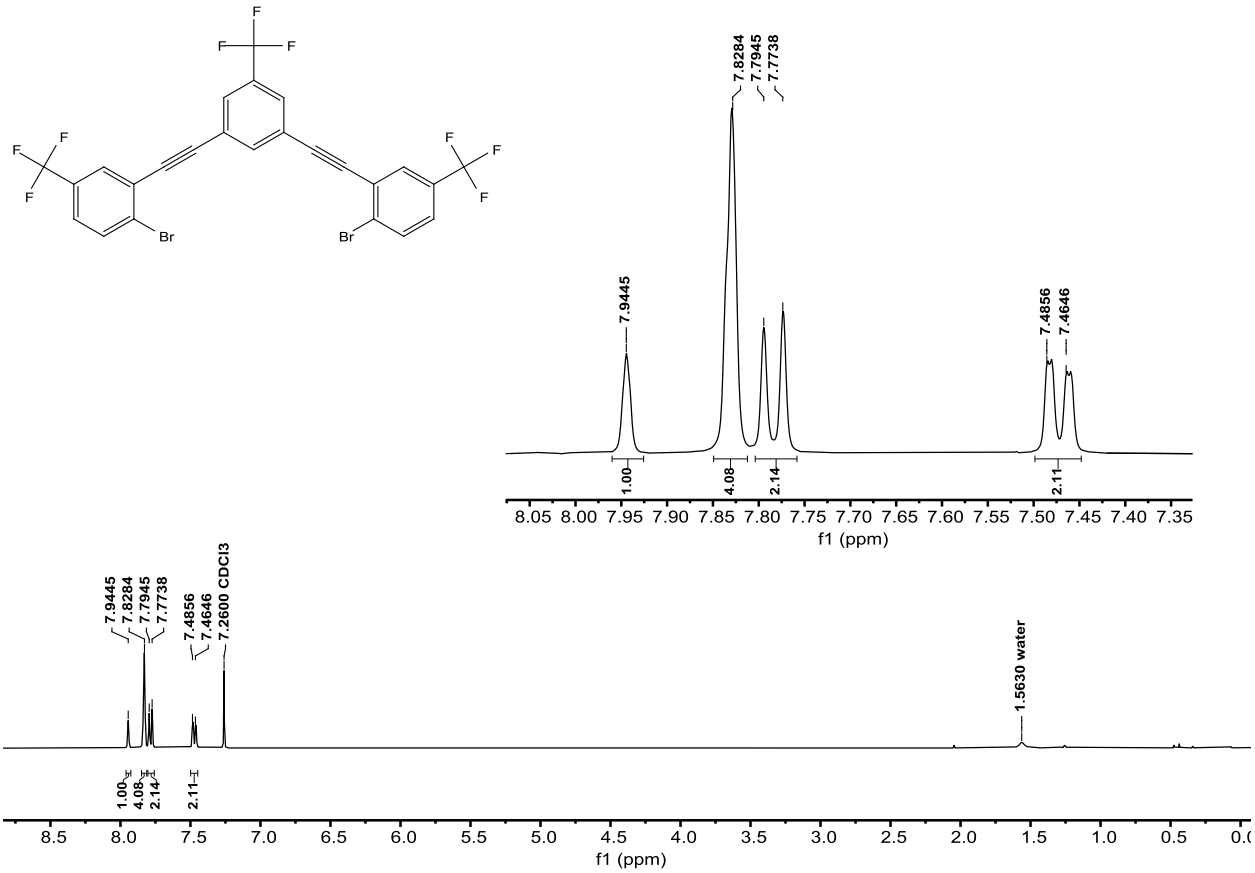

Figure S137. ^{1}H NMR of **nHBeXBBr** (400 MHz, $CDCl_3$).

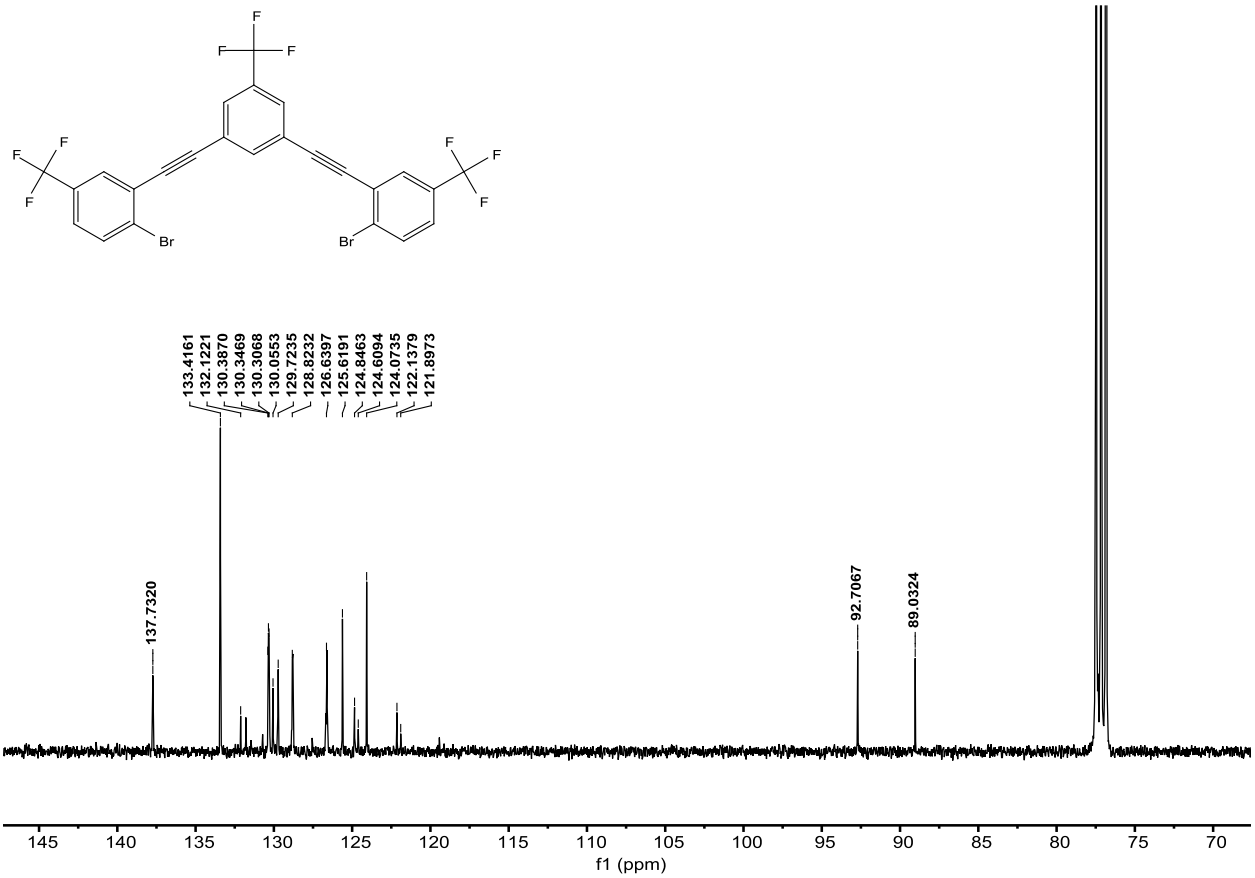

Figure S138. ^{13}C NMR of **nHBeXBBr** (100 MHz, $CDCl_3$).

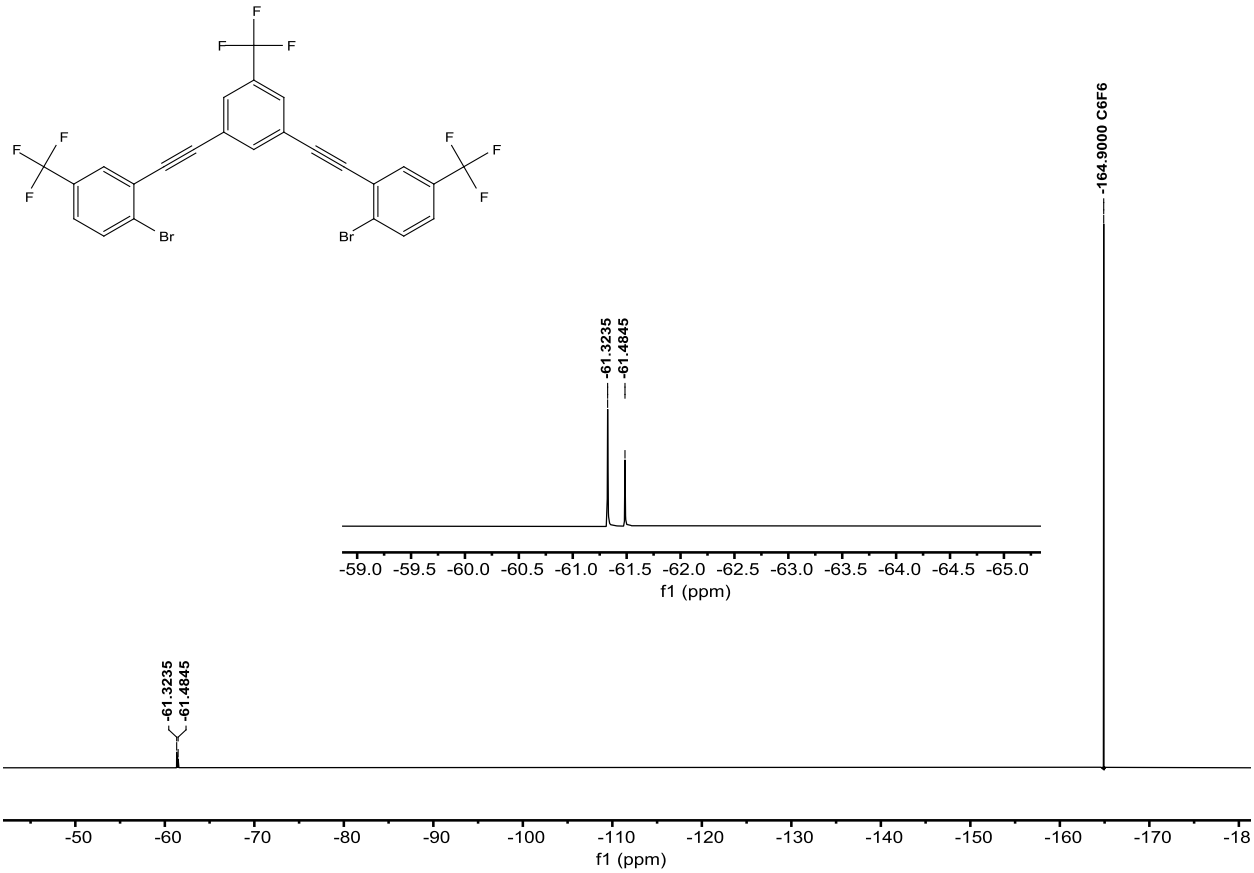

Figure S139. ^{19}F NMR of **nHBeXBBr** (376 MHz, $CDCl_3$). Hexafluorobenzene (C_6F_6) internal reference.

2,6-bis(2-ethynyl-4-(trifluoromethyl)iodophenyl)-4-trifluoromethylbenzene (nHBeXB). **nHBeXBBr** (0.200 g, 0.313 mmol), copper iodide (0.006 g, 0.030 mmol), sodium iodide (0.200 g, 1.33 mmol) were added to a 10-20 mL microwave reaction vial containing a stir bar and dissolved in 13 mL 1,4-dioxane. To the vibrant yellow reaction mixture, trans-N,N'-dimethylcyclohexane-1,2-diamine (0.1 mL) was added. The microwave vial was sealed and placed in a Biotage Initiator+ microwave reactor for 17 hours at 150 ˚C. After cooling, the reaction was run through pipet silica plug with EtOAc to remove catalysts and salts. The EtOAc crude was then ran through GCMS in order to obtain % conversion of bromines to iodines. If the conversion from bromine to iodine was 99% or greater, then the reaction was concentrated. The beige/yellow product (0.144 g, 63%) was obtained after purified via high performance liquid chromatography (reverse phase column gradient from 80% water/20% acetonitrile to 100% acetonitrile).

^{1}H NMR (400 MHz, $CDCl_3$): δ (ppm) = 8.04 (d, J = 8.3 Hz, 2H), 7.97 (s, 1H), 7.84 (s, 2H), 7.79 (s, 2H), 7.30 (d, J = 8.3 Hz, 2H).

^{13}C NMR (100 MHz, $CDCl_3$): δ (ppm) = 139.73, 137.58, 132.15 (q, J = 34.2 Hz), 131.21 (q, J = 32.8 Hz), 130.04, 129.32 (q, J = 3.7 Hz), 128.72(q, J = 4.0 Hz), 126.42 (q, J = 3.7 Hz), 124.12, 123.62 (q, J = 270.5 Hz), 123.27 (q, J = 271.6 Hz), 105.46, 92.62, 91.82.

^{19}F NMR (376 MHz, $CDCl_3$): δ (ppm) = –61.51, -61.57.

Elemental analysis, Found: C, 42.29; H, 1.14%. Calc. for $C_{25}H_9I_2F_9$: C, 40.90; H, 1.24%.

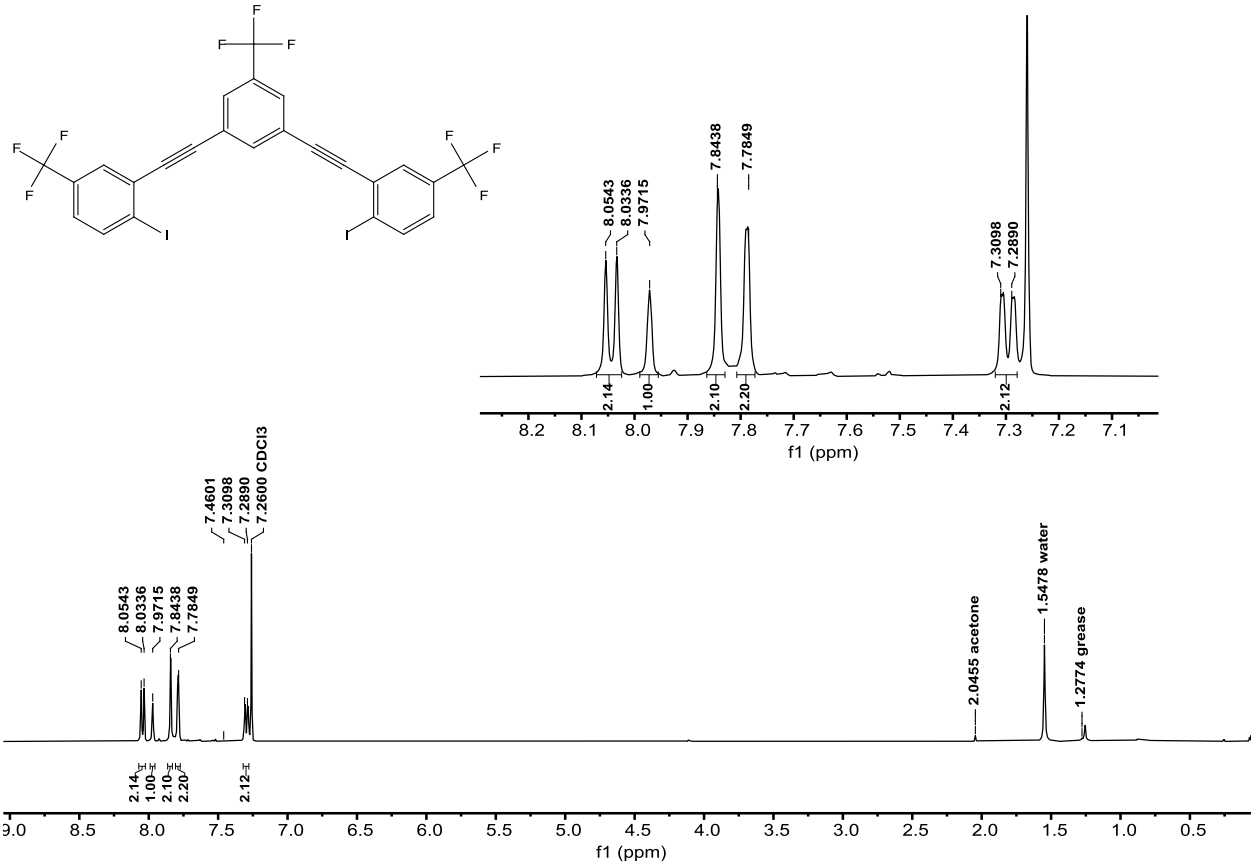

Figure S140. ^{1}H NMR of **nHBeXB** (400 MHz, $CDCl_3$).

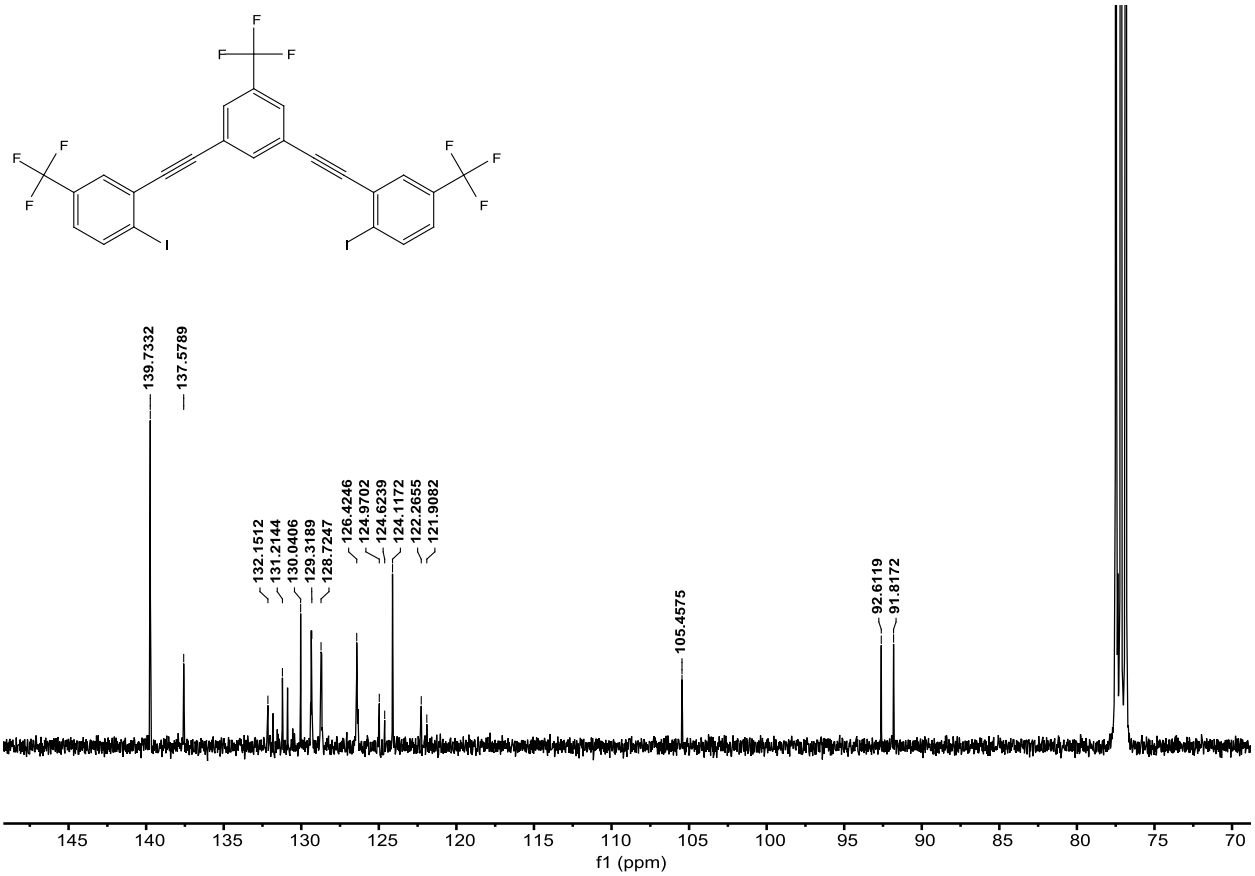

Figure S141. ^{13}C NMR of **nHBeXB** (100 MHz, $CDCl_3$).

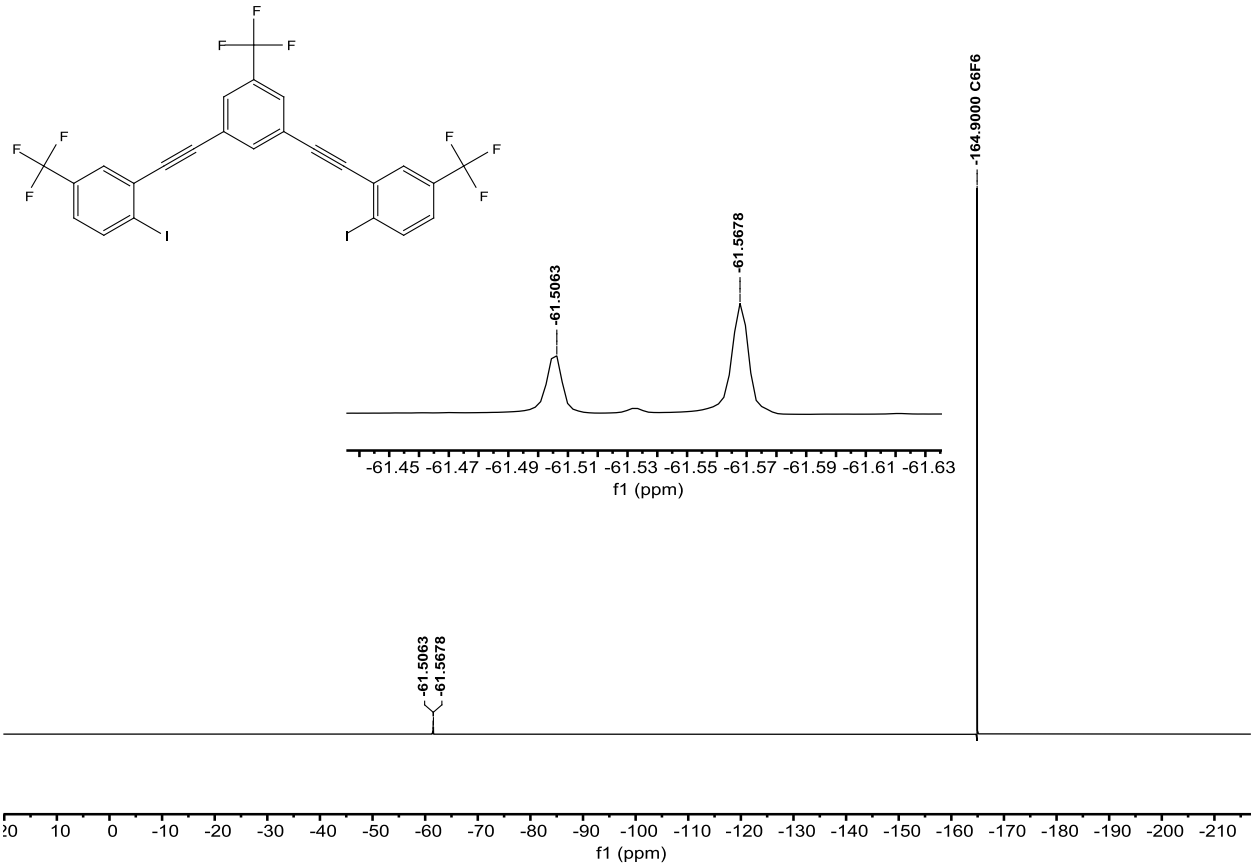

Figure S142. ^{19}F NMR of **nHBeXB** (376 MHz, $CDCl_3$). Hexafluorobenzene (C_6F_6) internal reference.

NMR titration Details and Data

All experiments were performed on a Varian Drive Direct 500 MHz NMR Spectrometer. C_6D_6 was dried over 3 Å molecular sieves. THA^+ salts (Cl^-, Br^-, I^-) was dried under vacuum and stored in a desiccator.

Stock solutions of all receptors (3.993-5.745 mM) were prepared in 1.4 mL of deuterated benzene (C_6D_6). 0.500 mL aliquots from each stock solution were syringed into three separate NMR tubes with screw caps and septa. The stock solution of each host was then used to make guest solutions. After obtaining free-host spectra of each receptor, aliquots of corresponding guest solution were added to their respective NMR tubes. Spectra were obtained after each addition (20x). A constant host concentration was maintained, while THA iodide salt concentrations gradually increased throughout titration (see data below). Intuitions of stoichiometric displacement led to the stepwise anion exchange model:

$H + G \rightleftharpoons HG$, $K_{11} = [HG]/[H][G]$

Dimerization and higher order binding were ruled out due to the emergence of an obvious pattern in residuals, unrealistic assigned shifts, poor convergence, and/or larger standard deviations. Bindfit[5] was used to refine the isothermal fits of multiple signals simultaneously. Association constants for binding of THA iodide to all receptors are shown in Table S1. Full

binding data and fitting parameters for each titration can be obtained from the Bindfit[5] using the following links.

Table S1. Association constants for binding of THA iodide to all receptors in C_6D_6 at 298 K.

Receptor	Assay 1 (M^{-1})	Assay 2 (M^{-1})	Assay 3 (M^{-1})	Average (M^{-1})
G3XB	428.8	406.5	410.8	415.6
2F-G3XB	152.9	177.4	179.6	170.0
2H-G3XB	69.9	75.5	70.3	71.9
2Me-G3XB	51.1	44.9	46.6	47.5
2*t*Bu-G3XB	54.1	51.0	49.2	51.4
2MeO-G3XB	60.2	63.6	63.2	62.4
Cl-G3XB	330.0	317.7	345.4	331.1
F-G3XB	236.4	274.4	241.1	250.7
H-G3XB	194.6	199.1	188.8	194.2
Me-G3XB	182.0	171.7	170.2	174.6
nHBeXB	12.4	4.4	8.0	8.3
G3HB	36.7	22.5	23.2	27.5

G3XB with THA iodide

Assay 1 K_a= 428.8 M^{-1} http://app.supramolecular.org/bindfit/view/d05dc4b3-cdea-4bc5-a05a-cf9ff564b20e

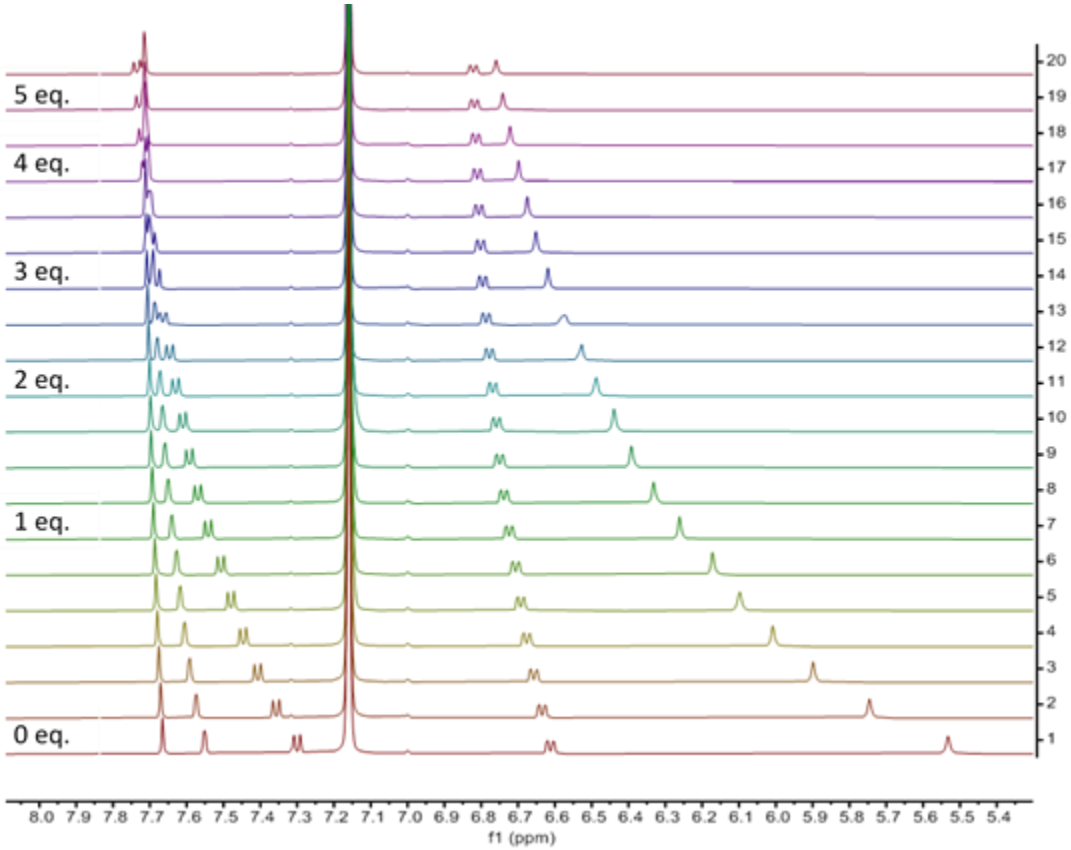

Figure S143-1. ^{1}H NMR spectra of **G3XB** upon addition of increasing equivalents of THA·I (C_6D_6, 298 K, 500 MHz).

Assay 2 K_a= 406.5 M^{-1} http://app.supramolecular.org/bindfit/view/f6b13944-604f-4a0d-89a6-894a7605e731

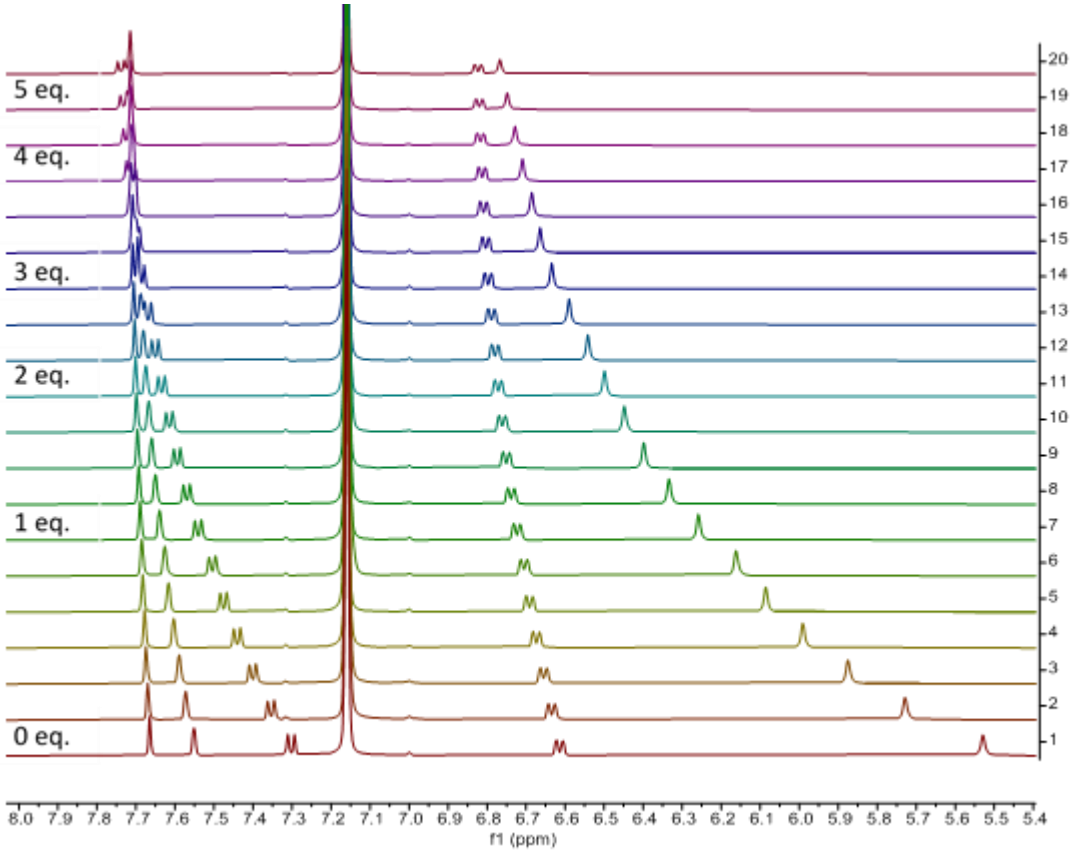

Figure S143-2. ^{1}H NMR spectra of **G3XB** upon addition of increasing equivalents of THA·I (C_6D_6, 298 K, 500 MHz).

Assay 3 K_a= 410.8 M^{-1} http://app.supramolecular.org/bindfit/view/d6cdf7b6-4e20-40a2-8af2-91b2beade8c0

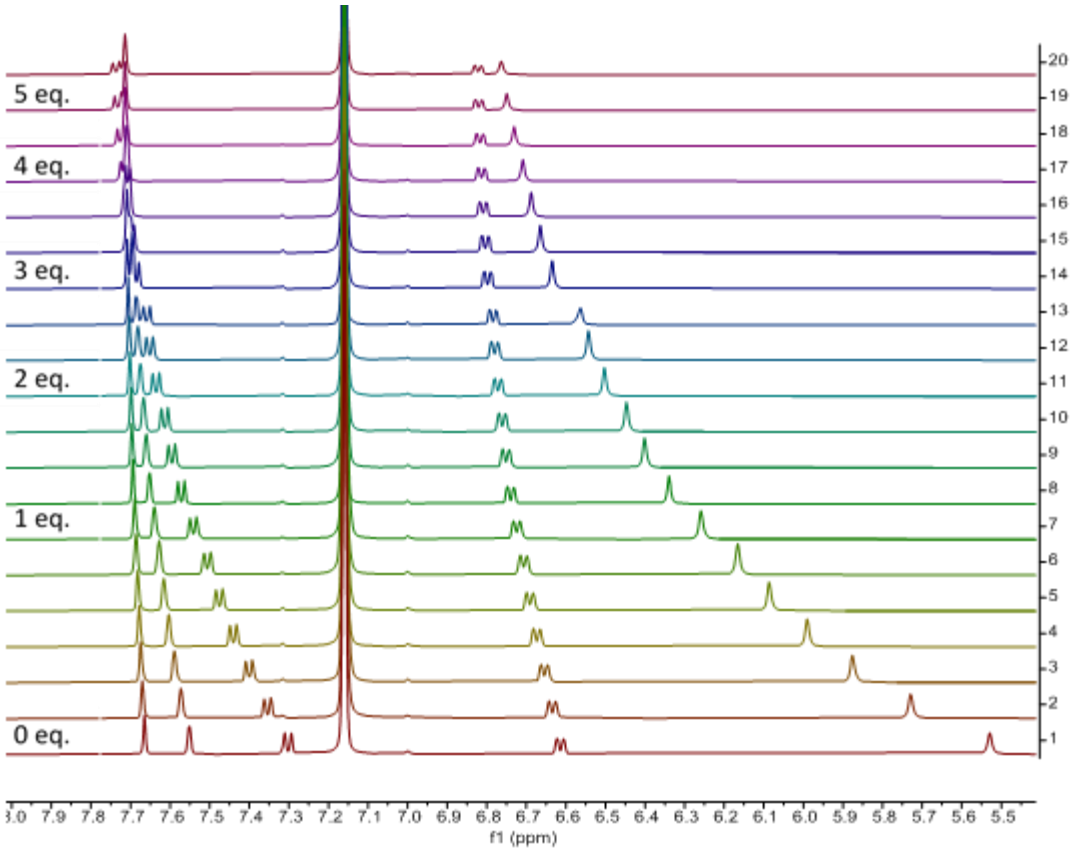

Figure S143-3. ^{1}H NMR spectra of **G3XB** upon addition of increasing equivalents of THA·I (C_6D_6, 298 K, 500 MHz).

2F-G3XB with THA iodide

Assay 1 K_a= 152.9 M^{-1} http://app.supramolecular.org/bindfit/view/e2455db7-87fd-4a8d-b961-b6d6f52084b5

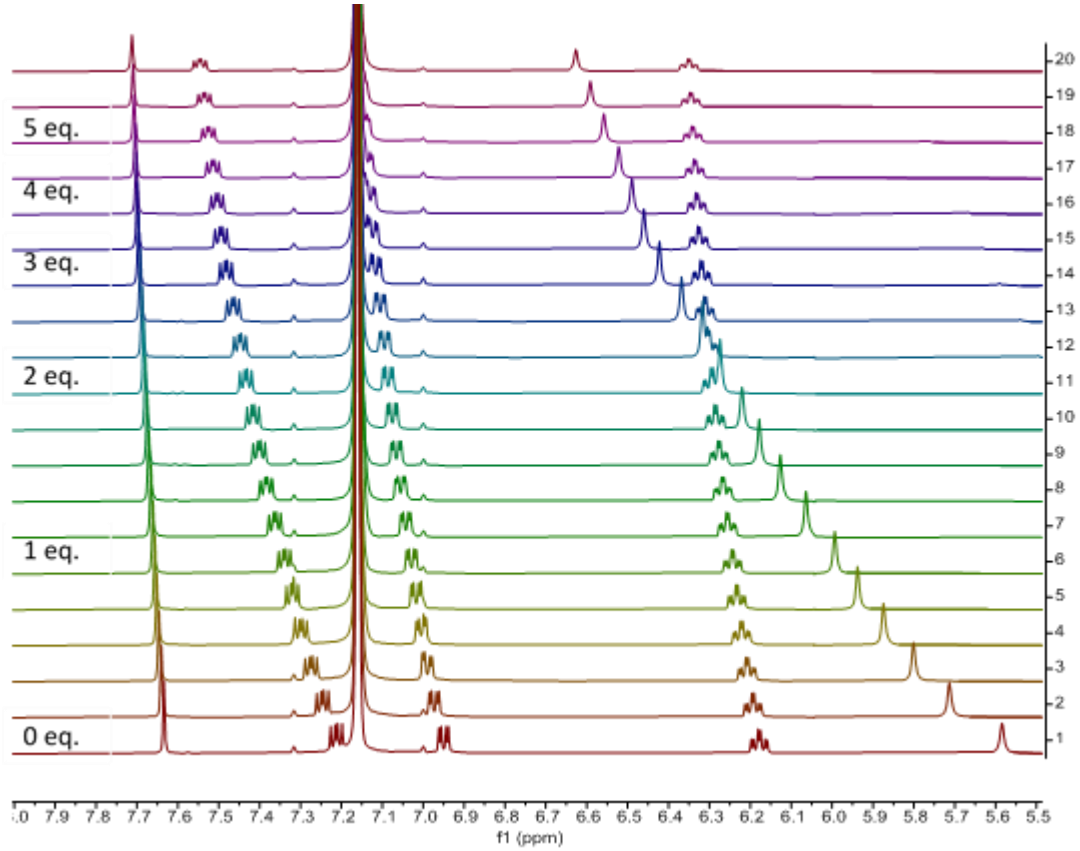

Figure S144-1. ^{1}H NMR spectra of **2F-G3XB** upon addition of increasing equivalents of THA·I (C_6D_6, 298 K, 500 MHz).

Assay 2 K_a= 177.4 M^{-1} http://app.supramolecular.org/bindfit/view/2bf8af11-212f-4434-809e-b11fe57f9649

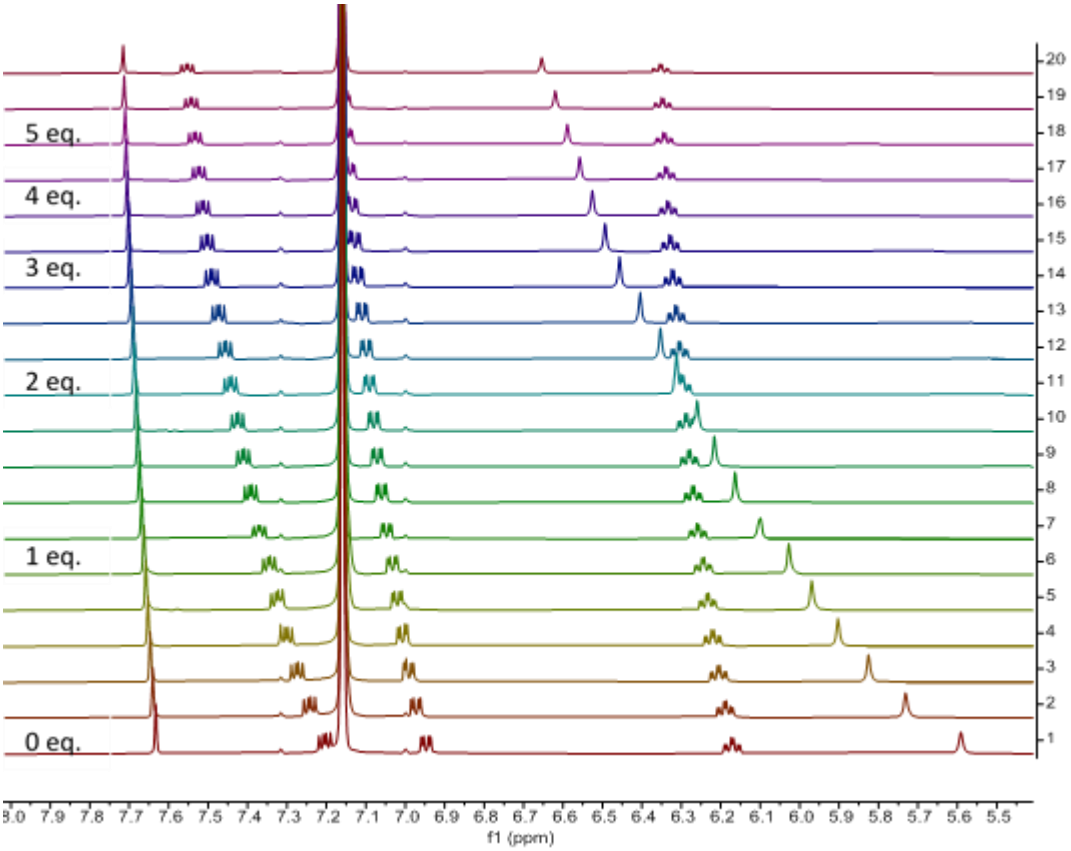

Figure S144-2. ^{1}H NMR spectra of **2F-G3XB** upon addition of increasing equivalents of THA·I (C_6D_6, 298 K, 500 MHz).

Assay 3 K_a= 179.6 M^{-1} http://app.supramolecular.org/bindfit/view/3646ae56-682e-467c-8f3f-0c1e1cfcb685

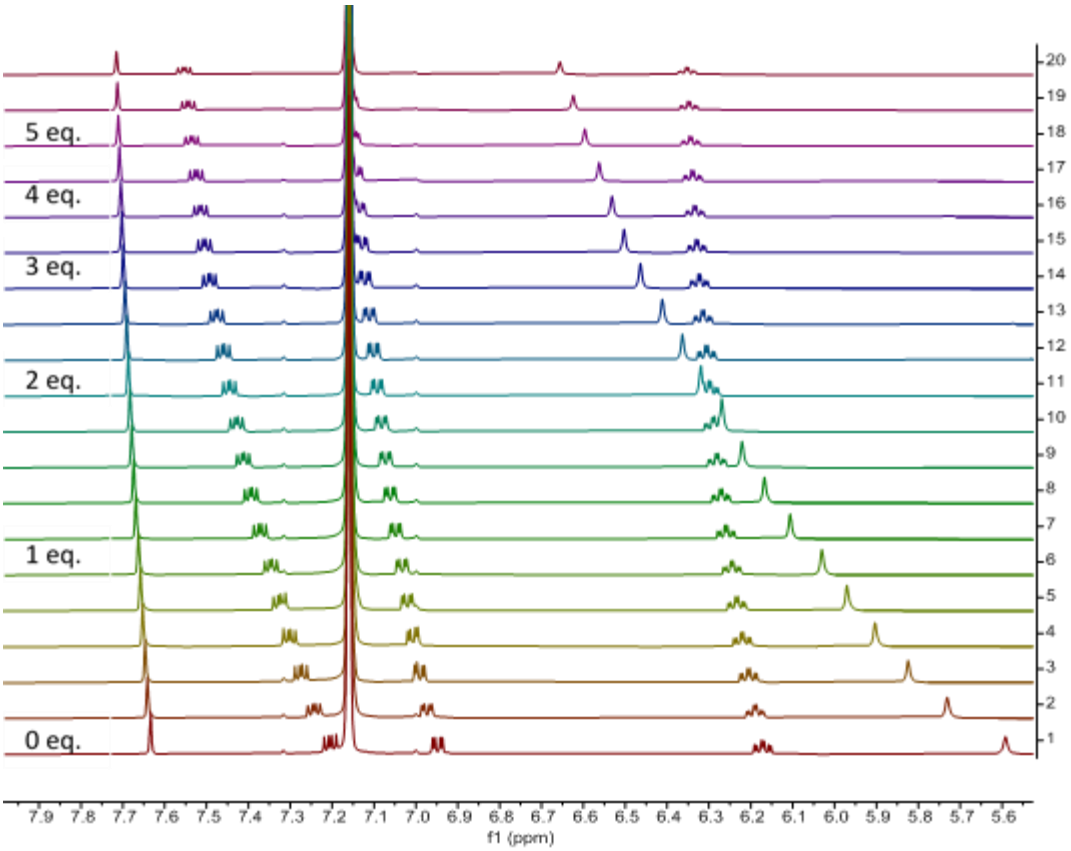

Figure S144-3. ^{1}H NMR spectra of **2F-G3XB** upon addition of increasing equivalents of THA·I (C_6D_6, 298 K, 500 MHz).

2H-G3XB with THA iodide

Assay 1 K_a= 69.9 M^{-1} http://app.supramolecular.org/bindfit/view/4e544414-0f49-474d-b021-4730b8a315ea

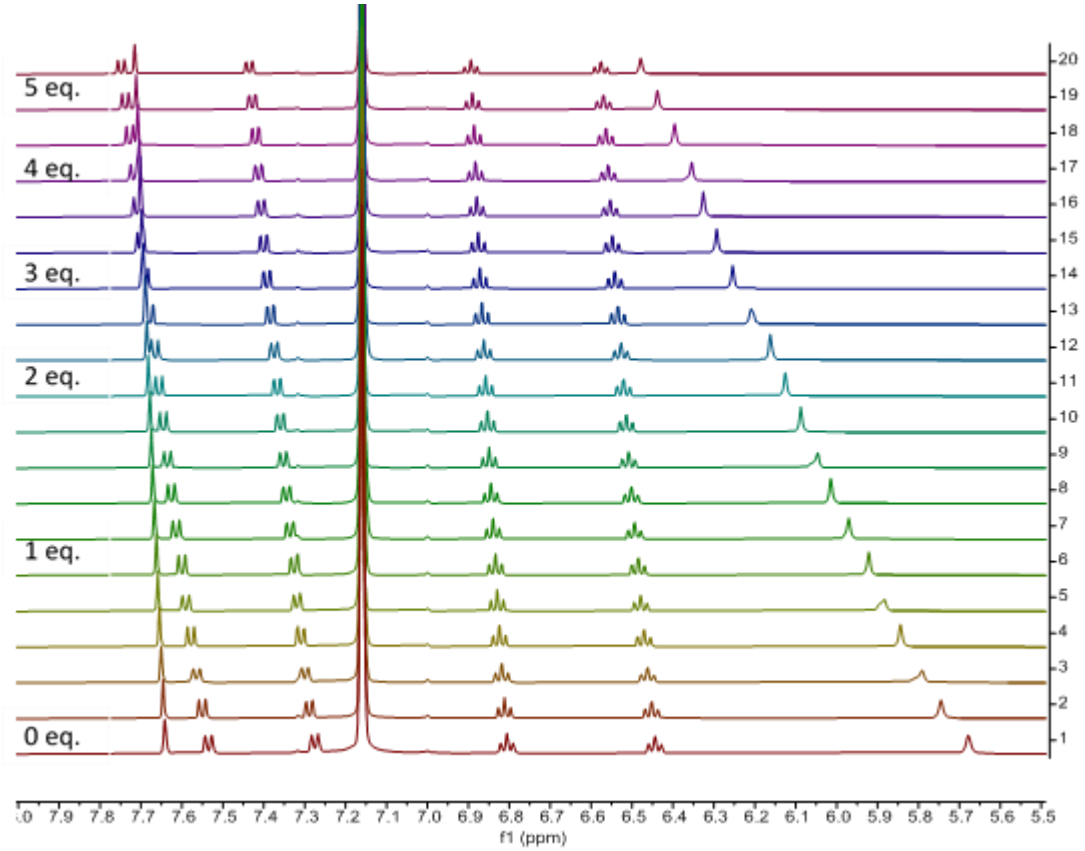

Figure S145-1. ^{1}H NMR spectra of **2H-G3XB** upon addition of increasing equivalents of THA·I (C_6D_6, 298 K, 500 MHz).

Assay 2 K_a= 75.5 M^{-1} http://app.supramolecular.org/bindfit/view/31ef807a-a956-4372-9614-45f31dd9c034

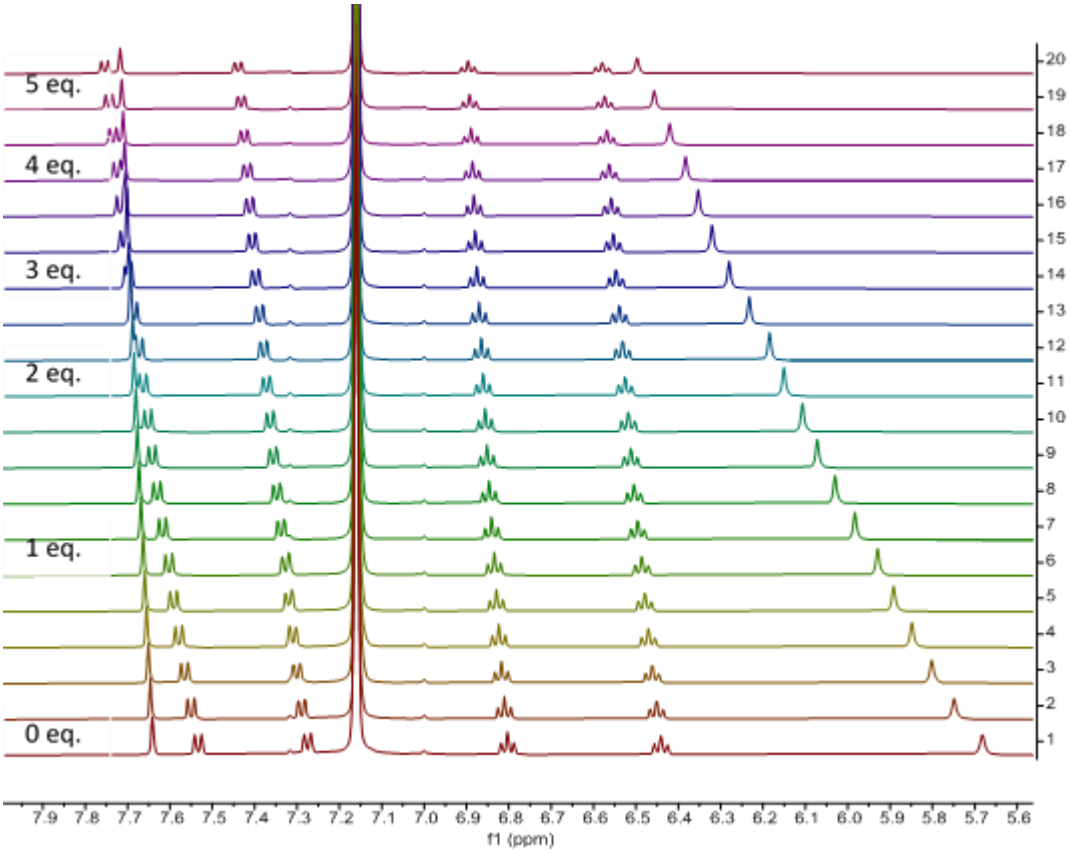

Figure S145-2. ^{1}H NMR spectra of **2H-G3XB** upon addition of increasing equivalents of THA·I (C_6D_6, 298 K, 500 MHz).

Assay 3 K_a= 70.3 M^{-1} http://app.supramolecular.org/bindfit/view/f27bf235-649a-45d9-a5f8-97a8130e9fcc

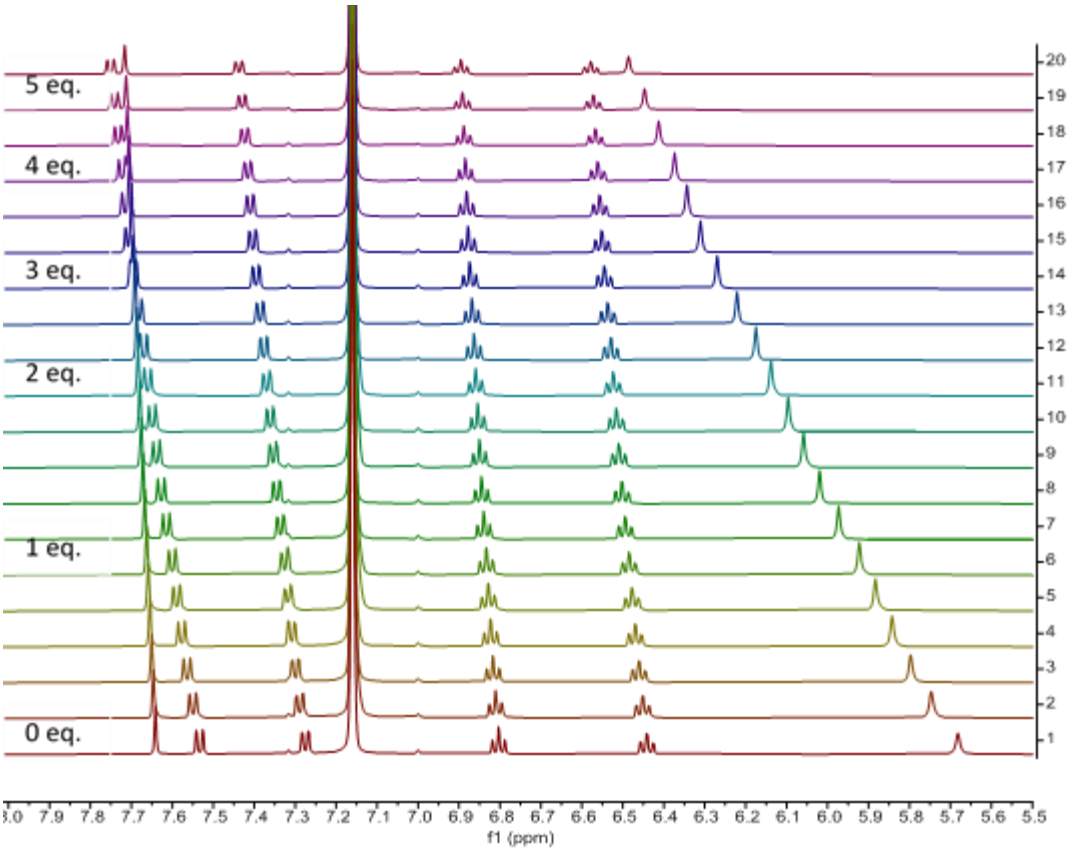

Figure S145-3. ^{1}H NMR spectra of **2H-G3XB** upon addition of increasing equivalents of THA·I (C_6D_6, 298 K, 500 MHz).

2Me-G3XB with THA iodide

Assay 1 K_a= 51.1 M^{-1} http://app.supramolecular.org/bindfit/view/f3b0725c-ef3b-4907-9cc0-439160c61860

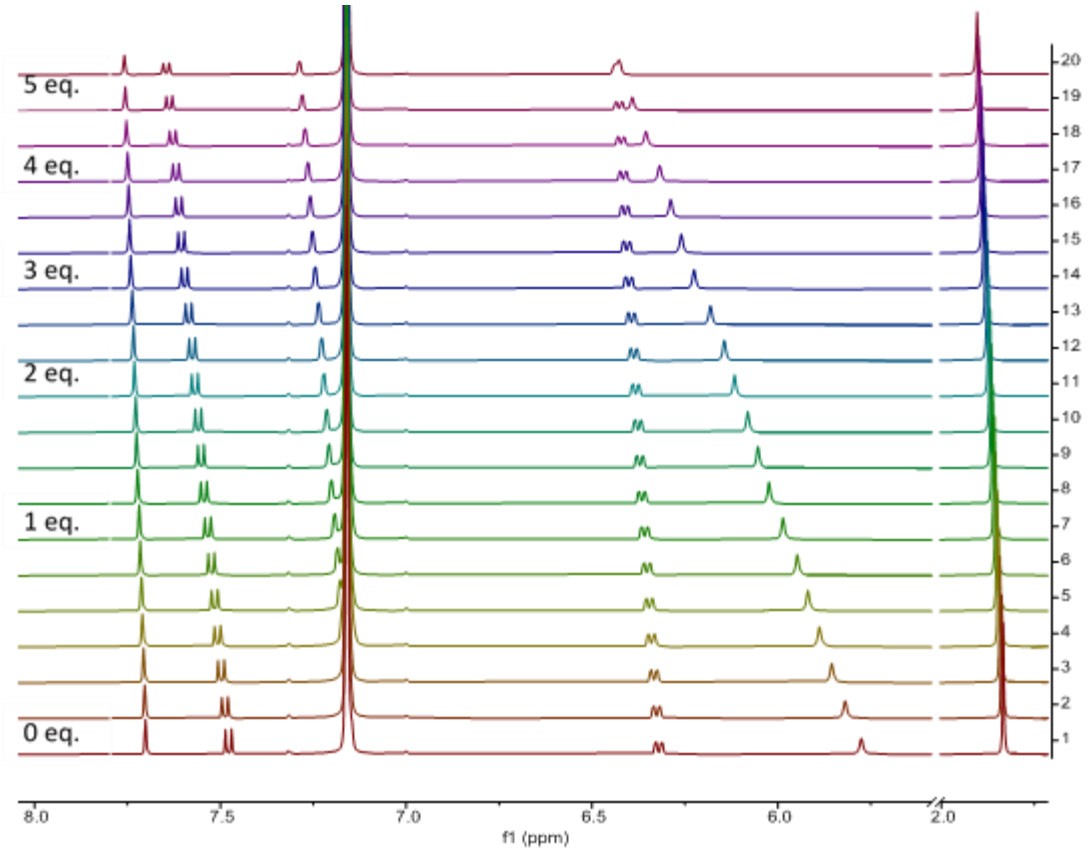

Figure S146-1. ^{1}H NMR spectra of **2Me-G3XB** upon addition of increasing equivalents of THA·I (C_6D_6, 298 K, 500 MHz).

Assay 2 K_a= 44.9 M^{-1} http://app.supramolecular.org/bindfit/view/a83b6928-477c-47d9-b2ef-a5bb372d5e63

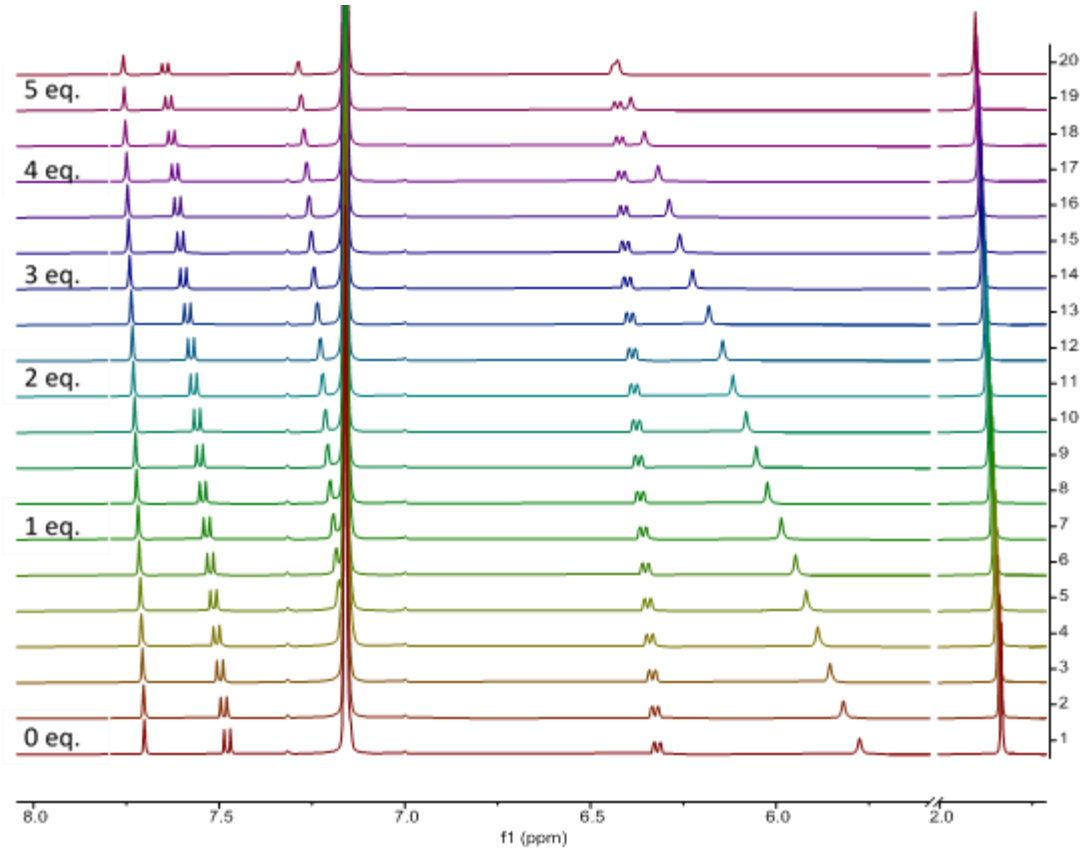

Figure S146-2. ^{1}H NMR spectra of **2Me-G3XB** upon addition of increasing equivalents of THA·I (C_6D_6, 298 K, 500 MHz).

Assay 3 K_a= 46.6 M^{-1} http://app.supramolecular.org/bindfit/view/54c86164-8816-47ad-b588-8eaad5e20311

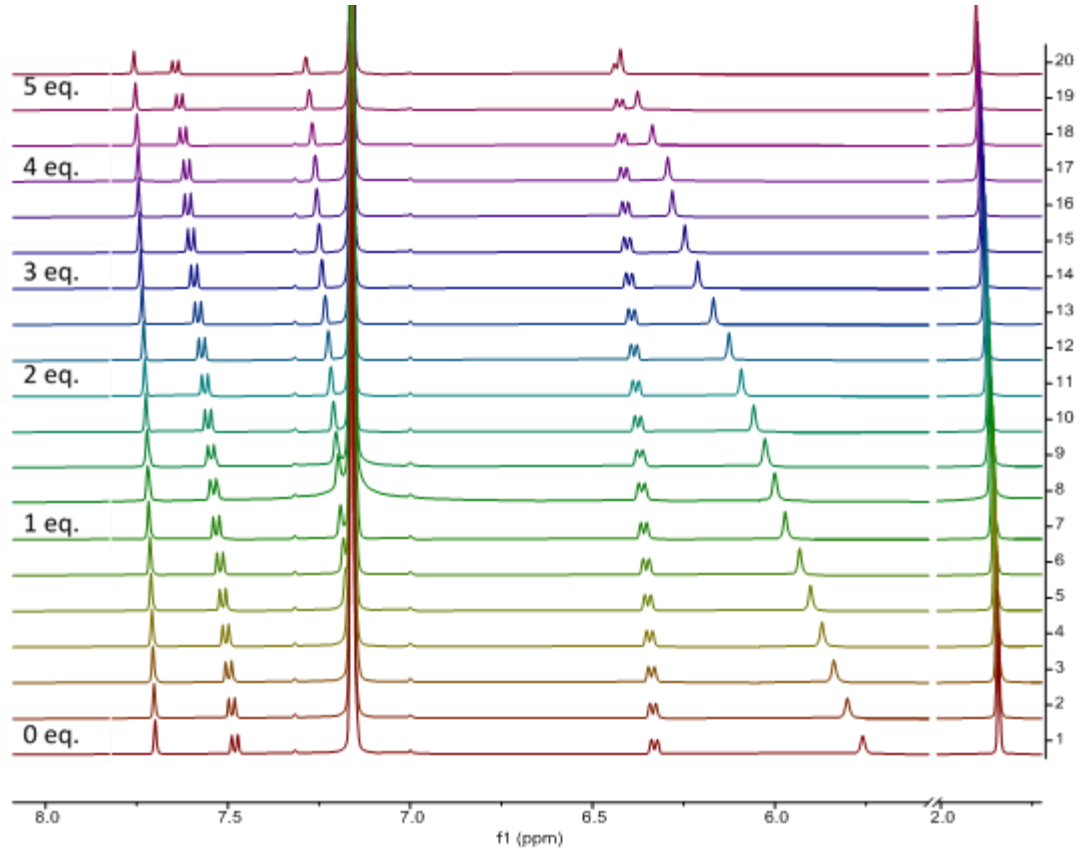

Figure S146-3. ^{1}H NMR spectra of **2Me-G3XB** upon addition of increasing equivalents of THA·I (C_6D_6, 298 K, 500 MHz).

2*t*Bu-G3XB with THA iodide

Assay 1 K_a= 54.1 M^{-1} http://app.supramolecular.org/bindfit/view/683b035e-6918-4f6e-8995-c71aca7c4dcd

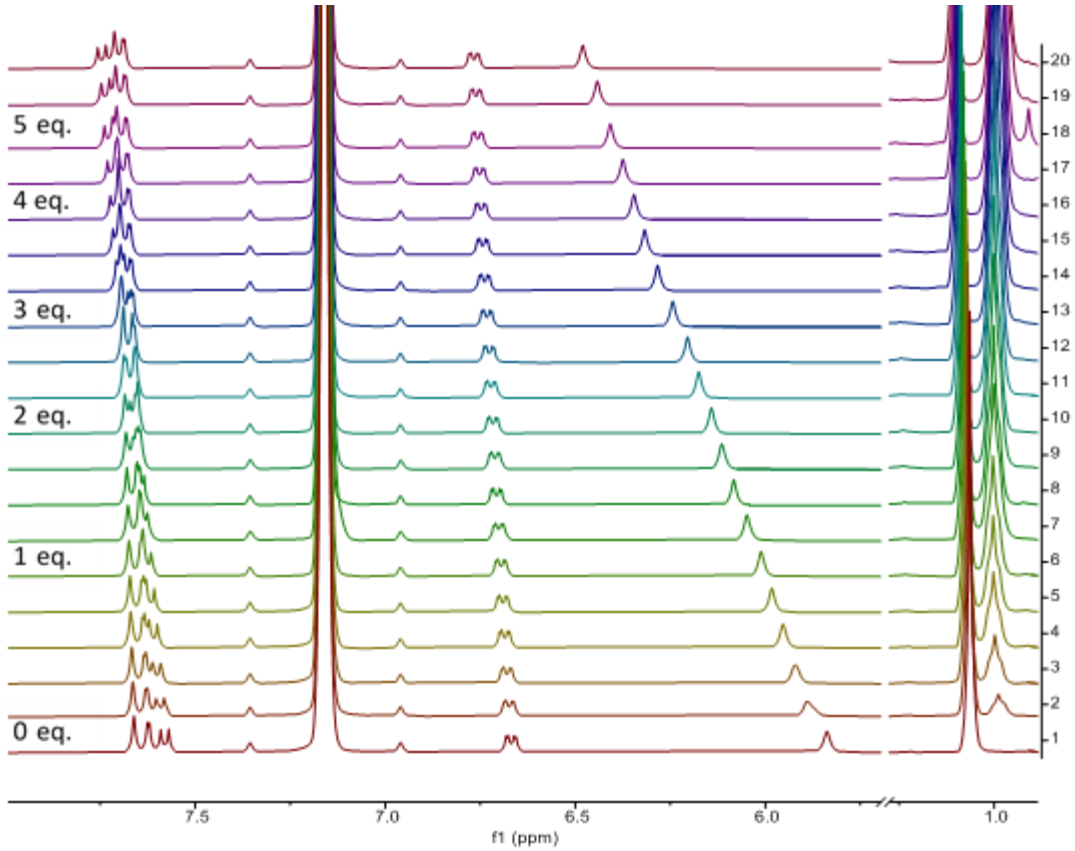

Figure S147-1. ^{1}H NMR spectra of **2*t*Bu-G3XB** upon addition of increasing equivalents of THA·I (C_6D_6, 298 K, 400 MHz).

Assay 2 K_a= 51.0 M^{-1} http://app.supramolecular.org/bindfit/view/fd255dc6-e87a-4e8c-84ca-b1f17ef54f0a

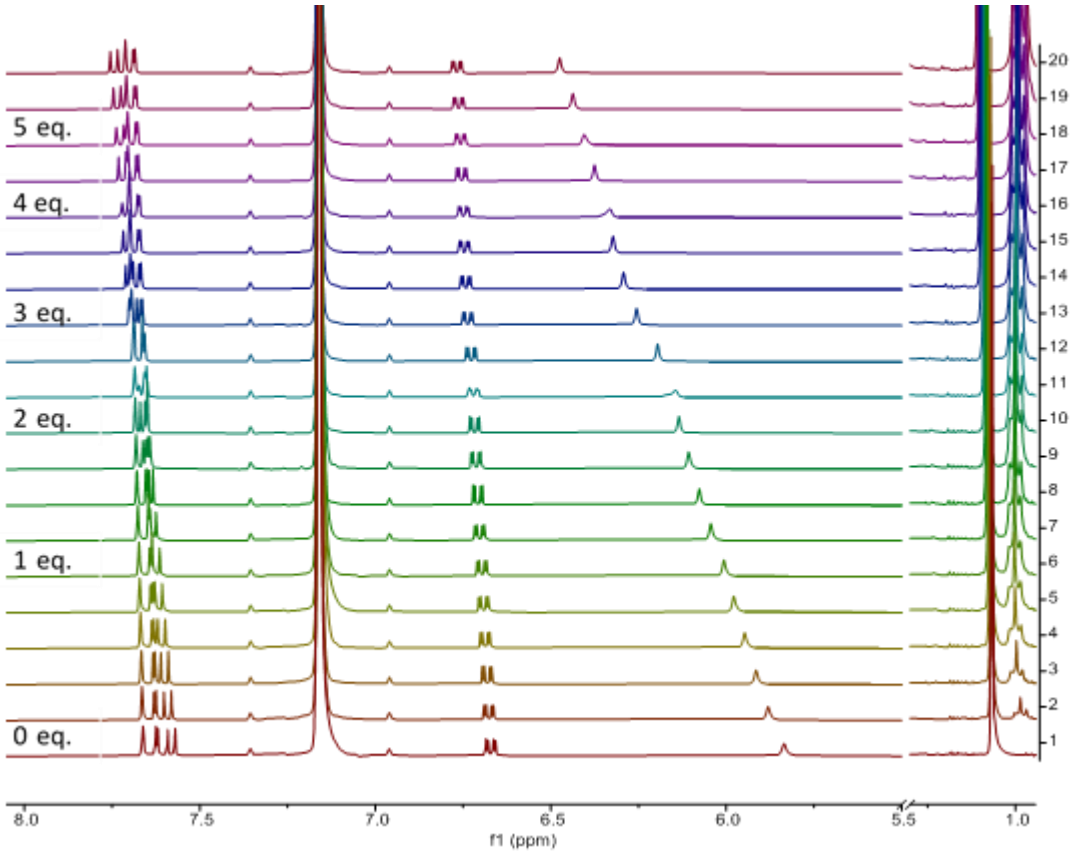

Figure S147-2. ^{1}H NMR spectra of **2*t*Bu-G3XB** upon addition of increasing equivalents of THA·I (C_6D_6, 298 K, 400 MHz).

Assay 3 K_a= 49.2 M^{-1} http://app.supramolecular.org/bindfit/view/429c33a3-777b-42b5-b81f-4d1995dc04bd

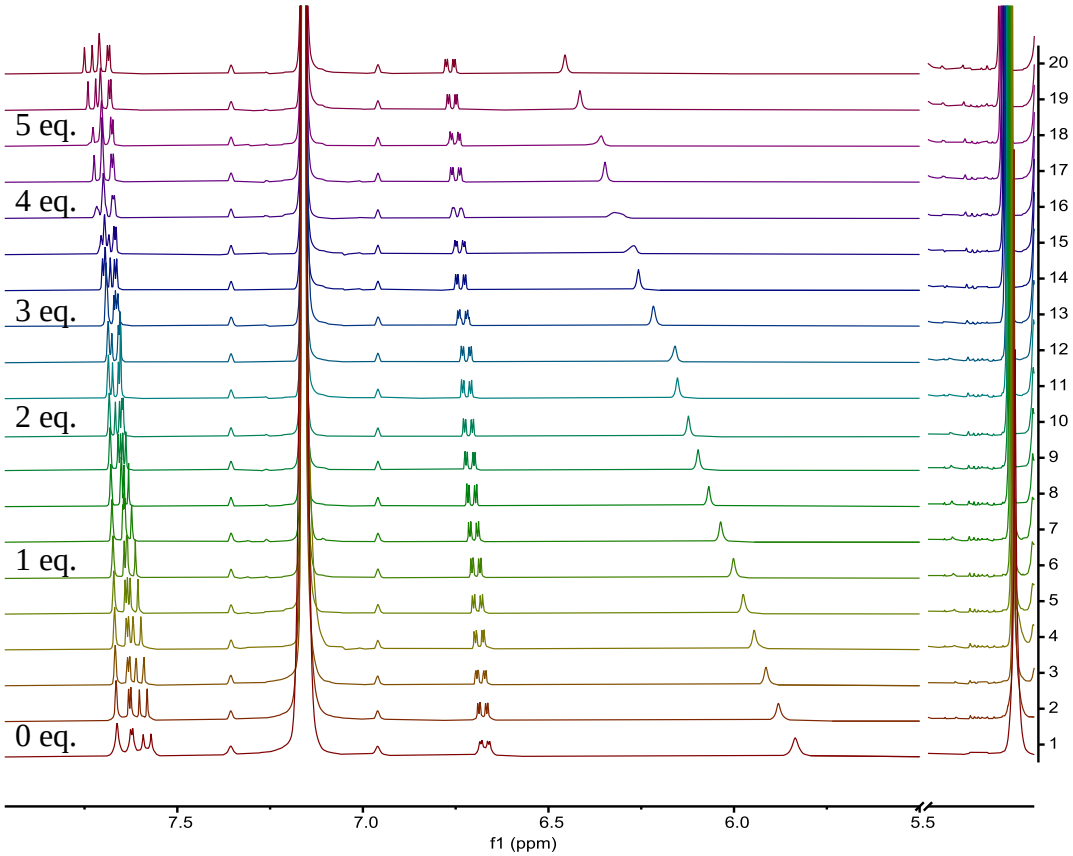

Figure S147-3. ^{1}H NMR spectra of **2*t*Bu-G3XB** upon addition of increasing equivalents of THA·I (C_6D_6, 298 K, 400 MHz).

2MeO-G3XB with THA iodide

Assay 1 K_a= 60.2 M^{-1} http://app.supramolecular.org/bindfit/view/e2d156d9-6430-4b9a-8181-8ba092d2dc8a

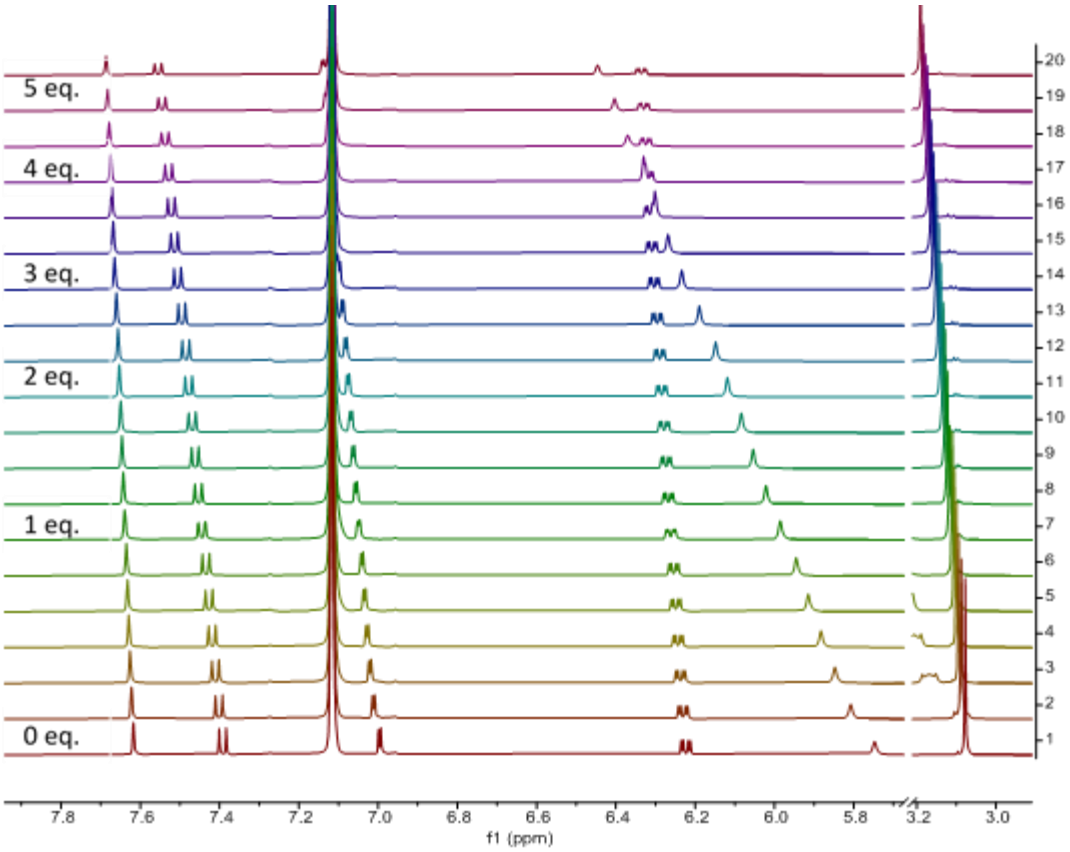

Figure S148-1. ^{1}H NMR spectra of **2MeO-G3XB** upon addition of increasing equivalents of THA·I (C_6D_6, 298 K, 500 MHz).

Assay 2 K_a= 63.6 M^{-1} http://app.supramolecular.org/bindfit/view/911973d0-3399-4738-92a4-fa05f18e5959

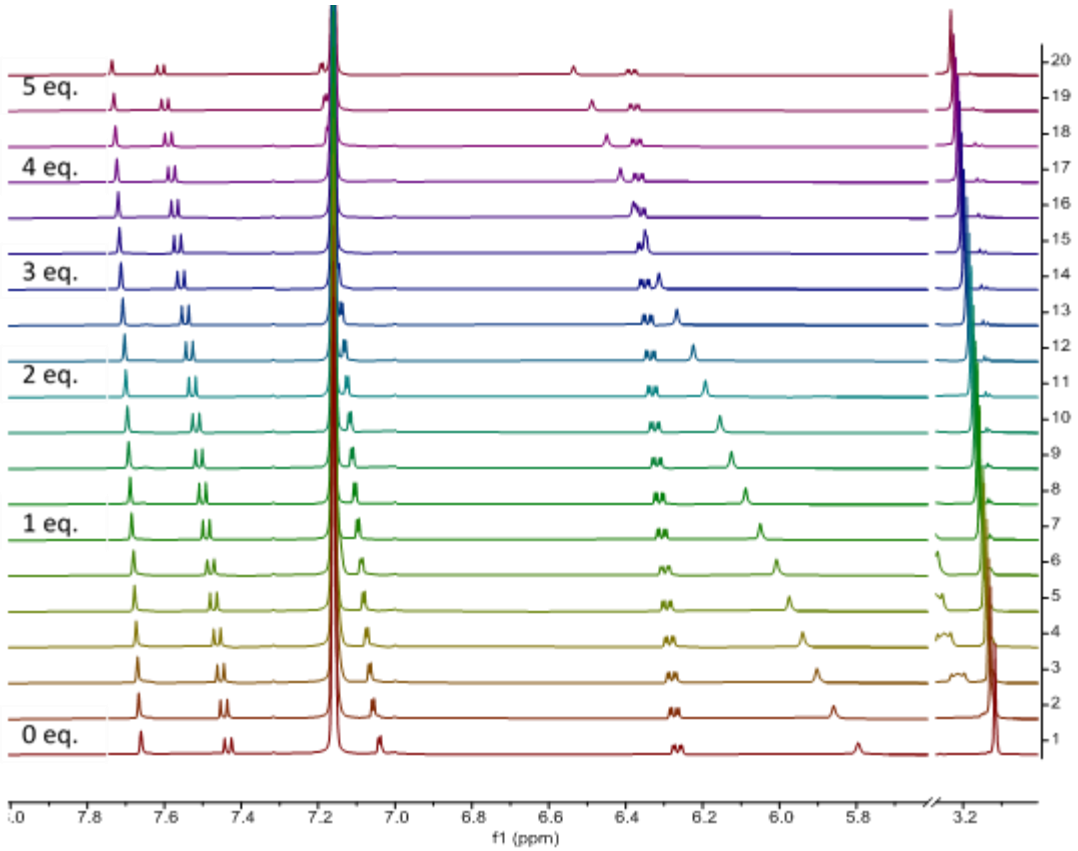

Figure S148-2. ^{1}H NMR spectra of **2MeO-G3XB** upon addition of increasing equivalents of THA·I (C_6D_6, 298 K, 500 MHz).

Assay 3 K_a= 63.2 M^{-1} http://app.supramolecular.org/bindfit/view/c15738b4-3ebf-430b-95e8-2cb0a3388a03

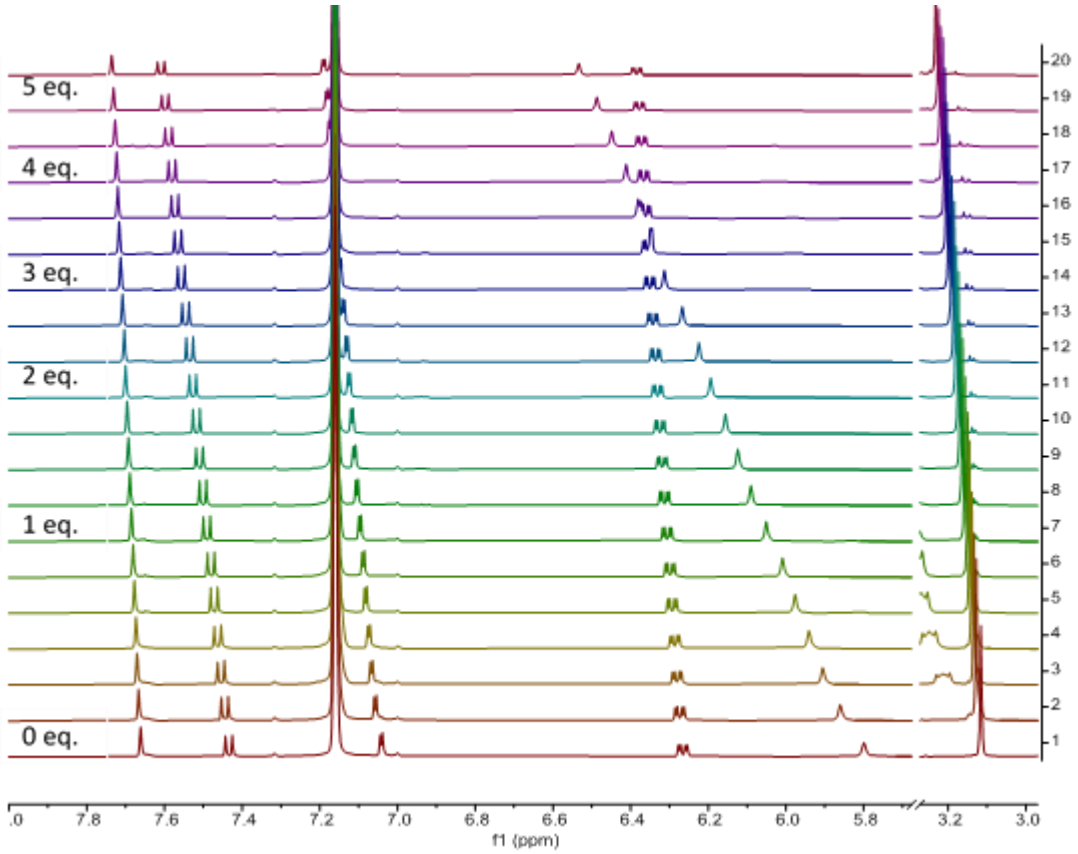

Figure S148-3. ^{1}H NMR spectra of **2MeO-G3XB** upon addition of increasing equivalents of THA·I (C_6D_6, 298 K, 500 MHz).

Cl-G3XB with THA iodide

Assay 1 K_a=330.0 M^{-1} http://app.supramolecular.org/bindfit/view/75f56ee4-d8a9-4703-9cae-0c7493e2ca0a

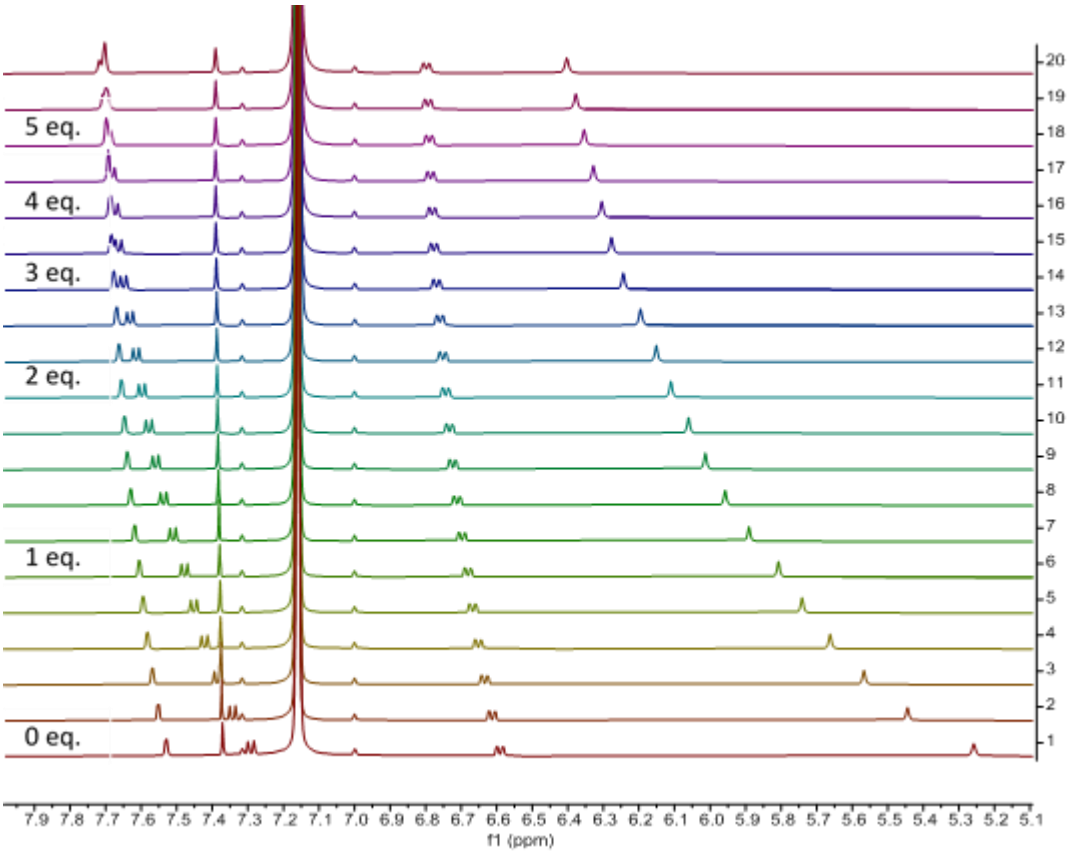

Figure S149-1. ^{1}H NMR spectra of **Cl-G3XB** upon addition of increasing equivalents of THA·I (C_6D_6, 298 K, 500 MHz).

Assay 2 K_a=317.7 M^{-1} http://app.supramolecular.org/bindfit/view/f0c61398-8b18-4b85-89cf-594c0491549e

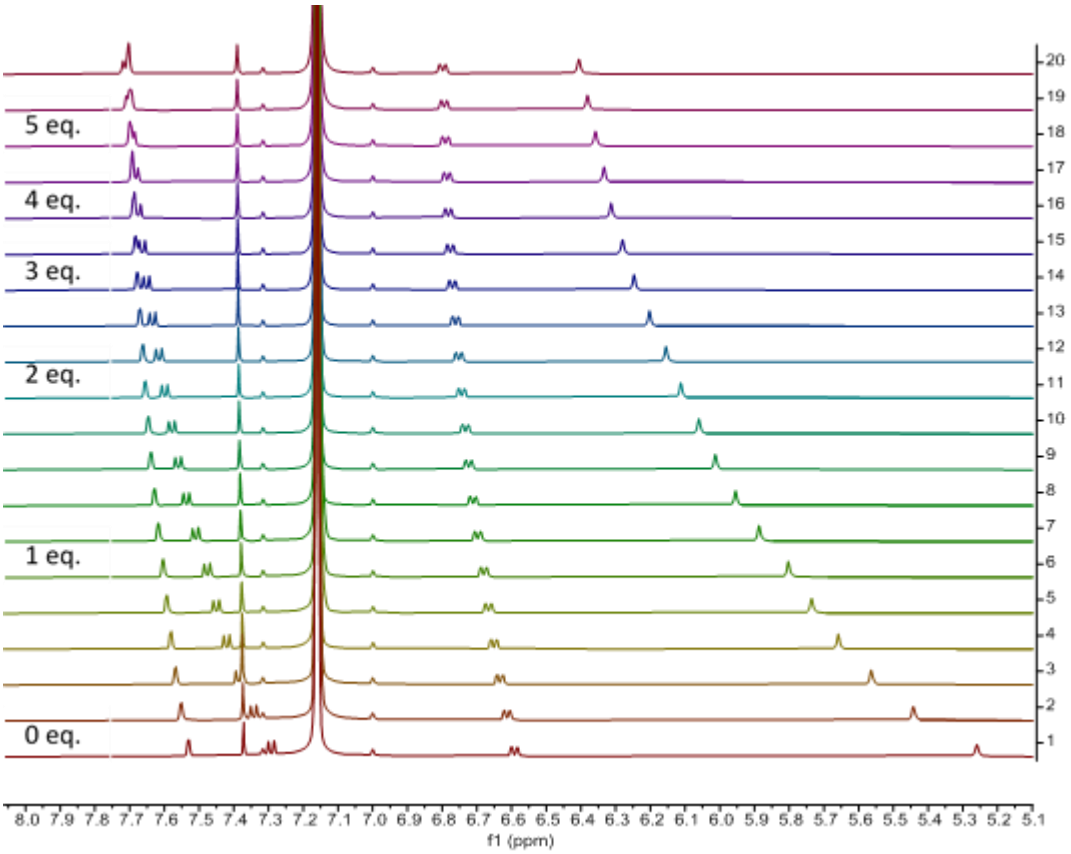

Figure S149-2. ^{1}H NMR spectra of **Cl-G3XB** upon addition of increasing equivalents of THA·I (C_6D_6, 298 K, 500 MHz).

Assay 3 K_a= 345.4 M^{-1} http://app.supramolecular.org/bindfit/view/1cb0201b-3798-4796-9753-9e3bc55ccd83

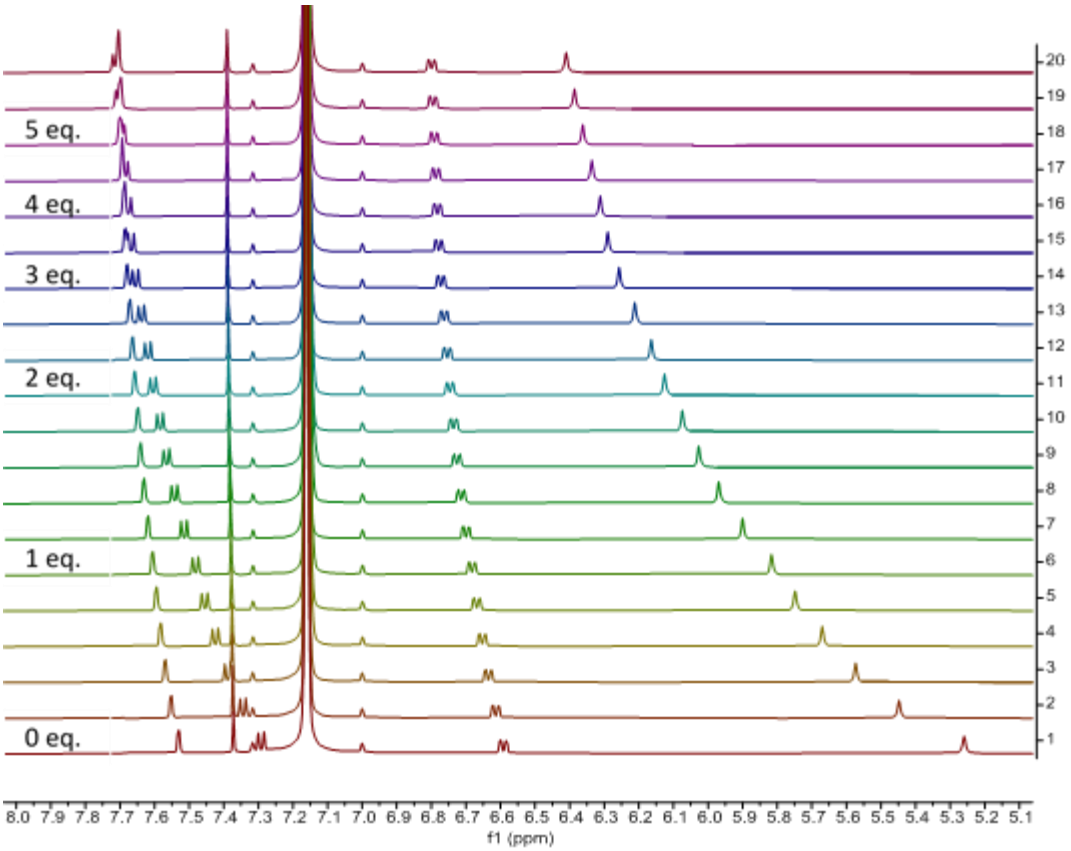

Figure S149-3. ^{1}H NMR spectra of **Cl-G3XB** upon addition of increasing equivalents of THA·I (C_6D_6, 298 K, 500 MHz).

F-G3XB with THA iodide

Assay 1 K_a= 236.4 M^{-1} http://app.supramolecular.org/bindfit/view/7b565776-3cc2-4956-ae6e-249da1dc7ee6

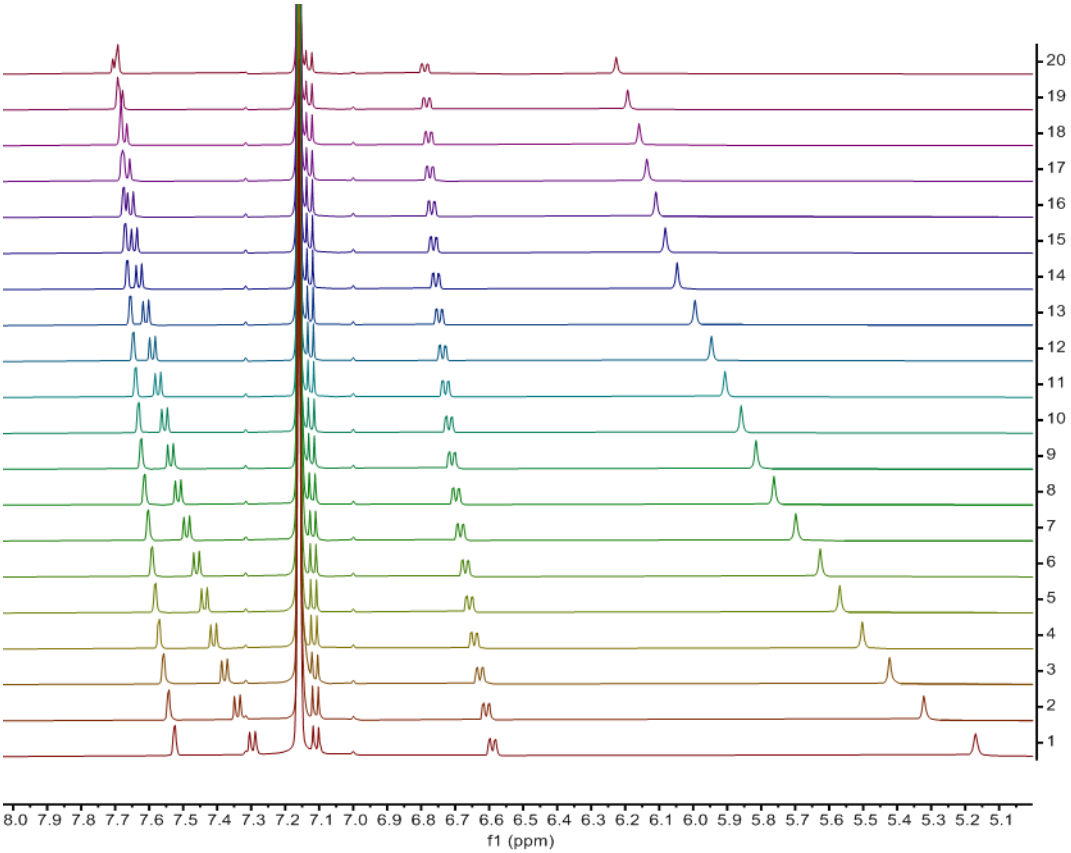

Figure S150-1. ^{1}H NMR spectra of **F-G3XB** upon addition of increasing equivalents of THA·I (C_6D_6, 298 K, 500 MHz).

Assay 2 K_a= 274.4 M^{-1} http://app.supramolecular.org/bindfit/view/a5ed5e27-8f4b-43a7-975b-1f0fb3b071b8

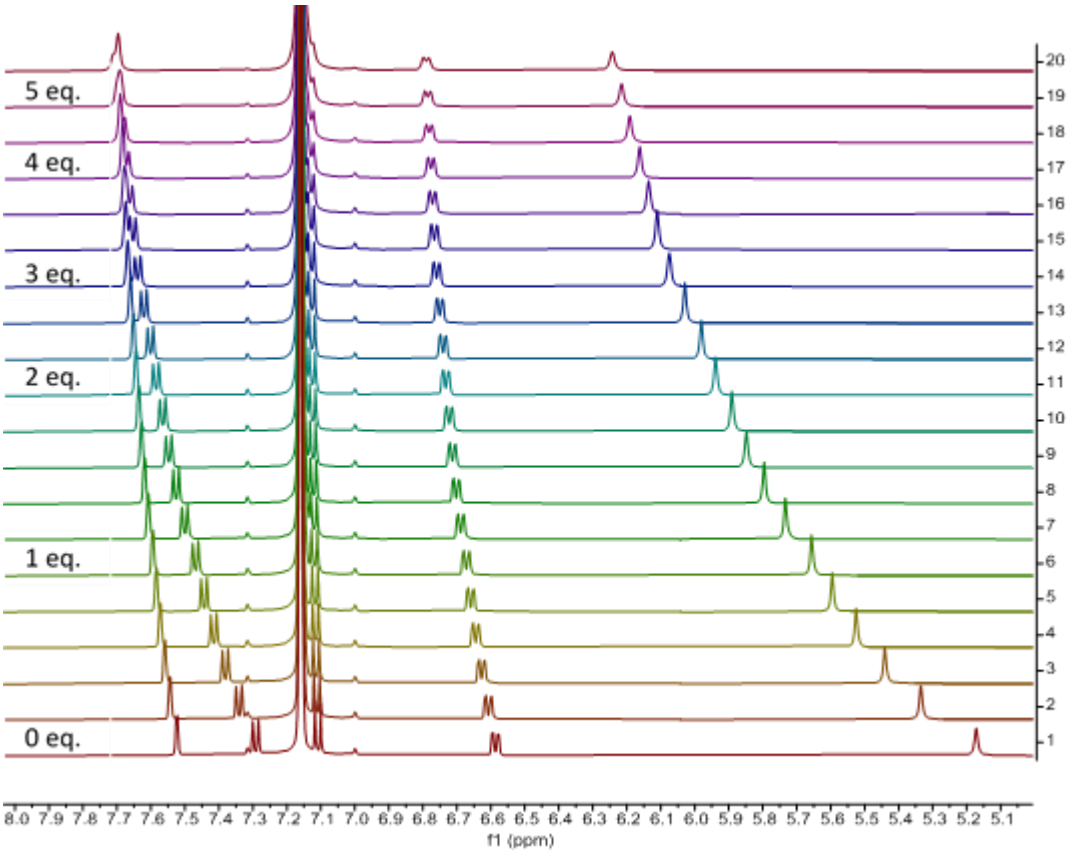

Figure S150-2. ^{1}H NMR spectra of **F-G3XB** upon addition of increasing equivalents of THA·I (C_6D_6, 298 K, 500 MHz).

Assay 3 K_a= 241.1 M^{-1} http://app.supramolecular.org/bindfit/view/ed534960-85cd-4a81-bb80-9e35b275c9d0

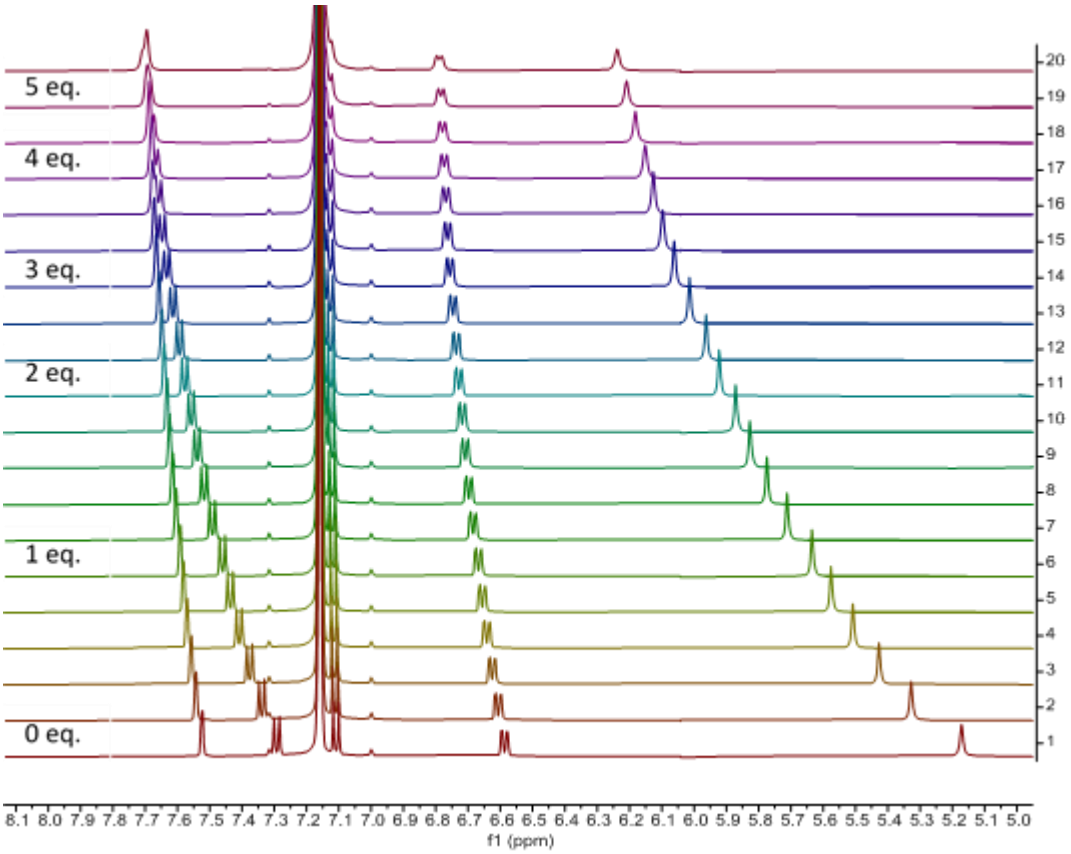

Figure S150-3. ^{1}H NMR spectra of **F-G3XB** upon addition of increasing equivalents of THA·I (C_6D_6, 298 K, 500 MHz).

H-G3XB with THA iodide

Assay 1 K_a= 194.6 M^{-1} http://app.supramolecular.org/bindfit/view/17befb01-d3f6-4d27-bf34-4c9c67c9ca8c

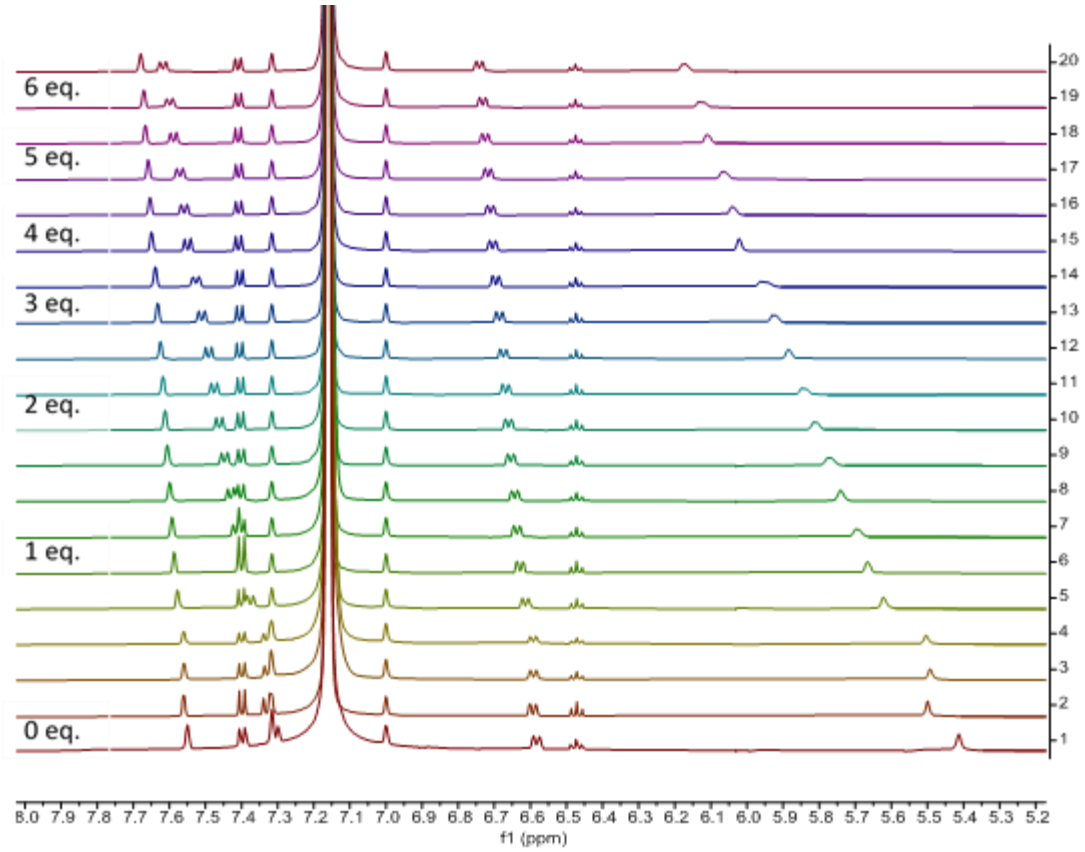

Figure S151-1. ^{1}H NMR spectra of **H-G3XB** upon addition of increasing equivalents of THA·I (C_6D_6, 298 K, 500 MHz).

Assay 2 K_a= 199.1 M^{-1} http://app.supramolecular.org/bindfit/view/8c81c119-d5b1-408a-a314-c9c82af2eac8

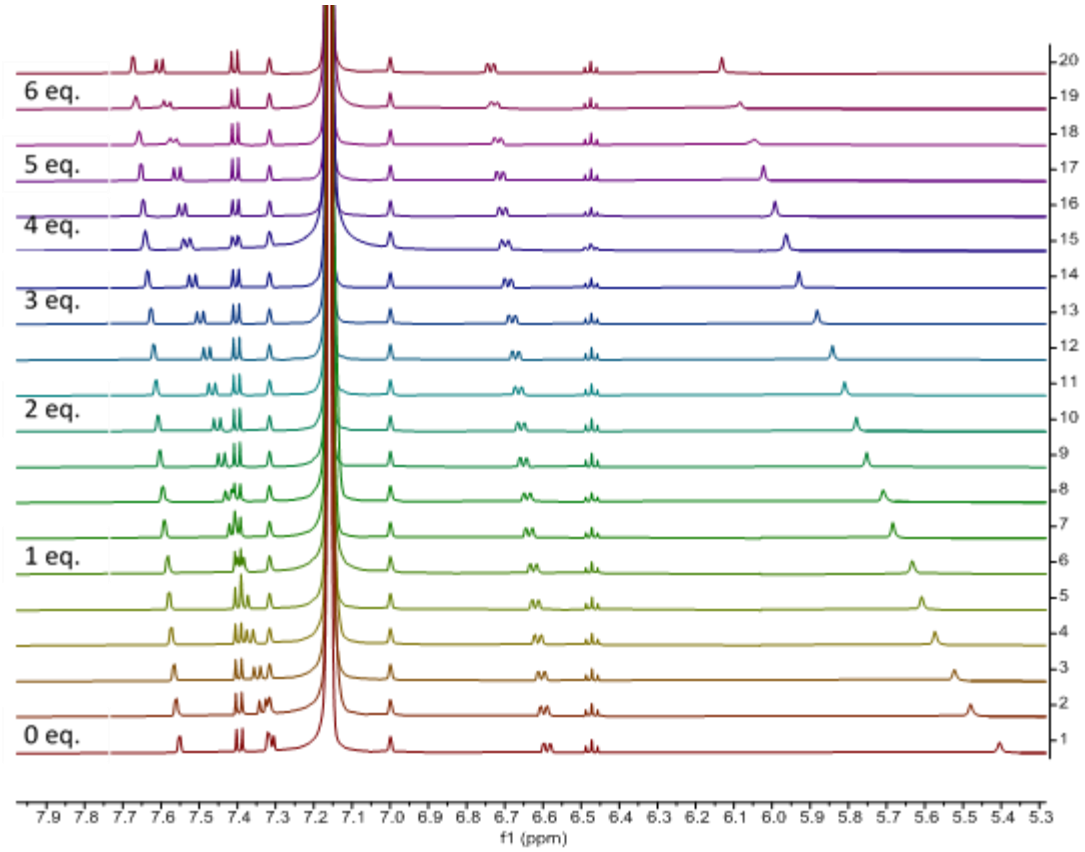

Figure S151-2. ^{1}H NMR spectra of **H-G3XB** upon addition of increasing equivalents of THA·I (C_6D_6, 298 K, 500 MHz).

Assay 3 K_a= 188.8 M^{-1} http://app.supramolecular.org/bindfit/view/f9dda397-b6ad-4f30-9b80-56fea76e0b2c

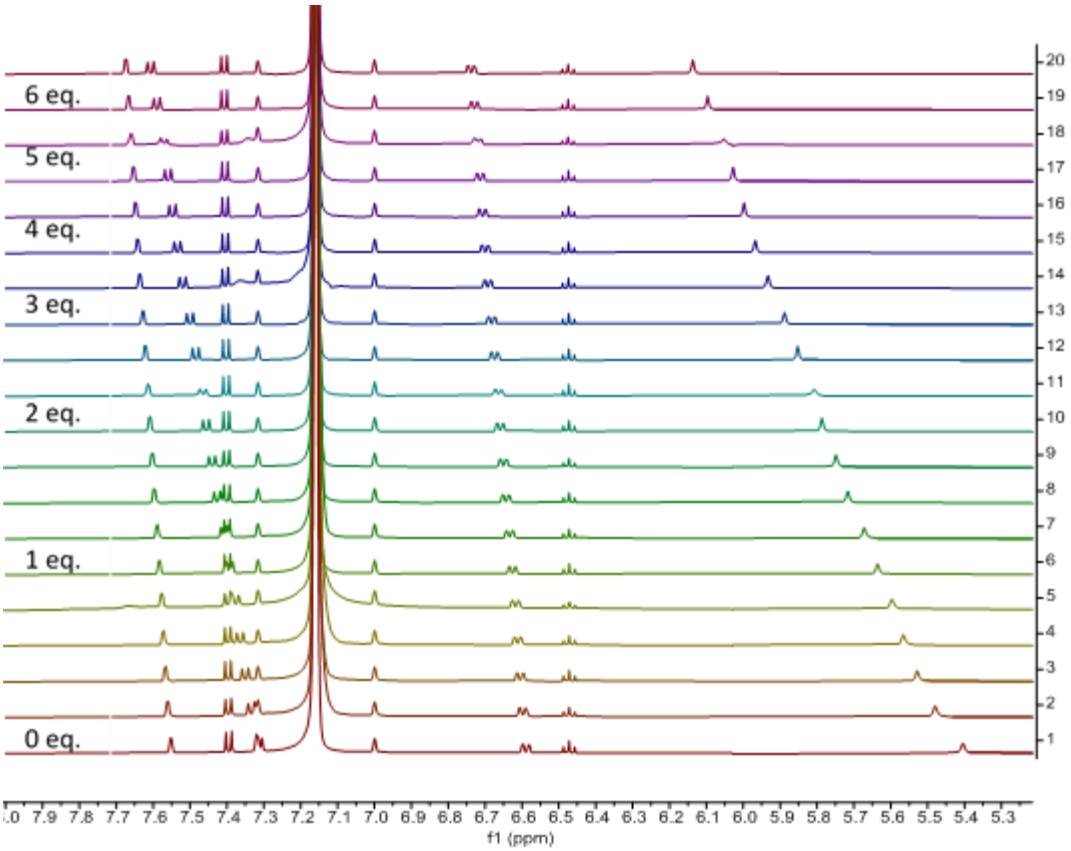

Figure S151-3. ^{1}H NMR spectra of **H-G3XB** upon addition of increasing equivalents of THA·I (C_6D_6, 298 K, 500 MHz).

Me-G3XB with THA iodide

Assay 1 K_a= 182.0 M^{-1} http://app.supramolecular.org/bindfit/view/c2346362-48e8-41e3-90c1-53aae0eb5eeb

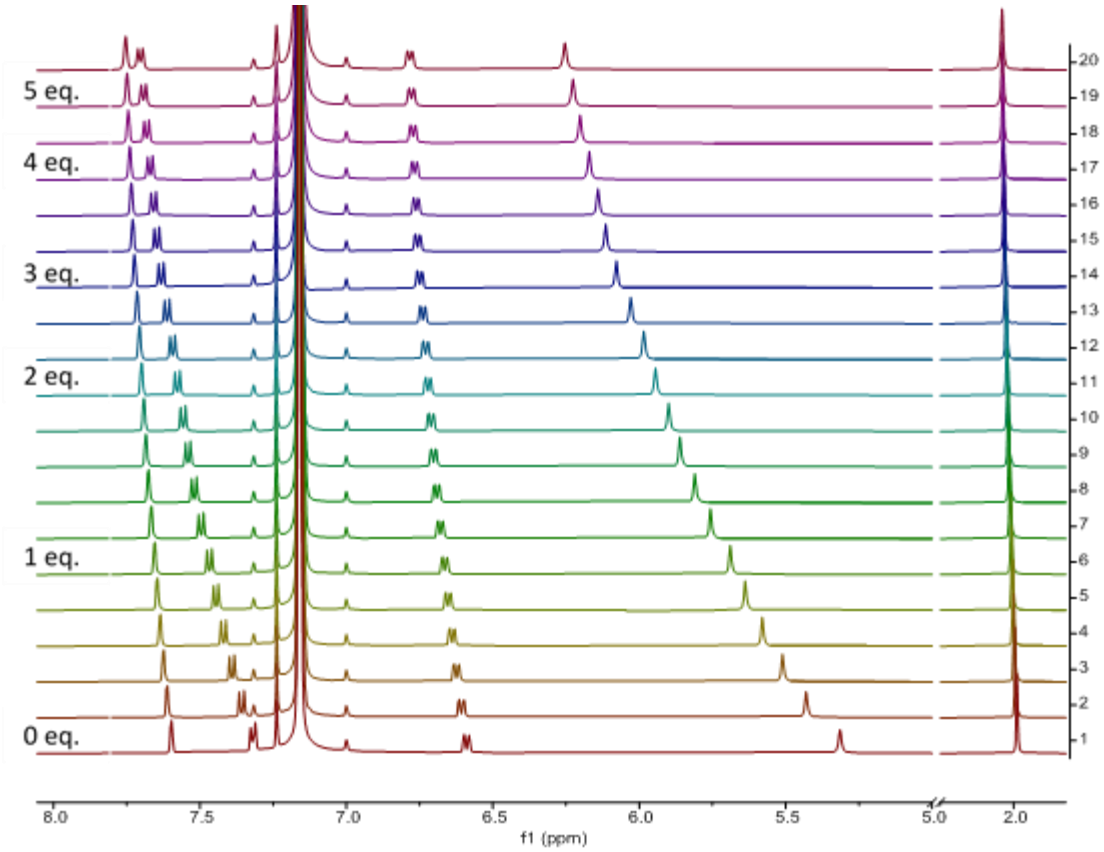

Figure S152-1. ^{1}H NMR spectra of **Me-G3XB** upon addition of increasing equivalents of THA·I (C_6D_6, 298 K, 500 MHz).

Assay 2 K_a= 171.7 M^{-1} http://app.supramolecular.org/bindfit/view/d3632f46-0eea-411e-9b0f-4a90ccbbbed8

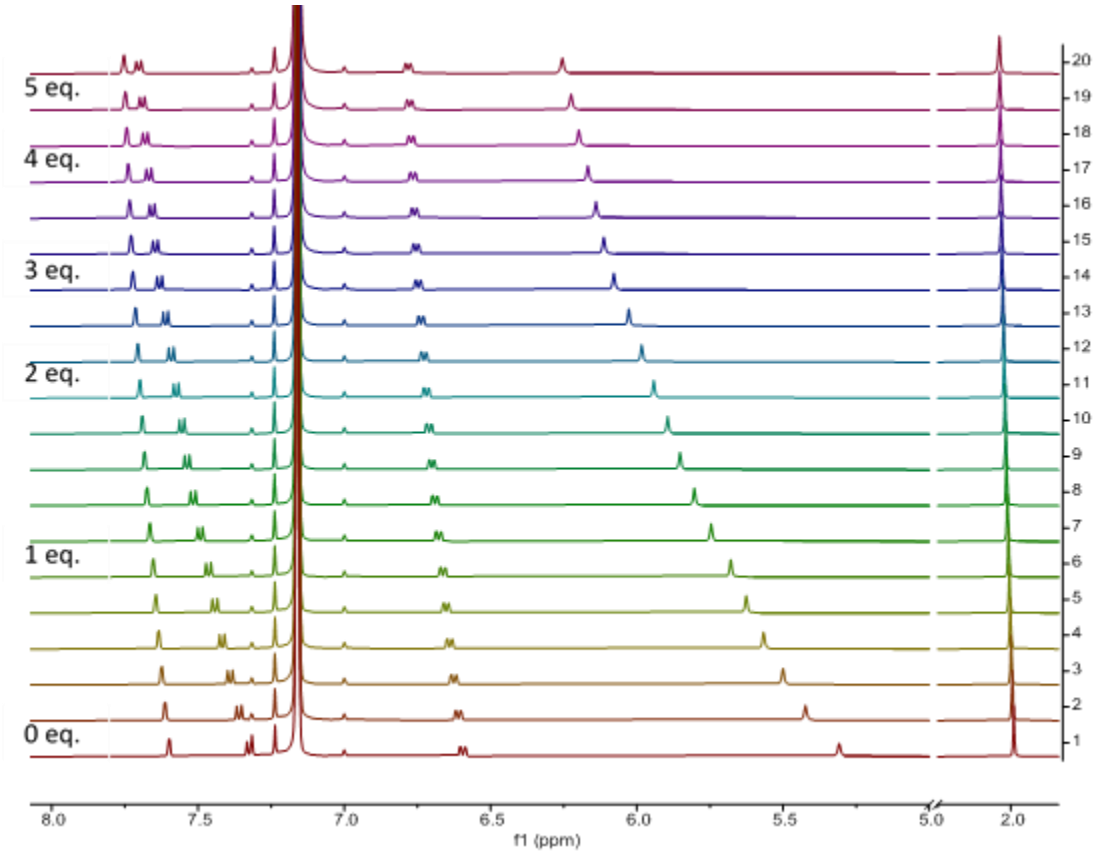

Figure S152-2. ^{1}H NMR spectra of **Me-G3XB** upon addition of increasing equivalents of THA·I (C_6D_6, 298 K, 500 MHz).

Assay 3 K_a= 170.2 M^{-1} http://app.supramolecular.org/bindfit/view/74be5d95-2df8-47cf-905a-4cda87ec7d65

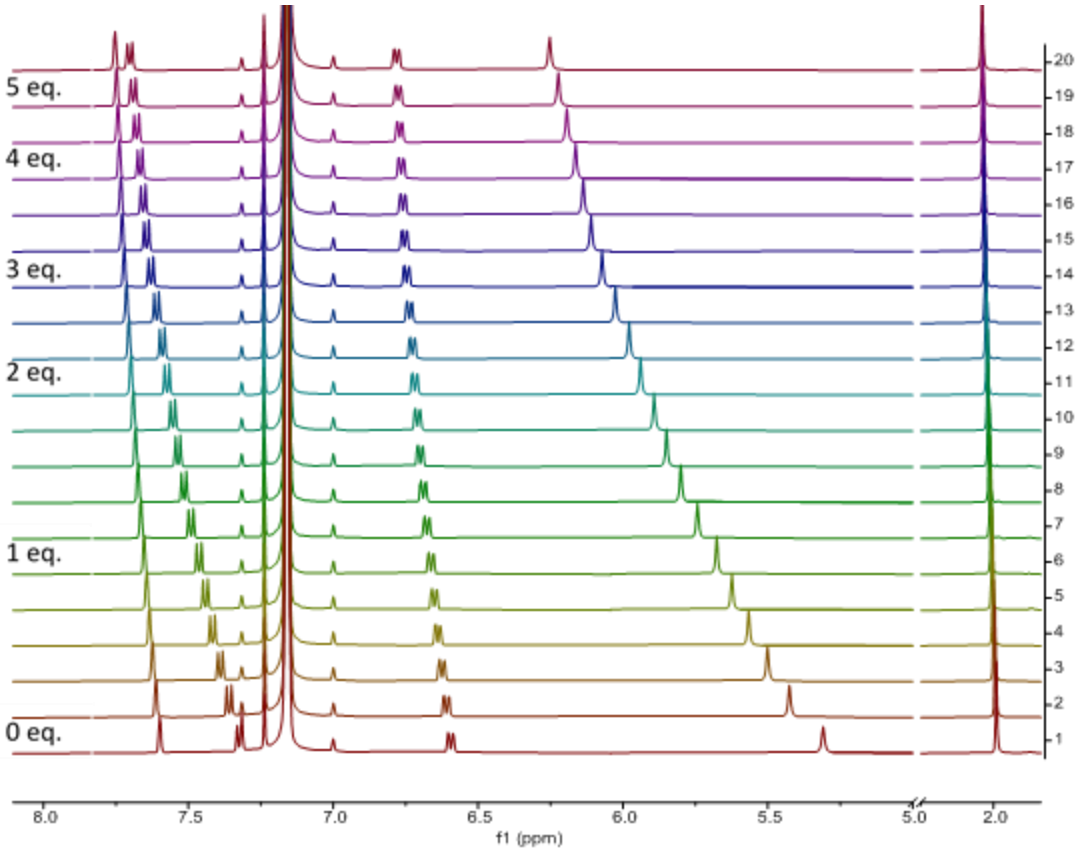

Figure S153-3. ^{1}H NMR spectra of **Me-G3XB** upon addition of increasing equivalents of THA·I (C_6D_6, 298 K, 500 MHz).

nHBeXB with THA iodide

Assay 1 K_a= 12.4 M^{-1} http://app.supramolecular.org/bindfit/view/7e08d321-604f-45b4-869d-2dd0451a9fea

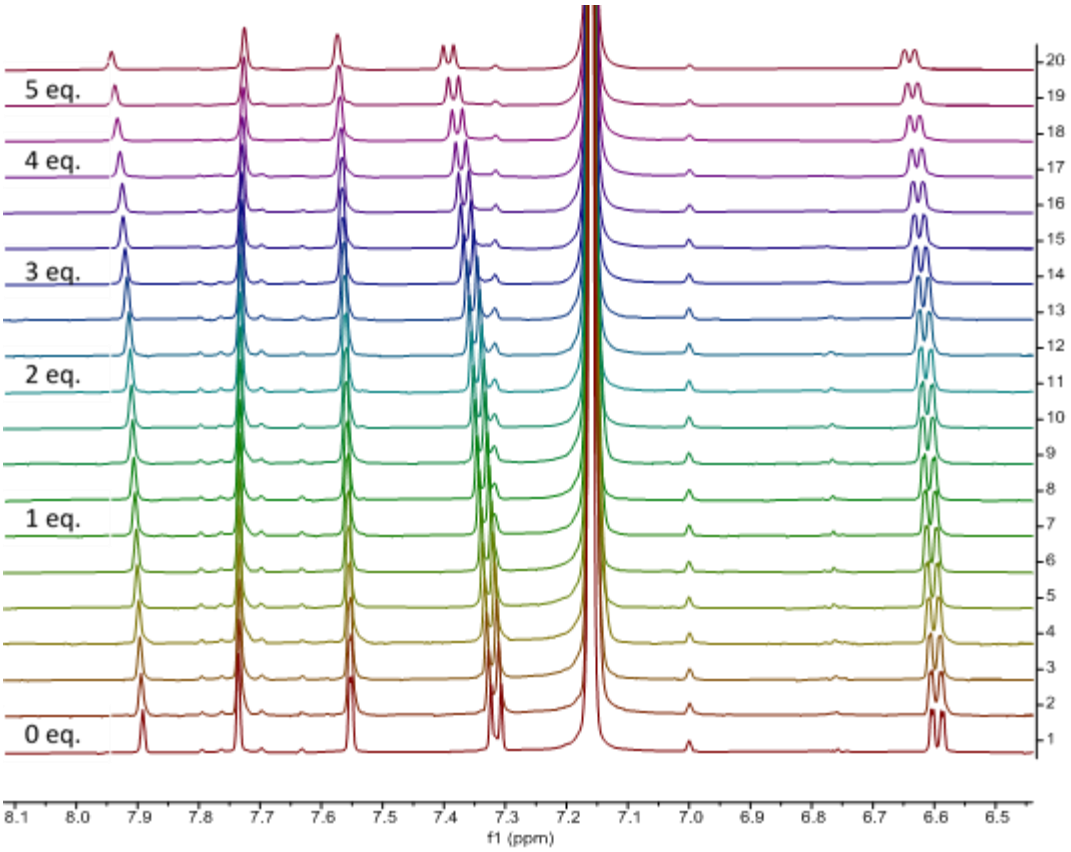

Figure S154-1. ^{1}H NMR spectra of **nHBeXB** upon addition of increasing equivalents of THA·I (C_6D_6, 298 K, 500 MHz).

Assay 2 K_a= 4.4 M^{-1} http://app.supramolecular.org/bindfit/view/29d125a6-7c77-4292-83bb-9e8b03dbcd1b

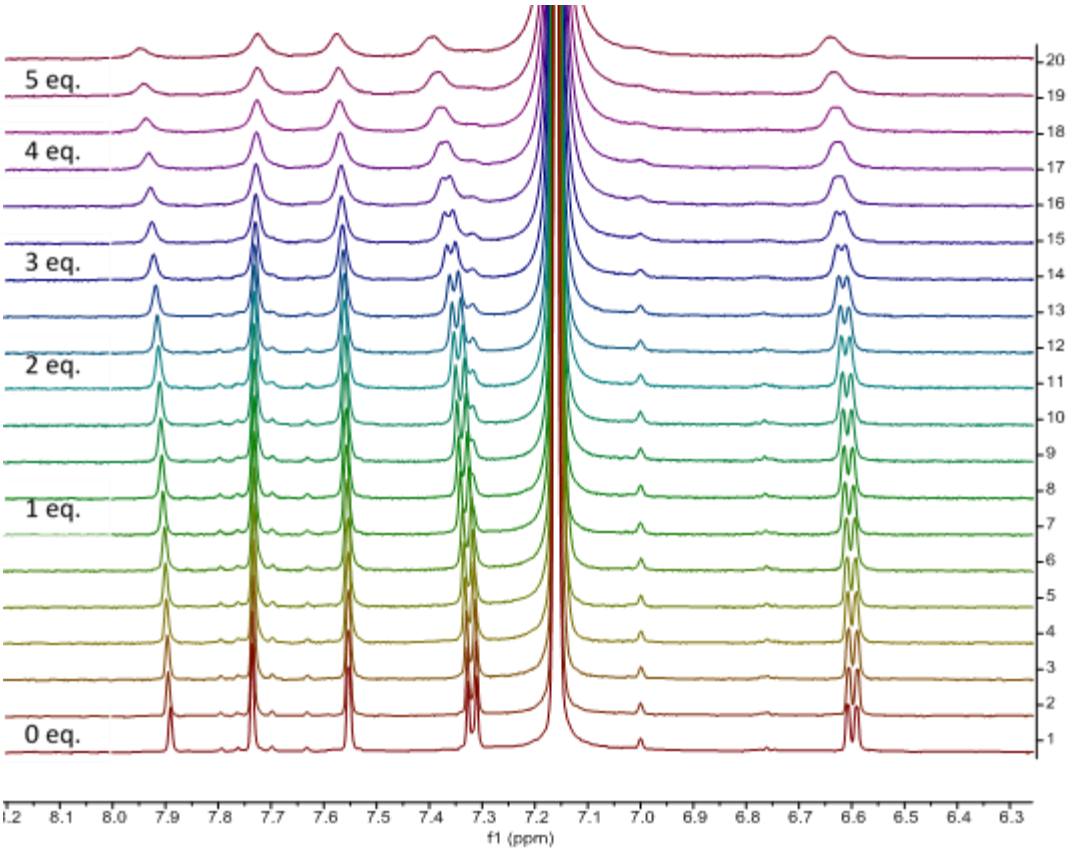

Figure S154-2. ^{1}H NMR spectra of **nHBeXB** upon addition of increasing equivalents of THA·I (C_6D_6, 298 K, 500 MHz).

Assay 3 K_a= 8.0 M^{-1} http://app.supramolecular.org/bindfit/view/da8fec06-3b2f-4e26-8bd9-0b9467705ec2

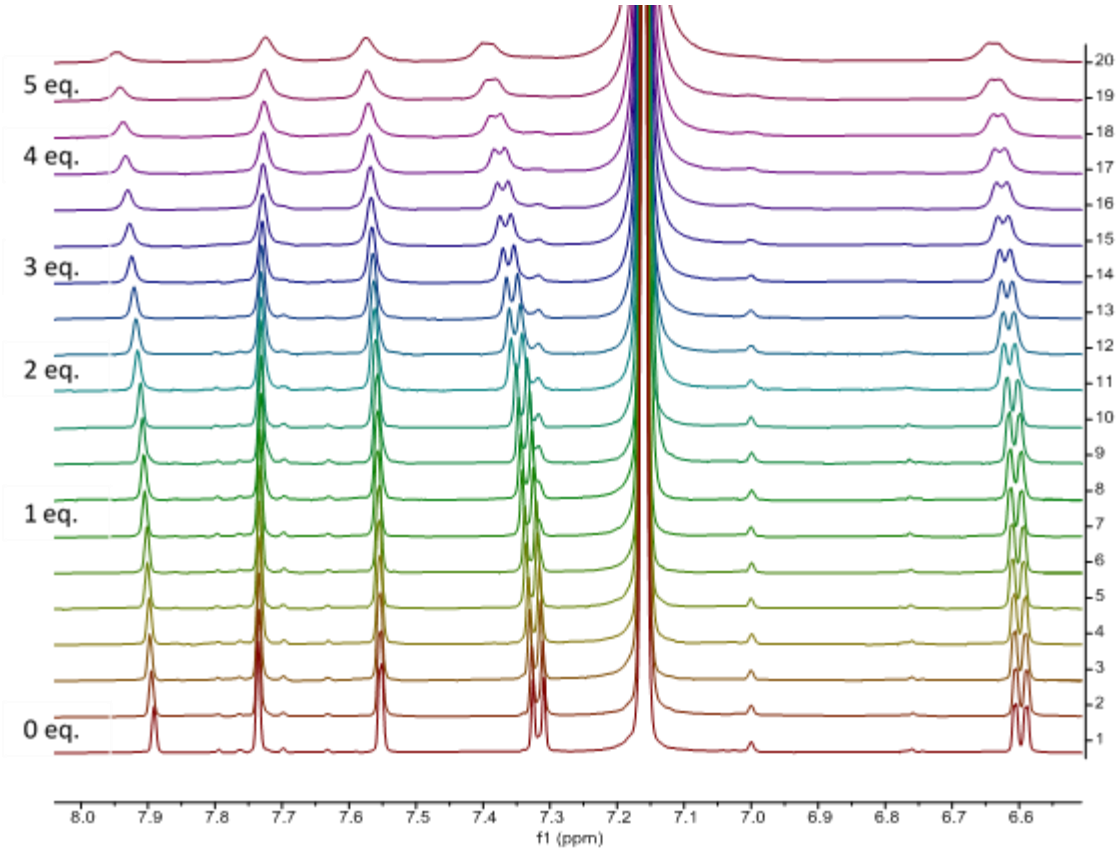

Figure S154-3. ^{1}H NMR spectra of **nHBeXB** upon addition of increasing equivalents of THA·I (C_6D_6, 298 K, 500 MHz).

G3HB with THA iodide

Assay 1 K_a= 36.8 M^{-1} http://app.supramolecular.org/bindfit/view/6847ebbe-5e75-417c-a18f-3b9e06f6c3fe

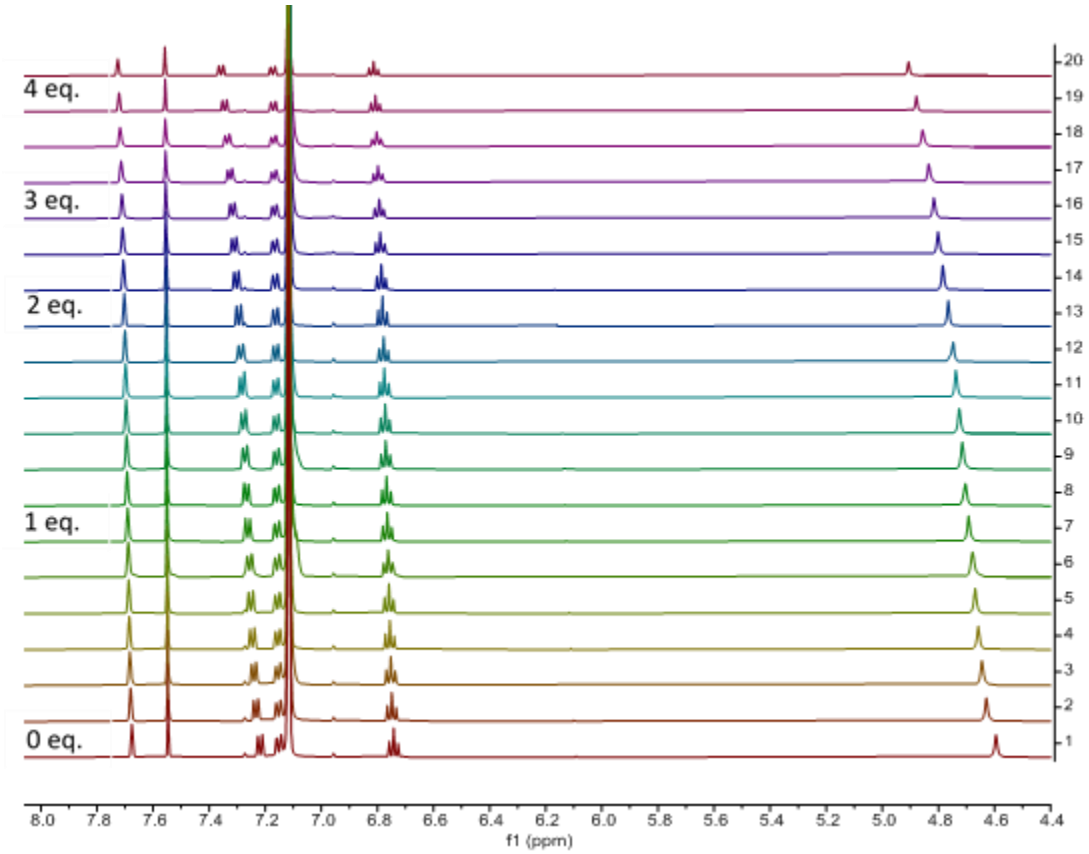

Figure S155-1. ^{1}H NMR spectra of **G3HB** upon addition of increasing equivalents of THA·I (C_6D_6, 298 K, 500 MHz).

Assay 2 K_a= 22.5 M^{-1} http://app.supramolecular.org/bindfit/view/29553f62-9021-445b-85b1-32cd17529328

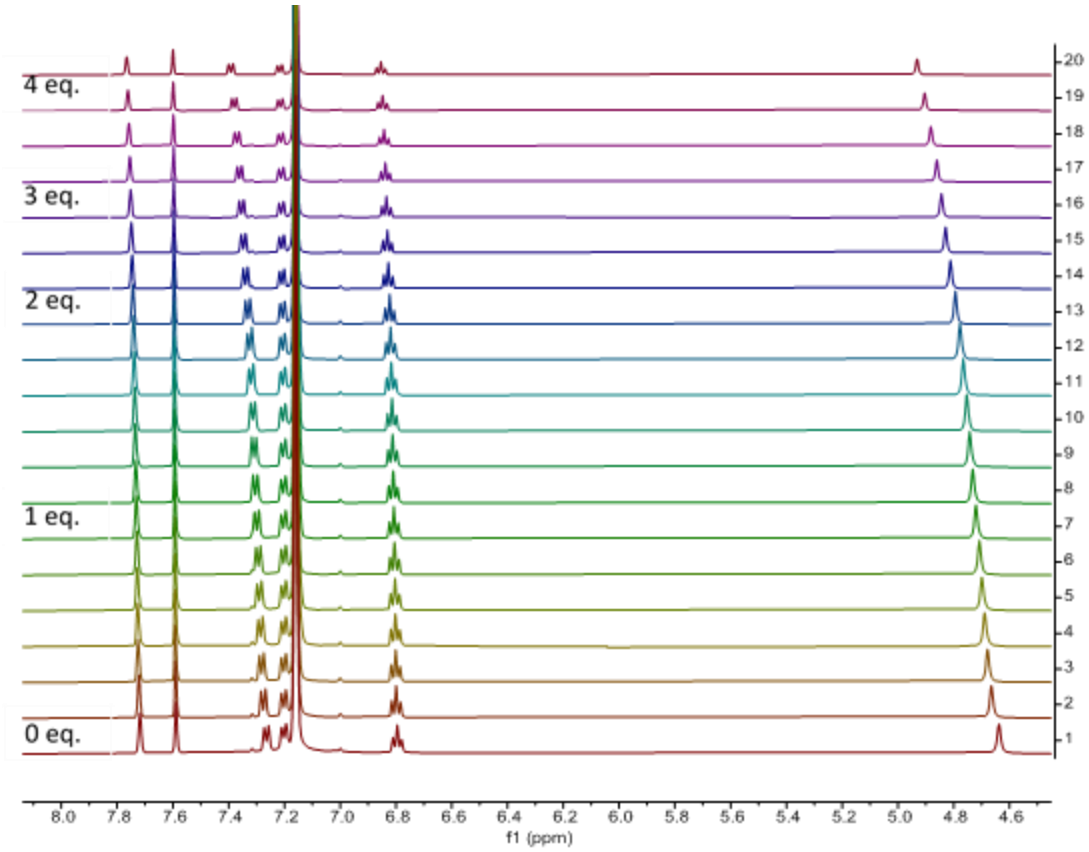

Figure S155-2. ^{1}H NMR spectra of **G3HB** upon addition of increasing equivalents of THA·I (C_6D_6, 298 K, 500 MHz).

Assay 3 K_a= 23.2 M^{-1} http://app.supramolecular.org/bindfit/view/ff9ef97c-9dea-47c3-865d-9a8fab9e4b50

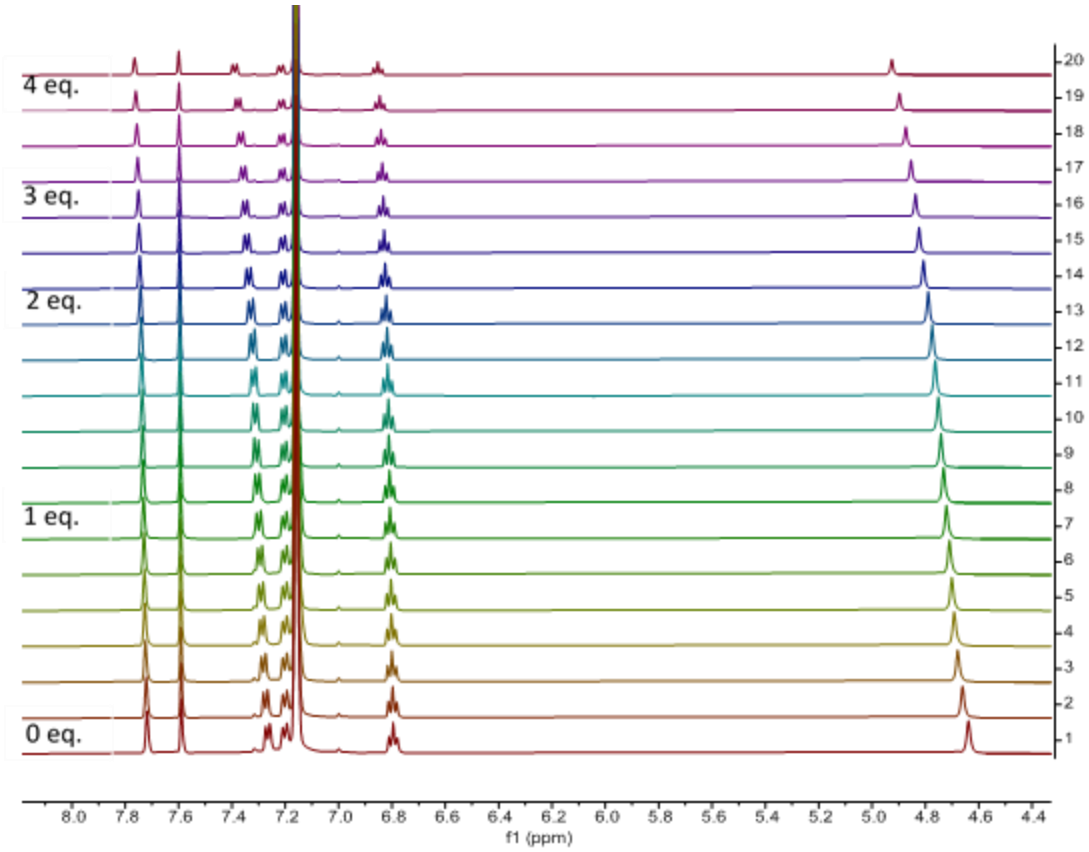

Figure S155-3. ^{1}H NMR spectra of **G3HB** upon addition of increasing equivalents of THA·I (C_6D_6, 298 K, 500 MHz).

Linear free energy relationships

Besides Hammett parameters, we also plotted the association constants obtained from NMR titrations with other parameters including Taft's σ_I, σ_R[6] and Dobrowolski's sEDA, pEDA[7].

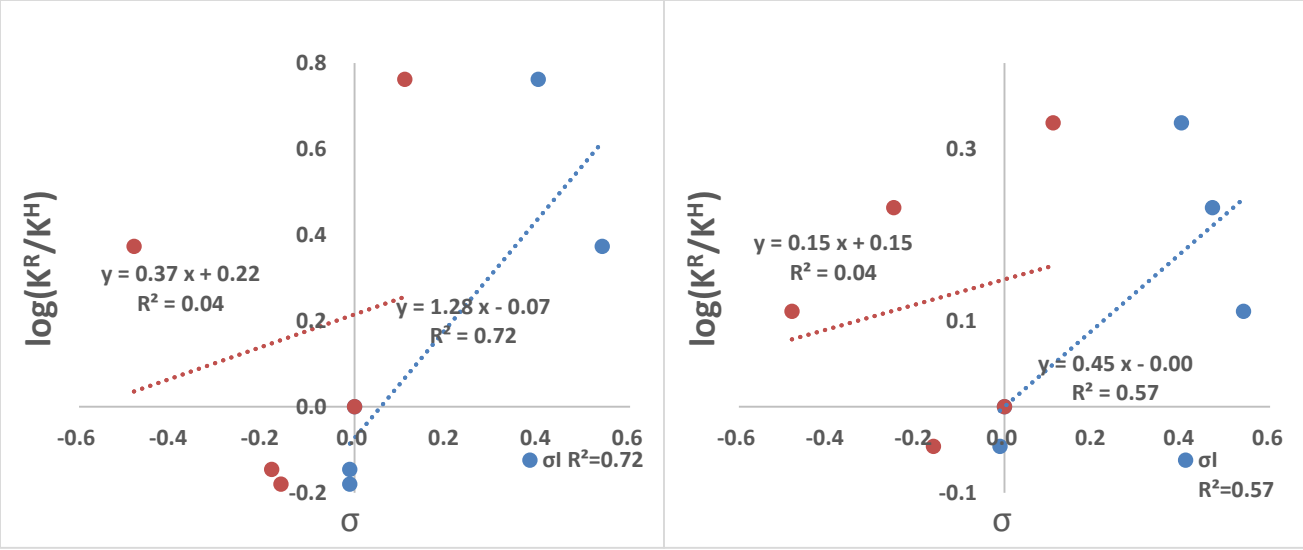

Figure S156. Normalized Hammett plots of K values of **2R$_2$-G3XB** (Left) and **R$_1$-G3XB** (Right) with σI (Blue) and σR (Orange).

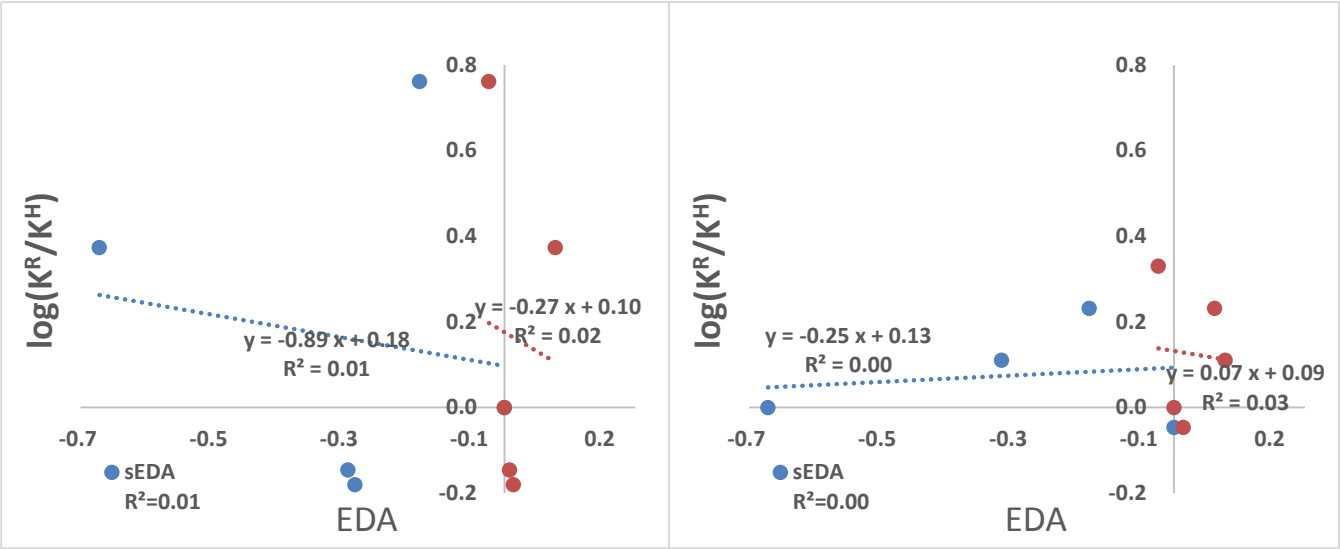

Figure S157. Normalized Hammett plots of K values of **2R$_2$-G3XB** (Left) and **R$_1$-G3XB** (Right) with sEDA (Blue) and pEDA (Orange).

Computaions

Calculations were carried out with the Gaussian 16 suite of programs using M062X functional employing the def2TZVPP basis set for all atoms except iodine. For iodine LANL2DZdp and effective core potential (ECP) were used. The LANL2DZdp ECP basis set was downloaded from the EMSL Basis Set Exchange (https://bse.pnl.gov/bse/portal).

Table S3-1. Computation results summary

	$V_{s,max}$ (kcal/mol)	$V_{s,min}$ (kcal/mol)	SPE (kcal/mol)		$V_{s,max}$(HBed) (kcal/mol)	$V_{s,max}$(non-HBed) (kcal/mol)	SPE (kcal/mol)	$\Delta V_{s,max}$ (kcal/mol)		$V_{s,max}$ (kcal/mol)	SPE (kcal/mol)
G3XB	32.05	-1.11	-1573352.23	**G3XB-S**	31.45	24.46	-1573350.70	6.99	**G3XB-W**	24.64	-1573349.12
2F-G3XB	28.40	-4.14	-1274864.51	**2F-G3XB-S**	28.52	20.94	-1274862.74	7.58			
2H-G3XB	24.98	-7.22	-1150303.91	**2H-G3XB-S**	26.05	17.95	-1150302.08	8.10			
2Me-G3XB	23.03	-9.43	-1199640.14	**2Me-G3XB-S**	24.69	16.94	-1199638.23	7.75			
2MeO-G3XB	22.96	-8.87	-1294035.26	**2MeO-G3XB-S**	23.25	15.73	-1294032.74	7.52			
2*t*Bu-G3XB	22.41	-11.14	-1347636.51	**2*t*Bu-G3XB-S**	24.37	16.15	-1347634.36	8.18			
Cl-G3XB	30.84		-1650226.19	**Cl-G3XB-S**	29.85	24.16	-1650224.76	5.69			
F-G3XB	30.12		-1424105.19	**F-G3XB-S**	29.33	24.61	-1424103.85	4.72			
H-G3XB	28.72		-1361826.55	**H-G3XB-S**	28.08	24.07	-1361825.11	4.01			
Me-G3XB	28.11		-1386493.72	**Me-G3XB-S**	27.36	24.04	-1386492.36	3.32			
G3HB											
nHBeXB	28.03		-1538603.60	**nHBeXB-S**	26.64	25.39	-1538603.61				

Table S3-2. Computation results summary continued

Dihedral Freeze	$V_{s,max}$(HBed) (kcal/mol)	$V_{s,max}$(non-HBed) (kcal/mol)	$\Delta V_{s,max}$ (kcal/mol)
G3XB-S	31.62	24.98	6.65
2F-G3XB-S	28.67	20.85	7.82
2H-G3XB-S	26.17	18.28	7.89
2Me-G3XB-S	24.99	16.46	8.53
2MeO-G3XB-S	23.31	15.73	7.58
2*t*Bu-G3XB-S	24.67	16.06	8.61

G3XB bidentate

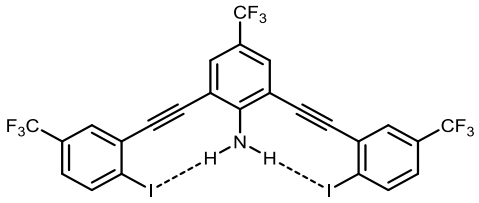

Coordinates for **G3XB bidentate**:

0 1

I	2.9778167	-2.7396896	-0.3462496
C	0.0111348	5.4783418	0.0113884
N	-0.0015477	-0.1739476	0.0079975
H	0.8673365	-0.6824503	-0.0002460
H	-0.8707141	-0.6820348	0.0141493
C	7.1194457	-1.5729951	-0.0511001
C	4.6677710	-0.2193214	-0.0446361
C	4.7227050	-1.6123268	-0.1631284
C	3.4442640	0.5082846	-0.0371995
C	1.2154129	1.8974180	-0.0178372
C	2.4390423	1.1733689	-0.0288475
C	5.9388684	-2.2829825	-0.1661045
H	5.9607287	-3.3588905	-0.2585033
C	-0.0013717	1.1717394	-0.0009224
C	-2.4408280	1.1761420	0.0156468
C	1.1989788	3.2861319	-0.0272539
H	2.1385803	3.8209328	-0.0446999
C	-1.2164467	1.8986306	0.0030879
C	-3.4466567	0.5119105	0.0269671
C	-0.0003083	3.9813980	-0.0247885
C	5.8756692	0.4830954	0.0708923
H	5.8469550	1.5588241	0.1636559
C	7.0796411	-0.1883958	0.0670550
C	-1.1993217	3.2885593	-0.0086554
H	-2.1383377	3.8237698	-0.0105614
C	-7.1234836	-1.5665715	0.0470892
C	-4.6706862	-0.2146754	0.0368664
C	-7.0823230	-0.1828566	-0.0807222
C	-5.8778614	0.4877231	-0.0864855
C	-4.7270483	-1.6067718	0.1652057
C	-5.9436998	-2.2765372	0.1699948
H	-5.9665497	-3.3517460	0.2700410
I	-2.9834987	-2.7341139	0.3608386
H	-5.8481493	1.5627551	-0.1867250
F	-1.1200125	6.0004797	-0.4758799

F	1.0265030	5.9863056	-0.6986026
F	0.1470914	5.9512746	1.2605097
C	8.3797316	0.5576216	0.1893799
F	9.0773888	0.1473314	1.2558848
F	8.2008776	1.8736697	0.3106732
F	9.1590296	0.3556154	-0.8804797
C	-8.3815398	0.5632183	-0.2115550
F	-9.1653657	0.3660315	0.8558880
F	-9.0750252	0.1488289	-1.2792251
F	-8.2015954	1.8786786	-0.3376366
H	-8.0729711	-2.0848137	0.0502089
H	8.0685407	-2.0919666	-0.0527297

G3XB S conformation

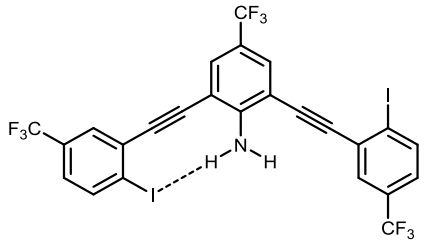

Coordinates for **G3XB-S**:

0 1

I	5.8844208	2.0037635	-0.5392262
C	-0.0025468	5.1285307	0.3759551
N	-0.2235464	-0.5121546	0.0530508
H	0.6267284	-1.0358890	-0.0541402
H	-1.1073377	-0.9827150	-0.0545641
C	6.8446987	-2.1653467	0.0392177
C	4.4999818	-0.6388215	0.0831043
C	5.7405074	-0.0419894	-0.1748174
C	3.2878308	0.1085954	0.1105293
C	1.0678897	1.5134913	0.1633647
C	2.2728584	0.7575554	0.1357951
C	6.9022619	-0.8037983	-0.1948461
H	7.8513904	-0.3291387	-0.3961245
C	-0.1732938	0.8345333	0.1141673
C	-2.6096540	0.9244354	0.0797011
C	1.1013429	2.8999388	0.2324677
H	2.0613276	3.3975793	0.2625916
C	-1.3610290	1.6019768	0.1394670
C	-3.6366992	0.2958869	0.0243188
C	-0.0729893	3.6372025	0.2567611

C	4.4611658	-2.0186659	0.3211809
H	3.5110193	-2.4890095	0.5280224
C	5.6187313	-2.7675189	0.2968443
C	-1.2953604	2.9894890	0.2128494
H	-2.2147987	3.5571948	0.2266763
C	-7.3803795	-1.6514901	-0.1501949
C	-4.8841405	-0.3871513	-0.0373253
C	-7.2956429	-0.2724157	0.0037775
C	-6.0695248	0.3552330	0.0599181
C	-4.9842454	-1.7741656	-0.1918396
C	-6.2226152	-2.4005317	-0.2478627
H	-6.2796082	-3.4725296	-0.3675508
I	-3.2755106	-2.9595048	-0.3452188
H	-6.0058239	1.4267480	0.1799622
F	-1.1350405	5.7184721	-0.0214132
F	0.9949368	5.6395134	-0.3574748
F	0.2164197	5.5225369	1.6402318
C	5.5846423	-4.2480977	0.5545520
F	6.1107013	-4.9340413	-0.4677333
F	4.3430003	-4.7020505	0.7419466
F	6.2961695	-4.5720520	1.6412130
C	-8.5719170	0.5161626	0.1092875
F	-9.3032817	0.1192128	1.1581073
F	-9.3368225	0.3513998	-0.9771048
F	-8.3509605	1.8240859	0.2480959
H	-8.3466211	-2.1359236	-0.1932057
H	7.7489691	-2.7588730	0.0215081

G3XB W conformation

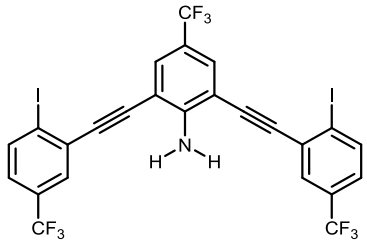

Coordinates for **G3XB-W**:

0 1

I	6.0338196	-1.9098178	-0.3151856
C	-0.0000747	-4.7563945	0.5001288
N	-0.0000173	0.8796073	-0.0021362
H	0.8626034	1.3512258	-0.2112487
H	-0.8626316	1.3512086	-0.2113135
C	7.1234483	2.2619556	-0.1139124

C	4.7237799	0.8261936	-0.0152305
C	5.9499326	0.1657121	-0.1626960
C	3.4847547	0.1259633	0.0388682
C	1.2142877	-1.1919612	0.1538317
C	2.4461322	-0.4826213	0.0909674
C	7.1390129	0.8827485	-0.2102806
H	8.0766035	0.3587948	-0.3237636
C	-0.0000015	-0.4720600	0.0921002
C	-2.4461363	-0.4826292	0.0909844
C	1.1993217	-2.5773791	0.2697405
H	2.1407764	-3.1077903	0.3089121
C	-1.2142948	-1.1919793	0.1538481
C	-3.4847510	0.1259659	0.0388738
C	0.0000185	-3.2683616	0.3257243
C	4.7273031	2.2234881	0.0838454
H	3.7883215	2.7437158	0.2042417
C	5.9119160	2.9272739	0.0331116
C	-1.1993062	-2.5773802	0.2697573
H	-2.1407546	-3.1078109	0.3089402
C	-7.1233777	2.2620633	-0.1139382
C	-4.7237637	0.8262240	-0.0152312
C	-5.9118321	2.9273404	0.0331504
C	-4.7272425	2.2235122	0.0839026
C	-5.9499306	0.1657778	-0.1627585
C	-7.1389833	0.8828591	-0.2103556
H	-8.0765872	0.3589414	-0.3238974
I	-6.0338764	-1.9097454	-0.3152982
H	-3.7882464	2.7437017	0.2043530
F	-1.0784994	-5.3239887	-0.0527250
F	-0.0013405	-5.1107000	1.7945725
F	1.0794411	-5.3239090	-0.0506414
C	5.9234656	4.4267691	0.1392399
F	6.6260139	4.8361829	1.2025530
F	4.6950073	4.9369365	0.2528794
F	6.4913166	4.9876123	-0.9357204
C	-5.9233239	4.4268293	0.1394079
F	-6.6256816	4.8361926	1.2028662
F	-6.4913363	4.9877758	-0.9354082
F	-4.6948296	4.9369516	0.2528886
H	-8.0491313	2.8204041	-0.1527745
H	8.0492237	2.8202630	-0.1527130

2F-G3XB bidentate

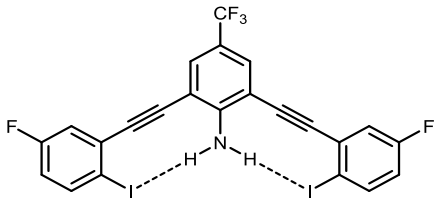

Coordinates for **2F-G3XB bidentate**:

0 1

I	2.9677784	-2.6096644	-0.0150579
C	-0.0147241	5.6193306	0.0098570
N	0.0020129	-0.0321476	0.0043696
H	0.8715768	-0.5401546	0.0075899
H	-0.8667414	-0.5415180	0.0056261
C	7.1244145	-1.4338020	0.0010375
C	4.6699090	-0.0741043	-0.0031239
C	4.7182853	-1.4743409	-0.0064263
C	3.4466610	0.6547417	-0.0051574
C	1.2158940	2.0407521	-0.0086576
C	2.4407665	1.3188937	-0.0071285
C	5.9337938	-2.1423149	-0.0043189
H	5.9542695	-3.2223508	-0.0068891
C	0.0010596	1.3129797	-0.0034724
C	-2.4397475	1.3133005	-0.0110250
C	1.1977193	3.4305876	-0.0186170
H	2.1364724	3.9661488	-0.0268314
C	-1.2165082	2.0381743	-0.0107773
C	-3.4442405	0.6471380	-0.0103856
C	-0.0017449	4.1228952	-0.0267773
C	5.8768192	0.6351977	0.0023162
H	5.8753414	1.7152623	0.0050325
C	7.0686742	-0.0526774	0.0042329
C	-1.2007024	3.4266915	-0.0213990
H	-2.1407883	3.9608306	-0.0320697
C	-7.1179839	-1.4482646	-0.0128230
C	-4.6661360	-0.0840712	-0.0106436
C	-7.0648298	-0.0671212	-0.0277227
C	-5.8742437	0.6229661	-0.0269558
C	-4.7118292	-1.4842945	0.0045026
C	-5.9261052	-2.1545094	0.0033706
H	-5.9446414	-3.2345131	0.0151471
I	-2.9592432	-2.6161293	0.0294302
H	-5.8746975	1.7029679	-0.0389505
F	-1.0292758	6.1273713	-0.7019700
F	1.1167248	6.1437852	-0.4748658

F	-0.1540425	6.0929048	1.2587817
F	8.2115926	0.6409132	0.0094714
F	-8.2089796	0.6242227	-0.0435438
H	-8.0740805	-1.9512497	-0.0140364
H	8.0814508	-1.9349903	0.0027674

2F-G3XB S conformation

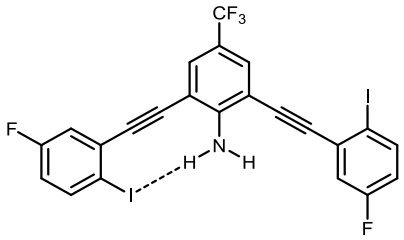

Coordinates for **2F-G3XB-S**:

0 1

I	5.8126004	0.6646000	-0.3983000
C	0.6187000	4.7595003	0.2964000
N	-0.6557000	-0.7445001	0.0725000
H	0.0816000	-1.4201001	-0.0214000
H	-1.6112001	-1.0415001	-0.0426000
C	6.0593004	-3.6182003	0.1490000
C	3.9917003	-1.7247001	0.1415000
C	5.3222004	-1.3347001	-0.0686000
C	2.9212002	-0.7848001	0.1447000
C	0.9948001	1.0024001	0.1536000
C	2.0378001	0.0347000	0.1499000
C	6.3401005	-2.2775002	-0.0620000
H	7.3613005	-1.9645001	-0.2234000
C	-0.3516000	0.5697000	0.1056000
C	-2.7271002	1.1188001	0.0389000
C	1.2903001	2.3590002	0.1984000
H	2.3271002	2.6653002	0.2292000
C	-1.3730001	1.5484001	0.1021000
C	-3.8546003	0.6969001	-0.0203000
C	0.2769000	3.3050002	0.1965000
C	3.7147003	-3.0792002	0.3563000
H	2.7017002	-3.4126002	0.5278000
C	4.7450003	-3.9917003	0.3542000
C	-1.0460001	2.8991002	0.1498000
H	-1.8414001	3.6308003	0.1418000
C	-7.9019006	-0.5111000	-0.2342000
C	-5.2086004	0.2616000	-0.0915000
C	-7.5368006	0.8220001	-0.2301000

C	-6.2226005	1.2243001	-0.1611000
C	-5.5708004	-1.0918001	-0.0954000
C	-6.9035005	-1.4695001	-0.1660000
H	-7.1670005	-2.5171002	-0.1676000
I	-4.1227003	-2.5903002	0.0109000
H	-5.9777005	2.2762002	-0.1606000
F	-0.3439000	5.5370004	-0.2134000
F	1.7543001	5.0515004	-0.3498000
F	0.7940001	5.1501004	1.5690001
F	4.4611003	-5.2828004	0.5602000
F	-8.4923006	1.7546001	-0.2960000
H	-8.9457006	-0.7842001	-0.2898000
H	6.8395005	-4.3655003	0.1564000

2H-G3XB bidentate

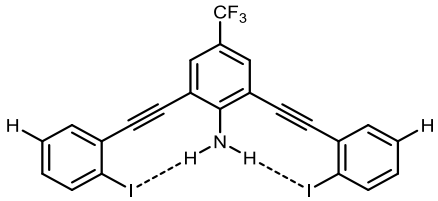

Coordinates for **2H-G3XB bidentate**:

0 1

I	2.9426820	-2.5931106	0.0094086
C	0.0537267	5.6561503	0.0038087
N	-0.0054434	0.0063102	-0.0011298
H	0.8619398	-0.5053422	-0.0006533
H	-0.8768550	-0.4985523	0.0003256
C	7.1026303	-1.4359426	-0.0081033
C	4.6607494	-0.0691552	-0.0060041
C	4.7025736	-1.4686389	-0.0005650
C	3.4415281	0.6672594	-0.0052509
C	1.2215016	2.0716491	-0.0042247
C	2.4414556	1.3402750	-0.0049052
C	5.9120313	-2.1464922	-0.0016011
H	5.9230406	-3.2268269	0.0026466
C	-0.0004917	1.3517605	-0.0023412
C	-2.4391833	1.3650370	-0.0024905
C	1.2100301	3.4587429	-0.0065101
H	2.1524162	3.9901014	-0.0094792
C	-1.2118200	2.0831568	-0.0029889
C	-3.4463038	0.7023031	-0.0018485
C	0.0124647	4.1605091	-0.0072319
C	5.8775993	0.6260023	-0.0125307

H	5.8497631	1.7066081	-0.0167827
C	7.0838541	-0.0476061	-0.0135682
C	-1.1888030	3.4742246	-0.0048484
H	-2.1254253	4.0126222	-0.0062681
C	-7.1272979	-1.3664638	0.0003494
C	-4.6724313	-0.0222894	-0.0011295
C	-7.0954051	0.0216743	0.0007117
C	-5.8829462	0.6840371	-0.0000124
C	-4.7276720	-1.4213718	-0.0015008
C	-5.9433516	-2.0880292	-0.0007567
H	-5.9643320	-3.1682461	-0.0010486
I	-2.9782384	-2.5622915	-0.0032899
H	-5.8451085	1.7643482	0.0002785
F	-1.1637956	6.1986178	-0.0993220
F	0.7916855	6.1438931	-1.0053999
F	0.6028271	6.1355054	1.1314933
H	8.0099384	0.5100541	-0.0187005
H	-8.0162228	0.5880377	0.0015772
H	-8.0718953	-1.8926147	0.0009286
H	8.0422436	-1.9709514	-0.0088971

2H-G3XB S conformation

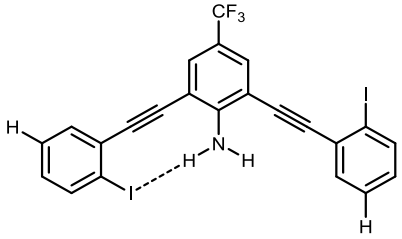

Coordinates for **2H-G3XB-S**:

0 1

I	5.7577752	0.1164299	-0.2900239
C	0.8348525	4.6384819	0.1563167
N	-0.8212901	-0.7660395	0.0963505
H	-0.1329341	-1.4926216	0.0108011
H	-1.7951003	-0.9962522	-0.0187599
C	5.5973291	-4.1674755	0.2638444
C	3.7166931	-2.0995743	0.1945547
C	5.0818538	-1.8327834	0.0227992
C	2.7335314	-1.0685560	0.1654104
C	0.9493517	0.8607832	0.1212577
C	1.9182475	-0.1812681	0.1448006
C	6.0125579	-2.8603577	0.0581235
H	7.0612629	-2.6376597	-0.0755699

C	-0.4244874	0.5243828	0.0896781
C	-2.7568786	1.2362211	0.0219528
C	1.3402424	2.1939585	0.1256194
H	2.3960014	2.4274420	0.1441448
C	-1.3751882	1.5715642	0.0629372
C	-3.9116800	0.8921236	-0.0132446
C	0.3958978	3.2084139	0.0991379
C	3.3217610	-3.4269955	0.4028819
H	2.2699396	-3.6357201	0.5418272
C	4.2493238	-4.4507049	0.4366729
C	-0.9532178	2.8960150	0.0699043
H	-1.6948937	3.6818611	0.0437797
C	-8.0325750	-0.0194733	-0.1352774
C	-5.2947147	0.5542360	-0.0543816
C	-7.5996349	1.2995766	-0.1159863
C	-6.2476746	1.5816040	-0.0760893
C	-5.7532289	-0.7684578	-0.0744427
C	-7.1093439	-1.0538144	-0.1146393
H	-7.4428006	-2.0813310	-0.1296276
I	-4.4095310	-2.3675363	-0.0443393
H	-5.8980626	2.6043495	-0.0607076
F	-0.0487017	5.4582224	-0.4271377
F	2.0142747	4.8255347	-0.4485516
F	0.9814303	5.0721710	1.4190234
H	3.9218406	-5.4680729	0.5991456
H	-8.3162749	2.1087877	-0.1320334
H	-9.0887356	-0.2489382	-0.1665894
H	6.3307090	-4.9616801	0.2893967

2Me-G3XB bidentate

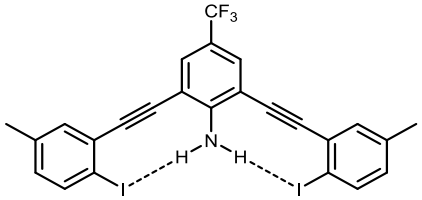

Coordinates for **2Me-G3XB bidentate**:

0 1

I	2.9646706	-2.6111428	0.2748366
C	-0.0155659	5.6095114	0.0091426
N	0.0020403	-0.0402137	0.0039999
H	0.8717356	-0.5479056	-0.0030146
H	-0.8668330	-0.5492489	0.0117484
C	7.1065439	-1.4399278	-0.0780195

C	4.6646825	-0.0943323	-0.0458859
C	4.7117459	-1.4863778	0.0690729
C	3.4443037	0.6403480	-0.0351364
C	1.2163168	2.0320002	-0.0208486
C	2.4407327	1.3084176	-0.0294344
C	5.9280851	-2.1534363	0.0526407
H	5.9527768	-3.2299736	0.1423342
C	0.0010311	1.3051223	-0.0043221
C	-2.4399649	1.3027857	0.0099320
C	1.1977753	3.4217009	-0.0318000
H	2.1364356	3.9570894	-0.0492461
C	-1.2172152	2.0294290	-0.0002776
C	-3.4420193	0.6325938	0.0190759
C	-0.0020021	4.1138914	-0.0277889
C	5.8759268	0.6004649	-0.1766051
H	5.8357362	1.6781813	-0.2654624
C	7.0974553	-0.0501808	-0.1945672
C	-1.2011943	3.4177109	-0.0099859
H	-2.1413904	3.9517579	-0.0111707
C	-7.1000867	-1.4545932	0.0707880
C	-4.6609456	-0.1045283	0.0332803
C	-7.0940902	-0.0639182	0.1757394
C	-5.8737973	0.5889812	0.1552572
C	-4.7048496	-1.4975709	-0.0700570
C	-5.9199157	-2.1668587	-0.0509850
H	-5.9422959	-3.2441444	-0.1317258
I	-2.9550177	-2.6204575	-0.2622128
H	-5.8359316	1.6674811	0.2351322
F	-1.0308044	6.1189763	-0.7019032
F	1.1152121	6.1363366	-0.4759412
F	-0.1548202	6.0848282	1.2581794
C	8.3850132	0.7117449	-0.3370439
C	-8.3834831	0.6965527	0.3090428
H	-8.0421659	-1.9886893	0.0844441
H	8.0496542	-1.9722427	-0.0895318
H	8.2053320	1.7827826	-0.4022574
H	8.9206363	0.4011645	-1.2347435
H	9.0400353	0.5272024	0.5149550
H	-8.2062456	1.7685861	0.3636898
H	-8.9194084	0.3938342	1.2092520
H	-9.0371437	0.5019806	-0.5417642

2Me-G3XB S conformation

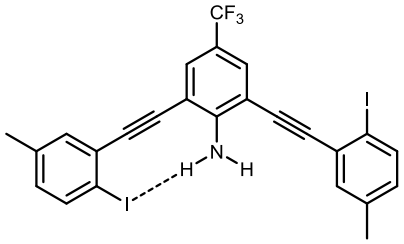

Coordinates for **2Me-G3XB-S**:

0 1

I	5.8345231	0.6955690	-0.4249696
C	0.5767275	4.7861550	0.3105710
N	-0.6309208	-0.7315336	0.0804033
H	0.1158566	-1.3941142	-0.0318829
H	-1.5816062	-1.0374442	-0.0514047
C	6.0441560	-3.5811449	0.1669379
C	4.0072774	-1.6811573	0.1494180
C	5.3342308	-1.2986090	-0.0730139
C	2.9377601	-0.7393765	0.1514153
C	0.9986276	1.0347786	0.1620502
C	2.0507825	0.0764866	0.1573423
C	6.3448491	-2.2495899	-0.0614307
H	7.3680179	-1.9463347	-0.2310427
C	-0.3428269	0.5873410	0.1130972
C	-2.7254430	1.1057136	0.0471676
C	1.2778709	2.3945874	0.2089635
H	2.3109366	2.7132100	0.2402373
C	-1.3765582	1.5526140	0.1111258
C	-3.8471296	0.6679899	-0.0125924
C	0.2527485	3.3283351	0.2083265
C	3.7337286	-3.0363007	0.3801934
H	2.7064128	-3.3266973	0.5593796
C	4.7317470	-3.9954329	0.3908632
C	-1.0654475	2.9069623	0.1611412
H	-1.8695678	3.6290499	0.1542743
C	-7.8683475	-0.5669017	-0.2219119
C	-5.1958724	0.2152892	-0.0831246
C	-7.5607714	0.7933577	-0.2047174
C	-6.2286212	1.1625997	-0.1359642
C	-5.5410819	-1.1387258	-0.1021581
C	-6.8716261	-1.5255184	-0.1713859
H	-7.1274478	-2.5753208	-0.1852736
I	-4.0767430	-2.6248140	-0.0215110
H	-5.9576061	2.2101156	-0.1211871
F	-0.3958500	5.5540572	-0.1963879

F	1.7078124	5.0948122	-0.3362573
F	0.7489060	5.1780148	1.5837449
C	4.4193384	-5.4454892	0.6328456
H	4.6618725	-6.0446848	-0.2456690
H	3.3652494	-5.5902651	0.8608066
H	5.0050520	-5.8347696	1.4658932
C	-8.6539194	1.8231585	-0.2598087
H	-9.3339176	1.7104601	0.5851582
H	-9.2430970	1.7132192	-1.1707764
H	-8.2478589	2.8322323	-0.2372509
H	-8.9033382	-0.8813269	-0.2755849
H	6.8441292	-4.3113012	0.1729672

2*t*Bu-G3XB bidentate

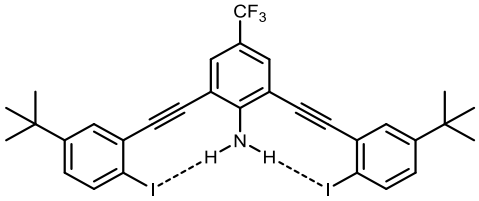

Coordinates for **2*t*BuG3XB bidentate**:

0 1

I	2.9590790	-2.7471867	0.3474641
C	-0.0117364	5.4754927	0.0109845
N	0.0017177	-0.1741229	0.0049849
H	0.8711138	-0.6821653	0.0182635
H	-0.8674337	-0.6826595	-0.0009859
C	7.1032327	-1.5688572	0.0509412
C	4.6643910	-0.2317019	0.0420982
C	4.7073447	-1.6212303	0.1636017
C	3.4443828	0.5041539	0.0311886
C	1.2173905	1.8974380	0.0039260
C	2.4413872	1.1730661	0.0184128
C	5.9258016	-2.2843465	0.1676250
H	5.9533306	-3.3604582	0.2620500
C	0.0014986	1.1713165	-0.0025240
C	-2.4393781	1.1700854	-0.0334309
C	1.1997417	3.2870691	-0.0075549
H	2.1388438	3.8220140	-0.0073003
C	-1.2162114	1.8961391	-0.0212773
C	-3.4418492	0.5004139	-0.0422280
C	0.0003798	3.9799558	-0.0262690
C	5.8772629	0.4664167	-0.0743548
H	5.8154914	1.5403520	-0.1674658

C	7.1045465	-0.1762623	-0.0727046
C	-1.1992744	3.2844956	-0.0308226
H	-2.1389844	3.8190021	-0.0498165
C	-7.0989417	-1.5755657	-0.0528319
C	-4.6612748	-0.2365422	-0.0495904
C	-7.1015944	-0.1821307	0.0608539
C	-5.8748027	0.4615000	0.0598767
C	-4.7028290	-1.6269355	-0.1610928
C	-5.9207789	-2.2909985	-0.1623637
H	-5.9473456	-3.3677804	-0.2490491
I	-2.9532959	-2.7526196	-0.3339462
H	-5.8139921	1.5361228	0.1453278
F	-1.0222941	5.9865853	-0.7054682
F	1.1224834	6.0011496	-0.4676540
F	-0.1568615	5.9509297	1.2594062
C	8.4293470	0.5717438	-0.2003671
C	-8.4271864	0.5657191	0.1809900
H	-8.0339675	-2.1202993	-0.0562001
H	8.0386876	-2.1128352	0.0566464
C	8.2293995	2.0816655	-0.3241367
C	-8.2285679	2.0765867	0.2950205
H	9.2009987	2.5684543	-0.4123214
H	7.7284439	2.4940827	0.5527754
H	7.6463860	2.3386732	-1.2095869
H	-9.2006741	2.5632170	0.3783159
H	-7.7264354	2.4835577	-0.5837598
H	-7.6472667	2.3398964	1.1797463
C	-9.2819543	0.2808325	-1.0618022
C	-9.1695710	0.0779045	1.4329107
H	-8.5791272	0.2665304	2.3303003
H	-9.3804632	-0.9903028	1.3846944
H	-10.1206630	0.6040112	1.5299606
C	9.2867081	0.2958561	1.0426648
C	9.1696958	0.0760811	-1.4504140
H	8.7788933	0.6364115	1.9458117
H	10.2381134	0.8242918	0.9628725
H	9.5016360	-0.7666764	1.1553416
H	8.5773602	0.2582231	-2.3478974
H	9.3814663	-0.9916257	-1.3954250
H	10.1202017	0.6022332	-1.5528373
H	-8.7726222	0.6156039	-1.9662561
H	-10.2338532	0.8091623	-0.9874064
H	-9.4959739	-0.7825883	-1.1676745

2*t*Bu-G3XB S conformation

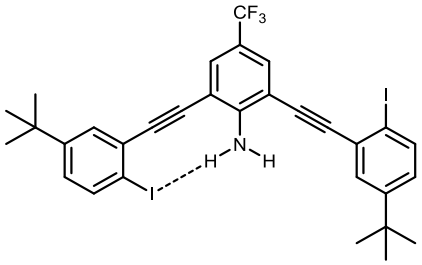

Coordinates for **2*t*Bu-G3XB-S**:

0 1

I	5.8759896	2.0307369	-0.6482970
C	-0.0257677	5.1286818	0.4635703
N	-0.1990384	-0.5058303	0.0399261
H	0.6576898	-1.0069796	-0.1161618
H	-1.0757009	-0.9781869	-0.1127251
C	6.8399465	-2.1334158	0.0347702
C	4.5141474	-0.6047665	0.0821772
C	5.7445564	-0.0072930	-0.2247456
C	3.2983503	0.1393872	0.1178569
C	1.0699166	1.5312695	0.1931960
C	2.2812228	0.7846030	0.1530378
C	6.8948156	-0.7739150	-0.2465707
H	7.8428832	-0.3130226	-0.4844519
C	-0.1653366	0.8418934	0.1262005
C	-2.6024720	0.9031064	0.0943354
C	1.0881406	2.9147954	0.2947365
H	2.0430208	3.4218857	0.3406577
C	-1.3609941	1.5935821	0.1691325
C	-3.6222142	0.2638814	0.0246133
C	-0.0955996	3.6389277	0.3364080
C	4.4907780	-1.9726706	0.3633136
H	3.5329787	-2.4135283	0.6070349
C	5.6371149	-2.7606717	0.3471436
C	-1.3103272	2.9805511	0.2755856
H	-2.2357906	3.5370058	0.3053947
C	-7.3371625	-1.7077051	-0.1879428
C	-4.8609613	-0.4363369	-0.0520901
C	-7.3041877	-0.3277187	-0.0060763
C	-6.0551379	0.2811086	0.0581345
C	-4.9376469	-1.8229665	-0.2346955
C	-6.1678626	-2.4490326	-0.3014534
H	-6.2218618	-3.5191159	-0.4424286
I	-3.2122314	-2.9852093	-0.4130537
F	-1.2306512	5.7023495	0.3757535

F	0.7441374	5.6763096	-0.4885545
F	0.5044260	5.5082811	1.6368344
C	5.5330078	-4.2496851	0.6712711
C	-8.5644273	0.5255278	0.1227306
H	-8.2797192	-2.2319922	-0.2449313
H	7.7614160	-2.6962920	0.0066486
C	6.8909020	-4.9475144	0.6008458
C	-9.8372216	-0.3154906	0.0308714
H	-10.7070715	0.3345210	0.1284735
H	-9.8858960	-1.0590590	0.8276951
H	-9.9112780	-0.8292020	-0.9287043
H	6.7666254	-6.0042555	0.8388816
H	7.5969706	-4.5254431	1.3173191
H	7.3264237	-4.8793415	-0.3970457
C	-8.5542568	1.2433526	1.4794907
H	-8.5334075	0.5229522	2.2981286
H	-9.4515136	1.8557116	1.5828289
H	-7.6883169	1.8969520	1.5821168
C	-8.5883996	1.5668326	-1.0047808

2MeO-G3XB bidentate

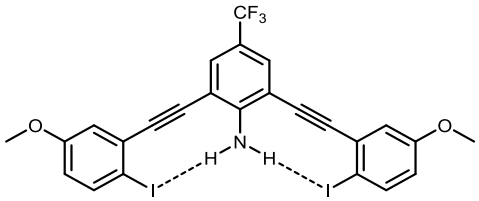

Coordinates for **2MeO-G3XB bidentate**:

0 1

I	2.9505845	-2.7223297	0.0140013
C	-0.0130552	5.5124485	0.0125191
N	0.0022144	-0.1372898	0.0058355
H	0.8717900	-0.6456915	0.0066149
H	-0.8667688	-0.6466719	0.0065441
C	7.1055209	-1.5471748	-0.0050216
C	4.6642964	-0.1942129	-0.0055345
C	4.7020424	-1.5885701	0.0023808
C	3.4443698	0.5420916	-0.0062896
C	1.2171430	1.9346256	-0.0081017
C	2.4414562	1.2110668	-0.0074879
C	5.9226193	-2.2549464	0.0025869
H	5.9449465	-3.3352170	0.0087211
C	0.0015541	1.2074791	-0.0020983
C	-2.4394399	1.2065928	-0.0079615

C	1.1988502	3.3241880	-0.0179647
H	2.1376776	3.8595235	-0.0268314
C	-1.2164387	1.9325986	-0.0083826
C	-3.4413406	0.5362029	-0.0067369
C	-0.0006602	4.0169443	-0.0251291
C	5.8737762	0.5193043	-0.0132695
H	5.8242049	1.5969514	-0.0193406
C	7.0861093	-0.1508996	-0.0130222
C	-1.1999177	3.3208618	-0.0187028
H	-2.1398498	3.8552166	-0.0284983
C	-7.1001553	-1.5569650	-0.0041618
C	-4.6604679	-0.2014937	-0.0057221
C	-7.0822868	-0.1606582	-0.0071783
C	-5.8706456	0.5108221	-0.0079475
C	-4.6966097	-1.5958990	-0.0027139
C	-5.9164986	-2.2635383	-0.0019523
H	-5.9377097	-3.3438309	0.0003736
I	-2.9439152	-2.7277489	0.0005196
H	-5.8222246	1.5885346	-0.0102327
F	-1.0294265	6.0231083	-0.6959916
F	1.1172233	6.0385064	-0.4749420
F	-0.1486409	5.9876282	1.2620135
O	8.2919767	0.4589672	-0.0201468
O	-8.2887858	0.4479369	-0.0091545
H	-8.0542253	-2.0648703	-0.0035895
H	8.0601335	-2.0540574	-0.0049576
C	8.3174975	1.8702218	-0.0287750
C	-8.3158317	1.8591982	-0.0121224
H	9.3651783	2.1543211	-0.0336675
H	7.8337955	2.2778259	0.8617383
H	7.8283974	2.2669972	-0.9212254
H	-9.3638266	2.1421883	-0.0133047
H	-7.8293710	2.2600504	-0.9041844
H	-7.8303727	2.2637728	0.8788158

2MeO-G3XB S conformation

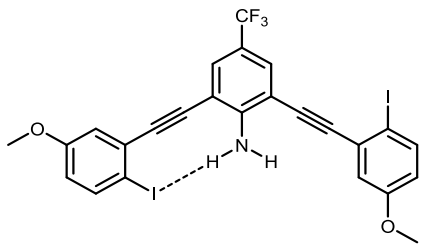

Coordinates for **2MeO-G3XB-S**:

0 1

I	5.8855740	1.2594806	-0.2342502
C	0.3458913	4.9379282	0.1711974
N	-0.4852575	-0.6515994	0.0514540
H	0.3039796	-1.2686033	-0.0205578
H	-1.4160340	-1.0287447	-0.0240516
C	6.3905553	-3.0332719	0.0544009
C	4.2083992	-1.2811686	0.0605672
C	5.5181012	-0.7858852	-0.0593281
C	3.0748526	-0.4166420	0.0669589
C	1.0205659	1.2220578	0.0800895
C	2.1356071	0.3380800	0.0732302
C	6.5866704	-1.6619617	-0.0608278
H	7.5929509	-1.2789718	-0.1532059
C	-0.2879156	0.6826873	0.0624731
C	-2.7018128	1.0379452	0.0363787
C	1.2065830	2.5982753	0.0994386
H	2.2158349	2.9871564	0.1072555
C	-1.3851796	1.5755416	0.0636184
C	-3.7941852	0.5293014	0.0110331
C	0.1200831	3.4599382	0.1007837
C	4.0194426	-2.6554677	0.1769670
H	3.0219976	-3.0596034	0.2748801
C	5.0979950	-3.5326143	0.1743349
C	-1.1668018	2.9484943	0.0847067
H	-2.0186603	3.6136616	0.0806109
C	-7.7349446	-0.9935512	-0.0761072
C	-5.1114190	-0.0142148	-0.0183358
C	-7.5034169	0.3779626	-0.0421868
C	-6.1982082	0.8564900	-0.0138344
C	-5.3584316	-1.3962271	-0.0523524
C	-6.6558404	-1.8691547	-0.0808567
H	-6.8395613	-2.9336291	-0.1071846
I	-3.7908790	-2.7740702	-0.0598207
H	-6.0335379	1.9240099	0.0121993
F	-0.6885336	5.6288668	-0.3233757
F	1.4375918	5.3109106	-0.5089021
F	0.5220179	5.3632856	1.4330768
O	4.7924460	-4.8453001	0.2936510
O	-8.4761534	1.3165579	-0.0344174
H	-8.7367052	-1.3943495	-0.0986169
H	7.2479754	-3.6887514	0.0494280
C	5.8582137	-5.7696466	0.3010762
C	-9.8164448	0.8764701	-0.0612986

H	-10.4297803	1.7720756	-0.0493298
H	-10.0481475	0.2655453	0.8141629
H	-10.0254496	0.3050041	-0.9685260
H	5.4075117	-6.7516411	0.4066215
H	6.5323235	-5.5870162	1.1410839
H	6.4230865	-5.7275210	-0.6330135

Cl-G3XB bidentate

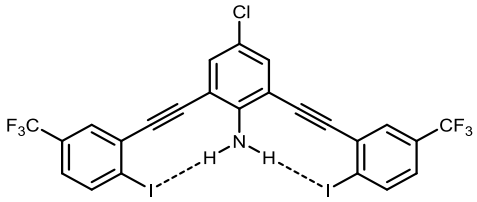

Coordinates for **Cl-G3XB bidentate**:

0 1

I	3.0044819	-2.4755100	-0.0549749
Cl	0.0000345	5.9789710	-0.1222959
N	-0.0000139	0.0873892	-0.0417882
H	0.8671318	-0.4144874	0.0548511
H	-0.8671607	-0.4144883	0.0548365
C	7.1409464	-1.2592923	0.0659764
C	4.6771222	0.0724899	0.0111693
C	4.7426461	-1.3252391	0.0028969
C	3.4482801	0.7897829	-0.0148094
C	1.2120720	2.1662339	-0.0547692
C	2.4385806	1.4481646	-0.0356368
C	5.9647389	-1.9848127	0.0303863
H	5.9944558	-3.0645325	0.0235876
C	-0.0000078	1.4386190	-0.0450889
C	-2.4385876	1.4481946	-0.0356610
C	1.1994054	3.5588488	-0.0787814
H	2.1355505	4.0982115	-0.0862587
C	-1.2120738	2.1662529	-0.0547833
C	-3.4482868	0.7898114	-0.0148469
C	0.0000146	4.2467277	-0.0919868
C	5.8809511	0.7905711	0.0473660
H	5.8442388	1.8700271	0.0540583
C	7.0907218	0.1300995	0.0739892
C	-1.1993825	3.5588700	-0.0787947
H	-2.1355223	4.0982427	-0.0862829
C	-7.1409422	-1.2592892	0.0658828
C	-4.6771243	0.0725140	0.0111152
C	-7.0907207	0.1301081	0.0740933

C	-5.8809598	0.7905857	0.0474892
C	-4.7426451	-1.3252084	0.0026526
C	-5.9647377	-1.9847961	0.0301196
H	-5.9944420	-3.0645151	0.0231683
I	-3.0044897	-2.4754821	-0.0554770
H	-5.8442470	1.8700411	0.0543338
C	8.3856977	0.8933359	0.1134548
F	9.0958393	0.5912504	1.2077749
F	8.1978365	2.2139457	0.1114674
F	9.1580769	0.5967110	-0.9393402
C	-8.3857012	0.8933259	0.1137475
F	-9.0957953	0.5910385	1.2080414
F	-9.1581202	0.5968814	-0.9390695
F	-8.1978514	2.2139386	0.1119867
H	-8.0944556	-1.7697103	0.0871304
H	8.0944585	-1.7697149	0.0872413

Cl-G3XB S conformation

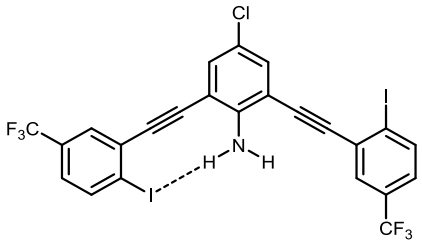

Coordinates for **Cl-G3XB-S**:

0 1

I	-5.8875688	2.2829669	0.5330351
Cl	0.0251806	5.6145805	-0.5743805
N	0.2108299	-0.2577320	-0.0851129
H	-0.6357400	-0.7520566	0.1362036
H	1.0880358	-0.7064947	0.1245467
C	-6.8456652	-1.8905321	-0.0161655
C	-4.5052239	-0.3580744	-0.0986216
C	-5.7437700	0.2360744	0.1739884
C	-3.2947436	0.3906438	-0.1466916
C	-1.0667300	1.7798960	-0.2469099
C	-2.2771735	1.0344391	-0.1937884
C	-6.9034166	-0.5281609	0.2129281
H	-7.8508023	-0.0548528	0.4252386
C	0.1662405	1.0957232	-0.1750790
C	2.6024520	1.1810071	-0.1458678
C	-1.0988226	3.1671544	-0.3674427

H	-2.0530597	3.6716254	-0.4199502
C	1.3542643	1.8569944	-0.2288618
C	3.6308613	0.5572272	-0.0661419
C	0.0789270	3.8899119	-0.4216046
C	-4.4664347	-1.7389866	-0.3317759
H	-3.5177782	-2.2069611	-0.5507524
C	-5.6216814	-2.4905696	-0.2880773
C	1.2990358	3.2437340	-0.3533924
H	2.2179052	3.8105319	-0.3934106
C	7.3776227	-1.3765699	0.1826384
C	4.8790973	-0.1212290	0.0212513
C	7.2908689	-0.0016264	-0.0039767
C	6.0637093	0.6213775	-0.0840908
C	4.9811749	-1.5041557	0.2089775
C	6.2207181	-2.1257545	0.2890480
H	6.2791265	-3.1945299	0.4342284
I	3.2737279	-2.6890541	0.3752127
H	5.9984374	1.6896720	-0.2292480
C	-5.5877014	-3.9718101	-0.5416778
F	-6.1106933	-4.6551325	0.4841495
F	-4.3467385	-4.4260812	-0.7315907
F	-6.3025796	-4.2992999	-1.6252847
C	8.5657564	0.7873001	-0.1203746
F	9.2947663	0.3822498	-1.1679339
F	9.3345126	0.6334563	0.9649970
F	8.3430502	2.0938835	-0.2704057
H	8.3445574	-1.8575552	0.2445357
H	-7.7480470	-2.4862697	0.0166023

F-G3XB bidentate

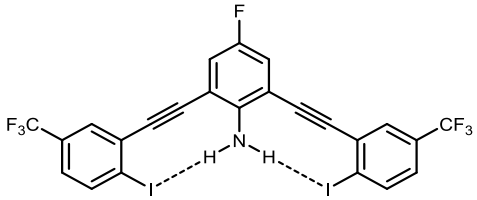

Coordinates for **F-G3XB bidentate**:

0 1

I	-2.9988322	-2.3109140	-0.1456544
F	0.0010717	5.7267431	-0.3540432
N	0.0001995	0.2426987	-0.0613461
H	-0.8627843	-0.2397408	0.1296771
H	0.8628595	-0.2399958	0.1306220
C	-7.1310854	-1.1084790	0.1461332

C	-4.6739969	0.2303227	0.0177584
C	-4.7365414	-1.1675114	-0.0065678
C	-3.4475924	0.9500164	-0.0437706
C	-1.2118090	2.3241595	-0.1474108
C	-2.4379427	1.6067568	-0.0953698
C	-5.9554730	-1.8303328	0.0574398
H	-5.9829556	-2.9099419	0.0381050
C	0.0003627	1.5992847	-0.1080204
C	2.4386155	1.6058458	-0.0960375
C	-1.2016101	3.7160337	-0.2302779
H	-2.1297845	4.2680636	-0.2612098
C	1.2127782	2.3237165	-0.1478915
C	3.4480189	0.9487348	-0.0442359
C	0.0008572	4.3862331	-0.2726935
C	-5.8770966	0.9447371	0.1079967
H	-5.8424044	2.0240621	0.1290924
C	-7.0836529	0.2807615	0.1708998
C	1.2030831	3.7155961	-0.2309740
H	2.1314536	4.2672683	-0.2623827
C	7.1318295	-1.1091934	0.1468215
C	4.6743972	0.2291568	0.0182673
C	7.0856337	0.2802919	0.1445485
C	5.8789098	0.9440178	0.0820025
C	4.7357633	-1.1689411	0.0203314
C	5.9548234	-1.8315010	0.0844542
H	5.9813869	-2.9113085	0.0847429
I	2.9963527	-2.3138953	-0.0786417
H	5.8454449	2.0236046	0.0804295
C	-8.3782436	1.0403010	0.2612149
F	-9.1521197	0.8130444	-0.8078677
F	-8.1898351	2.3583224	0.3436770
F	-9.0872549	0.6683576	1.3343011
C	8.3804047	1.0406239	0.2252115
F	9.2216010	0.6760866	-0.7503271
F	9.0109832	0.8065047	1.3832872
F	8.2025788	2.3591644	0.1282625
H	8.0829096	-1.6221548	0.1958292
H	-8.0819331	-1.6216540	0.1976198

F-G3XB S conformation

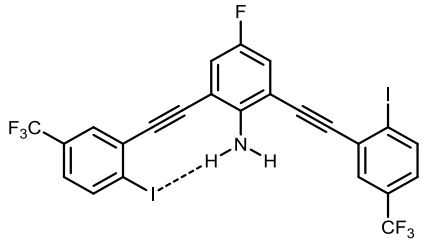

Coordinates for **F-G3XB-S**:

0 1

I	5.8868596	-2.4347896	0.5038344
F	-0.0425510	-5.3493153	-0.6871336
N	-0.2072426	0.1134535	-0.1137311
H	0.6348264	0.5860607	0.1667350
H	-1.0810458	0.5441350	0.1443116
C	6.8393775	1.7466239	0.0080451
C	4.5032670	0.2099318	-0.1094972
C	5.7411495	-0.3844060	0.1654304
C	3.2947603	-0.5404456	-0.1758205
C	1.0671115	-1.9268020	-0.3133905
C	2.2776315	-1.1833120	-0.2402270
C	6.8987658	0.3817786	0.2215383
H	7.8456900	-0.0918642	0.4350793
C	-0.1650101	-1.2440997	-0.2276385
C	-2.6011771	-1.3239457	-0.1991191
C	1.0999998	-3.3122299	-0.4661709
H	2.0462346	-3.8301839	-0.5303683
C	-1.3544486	-2.0002066	-0.2996269
C	-3.6291561	-0.7020059	-0.1016037
C	-0.0823364	-4.0156719	-0.5374411
C	4.4627870	1.5934478	-0.3266692
H	3.5144235	2.0613884	-0.5471371
C	5.6159369	2.3470718	-0.2654595
C	-1.3039416	-3.3853609	-0.4568116
H	-2.2154660	-3.9626061	-0.5118924
C	-7.3744836	1.2261504	0.2052259
C	-4.8768287	-0.0253414	0.0054589
C	-7.2887451	-0.1457187	-0.0032454
C	-6.0619673	-0.7667552	-0.1023206
C	-4.9777496	1.3545499	0.2153642
C	-6.2170169	1.9740708	0.3144370
H	-6.2746679	3.0404354	0.4766349
I	-3.2692413	2.5368406	0.3860503
H	-5.9974411	-1.8326750	-0.2642242
C	5.5804125	3.8310975	-0.5020766

F	6.1009517	4.5031753	0.5324325
F	4.3392935	4.2859369	-0.6888183
F	6.2967018	4.1719904	-1.5806626
C	-8.5640183	-0.9333734	-0.1231853
F	-9.2952740	-0.5201334	-1.1660308
F	-9.3305862	-0.7880688	0.9648914
F	-8.3419342	-2.2388678	-0.2840831
H	-8.3410519	1.7057115	0.2821085
H	7.7400918	2.3439764	0.0544424

H-G3XB bidentate

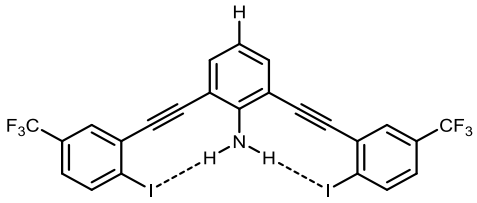

Coordinates for **H-G3XB bidentate**:

0 1

I	-2.9972002	-2.1570002	0.3511000
N	0.0000000	0.3969000	-0.0016000
H	-0.8685001	-0.1107000	0.0063000
H	0.8687001	-0.1107000	-0.0042000
C	-7.1335005	-0.9727001	0.0492000
C	-4.6734003	0.3703000	0.0398000
C	-4.7366003	-1.0223001	0.1629000
C	-3.4471002	1.0920001	0.0306000
C	-1.2134001	2.4740002	0.0088000
C	-2.4381002	1.7526001	0.0204000
C	-5.9560004	-1.6872001	0.1673000
H	-5.9825004	-2.7627002	0.2633000
C	0.0000000	1.7470001	-0.0008000
C	2.4381002	1.7527001	-0.0214000
C	-1.1943001	3.8673003	0.0073000
H	-2.1393002	4.3929003	0.0141000
C	1.2134001	2.4740002	-0.0102000
C	3.4471002	1.0921001	-0.0312000
C	0.0000000	4.5687003	-0.0006000
C	-5.8790004	1.0769001	-0.0788000
H	-5.8450004	2.1521002	-0.1752000
C	-7.0863005	0.4114000	-0.0735000
C	1.1942001	3.8673003	-0.0085000
H	2.1392002	4.3930003	-0.0150000
C	7.1335005	-0.9727001	-0.0482000

C	4.6734003	0.3704000	-0.0398000
C	7.0863005	0.4114000	0.0743000
C	5.8790004	1.0769001	0.0791000
C	4.7366003	-1.0222001	-0.1628000
C	5.9560004	-1.6872001	-0.1666000
H	5.9825004	-2.7627002	-0.2625000
I	2.9972002	-2.1569002	-0.3516000
H	5.8451004	2.1521002	0.1754000
C	-8.3821006	1.1634001	-0.1991000
F	-8.1974006	2.4789002	-0.3230000
F	-9.1648007	0.9683001	0.8699001
F	-9.0813007	0.7551001	-1.2658001
C	8.3820006	1.1633001	0.2004000
F	9.1650006	0.9685001	-0.8685001
F	9.0811006	0.7548001	1.2671001
F	8.1974006	2.4788002	0.3246000
H	8.0850006	-1.4872001	-0.0505000
H	-8.0850006	-1.4871001	0.0520000
H	-0.0001000	5.6485004	-0.0005000

H-G3XB S conformation

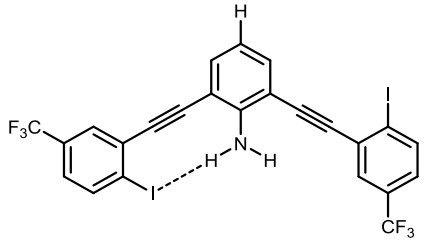

Coordinates for **H-G3XB-S**:

0 1

I	5.8856302	-2.5753849	0.4409753
H	-0.0492608	-5.2372218	-0.7767792
N	-0.2092416	-0.0251502	-0.1157810
H	0.6378872	0.4584852	0.1258917
H	-1.0860889	0.4151574	0.1120381
C	6.8417493	1.6131372	0.0186682
C	4.5026911	0.0800328	-0.1248143
C	5.7409925	-0.5190687	0.1382203
C	3.2938507	-0.6680473	-0.2040016
C	1.0671669	-2.0544309	-0.3656379
C	2.2767577	-1.3106386	-0.2794109
C	6.8995858	0.2445323	0.2069028
H	7.8461232	-0.2341849	0.4105881

C	-0.1661368	-1.3735008	-0.2652604
C	-2.6022971	-1.4538426	-0.2396925
C	1.0914697	-3.4360217	-0.5462406
H	2.0533913	-3.9253105	-0.6178395
C	-1.3562488	-2.1293684	-0.3524164
C	-3.6305788	-0.8332380	-0.1320592
C	-0.0816744	-4.1672321	-0.6346458
C	4.4644555	1.4676282	-0.3162983
H	3.5165036	1.9407053	-0.5272143
C	5.6182864	2.2191005	-0.2422243
C	-1.2963544	-3.5099343	-0.5371968
H	-2.2251772	-4.0600031	-0.6003874
C	-7.3778544	1.0885174	0.2056969
C	-4.8782382	-0.1591264	-0.0142590
C	-7.2908889	-0.2799351	-0.0238209
C	-6.0637867	-0.8986420	-0.1330058
C	-4.9811018	1.2172974	0.2169799
C	-6.2204960	1.8348819	0.3259128
H	-6.2783438	2.8985989	0.5046536
I	-3.2731196	2.3979568	0.4070787
H	-5.9986977	-1.9618975	-0.3111755
C	5.5834793	3.7071513	-0.4509774
F	6.1041924	4.3599341	0.5959286
F	4.3427129	4.1665075	-0.6295277
F	6.3001903	4.0683315	-1.5228969
C	-8.5653469	-1.0664939	-0.1563721
F	-9.2924207	-0.6446193	-1.1989634
F	-9.3373681	-0.9311560	0.9293151
F	-8.3428668	-2.3707900	-0.3278549
H	-8.3446068	1.5662954	0.2905146
H	7.7430484	2.2086967	0.0750242

Me-G3XB bidentate

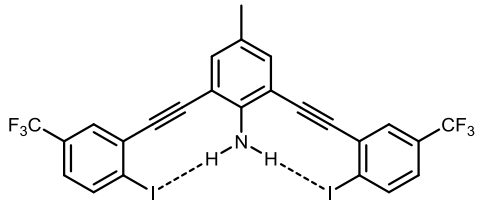

Coordinates for **Me-G3XB bidentate**:

0 1

I	-3.0128835	-2.3252616	-0.1553788
C	0.0013383	5.9118906	-0.4032012
N	0.0000786	0.2192494	-0.0610367

H	-0.8639668	-0.2658666	0.1172965
H	0.8637942	-0.2662246	0.1180285
C	-7.1403483	-1.1100450	0.1525313
C	-4.6774740	0.2215368	0.0218470
C	-4.7462850	-1.1761141	-0.0072159
C	-3.4490637	0.9368319	-0.0408726
C	-1.2080826	2.3032873	-0.1494467
C	-2.4365595	1.5899360	-0.0938517
C	-5.9672433	-1.8351456	0.0578893
H	-5.9981525	-2.9146109	0.0346921
C	0.0003150	1.5739539	-0.1119804
C	2.4371915	1.5888132	-0.0947814
C	-1.1860971	3.6947303	-0.2311459
H	-2.1334645	4.2185652	-0.2552940
C	1.2090471	2.3027188	-0.1500982
C	3.4494689	0.9353631	-0.0416401
C	0.0009545	4.4128823	-0.2787879
C	-5.8786823	0.9388867	0.1180831
H	-5.8400969	2.0179649	0.1429673
C	-7.0874032	0.2789624	0.1820823
C	1.1876956	3.6941523	-0.2320389
H	2.1353033	4.2175273	-0.2568556
C	7.1411609	-1.1107767	0.1530031
C	4.6778871	0.2202399	0.0220829
C	7.0894616	0.2785751	0.1555135
C	5.8805442	0.9381963	0.0918757
C	4.7455135	-1.1777732	0.0193976
C	5.9666233	-1.8364881	0.0846498
H	5.9966022	-2.9162260	0.0810663
I	3.0103090	-2.3286430	-0.0887905
H	5.8432171	2.0176235	0.0940635
H	0.8824052	6.3444208	0.0689138
H	-0.8811267	6.3446163	0.0660938
H	0.0030671	6.2190716	-1.4505657
C	-8.3786615	1.0428470	0.2784755
F	-9.1563051	0.8237292	-0.7899005
F	-8.1857552	2.3601514	0.3663535
F	-9.0875423	0.6693453	1.3513837
C	8.3808652	1.0433299	0.2426404
F	9.2273292	0.6851554	-0.7310412
F	9.0091735	0.8087955	1.4021443
F	8.1991271	2.3618507	0.1488387
H	8.0938714	-1.6205603	0.2028625
H	-8.0927917	-1.6201019	0.2048950

Me-G3XB S conformation

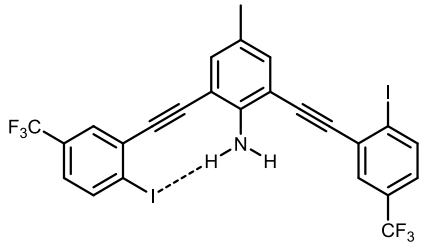

Coordinates for **Me-G3XB-S**:

0 1

I	5.8875365	-2.4305623	0.5031895
C	-0.0360083	-5.5357503	-0.7164516
N	-0.2063570	0.1367434	-0.1190666
H	0.6374890	0.6148334	0.1456681
H	-1.0810333	0.5731583	0.1253353
C	6.8487751	1.7493698	0.0138411
C	4.5072950	0.2172846	-0.1029610
C	5.7450883	-0.3789615	0.1685873
C	3.2970532	-0.5295988	-0.1687559
C	1.0636570	-1.9079034	-0.3070430
C	2.2771916	-1.1690310	-0.2330491
C	6.9048278	0.3839655	0.2243267
H	7.8508110	-0.0926865	0.4353681
C	-0.1648316	-1.2192839	-0.2283515
C	-2.5991894	-1.3062846	-0.1952500
C	1.0839337	-3.2939469	-0.4503677
H	2.0479018	-3.7849765	-0.5023012
C	-1.3506431	-1.9793925	-0.2950881
C	-3.6298222	-0.6875282	-0.0994159
C	-0.0822083	-4.0444557	-0.5260250
C	4.4709619	1.6017453	-0.3170379
H	3.5233803	2.0724533	-0.5348512
C	5.6259208	2.3526104	-0.2562537
C	-1.2891630	-3.3650874	-0.4429742
H	-2.2210007	-3.9146427	-0.4876023
C	-7.3827375	1.2290591	0.2052852
C	-4.8793918	-0.0151389	0.0064553
C	-7.2917608	-0.1442528	0.0083317
C	-6.0629046	-0.7612225	-0.0901236
C	-4.9863209	1.3662328	0.2045579
C	-6.2275525	1.9819453	0.3031981
H	-6.2883804	3.0495219	0.4561551
I	-3.2817765	2.5570366	0.3570557

H	-5.9947404	-1.8281984	-0.2431312
C	5.5932740	3.8370309	-0.4896961
F	6.1161986	4.5063448	0.5456817
F	4.3532091	4.2955367	-0.6746666
F	6.3096330	4.1791227	-1.5681885
C	-8.5640091	-0.9380064	-0.0992824
F	-9.3052284	-0.5327727	-1.1385189
F	-9.3241187	-0.7922462	0.9935864
F	-8.3378450	-2.2435266	-0.2565053
H	-8.3508649	1.7054758	0.2817154
H	7.7508885	2.3445735	0.0599401
H	-0.9308226	-6.0098534	-0.3158931
H	0.8296763	-5.9682281	-0.2164465
H	0.0306663	-5.7942913	-1.7747287

nHBeXB bidentate

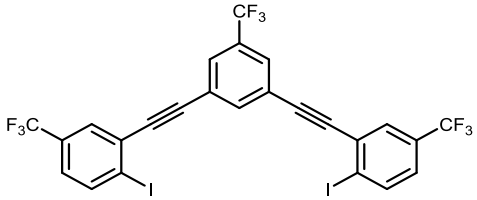

Coordinates for **nHBeXB bidentate**:

0 1

I	-2.9050544	-2.6853110	0.3614407
C	-0.0129098	5.4799344	-0.0057602
C	-7.0794848	-1.6307811	0.0529380
C	-4.6667739	-0.2176083	0.0440308
C	-4.6810610	-1.6117128	0.1702748
C	-3.4568216	0.5337664	0.0347393
C	-1.2090578	1.8989397	0.0180800
C	-2.4386620	1.1741947	0.0257591
C	-5.8815459	-2.3106993	0.1739383
H	-5.8769319	-3.3862454	0.2720601
C	0.0014586	1.2067987	0.0047972
C	2.4406745	1.1761761	-0.0094684
C	-1.2053855	3.2941913	0.0284566
H	-2.1406911	3.8356239	0.0447996
C	1.2102676	1.8994335	0.0028167
C	3.4597423	0.5372366	-0.0233615
C	0.0011059	3.9752432	0.0276180
C	-5.8894641	0.4550551	-0.0771059
H	-5.8872931	1.5307517	-0.1749154
C	-7.0766626	-0.2463947	-0.0721687

C	1.2068012	3.2963454	0.0140478
H	2.1418699	3.8372987	0.0176644
C	7.0846895	-1.6233295	-0.0585965
C	4.6704738	-0.2127457	-0.0384604
C	7.0805675	-0.2396877	0.0744555
C	5.8926391	0.4604754	0.0849449
C	4.6860835	-1.6061075	-0.1726733
C	5.8872966	-2.3037856	-0.1819511
H	5.8836733	-3.3787531	-0.2862945
I	2.9109997	-2.6805740	-0.3675284
H	5.8894866	1.5356028	0.1888196
F	1.1265560	6.0015688	0.4552051
F	-1.0115438	5.9808659	0.7281263
F	-0.1794049	5.9379472	-1.2532665
C	-8.3949163	0.4651719	-0.1999361
F	-9.0793143	0.0355395	-1.2675281
F	-8.2494658	1.7854797	-0.3236268
F	-9.1724206	0.2460969	0.8680214
C	8.3981945	0.4725111	0.2051181
F	9.1769719	0.2562536	-0.8624630
F	9.0817847	0.0410929	1.2725254
F	8.2517056	1.7924604	0.3315378
H	0.0016980	0.1257466	-0.0013476
H	-8.0150382	-2.1740345	0.0558051
H	8.0208115	-2.1655586	-0.0659254

nHBeXB S conformation

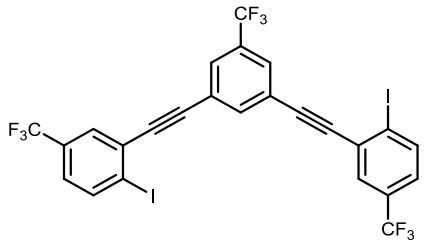

Coordinates for **nHBeXB-S**:

0 1

I	-5.9082569	2.0431822	0.0788376
C	0.0162489	5.0831801	-0.0627421
C	-6.8703310	-2.1639413	0.0013421
C	-4.5105461	-0.6641656	-0.0099292
C	-5.7603749	-0.0342647	0.0281485
C	-3.2890882	0.0684531	-0.0167376
C	-1.0484802	1.4453545	-0.0281618

C	-2.2541751	0.6816007	-0.0223746
C	-6.9306107	-0.7829169	0.0336917
H	-7.8876669	-0.2832661	0.0631667
C	0.1913150	0.8136766	-0.0238649
C	2.6312049	0.9009191	-0.0198380
C	-1.1143705	2.8429525	-0.0367216
H	-2.0768261	3.3334956	-0.0384502
C	1.3679388	1.5652520	-0.0275476
C	3.6785466	0.3093585	-0.0115429
C	0.0550517	3.5788640	-0.0404535
C	-4.4679124	-2.0637975	-0.0423085
H	-3.5076068	-2.5572788	-0.0728235
C	-5.6344966	-2.7991056	-0.0369276
C	1.2949679	2.9568368	-0.0362791
H	2.2026376	3.5446816	-0.0374335
C	7.3995860	-1.6812679	0.0233770
C	4.9228279	-0.3838194	0.0000895
C	7.3339176	-0.2929444	0.0061911
C	6.1148021	0.3516690	-0.0049971
C	5.0002905	-1.7816167	0.0169342
C	6.2325752	-2.4228774	0.0284809
H	6.2768149	-3.5020137	0.0408356
I	3.2735629	-2.9477679	0.0242326
H	6.0639457	1.4305352	-0.0192238
F	0.7340194	5.6047943	0.9391348
F	-1.2253948	5.5591963	0.0443120
F	0.5328853	5.5669594	-1.1992621
C	-5.5999150	-4.3018274	-0.0637940
F	-6.1392956	-4.8221565	1.0460248
F	-4.3579692	-4.7794757	-0.1644451
F	-6.3011139	-4.7877323	-1.0955260
C	8.6192420	0.4871144	0.0126693
F	9.4198950	0.1164977	-0.9941007
F	9.3064245	0.2847541	1.1441751
F	8.4162488	1.8008868	-0.1001384
H	8.3598068	-2.1795395	0.0309704
H	-7.7811934	-2.7476417	0.0047008
H	0.2482856	-0.2655621	-0.0162549

G3HB bidentate

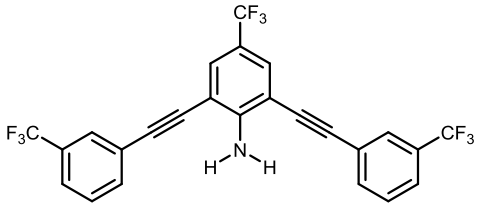

Coordinates for **G3HB bidentate**:

0 1

H	3.8211248	-3.0153264	-1.1781052
C	0.0111564	4.4211812	-0.2321958
N	-0.0028983	-1.2371315	-0.3090547
H	0.8581874	-1.7159598	-0.1073313
H	-0.8641657	-1.7157593	-0.1075718
C	7.0760756	-2.6971833	-0.3088310
C	4.6842477	-1.2615903	-0.2998216
C	4.7265440	-2.5670085	-0.7930016
C	3.4601091	-0.5252114	-0.2925763
C	1.2132361	0.8406200	-0.2838152
C	2.4413588	0.1186766	-0.2874817
C	5.9162103	-3.2778106	-0.7949257
H	5.9381755	-4.2883111	-1.1782063
C	-0.0028651	0.1205861	-0.2822737
C	-2.4458732	0.1209860	-0.2865454
C	1.1978373	2.2299460	-0.2814591
H	2.1376493	2.7645197	-0.2863635
C	-1.2170550	0.8415387	-0.2833336
C	-3.4651021	-0.5222438	-0.2913698
C	-0.0019231	2.9238266	-0.2815358
C	5.8557349	-0.6765136	0.1895434
H	5.8311244	0.3319153	0.5758339
C	7.0350839	-1.3969542	0.1805169
C	-1.2012088	2.2323524	-0.2805305
H	-2.1403743	2.7670015	-0.2843677
C	-7.0820993	-2.6926696	-0.3065565
C	-4.6895849	-1.2579955	-0.2982914
C	-7.0408607	-1.3916465	0.1806316
C	-5.8612092	-0.6716767	0.1892758
C	-4.7321710	-2.5642394	-0.7893357
C	-5.9221161	-3.2745560	-0.7908819
H	-5.9442233	-4.2856929	-1.1724810
H	-3.8266868	-3.0135909	-1.1730820
H	-5.8364662	0.3373745	0.5739258
F	-1.1249129	4.9488809	-0.7005473
F	1.0182553	4.9343152	-0.9499093

F	0.1636239	4.8808036	1.0197713
C	8.3119129	-0.7763597	0.6770681
F	8.9691047	-1.6005728	1.5022003
F	8.0994481	0.3642757	1.3367108
F	9.1463571	-0.4998111	-0.3341397
C	-8.3177437	-0.7696121	0.6752059
F	-8.9764198	-1.5924436	1.5005402
F	-9.1509695	-0.4934983	-0.3371465
F	-8.1051515	0.3715874	1.3338643
H	-8.0144321	-3.2409187	-0.3016378
H	8.0081860	-3.2458201	-0.3042037

G3XB S conformation dihedral freeze

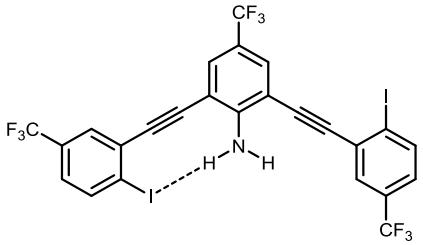

Coordinates for **G3XB-S-dhf**:

0 1

I	-5.9080738	2.0521259	0.0306599
C	-0.0142076	5.1148793	-0.0353816
N	0.2354904	-0.5332595	-0.0200982
H	-0.6123821	-1.0706734	0.0018482
H	1.1236114	-1.0071396	-0.0008309
C	-6.8692945	-2.1561894	0.0060159
C	-4.5072034	-0.6551999	0.0040620
C	-5.7584542	-0.0255032	0.0150666
C	-3.2880497	0.0806676	0.0014693
C	-1.0683595	1.4867714	-0.0053965
C	-2.2705841	0.7263583	-0.0015279
C	-6.9283533	-0.7747504	0.0161921
H	-7.8854151	-0.2742433	0.0245626
C	0.1766432	0.8134351	-0.0115903
C	2.6132429	0.9168292	-0.0072846
C	-1.1100279	2.8751879	0.0023097
H	-2.0730976	3.3673863	0.0125514
C	1.3602015	1.5886573	-0.0084396
C	3.6450722	0.2936965	-0.0058428
C	0.0594759	3.6195360	0.0048920
C	-4.4667772	-2.0553118	-0.0063954
H	-3.5082315	-2.5530653	-0.0167088

C	-5.6329272	-2.7910904	-0.0056764
C	1.2860016	2.9772250	-0.0020416
H	2.2022385	3.5504462	0.0046178
C	7.4055199	-1.6288292	0.0076891
C	4.8983356	-0.3812879	-0.0019319
C	7.3088058	-0.2420347	0.0114348
C	6.0771550	0.3774124	0.0070996
C	5.0104265	-1.7759984	-0.0059774
C	6.2541314	-2.3940427	-0.0012487
H	6.3204773	-3.4721716	-0.0051804
I	3.3114184	-2.9852374	-0.0200732
H	6.0041359	1.4550657	0.0090940
F	1.0947375	5.6848849	0.4491953
F	-1.0489753	5.5822266	0.6742308
F	-0.1708015	5.5775738	-1.2857653
C	-5.5961016	-4.2938196	-0.0087527
F	-6.1444266	-4.7983626	1.1037030
F	-4.3515257	-4.7709661	-0.0897277
F	-6.2854125	-4.7976574	-1.0395182
C	8.5773313	0.5655398	0.0348848
F	9.3947930	0.2175137	-0.9662181
F	9.2570714	0.3704256	1.1720131
F	8.3473476	1.8749785	-0.0720855
H	8.3759428	-2.1066735	0.0097844
H	-7.7802649	-2.7395872	0.0056331

2F-G3XB S conformation dihedral freeze

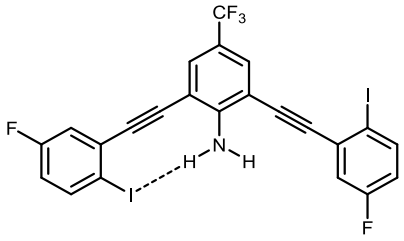

Coordinates for **2F-G3XB-S-dhf**:

0 1

I	5.8511034	0.6698532	-0.0188525
C	0.6289491	4.7631124	0.0226575
N	-0.6618586	-0.7403989	0.0079139
H	0.0721927	-1.4254366	0.0041807
H	-1.6226708	-1.0416940	0.0026787
C	6.0298416	-3.6509700	0.0052489
C	3.9777834	-1.7400724	0.0010200
C	5.3238820	-1.3471248	-0.0057661

C	2.9138597	-0.7928893	-0.0007831
C	0.9945737	1.0017980	-0.0035004
C	2.0344348	0.0309399	-0.0022856
C	6.3335860	-2.2986829	-0.0035839
H	7.3668420	-1.9834802	-0.0087213
C	-0.3538219	0.5718514	0.0003713
C	-2.7291238	1.1253664	-0.0089729
C	1.2938562	2.3583306	-0.0118805
H	2.3317449	2.6624071	-0.0194103
C	-1.3731142	1.5533097	-0.0066699
C	-3.8583727	0.7039051	-0.0102404
C	0.2829393	3.3068608	-0.0189136
C	3.6774854	-3.1066710	0.0099489
H	2.6514903	-3.4443023	0.0154935
C	4.7004273	-4.0272426	0.0118484
C	-1.0418189	2.9035491	-0.0149145
H	-1.8355479	3.6371236	-0.0247772
C	-7.9131114	-0.4984393	-0.0163747
C	-5.2147300	0.2702045	-0.0121696
C	-7.5462150	0.8342321	-0.0246928
C	-6.2295685	1.2343645	-0.0227882
C	-5.5787858	-1.0826364	-0.0035637
C	-6.9139537	-1.4582485	-0.0056973
H	-7.1787256	-2.5055756	0.0011200
I	-4.1306980	-2.5844831	0.0138977
H	-5.9834517	2.2859836	-0.0295545
F	-0.3398124	5.5237869	-0.5008145
F	1.7552557	5.0288808	-0.6502640
F	0.8232512	5.1994868	1.2775631
F	4.3937903	-5.3294957	0.0204499
F	-8.5024075	1.7683387	-0.0349896
H	-8.9587468	-0.7700230	-0.0181973
H	6.8036879	-4.4048816	0.0071025

2H-G3XB S conformation dihedral freeze

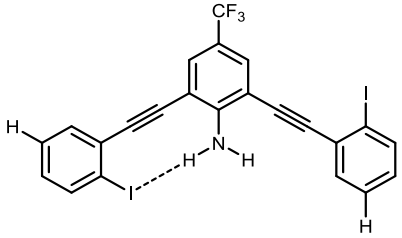

Coordinates for **2H-G3XB-S-dhf**:

0 1

I	5.7651500	0.1406116	-0.0155438
C	0.8569622	4.6138160	0.0175916
N	-0.8315873	-0.7798549	0.0073546
H	-0.1491979	-1.5163654	-0.0037167
H	-1.8120227	-1.0088086	-0.0055894
C	5.6160807	-4.1785427	0.0146770
C	3.7190429	-2.1240517	0.0047434
C	5.0904277	-1.8337565	-0.0006726
C	2.7293709	-1.0990229	0.0000796
C	0.9492882	0.8345410	-0.0065077
C	1.9134554	-0.2119911	-0.0035176
C	6.0288873	-2.8546903	0.0042660
H	7.0819219	-2.6134386	0.0001004
C	-0.4270839	0.5065234	-0.0028416
C	-2.7560168	1.2337087	-0.0128162
C	1.3484216	2.1653927	-0.0158867
H	2.4057893	2.3919480	-0.0234114
C	-1.3716917	1.5601872	-0.0110694
C	-3.9136914	0.8974847	-0.0129524
C	0.4103998	3.1857021	-0.0240998
C	3.3265702	-3.4683383	0.0153621
H	2.2697193	-3.6968043	0.0199520
C	4.2621869	-4.4852990	0.0203033
C	-0.9411483	2.8815566	-0.0199438
H	-1.6782643	3.6721381	-0.0307185
C	-8.0429002	0.0158057	-0.0136422
C	-5.2997094	0.5696003	-0.0131060
C	-7.5999515	1.3316372	-0.0233566
C	-6.2454050	1.6038377	-0.0231436
C	-5.7683100	-0.7496623	-0.0038889
C	-7.1270114	-1.0252311	-0.0040167
H	-7.4682671	-2.0502646	0.0033384
I	-4.4357824	-2.3584483	0.0098211
H	-5.8880422	2.6239910	-0.0305626
F	-0.0219736	5.4315407	-0.5760491
F	2.0378896	4.7882805	-0.5877149
F	1.0034239	5.0612857	1.2756153
H	3.9362068	-5.5159956	0.0285797
H	-8.3108317	2.1460377	-0.0310670
H	-9.1011586	-0.2059626	-0.0136324
H	6.3556766	-4.9673548	0.0185212

2Me-G3XB S conformation dihedral freeze

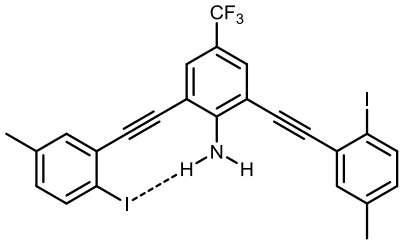

Coordinates for **2Me-G3XB-S-dhf**:

0 1

I	5.8749014	0.7024849	-0.0205846
C	0.5912602	4.7883561	0.0244101
N	-0.6393423	-0.7274005	0.0110345
H	0.1035159	-1.4028172	-0.0033907
H	-1.5967990	-1.0388845	-0.0031151
C	6.0132989	-3.6174651	0.0051613
C	3.9918615	-1.7003311	0.0003902
C	5.3357384	-1.3124212	-0.0068199
C	2.9288127	-0.7514920	-0.0014015
C	0.9982693	1.0319441	-0.0030941
C	2.0462344	0.0693039	-0.0025321
C	6.3382077	-2.2721714	-0.0043872
H	7.3741997	-1.9650105	-0.0098271
C	-0.3458214	0.5887476	0.0014610
C	-2.7275519	1.1142187	-0.0077843
C	1.2829884	2.3914489	-0.0115635
H	2.3175527	2.7065311	-0.0196053
C	-1.3762688	1.5581881	-0.0052697
C	-3.8512066	0.6773962	-0.0096135
C	0.2614660	3.3289840	-0.0179821
C	3.6938573	-3.0700027	0.0101093
H	2.6527974	-3.3665210	0.0161233
C	4.6837231	-4.0373875	0.0126103
C	-1.0591097	2.9117688	-0.0133876
H	-1.8606446	3.6367580	-0.0228687
C	-7.8796758	-0.5521179	-0.0179821
C	-5.2023366	0.2263557	-0.0122593
C	-7.5696086	0.8076600	-0.0262755
C	-6.2351925	1.1749934	-0.0232981
C	-5.5502174	-1.1270820	-0.0040267
C	-6.8830649	-1.5120264	-0.0069488
H	-7.1407382	-2.5614474	-0.0004198
I	-4.0869937	-2.6161763	0.0143622
H	-5.9623086	2.2221049	-0.0295762
F	-0.3853364	5.5398013	-0.4995228

F	1.7151770	5.0684660	-0.6471869
F	0.7795618	5.2280890	1.2796773
C	4.3457185	-5.5017770	0.0230061
H	4.7555835	-5.9997974	-0.8562665
H	3.2690826	-5.6592744	0.0313669
H	4.7678745	-5.9901736	0.9018396
C	-8.6627115	1.8388927	-0.0379525
H	-9.3014401	1.7349142	0.8397067
H	-9.2951028	1.7218365	-0.9185423
H	-8.2546619	2.8473922	-0.0439583
H	-8.9164897	-0.8650654	-0.0200885
H	6.8072243	-4.3542073	0.0070433

2*t*Bu-G3XB S conformation dihedral freeze

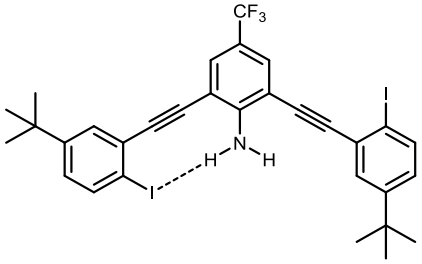

Coordinates for **2*t*Bu-G3XB-S-dhf**:

0 1

I	5.9143222	2.0948356	-0.0311834
C	-0.0126361	5.1210064	0.0367022
N	-0.2156995	-0.5269675	0.0233032
H	0.6380126	-1.0530850	-0.0293484
H	-1.0993485	-1.0076437	-0.0248304
C	6.8661697	-2.1270159	-0.0077946
C	4.5214839	-0.6254910	-0.0062726
C	5.7692027	0.0140856	-0.0163388
C	3.2979427	0.1059133	-0.0041634
C	1.0716457	1.5030572	0.0037203
C	2.2785865	0.7488702	-0.0008529
C	6.9283380	-0.7390809	-0.0170475
H	7.8893769	-0.2450725	-0.0249110
C	-0.1685883	0.8211888	0.0098461
C	-2.6062552	0.9010054	0.0039115
C	1.1022353	2.8915163	-0.0028107
H	2.0615282	3.3910894	-0.0126746
C	-1.3590074	1.5850703	0.0067952
C	-3.6310350	0.2660638	0.0006931
C	-0.0740427	3.6260872	-0.0050541
C	4.4910951	-2.0218160	0.0032010

H	3.5194470	-2.4980979	0.0120061
C	5.6461166	-2.7971106	0.0025376
C	-1.2956054	2.9740761	0.0010939
H	-2.2164257	3.5397436	-0.0056251
C	-7.3626802	-1.6849760	-0.0133389
C	-4.8757430	-0.4277234	-0.0035845
C	-7.3179770	-0.2933933	-0.0183845
C	-6.0636775	0.3080463	-0.0132532
C	-4.9642321	-1.8256042	0.0013986
C	-6.1997381	-2.4446952	-0.0035325
H	-6.2629097	-3.5235292	0.0002676
I	-3.2483964	-3.0155375	0.0169931
H	-5.9765682	1.3862958	-0.0169074
F	-1.1302744	5.6842347	-0.4386988
F	1.0123216	5.6005042	-0.6796904
F	0.1489542	5.5859567	1.2865194
H	-8.3097397	-2.2041828	-0.0170353
H	7.7951804	-2.6780183	-0.0087423
C	-8.5709625	0.5798354	-0.0293594
C	-8.5780413	1.4716265	1.2199682
C	-8.5626538	1.4621271	-1.2854183
C	-9.8510739	-0.2551165	-0.0340700
H	-8.5801839	0.8663176	2.1272647
H	-7.7069975	2.1257595	1.2519185
H	-9.4702319	2.0999094	1.2233773
H	-8.5531880	0.8499526	-2.1880553
H	-9.4549462	2.0899707	-1.3048124
H	-7.6915181	2.1164019	-1.3114025
H	-10.7152279	0.4096241	-0.0418950
H	-9.9126029	-0.8917719	-0.9178531
H	-9.9234937	-0.8850374	0.8537002
C	5.5319976	-4.3202625	0.0130922
C	4.7747357	-4.7641071	1.2722846
C	4.7626892	-4.7804426	-1.2328773
C	6.9022711	-4.9971800	0.0108586
H	5.3012067	-4.4453547	2.1726789
H	3.7684292	-4.3467428	1.3041524
H	4.6881314	-5.8517983	1.2909371
H	5.2803967	-4.4733525	-2.1423755
H	4.6760305	-5.8682806	-1.2366305
H	3.7560477	-4.3635496	-1.2603186
H	6.7704981	-6.0795024	0.0182087
H	7.4771298	-4.7373493	-0.8791199
H	7.4854177	-4.7263444	0.8921164

2MeO-G3XB S conformation dihedral freeze

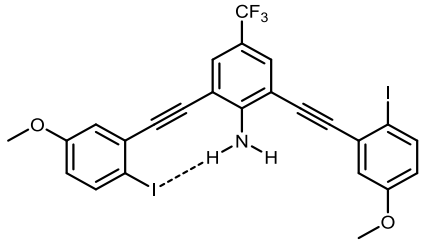

Coordinates for **2MeO-G3XB-S-dhf**:

0 1

I	5.8845788	1.2724940	-0.0293463
C	0.3546521	4.9278865	0.0313147
N	-0.4901411	-0.6604340	0.0153164
H	0.2974790	-1.2828766	-0.0100163
H	-1.4233076	-1.0381010	-0.0083632
C	6.4053185	-3.0277214	0.0043669
C	4.2126796	-1.2884571	-0.0015796
C	5.5233941	-0.7811981	-0.0100342
C	3.0749023	-0.4296410	-0.0026104
C	1.0205667	1.2090611	0.0001427
C	2.1342597	0.3234171	-0.0017550
C	6.5970580	-1.6509885	-0.0070416
H	7.6039639	-1.2586411	-0.0136432
C	-0.2892782	0.6727502	0.0052833
C	-2.7025689	1.0340470	-0.0023364
C	1.2099894	2.5850085	-0.0076635
H	2.2202360	2.9711984	-0.0165934
C	-1.3844264	1.5685087	0.0003114
C	-3.7966037	0.5283697	-0.0048941
C	0.1257810	3.4493601	-0.0118266
C	4.0281064	-2.6681940	0.0097939
H	3.0299456	-3.0822257	0.0170238
C	5.1118283	-3.5389420	0.0126675
C	-1.1624855	2.9409036	-0.0063381
H	-2.0127635	3.6081037	-0.0141263
C	-7.7429891	-0.9822963	-0.0164341
C	-5.1157517	-0.0111595	-0.0085071
C	-7.5065452	0.3887793	-0.0225240
C	-6.1995575	0.8632160	-0.0185498
C	-5.3677506	-1.3926973	-0.0023988
C	-6.6669082	-1.8615994	-0.0064233
H	-6.8544171	-2.9257170	-0.0016323
I	-3.8047782	-2.7756818	0.0136308

H	-6.0311212	1.9304511	-0.0234232
F	-0.6772554	5.6115889	-0.4785329
F	1.4487203	5.2860137	-0.6527652
F	0.5281515	5.3763325	1.2856051
O	4.8099997	-4.8578808	0.0240625
O	-8.4759996	1.3307747	-0.0322799
H	-8.7462523	-1.3799312	-0.0192647
H	7.2665967	-3.6781280	0.0065776
C	5.8806193	-5.7766408	0.0249127
C	-9.8179728	0.8950352	-0.0369884
H	-10.4280850	1.7928754	-0.0450215
H	-10.0451732	0.3092618	0.8566320
H	-10.0357891	0.2996444	-0.9265846
H	5.4320708	-6.7652532	0.0323902
H	6.5045241	-5.6539890	0.9131952
H	6.4971935	-5.6640923	-0.8697946

X-ray Diffraction Data

Single Crystal X-ray Diffraction Methods and Refinement

X-ray diffraction data were collected at 100 K (unless noted below) on a Bruker D8 Venture using MoKα-radiation (λ=0.71073 Å). Data have been corrected for absorption using SADABS[8] area detector absorption correction program. Using Olex2[9], the structure was solved with the SHELXT[10] structure solution program using Direct Methods and refined with the SHELXL[11] refinement package using least squares minimization. All non-hydrogen atoms were refined with anisotropic thermal parameters. Hydrogen atoms of the investigated structure were located from difference Fourier maps but finally their positions were placed in geometrically calculated positions and refined using a riding model. Isotropic thermal parameters of the placed hydrogen atoms were fixed to 1.2 times the *U* value of the atoms they are linked to (1.5 for methyl groups). Hydrogen atoms connected to heteroatoms were located from difference maps placed and refined. Calculations and refinement of structures were carried out using APEX3[12], SHELXTL[13], and Olex2 software. Specific and/or unique individual structure refinement details and crystal growth conditions are presented below.

Table S4-1. **Crystallographic Data**

Identification code	UMT_OB112	UMT_OB218	UMT_OB162	UMT_OB144	UMT_OB220
Manu Reference	G3XB	nHBeXB	G3HB-triclinic	G3HB-orthorhombic	2H-G3XB
CCDC Number	2023091	2238833	2023092	2023093	2238834
Empirical formula	$C_{25}H_{10}F_9I_2N$	$C_{25}H_9F_9I_2$	$C_{25}H_{12}F_9N$	$C_{25}H_{12}F_9N$	$C_{23}H_{12}F_3I_2N$
Formula weight	749.14	734.12	497.36	497.36	613.14

Temperature/K	105	100	100	100	100
Crystal system	monoclinic	monoclinic	triclinic	orthorhombic	monoclinic
Space group	$P2_1/c$	$P2_1/c$	P-1	Fdd2	$P2_1$
a/Å	17.0483(14)	18.7496(16)	7.9820(4)	37.842(3)	8.4061(3)
b/Å	4.7023(4)	4.7821(4)	7.9889(4)	50.545(4)	20.5959(7)
c/Å	30.687(3)	25.949(2)	17.3963(9)	8.9837(6)	12.3043(4)
α/°	90	90	84.337(2)	90	90
β/°	103.370(2)	94.215(2)	89.492(2)	90	108.6440(10)
γ/°	90	90	70.559(2)	90	90
Volume/$Å^3$	2393.4(3)	2320.4(3)	1040.62(9)	17183(2)	2018.47(12)
Z	4	4	2	32	4
$\rho_{calc}g/cm^3$	2.079	2.101	1.587	1.538	2.018
μ/mm^{-1}	2.714	2.796	0.150	0.145	3.152
F(000)	1416.0	1384.0	500.0	8000.0	1160.0
Crystal size/mm^3	0.46 × 0.02 × 0.01	0.46 × 0.02 × 0.01	0.39 × 0.07 × 0.02	0.55 × 0.32 × 0.09	0.12 × 0.07 × 0.01
Radiation	MoKα (λ = 0.71073)	MoKα (λ = 0.71073)	MoKα (λ = 0.71073)	MoKα (λ = 0.71073)	MoKα (λ = 0.71073)
2Θ range for data collection/°	6.146 to 55.072	5.184 to 50.118	5.414 to 55.106	5.25 to 52.936	5.114 to 55.074
Index ranges	-21 ≤ h ≤ 22, -6 ≤ k ≤ 6, -39 ≤ l ≤ 39	-22 ≤ h ≤ 22, -5 ≤ k ≤ 5, -28 ≤ l ≤ 30	-10 ≤ h ≤ 10, -10 ≤ k ≤ 10, -22 ≤ l ≤ 22	-47 ≤ h ≤ 47, -62 ≤ k ≤ 63, -11 ≤ l ≤ 11	-10 ≤ h ≤ 10, -26 ≤ k ≤ 26, -15 ≤ l ≤ 15
Reflections collected	51830	15943	47574	130424	75201
Independent reflections	5489 [R_{int} = 0.0667, R_{sigma} = 0.0419]	4089 [R_{int} = 0.0771, R_{sigma} = 0.0770]	4794 [R_{int} = 0.0459, R_{sigma} = 0.0252]	8847 [R_{int} = 0.0464, R_{sigma} = 0.0232]	9280 [R_{int} = 0.0447, R_{sigma} = 0.0250]
Data/restraints /parameters	5489/2/342	4089/21/353	4794/15/352	8847/37/703	9280/5/540
Goodness-of-fit on F^2	1.060	1.022	1.017	1.054	1.086
Final R indexes [I>=2σ (I)]	R_1 = 0.0364, wR_2 = 0.0734	R_1 = 0.0441, wR_2 = 0.0690	R_1 = 0.0390, wR_2 = 0.0892	R_1 = 0.0564, wR_2 = 0.1408	R_1 = 0.0254, wR_2 = 0.0559
Final R indexes [all data]	R_1 = 0.0598, wR_2 = 0.0805	R_1 = 0.0806, wR_2 = 0.0776	R_1 = 0.0600, wR_2 = 0.0991	R_1 = 0.0660, wR_2 = 0.1475	R_1 = 0.0312, wR_2 = 0.0579
Largest diff. peak/hole / e $Å^{-3}$	1.08/-0.81	0.66/-0.63	0.46/-0.31	0.64/-0.38	1.71/-0.36

Table S4-2. **Crystallographic Data Continued**

Identification code	UMT_OB229	UMT_OB227	UMT_OB129	UMT_OB148	UMT_OB196
Manu Reference	Me-G3XB	F-G3XB	G3XB-Cl^-	2H-G3XB-Cl^-	2Me-G3XB-Cl^-
CCDC number	2238835	2238836	2238837	2238838	2238839
Empirical formula	$C_{25}H_{13}F_6I_2N$	$C_{24}H_{10}F_7I_2N$	$C_{41}H_{46}ClF_9I_2N_2$	$C_{50}H_{67.69}Cl_{1.25}F_3I_2N_{2.25}$	$C_{41}H_{52}ClF_3I_2N_2$
Formula weight	695.16	699.13	1027.05	1055.37	919.09
Temperature/K	100	100	105	100	100
Crystal system	monoclinic	monoclinic	triclinic	tetragonal	triclinic
Space group	$P2_1/n$	C2/c	P-1	I-4	P-1
a/Å	18.182(4)	7.3702(7)	8.0763(5)	36.9115(18)	12.2702(5)
b/Å	4.5894(10)	18.1535(18)	15.6429(11)	36.9115(18)	13.0397(5)
c/Å	29.337(6)	34.027(3)	17.8668(12)	8.3724(4)	14.4541(6)
α/°	90	90	73.593(2)	90	107.965(2)
β/°	106.945(4)	94.009(2)	87.048(2)	90	108.3600(10)
γ/°	90	90	88.270(2)	90	93.925(2)
Volume/$Å^3$	2341.8(9)	4541.5(8)	2162.2(3)	11407.0(12)	2052.49(15)
Z	4	8	2	8	2
$\rho_{calc}g/cm^3$	1.972	2.045	1.578	1.229	1.487
μ/mm^{-1}	2.747	2.840	1.586	1.201	1.641
F(000)	1320.0	2640.0	1020.0	4302.0	924.0
Crystal size/mm^3	0.41 × 0.12 × 0.01	0.19 × 0.05 × 0.01	0.38 × 0.31 × 0.09	0.66 × 0.06 × 0.04	0.81 × 0.21 × 0.11
Radiation	MoKα (λ = 0.71073)	MoKα (λ = 0.71073)	MoKα (λ = 0.71073)	MoKα (λ = 0.71073)	MoKα (λ = 0.71073)
2Θ range for data collection/°	5.514 to 50.156	5.09 to 50.198	6.036 to 54.968	4.936 to 50.094	5.308 to 54.966
Index ranges	-20 ≤ h ≤ 21, -5 ≤ k ≤ 5, -34 ≤ l ≤ 34	-8 ≤ h ≤ 8, -21 ≤ k ≤ 21, -40 ≤ l ≤ 40	-10 ≤ h ≤ 10, -20 ≤ k ≤ 20, -23 ≤ l ≤ 23	-43 ≤ h ≤ 43, -43 ≤ k ≤ 43, -9 ≤ l ≤ 8	-15 ≤ h ≤ 15, -16 ≤ k ≤ 16, -18 ≤ l ≤ 18
Reflections collected	19640	47545	134813	86060	119487
Independent reflections	4155 [R_{int} = 0.0532, R_{sigma} = 0.0463]	4043 [R_{int} = 0.0621, R_{sigma} = 0.0319]	9902 [R_{int} = 0.0633, R_{sigma} = 0.0268]	10071 [R_{int} = 0.0551, R_{sigma} = 0.0288]	9379 [R_{int} = 0.0233, R_{sigma} = 0.0093]
Data/restraints/parameters	4155/2/316	4043/2/315	9902/2/508	10071/92/578	9379/97/524

Goodness-of-fit on F^2	1.179	1.183	1.146	1.052	1.152
Final R indexes [I>=2σ (I)]	R_1 = 0.0413, wR_2 = 0.0775	R_1 = 0.0404, wR_2 = 0.0634	R_1 = 0.0507, wR_2 = 0.1202	R_1 = 0.0334, wR_2 = 0.0697	R_1 = 0.0232, wR_2 = 0.0532
Final R indexes [all data]	R_1 = 0.0587, wR_2 = 0.0817	R_1 = 0.0556, wR_2 = 0.0667	R_1 = 0.0654, wR_2 = 0.1324	R_1 = 0.0408, wR_2 = 0.0736	R_1 = 0.0287, wR_2 = 0.0590
Largest diff. peak/hole / e $Å^{-3}$	1.38/-0.97	0.72/-0.64	2.37/-0.99	0.74/-0.38	1.37/-0.51

Table S4-3. **Crystallographic Data Continued**

Identification code	UMT_OB219
Manu Reference	H-G3XB-Cl^-
CCDC number	2238840
Empirical formula	$C_{48}H_{63}ClF_6I_2N_2$
Formula weight	1071.25
Temperature/ K	100
Crystal system	monoclinic
Space group	$P2_1/c$
a/Å	8.2189(5)
b/Å	22.0601(14)
c/Å	26.8587(18)
α/°	90
β/°	93.235(2)
γ/°	90
Volume/$Å^3$	4862.0(5)
Z	4
$\rho_{calc}g/cm^3$	1.463
μ/mm^{-1}	1.405
F(000)	2168.0
Crystal size/mm^3	0.26 × 0.21 × 0.2
Radiation	MoKα (λ = 0.71073)
2Θ range for data collection/°	5.296 to 61.15
Index ranges	-11 ≤ h ≤ 11, -31 ≤ k ≤ 31, -38 ≤ l ≤ 38

Reflections collected	181343
Independent reflections	14933 [R_{int} = 0.0493, R_{sigma} = 0.0237]
Data/restraints /parameters	14933/0/544
Goodness-of-fit on F^2	1.080
Final R indexes [I>=2σ (I)]	R_1 = 0.0293, wR_2 = 0.0665
Final R indexes [all data]	R_1 = 0.0405, wR_2 = 0.0707
Largest diff. peak/hole / e $Å^{-3}$	1.25/-0.72

Crystal Growth Conditions and Additional Refinement Details

G3XB

Diffraction quality crystals of **G3XB** were grown by vapor diffusion of diethyl ether into an ethyl acetate solution of **G3XB** resulting in yellow needles.

Diffraction data were collected at 105 K. The hydrogen atom locations of the aniline amine were found from the difference maps, placed, and refined with isotropic thermal parameters. Upon refinement the N—H bond distances reduced to an unreasonable length necessitating the use of bond distance restraints (DFIX 0.87 0.02).

---

nHBeXB

Colorless needles were obtained by slow evaporation of a methanol solution of the parent compound.

After initial refinement, it was apparent the trifluoromethyl (CF_3) group on the central benzene ring was disordered. The disorder was modeled over two positions using a PART instruction and tied to an individual free variable. Refinement of the free variable showed an approximate 70:30 disorder for the CF_3 group. The disorder model incorporated both bond length and thermal ellipsoid similarity restraints (SADI 0.02 and SIMU 0.08).

G3HB-triclinic

Diffraction quality crystals of **G3HB** were grown by slow evaporation of a benzene solution of **G3HB** resulting in colorless rods.

During anisotropic refinement, the fluorine atoms of one CF_3 group exhibited elongated ellipsoids suggesting disorder. The fluorine atoms of the CF_3 group were subsequently modeled over two positions using a PART instruction and tied to an individual free variable. Refinement of the free variable shows an approximate 57:43 disorder for the CF_3 group. In modeling the disorder, additional bond length (SADI 0.02) and thermal ellipsoid (SIMU 0.04 0.08) similarity restraints were utilized.

G3HB-orthorhombic

Diffraction quality crystals of **G3HB** were grown by vapor diffusion of diethyl ether into an ethyl acetate solution of **G3HB** resulting in colorless plates.

Several CF_3 groups displayed disorder. Two of the groups were modeled over two positions using a PART instruction and tied to an individual free variable. Refinement of the free variables shows an approximate 55:45 and 57:43 disorder for the CF_3 groups. The disorder of these CF_3 groups is likely dynamic in nature, and there was no improvement in the model by modeling this disorder of this group over 3 or more sites. One fluorine atom in the model presented has an elongated ellipsoid causing Level B Alert in the checkCIF suggesting further disorder. Attempts at producing suitable disorder model were unsuccessful. Contributing to the difficulty of finding was suitable model was the lack of observable secondary sites for the other fluorine atoms in the CF_3 group containing fluorine F8A. As such a model of simplicity was chosen for as a more complex disorder model would not significantly enhance the results and would necessitate several geometrical and thermal constraints.

2H-G3XB

Light yellow plates were grown from by slow evaporation of a acetone solution of **2H-G3XB.**

The hydrogen atoms of the amine required a N—H bond distance restraint (DFIX 0.87 0.02) due to unreasonable lengthening of the N—H bond upon initial refinement.

Me-G3XB

Yellow plank-like crystals of **Me-G3XB** were grown by slow evaporation of an diethyl ether and methanol solution of **Me-G3XB** and tetraphenylphosphonium chloride.

The hydrogen atoms of the amine required a N—H bond distance restraint (DFIX 0.87 0.02) due to unreasonable shortening of the N—H bond upon refinement.

F-G3XB

Yellow plates were grown by slow evaporation of an ethyl acetate and hexanes solution of **F-G3XB** and tetraphenylphosphonium iodide.

The hydrogen atoms of the amine required a N—H bond distance restraint (DFIX 0.87 0.02) due to unreasonable shortening of the N—H bond upon refinement.

G3XB-Cl^-

Colorless plates of **G3XB-Cl$^-$** were grown by vapor diffusion of hexanes into a benzene solution of **G3XB** and tetra-*n*-butyl ammonium chloride.

Diffraction data were collected at 105 K. The hydrogen atoms of the amine required a N—H bond distance restraint (DFIX 0.87 0.02) due to unreasonable shortening of the N—H bond upon refinement.

2H-G3XB-Cl$^-$

Colorless needles of **2H-G3XB-Cl$^-$** were grown by vapor diffusion of hexanes into a benzene solution of **2H-G3XB** and tetra-*n*-hexyl ammonium chloride.

Upon initial solution of the data, it was evident that one of the hexyl groups of the tetra-*n*-hexylammonium (THA) molecules was severely disordered. Subsequent modeling and refinement indicated that proximal to the hexyl disordered region a benzene molecule had partial occupancy. After several hours of considering disorder models we conceded. The various models we came up with to describe this region were not completely satisfactory, as the benzene molecule and the hexyl groups were always too close to each other, meaning the models were not chemically reasonable. All this despite evidence from the difference map the presence of a partially occupied benzene is present*, and the existence of THA hexyl group is undeniable. Our best overall disorder model described three locations of the disordered alkyl portion of the THA that were modeled and refined using free variables tied to a SUMP command to ensure full occupancy. To ensure a stable refinement here, various bond length and angle (1,3 distances) similarity restraints as well as thermal ellipsoids restraints and constraints were employed. The benzene molecule was geometrically constrained to a hexagonal shape, treated with a PART -1 command, and refined freely using a free variable. After treating the data in this manner there remained some diffuse electron density located in a channel that can be viewed by viewing a packing diagram down the crystallographic *c* axis. The disordered solvent in this channel was most likely hexane, considering the crystals were grown from a benzene/hexanes vapor diffusion. The SQUEEZE[14] routine within PLATON[15] was utilized to account for the residual, diffuse electron density and the model is refined against these data. A total of 78 electrons per unit cell were corrected for. Collectively this data led to an R_1 statistic ($I > 2\sigma(I)$) of 3.46%.

Considering the extensive use of restraints and constraints to model the disorder in a manner not fully chemically reasonable and the fact that no additional information is gained by modeling this region we ultimately decided to treat the disorder of hexyl chain and the benzene molecule using the SQUEEZE program. The program accounted for 412 electrons per unit cell (this included the diffuse solvent molecules found in the channels that propagate along the crystallographic *c* axis). Treating the data in this manner led to a minor improvement in the R_1 statistic to 3.35 % ($I > 2\sigma(I)$) over the model described in the previous paragraph.

*We considered that the benzene might not be located here and that potentially it could be intertwined hexyl disorder and the Q-peaks are just coincidentally in a roughly hexagonal shape. However, we feel this is unlikely. First, the crystals were grown using benzene, so the

presence of this species would be understandable. Second, for the hexyl group to reach several of the residual electron density peaks (of the benzene) the cation would need an additional carbon atom on the alkyl chain or the entire cation would need to be translated which the data do not support.

2Me-G3XB-Cl$^-$

Colorless prisms of **2Me-G3XB-Cl$^-$** were grown by vapor diffusion of hexanes into a benzene solution of **2Me-G3XB** and tetra-*n*-butyl ammonium chloride.

H-G3XB-Cl$^-$

Yellow Rods of **H-G3XB-Cl$^-$** were obtained by vapor diffusion of hexanes into a benzene solution of **H-G3XB** and tetra-*n*-butyl ammonium chloride.

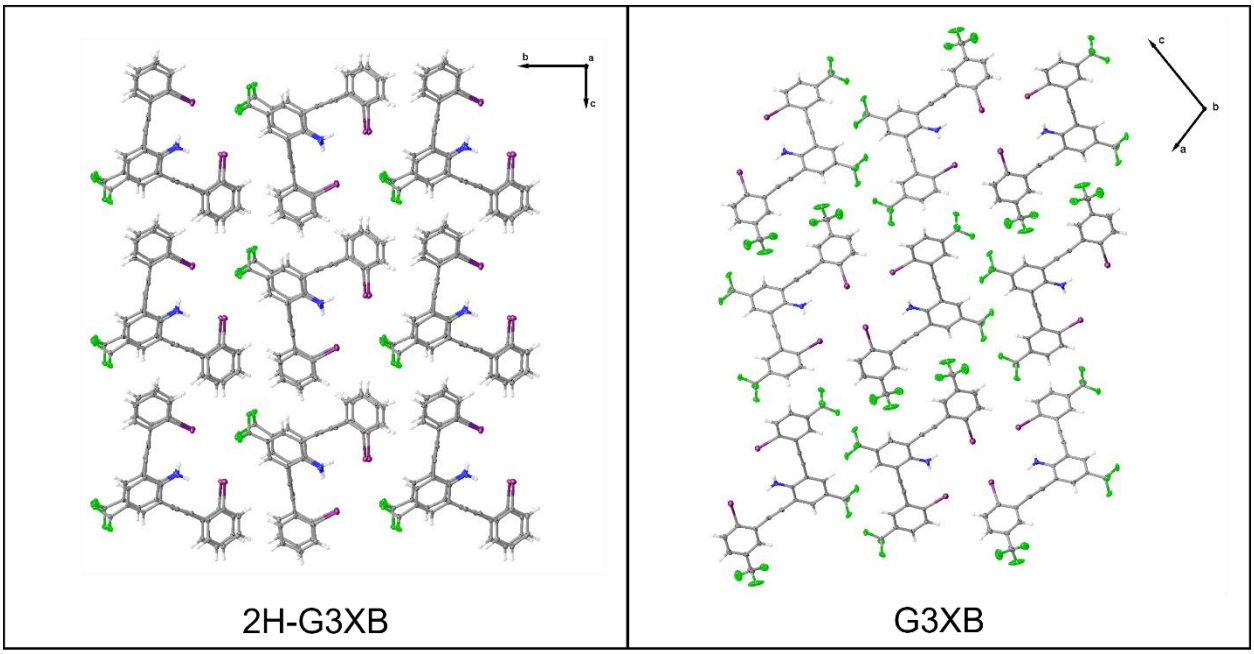

Figure S158. Crystal packing diagram showing one example of the long-range packing differences between **G3XB** and **2H-G3XB**. Thermal ellipsoids are drawn at the 50% probability level.

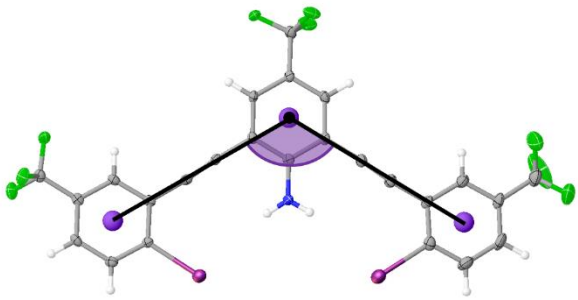

Figure S159**.** Image of **G3XB** showing the angle formed by the centroids of the three rings (i.e. flanking-core-flanking angle). Thermal ellipsoids are drawn at the 50% probability level.

Table S5. **Intramolecular HBing N-H…I distances of G3XB derivatives**

	Space group	N-H···I_1 (Å)	N-H···I_2 (Å)	Average (Å)
G3XB	$P2_1/c$	3.12	3.20	3.16
2H-G3XB	$P2_1$	3.16 / 3.16	3.00 / 2.99	3.08/3.08
Me-G3XB	$P2_1/n$	3.16	3.48	3.32
F-G3XB (S conformation)	C2/c	3.13		

Methoxy derivative

We also evaluated the **2R_2-G3XB** receptor containing methoxy substituent. The methoxy group at the *para* position is considered an electron withdrawing substituent by inductive/field effect, but electron-releasing by resonance effect. We initially assumed the *para* methoxy substituent would decrease the XB donor ability the most according to its Hammet parameter (σ_{para} = -0.268). However, noticed that the **2MeO-G3XB** derivative deviated from the expected electronic trend several times. For example, the difference between $\Delta V_{s,max}$ of **G3XB** and $\Delta V_{s,max}$ of **2MeO-G3XB** when ruling out the differences in planarity should tell us how **R_2** affect the iodine $V_{s,max}$ via intramolecular HBing. However, this value was not the highest as expected. Additionally, the **2MeO-G3XB** did not have the lowest association constant (K_a = 62 M^{-1}) among **2R_2-G3XB** derivatives. With this derivative included in the LFER analysis, a poor correlation is obtained for both σ_{meta} (R^2=0.88) and σ_{para} (R^2=0.89). This deviation from the expected trend potentially indicates a subtle interplay between preorganization and maximizing the XB donor strength and makes us question the utility of using the methoxy Hammett parameters for interpreting molecular recognition.

References

1. Riel, Asia Marie S., et al., *Chem. Sci.,* 2018, **9(26)**, 5828-5836.
2. Pollock J B, et al., *Journal of the American Chemical Society*, 2012, **134(25)**: 10607-10620.
3. Nair, Reji N., et al., *Topics in Catalysis* 2010, **53**, 1045-1047.
4. Asmus S, Beckendorf S, et al., *Chemistry–An Asian Journal*, 2014, **9(8)**: 2178-2186.
5. http://supramolecular.org/
6. M. Charton, *Progress in physical organic chemistry*, 1981, 119-251.
7. W. P. Ozimiński and J. C. Dobrowolski, *Journal of Physical Organic Chemistry*, 2009, **22**, 769-778.
8. Sheldrick, G. M. (1996). SADABS: Area Detector Absorption Correction; University of Göttingen, Germany.
9. Dolomanov, O.V.; Bourhis, L.J.; Gildea, R.J.; Howard, J.A.K.; Puschmann, H., (2009). J. Appl. Cryst., **42**, 339-341.
10. Sheldrick, G. M. (2015). *Acta Cryst.* **A71**, 3-8.
11. Sheldrick, G. M. (2015). *Acta Cryst.* **C71**, 3-8.
12. Bruker (2016). APEX3. Bruker AXS Inc., Madison, Wisconsin, USA.
13. Sheldrick, G.M. (2008). Acta Cryst. **A64**, 112-122.
14. Spek, A. L. (2015). Acta Cryst. **C71**, 9-18.
15. Spek, A. L. (2009). Acta Cryst. **D65**, 148-155.

Chapter 4

Synthesis of C-H HBeXB receptors

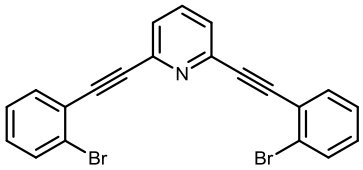

A flame dried Schlenk flask was charged with 2,6-diethynylpyridine (**1CoreDePro**) (0.2 g, 1.57 mmol), Bis(triphenylphosphine)palladium (II) dichloride (0.044 g, 0.06 mmol) and Copper (I) iodide (0.011 g, 0.06 mmol) and then sealed with a rubber septum. The Schlenk flask was then evacuated and backfilled with dry nitrogen gas three times. To a flame dried 50 ml round bottom flask was added tetrahydrofuran and triethylamine. The round bottom was sealed with a rubber septum and then sparged with dry nitrogen gas for 20 minutes, after which 2-bromo-iodobenzene (1.11 g, 3.93 mmol) was added and sparging resumed for 2 minutes. The 2-bromo-iodobenzene solution was then canula transferred to the Schlenk flask and stirred at room temperature overnight. The crude reaction mixture was concentrated and purified by silica gel column chromatography (5% ethyl acetate in hexanes) to afford **1Br** (0.448 g, 1.02 mmol, 65 % yield) as a white solid.

^{1}H NMR (500 MHz, $CDCl_3$) δ 7.71 (t, *J* = 7.4 Hz, 1H), 7.66 – 7.61 (m, 4H) (overlap of two doublets), 7.57 (d, *J* = 7.8 Hz, 2H), 7.32 (td, *J* = 7.6, 1.2 Hz, 2H), 7.23 (td, *J* = 7.8, 1.7 Hz, 2H).

^{13}C NMR (126 MHz, $CDCl_3$) δ 143.76, 136.59, 134.04, 132.65, 130.38, 127.26, 127.09, 126.07, 124.50, 92.47, 88.24.

HRMS (ESI pos) m/z for $C_{21}H_{12}Br_2N^+$ $[M+H]^+$: calculated:437.9311; found:437.9354

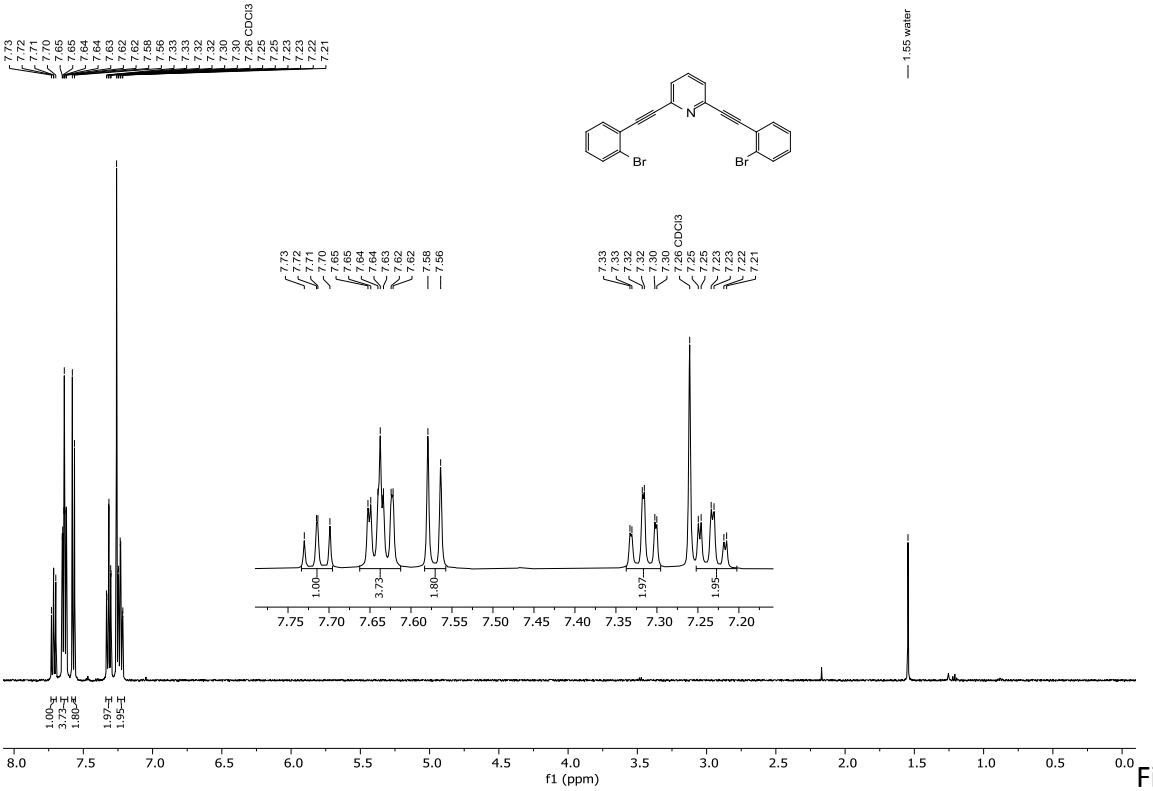

Figure S160. ^{1}H NMR spectrum of **1Br** (500 MHz, CDCl3)

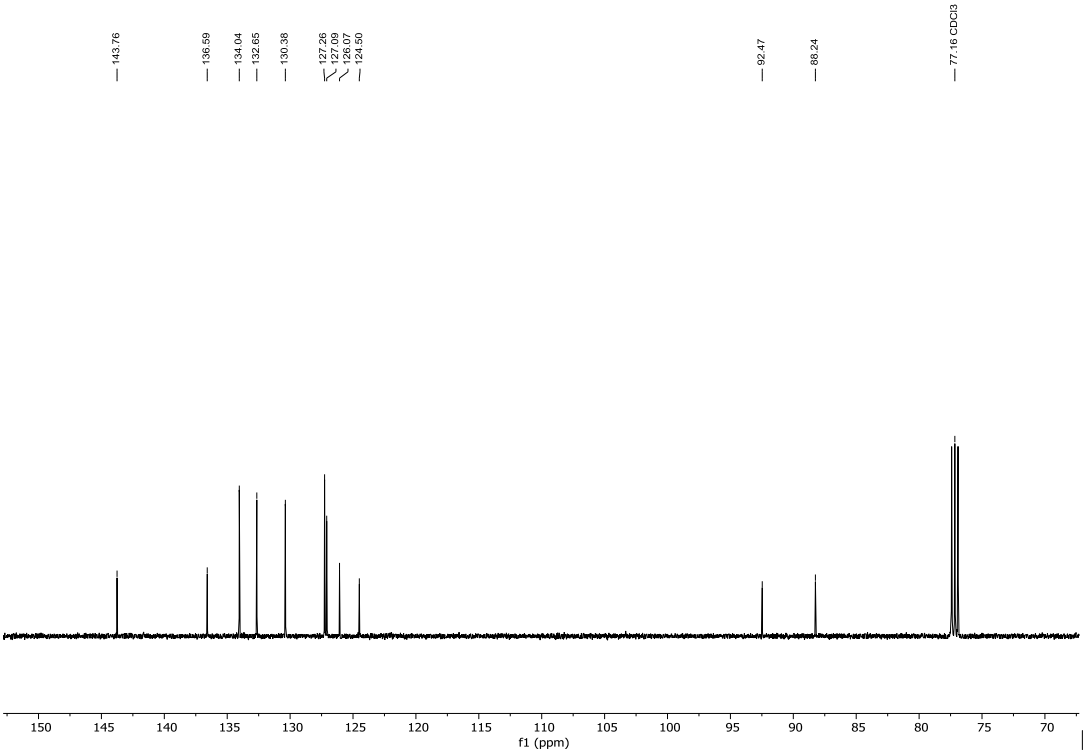

Figure S161. ^{13}C NMR spectrum of **1Br** (126 MHz, $CDCl_3$)

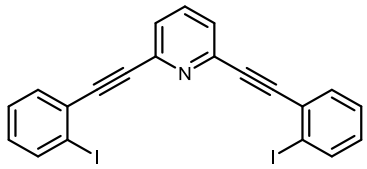

An oven dried round bottom (50 mL) was charged with **1Br** (0.10 g, 0.228 mmol) was subsequently dissolved in 20 mL of dry tetrahydrofuran and cooled to -67° C (dry ice and acetone bath). N-butyllithium (1.6 M in hexanes, 0.36 mL, 0.57 mmol) was added dropwise to the colorless solution producing a yellow solution that darkened overtime. The mixture was stirred for 30 min at -67° C. Iodine (0.29 g, 1.14 mmol) in 5 mL of tetrahydrofuran was cooled to -67° C then added dropwise. The resulting blood red solution was allowed to gradually warm to room temperature and stirred overnight. The crude reaction mixture was washed with a saturated aqueous sodium thiosulfate solution and extracted with diethyl ether. The organic layers were combined and dried with magnesium sulfate. The crude product was loaded onto C18 silica gel and subsequently purified via prep-HPLC to afford **1Neu** (0.1 g, 0.188 mmol, 82 % yield) as a beige solid.

^{1}H NMR (500 MHz, $CDCl_3$) δ 7.89 (d, *J* = 8.1 Hz, 1H), 7.73 (t, *J* = 7.2 Hz, 1H), 7.62 (dd, *J* = 7.8, 1.8 Hz, 2H), 7.61 (d, *J* = 7.8 Hz, 2H), 7.36 (t, *J* = 7.6 Hz, 1H), 7.07 (td, *J* = 7.8, 1.7 Hz, 2H).

^{13}C NMR (126 MHz, $CDCl_3$) δ 143.80, 138.95, 136.59, 133.39, 130.36, 128.87, 128.07, 127.06, 101.30, 91.74, 91.62.

HRMS (ESI pos) m/z for $C_{21}H_{12}I_2N^+$ $[M+H]^+$: calculated: 531.9054 found:531.9112

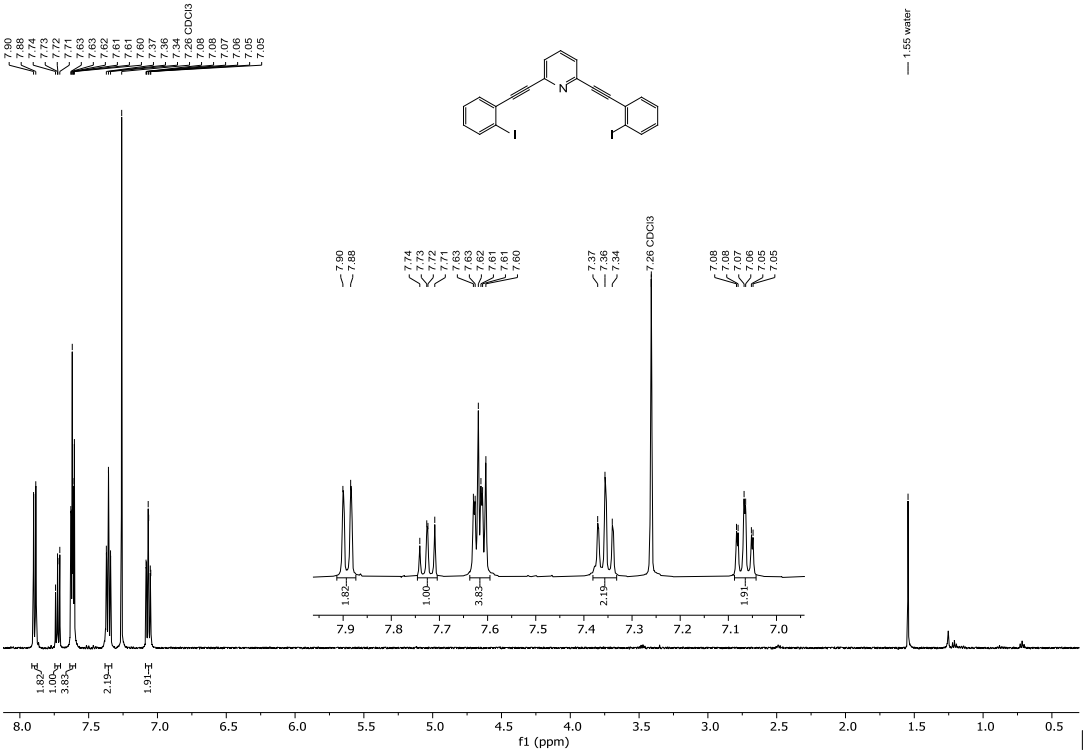

Figure S162. ^{1}H NMR spectrum of **1Neu** (500 MHz, CDCl3)

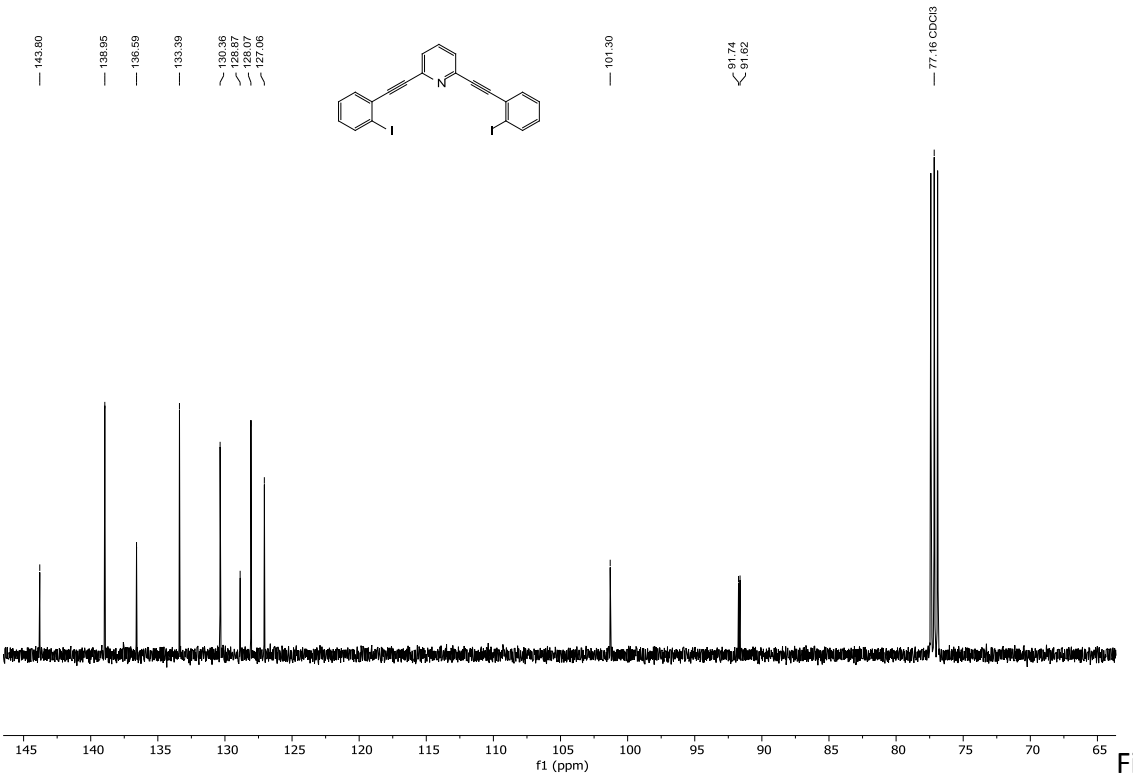

Figure S163. ^{13}C NMR spectrum of **1Neu** (126 MHz, $CDCl_3$)

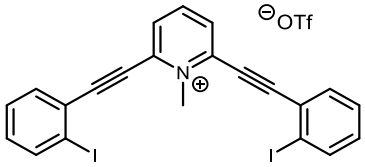

To a flame dried scintillation vial, **1Neu** (0.1 g, 0.188 mmol) was dissolved in 12ml of dry dichloromethane. Methyl trifluoromethanesulfonate(0.046 g, 0.28 mmol) was added dropwise to the solution, after which the vial was capped then allowed to stir at room temperature for 1-2 days. A light yellow precipitate formed, addition of diethyl ether facilitated further precipitation allowing **1** to be isolated by filtration. The solid was then washed with diethyl ether to afford **1** (0.12 g, 0.172 mmol, 91 % yield) as a light yellow solid.

^{1}H NMR (500 MHz, DMSO-d6) δ 8.63 (t, *J* = 8.0 Hz, 1H), 8.41 (d, *J* = 8.0 Hz, 2H), 8.10 (dd, *J* = 8.0, 1.1 Hz, 2H), 7.93 (dd, *J* = 7.7, 1.6 Hz, 2H), 7.63 (td, *J* = 7.6, 1.1 Hz, 2H), 7.39 (td, *J* = 7.8, 1.7 Hz, 2H), 4.71 (s, 3H).

^{13}C NMR (126 MHz, DMSO-d6) δ 144.12, 139.22, 138.28, 134.83, 133.24, 131.28, 128.78, 125.52, 106.53, 101.90, 83.37, 46.62. The ^{13}C resonance of the triflate anion (quartet with relative intensities of 1:3:3:1) was not observed)

^{19}F NMR (470 MHz, CD_3CN) δ -77.55

HRMS (ESI pos) m/z for $C_{22}H_{14}I_2N^+$ $[M]^+$: calculated: 545.9210 found: 545.9232

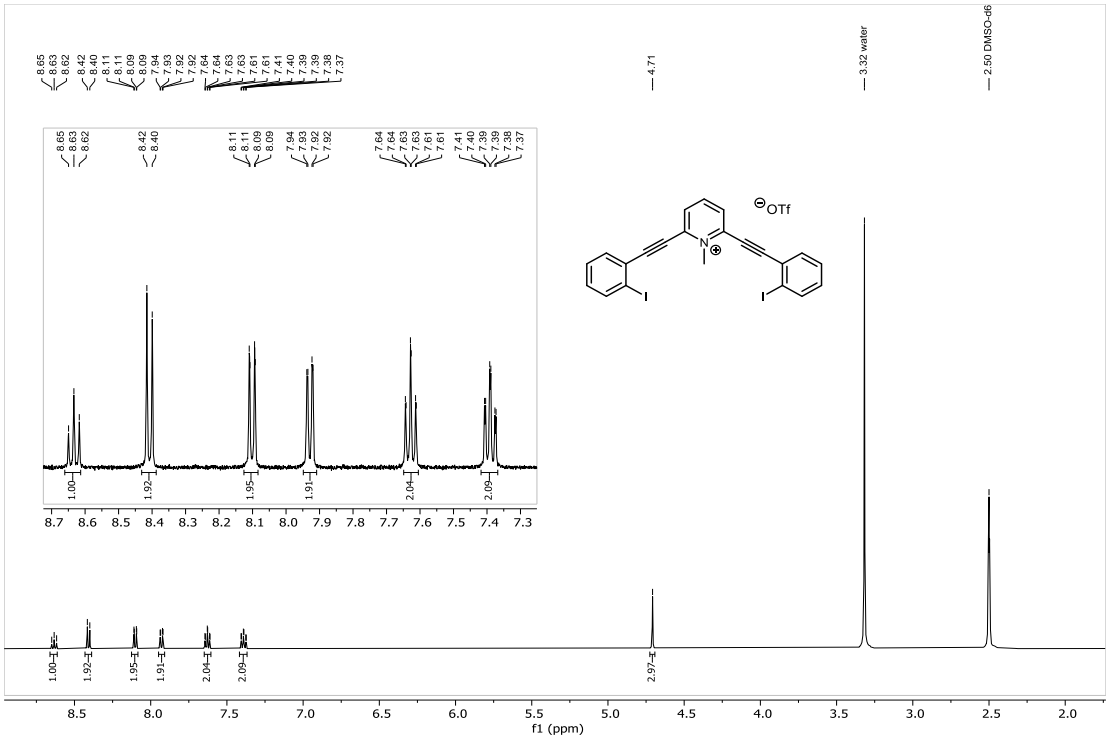

Figure S164. ^{1}H NMR spectrum of **1** (500 MHz, DMSO)

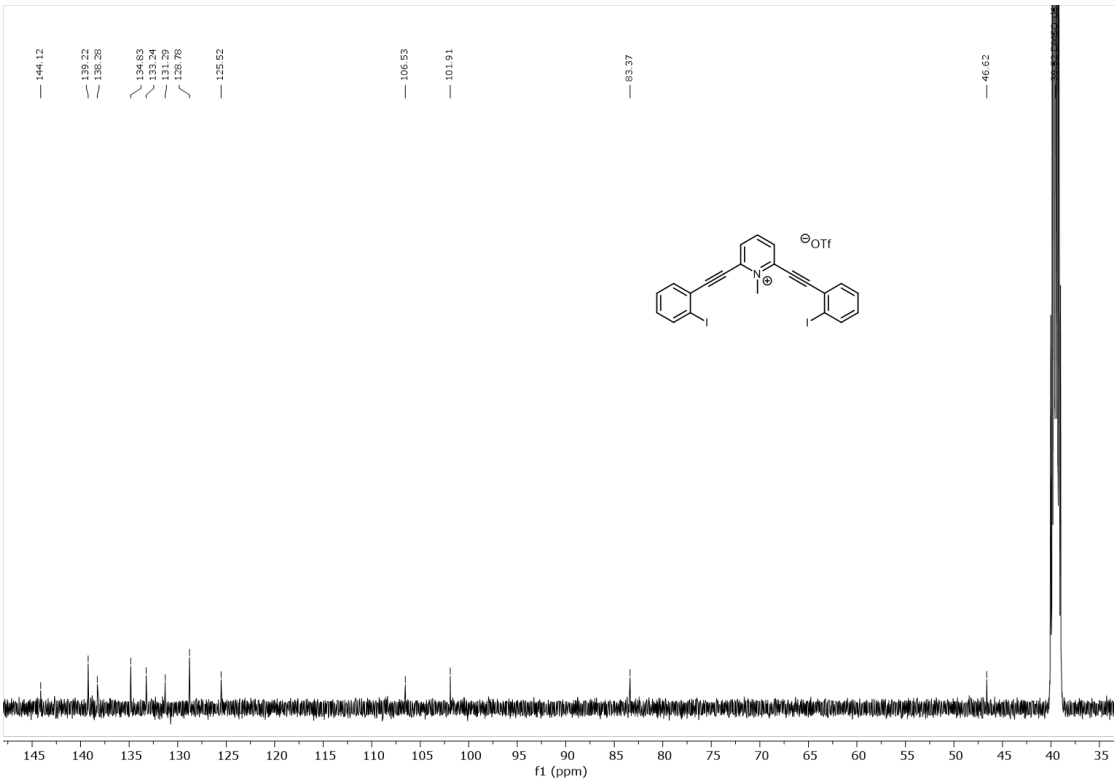

Figure S165 ^{13}C NMR spectrum of **1** (126 MHz, DMSO)

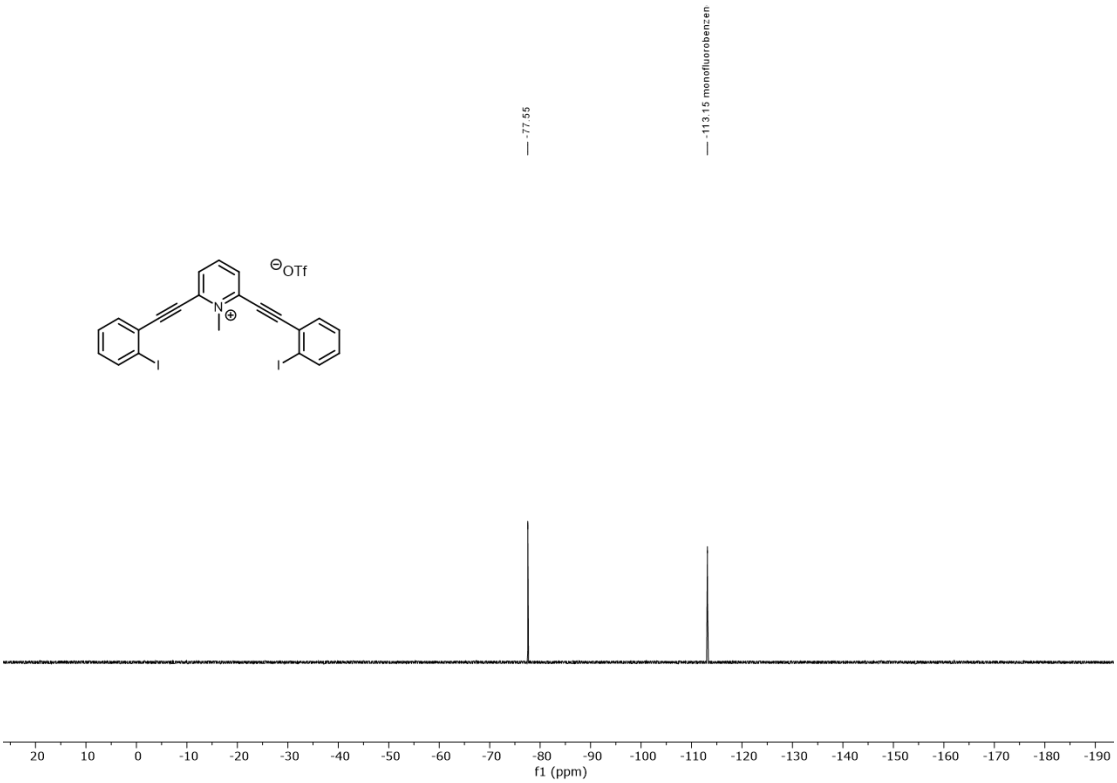

Figure S166 ^{19}F NMR spectrum of **1** (470 MHz, CD_3CN). C_6H_5F (monofluorobenzene) internal reference.

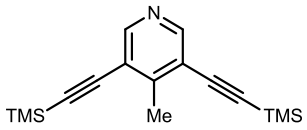

2CorePro synthesis and spectroscopic data in accordance with previously reported material. CrystEngComm (2017), 19, (23), 3094-3097.

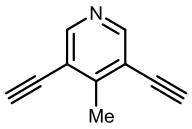

2CoreDePro synthesis and spectroscopic data in accordance with previously reported material. CrystEngComm (2017), 19, (23), 3094-3097.

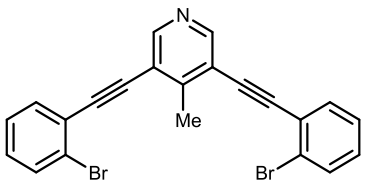

A flame dried Schlenk flask was charged with 3,5-diethynyl-4-methyl-pyridine (**2CoreDePro**) (0.3 g, 2.12 mmol), Bis(triphenylphosphine)palladium (II) dichloride (0.06 g, 0.085 mmol) and Copper (I) iodide (0.016 g, 0.085 mmol) and then sealed with a rubber septum. The Schlenk flask was then evacuated and backfilled with dry nitrogen gas three times. To a flame dried 50 ml round bottom flask was added tetrahydrofuran and triethylamine. The round bottom was sealed with a rubber septum and then sparged with dry nitrogen gas for 20 minutes, after which 2-bromo-iodobenzene (1.5 g, 5.31mmol) was added and sparging resumed for 2 minutes. The 2-bromo-iodobenzene solution was then canula transferred to the Schlenk flask and stirred at room temperature overnight. The crude reaction mixture was concentrated and purified by silica gel column chromatography (10% ethyl acetate in hexanes) to afford **2Br** (0.787 g, 1.74 mmol, 82 % yield) as a beige solid.

^{1}H NMR (500 MHz, $CDCl_3$) δ 8.67 (s, 2H), 7.65 (dd, *J* = 8.1, 1.2 Hz, 2H), 7.61 (dd, *J* = 7.7, 1.7 Hz, 2H), 7.34 (td, *J* = 7.6, 1.2 Hz, 2H), 7.24 (td, *J* = 7.8, 1.7 Hz, 2H), 2.81 (s, 3H).

^{13}C NMR (126 MHz, $CDCl_3$) δ 151.50, 151.04, 133.60, 132.74, 130.13, 127.31, 125.75, 124.97, 120.41, 94.98, 89.17, 19.46.

HRMS (ESI pos) m/z for $C_{22}H_{14}Br_2N^+$ $[M+H]^+$: calculated: 451.9467 found: 451.9479

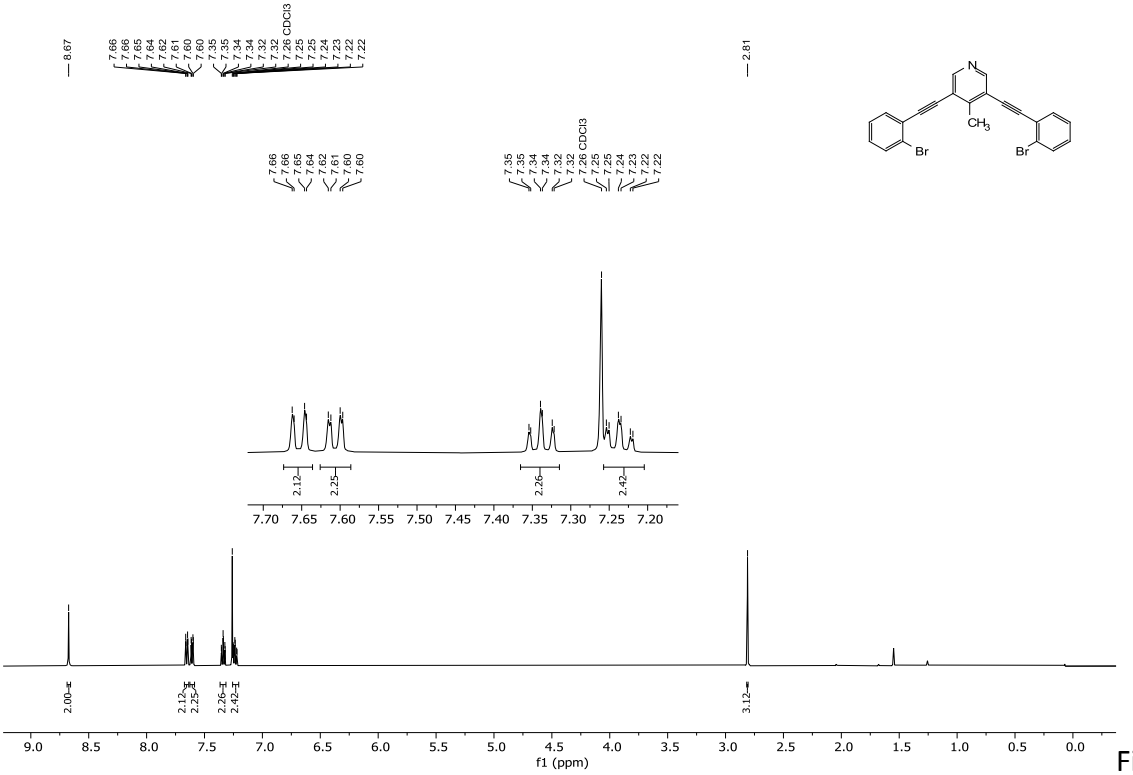

Figure S167. ^{1}H NMR spectrum of **2Br** (500 MHz, $CDCl_3$)

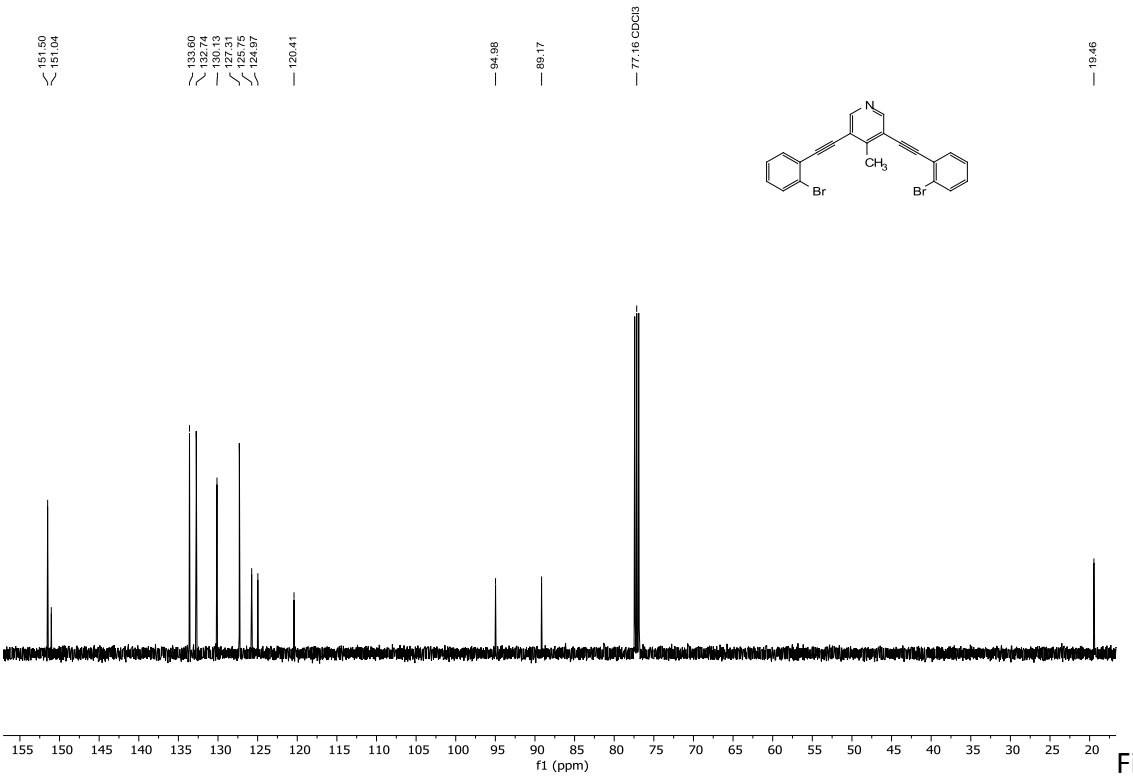

Figure S168. ^{13}C NMR spectrum of **2Br** (126 MHz, $CDCl_3$)

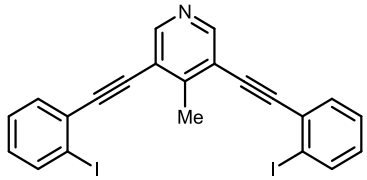

An oven dried round bottom (50 mL) was charged with **2Br** (0.2 g, 0.44 mmol) was subsequently dissolved in 20 mL of dry tetrahydrofuran and cooled to -67° C (dry ice and acetone bath). N-butyllithium (1.6 M in hexanes, 0.7 mL, 1.12 mmol) was added dropwise producing a deep beet red colored solution. The mixture was stirred for 30 min at -67° C. Iodine (0.56 g, 2.22 mmol) in 5 mL of tetrahydrofuran was cooled to -67° C then added dropwise. The resulting dark red solution was allowed to gradually warm to room temperature and stirred overnight. The crude reaction mixture was washed with a saturated aqueous sodium thiosulfate solution and extracted with diethyl ether. The organic layers were combined and dried with magnesium sulfate. The crude product was loaded onto C18 silica gel and subsequently purified via prep-HPLC to afford **2Neu** (0.089 g, 0.163 mmol, 37 %) as a light yellow solid.

^{1}H NMR (500 MHz, $CDCl_3$) δ 8.70 (s, 2H), 7.91 (dd, *J* = 7.9, 1.2 Hz, 2H), 7.59 (dd, *J* = 7.7, 1.6 Hz, 2H), 7.38 (td, *J* = 7.6, 1.1 Hz, 2H), 7.07 (td, *J* = 7.6, 1.7 Hz, 2H), 2.85 (s, 3H).

^{13}C NMR (126 MHz, $CDCl_3$, 50°C) δ 151.61, 150.84, 139.14, 133.08, 130.07, 129.60, 128.07, 120.50, 100.78, 98.28, 88.46, 19.86.

HRMS (ESI pos) m/z for $C_{22}H_{14}I_2N^+$ $[M+H]^+$: calculated:545.9210 found: 545.9189

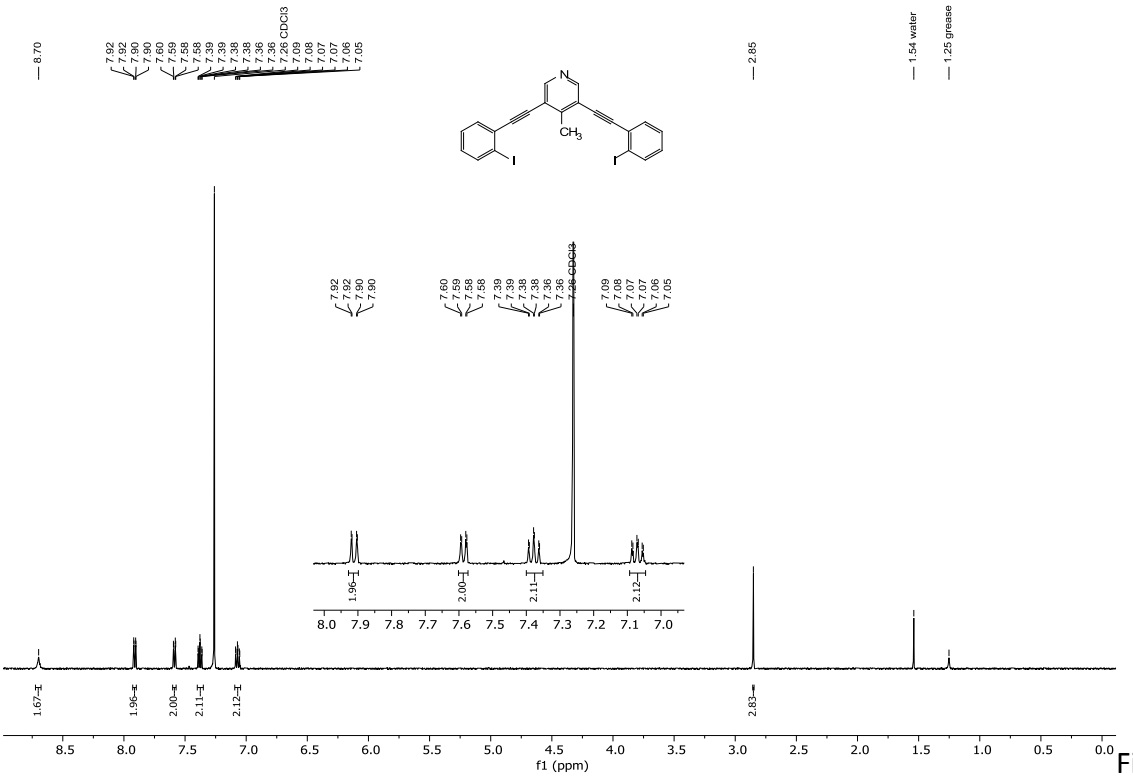

Figure S169. ^{1}H NMR spectrum of **2Neu** (500 MHz, $CDCl_3$)

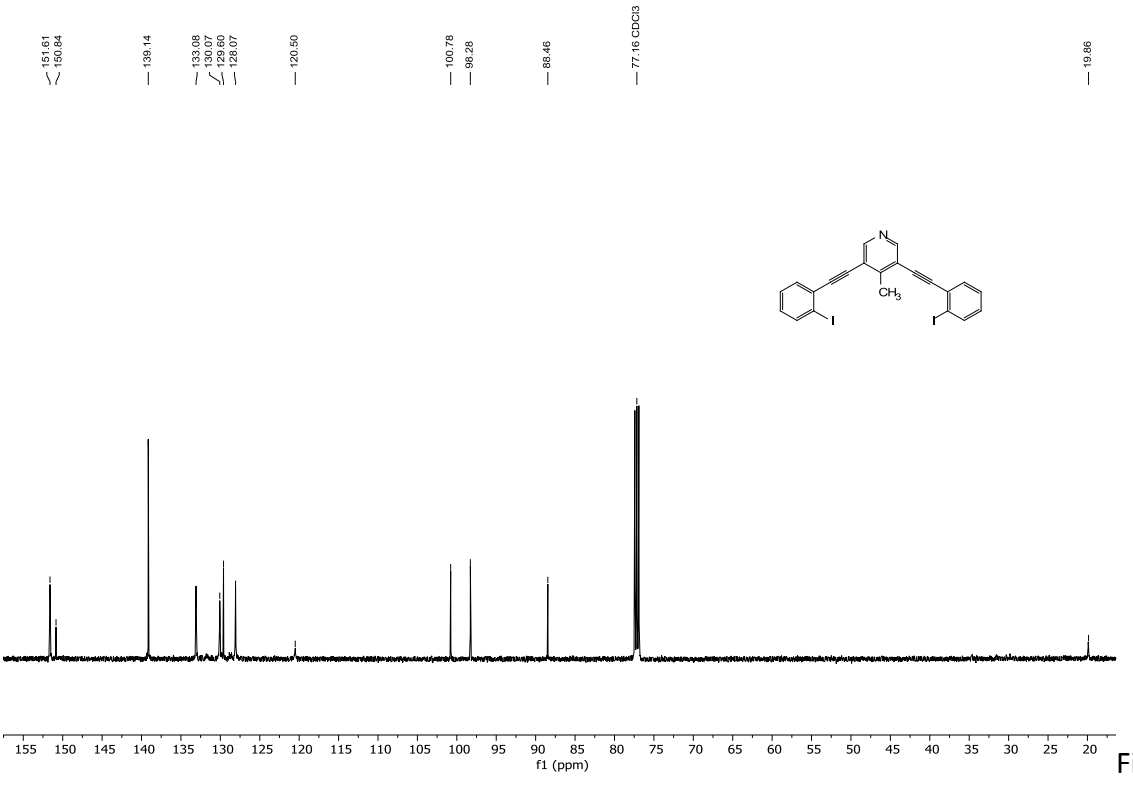

Figure S170. ^{13}C NMR spectrum of **2Neu** (126 MHz, $CDCl_3$)

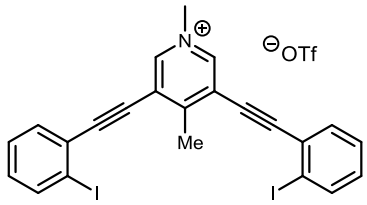

To a flame dried scintillation vial, **2Neu** (0.089 g, 0.163 mmol) was dissolved in 12ml of dry dichloromethane. Methyl trifluoromethanesulfonate (0.032 g, 0.2 mmol) was added dropwise to the solution, after which the vial was capped then allowed to stir at room temperature for 1-2 days. A white precipitate formed; diethyl ether was added to further the precipitation. The precipitate was isolated by filtration and washed with additional diethyl ether to afford **2** (0.105 g, 0.148 mmol, 91 % yield) as a white solid.

^{1}H NMR (500 MHz, CD_3CN) δ 8.73 (s, 2H), 8.02 (dd, *J* = 8.0, 1.2 Hz, 2H), 7.72 (dd, *J* = 7.7, 1.6 Hz, 2H), 7.52 (td, *J* = 7.6, 1.2 Hz, 2H), 7.26 (td, *J* = 7.8, 1.6 Hz, 2H), 4.27 (s, 4H), 3.07 (s, 3H).

^{13}C NMR (126 MHz, CD_3CN) δ 162.01, 146.27, 140.31, 134.74, 132.82, 129.64, 128.36, 125.27, 103.09, 101.01, 84.66, 49.09, 21.76. The ^{13}C resonance of the triflate anion (quartet with relative intensities of 1:3:3:1) was not observed)

^{19}F NMR (470 MHz, CD_3CN) δ -77.56.

HRMS (ESI pos) m/z for $C_{23}H_{16}I_2N^+$ [M]$^+$: calculated: 559.9367 found: 559.9342

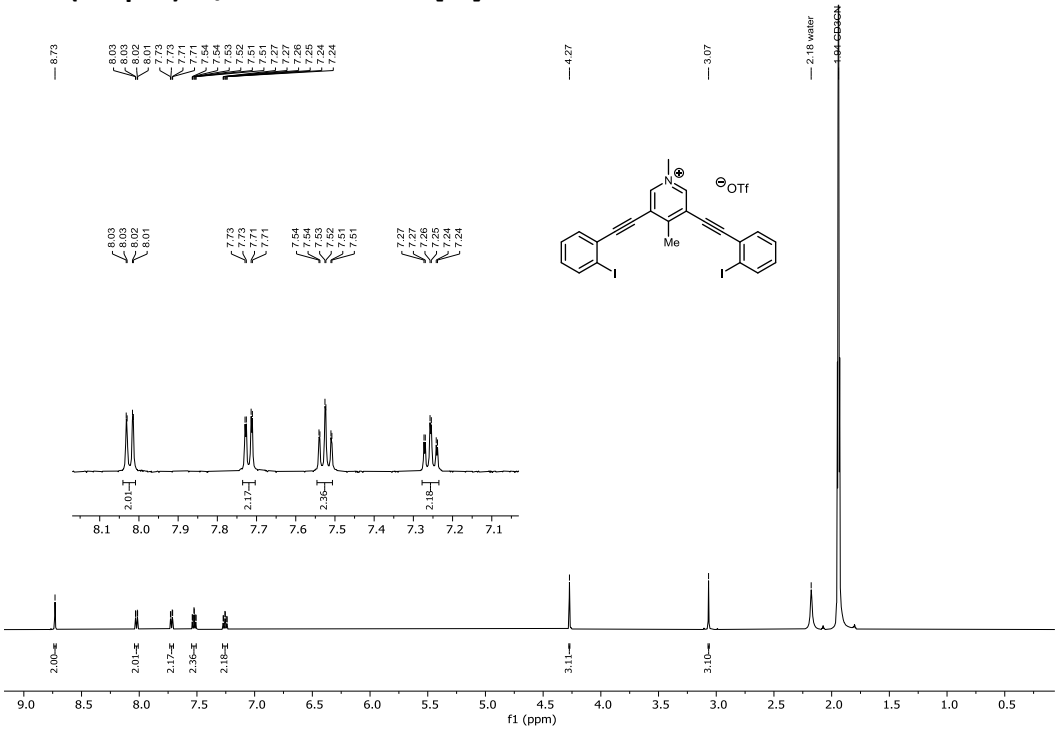

Figure S171. ^{1}H NMR spectrum of **2** (500 MHz, CD_3CN)

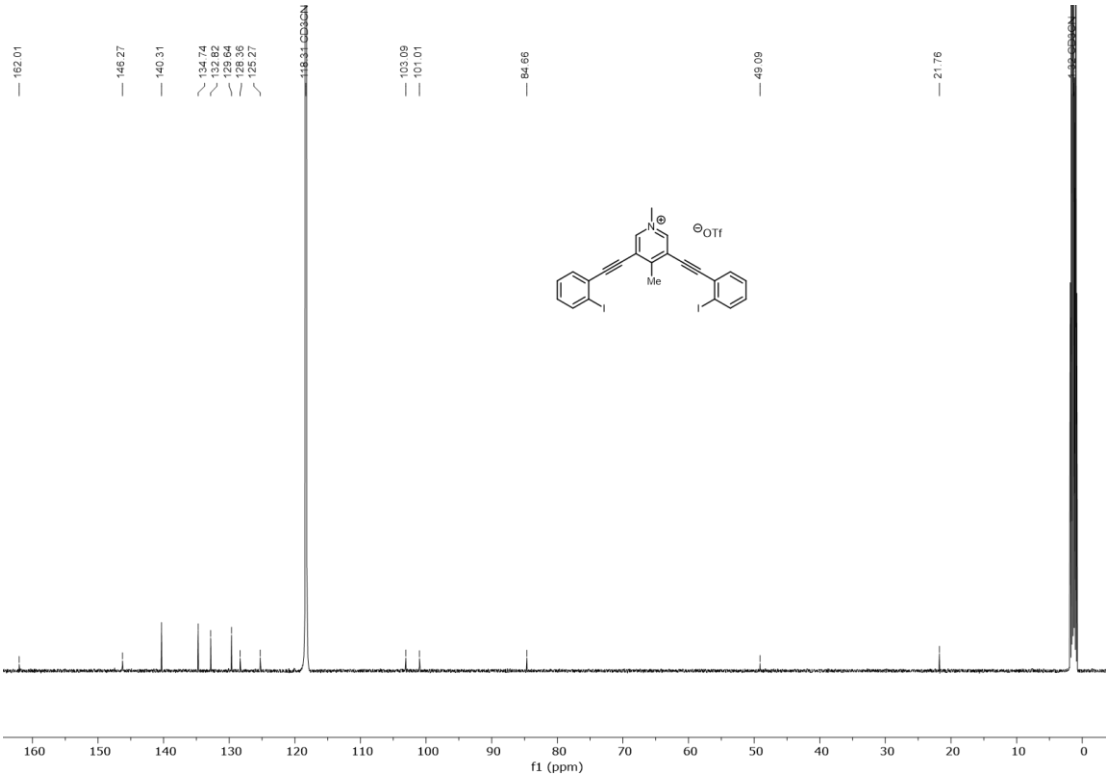

Figure S172. ^{13}C NMR spectrum of **2** (126 MHz, CD_3CN)

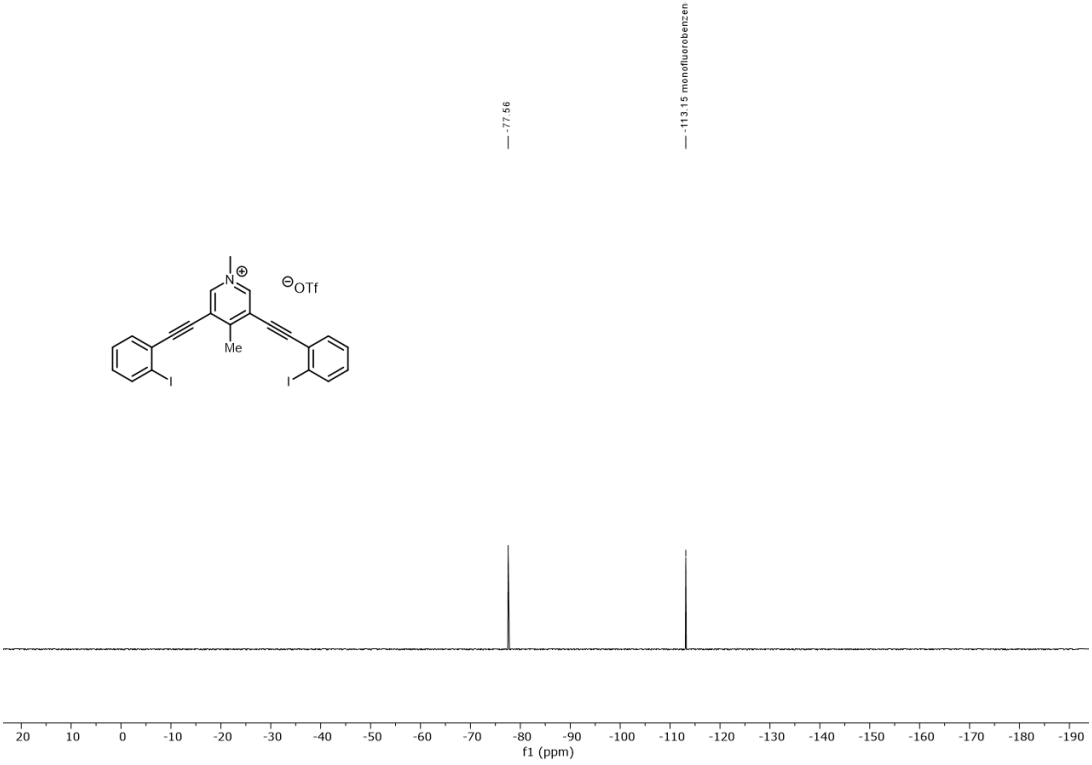

Figure S173. ^{19}F NMR spectrum of **2** (470 MHz, CD_3CN). C_6H_5F (monofluorobenzene) internal reference.

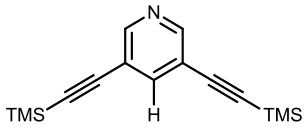

3CorePro Synthesis conducted according to previously reported procedure.

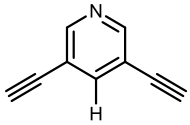

3CoreDePro Synthesis conducted according to previously reported procedure.

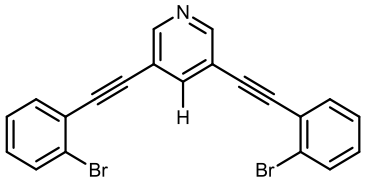

A flame dried Schlenk flask was charged with 3,5-diethynylpyridine (**3CoreDePro**) (0.16 g, 1.26 mmol), Bis(triphenylphosphine)palladium (II) dichloride (0.035 g, 0.05 mmol) and Copper (I) iodide (0.01 g, 0.05 mmol) and then sealed with a rubber septum. The Schlenk flask was then evacuated and backfilled with dry nitrogen gas three times. To a flame dried 50 ml round bottom flask was added tetrahydrofuran and triethylamine. The round bottom was sealed with a rubber septum and then sparged with dry nitrogen gas for 20 minutes, after which 2-bromo-iodobenzene (0.89 g, 3.14 mmol) was added and sparging resumed for 2 minutes. The 2-bromo-iodobenzene solution was then canula transferred to the Schlenk flask and stirred at room temperature overnight. The crude reaction mixture was concentrated and purified by silica gel column chromatography (5% ethyl acetate in hexanes) to afford **3Br** (0.433 g, 0.99 mmol, 79 %) as a white solid.

^{1}H NMR (500 MHz, $CDCl_3$) δ 8.75 (d, *J* = 2.0 Hz, 2H), 8.02 (t, *J* = 2.0 Hz, 1H), 7.65 (dd, *J* = 8.1, 1.2 Hz, 2H), 7.58 (dd, *J* = 7.7, 1.7 Hz, 2H), 7.33 (td, *J* = 7.6, 1.2 Hz, 2H), 7.24 (td, *J* = 7.7, 1.6 Hz, 2H).

^{13}C NMR (126 MHz, $CDCl_3$) δ 151.31, 140.79, 133.58, 132.76, 130.29, 127.32, 125.91, 124.66, 120.00, 91.96, 89.64.

HRMS (ESI pos) m/z for $C_{21}H_{12}Br_2N^+$ $[M+H]^+$: calculated: 437.9311 found: 437.9307

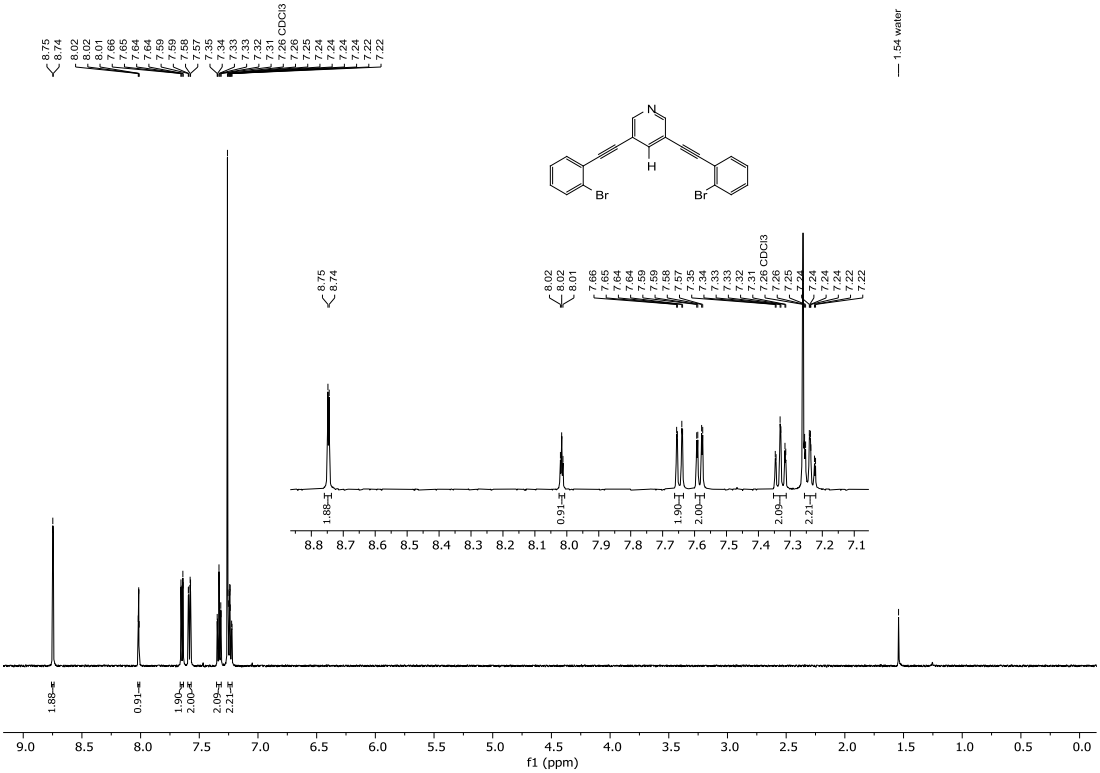

Figure S174. ^{1}H NMR spectrum of **3Br** (500 MHz, $CDCl_3$)

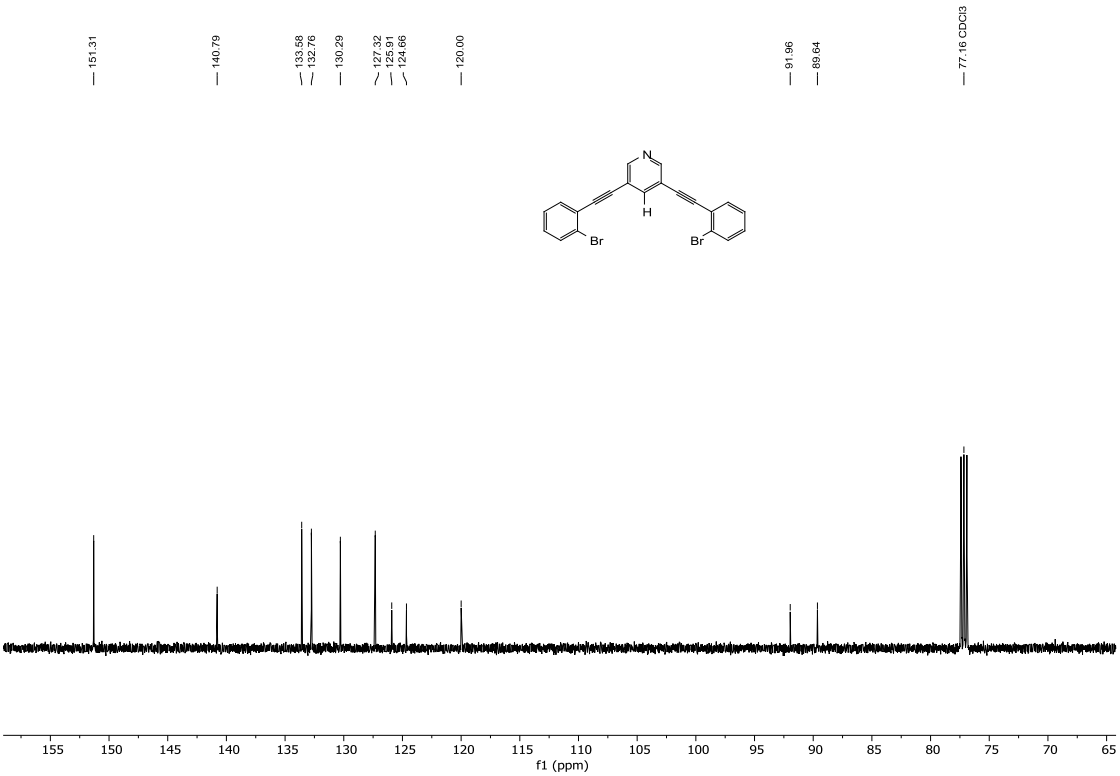

Figure S175. ^{13}C NMR spectrum of **3Br** (126 MHz, $CDCl_3$)

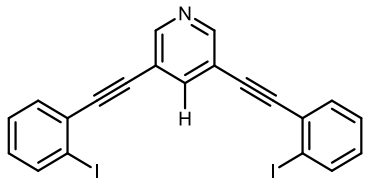

An oven dried round bottom (50 mL) was charged with **3Br** (0.2 g, 0.46 mmol) was subsequently dissolved in 20 mL of dry tetrahydrofuran and cooled to -67° C (dry ice and acetone bath). N-butyllithium (1.6 M in hexanes, 0.072 mL, 1.14 mmol) was added dropwise producing a red solution. The mixture was stirred for 30 min at -67° C. Iodine (0.58 g, 2.29 mmol) in 5 mL of tetrahydrofuran was cooled to -67° C then added dropwise. The resulting red solution was allowed to gradually warm to room temperature and stirred overnight. The crude reaction mixture was washed with a saturated aqueous sodium thiosulfate solution and extracted with diethyl ether. The organic layers were combined and dried with magnesium sulfate. The crude product was loaded onto C18 silica gel and subsequently purified via prep-HPLC to afford **3Neu** (0.103 g, 0.194mmol, 42%) as a very light yellow solid.

^{1}H NMR (500 MHz, $CDCl_3$) δ 8.77 (s, 2H), 8.04 (s, 1H), 7.91 (dd, *J* = 8.1, 1.2 Hz, 2H), 7.56 (dd, *J* = 7.7, 1.6 Hz, 2H), 7.37 (t, *J* = 7.6 Hz, 2H), 7.07 (td, *J* = 7.7, 1.7 Hz, 2H).

^{13}C NMR (126 MHz, $CDCl_3$, 50°) δ 151.31, 140.56, 139.15, 132.89, 130.22, 129.23, 128.10, 120.17, 101.24, 95.57, 88.96.

HRMS (ESI pos) m/z for $C_{21}H_{12}I_2N^+$ $[M+H]^+$: calculated: 531.9054 found: 531.9018

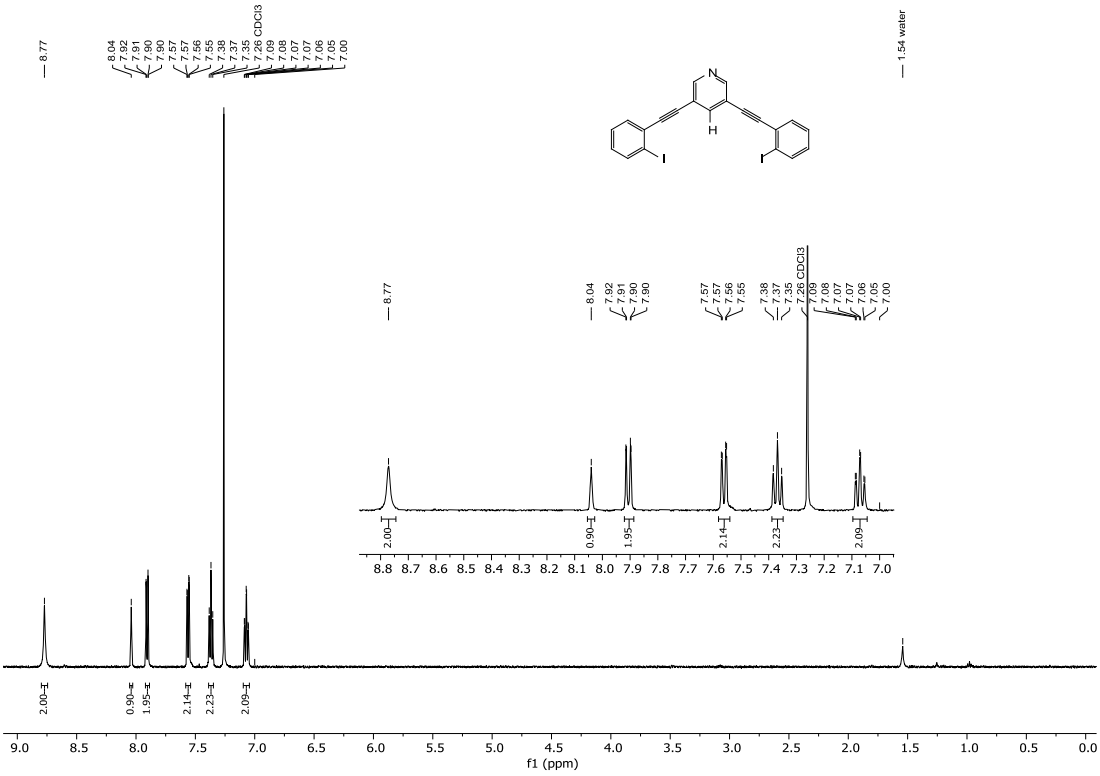

Figure S176. ^{1}H NMR spectrum of **3Neu** (500 MHz, $CDCl_3$)

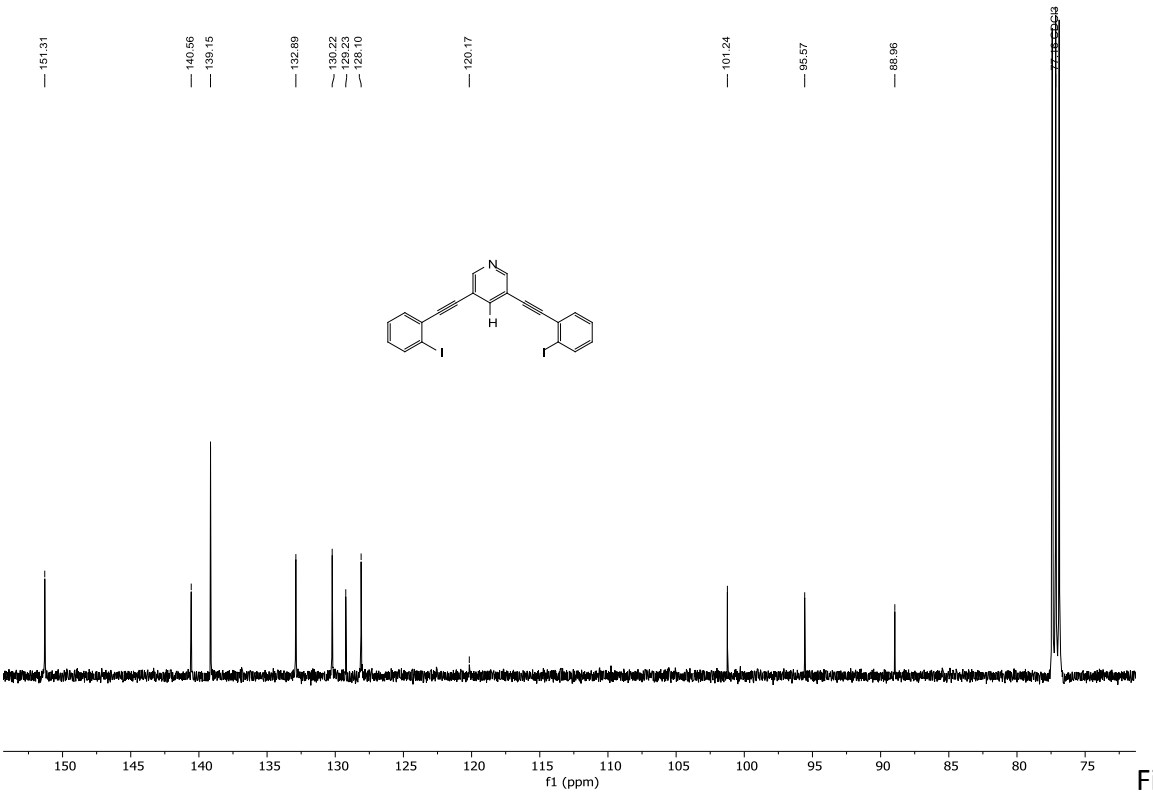

Figure S177. ^{13}C NMR spectrum of **3Neu** (126 MHz, $CDCl_3$, 50°C)

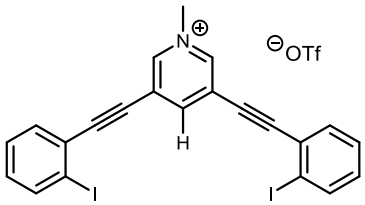

To a flame dried scintillation vial, **3Neu** (0.05 g, 0.094 mmol) was dissolved in 12ml of dry dichloromethane. Methyl trifluoromethanesulfonate(0.023 g, 0.141 mmol) was added dropwise to the solution, after which the vial was capped then allowed to stir at room temperature for 1-2 days. A white precipitate formed; diethyl ether was added to further the precipitation. The precipitate was isolated by filtration and washed with additional diethyl ether to afford **3** (0.06 g, 0.086 mmol, 91 % yield) as a white solid.

^{1}H NMR (500 MHz, CD_3CN) δ 8.81 (s, 2H), 8.68 (s, 1H), 8.02 (dd, *J* = 8.0, 1.1 Hz, 2H), 7.69 (dd, *J* = 7.7, 1.7 Hz, 2H), 7.52 (td, *J* = 7.6, 1.2 Hz, 2H), 7.26 (td, *J* = 7.8, 1.7 Hz, 2H).

^{13}C NMR (126 MHz, CD_3CN) δ 147.84, 146.09, 139.34, 133.55, 131.93, 128.68, 127.05, 124.22, 100.30, 99.53, 84.13, 48.87. The ^{13}C resonance of the triflate anion (quartet with relative intensities of 1:3:3:1) was not observed)

^{19}F NMR (470 MHz, CD_3CN) δ -77.55.

HRMS (ESI pos) m/z for $C_{22}H_{14}I_2N^+$ $[M]^+$: calculated: 545.9210 found: 545.9233

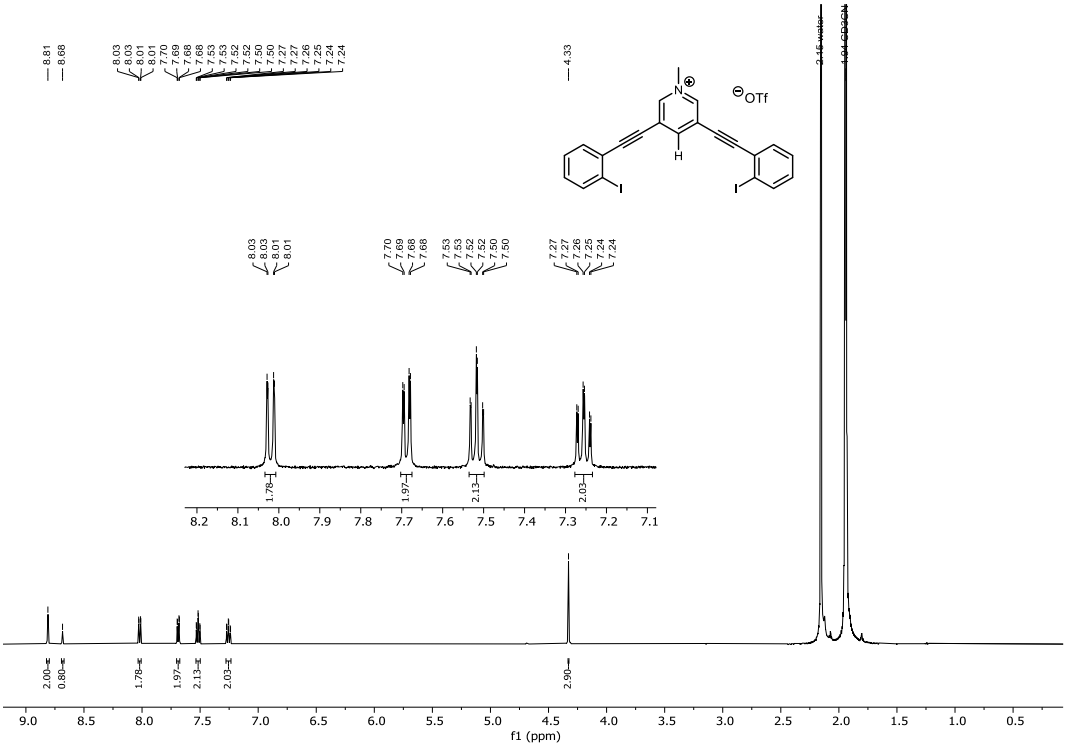

Figure S178. ^{1}H NMR spectrum of **3** (500 MHz, CD_3CN)

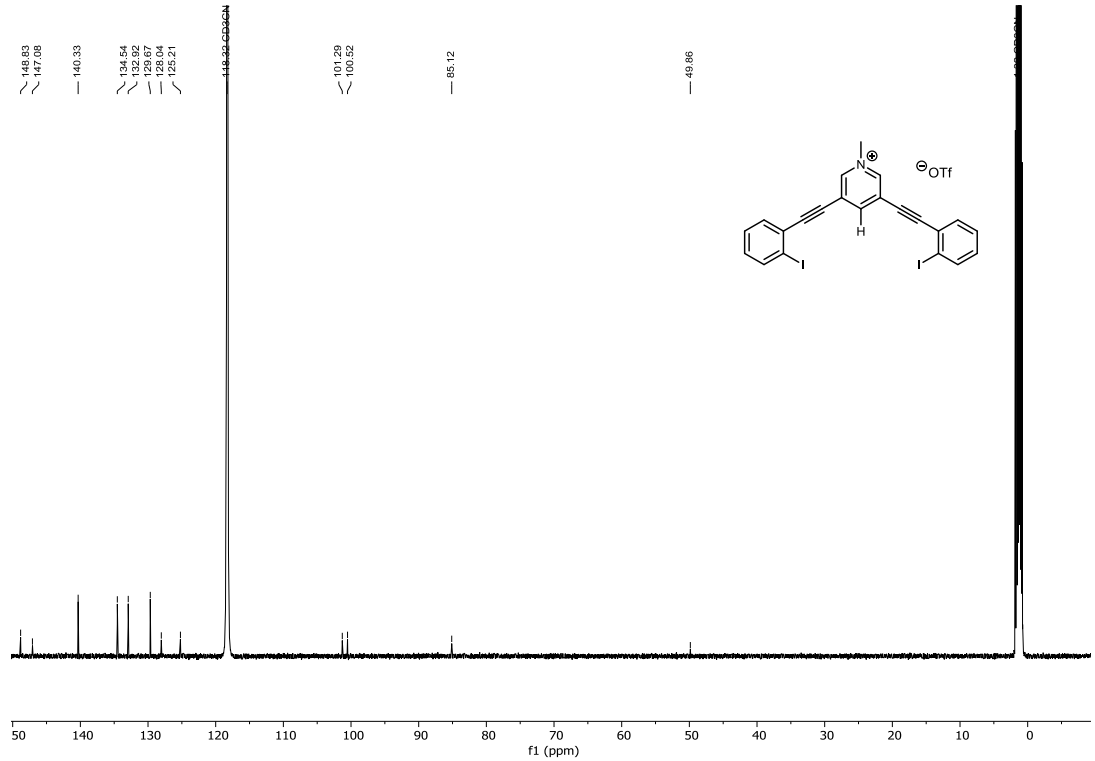

Figure S179. ^{13}C NMR spectrum of **3** (126 MHz, CD_3CN)

Figure S180. ^{19}F NMR spectrum of **3** (470 MHz, CD_3CN). C_6H_5F (monofluorobenzene) internal reference.

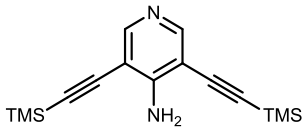

Synthesis adopted from.[10]

An oven dried Schlenk flask was charged with 3,5-dibromo-4-amino-pyridine (9.022 g, 35.7 mmol), bis(triphenylphosphine)palladium(II) dichloride (1.5 g, 2.14 mmol), and copper (I) iodide (0.68 g, 3.7 mmol) and subsequently vacuumed and backfilled with dry N_2 gas three times. While under nitrogen, the solid reagents were then dissolved in 180ml of dimethylformamide (DMF). To this stirring solution was added N,N-Diisopropylethylamine (31ml, 178.6 mmol) and trimethylsilylacetylene (10.52 g 107.2 mmol). The brown solution was then heated to 60°C and stirred for up to 2 days. Reaction progress was monitored by TLC and the reaction was pulled when consumption of starting material was observed. The reaction mixture was then run through a silica plug with a hexane/ethyl acetate solvent mixture (50:50) to remove any excess salts and catalysts. Subsequent removal of DMF, hexanes and ethyl acetate by roto-evaporation left a brown solid that was purified by silica gel column chromatography (15% ethyl acetate in hexanes) to afford **4CorePro** (5.54 g, 19.33 mmol, 54 % yield) as an off-white solid.

^{1}H NMR (500 MHz, $CDCl_3$) δ 8.27 (s, 2H), 5.20 (s, 2H), 0.27 (s, 18H).

^{13}C NMR (126 MHz, $CDCl_3$) δ 154.24, 151.77, 103.92, 103.55, 97.85, 0.07.

HRMS (ESI pos) m/z for $C_{15}H_{23}N_2Si_2^+$ [M+H]$^+$: calculated:287.1394 found: 287.1409

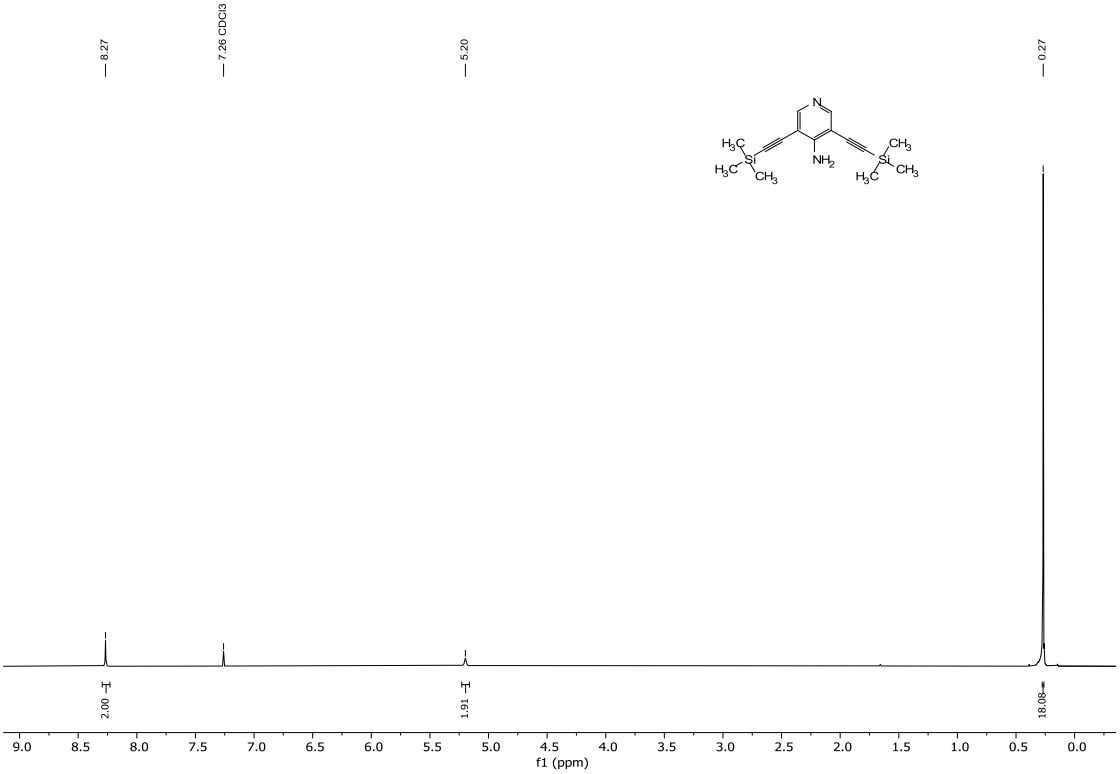

Figure S181. ^{1}H NMR spectrum of **4CorePro** (500 MHz, $CDCl_3$)

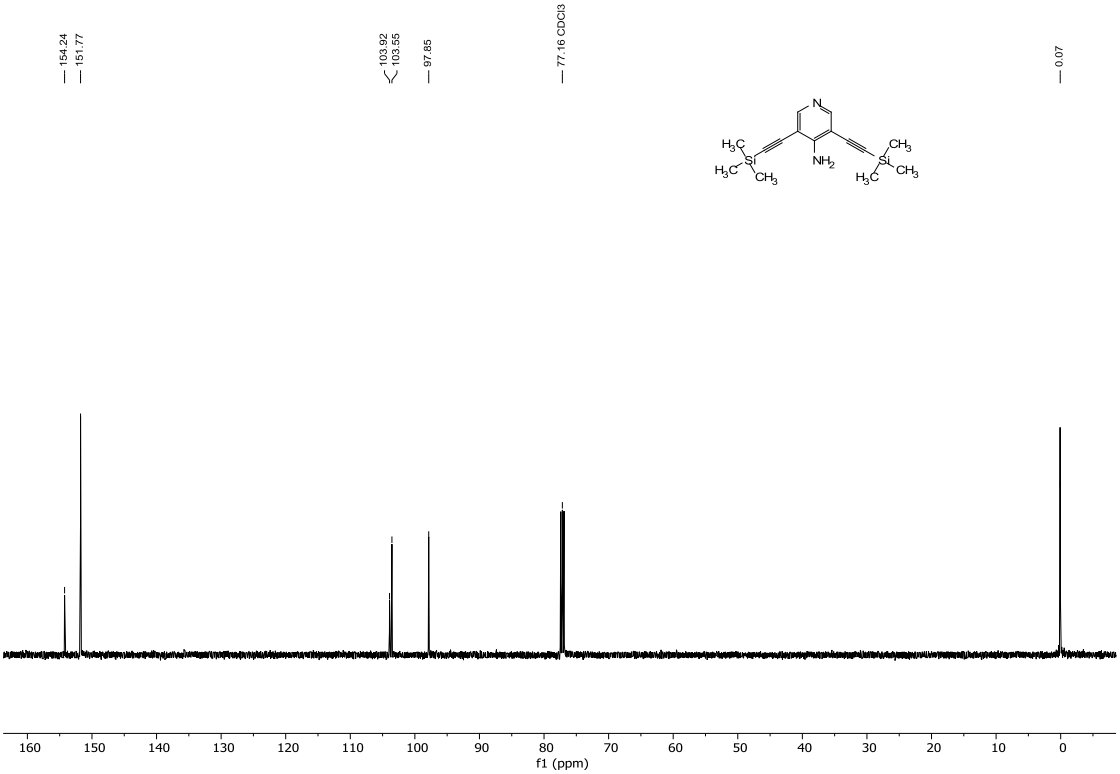

Figure S182. ^{13}C NMR spectrum of **4CorePro** (126 MHz, $CDCl_3$)

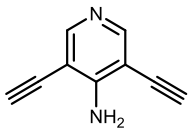

4CorePro (1.5 g, 5.24 mmol) was dissolved in 20 mL methanol and 20 mL DCM in a 250 mL round bottom flask. Potassium carbonate (1.81 g, 13.09 mmol) was added to the organic mixture. The reaction stirred vigorously for 4 hours at room temperature. The reaction progress was checked via TLC. When the reaction came to completion, water was added to quench the reaction. The crude product was extracted with ethyl acetate/hexanes (1:1) mix. The organic fractions were then dried over magnesium sulfate and vacuum filtered. The organic solution was reduced under vacuum producing an off-white solid of **4CoreDePro** (0.621 g, 4.37 mmol, 83%). Often the material can then be used in the next step without further purification. If further purification is needed, sublimation is suggested which will produce colorless crystals.
^{1}H NMR (500 MHz, $CDCl_3$) δ 8.34 (s, 2H), 5.25 (s, 2H), 3.50 (s, 2H).
^{13}C NMR (126 MHz, DMSO) δ 154.98, 151.89, 102.32, 88.62, 77.11.
HRMS (ESI pos) m/z for $C_9H_7N_2^+$ [M+H]$^+$: calculated: 143.0604 found: 143.0627

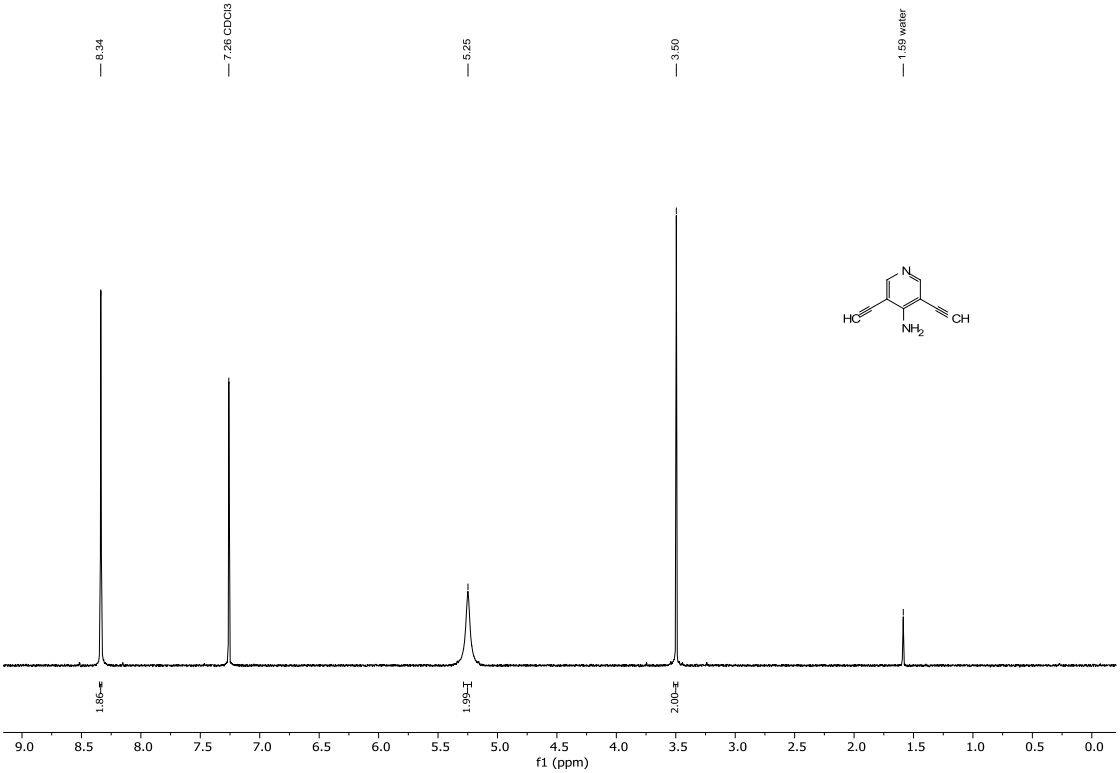

Figure S183. ^{1}H NMR spectrum of **4CoreDePro** (500 MHz, $CDCl_3$)

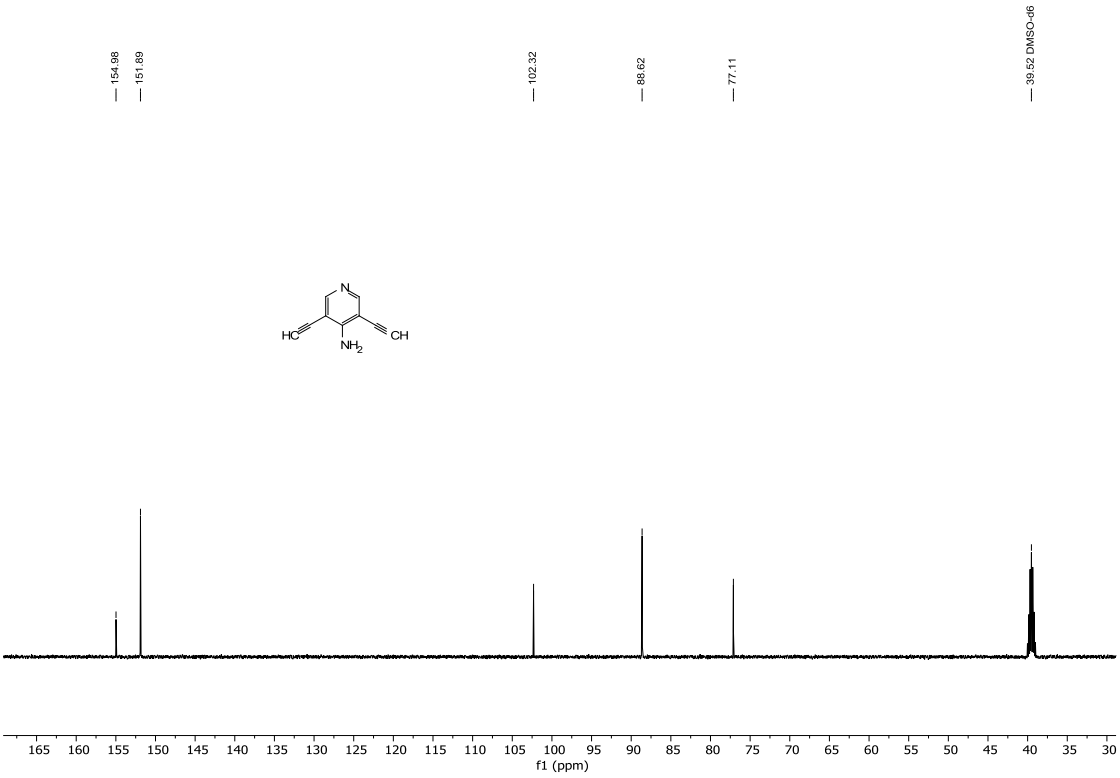

Figure S184. ^{13}C NMR spectrum of **4CoreDePro** (126 MHz, $CDCl_3$)

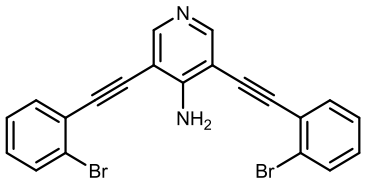

A flame dried Schlenk flask was charged with **4CoreDePro** (0.25 g, 1.76 mmol), Bis(triphenylphosphine)palladium (II) dichloride (0.05 g, 0.07 mmol) and Copper (I) iodide (0.013 g, 0.07 mmol) and then sealed with a rubber septum. The Schlenk flask was then evacuated and backfilled with dry nitrogen gas three times. To a flame dried 50 ml round bottom flask was added tetrahydrofuran and triethylamine. The round bottom was sealed with a rubber septum and then sparged with dry nitrogen gas for 20 minutes, after which 2-bromo-iodobenzene (1.24 g, 4.39 mmol) was added and sparging resumed for 2 minutes. The 2-bromo-iodobenzene solution was then canula transferred to the Schlenk flask and stirred at room temperature overnight. The crude reaction mixture was concentrated and purified by silica gel column chromatography (30% ethyl acetate in hexanes) to afford **4Br** (0.48 g, 1.06 mmol, 60 %) as a white solid.

^{1}H NMR (500 MHz, $CDCl_3$) δ 8.42 (s, 2H), 7.65 (d, *J* = 7.9 Hz, 2H), 7.60 (d, *J* = 7.9 Hz, 2H), 7.35 (t, *J* = 7.6 Hz, 2H), 7.23 (t, *J* = 7.8 Hz, 2H), 5.77 (s, 2H).

^{13}C NMR (126 MHz, $CDCl_3$) δ 154.32, 151.69, 133.15, 132.54, 129.98, 127.49, 125.33, 124.91, 103.78, 96.28, 87.25.

HRMS (ESI pos) m/z for $C_{21}H_{13}Br_2N_2^+$ $[M+H]^+$: calculated:452.9420 found:452.9448

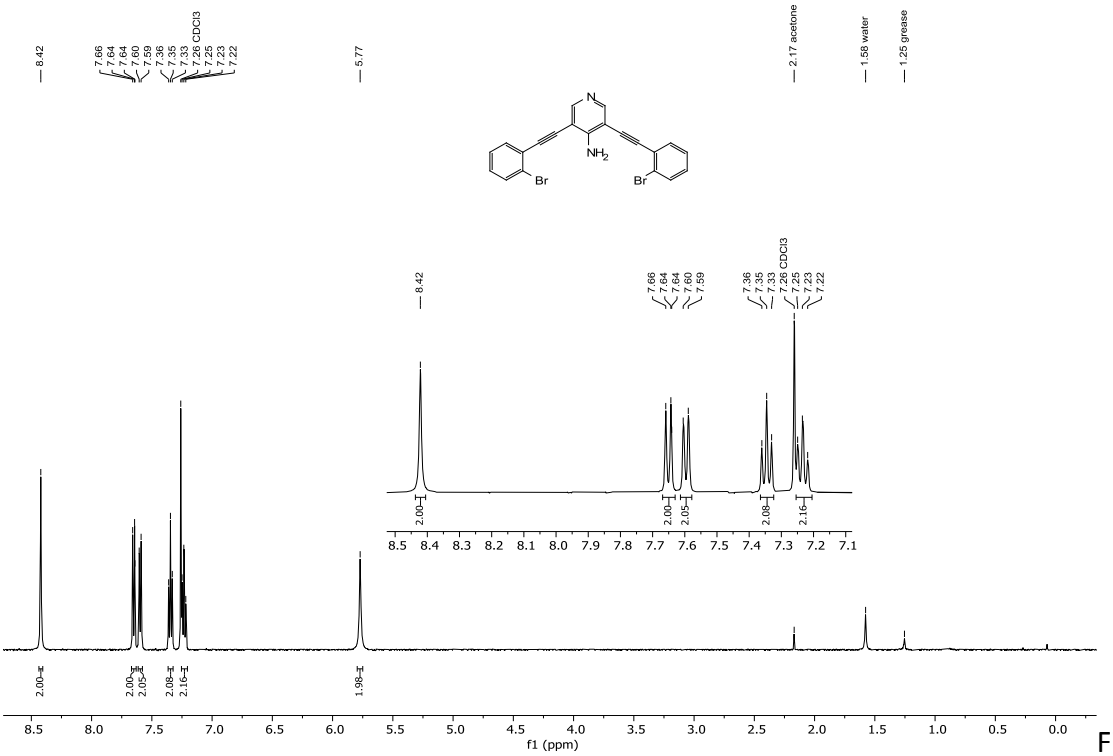

Figure S185. ^{1}H NMR spectrum of **4Br** (500 MHz, $CDCl_3$)

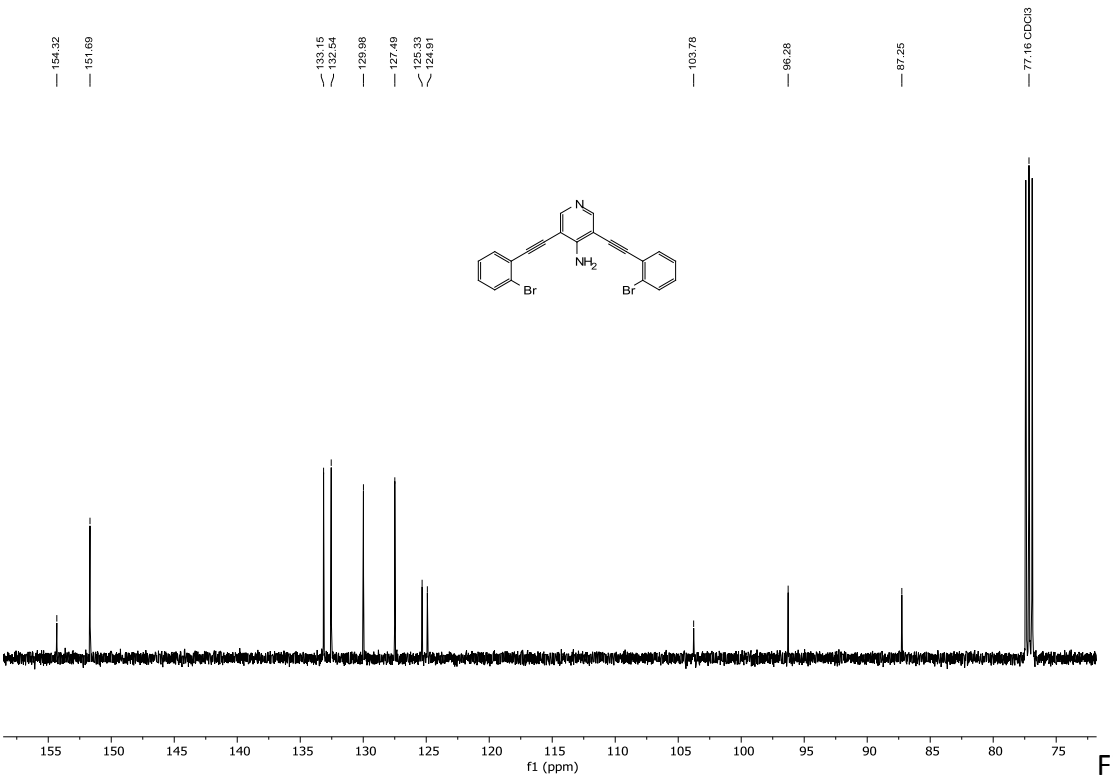

Figure S186. ^{13}C NMR spectrum of **4Br** (126 MHz, $CDCl_3$)

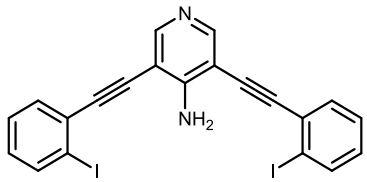

4Br (0.1 g, 0.22 mmol), copper iodide (0.004 g, 0.022 mmol), sodium iodide (0.13 g, 0.88 mmol) were added to a 10-20 mL microwave reaction vial containing a stir bar and dissolved in 10-15ml 1,4-dioxane. To the reaction mixture, transN,N'-dimethylcyclohexane-1,2-diamine (0.15 mL, 0.95 mmol) was added. The microwave vial was sealed and placed in a microwave. The reaction was performed in a Biotage Initiator+ microwave reactor for 16 hours at 150 ˚C. After cooling, an aliquot was run through pipet silica plug with EtOAc to remove catalysts and salts. The EtOAc crude was then ran through GCMS in order to obtain % conversion of bromines to iodines. If the reaction was unfinished, it would be submitted again at 30 min increments. When the reaction ran to completion, the crude reaction was run through a silica plug with EtOAc. The crude product was loaded onto C18 silica gel and subsequently purified via prep-HPLC to afford **4Neu** (0.028 g, 0.051 mmol, 23 % yield) as a beige solid.

^{1}H NMR (500 MHz, $CDCl_3$) δ 8.44 (s, 2H), 7.90 (dd, *J* = 8.1, 1.2 Hz, 2H), 7.58 (dd, *J* = 7.8, 1.6 Hz, 2H), 7.38 (td, *J* = 7.6, 1.2 Hz, 2H), 7.07 (td, *J* = 7.9, 1.7 Hz, 2H), 5.86 (s, 2H).

^{13}C NMR (126 MHz, $CDCl_3$, 45°C) δ 154.39, 151.91, 138.87, 132.74, 129.93, 129.52, 128.24, 103.89, 100.77, 99.49, 86.57.

HRMS (ESI pos) m/z for $C_{21}H_{13}I_2N_2^+$ $[M+H]^+$: calculated: 546.9163 found: 546.9183

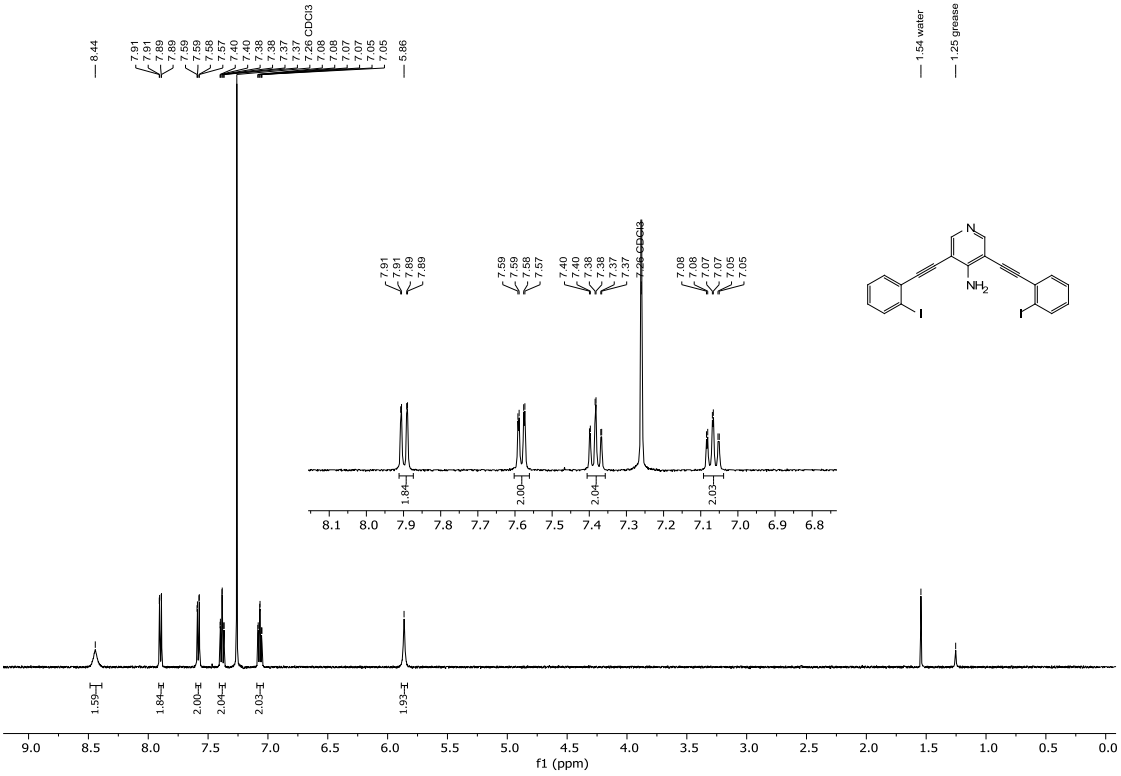

Figure S187. ^{1}H NMR spectrum of **4Neu** (500 MHz, $CDCl_3$)

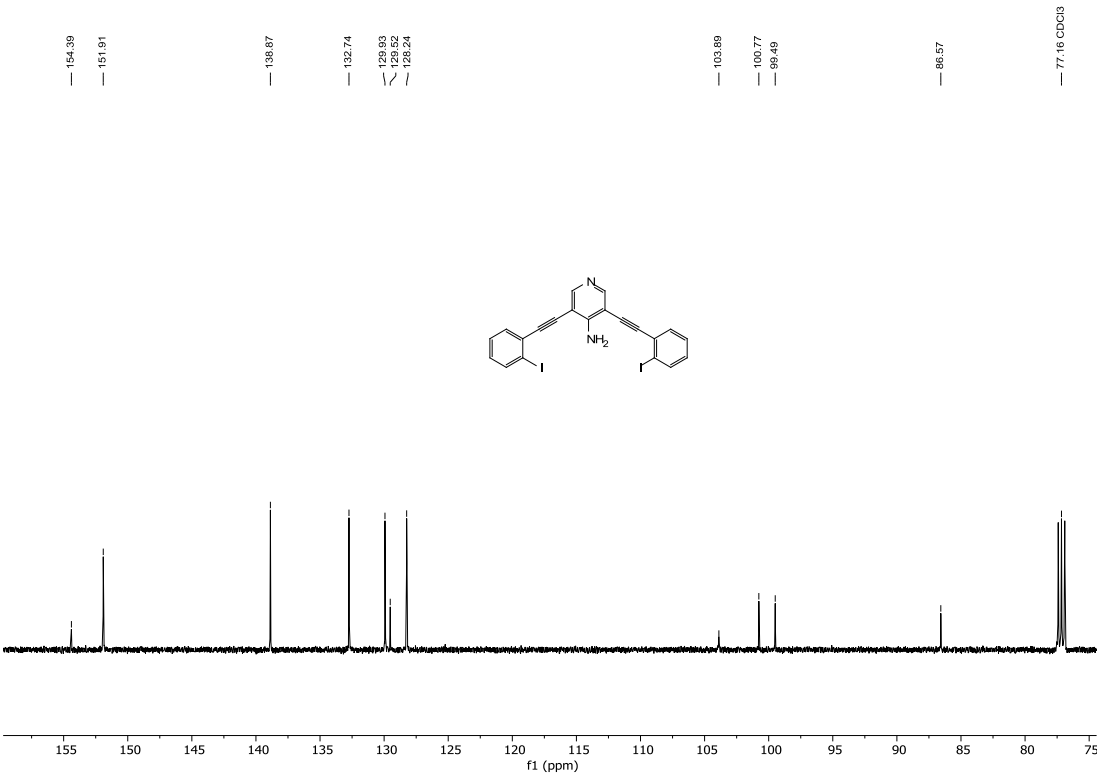

Figure S188. ^{13}C NMR spectrum of **4Neu** (126 MHz, $CDCl_3$, 45°C)

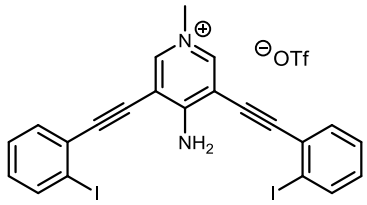

To a flame dried scintillation vial, **4Neu** (0.07 g, 0.128 mmol) was dissolved in 5 ml of dry dichloromethane. Methyl trifluoromethanesulfonate(0.033 g, 0.2 mmol) was added dropwise to the solution, after which the vial was capped then allowed to stir at room temperature for 1-2 days. A white precipitate formed; diethyl ether was added to further the precipitation. The precipitate was isolated by filtration and washed with additional diethyl ether to afford **4** (0.063 g, 0.089 mmol, 69 % yield) as a white solid.

^{1}H NMR (500 MHz, DMSO) δ 8.66 (s, 2H), 8.47 (s, 2H), 8.02 (dt, *J* = 8.1, 1.2 Hz, 2H), 7.82 (dt, *J* = 7.8, 1.4 Hz, 2H), 7.54 (tt, *J* = 7.6, 1.3 Hz, 2H), 7.25 (tt, *J* = 7.5, 1.5 Hz, 2H), 3.99 (s, 3H).

^{13}C NMR (126 MHz, DMSO) δ 156.71, 145.78, 138.70, 133.70, 131.37, 128.33, 127.41, 104.18, 101.46, 100.43, 82.09, 45.17. The ^{13}C resonance of the triflate anion (quartet with relative intensities of 1:3:3:1) was not observed)

^{19}F NMR (470 MHz, CD_3CN) δ -77.57.

HRMS (ESI pos) m/z for $C_{22}H_{15}I_2N_2^+$ [M]$^+$: calculated:560.9319 found: 560.9288

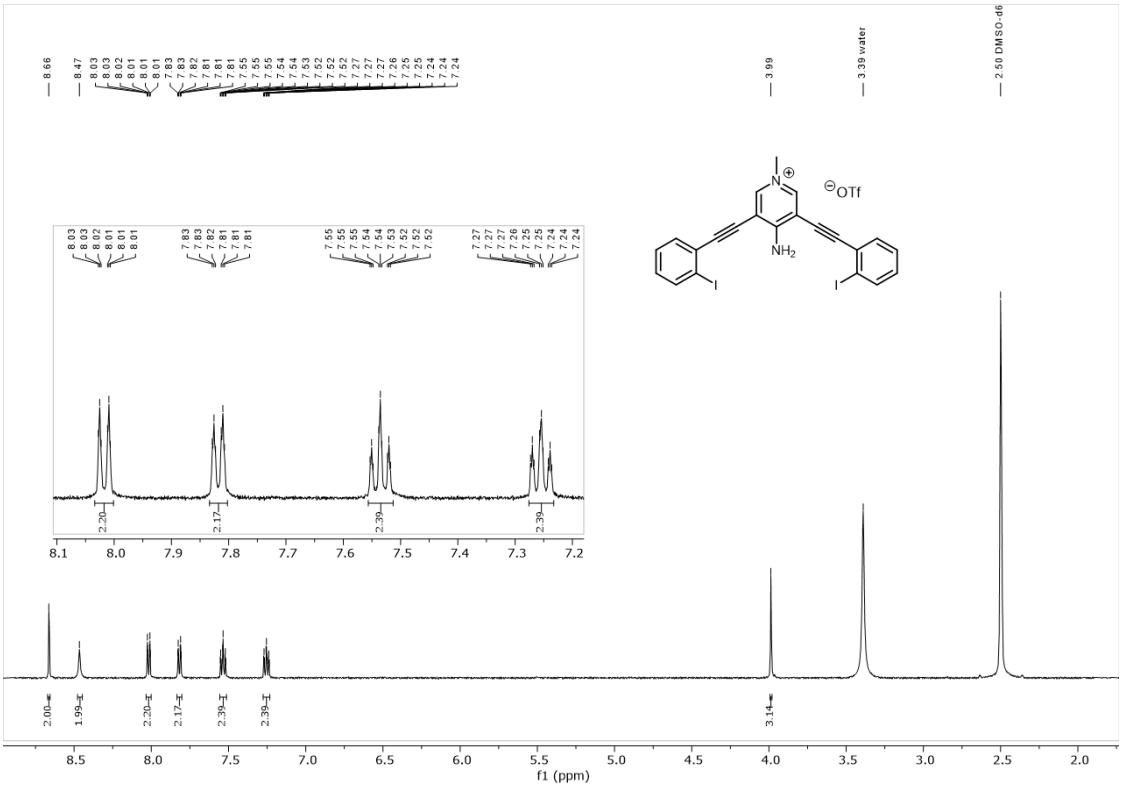

Figure S189. ^{1}H NMR spectrum of **4** (500 MHz, DMSO)

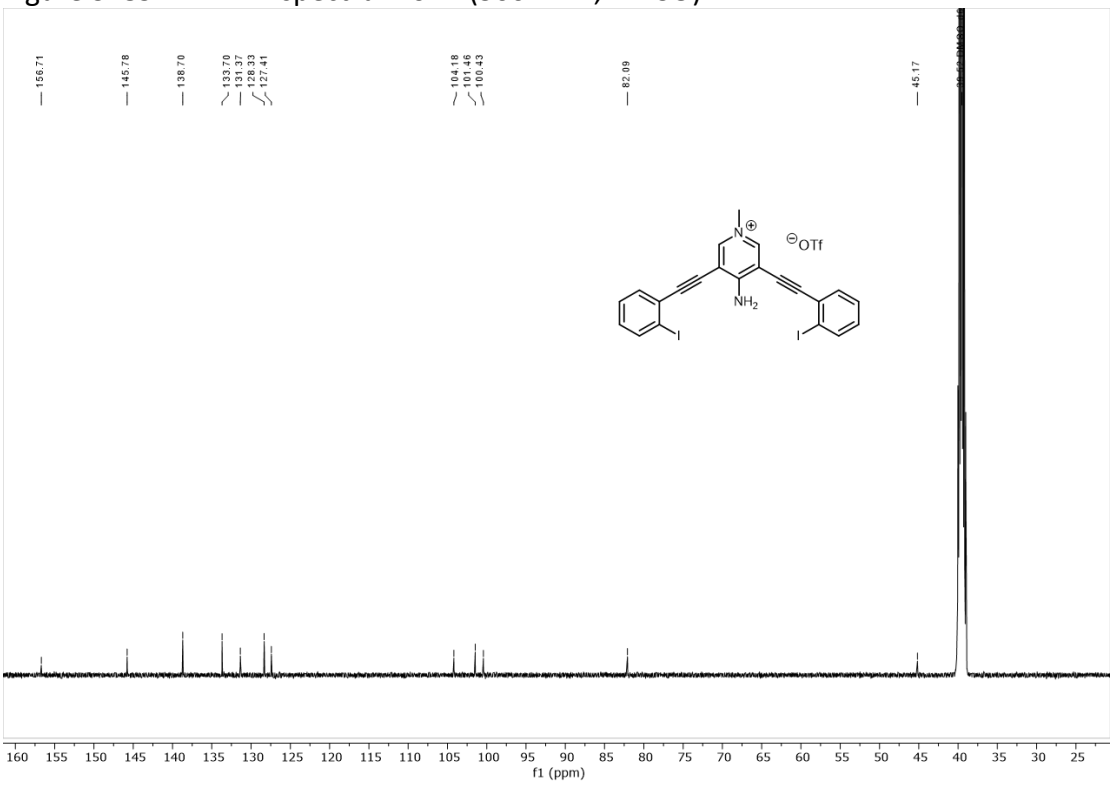

Figure S190. ^{13}C NMR spectrum of **4** (126 MHz, DMSO)

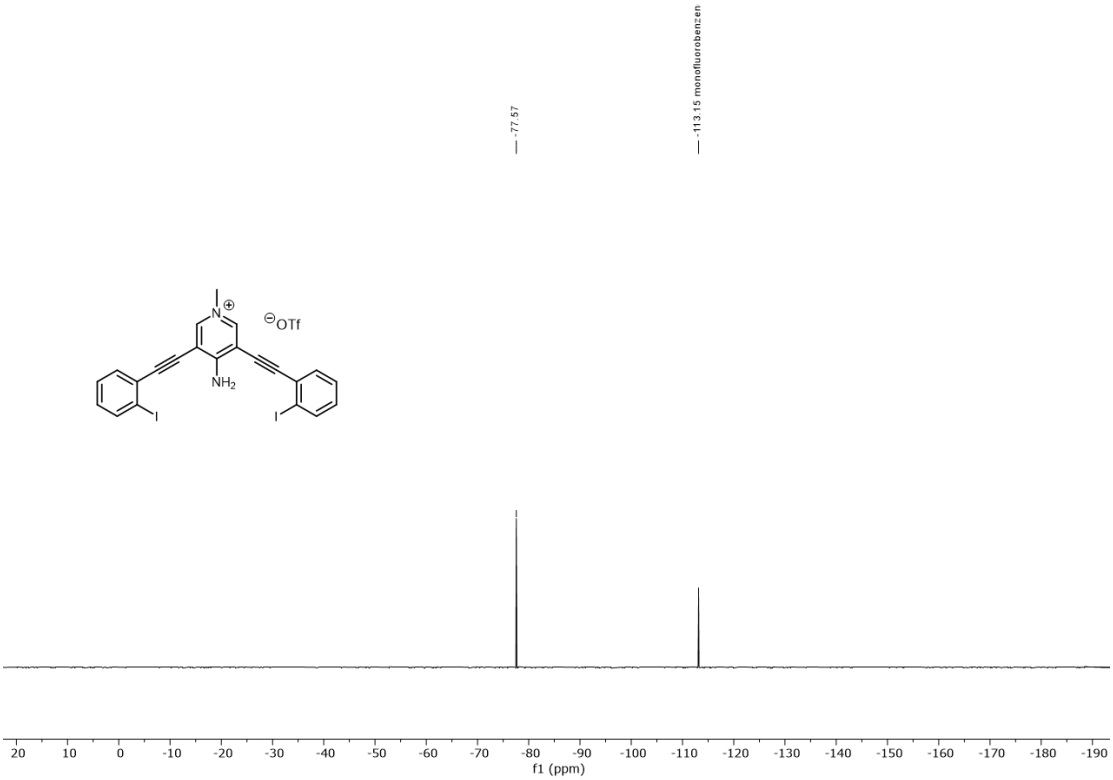

Figure S191. ^{19}F NMR spectrum of **4** (470 MHz, CD_3CN). C_6H_5F (monofluorobenzene) internal reference.

UV-Vis Titration Details and Data

UV-vis titrations were carried out on an Agilent Cary 60 UV-Vis spectrometer equipped with a Peltier 1x1 Cell Holder Accessory which can control the liquid sample temperature at 20 °C during the titrations. Association constants were determined by non-linear regression in Bindfit[17, 18] fitting the complete spectrum simultaneously. Hamilton gas-tight micro-syringes were used during serial dilutions and titrations. The reported association constants and errors were obtained from the average and standard deviation of three repeated titrations. Full binding data and fitting parameters for each titration can be obtained from the Bindfit using the links found below figures below.

Considering both the solubilities and changes of absorbance, the solvent mixture used in all titrations is made by 90% spectra grade Tetrahydrofuran, 9.9% spectra grade Dimethyl sulfoxide, and 0.1% deionized water. A stock solution of **1-4** was prepared with the solvent mixture. The stock solution of each host was then used to make TBA Bromide guest solutions. An aliquot (2.0 mL) of the stock host solution was transferred to a quartz cuvette with cap and a magnetic stir bar as the starting volume. Aliquots of guest solution were added to the cuvette, after each addition and stirring for three minutes, a spectrum was recorded.

Table S6. Association constants for binding of TBA bromide to all receptors in 90% THF/9.9% DMSO/0.1% deionized H_2O solvent system at 293 K.

Receptor	Assay 1 (M^{-1})	Assay 2 (M^{-1})	Assay 3 (M^{-1})	**Average (M^{-1})**

1	25516	27268	25182	**25989 ±915**
2	16940	11189	16181	**14700 ±2551**
3	12511	10300	13529	**12113 ±1348**
4	19417	16997	18654	**18356 ±1010**

1 with TBA bromide

Assay 1 K_a= 25516 M^{-1} http://app.supramolecular.org/bindfit/view/bc8348fa-c18f-4738-a858-6afee54be274

Assay 2 K_a= 27268 M^{-1} http://app.supramolecular.org/bindfit/view/d0db7fb8-e521-422a-89f9-65a8afc351dd

Assay 3 K_a= 25182 M^{-1} http://app.supramolecular.org/bindfit/view/80d9e25a-a4a8-4829-ab9e-ab413d6650cf

2 with TBA bromide

Assay 1 K_a= 16940 M^{-1} http://app.supramolecular.org/bindfit/view/67f16bc8-3f4f-40b6-a488-0e53de34ae04

Assay 2 K_a= 11189 M^{-1} http://app.supramolecular.org/bindfit/view/f35feff3-f714-4875-92ae-a7e9fc66cf5c

Assay 3 K_a= 16181 M^{-1} http://app.supramolecular.org/bindfit/view/0134f156-85a4-492a-90c9-51c19ab9d406

3 with TBA bromide

Assay 1 K_a= 12511 M^{-1} http://app.supramolecular.org/bindfit/view/25834360-3d81-4204-abda-afb68c0b3b57

Assay 2 K_a= 10300 M^{-1} http://app.supramolecular.org/bindfit/view/78e57c1c-3dde-48e2-8601-0ecbb7e80fc5

Assay 3 K_a= 13529 M^{-1} http://app.supramolecular.org/bindfit/view/9a833e73-82cd-40fc-aadc-1c983a81025e

4 with TBA bromide

Assay 1 K_a= 19417 M^{-1} http://app.supramolecular.org/bindfit/view/339d3d49-a9e4-4c6f-b716-2b9bc59a0c02

Assay 2 K_a= 16997 M^{-1} http://app.supramolecular.org/bindfit/view/b56dd4e1-3cc5-494f-8772-4b704f48a1da

Assay 3 K_a= 18654 M^{-1} http://app.supramolecular.org/bindfit/view/16b0f1e1-2ff0-4b28-b7f5-6454fab4b65f

References

1. Sheldrick, G. M. (1996). SADABS: Area Detector Absorption Correction; University of Göttingen, Germany.

2. Dolomanov, O.V.; Bourhis, L.J.; Gildea, R.J.; Howard, J.A.K.; Puschmann, H., (2009). J. Appl. Cryst., 42, 339-341.

3. Sheldrick, G. M. (2015).Acta Cryst.A71, 3-8.
4. Sheldrick, G. M. (2015).Acta Cryst.C71, 3-8.
5. Bruker (2016). APEX3. Bruker AXSInc., Madison, Wisconsin, USA.
6. Sheldrick, G.M. (2008). Acta Cryst. A64, 112-122.
7. Scattergood, P.A.; Roberts, J.; Omar, S.A.E.; Elliott, P.I., (2019) Inorg. Chem., 58(13), 8607-8621.
8. Hou, Y.; Cao, S.; Li, X.; Pei, Y.; Wang, B.; Wang, L.; Pei, Z., (2014) ACS Appl. Mater. Interfaces, 6(19), 16909-16917.
9. Bosch, E.; Barnes, B.L., (2000) Organometallics, 19(25), 5522-5524.
10. Riel, A.S.M,; Decato, D.A.; Sun, J.; Massena, C.J.; Jessop, M.J.; Berryman, O.B., (2018) Chem. Sci., 9, 5828-5836.
11. Zhao, Y.; Truhlar, D.G., (2008) Theor Chem Account 120, 215–241.
12. Frisch, M. J.; Trucks, G. W.; Schlegel, H. B.; Scuseria, G. E.; Robb, M. A.; Cheeseman, J. R.; Scalmani, G.; Barone, V.; Mennucci, B.; Petersson, G. A.; Nakatsuji, H.; Caricato, M.; Li, X.; Hratchian, H. P.; Izmaylov, A. F.; Bloino, J.; Zheng, G.; Sonnenberg, J. L.; Hada, M.; Ehara, M.; Toyota, K.; Fukuda, R.; Hasegawa, J.; Ishida, M.; Nakajima, T.; Honda, Y.; Kitao, O.; Nakai, H.; Vreven, T.; Montgomery, J. A. J.; Peralta, J. E.; Ogliaro, F.; Bearpark, M.; Heyd, J. J.; Brothers, E.; Kudin, K. N.; Staroverov, V. N.; Kobayashi, R.; Normand, J.; Raghavachari, K.; Rendell, A.; Burant, J. C.; Iyengar, S. S.; Tomasi, J.; Cossi, M.; Rega, N.; Millam, N. J.; Klene, M.; Knox, J. E.; Cross, J. B.; Bakken, V.; Adamo, C.; Jaramillo, J.; Gomperts, R.; Stratmann, R. E.; Yazyev, O.; Austin, A. J.; Cammi, R.; Pomelli, C.; Ochterski, J. W.; Martin, R. L.; Morokuma, K.; Zakrzewski, V. G.; Voth, G. A.; Salvador, P.; Dannenberg, J. J.; Dapprich, S.; Daniels, A. D.; Farkas, O.; Foresman, J. B.; Ortiz, J. V.; Cioslowski, J.; Fox, D. J. Gaussian, Inc.: Wallingford, CT 2009.
13. Weigend, F.; Ahlrichs, R., (2005) Phys. Chem. Chem. Phys. 7, 3297.
14. Peterson, K.A., (2003) J. Chem. Phys. 119, 11113-11123.
15. Pritchard, B.P.; Altarawy, D.; Didier, B.; Gibsom, T.D.; Windus, T.L., (2019) J. Chem. Inf. Model. 59, 4814-4820
16. Boys, F.; Bernardi, F., (1970) Mol. Phys. 19, 553.
17. http://supramolecular.org/
18. Hibbert, D.B.; Thordarson, P.; (2016) Chem. Commun., 52, 12792-12805.